Siddharth Ramachandran

OPTICAL AND FIBER COMMUNICATIONS REPORTS 5

Fiber Based Dispersion Compensation

Springer

OPTICAL AND FIBER COMMUNICATIONS REPORTS

OPTICAL AND FIBER COMMUNICATIONS REPORTS

The Optical and Fiber Communications Reports (OFCR) book series provides a survey of selected topics at the forefront of research. Each book is a topical collection of contributions from leading research scientists that gives an up-to-date and broad-spectrum overview of various subjects.
The main topics in this expanding field will cover for example:

- specialty fibers (periodic fibers, holey fibers, erbium-doped fibers)
- broadband lasers
- optical switching (MEMS or others)
- polarization and chromatic mode dispersion and compensation
- long-haul transmission
- optical networks (LAN, MAN, WAN)
- protection and restoration
- further topics of contemporary interest.

Including both general information and a highly technical presentation of the results, this series satisfies the needs of experts as well as graduates and researchers starting in the field. Books in this series establish themselves as comprehensive guides and reference texts following the impressive evolution of this area of science and technology.
The editors encourage prospective authors to correspond with them in advance of submitting a manuscript. Submission of manuscripts should be made to one of the editors. See also http://springeronline.com/series/ 4810.

Siddharth Ramachandran

Fiber Based Dispersion Compensation

Springer

Siddharth Ramachandran
OFS Laboratories
600-700 Mountain Avenue
Murray Hill, NJ 07974
USA
sidr@ofsoptics.com

ISBN 978-0-387-40347-2 e-ISBN 978-0-387-48948-3

Library of Congress Control Number: 2006939944

Printed on acid-free paper

9 8 7 6 5 4 3 2 1

springer.com

Contents

DOI: 10.1007/s10297-007-0084-x
Originally published in J. Opt. Fiber. Commun. Rep. 4, 1–18 (2007)

Introduction and overview

Siddharth Ramachandran

OFS Laboratories, Murray Hill, NJ 07974, USA

A pulse of light temporally dilates or compresses because of dispersion as a result of the fact that in all media except vacuum, the group velocity of light depends on its wavelength. This phenomenon occurs, of course, in every travelling wave that carries energy, and in the context of light, has been exploited, utilized, or mitigated ever since short-pulse lasers emerged. Mode-locked lasers, for instance, depend critically on the "dispersion-map" of the path in which light travels in a laser cavity. Traditionally, optical techniques to control or compensate dispersion comprised devices that would provide wavelength-dependent delays, such as bulk-optic diffraction gratings or prisms.

With the advent of practical, long-haul optical fiber links in the 1980s, the need to manage dispersion in an optical communications network arose. In addition to the temporal distortion effects that pulses from mode-locked lasers experienced due to dispersion, a pulse train in a communications link also had to contend with intersymbol interference (ISI) arising from overlaps of adjacent pulses in a bit-stream. As a general rule of thumb, the amount of dispersion tolerated by an optical transmission line varies inversely proportionally to the square of the data-rate. For the early 2.5-Gb/s systems, the dispersion tolerance was greater than 30000 ps/nm. Hence a conventional single-mode fiber (SMF), with 17 ps/(km-nm) dispersion could be used for lengths as long as 2500 km without being limited by dispersion. However, as transmission lengths as well as bit rates grew, dispersion became the primary bottleneck that the optical network had to combat.

In the mid-1980s, this dispersion-management problem was addressed with a novel transmission fiber—the dispersion-shifted fiber (DSF), whose dispersion-zero was engineered to coincide with the signal wavelength of choice, at the low-loss wavelength of 1550 nm. However, the subsequent advantages of massive capacity enhancement in wavelength-multiplexed systems demanded that the transmission fiber be designed to possess some amount of dispersion so as to minimize nonlinear effects. This motivated the introduction of a new class of transmission fibers, and in 1993, AT&T Bell Laboratories unveiled the first non-zero dispersion-shifted fiber (NZDSF). This design

philosophy has dominated in one form or another since then, and virtually all optical-fiber links deployed in the world today comprise of either SMF or one of the multitudes of flavors of NZDSFs.

Thus, most transmission links today comprise fibers with positive (anomalous) dispersion, and the accumulated dispersion is managed by devices that provide equal magnitudes of negative dispersion. One of the first such proposals was envisaged by a team at AT&T Bell Labs (Lin, Kogelnik and Cohen) in 1980 at a time when the high bit-rate link was still in its infancy. One of the first demonstrations of a dispersion compensating device came in 1987 (Ouellette), which used a chirped fiber-Bragg grating to realize wavelength-dependent delay in a compact fiber-device. This was followed by demonstrations of specialty fibers that were designed to yield high negative dispersion in the wavelength range or interest—in 1992, a group from Corning (Antos and coworkers) used a specially designed SMF to realize negative dispersion, and simultaneously, an AT&T Bell Labs group (Poole and coworkers) demonstrated strong negative dispersion in the LP_{11} mode of a dual mode fiber. This class of fibers, called dispersion-compensating fibers (DCF), grew to dominate the application-space of dispersion compensation.

The mere existence of a variety of transmission fibers with different dispersive properties calls for a variety of performance metrics from today's dispersion compensating devices. In addition, the fact that nonlinear distortions in an optical link also depend critically on the dispersion-map has yielded another mandate for today's dispersion-compensating devices—they must not only provide specific dispersion, dispersion-slope and dispersion-curvature as a function of wavelength, they must also be designed keeping in mind their role in ultimately determining the nonlinear distortions a system accumulates. In other words, the properties of the dispersion-compensating module are one of the key parameters determining the performance of the entire network.

This book provides a detailed overview of the fiber-based technologies and devices that cover this application-space. It focuses on fiber-based devices for two reasons. Fiber-based devices are almost exclusively the only kind deployed in practical communications networks today, primarily because they have not only provided superior performance to other devices, but they have continued to improve in performance so that competing technologies have not been able to catch up. The second reason is that the subset of fiber-based devices alone represents so much variety that it was necessary to restrict the scope of this book to facilitate a detailed exposition of the most significant technologies. This is the first book devoted solely to dispersion compensation, and several of the chapters have been written by the research and development teams in the parts of industry that dominate the dispersion-compensation market today. This allows the reader to gain insight into the physics of the devices as well as the practical constraints in taking laboratory ideas into the field.

The book is organized in three sections. Section I comprising 5 chapters describes various aspects and realizations of dispersion-compensating fibers (DCF). In contrast to the early demonstrations in 1992, today's DCFs require highly complex waveguide realizations, because they are designed for optimizing the dispersion as well as nonlinearity in a system. Section II comprising 5 chapters describes the variety of novel fiber technologies that are being considered as viable alternatives to DCFs. Descriptions in these chapters necessarily use DCFs as a benchmark against which to measure their performance. Finally section III addresses the systems-level aspects of different device

technologies, hence connecting the physical-layer discussion of the previous sections with practical issues pertaining to the use of a device in a real network. A brief synopsis of each chapter is given below.

Chapter 1 ("Modeling dispersion in optical fibers: applications to dispersion tailoring and dispersion compensation", by Thyagarajan and Pal) provides a detailed introduction of the problem of dispersion compensation in an optical link. Starting from the theory of pulse propagation in a bulk medium, the chapter describes the additional dispersive contributions of a signal propagating in fiber waveguides. This leads to the generic "statement-of-problem" for dispersion compensation in terms of relevant properties of a DCF, such as magnitude of dispersion, relative dispersion slope (RDS) and effective area (A_{eff}), the optimization of which is the objective of the variety of device technologies this book covers.

Chapter 2 ("Fiber designs for high figure of merit and high slope dispersion compensating fibers", by Wandel and Kristensen) describes commercial realizations of DCFs with a focus on techniques to achieve high dispersion-slopes and high figures-of-merit. After a brief introduction describing the desired performance metrics for DCFs, the chapter describes a powerful technique to understand the design philosophy for realizing dispersive fiber-waveguides—the super-mode theory connects modal evolution in a waveguide to its dispersion, thereby providing a physically intuitive recipe for designing DCFs. In addition, the authors show that complementary scaling techniques allow connecting the influence of waveguide dimensions to wavelength, thereby providing a generalized recipe to design dispersive structures in any spectral range of interest. The theoretical treatment is followed by descriptions of commercial realizations of DCFs for three distinct problems that have been especially hard to tackle for dispersion-compensators: (a) the ability to obtain very high figures-of-merit (FOM defined as the ratio of dispersion to loss) in order to achieve compensators that mitigate nonlinearities, (b) the ability to achieve high RDS, as is needed for a variety of NZDSF-transmission fibers that have been recently deployed, and (c) the ability to make compact modules without sacrificing dispersive performance.

Chapter 3 ("Design optimization of dispersion compensating fibers and their packaging techniques", by Kato et al.) considers the development of DCFs taking into account the fact that such fiber waveguides necessarily have high index contrasts, which leads to compromised performance with respect to microbend losses and polarization mode dispersion (PMD). The authors describe an innovative technique that has now been commercialized, where this inherent trade-off is mitigated by packaging techniques—instead of tightly winding the fiber around spools, the authors describe the realization of modules where the fiber is suspended in resins thereby removing many of the mechanical perturbations that lead to high microbend losses and PMD. This novel packaging technique needs to be realized in schematics that do not compromise the stringent reliability and manufacturability of real-world devices, but it also lifts many of constraints in waveguide design and may lead to the possibility of achieving more complex dispersive characteristics from a fiber.

Chapter 4 ("Dispersion compensating fiber used as a transmission fiber: inverse/reverse dispersion fiber", by Mukasa et al.) analyzes the dispersion-compensation problem from a different perspective—instead of treating the dispersive fiber as a discrete unit that must be designed to provide optimal performance from a pre-existing transmission fiber, the authors describe a composite transmission line comprising more than one fiber type such that the need for a discrete dispersion-compensating element

is eliminated. Such hybrid fiber systems now require that the negative-dispersion fiber share a lot of the attributes of transmission fibers, such as the ability to cable them, and the ability to manufacture long lengths of the fibers in a cost-competitive manner. Such links have become the mainstay of under-sea links, which both require much greater optimization in light of the significantly longer distance they traverse, and can afford designing the entire link from "scratch." This chapter describes the design and commercial realizations of the negative-dispersion fibers used in such links.

Chapter 5 ("Dispersion compensating fibers for Raman applications", by Grüner-Nielsen et al.) describes an alternative use of DCFs that has become popular in the last 4–5 years. Since DCFs inherently have small $A_{\rm eff}$ they are media with high nonlinearities—indeed, this has been one of the limitations from a systems-design perspective. However, this enhanced nonlinearity can be exploited to one's advantage, since it also entails efficient Raman gain in these fibers. In general, Raman amplification in the DCF would invariably help the noise-figure of a system, since the DCF is no longer just a loss-element, but this also leads to new sources of noise due to double-Rayleigh back-scattering in the fiber. In addition, the properties of a DCF for optimal Raman gain may not necessarily be the same as the properties required for optimal dispersion-compensation. This chapter discusses the use of DCFs as Raman amplifiers, and the relevant design trade-offs involved in using the DCF as both a dispersion-compensator and Raman amplifier.

Section II, the section that describes alternative technologies, starts with two chapters—6 and 7—that describe a novel fiber for dispersion compensation. They describe the enhanced design flexibility available in fibers when signal propagation is realized in a higher order mode (HOM). Specifically, both the magnitude of dispersion and effective modal area can be much larger in these fibers, hence providing a multitude of benefits ranging from lower nonlinear impairments to lower loss and potentially lower cost as well as smaller size. However, this technology platform requires specialized mode conversion techniques to excite and maintain the signal in a single desired HOM. Chapter 6 ("Static and tunable dispersion management with higher order mode fibers", by Ramachandran and Yan) describes the use of in-fiber gratings to realize all-fiber devices, while Chapter 7 ("High-order mode based dispersion compensating modules using spatial mode conversion", by Tur et al.) describes the use of free-space phase plates to achieve mode conversion. Since the unique feature of these devices is signal propagation in one specified mode out of many existing modes in the fiber, the primary impairment that they suffer from is multi-path interference (MPI). Both chapters describe the origin, techniques for characterization, as well as the desired target levels of performance with respect to this impairment—in general, for practical applications in a telecom system, it is important to achieve an MPI of less than -40 dB. This technology is an attractive alternative to DCFs as evidenced by the fact that it is the only alternative technology that has achieved similar or better systems performance than a similar link with DCFs. However, it is not clear that the performance improvements are significant enough to displace an entrenched technology like DCF today. Since the significant advantage is lower nonlinear distortions, it is conceivable that future systems running at higher bit rates (and hence higher peak powers), will benefit from this technology. In addition, the diminished nonlinearities of these devices may make them attractive for alternative emerging applications such as high-power lasers and amplifiers.

Chapter 8 ("Control of dispersion in photonic crystal fibers", by Roberts et al.) discusses the use of a new class of fibers—photonic-crystal or air-silica-microstructured fiber—as DCFs. The physics of operation of these fibers is similar to standard fibers in that light is guided by total internal reflection. However, since an air-silica boundary represents a significantly larger index step in comparison to those achievable in (Germanium) doped fibers, waveguides with much larger index contrasts can be realized. The magnitude of dispersion achievable from a waveguide increases with the largest achievable index step in the fiber, as described in chapter 2. Hence, microstructured fibers can be used to realize DCFs with order of magnitude higher levels of dispersion. This chapter describes some experimental realizations with this technology, and also discusses the drawbacks. The main impairment also arises from the large index steps in these fibers—small fabrication perturbations lead to higher loss as well as birefringence. It remains to be seen if these fabrication problems have solutions that would facilitate exploiting this powerful technique to realizing DCFs.

Chapters 9 ("Broadband fiber Bragg gratings for dispersion management", by Brennan) and 10 ("Fiber-based tunable dispersion compensation", by Litchinitser et al.), the final chapters in the alternative-technologies section of this book, describe the use of Fiber-Bragg Gratings (FBG) as dispersion compensators. Chirped FBGs offer a versatile means to tailor group-delay as a function of wavelength, and since they can be made arbitrarily complex, a variety of dispersion and dispersion-slope values can be achieved from a device which is less than a meter long. Typically, fiber gratings are of lengths less than 10 cm, but to achieve dispersion compensation over bandwidths exceeding 30 nm (as needed for a practical system), they need to have meter length-scales. Chapter 9 provides a detailed discussion of the fabrication techniques needed to achieve long-length FBGs. Chapter 10, in contrast, deals for FBGs of "conventional" (5–15 cm) length. The focus of this chapter is dispersion compensation in a per-channel basis, with the added feature of tunability. Several techniques to tune the dispersion of FBGs are discussed, the primary one being a length-dependent thermal profile of choice. Both chapters discuss in detail the primary impairment arising from this technology, namely group-delay ripple. This impairment arises from the fact that local perturbations along the grating lead to large wavelength-dependent group-delay changes. Chapter 10 also describes theoretical investigations of the impacts that group-delay ripple have on a telecom link—an important conclusion is that the frequency of such ripple is just as important as its amplitude. FBGs have attracted a lot of attention as alternatives for dispersion compensation. Indeed, as described earlier, one of the first demonstrations of a dispersion compensator was a chirped FBG in 1987. However, the group-delay ripple problem has remained a severe impairment. Each device can lead to power penalties of 0.5 to 1 dB, making them unsuitable as a drop-in replacement for DCFs in spans that require a concatenation of more than 30–40 such devices. The utility of FBGs may lie more in "clean-up" applications, particularly as tunable compensators that can offer tweaks and corrections to the dispersion map after a network is laid out.

Section III, the last section of this book is devoted to systems considerations of dispersion compensation. Chapter 11 ("Impact of DCF properties on system design", by Essiambre et al.) is a comprehensive review of the theoretical impact a dispersion compensation technology has on a telecom link. The chapter starts with a detailed description of the architecture of a long-distance link, and analyzes the multitude of noise contributions, from amplifiers, nonlinearity, chromatic as well as polarization-mode dispersion, and studies their impact at the receiver. Thereafter, extensive simulations

explore the idea of dispersion-mapping in such links. This treatment provides valuable insight into the parameters a dispersion-compensating technology must achieve for optimal performance in a telecom link. In addition, this chapter also provides a summary of the alternative technologies not covered in this book—the dispersion-compensating devices that are not based on a fiber platform, thus providing a comprehensive higher-level view of this application space.

The book ends with Chapter 12 ("Survey of systems experiments demonstrating dispersion compensation technologies", by Garrett), which is an exhaustive compendium of a variety of systems experiments and demonstrations that highlight the impact of dispersion and dispersion compensation in a real world telecom link. This chapter covers most of the noteworthy systems experiments carried out through 2004, hence providing a unified reference with which to compare and contrast the variety of existing dispersion-compensating technologies today. As with Chapter 11, this chapter also discusses experiments that utilize non-fiber-based devices so as to provide a higher-level perspective.

DOI: 10.1007/s10297-005-0061-1
Originally published in J. Opt. Fiber. Commun. Rep. 3, 25–60 (2005)

Fiber designs for high figure of merit and high slope dispersion compensating fibers

Marie Wandel and Poul Kristensen

OFS Fitel Denmark I/S
Email: mwandel@ofsoptics.com

Abstract. When the first dispersion compensating fiber modules were introduced to the market in the mid '90s, the only requirement to the fiber was that it should have a negative dispersion. As the bit rate and the complexity of the optical communication systems have increased, several other requirements have been added such as low loss, low non-linearities and the ability of broadband dispersion compensation.

1. Introduction

When the first dispersion compensating fiber modules were introduced to the market in the mid '90s, the only requirement to the fiber was that it should have a negative dispersion. As the bit rate and the complexity of the optical communication systems have increased, several other requirements have been added such as low loss, low non-linearities and the ability of broadband dispersion compensation.

Especially the demand of dispersion compensating fiber modules for broadband dispersion compensation has driven the development of new dispersion compensating fibers, so now, even with more than 100 000 dispersion compensating fiber modules deployed in systems worldwide, improvements to dispersion compensating fiber modules are constantly being introduced.

As the systems continuously become more advanced, so does the dispersion compensating fiber module. In this paper the process of designing the advanced dispersion compensating fibers will be discussed. One of the challenges of designing dispersion compensating fibers is to meet the expectations of both end users and the manufacturer of the fiber.

The end users' expectation to the optical properties of the dispersion compensating fiber module is that it can deliver broadband dispersion compensation with low added

Fig. 1. Two dispersion compensating fiber modules. The module in back is a conventional dispersion compensating fiber module while the module in front is the dispersion compensating fiber module with reduced physical dimensions described in section 6.

loss and non-linearities to the system. Furthermore, the optical properties have to be stable in changing operating conditions with respect to temperature and humidity. As to the physical appearance of the module, the dispersion compensating fiber module normally consists of the dispersion compensating fiber wound onto a metallic spool with connectors spliced to each end of the fiber as shown in Fig. 1. These spools are placed in metal boxes designed to meet the space requirements of the end user. As will be discussed later in this paper, dispersion compensating fiber modules with reduced physical dimensions are currently being developed.

Beside the demands of the end users, the manufacturer of the dispersion compensating fibers also has some demands to the design of the dispersion compensating fiber. The most important issue here is how much the optical properties of the dispersion compensating fibers change with the small variations in the index profile of the fiber, which are unavoidable during the manufacturing process.

This paper will focus on some of the trade offs encountered during the process of designing and manufacturing dispersion compensating fibers. Three special cases will be considered: Dispersion compensating fibers with a high figure of merit, dispersion

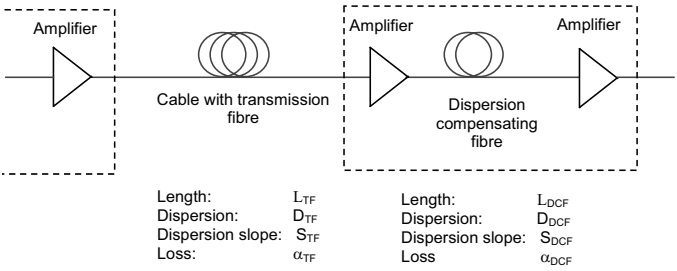

Fig. 2. Link consisting of cabled transmission fiber and amplifier with dispersion compensating fiber.

compensating fibers with a high dispersion slope and dispersion compensating fiber modules with reduced physical dimensions.

All three types of fiber represent a challenge with respect to fiber design as they either have extreme dispersion properties or bend loss properties. As will be discussed in this paper, several trade offs exist between the desired dispersion properties and properties such as bend losses and manufacturability.

First some basic requirements for dispersion compensation will be mentioned. Next, some of the basic considerations for designing dispersion compensating fibers will be discussed followed by a discussion of the major contributions to the attenuation of dispersion compensating fibers.

This leads to the discussion of the design of the three types of dispersion compensating fibers: the dispersion compensating fiber with a high figure of merit, the dispersion compensating fiber with a high dispersion slope and finally the dispersion compensating fiber with reduced physical dimensions.

At last the nonlinear impairments on the system from the dispersion compensating modules will be discussed, with a comparison of dispersion compensating modules with either a high figure of merit or a high dispersion slope.

2. Dispersion Compensation

Although dispersion compensating fibers can be cabled and used as a part of the transmission span, the common use of them is to place them as modules in the amplifier between two amplification stages as shown in Fig. 2.

Whether the dispersion of the transmission fiber should be fully compensated, or whether a slight over or under compensation is advantageous from a system point of view will not be considered here. For the rest of this paper, it will be assumed that the dispersion of the transmission fiber should be fully compensated.

The performance of a dispersion compensating fiber module over a wide wavelength range can be evaluated using the residual dispersion, which is the dispersion measured after the dispersion compensating fiber module in the receiver. The residual dispersion variation is the largest variation of the residual dispersion in the wavelength

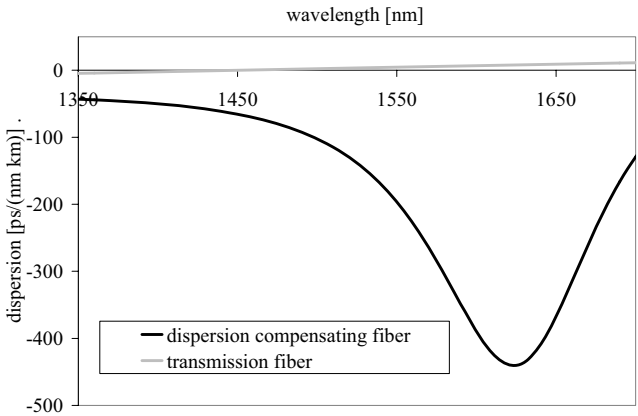

Fig. 3. Dispersion of transmission fiber and of dispersion compensating fiber. The dispersion slope of the transmission fiber is almost constant (dispersion curvature close to zero) for the entire wavelength range while the dispersion slope for the dispersion compensating fiber changes significantly making perfect dispersion match over a broad wavelength range impossible.

range considered. It has been shown that the theoretical tolerance on the residual dispersion variation for a non return to zero (NRZ) signal assuming a 1-dB eye-closure penalty is around 60 ps/nm at 40 Gb/s. [2]

The total residual dispersion D_{res} of the link shown in Fig. 2 is given by

$$D_{\mathrm{res}} = D_{\mathrm{TF}} L_{\mathrm{TF}} + D_{\mathrm{DCF}} L_{\mathrm{DCF}}. \tag{1}$$

The dispersion of any fiber or combination of fibers can be modeled by a Taylor expansion around the center wavelength as

$$D_(\lambda) = D(\lambda_0) + D'(\lambda_0)(\lambda - \lambda_0) + \frac{1}{2} D''(\lambda_0)(\lambda - \lambda_0)^2 + \frac{1}{6} D'''(\lambda_0)(\lambda - \lambda_0)^3 \ldots. \tag{2}$$

with D' being the first derivative of the dispersion (the dispersion slope, S), D'' the second derivative (the dispersion curvature C) and D''' the third derivative of the dispersion.

The dispersion of most transmission fibers is well described by including only the first two terms, the dispersion and the dispersion slope, in Eq. (2). Consequently, the dispersion of the perfect dispersion compensating fiber should have a slope matching that of the transmission fiber while all higher order dispersion terms in Eq. (2) should be small. The dispersion of a transmission fiber and a dispersion compensating fiber are shown in Fig. 3. Higher order terms are by no means negligible for the dispersion of dispersion compensating fiber and several higher order terms must be included in the description of the residual dispersion of the system in Fig. 2.

If zero dispersion is desired after the dispersion compensating fiber module in the receiver, the length of the dispersion compensating fiber (L_{DCF}) is given as

$$L_{\mathrm{DCF}} = -\frac{D_{\mathrm{TF}}}{D_{\mathrm{DCF}}} L_{\mathrm{TF}}. \tag{3}$$

In order to compensate the dispersion over a large wavelength range, the dispersion slope must be compensated as well. The residual dispersion slope is expressed as

$$S_{\mathrm{res}} = S_{\mathrm{TF}} L_{\mathrm{TF}} + S_{\mathrm{DCF}} L_{\mathrm{DCF}}. \tag{4}$$

If Eq. (3) is inserted in Eq. (4), the condition for simultaneous dispersion and dispersion slope compensation is expressed as

$$\frac{S_{\mathrm{DCF}}}{D_{\mathrm{DCF}}} = \frac{S_{\mathrm{TF}}}{D_{\mathrm{TF}}}. \tag{5}$$

The ratio of dispersion slope to dispersion is defined as the relative dispersion slope (RDS) [3]:

$$\mathrm{RDS} = \frac{S}{D}. \tag{6}$$

It has often been stated that in order to achieve perfect dispersion compensation, the slope of the dispersion compensating fiber must match that of the transmission fiber. [4]

This is the case when the ratio of dispersion slope to dispersion [the relative dispersion slope (RDS)], is the same for the two fibers.

That perfect dispersion compensation would be obtained by matching the slopes of the two fibers would only be true if higher order terms from Eq. (2) such as the curvature were not needed to describe the dispersion of the dispersion compensating fiber. It is only true that slope match gives the lowest possible residual dispersion when the dispersion curvature is not considered.

The relative dispersion curvature (RDC), which is defined as

$$\mathrm{RDC} = \frac{C}{D} \tag{7}$$

can be used for calculating the total curvature of a link consisting of N fibers

$$C_{\mathrm{tot}} = \frac{1}{L} \sum_{i=1}^{i=N} \mathrm{RDC}_i D_{\mathrm{tot},i} \tag{8}$$

with RDC_i being the relative dispersion curvature of fiber i, $D_{\mathrm{tot},i}$ the total dispersion of fiber i and L the length of the link. This expression is useful if the dispersion curvature of a link consisting of fibers with high dispersion curvatures is to be minimized. [5]

As mentioned previously, since the dispersion of the transmission fiber is well described by the first two terms in Eq. (2), all higher order terms, and thereby the curvature—and relative dispersion curvature for the dispersion compensating fiber should be as small as possible in order to obtain a low total dispersion curvature and thereby a low residual dispersion.

Figure 4 shows the residual dispersion of 4 links of the same type as shown in Fig. 2. The transmission fiber is a TrueWave® RS (Table 1) and the four different dispersion compensating fibers are all realized fibers.

The residual dispersion of the link is calculated from the measured dispersions of the transmission and dispersion compensating fibers.

The residual dispersion variation is one way to measure the quality of the dispersion compensation. Another is usable bandwidth, which can be defined as the bandwidth

Table 1. Dispersion, dispersion slope and relative dispersion slope (RDS) of transmission fibers at 1550 nm.

	Dispersion [ps/nm·km]	Dispersion slope [ps/nm^{2}km]	RDS [nm^{-1}]
Standard single-mode optical fiber (SSMF)			
ITU: G.652	16.5	0.058	0.0036
Non-zero dispersion-shifted single-mode optical fiber (NZDF): ITU: G.655			
TrueWave® REACH fiber	7.1	0.042	0.0058
TeraLight* fiber	8	0.058	0.0073
TrueWave® RS fiber	4.5	0.045	0.010
ELEAF* fiber	4.2	0.085	0.02
Dispersion shifted single-mode optical fiber (DSF)			
(at 1590 nm) ITU:G.653	2.8	0.07	0.025

*TeraLight is a registered trademark of Alcatel; LEAF is a registered trademark of Corning.

for which the residual dispersion variation is below a given value. [6] In Fig. 4 the usable bandwidth is shown as the bandwidth where the residual dispersion variation is within 0.2 ps/(nm km) corresponding to a theoretical transmission length of 300 km of a NRZ signal at 40 Gb/s assuming the transmission length to be limited by the dispersion only. [2]

In Fig. 4(a) the RDS of the transmission fiber is different from the RDS of the dispersion compensating fiber and the usable bandwidth is limited to 12 nm by the slope mismatch.

In Fig. 4(b) the dispersion slopes of the two fibers are matched resulting in a usable bandwidth that is only limited by the dispersion curvature of the dispersion compensating fiber. By reducing the curvature of the dispersion compensating fiber and keeping the slopes matched, an improvement in usable bandwidth can be obtained as shown in Fig. 4(c), but the improvement is only from the usable bandwidth of 51 nm in Fig. 4(b) to the usable bandwidth of 57 nm in Fig. 4(c). The largest usable bandwidth can be obtained if the curvature of the dispersion compensating fiber is minimized while allowing a small slope mismatch as shown in Fig. 4(d). This figure shows the same dispersion compensating fiber as in Fig. 4(c) but the transmission fiber of Figure 4d has a slightly lower dispersion slope. This overcompensation of the dispersion slope results in a usable bandwidth of 82 nm and is an example of how slope match is not always desirable in order to obtain a large usable bandwidth.

Whether the slopes should be perfectly matched for dispersion compensating fibers with low curvature depends of course on the requirements to the residual dispersion. In Fig. 4(c), even though the usable bandwidth as defined above is smaller than in Fig. 4(d), the residual dispersion variation from 1550 to 1570 nm is less than 0.01 ps/(nm km) and for some applications a low residual dispersion is more important than a large usable bandwidth.

Typical dispersions and RDS values for a number of commonly used transmission fibers at 1550 nm are listed in Table 1.

Of the transmission fibers listed in Table 1, standard single mode fiber (SSMF) has the highest dispersion and thus the highest need for dispersion compensating. The ITU: G.655 Non Zero Dispersion-shifted single-mode optical Fibers (NZDF) of Table 1 were developed in order to reduce the need for dispersion compensation, but

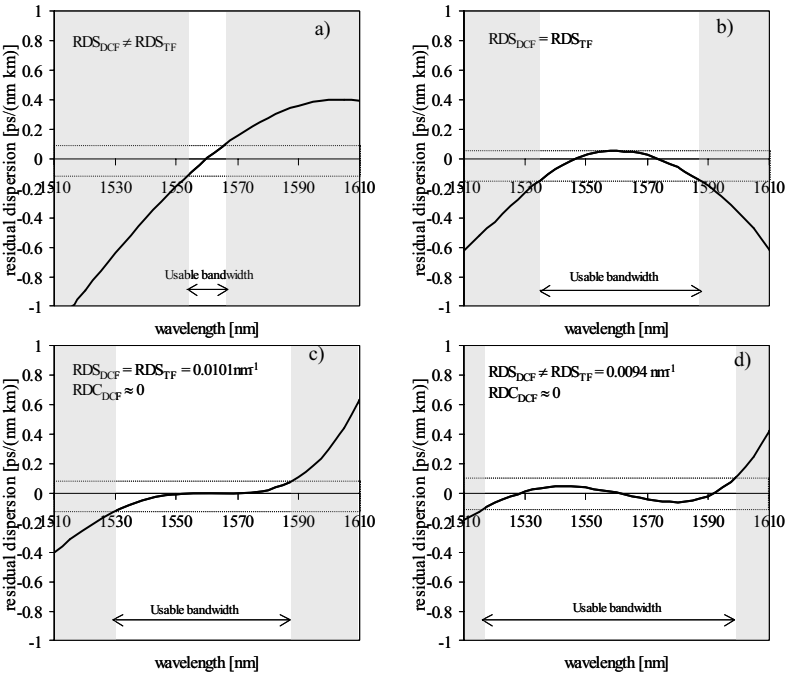

Fig. 4. Residual dispersion variation and usable bandwidth of 4 links consisting of a NZDF (TrueWave®RS) and a dispersion compensating fiber. The usable bandwidth is defined here as the bandwidth for which the residual dispersion is within 0.2 ps/(nm km). (a) RDS of the transmission fiber and the dispersion compensating fiber do not match. (b) RDS of the transmission fiber and the dispersion compensating fiber are matched. (c) RDS of the transmission fiber and the dispersion compensating fiber are matched. The curvature of the dispersion compensating fiber is low. (d) RDS of the transmission fiber is slightly lower than the RDS of the dispersion compensating fiber. The curvature of the dispersion compensating fiber is low.

as the bit rate of the systems increases, the control of the dispersion becomes more important and even the low dispersion of the NZDF requires compensation. Dispersion compensating fiber modules with slope match to all commonly installed transmission fibers are available.

The main challenge when designing dispersion compensating fibers for ITU: G.652 standard single mode fiber (SSMF) is to lower the attenuation of the dispersion compensating fiber module. During the past decade the attenuation of dispersion compensating fiber modules for 100 km SSMF have decreased from 9.5 to less than 5 dB but further improvement is still possible. Another challenge for dispersion compensating fiber modules for SSMF is to reduce the physical size of the dispersion compensating fiber module which will reduce the space requirements as well as the material costs.

For the non-zero dispersion fibers (NZDF) with low dispersion slope below 0.01 nm^{-1}, dispersion compensating fiber modules can easily be designed. The challenge

for designing dispersion compensating fibers for NZDF lies with the high slope NZDF with RDS above 0.01 nm^{-1}.

In this paper some of the trade offs, which must be considered when designing dispersion compensating fibers will be discussed. Three cases will be discussed: Dispersion compensating fibers with high figure of merit (FOM) for SSMF, dispersion compensating fibers with high dispersion slope and dispersion compensating fibers for SSMF with reduced physical dimensions.

3. Designing Dispersion Compensating Fibers

The dispersion compensating fibers considered in this paper all have triple clad index profiles with a core surrounded by a region with depressed index (the trench) followed by a raised ring (Figure 5a). This type of fiber is sometimes described as a dual concentric core fiber. Other designs for dispersion compensating fibers have been reported such as a quintuple clad fiber [7] or W-shaped profiles. [8] However, as most of the achieved dispersion properties can be obtained with a triple clad index profile as well, [9] only this type of profiles will be discussed here.

The dispersion is related to the second derivative of the propagation constant (β) by

$$D = \frac{-2\pi c}{\lambda^2}\frac{d^2\beta}{d\omega^2}. \tag{9}$$

The second derivative of the propagation constant is given by

$$\frac{d^2\beta}{d\omega^2} = \frac{1}{c}\left(2\frac{dn_e}{d\omega} + \omega\frac{d^2n_e}{d\omega^2}\right) \tag{10}$$

with ω being the frequency and n_e the effective index.

The propagation constant can be written in terms of the free space wave number and the effective index:

$$\beta = k_0 n_e \tag{11}$$

with the free-space wave number k_0 defined as

$$k_0 = \frac{\omega}{c} = \frac{2\pi}{\lambda} \tag{12}$$

and the effective index as

$$n_e = \Delta n_e + n_0 \tag{13}$$

with Δn_e being the effective index difference and n_0 the refractive index of the cladding the dispersion can be written as

$$D = \frac{-2\pi c}{\lambda^2}\frac{d^2k_0\Delta n_e}{d\omega^2} + \frac{-2\pi c}{\lambda^2}\frac{d^2k_0 n_0}{d\omega^2} = D_{\text{waveguide}} + D_{\text{material}} \tag{14}$$

with the first term giving the waveguide dispersion and the second term giving the material (or cladding) dispersion.

The propagation properties in a fiber with a triple clad index profile can be understood by considering the two guiding regions, the core and the ring regions separately. In Figs. 5(b) and (c) the two guiding regions are shown. The core index profile has

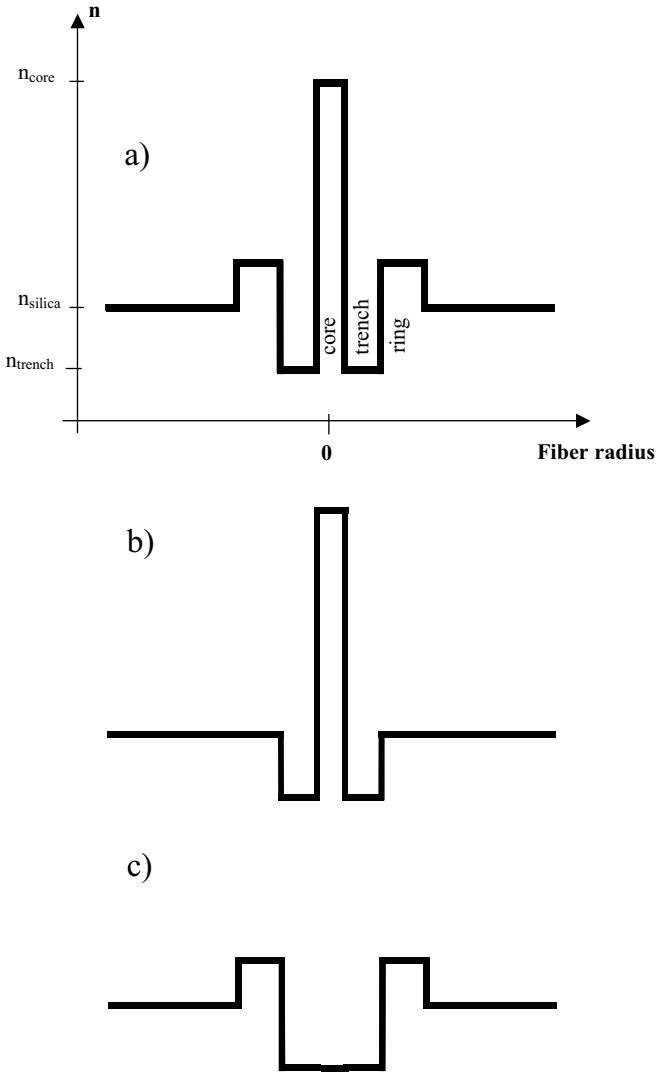

Fig. 5. Triple clad index profile. (a) The core is surrounded by the deeply down-doped trench followed by a raised ring. The core and ring are doped with germanium in order to increase the refractive index with respect to silica while the trench is doped with fluorine to lower the refractive index. (b) The index profile for the core guide. (c) The index profile for the ring guide.

been obtained by removing the ring from the triple clad index profile while the ring profile has been obtained by removing the core from the triple clad index profile.

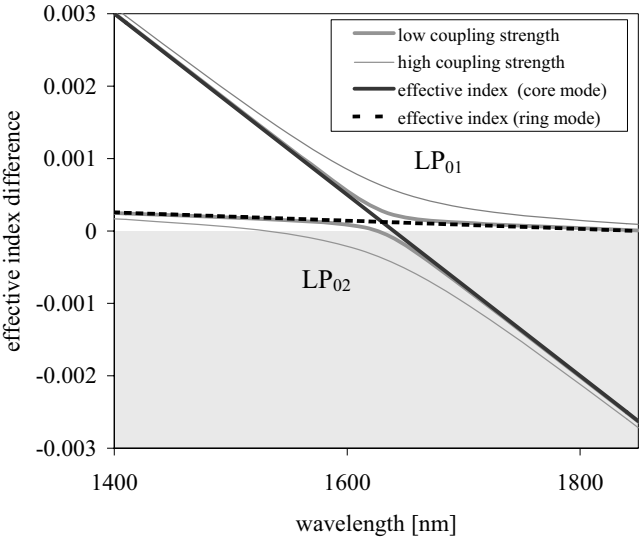

Fig. 6. Effective index differences for core-, ring-, LP_{01} and LP_{02} modes. The LP_{01} and LP_{02} modes are shown for high and low coupling strengths between the core and ring modes. A high coupling strength results in a low curvature at the cross over point while a low coupling strength results in a high curvature. The modes are not guided for $n_{\text{eff}} < 0$.

Using this supermode approach can be a powerful way to gain an intuitive understanding of how changes in the index profile changes the propagation properties of the fiber.

The effective index of the combined modes can be described by

$$n_e = \frac{n_{e(\text{core})} + n_{e(\text{ring})}}{2} \pm \sqrt{\kappa^2 + \left(\frac{(n_{e(\text{core})} - n_{e(\text{ring})})^2}{4}\right)} \tag{15}$$

with $n_{e(\text{core})}$ being the effective index of the core mode, $n_{e(\text{ring})}$ the effective index of the ring mode and κ the coupling strength between the two modes. [9]

The effective index n_e of the LP_{01} mode of the combined system is shown in Fig. 6 for both a low and a high coupling strength between the core and ring along with the effective index of the core and the ring mode. At short wavelengths the effective index of the LP_{01} mode approaches that of the core mode, indicating that the LP_{01} mode is confined mainly to the core. At longer wavelengths the effective index of the LP_{01} mode approaches that of the ring, indicating that the mode is confined to the ring.

The cross over-point is where the effective indices of the core and ring modes intersect. The coupling strength between the two modes determines the curvature of the effective index difference in the cross-over point and thus the dispersion of the LP_{01} (and LP_{02}) mode. With a low coupling strength, the interaction between the core and ring mode is small and the curvature of the effective index difference will be high while the opposite is the case for a high coupling strength.

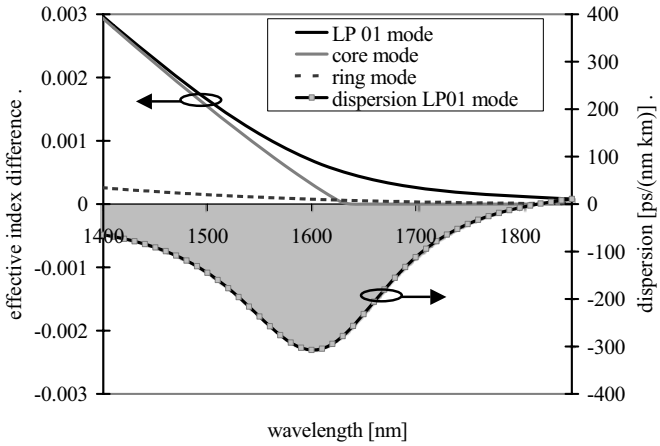

Fig. 7. The effective index difference of the ring, core and LP_{01} mode along with the resulting dispersion. Since the dispersion is the second derivative (curvature) of the effective index difference, the minimum of the dispersion curve is found at the wavelength for maximum curvature of the effective index.

As can be seen from Figure 7, the minimum of the dispersion of the LP_{01} mode occurs approximately were the curvature of the effective index difference reaches a maximum.

The first derivative of the propagation constant with respect to wavelength is the group delay. Consequently the area above the dispersion curve (shaded gray in Fig. 7) must be equal to the difference in group delay at the short and long wavelength side of the minimum of the dispersion curve. As the group delay of the LP_{01} mode approaches that of the core mode at short wavelengths and that of the ring mode at longer wavelengths, the area above the dispersion curve must be the same for different index profiles, unless the slope of the effective index difference of the core and ring modes changes significantly.

3.1. Scaling of the Triple Clad Index Profile

By changing the widths and indices of the triple clad index profile the dispersion curve given by Eq. (10) is changed. [10]

The scalar wave equation can be written as

$$\nabla^2_{r,\theta}\varphi + \frac{4\pi^2}{\lambda^2} 2n_0 \Delta n \varphi = \frac{4\pi^2}{\lambda^2} 2n_0 \Delta n_e \varphi \tag{16}$$

with $\nabla^2_{r,\theta}$ being the laplacian operator, Δn the refractive index difference, Δn_e the effective index difference and φ the scalar electric field. Terms in the order of Δn_e^2 and Δn^2 have been neglected.

If Eq. (16) is written for two different fiber profiles that are related to each other by

$$\Delta n^* = a\,\Delta n \tag{17}$$

and

$$r^* = b\,r \tag{18}$$

with * denoting the scaled profile, a being the index scale factor and b being the radius scale factor, Eq. (16) for the two index profiles will become the same if the effective index difference is scaled as

$$\Delta n_e^* = a\,\Delta n_e \tag{19}$$

and the wavelength is scaled as

$$\lambda^* = b\sqrt{a}\lambda. \tag{20}$$

Consequently the dispersion scales as

$$D^*_{\text{waveguide}} = \frac{-2\pi c}{\lambda^*}\frac{d^2 k_0^* \Delta n_e^*}{d\omega^{*2}} = \frac{\sqrt{a}}{b}\frac{-2\pi c}{\lambda}\frac{d^2 k_0 \Delta n_e}{d\omega^2} = \frac{\sqrt{a}}{b} D_{\text{waveguide}} \tag{21}$$

and the dispersion slope as

$$S^*_{\text{waveguide}} = \frac{dD^*_{\text{waveguide}}}{d\lambda^*} = \frac{d\left(\frac{\sqrt{a}}{b} D_{\text{waveguide}}\right)}{d(b\sqrt{a}\lambda)} = \frac{1}{b^2} S_{\text{waveguide}}. \tag{22}$$

If the radius scale factor b is related to the index scale factor a by

$$b = \frac{1}{\sqrt{a}}; \tag{23}$$

the relative dispersion slopes of the two fibers will be the same [Eqs. (6), (21) and (22)]:

$$\text{RDS}^*_{\text{waveguide}} = \text{RDS}_{\text{waveguide}}. \tag{24}$$

A consequence of this is that the effective index can be changed significantly without changing the waveguide dispersion.

The scaling only applies to the waveguide dispersion; consequently an error is introduced in the scaled dispersion due to the neglect of the material dispersion. But for most dispersion compensating fibers this error will be small since the material dispersion around 1550 nm is at the order of 20 ps/(nm km). An example is shown in Fig. 18 where a scaling of the radii of all layers of a triple clad index profile by a factor of 1.2 and a scaling of the indices by a factor of $1/\sqrt{1.2}$ results in an error of 3.7 ps/(nm km) on the dispersion of –158 ps/(nm km) of the scaled profile.

The scaling of the profile can be performed on the entire profile or on each of the guiding regions separately. So, by decreasing the core diameter, the wavelength where the effective index of the core and the ring mode intersects is decreased and thereby the wavelength of the minimum of the dispersion curve. The shift of the dispersion curve when the core width is changed can be used as a measure of how sensitive the design is to the small variations in core diameter, which are unavoidable during manufacturing.

By changing the width of the trench, the slope of the effective index difference for the core and ring modes remains largely unchanged. Consequently, the area under the dispersion curve is the same for fibers with different widths of the trench, but a significant change in the slope of the dispersion curve is seen. This will be treated further in section 5.

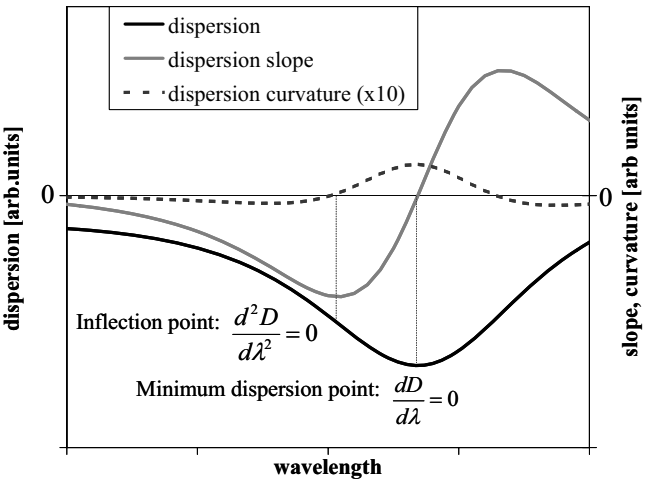

Fig. 8. Dispersion, dispersion slope and dispersion curvature for a dispersion compensating fiber. The dispersion curvature has been scaled with a factor of 10 in order to be plotted on the same axis as the dispersion slope. The minimum dispersion is found where $\frac{dD}{d\lambda} = 0$. The inflection point is where $\frac{d^2D}{d\lambda^2} = 0$. At wavelengths close to the inflection point, the dispersion curvature is low, resulting in a low residual dispersion. At wavelengths longer than the inflection point very negative dispersions can be obtained while at wavelengths shorter than the inflection point the maximum RDS can be found.

An important point on the dispersion curve is the inflection point (Fig. 8) where the second derivative of the dispersion, the curvature changes sign from negative to positive. The curvature around the inflection point is low and dispersion compensating fibers operating close to the inflection point can be used to obtain a very low residual dispersion as shown in Fig. 4(c)–(d). At wavelengths shorter than the inflection point the maximum value for RDS can be found while at wavelengths longer than the inflection point a very negative dispersion can be obtained. At the point of minimum dispersion, the curvature also reaches its maximum value; consequently the residual dispersion at this point will be high.

In the next sections some design strategies for dispersion compensating fibers with high negative dispersion, high dispersion slope and reduced physical dimensions will be discussed.

The properties of the fibers have been calculated solving the equation 16 using a finite elements formulation to obtain β and the fields of the guided modes.

Throughout this paper, simulated dispersion curves will be used to illustrate the design strategies for the various kinds of the dispersion compensating fibers.

4. Dispersion Compensating Fibers with a High Figure of Merit

While dispersion compensating fiber modules are necessary with respect to dispersion control, they decrease the performance of the system with respect to loss. The added loss from the dispersion compensating fiber module increases the need of amplification in the system thereby degrading the signal to noise ratio and adding cost.

The added loss from a dispersion compensating fiber module, $\alpha_{\mathrm{DCFmodule}}$ to a system can be expressed as

$$\alpha_{\mathrm{DCFmodule}} = L_{\mathrm{DCF}}\alpha_{\mathrm{DCF}} + \alpha_{\mathrm{splice}} + \alpha_{\mathrm{connector}} \tag{25}$$

with α_{DCF} being the attenuation coefficient of the dispersion compensating fiber (dB/km), L_{DCF} the length of dispersion compensating fiber in the module (km), α_{splice} the splice losses between the dispersion compensating fiber and the connectors and $\alpha_{\mathrm{connector}}$ the loss of the connector (dB).

As the length of dispersion compensating fiber can be expressed as

$$L_{\mathrm{DCF}} = D_{\mathrm{tot}}/D_{\mathrm{DCF}}$$

with D_{tot} being the accumulated dispersion on the transmission fiber, the length of dispersion compensating fiber in the module can be decreased by increasing the negative dispersion coefficient (D_{DCF}) on the dispersion compensating fiber.

This leads to a figure of merit for dispersion compensating fibers defined as

$$\mathrm{FOM} = \frac{-D_{\mathrm{DCF}}}{\alpha_{\mathrm{DCF}}}. \tag{26}$$

A high figure of merit signifies that the dispersion compensating fiber module adds less loss to the system.

Since the accumulated dispersion on NZDF is lower than on SSMF a high figure of merit is particularly interesting for a dispersion compensating fiber with slope match to SSMF than for one with slope match to NZDF. 100 km SSMF will accumulate a dispersion of 1650 ps/nm compared to the 450 ps/nm accumulated dispersion on 100 km of NZDF. Consequently, a module with a fiber designed to compensate the dispersion of NZDF will need a shorter length of dispersion compensating fiber and less loss will be added to the system.

Thus, the two strategies for increasing the figure of merit is to either decrease the attenuation of the dispersion compensating fiber or to increase the negative dispersion.

There are however limitations to how negative a dispersion is desirable. Dispersion compensating fibers with dispersions as negative as –1800 ps/(nm km) have been demonstrated, [11,12] but as this very negative dispersion can only be reached within a very narrow wavelength range, the dispersion properties of such a fiber will be very sensitive to variations in core diameter during manufacturing. Consequently, this design of a dispersion compensating fiber is not very desirable for a fiber manufacturer.

Other reports of dispersion compensating fibers that have more manufacturable designs include a fiber with a dispersion of –295 ps/(nm km), a FOM of 418 ps/(nm dB) and a RDS of 0.0004 nm^{-1} [13]. Another fiber has a negative dispersion of –302 ps/(nm km), a FOM of 459 ps/(nm dB) and a RDS of 0.0097 nm^{-1}.[14] None of these dispersion compensating fibers with high FOM published in the literature have slope match to SSMF.

4.1. Understanding the Attenuation of Dispersion Compensating Fibers

The attenuation of dispersion compensating fibers is typically in the range 0.4–0.7 dB/km depending on the fiber design. These values are high compared to the attenuation of less than 0.2 dB/km observed in transmission fibers.

The excess loss in dispersion compensating fibers is mainly design dependent, with bend and scattering losses as the main components. The attenuation of silica based optical fibers can be expressed as a sum of contributions:

$$\alpha_{\mathrm{tot}} = \alpha_{\mathrm{UV}} + \alpha_{\mathrm{IR}} + \alpha_{\mathrm{abs}} + \alpha_{\mathrm{scattering}} + \alpha_{\mathrm{waveguide}} \tag{27}$$

with α_{UV} being the attenuation due to absorption on electronics transitions, α_{IR} the attenuation due to multiphonon absorptions, α_{abs} the attenuation due to absorption on impurities or defects, $\alpha_{\mathrm{scattering}}$ the attenuation due to scattering and $\alpha_{\mathrm{waveguide}}$ the waveguide dependent attenuation.

The contributions to the attenuation from the first three terms in Equation 27 are roughly the same for both transmission and dispersion compensating fibers. It is mainly due to the last two terms $\alpha_{\mathrm{scattering}}$ and $\alpha_{\mathrm{waveguide}}$ that the dispersion compensating fibers have the high attenuation.

4.2. Attenuation Due to Scattering

The scattering losses of dispersion compensating fibers depend on fabrication method as well as the design of the fiber.

The scattering loss in germanium doped silica glasses can be expressed as

$$\alpha_{\mathrm{scattering}} = \alpha_{\mathrm{dens}} + \alpha_{\mathrm{conc}} + \alpha_{\mathrm{Bril}} + \alpha_{\mathrm{Raman}} + \alpha_{\mathrm{anomalous}} \tag{28}$$

α_{dens} being the elastic scattering due to density fluctuations in the glass, α_{conc} being the elastic scattering from concentration fluctuations, α_{Bril} being Brillouin scattering from acoustic phonons, α_{Raman} the scattering from optical phonons and $\alpha_{\mathrm{anomalous}}$ the scattering seen in fibers with a high index core. The first four contributions to the scattering losses show the same wavelength dependence:

$$\alpha_{\mathrm{scattering}} = \frac{C_{\mathrm{scattering}}}{\lambda^4}. \tag{29}$$

$C_{\mathrm{scattering}}$ being the scattering coefficient, which depends on glass composition and processing conditions. [15]

As $\alpha_{\mathrm{Raman}}$and α_{Bril} are both small compared to the other scattering losses, they will not be discussed further.

The scattering on density fluctuations (α_{dens}) is observed in all glasses. Density fluctuations are sometimes described as the dynamic fluctuations of the glass in the liquid state frozen in at the glass transition temperature (T_g). [16,17] The magnitude of the scattering on density fluctuations has been shown to be proportional to T_g, which is the temperature where a glass upon cooling reaches a viscosity of 10^{13} P. $T_g$depends on the cooling rate and the scattering due to density fluctuation can be lowered by controlling temperature during the fiber draw. [18,19]

α_{conc}, the scattering on concentration fluctuations, is observed in multicomponent glasses. In all glasses containing more than one component, regions will exist

where the concentration of one component is higher than the other. As the germanium concentration in the core increases, so does α_{conc}. [20]

The correlation lengths for the scatterings causing α_{dens} and α_{conc} are small compared to the wavelength of light. They are sometimes referred to as Rayleigh scattering due to the wavelength dependence of $1/\lambda^4$.

When the index of the core is increased, the scattering losses increases faster with germanium concentration than can be explained by the Rayleigh losses. This is due to another type of scattering losses, which are responsible for a large part of the added attenuation of dispersion compensating fibers: The anomalous loss.

The term $\alpha_{\mathrm{anomalous}}$ of Equation 28 is the scattering on fluctuations of the core diameter, which are induced during draw. The fluctuations causing the scattering are of larger than, but typically of the same order of magnitude as, the wavelength of the light in the longitudinal direction of the fiber while the fluctuations in the radial direction is smaller than 1 nm. For step index fibers with a high core index, $\alpha_{\mathrm{anomalous}}$ is the largest contribution to the total loss of dispersion compensating fibers. For a fiber with core diameter d_{core}, core index n_{core} and gradient of core profile γ, the anomalous scattering loss is

$$\alpha_{\mathrm{anomalous}} = D_{\mathrm{anomalous}} n_{\mathrm{core}}^2 \frac{\gamma^2}{d_{\mathrm{core}}^m \lambda^k (\gamma+2)^2} \tag{30}$$

with $D_{\mathrm{anomalous}}$ being the strength of the scattering. The exponents m and k depends on γ as shown in Table 2. According to Eq. (30) the anomalous loss can be lowered by decreasing the core index or by grading the core [21].

Table 2. Exponents for the anomalous loss expression.

γ	**m**	**k**
2 (quadratic index profile)	1.6	2.4
∞ (Step index profile)	1	3

For fibers produced using the Modified Chemical Vapor Deposition (MCVD) process, the central dip in the index profile contributes to the scattering losses as well. It has been shown [22,23] that scattering losses can be reduced significantly if the central dip is eliminated.

4.2.1. Waveguide dependent attenuation:

The last term in Eq. (27) is $\alpha_{\mathrm{waveguide}}$, the waveguide dependent attenuation. The most important contributions are macro and micro bend losses.

Macro bend losses. A dispersion compensating fiber in a module is used on a spool with a typical inner diameter of 100–200 mm. The propagation in the bend fiber can be described using the equivalent index profile: [24]

$$n_{\mathrm{equ}}^2 = n^2(r)\left[1 + 2\frac{r}{R}\cos(\phi)\right] \tag{31}$$

with $n(r)$ being the index profile of the undistorted fiber, r and ϕ the cylindrical coordinates of the fiber and R the bend radius of the fiber.

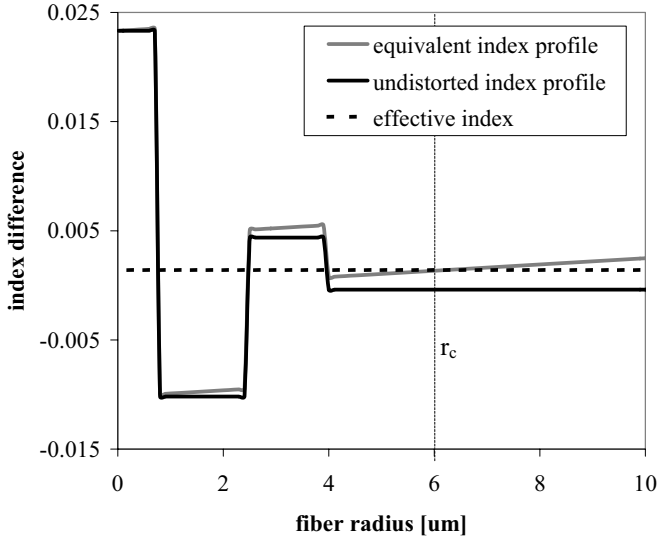

Fig. 9. The undistorted and the equivalent index profiles of a bend fiber. The vertical dotted line (rc) marks the radiation caustic, the radius where the mode becomes radiating.

The radius where the effective index intersects the equivalent index profile is the radiation caustic (r_c) outside which the field becomes radiating (Fig. 9). The macro bend losses can be reduced by either increasing the effective index, thereby increasing the radiation caustic, or by reducing the magnitude of the field at r_c by decreasing the effective area of the mode.

A side effect of increasing the effective index of the LP_{01} mode is that also the higher order modes will be more confined to the core thereby increasing their cut off wavelength. If the fiber supports higher order modes as well as the fundamental mode, the light traveling in the different modes can interfere, leading to noise due to modal MPI (multi path interference).

An interesting effect of bending the fiber is that as the propagation in the fiber changes with bend diameter so does the dispersion of the fiber. [26] It has been shown how the negative dispersion can be increased with decreasing bend diameters. [25,26] Unfortunately, this effect is most pronounced at the higher wavelengths where the effective index is small and the macro bend losses are high. It has been demonstrated on a multimoded dispersion compensating fiber where the minimum of the negative dispersion was shifted 40 nm by changing the bend radius from 6.6 to 25 cm. Since the change of dispersion is accompanied by a substantial increase of the fiber loss, it is unlikely that this effect can be utilized for making tunable dispersion compensating fibers. [27]

Micro bend losses. The fiber in a module experiences not only the macroscopic bend loss induced by the bend radius of the fiber on the module. Another source of attenuation

is the micro bend loss originating from the microscopic deformations caused by the pressure from the other fibers in the package.

The micro bend loss of the fiber is important not only for the overall attenuation of the fiber, but also for the performance of the dispersion compensating fiber module when subjected to temperature changes. When the dispersion compensating fiber module is subjected to an increase of temperature, the metallic spool on which the fiber is wound, will expand. The fiber will experience a pressure from the other turns of the fiber, which will act as a surface with deformation power spectrum Φ. This leads to microbend loss (α_{micro}) that can be expressed as [28]:

$$2\alpha_{\mathrm{micro}} = \sum_{p} C_{1p}^2 \Phi(\Delta\beta_{1p}), \tag{32}$$

where C_{1p} are the coupling coefficients between the LP_{01} mode and the cladding mode, LP_{1p} , ($p = 1, 2, \ldots$) and Φ is the deformation power spectrum of the fiber axis at spatial frequencies $\Delta\beta_{1p}$ corresponding to the difference in propagation constants between the LP_{01} and cladding modes ($\Delta\beta_{1p} = \beta_{01} - \beta_{1p}$).

The deformation spectrum experienced by the fiber depends on the stiffness of the fiber as well as of the ability of the coating to absorb the deformation. This leads to an expression for the micro bend loss of a fiber that experiences a linear pressure (F) onto a surface with the deformation spectrum Φ[29]:

$$2\alpha_{\mathrm{micro}} = \sqrt{\frac{2}{\pi}} \frac{DF}{H^2\sigma} \sum_{p=1}^{\infty} C_{1p}^2 \frac{1}{(\Delta\beta_{1p})^8} \Phi_s(\Delta\beta_{1p}) \tag{33}$$

with σ being related to the RMS value of the surface deformation, H the flexural rigidity (stiffness) and D the lateral rigidity of a coated fiber. The terms in front of the summation are all related to the mechanical properties of the fiber, whereas the terms inside the summation are related to the fiber index profile and the deformation spectrum.

Equation (33) shows that by increasing the fiber diameter and thereby the stiffness of the fiber, the micro bend losses can be reduced. Another possibility for reducing the micro bend losses is to change the ability of the coating to protect the fiber from deformation by absorbing the pressure.

As the terms inside the summation shows, the micro bend loss depends strongly on the difference in propagation constants ($\Delta\beta_{1p}$). So by choosing a design with large effective index difference, the micro bend loss can be minimized.

Splice losses. The second term in Eq. (25) describing the total loss of a dispersion compensating fiber module, α_{splice} is the losses arising from the splice between the dispersion compensating fiber and the standard single mode fiber pigtails. As the propagation of light in dispersion compensating fibers tend to be very sensitive towards small perturbations of the index profile, any such perturbations during the splice will induce some of the light to couple into higher order modes and increase the loss. The main problem lies in the fact that the small, non-Gaussian mode field of the dispersion compensating fiber must match the much larger Gaussian mode field of the standard single mode connector in order to yield low splice losses.

To reduce the splice losses several techniques have been proposed. By using Thermally Expanded Core (TEC) splicing, [32] tapering of the fusion splice [33] or fattening

the fusion splice [34] the cores of the dispersion compensating fiber and the standard single mode fiber can be modified to facilitate a smooth transition from one fiber to the other and thus minimize the splice losses. Another method uses an intermediate fiber, which can be spliced between the dispersion compensating fiber and the standard single mode fiber with a low loss. [35]

The different contributions to the attenuation of dispersion compensating fibers mentioned in the previous section all depend on the core index, but in different ways. If the core index is increased, the attenuation due to Rayleigh scattering and anomalous loss increases as well. The bend losses on the other hand decreases with higher core index as the effective index becomes higher and the light is more confined to the core, which again leads to a higher cutoff wavelength for the higher order modes.

This represents some of the trade offs encountered for the design of dispersion compensating fibers with high figure of merit. As will be shown in the next section, even more trade offs are introduced when the dispersion is considered as well.

4.3. Increasing the Negative Dispersion

Another way to lower the total losses of a dispersion compensating fiber module is to decrease the length of the dispersion compensating fiber [Eq. (25)]. This can be done by increasing the negative dispersion on the dispersion compensating fiber [Eq. (26)].

As discussed in a previous section, the dispersion curve can be moved with respect to operating wavelength by scaling the core. By changing only the trench, the dispersion curve can be made deeper and narrower without changing the area above the dispersion curve. These two operations can be used to increase the negative dispersion considerably and thereby show a way to increase the figure of merit.

Figure 10(a) shows the dispersion properties of two commercially available dispersion compensating fibers both with slope match to SSMF at 1550 nm. Fiber A has a dispersion of –120 ps/(nm km) while fiber B has a dispersion of –250 ps/(nm km).

The very negative dispersion of fiber B has been obtained by making the dispersion curve deeper and narrower by increasing the negative index of the trench (Fig. 11). Due to the low index of the trench region of fiber B, the overlap between the core and ring mode is small resulting in a high curvature of the effective index and consequently a very negative dispersion. The dispersion curve has been moved with respect to the operating wavelength by increasing the width of the core.

The measured optical properties of the two fibers at 1550 nm are shown in Table 3. Even though the dispersion of fiber B is more than twice as negative as that of fiber A, the attenuation has also increased from 0.43 dB/m to 0.58 dB/m so the figure of merit has only increased from 280 ps/(nm dB) to 430 ps/(nm dB).

Part of the increased attenuation can be explained by the higher anomalous loss due to the larger index difference between core and trench. Another part is due to increased bend loss sensitivity.

Figure 10(b) shows the simulated effective index difference and effective area for the two fibers. At 1550 nm, the effective index difference of fiber B is close to that of the ring mode. As the wavelength increases, the effective index difference decreases, thereby moving the radiation caustic closer to the core. This gives fiber B a high macro bend loss. The effective index difference of fiber A is larger, and the macro bend losses for this fiber are consequently much smaller.

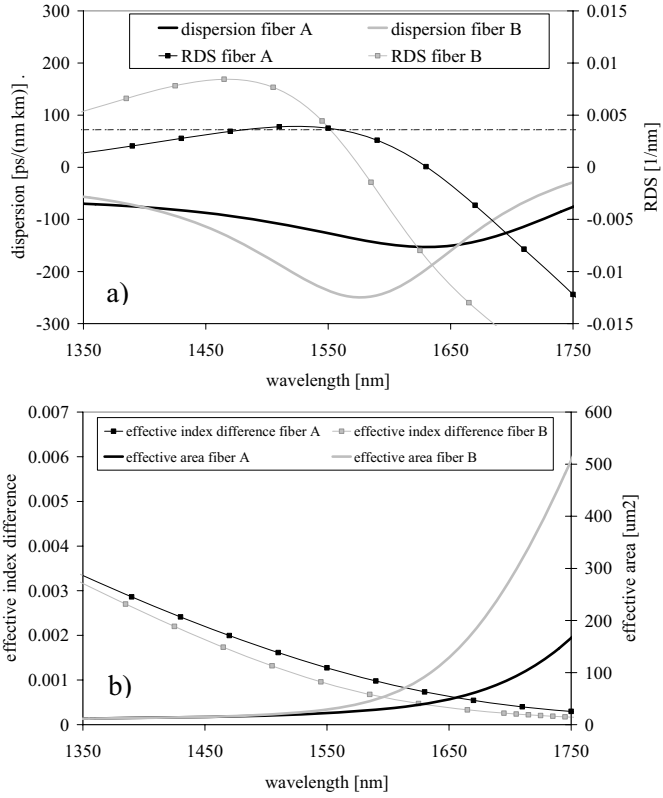

Fig. 10. Dispersion, RDS, effective index difference and effective area of the A and B fibers. Both fibers have an RDS of 0.0035 nm^{-1} at 1550 nm matching that of SSMF. Due to a higher curvature of the effective index of fiber B, the dispersion has been increased from the –120 ps/(nm km) of fiber A to –250 ps/(nm km).

Another consequence of the higher effective index difference of fiber A is that the micro bend losses for this fiber is lower than that of fiber B and consequently the stability of the fiber towards temperature changes is high.

Another draw back for fiber B is the higher residual dispersion. As the operating wavelength of fiber A is close to the inflection point of the dispersion curve, the curvature is very low whereas fiber B operates where the dispersion curvature is high resulting in a high residual dispersion.

A high residual dispersion is not the only consequence of the high dispersion curvature of fiber B. With a high curvature, the change in RDS with wavelength is high and the fiber is consequently very sensitive to the small variations in core diameter that are unavoidable during fiber production. In Fig. 12 the variation of RDS with core diameter is shown for fiber A and fiber B. Whereas the RDS of fiber A is relative insensitive to small variations of core diameter, even small variations of the

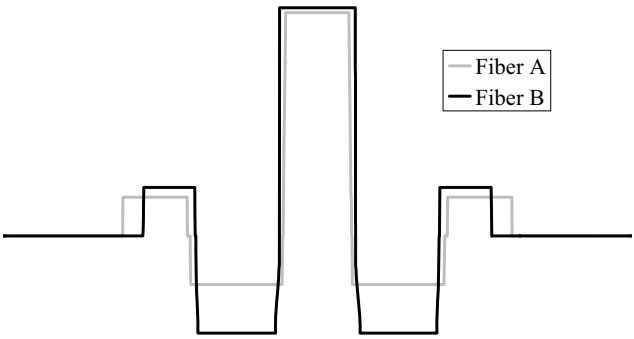

Fig. 11. Representative profiles for fibers A and B. The main difference between the index profiles of the two fibers is the refractive index of the trench region. Due to the lower refractive index of the trench region of fiber B, the overlap between the core and the ring mode is small resulting in a high curvature of the effective index and consequently a very negative dispersion.

Table 3. Optical properties measured at 1550 nm for 3 dispersion compensating fibers with slope match to standard single mode fiber (RDS = 0.0035 nm^{-1})

		Dispersion (ps/nm km)	Attenuation (dB/km)	Typical splice loss (dB)	FOM (ps/nm dB)	Residual dispersion variation (1530–1565 nm) (ps/nm km)
DCF A	Conventional DCF for SSMF	–120	0.43	0.35	280	± 0.02
DCF B	High FOM DCF for SSMF	–250	0.58	0.2	430	± 0.2
DCF C	Low loss DCF for SSMF	–170	0.46	0.3	370	± 0.1

core diameter of fiber B changes the RDS so slope match to SSMF can no longer be obtained.

The dispersion properties of fiber B are not the only properties that are very sensitive to variations of the core diameter. As shown previously (section 3) changing the core diameter corresponds to moving the dispersion curve with respect to wavelength. Consequently all other properties that change rapidly with wavelength will be very sensitive to any variations of the core diameter. This includes the effective area [Fig. 10(b)] and consequently the macro bend losses.

It is important however to keep in mind that even with the draw backs for fiber B presented above, it does have a higher figure of merit than fiber A, and for some applications a low attenuation of the dispersion compensating fiber module is more important than a low residual dispersion and high usable bandwidth.

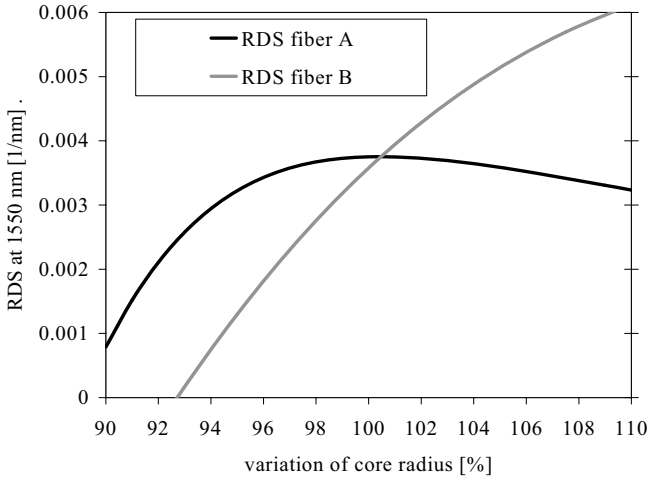

Fig. 12. RDS for fiber A and fiber B as function of variations of core radius. The RDS of fiber A is not very sensitive to variations in core radius, while for fiber B even small variations in core radius changes the RDS so slope match to SSMF can no longer be obtained.

Fibers A and B has been presented as representatives for two different design strategies: Optimizing the residual dispersion (fiber A) or optimizing the figure of merit (fiber B). It is of course possible to design a fiber that is somewhere in between the two. Fiber C of Table 3 is an example of such a fiber.

Figure 13 shows the residual dispersion variation of fibers A, B and C. Fiber C is designed to have both a high figure of merit of 370 ps/(nm dB) and a low residual dispersion of only ± 0.1 ps/(nm km). The low residual dispersion has been achieved by operating below, but closer to the inflection point than fiber B. Even though the dispersion at the inflection point is not as negative as that seen for fiber B, the figure of merit is high as the attenuation of the fiber is lower due to a design that is optimized with respect to the waveguide dependent losses.

As the fiber does not operate as close to the minimum of the dispersion curve as fiber B, more of the field is confined to the core resulting in lower bend losses. The index profiles has furthermore been optimized with respect to anomalous losses [Eq. (30)] by choosing a core index and core gradient that will give the right dispersion properties while minimizing the anomalous losses.

5. Dispersion Compensating Fibers with High Dispersion Slope

The dispersion compensating fibers described in the previous sections have all been designed to compensate the dispersion of standard single mode fiber (SSMF), which are the most commonly used type of fiber. As listed in Table 1 several other types of transmission fibers exist.

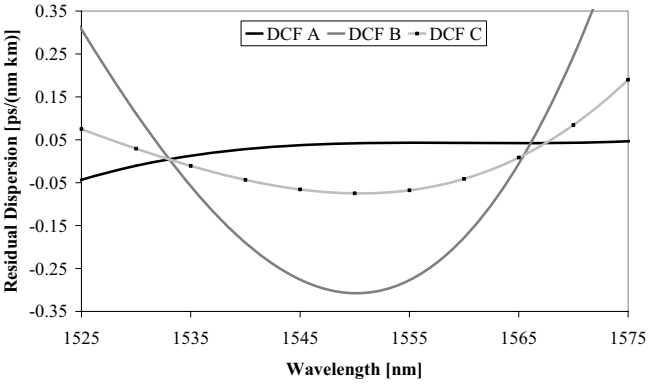

Fig. 13. Residual dispersion for SSMF compensated with fibers A, B or C. Fiber A is optimized for low residual dispersion. Fiber B is a high FOM fiber optimized to have a very negative dispersion. Fiber C is an intermediate fiber of A and B with a medium FOM and residual dispersion slightly higher than that of fiber A.

Historically, the dispersion shifted fibers (DSF) were designed to have zero dispersion at 1550 nm where the attenuation in silica fibers is lowest. For multi channel systems however, zero dispersion is a disadvantage since four wave mixing can occur between channels, resulting in interchannel crosstalk, which degrades the system performance. Currently, DSF is used mainly in the L-band where the dispersion is in the order of 2.8 ps/(nm km) and the RDS in the order of 0.025 nm^{-1} at 1590 nm.

The NZDF was designed to have less dispersion than SSMF at 1550 nm, but still enough dispersion to eliminate problems with four wave mixing. As shown in Table 1, they all have dispersion lower than 8 ps/(nm km) while the RDS values can be as high as 0.02 nm^{-1}.[30]

Even though the dispersion of the NZDF is reduced compared to SSMF, at high bit rates there is still a need for compensating this dispersion.

The dispersion of NZDF with RDS less than 0.01 nm^{-1} proves no challenge to compensate. [31] It has however proved to be a challenge to design dispersion compensating fibers for the NZDFs with RDS values above 0.01 nm^{-1} especially those where the RDS reaches values in the order of 0.02 nm^{-1}. [32–34]

5.1. Design

The basic index profile of dispersion compensating fibers with high dispersion slope is the triple clad index profile of Fig. 5. The complicated design of these fibers involves many trade offs especially between the dispersion properties and bend losses.

As an understanding of the different trade offs involved can be gained by investigating the effects of only changing a few parameters of the index profile, in this section only the width of the core and trench layer of the index profiles will be changed.

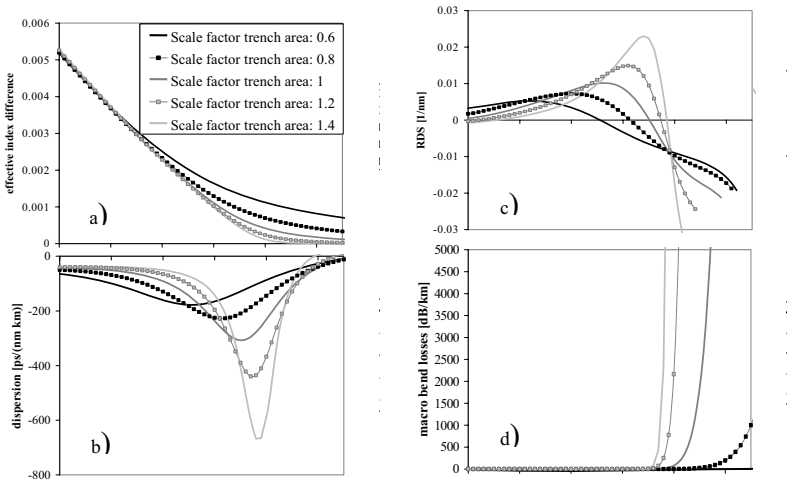

Fig. 14. The effect on effective index, dispersion, RDS and macro bend losses of changing the area of the trench of the triple clad index profile. (a) Increasing the area of the trench decreases the overlap between the core and ring mode. This causes an increase of the curvature of the effective index, resulting in a deep and narrow dispersion curve (b) with a high dispersion slope and consequently a higher RDS (c) Increasing the area of the trench reduces the wavelength for max RDS. The opposite effect is seen for the macro bend losses where the macro bend losses increases with increasing trench area (d) making the bandwidth, where the fiber has both a high RDS and low macrobend losses, very narrow.

The effect of changing the width of the trench from 0.6 to 1.4 (arbitrary units) on the dispersion, the RDS, the effective index difference and the macro bend losses as functions of wavelength is shown in Fig. 14.

When the diameter of the trench is increased, the overlap between core and ring modes is decreased and curvature of the effective index difference is increased resulting in a very negative dispersion [Eq. (9)]. As discussed in section 2, when the slope of the effective index difference remains largely unchanged at both the lower and higher wavelengths, the area above the dispersion curve must remain unchanged as well resulting in a more narrow dispersion curve with a high dispersion slope and consequently the possibility for high RDS values [Fig. 14(b)] shows the effect on macro bend losses of increasing the width of the trench. As the width of the trench increases, the wavelength for max RDS is reduced. The opposite effect is seen for the macro bend loss. When the width of the trench increases, so does the wavelength where the attenuation, due to macro bend losses become large making the bandwidth where the fiber has both a high RDS value and low losses very narrow. This can to some extend be counteracted by increasing the effective index, thereby increasing the radiation caustic. However, as for the fibers with high figure of merit, increasing the effective index will result in a higher cutoff wavelength, as higher order modes will be better confined to the core as well.

An important question is: When is the cutoff wavelength for the higher order modes too high? An investigation of the relation between cutoff wavelength and MPI

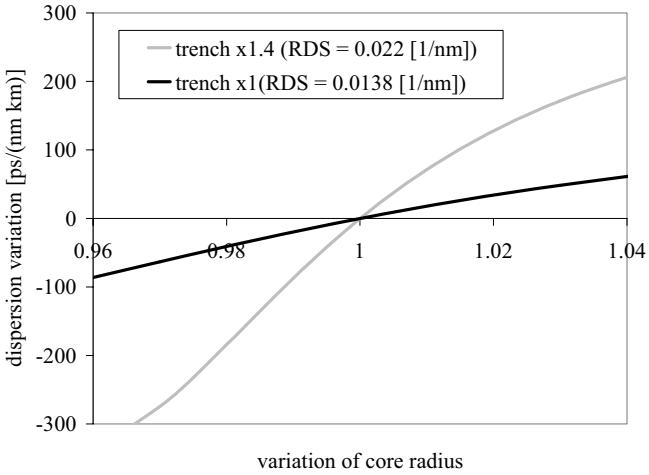

Fig. 15. Dispersion variation at the inflection point for two different scalings of the width of the trench. The sensitivity of the dispersion with respect to variation of the core radius is increased for increased width of the trench.

has been performed showing how dispersion compensating fibers with high dispersion slope have a higher MPI than dispersion compensating fibers with low dispersion slope, probably due to the higher cutoff wavelength of the high slope dispersion compensating fibers. [35] However, the investigation gives no conclusive answer as to what the maximum acceptable cutoff wavelength is with respect to MPI.

Another question is how to correctly measure the cutoff of dispersion compensating fibers. The cutoff wavelength can be considered as the wavelength where the higher order modes experience bend losses high enough so they no longer can be considered as being guided. This wavelength will of course depend on the bend diameter of the fiber on the module and the measurement of the cutoff wavelength will depend on the length of fiber measured as well. [36,37] The bending diameter of the dispersion compensating fiber during the measurement of the cutoff wavelength should be chosen to be slightly larger than the outer diameter of the dispersion compensating module thereby ensuring single mode operation of the fiber above the measured cutoff wavelength when the fiber is on the spool in the module.

Increasing the RDS by increasing the width of the trench not only increases the macro bend sensitivity of the fiber; it also increases the sensitivity of the dispersion to small variations in core diameter. Figure 15 shows the dispersion variation at the inflection point for two different scalings of the trench resulting in RDS values of 0.022 nm^{-1} and 0.0138 nm^{-1}. The scale factors for the width of the trench are given in the figure.

Naturally, as the dispersion slope increases, so does the sensitivity to small changes in core diameter, which makes it challenging to manufacture dispersion compensating fibers with high dispersion slopes.

Another trade off is the limitations imposed on the usable bandwidth by increasing the dispersion slope. [6,10] It was found that for fibers designed to operate at a wavelength close to the inflection point there is an inverse relationship between the usable bandwidth and RDS. This is true as long as the effective indices of the core and ring mode do not change significantly from fiber to fiber. If the effective indices of the core and ring mode do not change, the area above the dispersion curve is kept constant. Consequently, increasing the dispersion slope will cause the dispersion curve to become deep and narrow, thus decreasing the usable bandwidth. If the index of the core or ring region is changed, this relationship will no longer hold.

5.2. Combined Dispersion Compensating Fiber Module

Another possibility for making a dispersion compensating fiber module with a high dispersion slope is to use a combined module where the desired dispersion properties are obtained by combining two different fibers [38].

The dispersion of the combined module is

$$D_{\text{combined}} = D_{\text{DCF1}} L_{\text{DCF1}} + D_{\text{DCF2}} L_{\text{DCF2}} \tag{34}$$

and the slope is

$$S_{\text{combined}} = S_{\text{DCF1}} L_{\text{DCF1}} + S_{\text{DCF2}} L_{\text{DCF2}}. \tag{35}$$

Leading to a relative dispersion slope (RDS) for the combined module of:

$$\text{RDS}_{\text{combined}} = \frac{S_{\text{DCF1}} L_{\text{DCF1}} + S_{\text{DCF2}} L_{\text{DCF2}}}{D_{\text{DCF1}} L_{\text{DCF1}} + D_{\text{DCF2}} L_{\text{DCF2}}}. \tag{36}$$

If the two fibers in the combined module have negative dispersion it is possible to make a combined module with a RDS value between that of the two individual fibers. If however fiber 1 has a negative dispersion and fiber 2 a positive dispersion but a RDS value lower than that of fiber 1, it is possible to achieve a RDS for the combined module that is higher than the RDS of fiber 1. Consequently a dispersion compensating fiber module with a RDS value matching that of the high slope NZDF can be manufactured by combining a dispersion compensating fiber having a low RDS value of 0.015 nm^{-1} with for example SSMF fiber having a positive dispersion and a RDS of 0.0036 nm^{-1}.

As shown previously, a dispersion compensating fiber with a lower RDS is less sensitive to variations in core diameter and less likely to suffer from high macro bend losses. By using the method of the combined module it is thus possible to make a dispersion compensating fiber module with slope match to the high slope NZDF using a dispersion compensating fiber with a lower RDS.

As the length of both fibers in the combined module increases with the difference between $\text{RDS}_{\text{combined}}$ and RDS_{DCF1}, so does the attenuation of the module. This is however in some instances preferred to the difficulties associated with the production of a dispersion compensating fiber with slope match to the high slope NZDFs.

One of the reasons the combined module can offer an attractive solution, not only to the user, but also to the manufacturer is that the combination of two different fibers in the module can reduce the width of the RDS distribution as shown in Fig. 16. As the RDS of the combined module is controlled by the length of positive dispersion fiber, better control of the RDS can be achieved for the combined than for a single fiber solution.

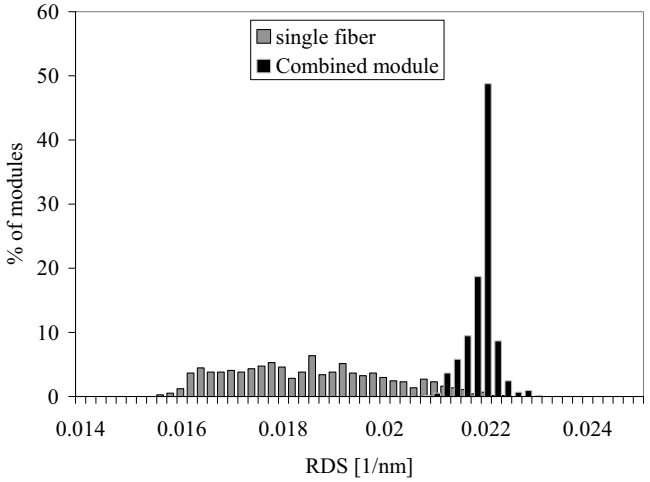

Fig. 16. The distribution of RDS values for the negative dispersion fiber and for the combined module. By making a combined module, the RDS distribution is narrowed significantly.

6. Dispersion Compensating Fiber Module with Reduced Physical Dimensions

In the previous sections the trade offs between dispersion properties and bend losses have been explored in order to design fibers with extreme dispersion properties such as a very negative dispersion or a high dispersion slope. It was found that the performance with respect to bend loss limits the obtainable dispersion properties.

The minimization of bend losses is also central when it comes to reducing the physical dimensions of a dispersion compensating fiber module.

Several approaches exist to reducing the size of the dispersion compensating fiber module. The approach to be discussed in this section is to reduce the diameter of the fiber *A*nd the inner diameter of the spool on which the fiber is wound in the dispersion compensating fiber module. Another strategy is to look at the packaging of the fiber in the dispersion compensating fiber module in order to reduce the microbend losses. [39,40]

6.1. Bend Losses

No matter how the challenge of decreasing the physical dimensions is approached, bend loss will limit the design:

If the approach to smaller physical dimensions is to decrease the fiber and/or coating diameter thereby decreasing the fiber volume, the microbend losses will be the limiting factor.

For a given fiber design Equation 33 reduces to

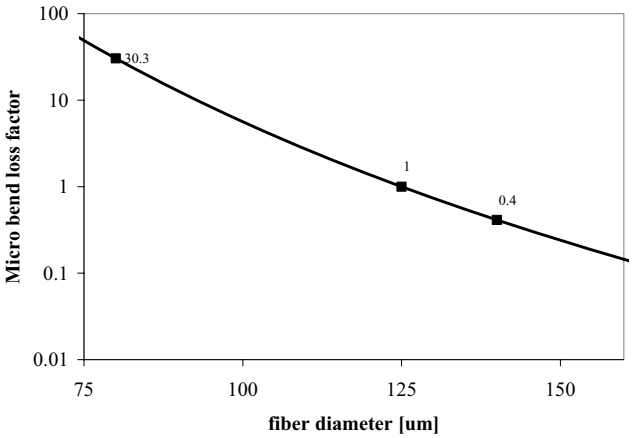

Fig. 17. Simulated micro bend loss factor as a function of fiber cladding (glass) diameter. The thickness of the coating is kept constant.

$$\alpha_{\text{micro}} \propto \frac{D}{H^2}. \tag{37}$$

For a given fiber design, the micro bend losses can be evaluated for different flexural and lateral rigidities of the fiber.

Expressions for the flexural rigidity (H) and lateral rigidity (D) of a double coated fiber has been derived in terms of the Young's modulus and the diameter of the fiber, primary and secondary coating layers [41]:

$$H = H_{\text{glass}} + H_{\text{sec.coat}} = \pi r_{\text{glass}}^4 E_{\text{glass}} + \pi (r_{\text{sec.coat}}^4 - r_{\text{prim.coat}}^4) E_{\text{sec.coat}} \tag{38}$$

and

$$D = E_1 + (E_2 - E_1) \left(\frac{E_1}{E_2}\right)^{2/3} \left(2\frac{r_2 - r_1}{r_2 - r_0}\right)^{2/3} \tag{39}$$

with E being Young's modulus and r the radius of the layer. Subscript 0 refers to the fiber, 1 to the primary coating and 2 to the secondary coating.

Figure 17 shows the micro bend loss as a function of fiber diameter for a given fiber design with the loss normalized to that of a fiber with diameter of 125 μm and a constant thickness of the coating layers.

If the fiber diameter is reduced from 125 to 80 μm, the microbend loss increases with a factor of 30. In order to achieve similar micro bend losses in an 80-μm fiber As in a 125-μm fiber, the micro bend loss performance must be increased by a factor of 30.

Another interesting point is that by increasing the fiber diameter, the microbend loss is improved. This effect has been utilized to fabricate a dispersion compensating fiber with high dispersion slope. The fiber diameter was increased to 140 μm thereby decreasing the microbend losses for an otherwise micro bend sensitive design. [34]

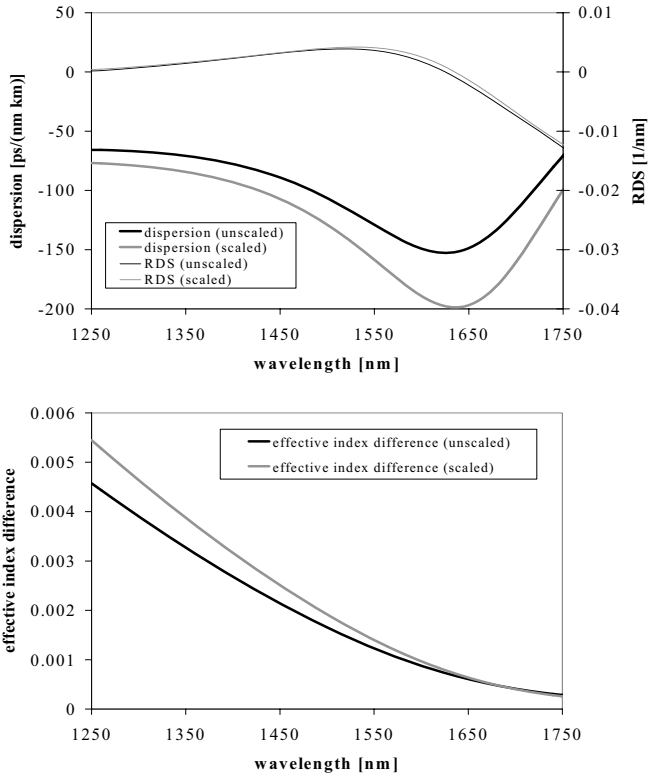

Fig. 18. The dispersion properties and effective index difference of a dispersion compensating fiber scaled as described in equation 12. By scaling the indices of all layers of a triple clad index profile with 1.2 and the areas of all layers by $1/\sqrt{1.2}$ both the effective index and the dispersion have been increased by a factor of 1.2 (Neglecting the material dispersion causes an error on the scaled dispersion of 3.7 ps/nm km). The only change in RDS due to the scaling of the profile is caused by the neglect of the material dispersion.

The main approach to improving the micro bend loss sensitivity of the dispersion compensating fiber is to increase the effective index difference.

The scaling outlined in section 3 [Eqs. (15)–(23)] shows how the effective index difference can be increased without significantly changing the dispersion properties.

Figure 18 shows the dispersion, RDS and effective index difference of two dispersion compensating fibers, where the scaled profile has been obtained from the unscaled by scaling the refractive indices of each layer by 1.2 and the widths by $1/\sqrt{1.2}$.

The RDS are almost unchanged by the scaling, while a large increase in effective index difference is observed, resulting in improved calculated micro bend losses of a factor of 5. [42] The error on the dispersion by neglecting material dispersion is of 3.7 ps/(nm km). This scaling is however not ideal as it would require the index of the core

to be increased by 20% which would greatly increase the attenuation of the fiber due to anomalous losses and Rayleigh scattering.

As discussed previously, increasing the effective index difference not only reduces the micro bend loss sensitivity, it also reduces the macro bend losses of the fiber.

The approach of increasing the effective index difference has been used to make a dispersion compensating fiber module with slope match to SSMF with reduced physical dimensions. [43] The properties of the fiber are listed in Table 4.

Table 4. Optical properties measured at 1550 nm for a dispersion compensating fiber with slope match to standard single mode fiber (RDS = 0.0035 nm^{-1}) and reduced physical dimensions.

	Dispersion (ps/nm km)	Attenuation (dB/km)	Typical splice loss (dB)	FOM (ps/nm dB)	Fiber diameter (μm)	Coating diameter (μm)	Residual dispersion variation (1530–1565 nm) (ps/nm km)
DCF for SSMF with reduced physical dimensions	–123	0.59	0.1	210	80	145	$\pm$0.02

The dispersion properties are comparable to that of fiber C of Table 3. Due to a higher core index, the attenuation is somewhat higher resulting in a FOM of only 210 ps/(nm dB). However, due to the improved bend loss performance, it has been possible to manufacture a dispersion compensating fiber module for compensating the dispersion of 70 km SSMF with a height of 22 mm and an outer diameter of 140 mm, which compared to an ordinary dispersion compensating fiber module with a height of 40 mm and an outer diameter of 199 mm, is a 4$\times$ reduction of the volume. Figure 1 shows a dispersion compensating fiber module with reduced physical dimensions in front of an ordinary module.

Since the design of the dispersion compensating fiber with reduced physical dimensions will be limited by the bend loss sensitivity, it will be more difficult to make a fiber that has both the reduced physical dimensions and extreme dispersion properties such as a very high dispersion slope or a very negative dispersion.

7. Nonlinear Phaseshift of Dispersion Compensating Fiber Modules

So far, the quality of a dispersion compensating fiber module has only been evaluated on the residual dispersion and the added loss to the system.

Dispersion and added loss are however not the only parameters which degrade the signal to noise ratio of the system. It has been shown that in systems with a low residual dispersion, the degradation of the signal can be linked to the nonlinear phaseshift of the dispersion compensating fiber module, which should be as small as possible. [44]

The nonlinear phaseshift (ϕ_{NL}) in a dispersion compensating fiber module in the configuration shown in Fig. 2 can be expressed as

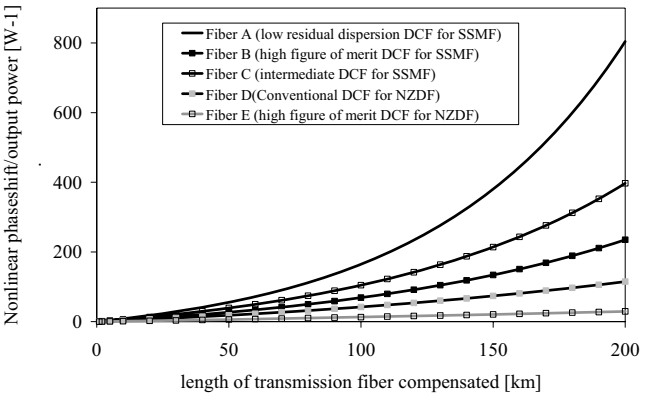

Fig. 19. The ratio of nonlinear phaseshift to output power as a function of length of transmission fiber compensated for dispersion compensating modules for SSMF and NZDF. The lowest nonlinear phaseshift is obtained for a high FOM dispersion compensating fiber module for NZDF.

$$\phi_{\mathrm{NL}} = \frac{2\pi n_2}{\lambda A_{\mathrm{eff}}} P L_{\mathrm{eff}} = \frac{2\pi n_2}{\lambda A_{\mathrm{eff}}} P_{in} \frac{(1 - \exp(-\alpha_{\mathrm{DCF}} L_{\mathrm{DCF}}))}{\alpha_{\mathrm{DCF}}} \tag{40}$$

with n_2 being the nonlinear refractive index, $\mathrm{A_{eff}}$ the effective area, P_{in} the input power to the dispersion compensating fiber module and L_{eff} the effective length. If the output power is kept constant, the signal to noise ratio can be assumed to be constant and P_{in} can be expressed as

$$P_{\mathrm{in}} = P_{\mathrm{out}} \exp(\alpha_{\mathrm{DCF}} L_{\mathrm{DCF}} + \alpha_{\mathrm{spl}}). \tag{41}$$

The ratio of nonlinear phaseshift to output power can now be calculated as

$$\frac{\phi_{NL}}{P_{\mathrm{out}}} = \frac{n_2 2\pi}{\lambda\alpha\ A_{\mathrm{eff}}} \exp\left(\alpha \frac{D_{\mathrm{tot}}}{D_{\mathrm{DCF}}} + \alpha_{\mathrm{sp}}\right) \left(1 - \exp\left(-\alpha \frac{D_{\mathrm{tot}}}{D_{\mathrm{DCF}}}\right)\right). \tag{42}$$

Using Eq. (42) the ratio of nonlinear phaseshift to output power can be evaluated for modules with different dispersion properties. [45] Figure 19 shows the ratio of nonlinear phaseshift to output power for the dispersion compensating fibers with slope match to SSMF listed in Table 3 as well as for two dispersion compensating fiber for NZDF (Table 5) with RDS values of 0.01 nm^{-1} matching that of TrueWave ® RS. Fiber E has the highest figure of merit reported for a dispersion compensating fiber of 459 ps/(nm dB). [14] This fiber is an example of how it can be easier to obtain a high figure of merit for a dispersion compensating fiber with a higher dispersion slope.

The ratio is shown as a function of length of transmission fiber compensated. It has been calculated using data from Tables 3 and 4 and n_2 of 2.7×10^{-20} for all fibers. n_2 has been measured for several dispersion compensating fibers using the CW beat signal method. [46]

The ratio of nonlinear phaseshift to output power depends mainly on the length of dispersion compensating fiber in the module. Consequently, the lowest ratio can

Table 5. Optical properties measured at 1550 nm for dispersion compensating fibers with slope match to Non Zero Dispersion Fibers (RDS = 0.01 nm^{-1})

		Dispersion (ps/nm km)	Attenuation (dB/km)	Typical splice loss (dB)	FOM (ps/nm dB)
DCF D	Conventional DCF for NZDF	–120	0.63	0.35	170
DCF E	High figure of merit DCF for NZDF	–302	0.66	0.3	459

be found for the dispersion compensating fiber for NZDF with high figure of merit. Not only does the lower accumulated dispersion on NZDF calls for shorter lengths of dispersion compensating fiber but the very negative dispersion of –302 ps/nm km reduces the required length of dispersion compensating fiber further. This also explains that even though fiber D has the lowest figure of merit of the 5 fibers, the ratio of nonlinear phaseshift to output power is only slightly higher than that for fiber E.

A higher ratio is seen for fiber B with the high figure of merit for compensating SSMF. This is again due to the shorter length of fiber needed in the module. As the figure of merit decreases, the ratio of nonlinear phaseshift to output power increases giving fiber A the highest ratio of the five fibers.

The lower ratio of nonlinear phaseshift to output power for the dispersion compensating fiber with high figure of merit is mainly due to the shorter length of fiber needed in a module, so the same effect on the nonlinear phaseshift would not be observed if the improvement in figure of merit was due to an improvement of the attenuation of the dispersion compensating fiber. [40,47]

8. Summary

In this paper it has been shown how the dispersion properties of the dispersion compensating fiber can be tailored by scaling the index profile.

The trade offs associated with the design of dispersion compensating fibers with extreme dispersion properties such as a very negative dispersion or very high dispersion slope has been discussed and it has been found that the main trade offs is between the desired dispersion properties and properties such as manufacturability and bending losses.

If less extreme dispersion properties can be accepted, it is possible to optimize the bend loss to a degree that makes it possible to manufacture a dispersion compensating fiber module with reduced physical dimensions.

For the fiber with a high figure of merit it was shown how increasing the negative dispersion by operating closer to the minimum of the dispersion curve can give problems with bend losses as the effective index difference at this wavelength is low.

It was also shown how increasing the figure of merit by increasing the negative dispersion of the dispersion compensating fiber, thus decreasing the length of fiber needed in a module, improves the performance of the module with respect to nonlinearities.

For fibers with high dispersion slope, increasing the dispersion slope will cause the usable bandwidth to be smaller as the dispersion curve becomes narrower with increasing RDS. As for the dispersion compensating fibers with high figure of merit, the bend losses are usually high for this type of fiber. The improvement of macro bend losses will usually cause the cutoff wavelength to increase giving problems with MPI.

It has also been shown how a dispersion compensating fiber module with slope match to the high slope NZDFs (RDS = 0.02 nm^{-1}) can be manufactured by combining a dispersion compensating fiber having a lower RDS value with a positive dispersion fiber having a lower RDS than the dispersion compensating fiber. The advantages of this solution are a better control of the RDS of the module, and a dispersion compensating fiber with lower bend losses and better manufacturability.

Finally, by improving the bend loss performance a dispersion compensating fiber module with reduced physical dimensions have been manufactured.

References

1. L.E. Nelson, Optical Fibers for High-Capacity WDM, Long haul systems, IEICE Trans. Electron., **E86-C** (5), 693–698 (2003).
2. L. Grüner-Nielsen, S.N. Knudsen, T. Veng, B. Edvold, C.C. Larsen, Design and manufacture of dispersion compensating fibre for simultaneous compensation of dispersion and dispersion slope, OFC/IOOC'99 Optical Fiber Communication Conference and the International Conference on Integrated Optics and Optical Fiber Communications (1999), vol. 2, pp. 232–234.
3. L. Grüner-Nielsen, S.N. Knudsen, B. Edvold, T. Veng, D. Magnussen, C.C. Larsen, H. Damsgaard, Dispersion compensating fibers, Opt. Fiber Technol., **6**, 164–180 (2000).
4. L. Grüner-Nielsen, B. Edvold, Status and future promises for dispersion compensating fibres, Proceedings of 2002 European Conference on Optical Communications, Paper 6.1.1.
5. J. Rathje, L. Grüner-Nielsen, Relationship between relative dispersion slope of a transmission fiber and the usable bandwidth after dispersion compensating, Proceedings of 2002 European Conference on Optical Communications, Paper P1.23.
6. J.U. Jeon, H.K. Seo, Y.T. Lee, Wide-band High Negative Dispersion-Flattened Fiber, Proceedings of 2002 European Conference on Optical Communications, Paper P1.35.
7. T. Wang, Y. Cao, J. Luo, Dispersion compensation fiber working in U band, Proceedings of 2003 Optical Fiber Communications, Paper MF2.
8. J. Rathje, M. Andersen, L. Grüner-Nielsen, Dispersion Compensating fiber for identical compensation in the S, C and L band, Proceedings of 2003 Optical Fiber Communications, Paper FK6.
9. V.M. Schneider, J.A. West, Analysis of wideband dispersion slope compensating optical fibres by supermode theory; Electron. Lett., **38** (7), 306–307 (2002).
10. P. Kristensen, Design of dispersion compensating fiber, Proceedings of 2004 European Conference on Optical Communications, Paper We3.31.
11. J.L. Auguste, J.M. Blondy, J. Maury, J. Marcou, B. Dussardier, G. Monnom, R. Jindal, K. Thyagarajan, B.P. Pal, Conception, realization and characterization of a very high negative chromatic dispersion fiber, Optical Fiber Technology, **8**, 89–105 (2002).
12. J.-L. Auguste, R. Jindal, J.-M. Blondy, M. Clapeau, J. Marcou, B. Dussardier, G. Monnom, D.B. Ostrowsky, B.P. Pal, K. Thygarajan, –1800 ps/(nm km) chromatic dispersion at 1.55 micron in dual concentric core fibre, Electron. Lett., **36** (20), 1689 (2000).

13. D.W. Hawtof, G.E. Berkey, A.J. Antos, High figure of merit dispersion compensating fiber, Proceedings of 1996 Optical Fiber Communications, Paper PD6.

14. M. Wandel, T. Veng, Q. Le, L. Grüner-Nielsen, Dispersion compensating fibre with a high figure of merit; Proceedings of 2001 European Conference on Optical Communications, Paper PD.A.1.4.

15. M.E. Lines, Scattering Losses in optic fiber materials II. Numerical estimates, J. Appl. Phys., **55** (11), 4058–4063 (1996).

16. M.E. Lines, Optical losses from compositional fluctuations in three-component glasses, J. Non-crystalline Solids, **195**, 249–260 (1996).

17. K. Saito, A.J. Ikushima, Reduction of light-scattering loss in silica glass by the structural relaxation of "frozen-in" density fluctuations, Appl. Phys. Lett., **70** (26), 3504–3506 (1997).

18. S. Sakaguchi, S. Todoriki, Rayleigh Scattering of silica core optical fiber after heat treatment, Appl. Opt., **37** (33), 7708–7711 (1998).

19. C. Brehm, P. Dupont, G. Lavanant, P. Ledoux, C. Le Sergent, C. Reinaudo, J.M. Saugrain, M. Carratt, R. Jocteur, Improved drawing conditions for very low loss 1.55 my dispersion shifted fiber, Fiber Integrated Opt., **7**, 333–341 (1988).

20. P. Guenot, P. Nouchi, P. Poumellec, Influence of drawing temperature on light scattering properties of single mode fibers, Proceedings of the 1999 Optical Fiber Communications, paper ThG2.

21. M. Ohashi, K. Shiraki, K. Tajima, Optical loss property of silica-based single mode fibers, J. Lightwave Technol., **10** (5), 539–543 (1992).

22. M.E. Lines, W.A. Reed, D.J. DiGiovanni, J.R. Hamblin, Explanation of anomalous loss in high delta singlemode fibres, Electron. Lett., **35**, 12 (1999).

23. M.M. Bubnov, S.L. Semjonov, M.E. Likhachev, E.M. Dianov, V.F. Khopin, M.Y. Salganskii, A.N. Guryanov, J.C. Fajardo, D.V. Kuksenkov, J. Koh, P. Mazumder, Optical loss reduction in highly GeO2-doped single-mode MCVD fibers by refining refractive index profile, Proceedings of 2003 European Conference on Optical Communications, Paper Tu1.7.3.

24. M.M. Bubnov, S.L. Semjonov, M.E. Likhachev, E.M. Dianov, V.F. Khopin, M.Y. Salganskii, A.N. Guryanov, J.C. Fajardo, D.V. Kuksenkov, J. Koh, P. Mazumder, On the origin of excess loss in highly GeO_2 doped single-mode MCVD fibers, IEEE Photon. Technol. Lett., **16** (8), 1870–1872 (2004).

25. S.B. Andreasen, New bending loss formula explaining bends on the loss curve, Electron. Lett., **23** (21), 1138–1139 (1987).

26. M. Kato, T. Sugie, K. Okamoto, Generation of Negative third-order Dispersion in Coiled Single-Mode Fibers, IEEE Photon. Technol. Lett., **13** (5), 463–465 (2001).

27. F. Koch, S.V. Chernikov, J.R. Taylor, L. Grüner-Nielsen, Effect of macro-bending on dispersion of dispersion compensating fibres, Electron. Lett., **35**, 8 (1999).

28. I.J. Blewett, Effect of bending on chromatic dispersion of singlemode optical fibres; Electronic Letters, **30** (7), 592–593 (1994).

29. S. Février, J.-L. Auguste, J.-M. Blondy, A. Peyrilloux, P. Roy, D. Pagnoux, Accurate tuning of the highly negative chromatic dispersion wavelength into a dual concentric core fibre by macro-bending, Proceedings of 2002 European Conference on Optical Communications, Paper P1.8.

30. D. Marcuse, Microdeformation losses of single-mode fibers, Appl. Opt. **23** (7), 1082–1091 (1984).

31. D. Gloge, Optical fiber packaging and its influence on fiber straightness and loss, Bell Syst. Techn. J., **54** (2), 245–262 (1975) .
32. Y. Ohtera, O. Hanaizumi, S. Kawakami, Numerical Analysis of Eigenmodes and Splice Losses of Thermally Diffused Expanded Core Fibers, J. Lightwave Technol., **17** (12), 2675–2681 (1999).
33. D.B. Mortimore, J.V. Wright, Low-loss joints between dissimilar fibres by tapering fusion splices, Electron. Lett., **22** (6), 318–319 (1986).
34. E.M. O'Brien, C.D. Hussey, Low-loss fattened fusion splices between different fibers, Electron. Lett., **35** (2), 168–169 (1999).
35. B. Edvold, L. Grüner-Nielsen, New technique for reducing the splice loss to dispersion compensating fiber, Proceedings of 22nd European Conference on Optical Communication (1996), Paper TuP.07.
36. J. Refi, Optical Fibers for Optical Networking, Bell Labs Techn. J., January–March 1999, pp. 246–261.
37. Q. Le, T. Veng, L. Grüner-Nielsen, New dispersion compensating module for compensation of dispersion and dispersion slope of non-zero dispersion fibres in the C-band, Proceedings of 2001 Optical Fiber Communications, Paper TuH5.
38. V. Srikant, Broadband dispersion and dispersion slope compensation in high bit rate and ultra long haul systems, Proceedings of 2001 Optical Fiber Communications, Paper TuH1.
39. M. Wandel, P. Kristensen, T. Veng, Y. Qian, Q. Le, L .Grüner-Nielsen, Dispersion compensating fibers for non-zero dispersion fibers, Proceedings of 2002 Optical Fiber Communications, Paper WU1.
40. H. Hatayama, M. Hirano, T. Yokokawa, T. Kato, M. Onishi, E. Sasaoka, Dispersion compensating fiber for large-A_{eff} NZ-DSF with low residual dispersion by the technique of suppressing the micro-bending loss, Proceedings of 2003 European Conference on Optical Communications, Paper We 4.P.32.
41. W. Zheng, H.P. Sardesai, M.G. Taylor, D.L. Craig, J. Fowlkes, J.R. Simpson, Measurement and system impact of multipath interference from dispersion compensating fiber modules, IEEE Trans. Instrumentation Measurement, **53** (1), 15–23 (2004).
42. M. Ohashi, N. Shibata, K. Sato, Evaluation of length dependence of cutoff wavelength in a cabled fiber, Opt. Lett., **13** (12), 1123–1125 (1988).
43. K. Kitayama, M. Ohashi, Y. Ishida, Length dependence of effective cutoff wavelength in single mode fibers, J. Lightwave Technol., **2** (5), 629–633 (1984).
44. L.V. Jørgensen, J.S. Andersen, S. Primdahl, M.N. Andersen, B. Edvold, Next generation dispersion compensating modules for 40 Gbit/s systems, Proceedings of 2002 NFOEC, pp. 1171–1182.
45. T. Yokokawa, T. Kato, T. Fujii, Y. Yamamoto, N. Honma, A. Kataoka, M. Onishi, E. Sasaoka, K. Okamoto, Dispersion compensating fiber with large negative dispersion around –300 ps/nm/km and its application to compact module for dispersion adjustment; Proceedings of 2003 Optical Fiber Communications, Paper FK5.
46. T. Kato, M. Hirano, K. Fukuda, A. Tada, M. Onishi, M. Nishimura, Design optimization of dispersion compensating fiber for NZ-DSF considering nonlinearity and packaging performance, Proceedings of 2001 Optical Fiber Communications, Paper TuS6.
47. F. Cocchini, The lateral rigidity of double-coated optical fibers, J. Lightwave Technol., **13** (8), 1706–1710 (1995).
48. K. Petermann, Theory of microbending loss in monomode fibers with arbitrary index profile, Archiv. Elektron. Ubertragungstechn., **30** (9), 227–342 (1976).

49. P. Kristensen, M.N. Andersen, B. Edvold, T. Veng, L. Grüner-Nielsen, Dispersion and slope compensating module for G.652 fiber with $\times 4$ reduced physical dimensions, Proceedings of 2003 European Conference on Optical Communications, Paper We4.P.15.

50. A.R. Chraplyvy, Limitations on Lightwave Communications imposed by optical-fiber nonlinearities, J. Lightwave Technol., **8** (10), 1548–1557 (1990).

51. L. Grüner-Nielsen, Dispersion compensation, techniques and system requirements, Proceedings of 2003 European Conference on Optical Communications, Paper Mo4.7.1.

52. A. Boskovic, S.V. Chernikov, J.R. Taylor, L. Grüner-Nielsen, O.A. Levring, Direct continous-wave measurement of n_2 in various types of telecommunication fiber at 1.55 mum, Opt. Lett., **21** (24), 1966–1968 (1996).

53. P. Sillard, B. Dany, A. Bertaina, L. Curinckx, C. Bastide, O. Courtois, J.-C. Antona, S. Bigo, Simple Criterion of Quality to evaluate DCM impact on WDM system performance, Proceedings of 2004 Optical Fiber Communications.

DOI: 10.1007/s10297-006-0074-4
Originally published in J. Opt. Fiber. Commun. Rep. 4, 86–109 (2007)

Design optimization of dispersion compensating fibers and their packaging techniques

T. Kato, M. Hirano, T. Fujii, T. Yokokawa, Y. Yamamoto and M. Onishi

Sumitomo Electric Industries, Ltd.

Abstract. Design optimization of dispersion compensating fibers (DCFs) based on the fundamental mode is described considering the packaging technique. Optical performances of the DCF modules are mainly limited by the macro-, micro-bending loss and the polarization mode dispersion that strongly depend on the module structure. Two types of DCF modules are demonstrated as examples. Bobbin-less module structure that mitigates the bending limit is also described.

1. Introduction

Fiber-based dispersion compensation is an attractive technique to upgrade the systems because of its dispersion characteristics and compatibility to transmission fibers. Dispersion compensating fiber (DCF) was proposed to equalize the pulse distortion in 1980 [1]. In the early 1990s, numerous DCFs [2–6] were proposed and developed for commercial use. They were initially developed to upgrade the existing systems using 1.3 μm standard single-mode fibers (SSMFs) to higher bit-rate systems [7,8] or long distance transmission [9] in the 1.55-μm windows. The DCFs are designed to have large negative dispersion at 1.55 μm to compensate for the positive dispersion of the SSMFs typically having 17 ps/nm/km. With the development of the wavelength division multiplexing (WDM) techniques for large capacity transmission systems [10], DCFs to compensate for the dispersion slope of the SSMFs as well as the dispersion have been required and developed. The DCFs have also been developed to upgrade the systems using the non-zero dispersion shifted fibers (NZ-DSF) which have relatively low dispersion and high dispersion slope [11–16]. In order to have a large negative dispersion or low optical nonlinearity, the DCFs based on the higher-order mode like LP_{11} or LP_{02} were also proposed and developed [17–19]. The DCFs having an extremely

large negative dispersion or DCFs compensating for the loss as well as the dispersion of the transmission fibers simultaneously were also proposed and demonstrated [20,21].

In order to realize compactly packaged and high performance DCF modules, other optical performances of the DCFs such as attenuation, polarization mode dispersion (PMD), optical nonlinearities and bending characteristics have been considered in their designs. The bending loss is especially critical issue to limiting the performance of the DCF modules. Therefore the packaging technique including optical or mechanical reliabilities deserves much focus.

In this paper, design optimization of the DCFs based on the fundamental mode is demonstrated considering the packaging performances. Actually fabricated high performance DCF modules are shown. A novel bobbin-less packaging technique is also demonstrated to improve the performance of the DCF modules.

2. Fiber Design and Module Performance

2.1. General Requirement for DCF Module

Dispersion compensating fiber modules (DCFMs) are consisted of dispersion compensating fibers (DCFs) and pigtail fibers at both ends of the DCFs to connect to the transmission fibers, such as standard single mode fibers (SSMFs) or non-zero dispersion shifted fibers (NZ-DSFs). The lengths of the DCFs are determined to cancel out the accumulated dispersion of the transmission fibers within the proper amount of residual dispersion [22]. Various characteristics of the DCFs in addition to the dispersion must be considered to realize the high performance DCFMs. The general requirements for the DCFMs are given below.

(a) Exactly matched dispersion for transmission fibers
(b) Low insertion loss
(c) Low polarization mode dispersion (PMD)
(d) Low nonlinearity
(e) Small packaging size
(f) Stability for environmental variation

Cancellation of the accumulated dispersion over the signal wavelengths is required for the wavelength division multiplexing (WDM) transmission. The dispersion slope compensation ratio (DSCR) defined by Eq. (1) is introduced to represent the excellence in terms of the dispersion characteristics.

$$\mathrm{DSCR} = (S_{\mathrm{DCF}}/D_{\mathrm{DCF}})/(S_{\mathrm{TF}}/D_{\mathrm{TF}}) \tag{1}$$

where D_{TF}, S_{TF}, D_{DCF} and S_{DCF} represent the dispersion and the dispersion slope of the transmission fiber and the DCF. The DSCR of 100% is the best DCF for the WDM transmission.

In order to keep the high signal to noise ratio (S/N), the insertion loss of the DCFM is expected to be as small as possible. The total accumulated dispersion to cancel out by the DCFM is determined in advance, so the figure of merit (FOM) defined by Eq. (2) has been introduced to express the excellence of the DCF in terms of the attenuation.

$$\mathrm{FOM} = D/\alpha, \tag{2}$$

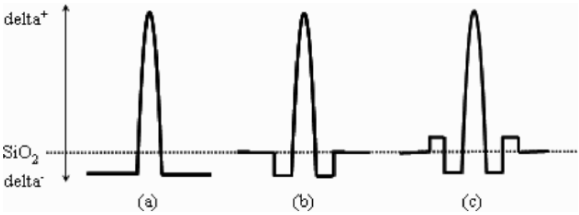

Fig. 1. Schematic diagram of the index profiles with (a) matched cladding, (b) double cladding (W-shape) and (c) triple cladding.

where D and α represent the dispersion and the attenuation of the DCF. In general, the mode field diameter of the DCF based on the fundamental mode is relatively small, so the splice loss between the DCF and the pigtail fiber is notable because of the mode field mismatch. Therefore the low splice techniques such as the thermal diffusion of the dopant [23–26] or the use of an intermediate fiber [27] is required to reduce the insertion loss.

Low PMD is required for the DCFM to realize high-speed transmission systems. It is well known that the PMD occurs by winding the fiber at a small diameter because of the bend-induced birefringence [28]. Therefore the bend-induced PMD must be carefully considered in the design of the DCFM package in addition to reducing the PMD of the DCF itself.

Optical nonlinearities [29] such as self-phase-modulation (SPM) and cross-phase-modulation (XPM) are also critical issues in the high-speed transmission systems. The optical nonlinearities occurring in the DCFM depend on the fiber length and the input power as well as the nonlinear coefficient of the DCF itself. Therefore various parameters of the DCF should be considered to minimize the effect of the nonlinearities.

The size of the DCFM and the stability for the environmental variation should also be considered in practical use. In general, the DCFMs are placed after the transmitter, in the amplifier, or before the receiver in the terminal buildings having limited spaces. The macro- and micro- bending performance of the DCF is essential to realize the compact package and stable optical characteristics of the DCFM against environmental variation such as temperature.

The DCFs are designed in their refractive index profiles while considering these requirements for the DCFMs. The schematic diagram of the index profiles widely used for the DCFs is shown in Fig. 1.

The matched cladding type of DCF which compensates for only dispersion of the transmission fibers is used for a single channel transmission. The double cladding (W-shape) and triple cladding type of DCFs which compensate for both dispersion and dispersion slope simultaneously are used for the WDM transmission. In this section, the design optimization for two types of DCFM has been set apart and demonstrated as examples. One is the DCFM for the NZ-DSF whose design is determined by the optical nonlinearities, maintaining good microbending performance. Another is the quite small size of DCFM to compensate for the small amount of the dispersion whose design is determined by the macrobending performance and the bend-induced PMD.

These means to optimize the design of the DCF are applicable to other DCFM designs for different transmission fibers.

2.2. DCF Module for NZ-DSF

The NZ-DSFs [16,30–32] have been widely installed for large capacity transmission employing the WDM technology. The DCFs [11–16] which compensate for both dispersion and dispersion slope of the NZ-DSFs are also necessary when these lines are intended to be upgraded to the wide-band, high bit-rate transmission systems, such as 10 Gb/s or higher [32–34]. The DCF to compensate for both the dispersion and dispersion slope of the SSMF typically has the dispersion and dispersion slope of –100 ps/nm/km, –0.34 ps/nm^2/km, respectively. They are intended to match the dispersion characteristics of the SSMF. On the other hand, the NZ-DSF has a relatively large dispersion slope to the dispersion compared with the SSMF. Table 1 summarizes the typical dispersion characteristics of the SSMF and the NZ-DSFs.

Table 1. Typical dispersion characteristics of transmission fibers at 1.55 μm.

Fiber Type	A_{eff} [μm^2]	Dispersion, D [ps/nm/km]	Dispersion Slope S [ps/nm^2/km]	S/D [1/nm]
SMF	85	+17	+0.06	0.0035
NZ-DSF with large effective area [27]	70	+4	+0.09	0.023
NZ-DSF with low dispersion slope [28]	55	+4.5	+0.045	0.010
NZ-DSF with medium dispersion [15,29]	65	+8	+0.06	0.0075

It shows that the NZ-DSFs have a large dispersion slope ratio, S/D compared with the SSMF. The negative dispersion slope of the DCF is produced by the large waveguide dispersion near the cutoff of the fundamental mode. Therefore it is difficult to realize the DCF having a large negative dispersion slope that maintains the same dispersion because the design of the DCF tends to become a more bend-sensitive one. In [13], the DCF with the large dispersion slope ratio of 0.018 [1/nm] has been reported, but it is difficult to compensate perfectly for the dispersion slope of the NZ-DSF with a large dispersion slope ratio by using one kind of DCF. The packaging technique is a more prominent issue to realize a module using such bend-sensitive fiber. Moreover, for these high-speed systems, the fiber nonlinearity occurring in the DCFs is also one of the main factors to limit the transmission performance.

In this section, the optimum designs of the DCFs for two types of NZ-DSFs have been explored considering both nonlinear phase shifts induced by the self-phase modulation and the bending performance required for packaging. In addition, actually fabricated high performance DCFs and DCFMs have been demonstrated.

The DCF has relatively high nonlinearity because of its small effective area (A_{eff}) and a high nonlinear refractive index (n_2). The self-phase modulation (SPM) is an especially serious problem limiting the transmission performance of the DCF, while four-wave mixing (FWM) seldom occurs because of its large chromatic dispersion. We have examined the SPM effect quantitatively by calculating the nonlinear phase shift caused by the SPM. The SPM-induced phase shift is expressed by the equation [29]

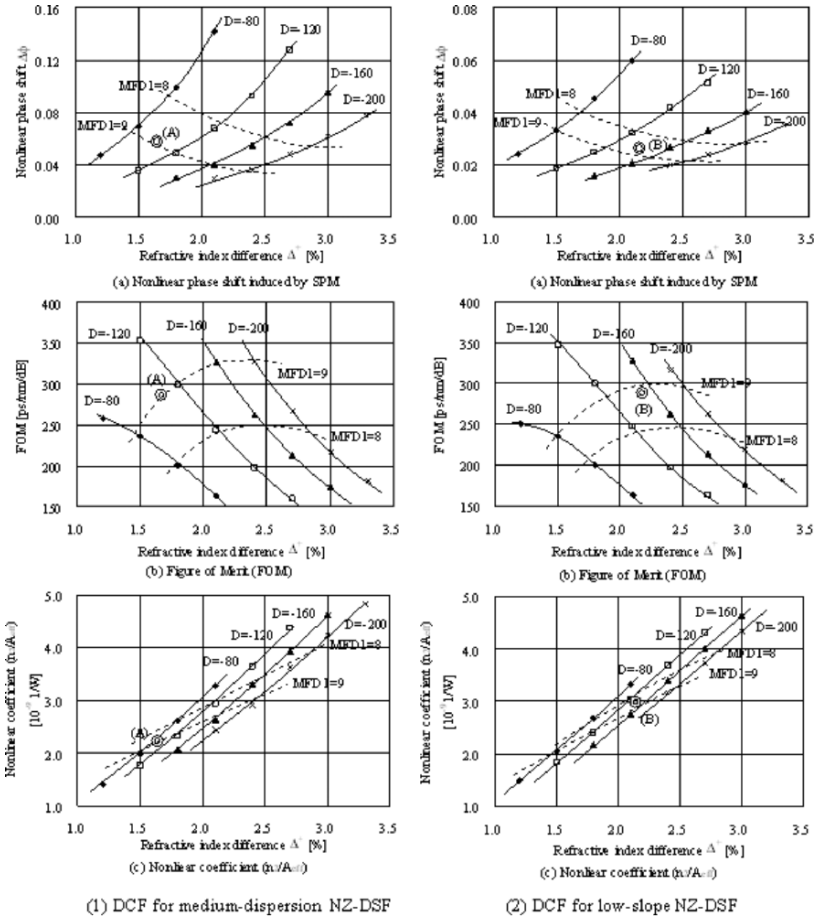

Fig. 2. DCF design optimization diagrams for two types of NZ-DSF.

$$\Phi = \frac{2\pi}{\lambda}\frac{n_2}{A_{\text{eff}}} L_{\text{eff}} P_0, \tag{3}$$

where L_{eff} is the effective length of the DCF. The length of the DCF is determined so as to compensate for 100-km-long NZ-DSF. P_0 is the signal power launched into the DCF. In order to keep the signal to noise ratio (S/N) constant at the output end of the DCF, P_0 is adjusted so as to give the same power at the output [35]. The output power of the DCF is assumed to be –3 dBm for the dual-stage amplifier where the DCFM is placed between two amplifiers. Two types of NZ-DSFs have been considered here. One is a medium-dispersion type NZ-DSF and the other is a low-slope type NZ-DSF listed in Table 1.

Figures 2 (1) and (2) show calculation results of the nonlinear phase shift, the figure of merit (FOM) and the nonlinear coefficient (n_2/A_{eff}) as a function of the refractive

index difference, Δ^+ of the DCFs. In this case, the refractive index profile with triple cladding has been adopted because of its relatively good bending performance. The fiber characteristics have been calculated by the finite element (FEM) method [36]. The transmission loss has been estimated from the empirical dependence on the GeO_2 concentration in the core, and the nonlinear refractive index has also been estimated by using the dependence on the GeO_2 concentration determined by the XPM method [37]. In Fig. 2 (1) and (2), the dispersion value D, is set to several levels while maintaining perfect compensation of the dispersion slope. Bending performance, especially microbending performance is an important factor governing the packaging performance because the winding diameter of the fiber is usually determined so as not to cause macrobending loss. In Fig. 2 (1) and (2), calculation results of the mode field diameter, 2ω by Petermann's first definition (MFD1) are also shown [38]. It is expressed by

$$2\omega = 2\sqrt{2\int_0^\infty \phi^2(r)r^3dr \Big/ \int_0^\infty \phi^2(r)rdr}, \tag{4}$$

where $\phi(r)$ is the electrical distribution in the radial direction. MFD1 is believed to well represent the microbending performance [38,39]. By comparing the calculated MFD1 with the loss increase observed in actually fabricated DCFMs, the maximum allowable MFD1 has been estimated. Here, a newly developed bobbin-less DCF module has been used. In this module, the bobbin to wind the fiber is removed and the fiber is suspended in a bed of resin, so that the bending loss caused by the winding tension or the weight of the fiber itself is minimized. The details of this bobbin-less DCF module are described in section 3.1. The MFD1 of around 9 μm is the maximum limit to sufficiently suppress loss increase in the entire C-band.

From Figs. 2 (1) and (2), the phase shifts are found to be minimized with Δ^+ of 2.5 $\sim$ 2.7 % for both cases. When the refractive index difference Δ^+ is too small, FOM deteriorates due to small absolute dispersion. When the refractive index difference Δ^+ is too high, FOM also deteriorates because of increased fiber attenuation. It is found that obtaining the highest FOM is the most effective means to also suppress the SPM-induced phase shift in spite of an increase in the nonlinear coefficient $(n_2/A_{\rm eff})$. The DCF optimized for the medium-dispersion NZ-DSF has a better FOM and lower nonlinear coefficient than those for the low-slope NZ-DSF. This is because medium-dispersion NZ-DSF has a lower dispersion slope ratio, S/D which makes it easier to design the DCF with maintaining the good bending performance. The phase shift in the DCF for medium-dispersion NZ-DSF, however, is larger than that for the low-slope NZ-DSF, because of the large amount of the accumulated dispersion.

Table 2 summarizes characteristics of fabricated DCFs. The dispersion slope compensation ratios are 110% and 123% for the medium-dispersion NZ-DSF, and 82% and 92% for the low-slope NZ-DSF, respectively. Figure 3 shows spectral dispersion characteristics and loss spectra of the bobbin-less DCF modules fabricated using these fibers. Loss increase over the entire C-band has been suppressed well in both DCF modules, especially in Type B. The loss increase at a longer wavelength is less noticeable in Type B than in Type A. This suggests that the absolute dispersion value and FOM of Type B can be further enlarged while maintaining a sufficiently low loss increase in the C-band.

The bobbin-less DCFM with the fabricated DCF has also been evaluated. This DCFM compensates for the dispersion of the 50-km-long medium-dispersion type

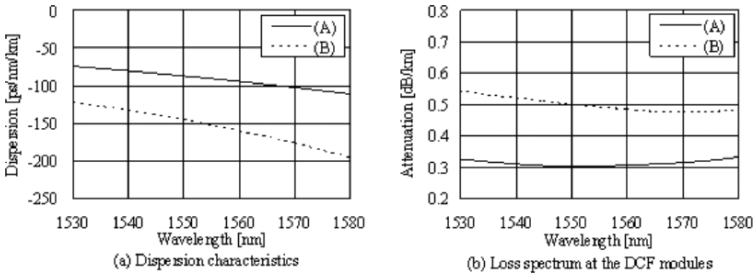

Fig. 3. Dispersion and loss spectra of the modules using two types of DCF listed in Table 2 [16].

Table 2. Characteristics of fabricated DCFs measured at 1.55 μm.

No.	Δ^+ [%]	Loss [dB/km]	Dispersion [ps/nm/km]	Slope [ps/nm^2/km]	FOM [ps/nm/dB]	A_{eff} [μm^2]	Φ SPM (medium-disp.)	Φ SPM) (Low-slope)
(A)	1.6	0.30	–87	–0.71	290	19	0.057	0.030
(B)	2.2	0.50	–145	–1.34	290	15	0.053	0.026

NZ-DSF. Table 3 summarizes the characteristics of the DCFM. Figure 4 shows the insertion loss including splice loss and the averaged dispersion when the NZ-DSF and the DCFM are concatenated. The splice loss between the DCF and the SSMF as a pigtail fiber is around 0.2 dB at 1.55 μm per splice by using the heat treatment. The low residual dispersion below $\pm$0.08 ps/nm/km has been obtained in the C-band. This DCFM having the characteristics such as low nonlinearities, low insertion loss and low residual dispersion leads to realizing the high-bit rate transmission systems.

Table 3. Characteristics of fabricated DCFM measured at 1.55 μm.

Items	Characteristics
Dispersion	–420 ps/nm
Dispersion Slope	–3.9 ps/nm^2
PMD	0.29 ps
Module Insertion Loss	1.9 dB
Size (W*D*H)	230*230*40mm

2.3. Compact DCF Module for Dispersion Adjustment

The DCFs have contributed to upgrade the transmission lines owing to their various advantages such as broad bandwidth and low insertion loss. Recent progress in the high bit-rate transmission systems such as 40 Gb/s requires the precise tuning of the residual dispersion over entire signal wavelengths [32,34]. In addition, some of the metro-core systems require the dispersion compensation according to their system lengths or bit

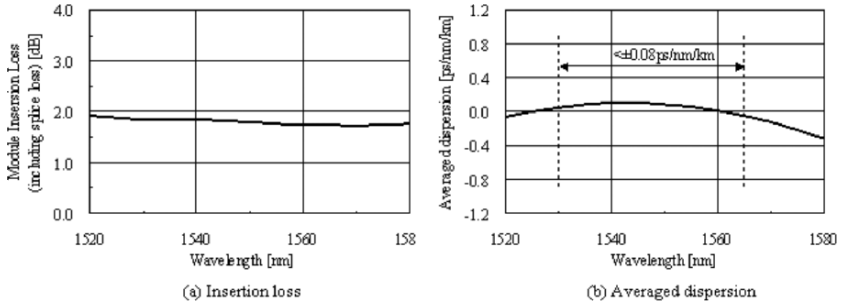

Fig. 4. Insertion loss of the DCFM and averaged dispersion when the NZ-DSF and DCFM are concatenated.

rates. Furthermore, in the high-speed, cost effective systems, the signal chirping of the directly modulated lasers must be compensated at the transmitter. For these purposes, it is strongly considered that a new class of DCFM with a low insertion loss and an extremely small package is indispensable for adjusting a relatively small amount of the dispersion. In order to realize a small package, the length of DCF must be short, less than 1 km, which is also beneficial to low-cost designing.

In this section, the DCF with a quite large negative dispersion around –300 ps/nm/km has been explored while maintaining good bending performance. In this case, the macrobending loss or the bend-induced PMD are the limiting factors to realize the high performance DCFM because the smallest possible winding diameter of the coil is required. In the fiber design, a flattened dispersion performance is also considered in order to apply the DCF to both C- and L-bands. Based on the optimization of the index profile, several DCFs have been actually fabricated which have large negative dispersion of –300 ps/nm/km while maintaining good bending performance.

The refractive index profile of the DCF used in this study is the triple cladding type shown in Fig. 1. The calculation results by the FEM method for the macrobending loss [40] as a function of the absolute values for the chromatic dispersion are shown in Fig. 5. Two bending diameters of 20 and 60 mm are picked up in this figure. As shown in section 2.2, the large refractive index difference, Δ^+ is preferable to realize the large negative dispersion while maintaining good bending performance. Therefore the Δ^+ is fixed at 2.7%, and Δ^- is set to be –0.3, –0.5% and –0.7% in this calculation. The radii of the core, the first cladding and the second cladding are adjusted so as to realize the flattened dispersion spectrum and to make the cutoff wavelength to be 1450 nm.

Figure 5 shows that the macro-bending loss increases with the large absolute value of the dispersion, $|D|$ and it is dramatically improved by reducing the Δ^-. For example, in the case of $|D|$ of 300 ps/nm/km, the bending loss at 60 mmϕ is about 3 dB/km for the $\Delta^-$of –0.3%, but it is improved to 10^{-6} dB/km by employing the $\Delta^-$of –0.7%. Several DCFs have been fabricated based on this calculation. Measurement results for the bending loss at 20 mmϕ are plotted in Fig. 5, indicating good agreement with the calculation results. Other characteristics of the fabricated DCFs with the Δ^- of –0.7% are also listed in Table 4. These are measured with a bobbin having a diameter of 280

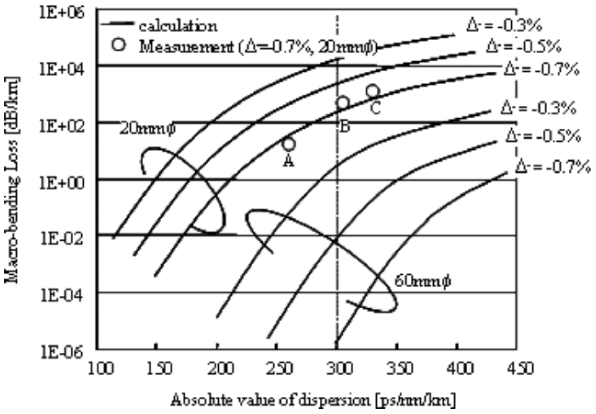

Fig. 5. Calculation results for the macro-bending loss at a diameter of 20 and 60 mm.

mm. A large negative dispersion of –330 ps/nm/km is realized, and the FOM is as high as 314 ps/nm/dB.

Table 4. Characteristics of the fabricated DCF at 1550 nm.

Loss [dB/km]	Dispersion [ps/nm/km]	Slope [ps/nm^2/km]	FOM [ps/nm/dB]	A_{eff}] [μm^2]
1.05	–330	–0.62	314	18

Figure 6 shows the dispersion characteristics and the loss spectra of the fabricated DCF. The dispersion variances in the C-band and the L-band are small because of its low dispersion slope. This is favorable for practical use because one can use the same module to compensate for the same amount of the dispersion at other signal wavelengths. Figure 6 shows that the attenuation is degraded by winding the fiber on a small coil with a diameter of 60 mmϕ. It is, however, dramatically improved by winding it on the bobbin-less module described in section 3.1. This fact and the calculation result of the macrobending loss in Fig. 6 indicate that the loss increase is caused by the micro-bending loss, not by the macro-bending loss.

When the fiber is wound at a small diameter to realize a compact package module, the bend-induced PMD should be also considered. It is well known that the PMD of a bent fiber is increased because of bending-induced birefringence, $\Delta\beta$ which is expressed [28] by

$$\Delta\beta = 0.25kn^3(p_{11} - p_{12})(1 + \upsilon)d^2/D^2, \tag{5}$$

where k denotes a wave number, n is a refractive index of the fiber core, p_{ii} are strain-optical coefficients, υ is a Poisson's ratio, d is a fiber diameter, and D is a bending diameter. Taking into account the mode coupling, bend-induced PMD, $\Delta\tau$ is expressed by [41]

$$\Delta\tau = \sqrt{hL} \times (\Delta\beta/kc) \quad \text{for } L/h \ll 1, \tag{6}$$

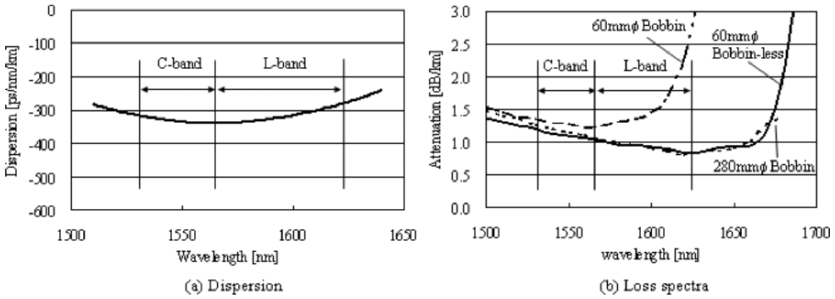

Fig. 6. Dispersion characteristics and loss spectra for fabricated DCF.

where L denotes fiber length, c is the velocity of light, h is coupling length. With the presence of the frequent mode coupling, PMD increases as the square root of the fiber length. By using the constant parameters for fused silica [28], $n = 1.46$, $p_{11} - p_{12} = -0.15$, $\nu = 0.17$ and the fiber diameter of 125 μm, Eq. (6) is rewritten by

$$\Delta\tau = 7.1\sqrt{hL}/D^2. \tag{7}$$

Equation (7) indicates that the bend-induced PMD increases according to the square of the smaller winding diameter. Figure 7 shows the relationship between the winding diameter and the PMD for two types of module structures. The PMD of the test fiber is below 0.03 ps/r-km when it is wound at a diameter of 280 mm with no tension. The PMD increases with the small winding diameter and the PMD with the conventional bobbin structure wound with a tension of 50 g is larger than that of the bobbin-less structure. The degradation of the PMD can be explained with the lateral force from the bobbin caused by a winding tension. Considering the degradation of the bend-induced PMD, the winding diameter should be around 40 $\sim$ 60 mm.

Compact dispersion adjusting modules have been actually fabricated by employing the newly designed DCFs. The appearance of the package is shown in Fig. 8. The insertion loss spectra for two types of the dispersion adjusting modules are shown in Fig. 9. The splice loss between the DCF and the SSMF is around 0.2 dB per splice by heat treatment. Table 4 summarizes the characteristics of the fabricated dispersion adjusting modules with the total dispersion of –100 and –300 ps/nm. Quite small sizes of 110*110*10 mm (for –100 ps/nm) and 100*120*20 mm (for –300 ps/nm) have been realized, which are one-tenth volume in comparison with that for the conventional DCF module.

2.4. Splicing Technique

In general, the DCF has a relatively small mode field diameter to design the index profile keeping a large negative dispersion and good bending performance. If a special splicing technique is not used, the splice loss is large between transmission fiber like SSMF and the DCF because of the mode field mismatch. Therefore in the DCF module, the SSMF or other transmission fibers are concatenated with a special splicing technique

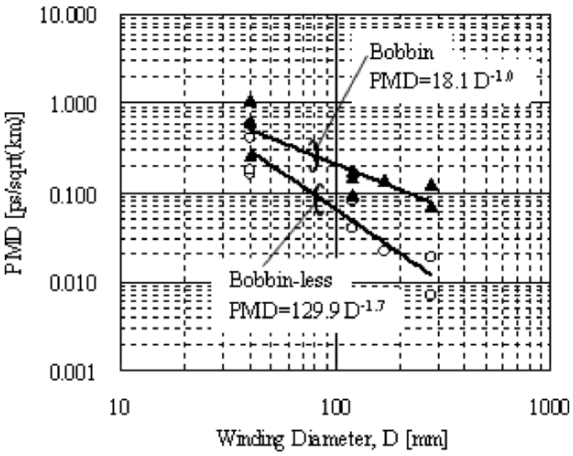

Fig. 7. Relationship between wounding diameter and PMD.

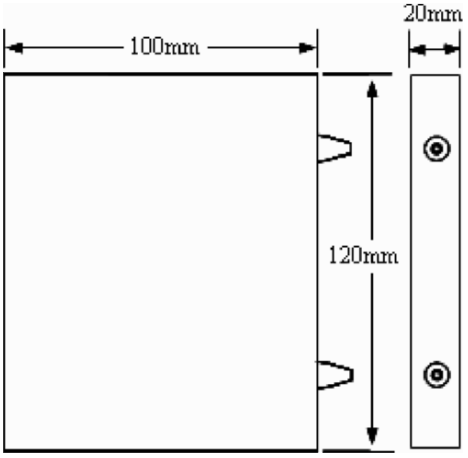

Fig. 8. Package appearance of compact dispersion adjusting module (Module-2).

at both ends of the DCF. While the use of connectors is one means to splice the fiber, the fusion splice is mainly used for the DCF module because it has a relatively low reflexivity, long-term reliability and easiness for special techniques like the thermally expanding core technique [23–26].

The splice loss by the mode field mismatch is calculated by [42]

$$L = -10 \log \left(\frac{2\omega_1 \omega_2}{\omega_1^2 + \omega_2^2} \right)^2, \tag{8}$$

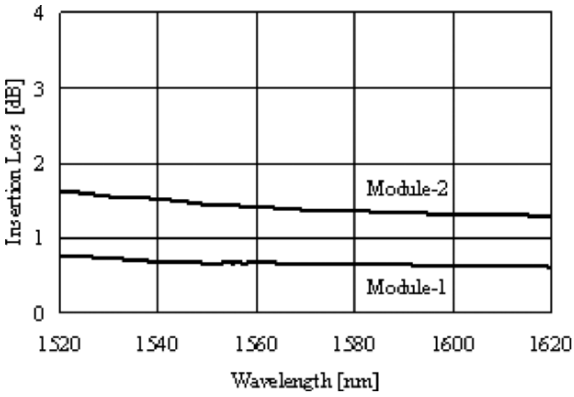

Fig. 9. Insertion loss including splice loss for two types of dispersion adjusting modules.

Table 5. Characteristics of the fabricated dispersion adjusting modules at 1550 nm.

Items	Module-1	Module-2
Dispersion	–100 ps/nm	–311 ps/nm
Dispersion Slope	–0.05 ps^2/nm	–0.10 ps^2/nm
Insertion Loss	0.7 dB	1.5 dB
PMD	0.20 ps	0.26 ps
Size (W*D*H)	110*110*10 mm	100*120*20 mm

where ω_1 and ω_2 are half of the mode field diameters, which are defined by Petermann's second definition [43,44]. It is expressed by

$$2\omega = 2\sqrt{2\int_0^\infty \phi^2(r)dr \Big/ \int_0^\infty \left(\frac{d\phi(r)}{dr}\right)^2 r\,dr}, \tag{9}$$

where $\phi(r)$ is the electrical distribution in the radial direction. The typical mode field diameters of the SSMF and the DCF defined by Eq. (9) are about 10 and 5 μm at 1.55 μm, respectively. The splice loss between them is then 2 dB by Eq. (8). In the DCF module, there are two splice points between the SSMF and the DCF which increase the insertion loss by 4 dB.

One method to reduce the splice loss caused by the mode field mismatch is to use an intermediate fiber [27] having a mode field diameter between those of SSMF and DCF. For example, if the DSF having the mode field diameter of 8 μm is used, the splice losses between the SSMF and the DSF, the DSF and the DCF are 0.2 and 0.9 dB, respectively. The total splice loss is 2.2 dB which is half of that of the directly spliced case.

Another method to reduce the splice loss is to use the thermally expansion core (TEC) technique [23–26]. In general, the DCF has a large Germanium concentration in

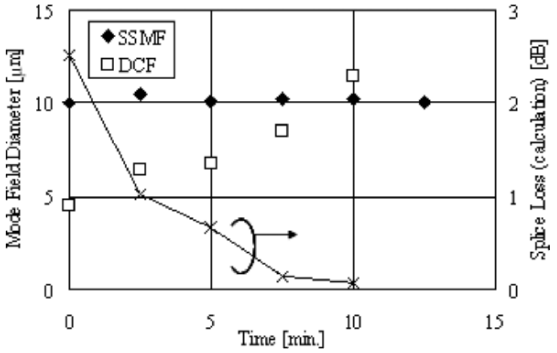

Fig. 10. Measurement results of the mode field diameters by heat treatment and calculation result of splice loss.

the core compared to the SSMF. The large amount of Germanium concentration in the core easily spreads by heat treatment such as additional arc splicing [26] or the use of a gas burner having a temperature of one thousand several hundred degrees [23–25]. The mode field diameter of the DCF by heat treatment is then enlarged rapidly compared to the SSMF. Figure 10 shows the measurement results of the mode field diameters at 1.55 μm for the SSMF and the DCF with the matched cladding when their facets are heated. It also shows the calculation result of the splice loss by Eq. (8). It is found that the mode field diameter of the DCF matched to that of the SSMF by the heat treatment and the splice loss can be reduced with the TEC technique. In general, the heat treatment is done to monitor the lowest possible splice loss after the fusion splice. In the case of the TEC technique, it is also important to reduce the longitudinal change of the refractive index profile. It causes an additional loss increase, so the conditions of the heat treatment to change it smoothly must be well adjusted, especially for the DCF with the double or the triple cladding. In [45], the effectiveness of the intermediate fiber doped with the fluorine in the ring is reported considering the thermal diffusion of the fluorine in the DCF.

3. Novel Packaging Technique

3.1. Stress-Free Module Structure

With the increase of the transmission capacity, the requirements for the dispersion compensating fiber module (DCFM) become increasingly severe to realize the high performance transmission lines in wavelength division multiplexing (WDM) systems. As described in section 2, the bending performance is the main factor to limit the performance of the DCF modules. Therefore in this section, a novel packaging technique to reduce the effect of the microbending loss has been explored, and reliability test results have also been conducted.

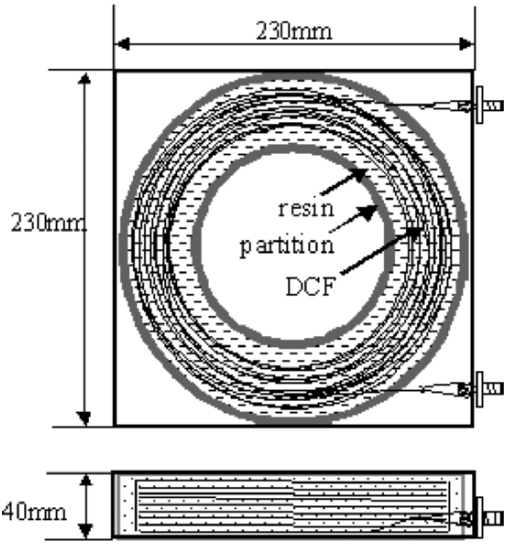

Fig. 11. Structure of the stress free coil.

In general, the DCFM is consisted of a several km long DCF winding on a coil of a small diameter with a tension and a pigtail fiber to connect with the transmission fiber. They are tightly packaged into a small box of around a 230*230*40 mm size. It causes difficulties in stability against environmental variations, especially loss variation caused by the microbending loss at longer wavelength. Thermal expansion of the bobbin also causes loss variation in the DCFM. The performance of the DCFM is mainly limited by the bending loss, so if a novel module structure to reduce the microbending loss is realized, a higher performance DCFM can be obtained. Therefore in this section, a novel structure of the DCF module is demonstrated. It should be designed to remove the strain applied to the fiber as much as possible and to hold the fiber firmly and securely. For these purposes, the approach to coat the fiber in a flexible resin has been adopted as shown in Fig. 11. This structure involves effectively floating the fiber in a bed of resin, so that it is referred to as a Suspended-In-Resin coil (SIRCOIL). At first the DCF is wound on a small size bobbin in the usual manner and the bobbin is removed. The DCF and parts of the pigtail fibers including the splicing points are placed on a ring-type box. After the resin is poured into it, the resin is cured by heat and the DCFM with the SIRCOIL structure is fabricated. The strain caused by the winding tension or the weight of the fiber itself is removed in this coil. This structure also provides excellent reliability because the fiber is held firmly by the resin.

In order to confirm the effectiveness of the SIRCOIL structure, the loss performances of the DCFMs have been tested. First, three conditions of the loss spectra of the same fiber packaged into the modules have been evaluated, (a) the conventional module wound on the bobbin with 50 g tension, (b) the bundled fiber removed from the bobbin and (c) the same bundled fiber in the resin. The results are shown in Fig. 12.

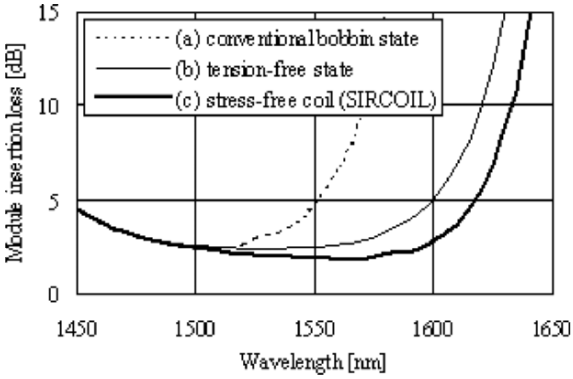

Fig. 12. Loss spectra for three conditions.

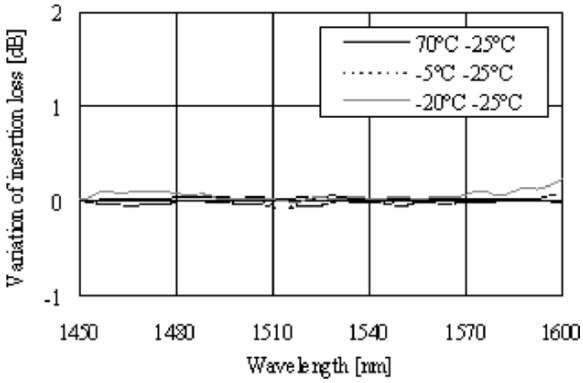

Fig. 13. Thermal characteristics of stress-free coil structure.

The more bend-sensitive DCF for NZ-DSF is chosen to clarify the effect of the lateral forces caused by the winding tension or the fiber's own weight. The loss increase at the longer wavelength side is clearly observed for the DCF with a conventional bobbin state. It is reduced with a tension free state produced by removing the bobbin. And it is suppressed further for the SIRCOIL condition. This is related to the fact that the suspension of the fiber in resin alleviates the strain imposed by the winding tension and the fiber's own weight. The loss characteristics against the temperature variation have also been evaluated. Figure 13 shows the wavelength dependency of the thermal characteristics of the DCF module with the SIRCOIL structure. No loss variation is observed from –20°C to 70°C. These figures indicate the effectiveness of the SIRCOIL structure.

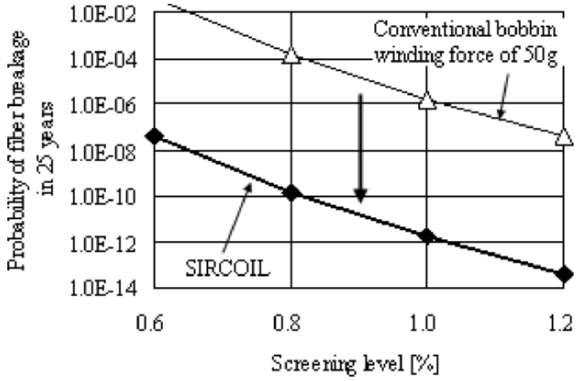

Fig. 14. Probability of fiber breakage in 25 years.

3.2. Reliability Test

The DCF modules with the SIRCOIL structure have strong advantages not only in the loss characteristics, but also in reliability. In this section, mechanical and optical reliabilities of the SIRCOIL structure have been demonstrated.

After screening, the probability of fiber breakage F_s is given by [46]

$$F_s \cong 1 - \exp\left(-N_p L \frac{m}{n-2} \frac{\sigma_s^n t_s}{\sigma_p^n t_p}\right). \tag{10}$$

Here, Table 6 summarizes the meanings of the parameters and values to calculate the probability of the fiber breakage. For long fibers, the winding diameter changes, for example, from 120 to 200 mmϕ. The strain by the fiber bend is estimated by averaging the bending diameter and the fiber length wound with its diameter. The strains in the conventional bobbin type of module occur by the fiber bend, winding tension and thermal expansion of the bobbin. On the other hand, in the SIRCOIL structure, the strains caused by the winding tension and the thermal expansion of the bobbin can be ignored. Therefore the strain occurring in the SIRCOIL structure is about half of that of the conventional bobbin structure. Figure 14 shows the calculation results of the probability of fiber breakage for two types of modules. It shows that over a 25-year period, the probability of breakage for the SIRCOIL structure is dramatically reduced compared with a conventional bobbin structure.

Before testing the optical performance in the SIRCOIL structure, it has been confirmed that the resin itself has high reliability throughout the thermal aging test and the damp heat test. Table 7 summarizes the test conditions to confirm the reliability of the SIRCOIL structure based on the Bellcore GR 63 [47].

Figures 15 and Table 8 show the results of each test. The variation of module insertion loss is less than 0.1 dB in every test. The resin has been maintained at a stable state and the SIRCOIL structure has not changed at all for a 2000 hr. damp heat test after sequential test 9.

Table 6. Parameters to calculate probability of fiber breakage.

Marks	Contents	Values
N_p	Number of breakages during screening test	0.065 times/km
L	Fiber Length	21 km
σ_s	Strain during the use as a module	0.125/bending diameter (120 $\sim$ 200mm)
	by fiber bend	*100 %
	by winding tension	0.045 % (50 g)
	by thermal expansion of the bobbin	0.062 % (difference of expansion coefficients for glass and aluminum, $\Delta T = \pm 27.5$ deg.)
σ_p	Strain during screening test	0.6 $\sim$ 1.2 %
t_s	Life time	25 years
t_p	Time of screening test	1 sec.
n	Coefficient of fatigue	20
m	Slope of distribution in a Weibull probability chart	10

Table 7. Reliability test conditions.

	Sequential Test	Conditions
1	Initial	–
2	Low Temp. Heat Shock 1st	–40°C for 72 h, transition rate: 30°C/hr to –40°C, <5 min. to 25°C
3	High Temp. Heat Shock 1st	70°C for 72 h, transition rate 30°C/hr to 70°C, <5 min. to 25°C
4	High Temp. Storage (Dry Heat)	85°C, <40% RH, 168 hr
5	Vibration	10 to 50 Hz@0.1 octave/min, 1.5 g along axis 1X per axis
6	Unpackaged Drop	4 inch drop on its base, 1X on 5 sides
7	Low Temp. Heat Shock 2nd	–40°C for 72 h, transition rate: 30°C/hr to –40C, <5 min. to 25°C
8	High Temp. Heat Shock 2nd	70°C for 72 h, transition rate 30°C/hr to 70°C, <5 min. to 25°C
9	High Temp. Storage (Damp Heat)	85°C, 85% RH, 168hr

Table 8. Reliability test results of each packaging.

DCFM Type	SIRCOIL structure DCF for NZ-DSF –393 ps/nm	Conventional bobbin DCM80 for SSMF –1360 ps/nm
Items	Variation of insertion loss at 1550 nm	
Vibration	< 0.1 dB	< 0.1 dB
Unpackaged Drop	< 0.1 dB	< 0.1 dB
Damp Heat	< 0.1 dB (2000 h)	< 0.1 dB (2000 h)

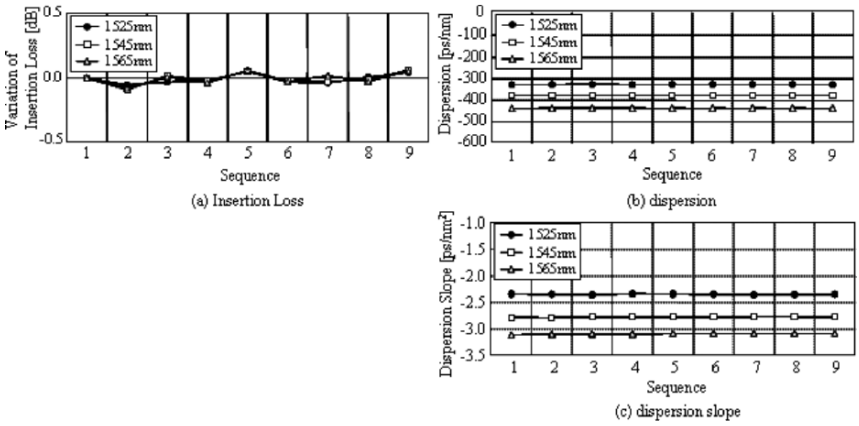

Fig. 15. Sequential test results for DCF module.

3.3. Application to Hybrid DCF Module

Dispersion and dispersion slope compensating fibers have contributed to realizing the WDM-based 10 Gb/s transmission systems. And in future 40 Gb/s systems, heightened precision control of the residual dispersion over the entire operating wavelength band is required [32,34]. However, while dispersion and dispersion slope are compensated at a center wavelength of the operating band, considerable residual dispersion remains at both ends of the band. This problem originates from the dispersion curvature, C, which is wavelength dependency on the dispersion slope and is given by [14]

$$C = \frac{dS}{d\lambda} = \frac{d^2D}{d\lambda^2} \ , \tag{11}$$

where D, S and λ are dispersion, dispersion slope and wavelength, respectively. The dispersion curvature of the transmission fibers is very low within the operating bandwidth. On the other hand, the conventional DCFs generally have a large negative curvature, i.e., convex dispersion properties. It originates from the wavelength dependency on the waveguide dispersion of the DCF. Therefore, it is essential to match the curvature of a DCF module with that of a transmission fiber in order to achieve a lower residual dispersion over the operating bandwidth. One approach [13] to reduce the curvature of the DCF is the careful tuning of the index profile to utilize the inflection point of the dispersion property. It may, however, be difficult to manufacture large volume DCFs with the same characteristics. Another approach [15] is to combine two DCFs with the opposite sign of the curvature to minimize it. The DCF described in section 2.3 has a large positive curvature (concave dispersion), so that combination of the conventional DCF with the negative curvature is expected to have a low curvature. It is, however, troublesome that two different DCFs including the splice point are packaged into the small box with the conventional bobbin. Usually, after splicing two DCFs wound on each bobbin, the splice point is re-coated and one fiber is re-wound on another fiber's bobbin. On the other hand, it is relatively easier to manufacture the

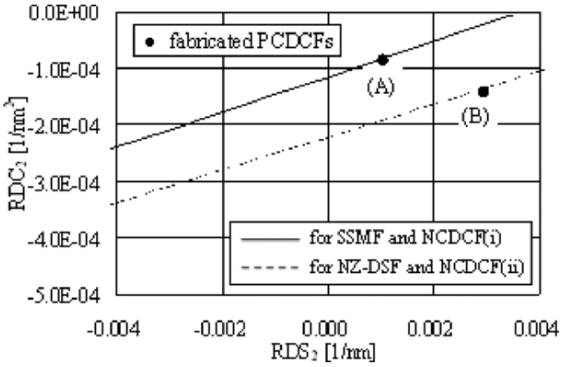

Fig. 16. Required relationship between RDS2 and RDC2 for PCDCF.

hybrid DCF module with the SIRCOIL structure. Two DCFs wound on each bobbin with different diameters are first prepared. After removing the bobbins, both DCFs are set in a box. The bend-sensitive DCF is placed outside to have a large bending diameter. After fusion splices are performed in the usual manner, the splice points between both DCFs and the pigtail fibers are also placed in it. The resin is poured into it and cured by heat, and the hybrid DCF module is then fabricated.

In this section, the hybrid DCF modules with the ultra-low residual dispersion over the entire C-band for an SSMF and NZ-DSFs have been demonstrated as one of the applications of the SIRCOIL structure. Those modules are composed of two DCFs with the positive curvature (PCDCF) and the negative curvature (NCDCF). The requirement to compensate for curvature as well as dispersion and dispersion slope simultaneously is summarized at first. Based on the estimation, the hybrid DCF modules are assembled while maintaining good module performance.

Table 9. Parameters of the fibers.

Parameter	Transmission fiber	NCDCF	PCDCF
Length [km]	L_0	L_1	L_2
Dispersion [ps/nm/km]	D_0	D_1	D_2
Slope [ps/nm^2/km]	S_0	S_1	S_2
Curvature [ps/nm^3/km]	C_0	C_1	C_2
RDS [1/nm]	$\mathrm{RDS}_0 = S_0/\ D_0$	$\mathrm{RDS}_1 = S_1/\ D_1$	$\mathrm{RDS}_2 = S_2/\ D_2$
RDC [1/nm^2]	$\mathrm{RDC}_0 = C_0/\ D_0$	$\mathrm{RDC}_1 = C_1/\ D_1$	$\mathrm{RDC}_2 = C_2/\ D_2$

At first, the requirement is given for a link consisting of a transmission fiber and a hybrid DCF module with the NCDCF and the PCDCF. The fiber parameters are defined in Table 9. When the curvature as well as dispersion and dispersion slope of the hybrid DCF module is ideally matched with those of the transmission fiber, the link satisfies

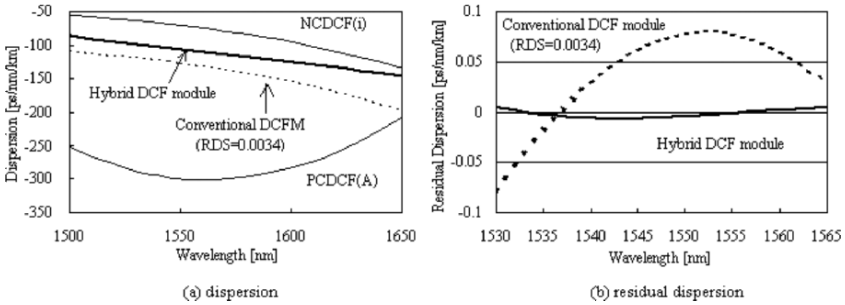

Fig. 17. Dispersion characteristics for hybrid and conventional DCFM for SMF.

$$\begin{cases} D_1L_1 + D_2L_2 = -D_0L_0, \\ S_1L_1 + S_2L_2 = -S_0L_0, \\ C_1L_1 + C_2L_2 = -C_0L_0. \end{cases} \tag{12}$$

Introducing the relative dispersion slope as RDS_i=S_i/D_i and the relative dispersion curvature as RDC_i=C_i/D_i (where $i = 0$, 1 or 2), Eq. (12) leads to

$$\mathrm{RDC}_2 = \frac{1}{\mathrm{RDS}_1 - \mathrm{RDS}_0} \left\{ \mathrm{RDC}_0 \left(\mathrm{RDS}_1 - \mathrm{RDS}_2 \right) - \mathrm{RDC}_1 (\mathrm{RDS}_0 - \mathrm{RDS}_2) \right\} . \tag{13}$$

Figure 16 shows the required relationship between RDS_2 and RDS_2 for the PCDCF. The solid line shows the calculation result of the SSMF with $(\mathrm{RDS}_0, \mathrm{RDC}_0)$ = (0.0034, -5.27×10^{-6}). The NCDCF(i) with $(\mathrm{RDS}_1, \mathrm{RDC}_1)$ = (0.0054, 5.37×10^{-5}) is chosen in this case. The broken line shows the calculation result for the medium dispersion type of the NZ-DSF with (RDS_0, RDC_0) = (0.0075, -3.21×10^{-6}). In this case the NCDCF(ii) with $(\mathrm{RDS}_1, \mathrm{RDC}_1)$ = (0.0201, 3.65×10^{-4}) is used. The fabricated PCDCFs are also plotted in Fig. 16. The PCDCF(A) and the PCDCF(B) satisfy Eq. (13) for each case.

Figure 17 shows the dispersion spectra of the NCDCF(i), the PCDCF(A) and the hybrid DCF module composed of those DCFs, in addition to a conventional DCF for SSMF. Almost linear dispersion property, namely small curvature is obtained in the hybrid DCF module. The residual dispersion for the link consisting of 100 km SSMF and the hybrid module which is composed of 13.4 km NCDCF(i) and 2.5 km PCDCF(A) is also illustrated in Fig. 17. The residual dispersion is remarkably flattened in comparison with the conventional one, and it is reduced to $\pm$0.0056 ps/nm/km in C-band (1530–1565 nm).

In the same manner, the hybrid DCFM for medium-dispersion NZ-DSF consisting of the NCDCF(ii) and the PCDCF(B) has been explored. The lengths of the NCDCF(ii) and the PCDCF(B) are 1.15 and 1.84 km, respectively for a 100-km length NZ-DSF. The residual dispersion shown in Fig. 18 is as low as $\pm$0.0050 ps/nm/km in C-band.

Table 10 summarizes the characteristics of the assembled hybrid DCF modules. The insertion loss and the PMD are sufficiently low for the commercial use owing to a large negative dispersion of the PCDCFs around –300 ps/nm/km shown in Figs. 17 and 18.

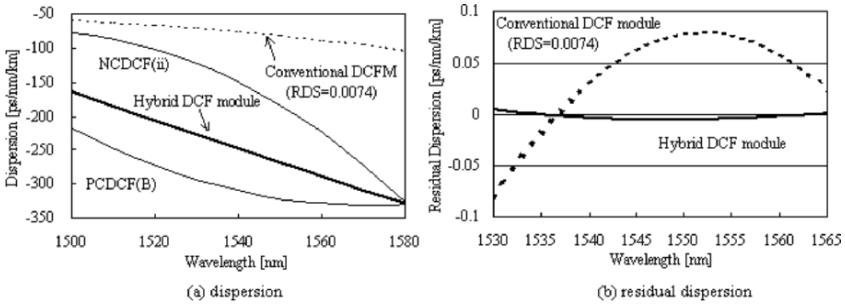

Fig. 18. Dispersion characteristics for hybrid and conventional DCFM for NZ-DSF.

Table 10. Characteristics of the hybrid DCF modules for 100 km transmission fibers at 1550 nm.

Transmission fiber	RDS [1/nm]	Insertion loss (including splice loss) [dB]	PMD [ps]
SSMF	0.0035	8.4	0.48
NZ-DSF	0.0075	4.1	0.29

4. Summary

In this paper, design optimization of the DCFs has been demonstrated considering the packaging technique. Optical performances of the DCFM are mainly limited by the macro-, micro-bending loss and the PMD which depend on the module structure. First, the design of the DCFM having the low nonlinearities has been explored. In this case, there is a trade-off between the optical nonlinearities and the microbending loss, so the module structure to reduce the microbending loss should be considered. At the same time, it has been revealed that the design to obtain a high FOM is also effective for suppressing the nonlinearities even with the same microbending performance. Second, the compact packaged DCFM has been explored to adjust a small amount of the dispersion. In this case, the macrobending loss and the PMD are critical issues because the possible smallest bending diameter must be achieved. Throughout this paper, the effect of the novel bobbin-less module structure has been described. In this module, the fiber is suspended in the resin, so it reduces the microbending loss dramatically. By using this novel module structure, high performance DCFMs have been realized. As one of the applications of the novel coil structure, the hybrid-DCFM has also been demonstrated to cancel out the higher order dispersion consisting of two types DCFs in the same module.

References

1. C. Lin, H. Kogelnik, and L.G. Cohen, "Optical pulse equalization of low-dispersion transmission in single-mode fibers in the 1.3–1.7 μm spectral region," Opt. Lett. **5** (11), 476–478 (1980).
2. H. Izadpanah, C. Lin, J.L. Gimlett, A.J. Antos, D.W. Hall, and D.K. Smith, "Dispersion compensation in 1310 nm optimized SMF's using optical equalizer fibre, EDFAs and 1310/1550 WDM," Electron. Lett. **28** (15), 1469–1470 (1992).
3. A.M. Vengsarkar and W.A. Reed, "Dispersion-compensating single-mode fibers: efficient designs for first- and second-order compensation," Opt. Lett. **18** (11), 924–926 (1993).
4. A.J. Antos and D.K. Smith, "Design and characterization of dispersion compensating fiber based on the LP_{01} mode," J. Lightwave Technol. **12** (10), 1739–1745 (1994).
5. A. Bjarklev, T. Rasmussen, O. Lumhol, K. Rottwitt, and M. Helmer, "Optimal design of single-cladded dispersion-compensating optical fibers," Opt. Lett. **19** (7), 457–459 (1994).
6. M. Onishi, Y. Koyano, M. Shigematsu, H. Kanamori, and M. Nishimura, "Dispersion compensating fibre with a high figure of merit of 250 ps/nm/dB," Electron. Lett. **30** (2), 161–163 (1994).
7. C.D. Chen, J.-M.P. Delavaux, B.W. Hakki, O. Mizuhara, T.V. Nguyen, R.J. Nuyts, K. Ogawa, Y.K. Park, R.E. Tench, L.D. Tzeng, and P.D. Yeates, "Field experiment of 10 Gbit/s, 360 km transmission through embedded standard (non-DSF) fibre cables," Electron. Lett. **30** (14), 1159–1160 (1994).
8. A.D. Ellis and D.M. Spirit, "Unrepeatered transmission over 80 km standard fibre at 40 Gb/s," Electron. Lett. **30** (1), 72–73 (1994).
9. M. Kakui, T. Kato, T. Kashiwada, K. Nakazato, C. Fukuda, M. Onishi, and M. Nishimura, "2.4 Gbit/s repeaterless transmission over 306 km non-dispersion-shifted fibre using directly modulated DFB-LD and dispersion compensating fibre," Electron. Lett. **31** (1), 51–52 (1995).
10. R.W. Tkach, R.M. Derosier, A.H. Gnauck, A.M. Vengsarkar, D.W. Peckham, J.L. Zyskind, J.W. Sulfoff, and A.R. Chraplyvy, "Transmission of eight 20 Gb/s channels over 232 km of conventional single-mode fiber," Photon. Technol. Lett. **7** (11), 1369–1371 (1995).
11. M. Onishi, T. Kashiwada, Y. Koyano, Y. Ishiguro, M. Nishimura, and H. Kanamori, "Third-order dispersion compensating fibres for non-zero dispersion shifted fibre links," Electron. Lett. **32**, 25 (1996).
12. L.G. Nielsen, S.N. Knudsen, B. Edvold, T. Veng, D. Maganussen, C.C. Larsen, and H. Damsgaard, "Dispersion compensating fibers," Opt. Fiber Technol. **6** (2), 164–180 (2000).
13. M. Wandel et al., "Dispersion compensating fibers for non-zero dispersion fibers," in Technical digest of OFC2002, WU1 (2002).
14. L. Grüner-Nielsen et al., "Status and future promises for dispersion compensating fibres," in Proceedings of ECOC2002, Paper 6.1.1, 2002.
15. L.V. Jorgensen et al., "Next generation dispersion compensating modules for 40 Gbit/s systems," in Technical Proceedings of NFOEC2002, pp.1171–1182, 2002.
16. T. Kato, M. Hirano, A. Tada, K. Fukuda, T. Fujii, T. Ooishi, Y. Yokoyama, M. Yoshida, and M. Onishi, "Dispersion flattened transmission line consisting of wide-band non-zero dispersion shifted fiber and dispersion compensating fiber module," Opt. Fiber Technol. **8** (2), 231–239 (2002).

17. C.D. Poole, J.M. Wiesenfeld, and A.R. McCormick, "Broadband dispersion compensation by using the higher-order spatial mode in a two mode fiber," Opt. Lett. **17** (14), 985–987 (1992).

18. A.H. Gnauck, L.D. Garrett, Y. Danziger, U. Levy, and M. Tur, "Dispersion and dispersion-slope compensation of NZDSF over the entire C band using higher-order-mode fibre," Electron. Lett. **36** (23), 1946–1947 (2000).

19. S. Ghalmi, S. Ramachandran, E. Monberg, Z. Wang, M. Yan, F. Dimarcello, W. Reed, P. Wisk, and J. Fleming, "Low-loss, all-fibre higher-order-mode dispersion compensators for lumped or multi-span compensation," Electron. Lett. **38** (24), 1507–1508 (2002).

20. P. Palai, K. Thyanarajan, and B.P. Pal, "Erbium-doped dispersion compensating fiber for simultaneous compensation of loss and dispersion," Opt. Fiber Technol. **3** (3), 149–153 (1997).

21. J.L. Auguste, J.M. Blondy, J. Mauny, J. Marcou, B. Dussardier, G. Monnom, R. Jinclal, K. Thyagarajan, and B.P. Pal, "Conception, realization and characterization of a very high negative chromatic dispersion fiber," Opt. Fiber Technol. **8** (1), 89–105 (2002).

22. R.J. Nuyts, Y.K. Park, and P. Gallion, "Dispersion equalization of a 10 Gb/s repeatered transmission system using dispersion compensating fibers," J. Lightwave Technol. **15** (1), 31–42 (1997).

23. J.T. Krause, W.A. Reed and K.L. Walker, "Splice loss of single mode fibre as related to fusion time, temperature and index profile alteration," J. Lighwave Technol. **4** (7), 837–840 (1986).

24. D.B. Mortimore and J.V. Wright, "Low-loss joints between dissimilar fibres by tapering fusion splices," Electron. Lett. **22** (6), 318–319 (1986).

25. K. Shiraish, Y. Aizawa, and S. Kawakami, "Beam expanding fiber using thermal diffusion of the dopant," J. Lightwave Technol. **8** (8), 1151–1161 (1990).

26. H.Y. Tam, "Simple fusion splicing technique for reducing splicing loss between standard single mode fibres and erbium-doped fibre," Electron. Lett. **27** (17), 1597–1599 (1991).

27. M.J. Holmes, F.P. Payne, and D.M. Spirit, "Matching fibres for low loss coupling into fiber applications," Electron. Lett. **26** (25), 2102–2104 (1990).

28. R. Ulrich, S.C. Rashleigh, and W. Eickhoff, "Bending-induced birefringence in single-mode fibers," Opt. Lett. **5** (6), 273–275 (1980).

29. G.P. Agrawal, *Nonlinear Fiber Optics* (Academic Press, Boston, 1989).

30. S. Tsuda and V.L. daSilva, "Transmission of 80 $\times$10 Gbit/s WDM channels with 50 GHz spacing over 500 km of LEAF® fiber," in Technical digest of OFC'2000, TuJ6-1, pp. 149–151 (2000).

31. D.W. Peckham, A.F. Judy and R.B. Kummer, "Reduced dispersion slope, non-zero dispersion fiber," in Proceeding of ECOC'98, vol. 1, pp.139–140, 1998.

32. S. Bigo, E. Lach, Y. Frignac, D. Hamoir, P. Sillard, W. Idler, S. Gauchard, A. Bertaina, S. Borne, L. Lorcy, N. Torabi, B. Franz, P. Nouchi, P. Guenot, L. Fleury, G. Wien, G. Le Ber, R. Fritschi, B. Junginger, M. Kaiser, D. Bayart, G. Veith, J.-P. Hamaide, and J.-L. Beylat, "Transmission of 32 ETDM channels at 40 Gbit/s (1.28 Tbit/s capacity) over 3 $\times$ 100 km of TeraLight$^{\mathrm{TM}}$ fibre," Electron. Lett. **37** (7), 448–449 (2001).

33. S. Gurib, A. Bertaina, S. Gauchard, S. Bigo, J.-P. Hamaide, J.-L. Beylat, L.-A. de Montmorillon, R. Sauvageon, P. Nouchi, J.-C. Rousseau, and J.-F. Chariot, "Experimental evaluation of Teralight$^{\mathrm{TM}}$ resistance to cross-nonlinear effects for channel spacings down to 50 GHz," Electron. Lett. **36** (11), 959–961 (2000).

34. B. Zhu, L. Leng, L.E. Nelson, Y. Qian, L. Cowsar, S. Stulz, C. Doerr, L. Stulz, S. Chandrasekhar, S. Radic, D. Vengsarkar, Z. Chen, J. Park, K.S. Feder, H. Thiele, J. Bromage, L. Gruner-Nielsen, and S. Knudsen, "3.08 Tbit/s (77 × 42.7 Gbit/s) WDM transmission over 1200 km fibre with 100 km repeater spacing using dual C- and L-band hybrid Raman/erbium-doped inline amplifiers," Electron. Lett. **37** (13), 844–845 (2001).

35. S.N. Knudsen, M.Ø. Pedersen, and L. Grüner-Nielsen, "Optimization of dispersion compensating fibres for cabled long-haul applications," Electron. Lett. **36** (25), 2067–2068 (2000).

36. K. Okamoto, "Comparison of calculated and measured impulse responses of optical fibers," Appl. Opt. **18** (13), 2199 (1979).

37. T. Kato, Y. Suetsugu, and M. Nishimura, "Estimation of nonlinear refractive index in various silica-based glasses for optical fibers, " Opt. Lett. **20** (22), 2279 (1995).

38. K. Petermann, "Microbending loss in monomode fibers," Electron. Lett. **12** (4), 107–109 (1976).

39. K. Petermann, "Theory of microbending loss in monomode fibers with arbitrary refractive index profile," Arch. Elektron. Übertr. **30**, 337 (1976).

40. J. Sakai and T. Kimura, "Bending loss of propagation mode in arbitrary index profile optical fibers," Appl. Opt. **17** (10), 1499–1506 (1978).

41. N. Gisin, J.-P.V. der Weid, and J.-P. Pellaux, "Polarization mode dispersion of short and long single-mode fibers," J. Lightwave Technol. **9** (7), 821–827 (1991).

42. D. Marcuse, "Loss analysis of single-mode fiber splices," Bell Sys. Tech. J. **56** (5), 703–718 (1977).

43. K. Petermann, "Constraints for fundamental-mode spot size for broadband dispersion - compensated single-mode fibres," Electron. Lett. **19** (18), 712–714 (1983).

44. C. Pask, "Physical interpretation of Petermann's strange spot size for single-mode fibres," Electron. Lett. **20** (3), 144–145 (1984).

45. B. Edvold and L. -G. Nielsen, "New technique for reducing the splice loss to dispersion compensating fiber," in Proceeding of ECOC'96, pp. 2.245–2.248, 1996.

46. Y. Mitsunaga, Y. Katsuyama, H. Kobayashi and Y. Ishida, "Failure prediction for long length optical fiber based on proof testing," J. Appl. Phys. **53** (7), 4847–4853 (1982).

47. GR-63 BELLCORE, "Network Equipment-Building Systems (NEBS) Requirement," 1995.

DOI: 10.1007/s10297-006-0073-5
Originally published in J. Opt. Fiber. Commun. Rep. 3, 292–339 (2006)

Dispersion compensating fiber used as a transmission fiber: inverse/reverse dispersion fiber

Kazunori Mukasa, Katsunori Imamura, Iwao Shimotakahara,
Takeshi Yagi and Kunio Kokura

Furukawa Electric Co., Ltd. Fitel-Photonics Laboratory
6, Yawata-Kaigandori, Ichihara, Chiba 290-8555 Japan
Email : mukasa@ch.furukawa.co.jp

Abstract. This paper gives an overview of IDF/RDF fiber design and development for submarine system. It starts with the concept of dispersion management line and its difference from the conventional DCF used in a module. Then it reviews the fiber design details and optical properties of various types of fibers used as parts of dispersion management lines. Fiber splicing issues using MFD expanding method and a brief summary of transmission experiments using the dispersion management lines are also included. Finally, we discussed a medial dispersion alternative comprising a positive and negative medial dispersion fiber and future optical properties improvements possibilities.

1. General Information About IDF/RDF

1.1. What is IDF?—General Information

Over the years, many innovative technologies opened the new era of optical telecommunication. A silica-based optical fiber with attenuation loss less than 20 dB/km, semiconductor lasers operating in a room temperature and erbium doped fiber amplifiers (EDFAs) are some of them. In addition to these, wavelength division multiplexing (WDM) transmission technology certainly opened the new era of wide-band high-capacity optical transmission [1–3]. WDM technology has been widely accepted because it met the strong requirement for rapidly increasing data-rate at that time. The improvement of EDFAs to be able to amplify over a wide range of wavelengths simultaneously also accelerated the spreading use of WDM technology [4].

On the other hand, silica-based optical fibers have been a mainstay for modern communication systems. Stimulated by the new innovative technologies, transmission fibers have been continuously evolving from multi-mode fiber (MMF) to 1.31 μm single mode fiber (SMF) and dispersion-shifted fiber (DSF) to better fit the capacity increase. WDM transmission technology also required new types of optical fiber, and non-zero dispersion shifted fiber (NZ-DSF) was developed to cope with GVD limitations, while suppressing the noise signal caused by the four wave mixing (FWM) phenomenon. Zero dispersion wavelengths were slightly shifted toward either longer or shorter wavelengths from zero dispersion DSF and strongly reduced the impact of cross-nonlinear effect. However, NZ-DSFs have some limitations to the realization of long-haul high-capacity WDM transmission, such as tradeoff of low dispersion slope and large A_{eff}. To realize a long haul transmission, a large A_{eff} is essential to avoid nonlinear signal distortion by Self Phase Modulation (SPM) and Cross Phase Modulation (XPM). Meanwhile, enlargement of A_{eff} significantly increases dispersion slope of NZ-DSF and transmission capacity was limited by a large dispersion slope that causes signal distortion due to accumulated dispersion especially at the edge of the channels.

To solve these problems, transmission lines using two fiber combinations, namely dispersion managed/management line, were proposed. For example, dispersion management lines consisted of standard SMF plus –NZ-DSF or +NZ-DSF plus –NZ-DSF and their performances without the need of dispersion compensating device were reported [5,6], but their distances and capacities were limited due to large dispersion slope and high nonlinearity. Total optical properties in addition to individual fiber properties of SMF plus –NZ-DSF and +/- NZ-DSF combination are shown in Tables 1 and 2. Total A_{eff} is equivalent A_{eff} that is calculated by considering fiber nonlinearity and power density using Eq. (1), wherein n_2 is a nonlinear refractive index, A_{eff} is the effective core area of each fiber and α is attenuation loss of each fiber. The splice loss was assumed to be 0.1 dB and the span length was set at 50 km, both were typical values for submarine system requirements. By calculating the product of the integral of power density along the fiber length and fiber nonlinearity using this equation, total non linear phase shift can be estimated. Accumulated dispersion is the maximum value within a 50-km span, that affects the system performance so much in the case of transmissions beyond 40 Gb/s as explained later:

$$\phi = \int_0^L \frac{n_2(Z)}{A_{\mathrm{eff}}(Z)} \exp(-\alpha Z) dZ. \tag{1}$$

Table 1. Typical optical properties of standard SMF and +/- NZ-DSF at 1550 nm [5,6]

	Dispersion [ps/nm/km]	Slope [ps/nm^2/km]	RDS [/nm]	Loss [dB/km]	A_{eff} [μm^2]
SMF	16.5	0.060	0.0036	0.185	75
NZ-DSF +	3	0.060	0.003	0.21	50
NZ-DSF -	–3	0.060	0.003	0.21	50

As shown in Table 2, the total dispersion slope was as large as a value of 0.06 ps/nm^2/km because both fibers had a positive dispersion slope. Though total dispersion

of a single channel can be managed to nearly zero by combining plus and minus dispersion value fibers, the dispersion effect must also be considered at other channels due to the dispersion slope. Furthermore, the equivalent $A_{\rm eff}$ of these lines ranged from 50 to 55 μm^2. This value is comparable with initial SMF+IDF, but much smaller than improved SMF+IDF which will be described in detail later. Enlargement of $A_{\rm eff}$ with NZ-DSFs have also been reported, but all of them had smaller $A_{\rm eff}$ than that of SMF, developed for 1.55 μm transmission called Cutoff Shifted Fiber (CSF), with $A_{\rm eff}$ about 80 μm^2. To realize transoceanic distance, high-capacity transmission, a totally flat dispersion line at the operating wavelength range, such as 1530 to 1570 nm with non-zero dispersion and large $A_{\rm eff}$ at each portion to avoid impairment due to nonlinearity, is desirable for WDM transmission.

Table 2. Optical properties of SMF plus –NZ-DSF and +NZ-DSF plus –NZ-DSF of a 50-km span at 1550 nm (splice loss was assumed 0.1 dB).

Combination	Accumulated Disp$^{(1)}$ [ps/nm]	Disp. Slope [ps/nm^2/km]	Loss [dB/km]	$A_{\rm eff}{}^{(2)}$ [mm^2]
SMF plus -NZ-DSF	126	0.060	0.208	56.1
+NZ-DSF plus -NZ-DSF	75	0.060	0.212	49.9

(1) Maximum accumulated dispersion in a 50-km span; (2) equivalent $A_{\rm eff}$

To achieve desirable dispersion for WDM transmission, a new type of single mode fiber which has inverse/reverse dispersion and a dispersion slope against SMF, refered to as an inverse/reverse dispersion fiber (IDF/RDF), was proposed [7]. Transmission lines comprised of SMF plus IDF type fiber are also called Dispersion Management Line (DML) or Dispersion Management Fiber (DMF). It might be confusing that transmission lines consisting of a SMF plus –NZ-DSF and a +/- NZ-DSF combination are also known as DML/DMF, but recently DML/DMF generally indicates that a transmission line consists of a + dispersion/slope fiber and a – dispersion/slope fiber such as SMF plus IDF. IDF shows negative dispersion and slope, inverse to those of SMF. The ratio of dispersion and its slope around 1.55 μm should be equal to that of SMF, so wide-band dispersion flatness will be obtained by SMF plus IDF. The nonlinearity of IDF, that showed improved performance from the DCFs, but is still one order larger compared with SMF, could be compensated by putting SMF first then IDF after EDFA. The transmission power is decreased by SMF attenuation, and a less nonlinear effect is induced in IDF due to decreased power. SMF plus IDF was widely accepted as a next-generation WDM transmission line, because IDF induced many inherent advantages of SMF such as low nonlinearity and low loss. Though DML is difficult to install into a short length terrestrial system due to the flexibility of span length required, many investigations have been done to confirm an adaptability of DML for transoceanic systems where fixed span length is generally used, because optical properties were better than any other types of transmission lines. It should be worth noting that NZ-DSFs in addition with DCFs have now been improved and made adaptable to high-capacity terrestrial systems. These improvements include a reduction of the dispersion slope and an enlargement of $A_{\rm eff}$. Some types of NZ-DSF for a terrestrial system are shown in Table 3 with improved SMF for a submarine system. At present, all of them have became commercially available, but considering

submarine system requirements such as large A_{eff}, low RDS (Relative dispersion slope; related to the easiness of dispersion compensation and described in section 2.1) and low attenuation loss properties, improved SMF shows the highest performance. Note new type of positive dispersion fiber (P-MDF), which has medial dispersion of SMF and NZ-DSF, has proposed recently and showed suitable performances for high-bit-rate transmission. These developments will be explained in section 4.1.

Table 3. Optical properties of various types of NZ-DSF for terrestrial system and improved SMF at 1550 nm.

	Dispersion [ps/nm/km]	Slope [ps/nm^2/km]	RDS [/nm]	Loss [dB/km]	A_{eff} [μm^2]
SMF	20	0.060	0.0036	0.17	110
NZ-DSF 1	5	0.090	0.0180	0.20	72
NZ-DSF 2	8	0.060	0.0075	0.20	65
NZ-DSF 3	8	0.045	0.0056	0.20	55
NZ-DSF 4	6	0.020	0.0033	0.20	45

The authors will explain about SMF plus IDF development for a submarine system mainly in this paper.

1.2. Differences Between IDF and DCF

There are many references that are devoted to the topics of various types of DCFs as well as IDFs. However, differences between IDF and DCF which at times are quite confusing will be explained very briefly in this section. DCFM stands for Dispersion compensation fibers used as module. Many types of DCFMs, which compensate a 1.55 μm region dispersion of a constructed SMF network at wide wavelength range, have been developed and widely used before the development of IDF [8–11]. In addition, DCFs for NZ-DSFs have also become possible by fiber technology improvements [12–15]. In these references, design issues and optical properties of DCFs are thoroughly explained. Though NZ-DSF+DCF or SMF+DCF also seemed to be applicable for a submarine cable system, DCF is not always suitable to be used in a cable, because of its relatively high attenuation loss and nonlinear properties.

Both DCF and IDF were used as dispersion compensating fiber for positive dispersion and dispersion slope fiber, but DCF was developed to be used as a module as shown in Fig. 1, and IDF is developed to be used as a transmission cable as shown in Fig. 2. To adapt for each application, the required optical properties were different for DCF and IDF. The typical optical properties are shown in Table 4. As shown in Table 4, DCF and IDF each have some unique optical properties. DCF has a large absolute dispersion value larger than 100 ps/nm/km in general, as shown in [8–11], because a large dispersion makes it possible to reduce the module size. To prevent the bending loss increase within the small sized package, the bending loss of DCF is designed to be low enough. On the other hand, IDF has a larger macro- and micro-bending loss because the required bending loss is not so restricted for a cable application compared to a module application. In addition, the absolute dispersion value is not so large because it will not be used as the small package, but as certain length of cable. By allowing

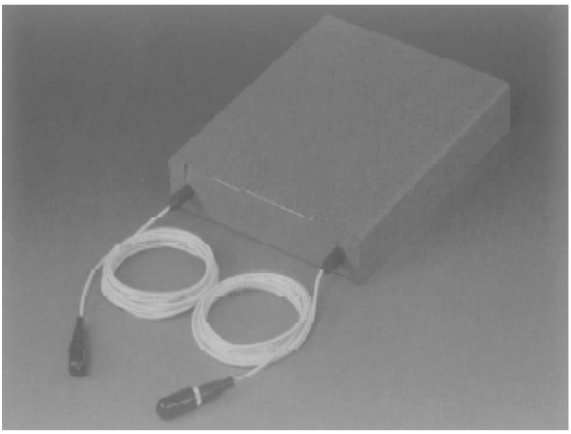

Fig. 1. An example of DCF module pictures used to compensate SMF or NZ-DSF.

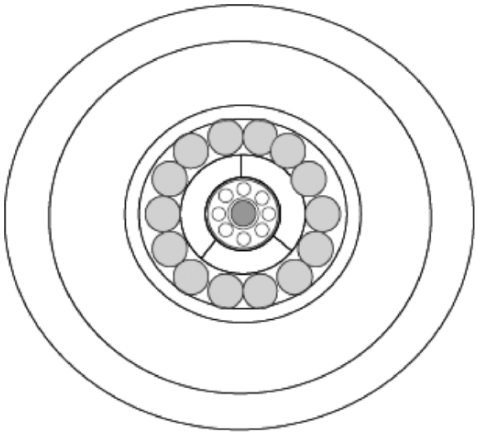

Fig. 2. An example of cross sectional images of a submarine cable.

a smaller absolute dispersion and larger bending loss, IDF has some advantageous properties for a long-haul transmission such as a large A_{eff}, low attenuation loss and low PMD compared to DCF type fiber.

IDFs with dispersion around –45 ps/nm/km are used as standard IDF now and most DML system experiments were done with this type of IDFs. This IDF has successfully solved a nonlinear problem caused by initial IDF with dispersion of about –20 ps/nm/km by increasing absolute dispersion. Other than IDF-45E, IDF with dispersion of about –60 ps/nm/km and IDF having dispersion the same as with initial

IDF, but larger A_{eff} and lower loss, were also developed and reported. These will be explained in section 2 (initial IDF) and section 3 (Improved IDF; IDF-45E and other suggestions). It is also important to note that alternative DML, consisting of positive and negative Medial Dispersion Fiber (MDF), one of the biggest candidates of next generation submarine fiber, was also developed and reported. Initial MDF with absolute dispersion of about 14 ps/nm/km and further improvement with SMF+IDF and MDF will be explained in section 4. A brief summary of transmission experiments with DMLs is also included.

Table 4. Typical optical properties of DCF used for a module and IDFs used for a submarine transmission system.

	Dispersion [ps/nm/km]	Slope [ps/nm^2/km]	RDS [/nm]	Loss [dB/km]	A_{eff} [μm^2]	λ_c [nm]	PMD [ps/rkm]	Bend(*) [dB/m]
DCF	–120	–0.360	0.003	0.47	17	< 1300	0.15	0.1
IDF(1)	–20	–0.060	0.003	0.23	32	< 1300	0.05	8
IDF(2)	–40	–0.120	0.003	0.24	28	< 1300	0.05	8
IDF(3)	–60	–0.180	0.003	0.26	25	< 1300	0.06	8

(*) Bending loss increase at 20 mm diameter

2. Development of Initial IDF/RDF

2.1. Design and Concept of Initial IDF

Initial IDF was designed with the idea of providing a dispersion compensation for standard SMF in the same way as DCFMs, so not only dispersion characteristics of IDF itself but also total dispersion characteristics connecting SMF plus IDF are very important [7]. Obtained dispersion flatness by SMF plus IDF should be indicated by the Eq. (2).

The closer the CR (Compensating Rate) is to 100%, the more dispersion flatness will be obtained in a total line. In other words, the Relative Dispersion to Slope (RDS) same as that of SMF is desirable for wide band dispersion flatness. The attraction of SMF+IDF comes from a total dispersion flatness imposed by an optimal two fiber combination:

$$\text{Dispersion Compensating Rate}[\%] = \frac{\text{RDS}_{\text{IDF}}}{\text{RDS}_{\text{SMF}}} \times 100, \tag{2}$$

$$\text{RDS} = \text{Relative Dispersion Slope} = \text{D.Slope/Dispersion}.$$

Several types of index profiles have been reported to achieve such dispersion characteristics [8–15]. Among them, a W-shaped profile as shown in Fig. 3 was chosen for initial IDF, because it is a relatively simple structure and easy to fabricate by the Vapor Axial Deposition (VAD) method. VAD technology is a well-optimized and established technology using chemical reactions, and many low loss fibers were reported with high purity VAD glass [as 16]. A wide range of parameters can be selected for the W-shaped profile, which will give various absolute dispersion slopes. Initial IDF was

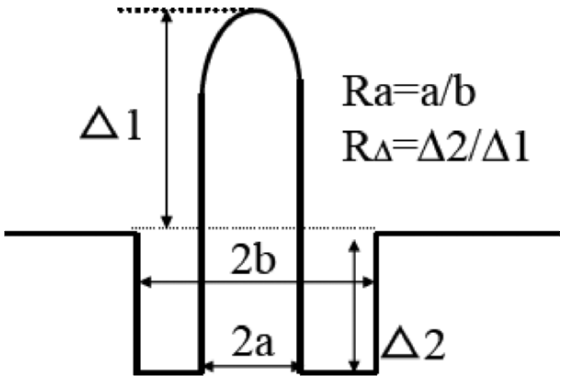

Fig. 3. A W-shaped core profile used for initial IDF [7].

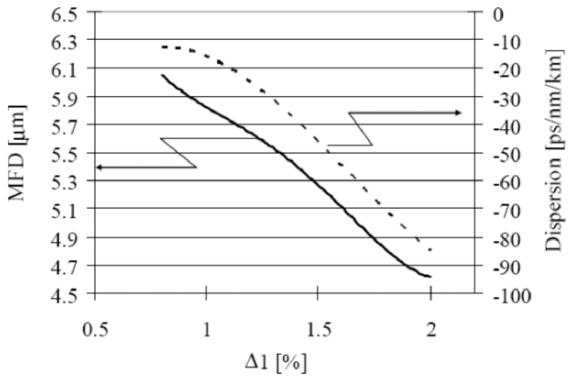

Fig. 4. The relation of $\Delta 1$ of IDF with a W-shaped profile vs. MFD and dispersion [7].

developed by targeting the same absolute dispersion with that of SMF. This means an approximately 1:1 length ratio of SMF and IDF will be jointed to construct a network.

The smaller center core Δ (relative refractive index difference) value, than that of DCF, was selected. The aim was to achieve low loss and nonlinearity. The relation between Δx vs. MFD and the dispersion of W-shaped IDF is illustrated in Fig. 4. By decreasing center core Δs the absolute dispersion is getting smaller while MFD is getting larger as shown in Fig. 4.

The larger MFD is very important because the signal distortion due to the nonlinearity of optical fiber (Φ) is expressed as

$$\Phi \propto PL_{\text{eff}} \frac{n_2}{(\text{MFD})^2}. \tag{3}$$

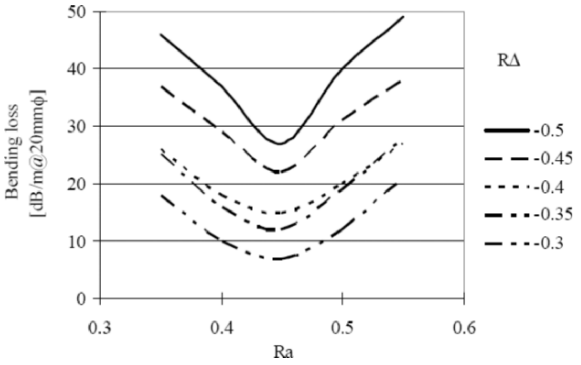

Fig. 5. The relation of bending loss of 20 mmϕ to Ra and $R\Delta$ of IDF with a W-shaped profile [7].

The effective core area (A_{eff}) is proportional to (MFD)^2, so A_{eff} is more commonly used to express a nonlinear property. The calculated A_{eff} was as large as 24 μm^2, which indicates improved nonlinearity from DCF with an A_{eff} of 17 μm^2. Meanwhile, fibers become weak against macro-bending and micro-bending loss when Δx is too low, because the propagation mode becomes leaky. By optimizing Δ value and adjusting other parameters such as Ra and $R\Delta$, a solution for the required dispersion property could be obtained without a bending-loss increase. Figure 5 shows a simulation result indicating how to suppress bending loss of W-shaped IDF by means of parameters optimization. The attenuation loss is expected to be small and stable for cabling because of a small $\Delta 1$ but the optimized bending properties. Simulated cutoff wavelength was as low as 800 nm in the case of initial RDF and did not affect other optical properties at all, but in general, cutoff wavelength also has a tradeoff relation with compensating rate, A_{eff} and bending loss, and must be considered.

Table 5. First fabrication results of initial IDF obtained in lab of Furukawa Electric (1550 nm) [7].

	Dispersion [ps/nm/km]	Slope [ps/nm^2/km]	RDS [/nm]	Loss [dB/km]	A_{eff} [μm^2]	λ_c [nm]	PMD [ps/rkm]	Bend(*) [dB/m]
No.1	–15.6	–0.046	0.003	0.25	24	830	0.07	5

(*) Bending loss increase at 20 mm diameter

The initial IDF with W-shaped profile was fabricated by the VAD method. The center core, the side core and the clad are made of SiO_2/GeO_2, SiO_2/F and pure SiO_2, respectively. The first fabrication results of initial IDF in the lab of Furukawa Electric are shown in Table 5 [7]. Because many tradeoffs were considered in the design stage, almost the same dispersion and dispersion slope with those of SMF were obtained with a negative sign and A_{eff} was successfully enlarged to 24 μm^2. Most of the optical properties showed a good agreement with the simulated values. Other optical properties

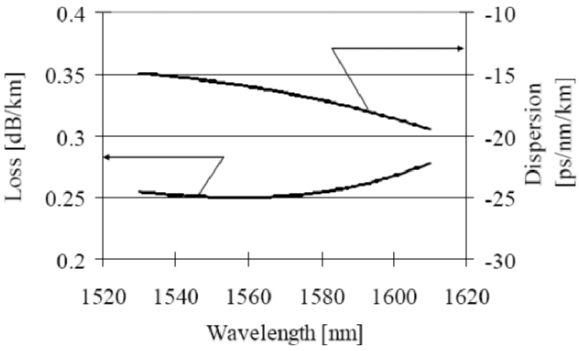

Fig. 6. Attenuation and dispersion spectrum over 1530–1610 nm of initial IDF [7].

such as bending loss and PMD were also low enough. For bending loss properties, not only the macro-bending loss but also the micro-bending loss properties were confirmed with developed IDFs. There are several methods proposed to measure micro-bending performance, but the authors selected a winding method [17] using #1000 sandpaper and 250 mm diameter bobbin where fiber was wound up to create 100 g tension. The tests were repeated three times at least each to increase the reliability of the data. The loss increase at 1550 nm was less than 0.2 dB/km that is comparable with the standard SMF, so cable performance was expected to be good.

A dispersion and attenuation loss spectrum of the initial IDF is shown in Fig. 6, and a low and flat attenuation loss spectrum was confirmed over wide-band by considering bending loss and cutoff properties. Though the propagation loss edge of IDF was close to operation range due to a W-shaped profile, the fiber loss was stable up to 1570 nm. Dispersion curvature is also an important issue considering the wide-band transmission. A dispersion slope became steeper in longer wavelength, but within C-Band, it showed a relatively straight dispersion line. The total performance with SMF will be explained in section 2.2.

After the first trial, much adjustment and optimization had been done with initial IDF through mass-productivity confirmation. Table 6 shows typical characteristics of mass-produced initial IDF (About 10,000 km) in addition with typical DCF properties. The typical absolute dispersion had been slightly enlarged from a lab-obtained value keeping a high compensating rate for SMF. Attenuation loss was reduced about 0.240 dB/km as a typical value. These optical properties could be obtained stably by a long-term design and process optimization.

2.2. Splicing and Total Optical Property with SMF

This IDF is connected with SMF, both of which are approximately same length, to construct a network as shown in Fig. 7.

The advantage of choosing SMF as a counterpart is its low attenuation and low nonlinearity. Though the attenuation of IDF was 0.24 dB/km, the average loss of repeater span would be 0.215 dB/km, because the attenuation of SMF is as low as 0.19

Table 6. Typical characteristics of mass-produced initial IDFs and DCFs (1550 nm).

Optical properties	Initial IDF	DCF
Clad diameter [mm]	125.0±1.0	125.0±1.0
Clad non-circularity [%]	0.1	0.1
Core ovality [mm]	0.1	0.1
Loss [dB/km] @1550 nm	0.24	0.5
Dispersion [ps/nm/km] @1550 nm	–20±5.0	–100
RDS [/nm] @1550 nm	0.0029	0.0035
Compensate rate [%] @1550 nm	94	100
λ_c [nm]	820	800
MFD [mm] @1550 nm	5.6	4.8
A_{eff} [mm^2] @1550 nm	24	18
Nonlinear coefficient [1/W]	12.4×10^{-10}	20×10^{-10}
Bend loss at 20ϕ [dB/m] @1550 nm	10	1
PMD [ps/rkm]	0.07	0.2
Proof test level	>1.0%	>1.0%

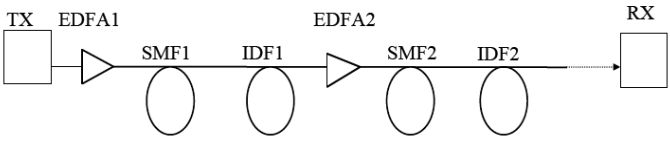

Fig. 7. An example of system configurations consisted of SMF+IDF used for a submarine transmission system [7].

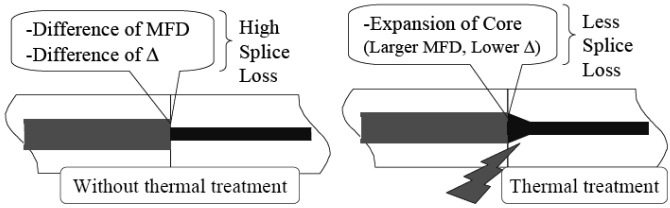

Fig. 8. An image figure of the SMF-IDF splice (Left: Conventional, Right: MEX), wherein MEX means a Mode Field Diameter expanding thermal splice.

dB/km. As described in sections 1.1 and 1.2, the improvement of IDF nonlinearity from DCFM was indicated. However, the nonlinearity was still one order larger compared with SMF. This could be reduced by putting SMF after EDFA and IDF after SMF as shown in Fig. 7.

A compensating rate for SMF was more than 90% so the dispersion from 1530 to 1565 nm was within a range of ±0.1 ps/nm/km, which will be depicted later. SMF plus

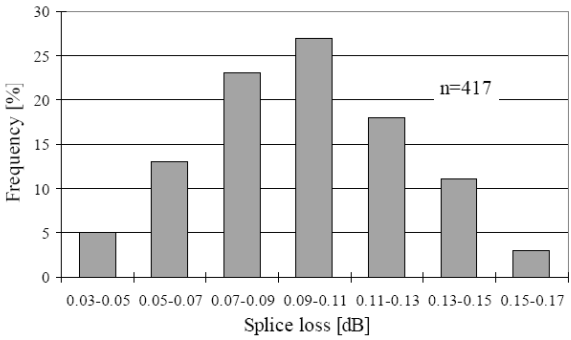

Fig. 9. Splice loss distributions of SMF-IDF by MEX (MFD Expanding) technique.

IDF seemed to be a promising candidate for the future transmission line for the points stated earlier. However, a large splice loss was one of the biggest hindrances to be solved at that time. The splice loss of SMF plus initial IDF using a commercially available splicing machine was about 1.0 dB/splice, because of MFD and delta mismatch. A splice loss of SMF-SMF is less than 0.1 dB/splice, so splice loss of SMF-IDF was too high to be adapted into a real system. By optimizing a splice loss condition such as arc power and discharge time, the splice loss of SMF-IDF could be reduced about 0.7 dB, but 0.7 dB/splice is still high. We developed thermal MFD expansion (MEX) splice technique. The MEX splice technique is very effective to reduce the splice loss (Fig. 8).

The MEX splicing uses a thermal treatment with a small amount of flame. GeO_2 is efficiently diffused by the thermal treatment, causing an expansion of the electric field by a profile change due to GeO_2 diffusion, especially that of IDF expands easily because IDF contains larger amount of GeO_2 than SMF does. However, if the treatment time is too long, the GeO_2 of IDF expands into too broad of a range and the A_{eff} becomes larger than SMF, so it is very important to stop the treatment at the appropriate time while monitoring the splice loss value change. By using the MEX splice, the splice loss of SMF plus IDF became about 0.1 dB as shown in Fig. 9.

The problem of high splicing loss is not limited only for SMF-IDF, but also IDF-IDF. MFD and Δ are almost the same for IDF-IDF, but an axial discrepancy affects more seriously by small MFD fiber homogeneous splices. Fortunately, this problem was also solved by MEX splice technique.

Table 7. Typical optical properties of commercial-available three types of SMF.

	Dispersion [ps/nm/km]	Slope [ps/nm^2/km]	RDS [/nm]	Loss [dB/km]	A_{eff} [μm^2]
SMF	16.5	0.060	0.0036	0.185	75
CSF	18.5	0.060	0.0032	0.185	83
FF-SMF	18.5	0.060	0.0032	0.172	75

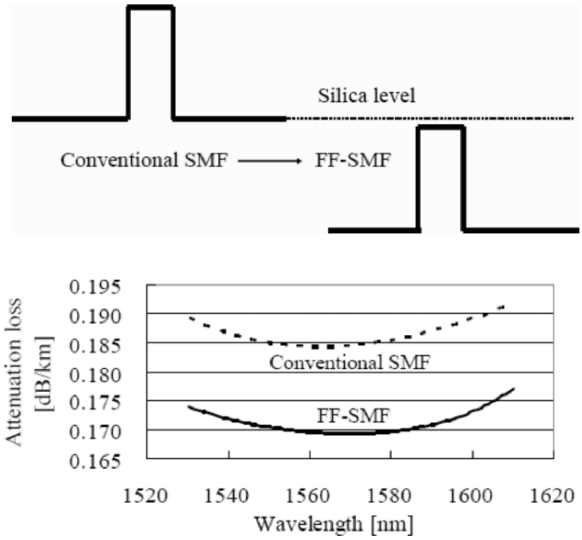

Fig. 10. A method and a result regarding to attenuation loss reduction with SMF by FF method. *Top*: Profile of Conventional SMF(Left) and FF-SMF(Right). *Bottom*: Attenuation loss spectrum of conventional SMF and FF-SMF.

There were three types of SMF available in the market when initial IDF was developed. Optical properties of these three types of SMF are shown in Table 7.

Table 8. Total optical properties of SMF plus initial IDF at 1550 nm assuming span length of 50 km and splice loss of 0.1 dB [7].

	Dispersion$^{(1)}$ [ps/nm/km]	Slope [ps/nm^2/km]	Loss [dB/km]	$A_{\mathrm{eff}}{}^{(2)}$ [μm^2]
SMF	0(452)	0.007	0.212	49.6
CSF	0(480)	0.003	0.213	50.5
FF-SMF	0(480)	0.003	0.207	46.6

(1) Total dispersion (Maximum accumulated dispersion in a 50-km span); (2) equivalent A_{eff}

In particular, FF-SMF (FF-SMF stands for Fully Fluorine doped SMF) is very attractive because of its very low attenuation loss and small RDS. FF-SMF is sometimes referred to as Pure Silica Core SMF (PSCF) also [16]. In general, it is more difficult to compensate a dispersion slope of fibers with large RDS. Additionally, by using depressed cladding, the Rayleigh scattering loss of the center core was reduced by no GeO_2 doping as shown in Fig. 10. Figure 10(top) shows the attenuation loss spectrum of GeO_2 doped conventional SMF and FF-SMF. As clearly shown in Fig 10(bottom), FF-SMF showed lower attenuation loss, keeping a similar loss curve with SMF.

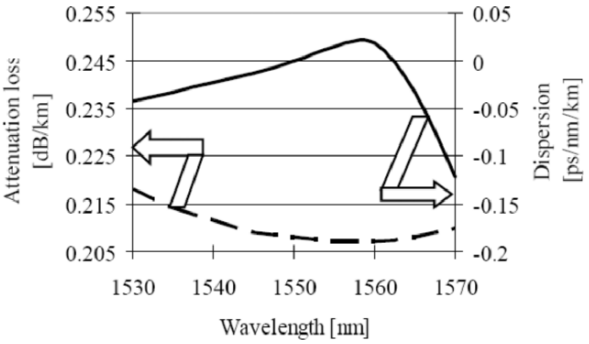

Fig. 11. An attenuation and dispersion spectrum of FF-SMF plus initial IDF over C-band.

Total optical properties of three types of SMF plus IDF were summarized in Table 8, and the dispersion and attenuation spectrum of FF-SMF plus initial IDF over C-Band is shown in Fig. 11. As shown in the table and figure, SMF plus IDF showed characteristics suitable for WDM transmission compared to NZ-DSF which have a trade-off relation with large A_{eff} and low dispersion slope. The dispersion curvature showed a relatively steep negative slope in a longer wavelength and it will become a problem in case of a L-Band transmission. With a W-shaped profile, it is very difficult to solve this problem by a profile optimization. In the case of L-Band transmission, it would be effective to use SMF, DSF or NZ-DSF as an L-band dispersion compensator to adjust the residual dispersion. However, it should be noted these technical challenges such as a L-band transmission have been investigated in lab-base even with transoceanic distance, but introducing these technologies into a field submarine system has been difficult due to electrical power supply problem, reliability problem and so on up until now.

2.3. Experimental Results Using SMF Plus Initial IDF

Many experimental transmission results have been reported using SMF plus initial IDF. Two typical NZ-DSFs used in a submarine system are shown in Table 9. These types of NZ-DSF have negative dispersion, so a positive dispersion fiber such as CSF is used as a dispersion compensating fiber. Figure 12 shows the accumulated dispersion characteristics of conventional NZ-DSF with local dispersion of –2 ps/nm/km plus CSF and SMF plus initial IDF.

The biggest difference between these two types of lines is wavelength dependence for dispersion. SMF plus IDF has a very small wavelength dependence of dispersion as shown in Fig. 11. On the other hand, NZ-DSF has a large wavelength dependence of dispersion due to its high dispersion slope. Figure 13 shows the dispersion spectrum of FF-SMF plus initial IDF and NZ-DSF. As clearly shown in the figure, NZ-DSF has a large wavelength dependence of dispersion. In other words, SMF plus IDF will not cause much difference in accumulated dispersion for each channel, but NZ-DSF causes a large difference in cases of a long distance transmission. This difference would cause a

Table 9. Typical optical properties of NZ-DSFs for a submarine system.

	Dispersion [ps/nm/km]	Slope [ps/nm^2/km]	Loss [dB/km]	A_{eff} [μm^2]	PMD [ps/rkm]
Type 1	–2(–100)*	0.090	0.215	70	0.05
Type 2	–2(–100)*	0.050	0.215	55	0.05

(*) Local dispersion (Maximum accumulated dispersion in a 50-km span)

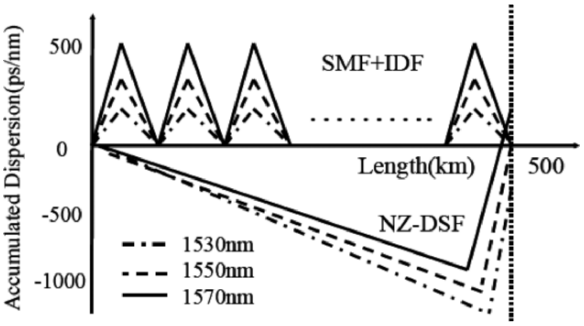

Fig. 12. Accumulated dispersion characteristics of 500 km consisted of negative dispersion NZ-DSF plus DC-CSF and SMF+IDF used for a submarine system.

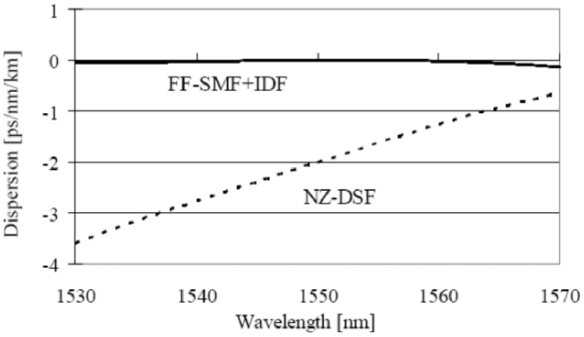

Fig. 13. Dispersion spectrum of SMF+IDF and NZ-DSF used for a submarine system over C-Band.

serious signal distortion due to an accumulated dispersion in edge channels. Dispersion at 1550 nm was compensated by dispersion compensating fibers such as CSF, but the dispersion slope was not compensated by CSF. SMF plus IDF is advantageous for wide-band WDM transmission. Many experimental transmission results have proven the high performance of SMF plus initial IDF [17,18]. For example, 10 Gb/s, 16 ch., and 8303 km transmission was reported in [17]. 40 Gb/s transmission was also reported

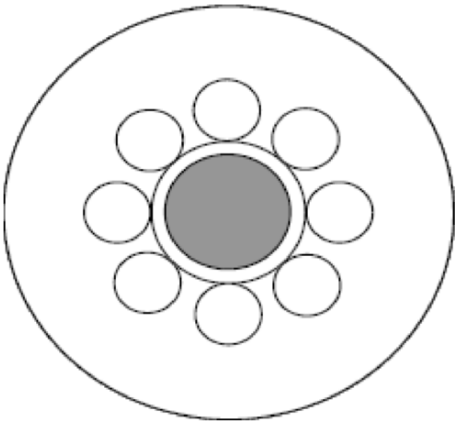

Fig. 14. The structure of IDF unit.

in [18]. Since then, improvements of NZ-DSFs have been done mainly aiming for a terrestrial system, while SMF plus IDF has been improved aiming for a transoceanic transmission system as described in section 1.1. This issue will be explained again in section 3.4.

2.4. Cabling Test for Initial IDF

As described in section 2.3, SMF plus initial IDF showed a very high performance as a long-haul transmission line, and micro-bending loss performance was examined with some samples after a mass-production. The micro-bending of IDFs showed comparable properties with conventional SMF. However, to confirm the cabling performance, more reliable data were required, so the authors have manufactured a submarine cable unit using initial IDFs and confirmed the optical and mechanical characteristics taking a practical condition into account. We fabricated 2.55 mmϕ tight-structured unit with 8 slots, which is widely used in Japan. IDF in slots are ultraviolet (UV) resin coated fibers with a diameter of 400 μm. Figure 14 shows the cross sectional figure of this cable unit. Five IDF cables that have typical optical properties were fabricated and measured to make sure of reliability of RDF cable data.

Table 10. Environmental test results of initial IDF units for a submarine use (1550 nm).

IDF properties	Condition	Variation
Temperature dependency loss	From –20 to 50 deg	$< +- 0.004$ dB
Lateral force	From 0 to 5 kgf/cm	$< +- 0.002$ dB
Water pressure	From 0 to 100 kgf/cm^2	$< +- 0.010$ dB

At first, attenuation, dispersion and PMD in the range of 1530 to 1570 nm were measured before and after unit fabrication. No significant change was observed before

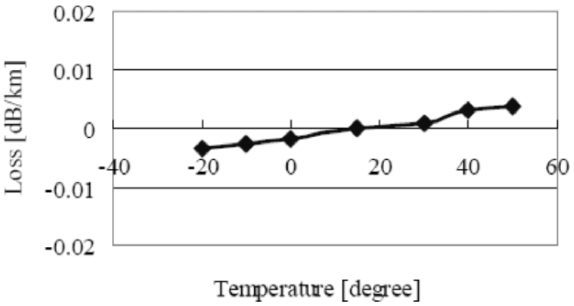

Fig. 15. Temperature dependence of IDF loss.

and after fabrication. Next, we investigated the unit optical properties by changing environments such as temperature, lateral force and water pressure. The results are summarized in Table 10. As shown in Table 10, the change of every evaluated optical property is confirmed to be within the same range as of conventional submarine fiber units. Figure 15 shows the temperature dependence of the attenuation loss. This dependency and levels were the same as conventional submarine fibers. These results show that initial IDF has reliable performances for a submarine use. Improvements of IDFs, which will be explained next, have been attempted so as not to exceed the bending loss (both macro- and micro-bending) of initial IDF. The performances of ribbon-slot cable and loose-tube cable using initial IDF were also confirmed and reported in [19,20], and reliable performances were also reported. With these fabrications and experiments of initial IDF, the performance potential and basic properties were well understood, and improvements have been done based on these results. Though initial IDFs have replaced by improved IDFs, the research of initial IDF was very important from this point of view.

3. Improvement of IDF/RDF Optical Properties

3.1. Improvement of SMF Properties

As described in section 2.3, 10-Gb/s-based long-haul WDM transmissions were actually realized by a new type of transmission line consisted of SMF and initial IDF. However, further improvements with SMF and IDF optical properties have been required to realize longer-haul and higher-capacity transmissions. Long-haul high-capacity transmissions were actually realized and reported by DML properties improvements such as a large A_{eff} and low attenuation loss while keeping a flat dispersion [21,22]. In [21,22], 1 Tb/s transoceanic transmissions were reported with improved DML. In this section, the authors will explain SMF optical properties improvements followed by IDF improvements. Total optical properties and their high performance will also be explained.

SMF is characterized with attenuation of about 0.19 dB/km and an A_{eff} of about 80 μm^2, and these optical properties are very attractive to obtain low nonlinearity in a

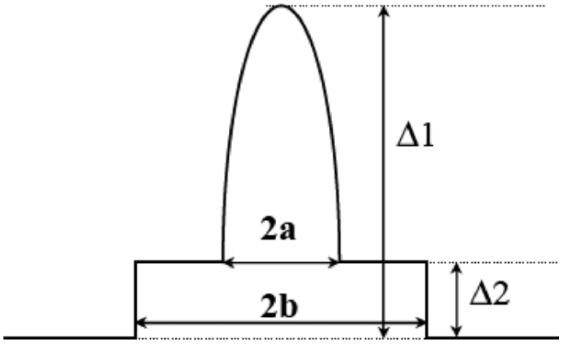

Fig. 16. A Dual Shaped Core (DSC) profile.

total line. However, the equivalent $A_{\rm eff}$ of SMF plus initial IDF was about 50 μm^2, and was still small compared to large-$A_{\rm eff}$ NZ-DSF, for example. To suppress nonlinear phenomena of a total line, small dispersion or large $A_{\rm eff}$ would be required for SMF. So a new type of SMF (Enlarged $A_{\rm eff}$ SMF: SMF-E) has been developed [23].

SMF-E is designed to achieve similar dispersion with conventional SMF, because large dispersion will shorten SMF length ratio and causes higher nonlinearity and higher loss in a total line. A Dual Shaped Core (DSC) profile (Fig. 16) was selected because of its simple structure and easy fabrication by VAD method and optimized to have as large as possible $A_{\rm eff}$. A DSC profile is also attractive for the aspect of low dispersion and large $A_{\rm eff}$. A wide range of parameters were searched for the DSC-profile. About the same $\Delta 1$ value with SMF was selected, because fibers become weak against bending loss when $\Delta 1$ is too low. Then, by optimizing the shape of the center coreand the side core, a solution for required properties was obtained. The authors used a DSC profile to enlarge $A_{\rm eff}$ while keeping low dispersion, but many results with a W-shaped profile (such as Ultra Wave SLA) have been reported also, as in [24]. These reported fibers have larger $A_{\rm eff}$ than that of SMF-E with a DSC profile of 100 μm^2, but the dispersion is generally a little larger, so the total performances are almost the same. Based on the simulation result, SMF-E was fabricated by VAD method. The fabrication results of SMF-E are shown in Table 11. An $A_{\rm eff}$ as large as 100 μm^2 were obtained keeping a low dispersion property. Also low attenuation and low PMD could be obtained. Cutoff wavelength measured by 2-m methods was about 1520 nm, but less than 1400 nm in cases measured by 22 m. The attenuation spectrum of SMF-E is shown in Fig. 17 where a very low and flat characteristic could be confirmed. Attenuation of 1550nm was about 0.19 dB/km and water peak loss (about 1385 nm) was only 0.295 dB/km.

As described above, SMF-E had successfully enlarged the $A_{\rm eff}$, keeping other characteristics about the same level with conventional SMF, by dual shaped core profile. As one of the next approaches, loss reduction with fully fluorine doped SMF-E was experimentally demonstrated. As shown in Fig. 18, most of the light transmits through

Table 11. Fabrication results of Enlarged A_{eff} SMF (SMF-E) with DSC profile at 1550 nm [23]

	Dispersion [ps/nm/km]	Slope [ps/nm^2/km]	RDS [/nm]	Loss [dB/km]	A_{eff} [μm^2]	λ_c [nm]	PMD [ps/rkm]	Bend(*) [dB/m]
No.1	17.5	0.062	0.0035	0.189	100	1520	0.04	5

(*) Bending loss increase at 20 mm diameter

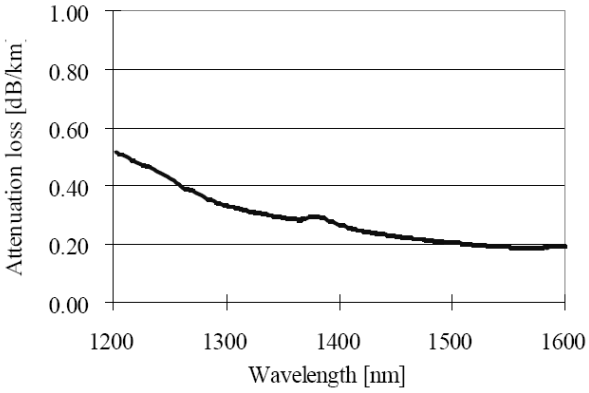

Fig. 17. Attenuation spectrum of SMF-E.

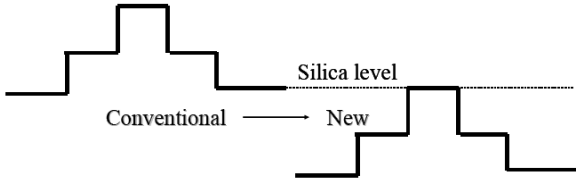

Fig. 18. Profiles of conventional SMF-E(left) and New FF type (right) The center core of the new profile is almost silica level while keeping the same structure as a conventional one [25].

the inside of the pure silica center-core that contains no GeO_2 doping and attenuation loss was effectively reduced [25] in the same way as the conventional FF-SMF.

Fabrication result of low loss SMF-E (Refered to as LL-SME hereafter) is shown in Table 12. And an attenuation spectrum of LL-SME is shown in Fig. 19. As shown in Table 12 and Fig. 19, very low attenuation was obtained keeping other optical properties about the same level with conventional SMF-E. The loss of the lowest wavelength was 0.166 dB/km. Water peak loss and local dispersion was a little larger than those of SMF-E, but still small enough. The difference of dispersion was mainly due to the difference of center core shape. Conventional SMF-E had α shaped profile attributing smaller dispersion, but it is very difficult to realize a shaped core with FF or PSC type

Table 12. Fabrication results of enlarged A_{eff} and Fully Fluorine doped SMF (LL-SME) at 1550 nm [25].

	Dispersion [ps/nm/km]	Slope [ps/nm^2/km]	RDS [/nm]	Loss [dB/km]	A_{eff} [μm^2]	λ_c [nm]	PMD [ps/rkm]	Bend(*) [dB/m]
No.1	19.5	0.060	0.0031	0.169	105	1510	0.04	5

(*) Bending loss increase at 20 mm diameter

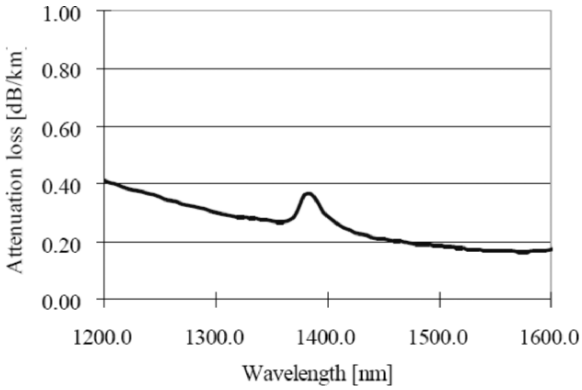

Fig. 19. Attenuation spectrum of LL-SME.

fiber, because of an absence of GeO_2 dopant and a step-like core profile is inevitable. Therefore the dispersion became a little larger. However, low attenuation loss and similar properties with SMF-E were confirmed. The A_{eff} became a little larger by changing the shape of the centre core, so comparable optical properties with SMF-E plus IDF were obtained with LL-SME plus IDF.

Other than a DSC profile, LL-SME with a W-shaped profile (as PSCF) has been also reported. In [26], PSCF with attenuation loss as low as 0.1488 dB/km at 1568 nm was successfully achieved and reported by reducing the Rayleigh scattering loss coefficient at 0.745 dB/km/μm^{-4}. The system impact of reducing attenuation loss was also analyzed and reported in [26]. Though optical properties with an optimized DSC profile were comparable with a W-shaped profile, macro bending loss is generally better with a W-shaped profile. Therefore W-shaped SMF-E (SLA type fiber) has become a standard positive dispersion fiber, and it has become a commercial base now.

3.2. Dispersion Enlargement with IDF

Initial IDFs had dispersion of about –20 ps/nm/km at 1550 nm, so SMF and IDF would be connected at about 1:1 length ratio. Though IDF is placed after SMF to suppress a nonlinear problem, the total equivalent A_{eff} was about 50 μm^2, because the A_{eff} of IDF is still small compared to SMF or NZ-DSF and the length of IDF is half of the total length. Thanks to the development of SMF-E, an equivalent A_{eff} of SMF-E plus initial

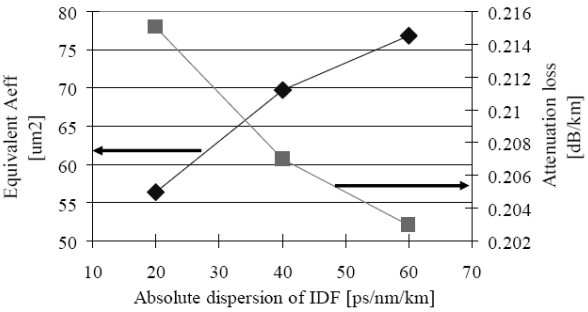

Fig. 20. Absolute dispersion of IDF with a W-shaped profile vs. equivalent Aeff and attenuation loss of 1550 nm.

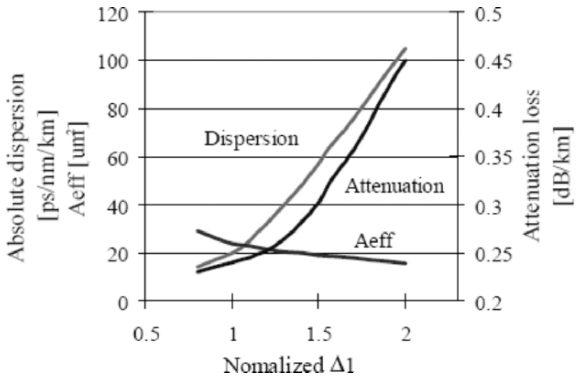

Fig. 21. A nomalized $\Delta 1$ setting that of initial IDF to 1.0 vs. optical properties of IDFs.

IDF was enlarged about 55 μm^2, but not a sufficient value compared to large A_{eff} NZ-DSFs. Equivalent A_{eff} can be drastically improved by changing the length ratio of SMF vs. IDF. Figure 20 shows an equivalent A_{eff} and attenuation loss of SMF-E plus IDF with local dispersion of –20, –40 and –60 ps/nm/km. Attenuation loss and the A_{eff} of IDF were assumed to be constant, at 0.240 dB/km and 24 μm^2 each. As shown in the figure, an absolute dispersion enlargement of IDF is very effective for the aspect of large equivalent A_{eff} and low attenuation loss of a total line. However, IDF has a tradeoff with large absolute dispersion vs. large A_{eff}, low attenuation loss and low PMD. In this section, the authors will explain how these trade-offs have been solved.

In the first stage, IDF with enlarged absolute dispersion was developed with a W-shaped profile. Figure 21 shows the optical properties of IDF changing a $\Delta 1$ value with a W-shaped profile. $\Delta 1$ was normalized setting an initial IDF $\Delta 1$ value as 1.0. As shown in the figure, $\Delta 1$ changes the dispersion property of IDF effectively. However, it

Table 13. Typical characteristics of IDF-20 and IDF-40 using a W-shaped profile at 1550 nm.

	Dispersion [ps/nm/km]	Slope [ps/nm^2/km]	RDS [/nm]	Loss [dB/km]	$A_{\rm eff}$ [μm^2]	λ_c [nm]	PMD [ps/rkm]	Bend(*) [dB/m]
IDF-20	–20	–0.060	0.003	0.24	24	820	0.07	10
IDF-40	–40	–0.120	0.003	0.26	21	800	0.10	5

(*) Bending loss increase at 20 mm diameter

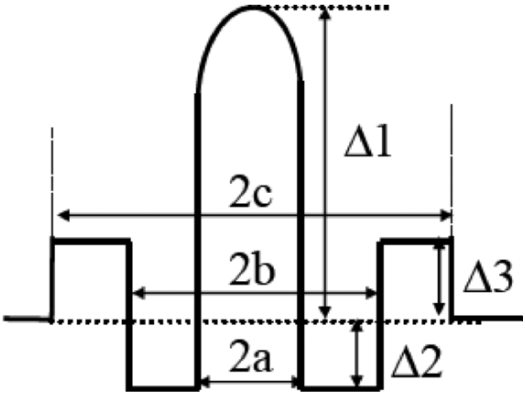

Fig. 22. W plus side-core layer profile.

is clearly shown that the enlargement of absolute dispersion accompanies smaller $A_{\rm eff}$ and higher attenuation loss. Table 13 shows the optical characteristics of conventional IDF (IDF-20) and Enlarged Dispersion IDF (IDF-40) that were actually fabricated by VAD method. Both IDF-20 and IDF-40 were designed with a W-shaped profile (Fig. 3). As shown in the table, large dispersion as –40 ps/nm/km was realized with IDF-40, but $A_{\rm eff}$ was 21μm^2 and attenuation loss became 0.26 dB/km. PMD also became larger and it also strictly limits transmission performance [27,28]. As aforementioned, the dispersion enlargement of IDF, which can be realized by changing a Δ1 value of a w-shaped profile, is advantageous for low nonlinear property in a total line, but it generally sacrifices $A_{\rm eff}$, loss and PMD properties.

These problems have been successfully solved by the selection of a new type of profile known as a W plus side-core layer profile (Fig. 22) [23,24]. For a high negative slope, a deep depressed layer in the side of center core is necessary, but the deep depressed layer makes it difficult to enlarge $A_{\rm eff}$ as being confirmed with IDF-40. However, a side core layer is very effective to enlarge $A_{\rm eff}$ while preventing a bending loss increase. An example of simulation results is shown in Fig. 23. We call this type of IDF as IDF-45E hereafter.

Based on the simulation results, IDF-45E was actually fabricated by the VAD method. The fabrication results of IDF-45E are shown in Table 14, No.1. Both negative dispersion and dispersion slope could be successfully achieved. Larger $A_{\rm eff}$ than

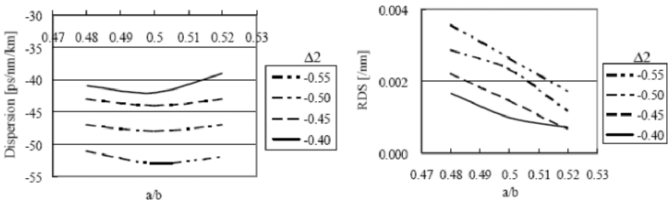

Fig. 23. Examples of enlarged dispersion IDF (IDF-45E) simulations [23] (left: Index profile values vs. dispersion, right: Index profile values vs. RDS).

initial IDF, about 28 μm^2, was obtained with large absolute dispersion value of about –45 ps/nm/km by the W plus side-core layer profile. It should be noted how low attenuation loss, PMD and bending loss could be obtained by the new type of profile. Additionally, while cutoff wavelength was of concern, it was short enough even if Raman amplification or S-Band transmission were to be adapted, though they have been difficult in the actual submarine system. Recently IDF-45E with low attenuation of 0.234 dB/km and a large $A_{\rm eff}$ of more than 30 μm^2 was also reported [29] and the reported results are shown in Table14, No.2. Currently, IDF-45E has become a standard IDF, so IDF itself generally means IDF-45E.

Table 14. Fabrication results of IDF-45E type fibers at 1550 nm.

	Dispersion [ps/nm/km]	Slope [ps/nm^2/km]	RDS [/nm]	Loss [dB/km]	$A_{\rm eff}$ [μm^2]	$\lambda_{\rm c}$ [nm]	PMD [ps/rkm]	Bend(*) [dB/m]
No.1 [23]	–45	–0.135	0.003	0.24	28	1450	0.06	5
No.2 [29]	–44	–0.128	0.0029	0.234	31.5	$<$1400	0.06	5

(*) Bending loss increase at 20 mm diameter

Other than IDF-45E, IDF-E with large dispersion like –60 ps/nm/km (IDF-60E) was also developed [30]. To avoid sacrificing $A_{\rm eff}$, attenuation loss and PMD property, a W plus side-core layer profile (Fig. 22) was selected again. Fabricated results of IDF-60E are shown in Table 15, and as shown in the table, about the same value of $A_{\rm eff}$ with initial IDF could be realized keeping large absolute dispersion of -60 ps/nm/km. Attenuation loss became a little larger than that of initial IDF but was still low. Total loss and $A_{\rm eff}$ could be improved because of a short length ratio of IDF. Though this fiber showed a comparable performance with IDF-45E, IDF-45E has become a standard IDF and a very high performance was reported as [29], so very few fabrication results have been reported after [30].

3.3. Attenuation and Nonlinearity Reduction with IDF

As described in section 3.2, a dispersion of initial IDF was about –20 ps/nm/km at 1.55 μm, and many investigations have been made in order to enlarge the absolute dispersion of IDF, because nonlinearity and attenuation of IDF are higher than SMF

Table 15. Fabrication results of IDF-60E at 1550 nm [30].

	Dispersion [ps/nm/km]	Slope [ps/nm^2/km]	RDS [/nm]	Loss [dB/km]	A_{eff} [μm^2]	λ_c [nm]	PMD [ps/rkm]	Bend(*) [dB/m]
No.1	–60	–0.220	0.0036	0.255	23	1500	0.04	3

(*) Bending loss increase at 20 mm diameter

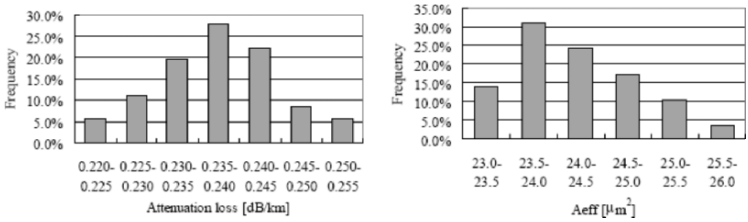

Fig. 24. The attenuation loss and A_{eff} distribution of initial IDF (left: attenuation; right; A_{eff}).

type fibers [23,24,29,30] and shortening IDF length is very effective to improve a total performance. Figure 24 shows the attenuation loss and A_{eff} distribution of initial IDFs.

The attenuation loss and A_{eff} were distributed in a much worse range compared to SMF type fibers. That is the reason why short-length IDF (enlarged-dispersion IDF) is very effective to improve the total optical properties. However, the large accumulated dispersion caused by enlarged dispersion of IDF, which generated no serious problem in case of 10 Gb/s transmissions, would cause a serious problem due to a SPM-GVD effect in case of 40 Gb/s transmissions [31]. To solve this problem, many couples configurations (such as a quadruple configuration) of SMF-E plus IDF-E have been proposed [31], but many couples configurations cause a system complexity. So, other than the enlarged dispersion IDF such as IDF-45E, the attenuation and nonlinearity reduction of IDF with low local dispersion of about –20 ps/nm/km have been researched in a laboratory base to enable long-haul 40-Gb/s transmissions [25,32]. Though no experimental transmission results have been reported with this IDF, because many researchers have been more commonly researched about some special technologies (such as new signal format, Raman amplification and so on) using more established SMF-E and IDF-45E fiber types (not only AB map, but also ABA or ABAB map to reduce the accumulated dispersion, for example) and a Medial Dispersion Fiber (MDF) that gives more sophisticated solution has already been developed (see section 4.1), to explore how far IDF can go in terms of low attenuation loss and a large A_{eff} has been quite interesting, and that kind of technological challenge will be explained here.

The selected index profile is a W plus side-core layer profile (Fig. 22) again, to prevent bending loss increase. The index profile was numerically optimized keeping dispersion to about –20 ps/nm/km and the RDS value to about 0.003/nm. Three factors were carefully considered based on the experience through initial IDF fabrication. First, optimum delta was carefully chosen, because delta has a great relationship with attenuation loss. If it is too high, Rayleigh scattering loss becomes larger, meanwhile

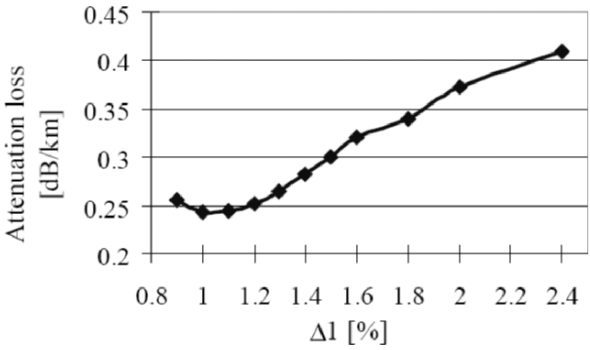

Fig. 25. The relation with the $\Delta 1$ and attenuation loss of initial IDF with a W-shaped profile.

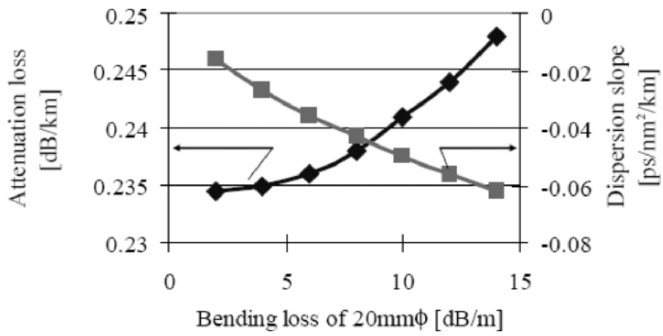

Fig. 26. The relation with bending loss (20 mmϕ) vs. attenuation loss and slope at 1550 nm of initial IDFs with a W-shaped profile.

if it is too low, the attenuation loss increased by a bending loss. Figure 25 shows the relation between $\Delta 1$ of W-shaped IDFs and attenuation loss.

As shown in the figure, the attenuation loss has a strong relationship with the $\Delta 1$, because $\Delta 1$ value strongly affects both Rayleigh scattering loss and a micro-bending loss increase. We also designed the IDF to have a low bending loss less than 5 dB/m at 20 mm diameter by means of the refractive index profiles optimization, because a relatively high bending-loss had increased to the attenuation of 1.55 μm in the case of initial IDF. Figure 26 shows the relationship between bending loss (of 20 mm diameter) of initial IDFs vs. attenuation loss and dispersion slope. Attenuation loss increased rapidly when the bending loss became larger than 5 dB/m. However, bending loss suppression and a high compensating rate had been a trade-off as part of the relationship with initial IDFs. The W plus side-core layer profile was very effective to solved this problem. OH induced loss was also suppressed to prevent a 1.55-μm loss increase by the fabrication process optimization. The relation between OH induced loss and 1550 nm loss of initial IDF was shown in Fig. 27. An OH induced peak also

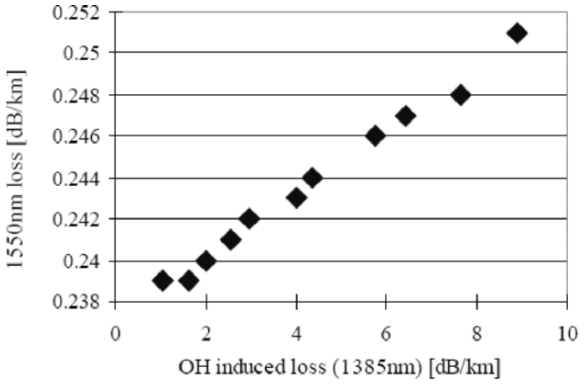

Fig. 27. The relation with OH induced loss and 1550 nm loss of initial IDF.

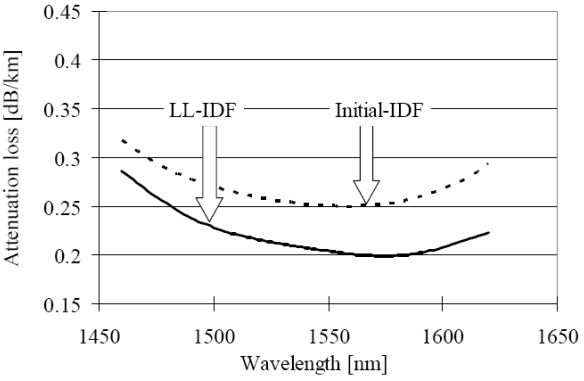

Fig. 28. The attenuation loss spectrum of LL-IDF and initial IDF over the three transmission bands (S,C and L-Band).

influenced 1550 nm attenuation loss. Actually, some of initial IDFs had large OH peaks and increased 1550 nm loss by the effect. It was one of the biggest challenges, but successfully solved by the experimental fabrication process optimizations, especially the sintering process conditions, such as gas composition, sintering time and sintering temperature.

Based on the simulation result, low-loss IDF (LL-IDF) was carefully fabricated to obtain very low loss considering the points mentioned before. The results of fabrication were shown in Table 16. Attenuation had a value as low as 0.205 dB/km, suppressing local dispersion at about the same level as initial IDF. A_{eff} was enlarged to 34 μm^2 so nonlinear phenomena would be suppressed. Figure 28 shows the attenuation spectrum of LL-IDF (The loss spectrum of initial IDF is also shown for comparison). As shown in Fig. 28, wide-band flatness, not only in C-Band and L-Band but also S-Band, was

Table 16. Fabrication results of LL-IDF at 1550 nm [25].

	Dispersion [ps/nm/km]	Slope [ps/nm^2/km]	RDS [/nm]	Loss [dB/km]	A_{eff} [μm^2]	λ_c [nm]	PMD [ps/rkm]	Bend(*) [dB/m]
No.1	–22	–0.077	0.0035	0.205	34	1500	0.05	0.6

(*) Bending loss increase at 20 mm diameter

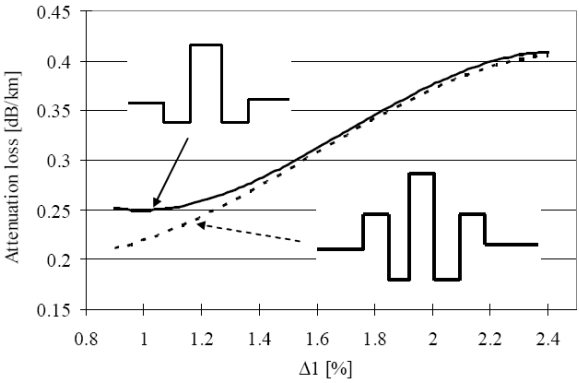

Fig. 29. $\Delta 1$ value of various IDFs with W-shaped profile and W+side-core layer profile vs. attenuation loss of 1550 nm.

confirmed because bending loss and OH loss (about 1.0 dB/km at 1385 nm water peak) were successfully suppressed. The attenuation loss of around 1570 nm was lower than 0.20 dB/km (0.196 dB/km at the lowest wavelength), and about the same level as SMF type fibers. This is the lowest value of dispersion compensating type fibers. We should add that a micro-bending loss of this RDF was about 0.1 dB/km which is comparable with conventional DSFs. Though the merit of this type of fiber became vague by the development of MDFs, to be described in section 4.1, this technology will be applied to improve IDF-45E, that is standard IDF now, and MDF loss properties.

After the development of initial IDF, IDF-E and LL-IDF, many types of IDFs with various $\Delta 1$ values have been fabricated. But from the point of view of low attenuation loss, a side core layer addition is very effective to prevent bending loss increase and to obtain lower loss especially in a low $\Delta 1$ region as shown in Fig. 29. Recently, most of IDFs or N-MDFs, which will be introduced later, are designed with the W+side-core layer profile or more complicated profiles to realize good optical performances without a bending loss increase. It should be worth adding that the authors mainly described the fabrication results obtained by the VAD method, but high performance SMFs and IDFs were also fabricated and reported by other methods such as a Modified Chemical Vapor Deposition (MCVD) method, an Outside Vapor Deposition (OVD) method, a Plasma Chemical Vapor Deposition (PCVD) method and so on, and they have become commercial-available all over the world now.

3.4. System Experiments Using Improved IDF

As described in section 2.3, SMF plus initial IDF showed very high transmission performances. However, total optical performances have been further improved with new types of SMF and IDF. The total optical properties of newly developed SMF plus IDF-E, connected each other to manage dispersion at 1.55 μm to be nearly zero in a 50-km span, are summarized in Table 17 with other types of optical links for comparison. The splice loss was assumed to be 0.1 dB; typical splice loss of DML and other fibers connections. From the calculation, the total equivalent A_{eff} was enlarged more than 70 μm^2. The equivalent A_{eff} of a conventional SMF plus initial IDF was less than 50 μm^2, so it would provide low nonlinearity. Improved NZ-DSF for a terrestrial system, especially large A_{eff} NZ-DSF, showed relatively large equivalent A_{eff} as 64 μm^2, but still smaller than that of DML, because the A_{eff} of NZ-DSF is smaller than SMF-E type fiber. The total dispersion slope was less than 0.01 ps/nm^2/km and the total attenuation loss was about 0.205 dB/km that is much better than that of SMF+DCF or NZ-DSF+DCF. In the case of LL-SME being used as a pre-fiber and IDF-E as a post-fiber, the total attenuation was further reduced to a ultra low value, such as 0.19 dB/km. Figure 30 shows the attenuation and dispersion spectrums of SMF-E plus IDF-45E. Both attenuation and dispersion are very flat in a wide range of wavelength from 1530 to 1580 nm. For example, dispersion deviation was $\pm$0.05 ps/nm/km over the whole C-band.

Table 17. Total optical properties of SMF-E plus IDF-E and other types of transmission lines at 1550 nm.

Combination	Accumulated Disp$^{(1)}$ [ps/nm]	Disp. Slope [ps/nm^2/km]	Loss [dB/km]	$A_{\text{eff}}{}^{(2)}$ [mm^2]	PMD [ps/rkm]
SMF-E+IDF-45E (2:1)	630	0.007	0.205	75.8	0.048
LL-SME+IDF-45E (2:1)	681	0.001	0.192	72.8	0.056
SMF-E+IDF-60E (3:1)	677	–0.002	0.206	75.2	0.041
LL-SME+IDF-60E (3:1)	735	–0.009	0.192	72.1	0.048
SMF-E+LL-IDF (1:1)	487	0.001	0.197	70.7	0.044
LL-SME+LL-IDF (1:1)	517	–0.004	0.188	67.1	0.045
Conventional SMF+initial IDF	452	0.007	0.212	49.6	0.054
Conventional FF+initial IDF	480	0.003	0.207	46.6	0.059
SMF+DCF	708	$<$0.005	0.233	56.2	0.044
NZ-DSF(Table3-No.1)+DCF	238	$<$0.005	0.221	63.6	0.053
NZ-DSF(Table3-No.2)+DCF	370	$<$0.005	0.232	56.2	0.054
NZ-DSF(Table3-No.3)+DCF	370	$<$ 0.005	0.232	48.3	0.054
NZ-DSF(Table3-No.4)+DCF	283	$<$ 0.005	0.221	41.4	0.052
SMF+Negative NZ-DSF	126	0.060	0.208	56.1	0.048
Positive NZ-DSF+ NegativeNZ-DSF	75	0.060	0.212	49.9	0.050

(1) Maximum accumulated dispersion in a 50-km span; (2) equivalent A_{eff}

Using new SMF-E plus IDF-45E type fiber, many experimental transmission results have been reported, and high performance was confirmed with SMF-E plus IDF-E [33–42]. The aggregate of 10 and 40 Gb/s transmission experimental results reported in ECOC'03 and OFC'04 are summarized in Fig. 31. As shown in the figure, both 10-

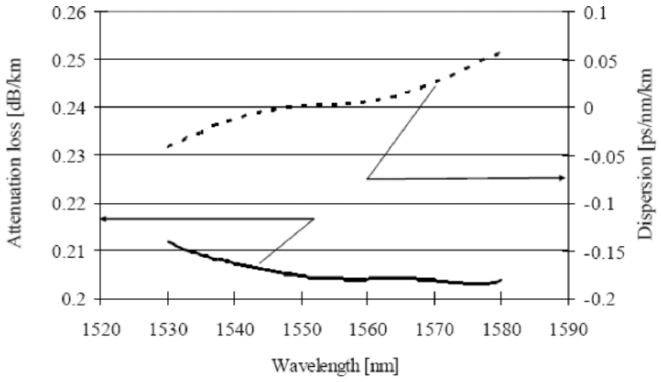

Fig. 30. An attenuation and dispersion spectrum of SMF-E plus IDF-45E [23].

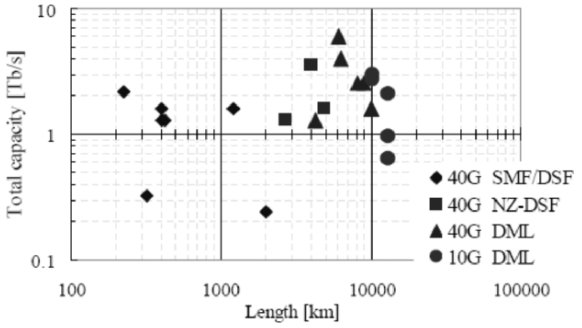

Fig. 31. Reported experimental transmission results of ECOC'03 and OFC'04.

and 40-Gb/s long-haul high-capacity transmissions have been realized by DML. Of course, it is just only the results of two recent conferences, and more detailed analysis will be needed to conclude the best transmission lines in terms of the best system performance. However, it is clearly seen that DML showed suitable properties for a long-haul high-capacity transmission.

As described before, new SMF-E plus IDF-45E are used as a standard DML. Equivalent A_{eff} SMF-E plus various types of IDFs are summarized in Fig. 32, and dispersion of –45 ps/nm/km shows good properties in terms of the balance between large equivalent A_{eff} and low attenuation loss. However, we need to pay attention that most of the DML transmission experiments use special techniques such as Raman amplification, special signal formats, advanced FEC, multiple fiber configurations, large diameter fibers and so on to realize a long-haul 40-Gb/s transmission. To realize a 40-Gb/s transmission without such special techniques, a transmission line with low accumulated dispersion of about the same level as NZ-DSF type is required [31].

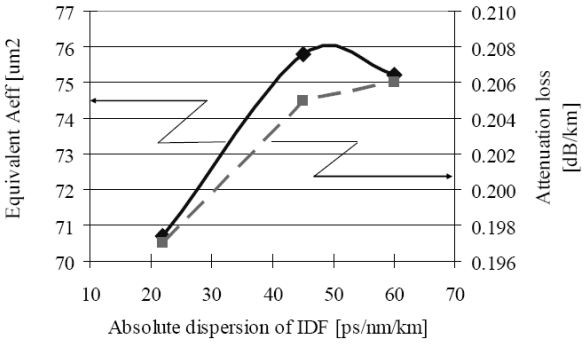

Fig. 32. Absolute dispersion of IDF-E vs. equivalent Aeff and atteanution loss.

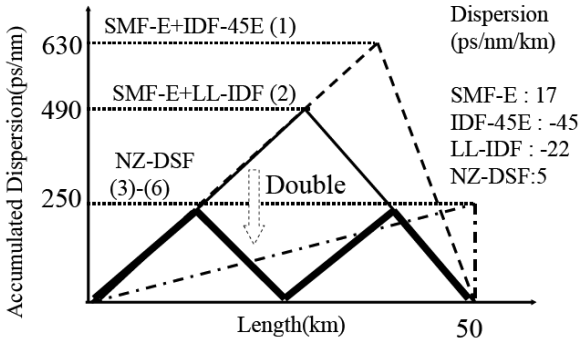

Fig. 33. Accumulated dispersion characteristics in a 50-km span of transmission lines consisted of SMF+IDF and NZ-DSFs.

Accumulated dispersion of SMF-E plus LL-IDF and various types of transmission line are shown in Fig. 33. Also in Fig. 33, the accumulated dispersion of SMF-E plus LL-IDF would be suppressed as low as conventional NZ-DSF by adapting only a double configuration (ABAB map). So a long-haul 40-Gb/s transmission would be enabled by using this transmission line in the future. Besides, SMF-E+LL-IDF showed lower attenuation loss than +IDF-45E. When LL-SME was used instead of SMF-E, the total attenuation loss was suppressed to 0.188 dB/km. This attenuation has been the lowest value as a dispersion management (flattened) transmission line up until now.

However, as described in previous section, using special techniques such as Raman amplification and advanced signal format with more established DML types such as SMF-E+IDF-45E (or NZ-DSF+DCF) has become more mainstream than using a new type of DML to realize the long-haul high-capacity 40-Gb/s transmission. In considering counter-transmission and lower accumulated dispersion, not-only a SMF-IDF (AB) configuration, but also a SMF-IDF-SMF (ABA) configuration was proposed [42],

Table 18. Total optical properties of SMF-E plus LL-IDF (AB map, ABA map and ABAB map) at 1550 nm.

Combination	Accumulated Disp$^{(1)}$ [ps/nm]	Disp. Slope [ps/nm^2/km]	Loss [dB/km]	$A_{\mathrm{eff}}{}^{(2)}$ [mm^2]	PMD [ps/rkm]
SMF-E+LL-IDF (AB map)	487	0.001	0.197	70.7	0.044
SMF-E+LL-IDF (ABA map)	244	0.001	0.200	56.5	0.044
SMF-E+LL-IDF (ABAB map)	244	0.001	0.202	60.7	0.044

(1) Maximum accumulated dispersion in a 50-km span; (2) equivalent A_{eff}

though they still required advanced techniques such as special signal formats, Raman amplification and so on to cancel the impairment due to an accumulated dispersion. Furthermore, a simpler configuration with MDF has been realized now, so experiments with a double configuration of SMF-E+LL-IDF have not been reported until now. Though an ABAB map or an ABA map of SMF-E+LL-IDF shows comparable performances with MDF in terms of an accumulated dispersion and attenuation loss as shown in Table 18, which will be explained in the next section, the equivalent A_{eff} of these maps are generally small, because IDF is placed in a relatively high intensity power transmitting part. Moreover, these configurations (ABA or ABAB configurations) might be still too complicated considering the actual installing and repairing, because even a simple AB map has many problems with actual installation such as repairing and splicing into a real system.

4. What Would Happen in the Future with IDF/RDF?

4.1. Development of MDF

Development of Initial MDF

As described in the section 3.3, a low-loss IDF (LL-IDF) was successfully developed. Attenuation of 0.205 dB/km was obtained keeping dispersion of about –20 ps/nm/km, fully dispersion slope compensation for SMF-E and large A_{eff} of 34 μm^2. The maximum accumulated dispersion of SMF-E plus LL-IDF in a 50-km span was suppressed about 500 ps/nm, so by using only a double configuration (ABAB map), the maximum accumulated dispersion was suppressed at about the same level with conventional NZ-DSF. That would be very advantageous considering the future high-bit-rate transmission of 40 Gb/s or above. However, in other words, we need to use a double configuration to suppress the maximum accumulated dispersion comparable with conventional NZ-DSF. Of course, a single configuration DML with low accumulated dispersion (preferably about the same level as conventional NZ-DSF) is more desirable. On the other hand, NZ-DSF+DCF line is difficult to adapt in a submarine system due to high attenuation loss and small equivalent A_{eff} as shown in the Table 17. Recently, an alternative transmission line consisted of Positive Medial Dispersion Fiber (P-MDF) and Negative Medial Dispersion Fiber (N-MDF) has been proposed to respond to the

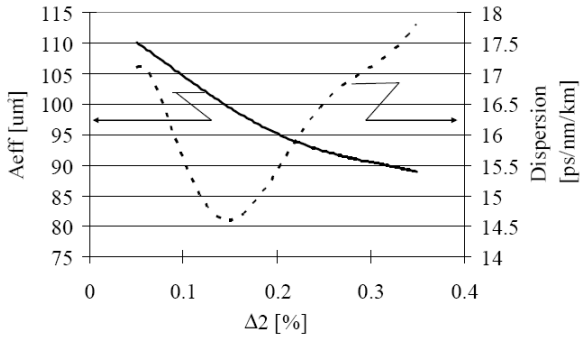

Fig. 34. An example of simulation results of initial P-MDF [43] ($\Delta 2$ of dual-shaped core profile vs. A_{eff} and dispersion).

requirements. The development of an initial MDF was reported in ECOC'00 [43] and many improved results have been reported after that.

Positive-Medial Dispersion Fiber (P-MDF) was designed to achieve the medial dispersion of NZ-DSF and SMF. It is more desirable to have as large an A_{eff} as the SMF-E type fiber to consider a submarine application. We have chosen a DSC-shaped profile (Fig. 16) again and the profile was numerically optimized keeping the center core delta a little larger than that of the conventional SMF so as not to impair bending loss properties. Then, by optimizing the shape of the center core and adjusting the side core carefully, low dispersion and a large A_{eff} were realized simultaneously. Figure 34 shows the correlation between $\Delta 2$ value (delta of side-core) and calculated dispersion and A_{eff} with optimized other profile parameters.

Table 19. First fabrication results of initial P-MDFs obtained in lab of Furukawa Electric at 1550 nm [43].

	Dispersion [ps/nm/km]	Slope [ps/nm^2/km]	RDS [/nm]	Loss [dB/km]	A_{eff} [μm^2]	λ_c [nm]	PMD [ps/rkm]	Bend(*) [dB/m]
No.1	14.7	0.070	0.0048	0.19	98	1560	0.04	3.5
No.2	14.6	0.068	0.0047	0.19	103	1702	0.05	2.5

(*) Bending loss increase at 20 mm diameter

As shown in the figure, a region of A_{eff} about 100 μm^2 and dispersion lower than 15 ps/nm/km surely existed. Based on the simulation result, P-MDF was fabricated by the VAD method in a laboratory. The fabrication results of the first two P-MDF samples are shown in Table 19. Medial dispersion of about 14 ps/nm/km was obtained with a large A_{eff} of about 100 μm^2. Medial dispersion with those of NZ-DSF and SMF were advantageous for the suppression of both FWM phenomenon and signal distortion due to dispersion. Other characteristics such as dispersion slope, attenuation and PMD showed very good performances. No. 2 had a longer λ_c of about 1700 nm, but it became less than 1500 nm in the case of a 22-m-measurement method.

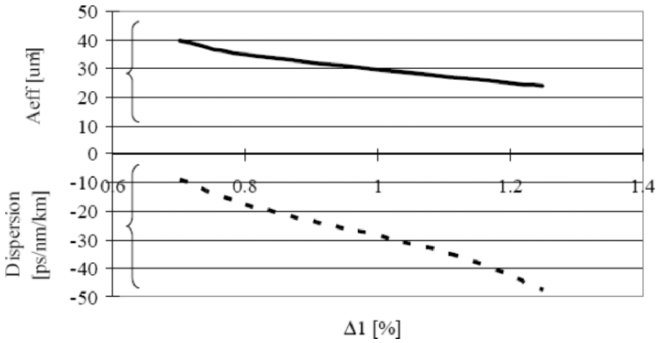

Fig. 35. The relation of $\Delta 1$ vs. A_{eff} and dispersion at 1550 nm with initial N-MDF [43].

Negative-Medial Dispersion Fiber (N-MDF) was also designed to achieve medial dispersion. It is more desirable to have a larger A_{eff} than that of IDF-45E (about 28 μm^2) because the longer N-MDF will be used to suppress the maximum accumulated dispersion, and the negative dispersion slope for the compensation of not only dispersion but also its slope of P-MDF. To achieve the negative dispersion slope, a depressed layer surrounding the center core is required, but this layer makes it difficult to enlarge the A_{eff} value as previously mentioned. To solve this impairment, the center core delta was designed as a low level (about a two-thirds value of conventional IDF) to provide not only a large A_{eff} but also low dispersion, loss and PMD, while a third-layer at the side of the depressed layer was added again and optimized to prevent the bending loss increase like IDF-E. Figure 35 shows the correlation of the center core delta vs. the calculated dispersion and MFD. A region with an A_{eff} of more than 35 μm^2 as well as negative medial dispersion and negative dispersion slope were selected for the initial N-MDF. N-MDF was fabricated based on simulation results. The fabrication results of N-MDF are shown in Table 20. The medial dispersion between NZ-DSF and SMF were obtained with a negative sign. Dispersion slope also showed negative values. Because initial N-MDF was designed aiming to obtain an A_{eff} as large as possible in the design stage, a very large A_{eff} was realized. Also low attenuation loss and PMD could be obtained with each fiber.

Table 20. First fabrication results of initial N-MDFs obtained in lab of Furukawa Electric at 1550 nm [43].

	Dispersion [ps/nm/km]	Slope [ps/nm^2/km]	RDS [/nm]	Loss [dB/km]	A_{eff} [μm^2]	λ_c [nm]	PMD [ps/rkm]	Bend(*) [dB/m]
No.1	–14.2	–0.038	0.0027	0.24	40	1432	0.06	16
No.2	–14.9	–0.083	0.0055	0.24	34	1257	0.07	15

(*) Bending loss increase at 20 mm diameter

With the initial P- and N-MDF, the medial dispersion of those of NZ-DSF and SMF were obtained with both positive and negative signs. These MDFs are connected with

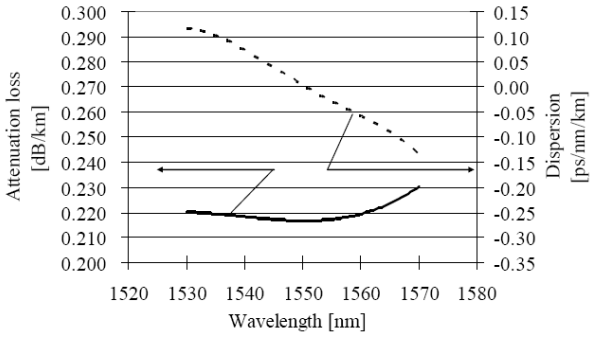

Fig. 36. Attenuation loss and dispersion spectrum of initial P-MDF plus N-MDF [43].

each other in about a 1:1 length ratio and dispersion flatness could be obtained in a total line. The total characteristics of P-MDF 01 and N-MDF 01/02 are summarized in Table 21. Both fibers have low local dispersion, so the maximum accumulated dispersion was kept small for a long distance. The dispersion slope at 1550 nm was about 0.01 ps/nm^2/km. The average loss of repeater span at 1550 nm was about 0.215 dB/km. The equivalent $A_{\rm eff}$ was as large as SMF-E plus IDF-E. An attenuation and dispersion spectrum of the link consisting of P-MDF1 with N-MDF2 is shown in Fig. 36. Both attenuation and dispersion flatness over 1530 to 1570 nm could be obtained.

Table 21. Optical properties of initial P-MDF plus N-MDF at 1550 nm [43].

Combination	Accumulated Disp$^{(1)}$ [ps/nm]	Disp. Slope [ps/nm^2/km]	Loss [dB/km]	$A_{\rm eff}{}^{(2)}$ [mm^2]	PMD [ps/rkm]
P-MDF 01+N-MDF 01	361	0.015	0.217	69.6	0.050
P-MDF 01+N-MDF 02	370	–0.006	0.217	65.1	0.055

(1) Maximum accumulated dispersion in a 50-km span; (2) equivalent $A_{\rm eff}$

As a result, this new type of link was confirmed to be very suitable for the high-bit-rate WDM transmission. Thus, we tried to start mass-productive confirmation with the initial MDF, but one big problem was left before that. The attenuation loss of N-MDF was 0.24 dB/km at 1.55 μm and it would affect total net-loss greatly because length of N-MDF would be about a half of the total line. Furthermore, attenuation of 1.58 μm was increased to 0.29 dB/km by the bending loss, so attenuation loss of longer wavelength was larger as shown in the Fig. 36. To achieve more reliable attenuation, a kind of compromise with N-MDF must be considered [44]. So, N-MDF was re-designed to achieve a low bending loss property, for example, 5 dB/m at 20 mm diameter, before mass-production. Fabrication results of re-designed N-MDF are shown in Table 22.

A bending loss of 20 mmϕ was suppressed about 7 and 4 dB/m, respectively. The characteristics are little inferior to the conventional ones for the aspect of a dispersion slope with N-MDF3 and $A_{\rm eff}$ with N-MDF4, but the low attenuation characteristics realized by suppressing bending loss increased. Attenuation loss of N-MDF was about

Table 22. Fabrication results of re-designed N-MDFs to obtain lower bending loss performance at 1550 nm [44].

	Dispersion [ps/nm/km]	Slope [ps/nm^2/km]	RDS [/nm]	Loss [dB/km]	A_{eff} [μm^2]	λ_c [nm]	PMD [ps/rkm]	Bend(*) [dB/m]
No. 3	–15.3	–0.030	0.0020	0.218	34	1198	0.06	7
No. 4	–13.2	–0.050	0.0038	0.215	32	1256	0.08	4

(*) Bending loss increase at 20 mm diameter

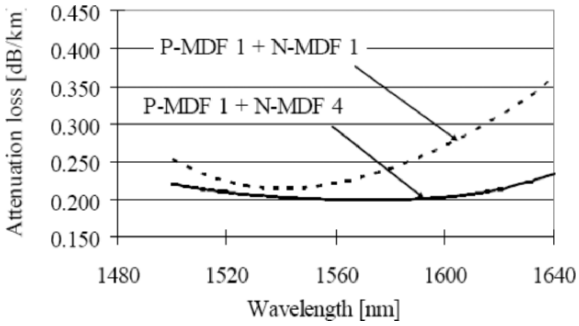

Fig. 37. Attenuation spectrum of initial P-MDF plus two types N-MDFs [43,44].

0.215–0.220 dB/km. Furthermore, loss of 1.58 μm was 0.227 dB/km for N-MDF3 and 0.213 dB/km for N-MDF4. It indicated the remarkable improvement from conventional N-MDF in terms of the total net-loss connecting with P-MDF as shown in Fig. 37, and mass-production was attempted with this type of N-MDF considering the higher reliability.

Table 23. Typical characteristics of mass-produced initial MDFs at 1550 nm.

MDF properties	P-MDF	N-MDF	Total
Clad diameter [mm]	125.0±1.0	125.0±1.0	
Clad non-circularity [%]	0.1	0.1	
Core ovality [mm]	0.1	0.1	
Loss [dB/km] @1550 nm	0.20	0.22	0.205
Dispersion [ps/nm/km] @1550 nm	14±3.0	–14±5.0	0(*350)
RDS [/nm] @1550 nm	0.0050	0.0046	
Compensate rate [%] @1550 nm	–	92	
λ_c [nm]	1500	1500	
A_{eff} [mm^2] @1550 nm	95	32	62
Bend loss at 20ϕ [dB/m] @1550 nm	10	5	
PMD [ps/rkm]	0.04	0.06	0.05

(*) Maximum accumulated dispersion in a 50-km span

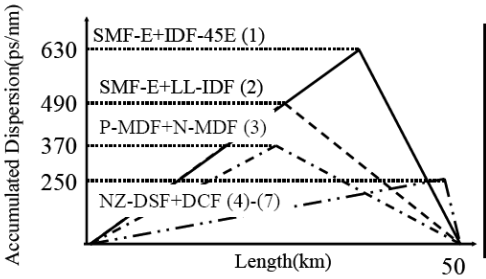

Line	Aeff	Loss
(1)	76	0.205
(2)	71	0.197
(3)	62	0.205
(4)	64	0.221
(5)	56	0.232
(6)	48	0.232
(7)	41	0.221

Fig. 38. Accumulated dispersion characteristics (50 km span) , Equivalent $A_{\rm eff}$ and total nett-loss for various types of transmission lines.

As described above, the initial design considerations have been accomplished, so we fabricated many samples to confirm the mass-productivity. The typical optical properties of P-MDF and N-MDF were shown in Table 23. They showed very reliable and high performances while maintaining a good mass-productivity due to their relatively simple index profiles. Tough a total equivalent $A_{\rm eff}$ was little impaired as $62\mu{\rm m}^2$, that is still almost the same value as with NZ-DSF(1)+DCF or SMF-E+LL-IDF ABAB map, because both P-MDF and N-MDF have a large $A_{\rm eff}$ each. The total attenuation loss was 0.205 dB/km that is much better than NZ-DSF(1)+DCF. SMF-E+LL-IDF ABAB map showed comparable low attenuation loss, but MDF is advantageous for the aspect of a simple single (AB) configuration due to its low accumulated dispersion characteristics.

The local dispersion of MDF is small and the total dispersion is very flat, so an accumulated dispersion is kept small over a wide range of wavelength. The accumulated dispersion characteristics of each type of dispersion management links are shown in Fig. 38 in addition with the equivalent $A_{\rm eff}$ and total attenuation loss property. As shown in Fig. 38, the MDF link is advantageous for the aspect of accumulated dispersion. The maximum accumulated dispersion of a 50km span is only 360 ps/nm and it is only 80% of SMF-E plus initial IDF and 60% of SMF-E plus IDF-E. Though the accumulated dispersion is still larger than NZ-DSF type fiber, a large $A_{\rm eff}$ and low attenuation loss was realized simultaneously.

Table 24. Fabrication results of MDF$^{\rm SD}$ at 1550 nm using conventional profiles [46].

	Dispersion [ps/nm/km]	Slope [ps/nm^2/km]	RDS [/nm]	Loss [dB/km]	$A_{\rm eff}$ [μm^2]	λ_c [nm]	PMD [ps/rkm]	Bend(*) [dB/m]
P-SD 01	10.8	0.060	0.0056	0.185	70	1265	0.03	4
P-SD 02	10.6	0.069	0.0065	0.187	81	1523	0.03	7
N-SD 01	–10.0	–0.055	0.0055	0.216	34	1440	0.03	7

(*) Bending loss increase at 20 mm diameter

Table 25. Total optical properties of initial P-MDF$^{\mathrm{SD}}$ plus N-MDF$^{\mathrm{SD}}$ at 1550 nm [46].

Combination	Accumulated Disp$^{(1)}$ [ps/nm]	Disp. Slope [ps/nm^2/km]	Loss [dB/km]	$A_{\mathrm{eff}}{}^{(2)}$ [mm^2]	PMD [ps/rkm]
P-MDF$^{\mathrm{SD}}$ 01+N-MDF$^{\mathrm{SD}}$ 01	260	0.000	0.201	53.8	0.030
P-MDF$^{\mathrm{SD}}$ 02+N-MDF$^{\mathrm{SD}}$ 01	260	0.005	0.202	58.6	0.030

(1) Maximum accumulated dispersion in a 50-km span; (2) equivalent A_{eff}

The merit of a MDF transmission line for the aspect of system performance was reported in [45]. In this report, an EDFA-based CS-RZ, 2 Tb/s (50 $\times$ 40 Gb/s) transmission over 6000 km was reported using Medial dispersion DML.

*The Development of Improved MDF with Suppressed Dispersion (*MDF$^{\mathrm{SD}}$)

The new type of dispersion management transmission line with MDF had successfully been developed as described in the previous subsection. Accumulated dispersion of MDF links were successfully reduced as 350 ps/nm with P-MDF plus N-MDF because of their small local absolute dispersion of about 14 ps/nm/km. However, an accumulated dispersion restricts the transmission performance especially for the high-bit-rate transmission. The accumulated dispersion of MDF link had been surely suppressed, but still large compared to NZ-DSF (+DCF) as shown in the Fig. 37. To solve this problem, further suppression of local dispersion with MDF, namely MDF with suppressed dispersion (MDF$^{\mathrm{SD}}$), was proposed using the conventional refractive index profile [46]. A W plus side-core layer profile (Fig. 22) was selected for both Positive-MDF^{SD}(P-MDF$^{\mathrm{SD}}$) and Negative-MDF$^{\mathrm{SD}}$(N-MDF$^{\mathrm{SD}}$), and local absolute dispersion was suppressed about 10–11 ps/nm/km, so the maximum accumulated dispersion comparable with NZ-DSF+DCF was realized as shown in Table 24 (individual) and Table 25 (total).

However, the equivalent A_{eff} of P-MDF$^{\mathrm{SD}}$ and N-MDF$^{\mathrm{SD}}$ was about 55 μm^2, smaller than the conventional MDF of 62 μm^2 and much smaller than SMF-E plus IDF-45E of 75 μm^2, so it is difficult to be adapted into a high-capacity submarine system. It is worth mentioning this type of fiber might be used as a next-generation terrestrial long-haul system. Exploring the possibility of adaptation to a terrestrial system will be very interesting in the future. The attenuation loss spectrum of P-MDF$^{\mathrm{SD}}$ No.1 is shown in Fig. 39. As shown in Fig. 39, the wide-band flatness, that is required for next-generation terrestrial system, can be confirmed.

The problem of MDF$^{\mathrm{SD}}$ has been successfully solved by Enlarged A_{eff} MDF (MDF$^{\mathrm{EA}}$) using new type of index profiles [47]. The selected index profiles of MDF$^{\mathrm{EA}}$ are shown in Fig. 40. With these profiles, suppressed absolute dispersion about 11 ps/nm/km and large A_{eff} as 110 μm^2 and 40 μm^2 each were obtained as shown in the Table 26.

The total characteristics of P-MDF$^{\mathrm{EA}}$ plus N-MDF$^{\mathrm{EA}}$ assuming the connection is about a 1:1 length were shown in Table 27. As shown in the table, the ultra low dispersion slope of 0.002 ps/nm^2/km and large equivalent A_{eff} of about 90 μm^2 were obtained simultaneously. The attenuation loss was 0.228 dB/km in total. The accumulated dispersion and PMD were low enough for the high-bit-rate transmission. Figure

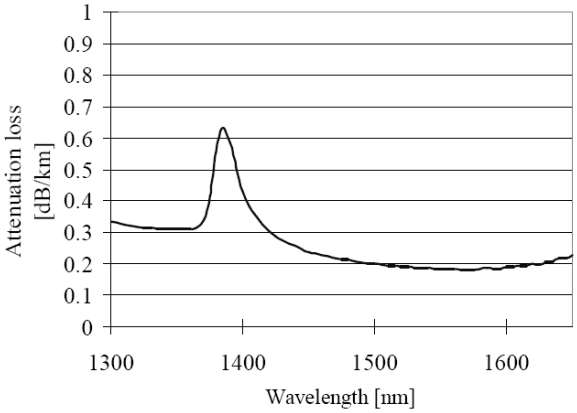

Fig. 39. Attenuation loss spectrum of P-MDF$^{\mathrm{SD}}$ No.1.

Table 26. Fabrication results of MDF$^{\mathrm{EA}}$ at 1550 nm using new types of profiles [47].

	Dispersion [ps/nm/km]	Slope [ps/nm^2/km]	RDS [/nm]	Loss [dB/km]	A_{eff} [μm^2]	λ_c [nm]	PMD [ps/rkm]	Bend(*) [dB/m]
P-MDF$^{\mathrm{EA}}$	11.1	0.069	0.0062	0.245	113	1473	0.04	13
N-MDF$^{\mathrm{EA}}$	–11.2	–0.065	0.0058	0.208	40	1498	0.03	10

(*) Bending loss increase at 20 mm diameter

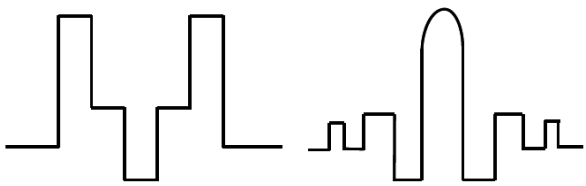

Fig. 40. Selected index profiles for MDFEA (left: Positive; right: Negative) to realize low dispersion and a large A_{eff} simultaneously [47].

41 shows the wavelength dependence of dispersion and attenuation. As shown in Fig. 41, both dispersion and attenuation show wide-band flatness not only C-Band and L-Band but extended to S-Band and XL-Band. The dispersion deviation from 1500 to 1650 nm was only within $\pm$0.2 ps/nm/km and the attenuation was lower than 0.30 dB/km. As a result, the possibility of optical properties improvements from initial MDF adaptability can be confirmed with MDF$^{\mathrm{EA}}$.

Nevertheless, some issues need to be considered with MDF$^{\mathrm{EA}}$, P-MDF$^{\mathrm{EA}}$ in particular. At first, a FWM phenomenon must be considered, because the dispersion is suppressed while the dispersion slope is as large as 0.07 ps/nm^2/km, so λ_0 would be

Table 27. Optical properties of P-MDF^{EA} plus N-MDF^{EA} at 1550 nm [47].

Combination	Accumulated Disp$^{(1)}$ ps[/nm]	Disp. Slope [ps/nm^2/km]	Loss [dB/km]	$A_{\rm eff}{}^{(2)}$ [mm^2]	PMD [ps/rkm]
P-MDF^{EA}+N-MDF^{EA}	279	0.002	0.228	88.3	0.035

(1) Maximum accumulated dispersion in a 50-km span; (2) equivalent $A_{\rm eff}$

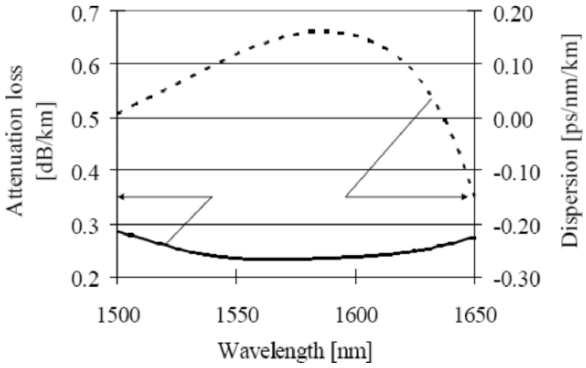

Fig. 41. An attenuation loss and dispersion spectrum of P-MDF^{EA}+N-MDF^{EA} [47].

shifted to a longer wavelength. If the dispersion in the transmission region is close to zero, noise signals are generated through FWM phenomenon [2]. Figure 42 shows the dispersion curvature of P-MDF^{EA} and the confirmed shifting of λ_0 to less than 1430 nm.

Another big issue is the splice loss of MDF^{EA}. In general, the centre-depressed profile as Fig. 40 (left) tends to generate a high splice loss because the electric field deviates from the Gaussian distribution. Figure 43 shows an example of the electric field distribution shapes of P-MDF^{EA}. However, the optimization of the MEX splice technique was also effective for these types of fibers and a splice loss lower than 0.1 dB was obtained for various combinations as shown in Table 28. The splice loss of a N-MDF^{EA} homogeneous splice was also less than 0.1 dB by MEX splicing. Finally, PMD and attenuation loss issue must be considered. Fibers with a complex profile like MDF^{EA} tend to have large attenuation loss and large PMD. Actually, the attenuation loss of P-MDF^{EA} was relatively large, but that of N-MDF^{EA} was very low in value. Additionally, the PMD of both fibers was suppressed in a low level by the core and clad non-circularity suppression with fabrication process optimization. Note loss reductions of P-MDF^{EA} type fiber were reported recently by means of the fabrication process optimization [48] and the index profile (especially $\Delta 1$) optimization [49]. Reported properties are shown in Table 29. In [49], loss reduction with conventional P-MDF was also reported, and low attenuation loss of 0.180 dB/km has achieved by the FF method.

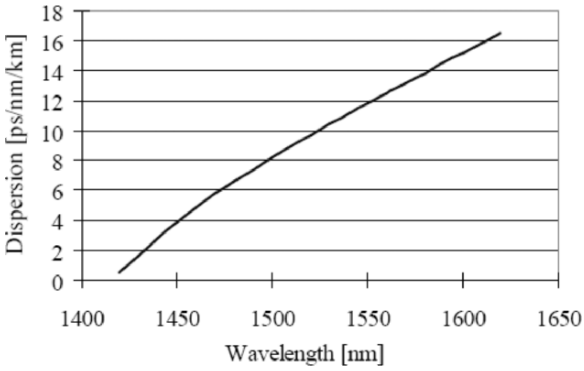

Fig. 42. Dispersion curvature of P-MDF$^{\mathrm{EA}}$.

4.2. Further Optical Property Improvement of Dispersion Management Lines

As having been explained, dispersion management transmission lines such as SMF plus IDF or P-MDF plus N-MDF have shown high performance for the long-haul WDM transmission. Recently, new transmission fibers with holes as Holey fiber (HF), Photonic Crystal Fiber (PCF) and Photonic Bandgap Fiber (PBGF) have been paid considerable attention, because the existence of holes can change optical properties drastically. The attenuation loss of these fibers has drastically decreased in these years [50,51]. But, up until now, the dispersion management line shows the highest performance, and various types of dispersion management transmission lines have been reported continuously. The Holey fibers might be adapted for a terrestrial system because of their wide-band transmission ability such as an endless single mode and low macro-bending loss performance, but the submarine systems generally use limited band-width, and reported performances around 1550nm, for example, were much worse than recently reported DML, though HF and PBGF are still in progress of potential explorations. I would like to finish this chapter by introducing some new topics of DMLs.

For SMF, one approach to improve the optical performance is to enlarge A_{eff}, and the other approach is to reduce the attenuation. However these two optical properties have been tradeoff because a large A_{eff} increase micro-bending loss and attenuation loss will be increased by micro-bending loss. In [52], one of the unique approaches was introduced to obtain low attenuation and very large A_{eff} simultaneously. The reported optical properties are shown in Table 30. The proposed method in this reference is to enlarge fiber diameter to prevent a micro-bend loss increase. By this method, the attenuation loss of 0.159 dB/km and ultra large A_{eff} as 211 $\mu\mathrm{m}^2$ were reported using the PSC technique and a W-shaped profile. Maybe this technique would be effective for IDF, because micro-bending loss restrict IDF characteristics improvement also.

The total optical properties with this SMF plus IDF of the Table14, No.2 are shown in Table 31. Though the accumulated dispersion is a large value, the ultra low dispersion slope, attenuation loss and nonlinearity were confirmed with this combination. It is, however, to be appreciated that many problems as handling and splicing will need

Table 28. The splice loss of MDF^{EA} and other fibers [47].

Fiber pairs	Typical value
P-MDF^{EA}+SMF	0.03 dB
P-MDF^{EA}+N-MDF^{EA}	0.08 dB
N-MDF^{EA}+SMF	0.07 dB

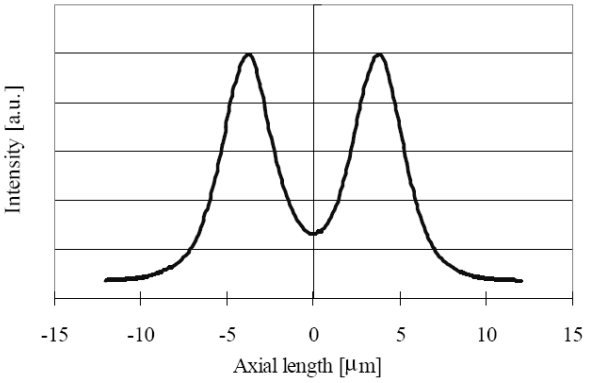

Fig. 43. An example of electric field distribution of P-MDF^{EA} with a ring profile.

Table 29. Reported results of low loss P-MDFs with a ring-profile at 1550 nm.

	Dispersion [ps/nm/km]	Slope [ps/nm^2/km]	RDS [/nm]	Loss [dB/km]	$A_{\rm eff}$ [μm^2]	PMD [ps/rkm]	Bend(*) [dB/m]
[48]	9.1	0.065	0.0071	0.212	96	0.06	–
[49]	13.5	0.068	0.0050	0.210	125	0.05	6

(*) Bending loss increase at 20 mm diameter

to be considered if such a technology is ever to achieve a real world deployment. Large macro-bending loss should be the other big issue to be carefully considered. As for IDF, IDF-45E fiber type has become the standard fiber and showed quite reliable performances in the commercial base so there seems to be little space to be improved. To adapt PSC or Fully Fluoride doped method for IDF seems to be interesting, but we have to say that IDF has deep depressed layer from the original structure and the PSC-method might increase the attenuation loss by the influence of higher fluorine doping layer. A prudent design consideration will be required to use this technique. Attenuation loss reduction of SMF and IDF will be still interesting. Up until now, the lowest loss of SMF has been 0.149 dB/km of [26] and IDF 0.196 dB/km of [25]. If we combine these two fibers, a dispersion flattened line with attenuation loss of 0.174 dB/km will be obtained. It is a tough value to break, but the authors believe a further reduction will be possible in the future by mean of profile and process optimization with a meticulous care.

The technical consideration of DML to be installed into a real submarine system is as important as optical properties improvements. One of the biggest issues that needs to be considered is splicing. The splice loss of SMF and IDF has been reduced as described in this paper, but to reduce splice loss without special technique, such as the thermal treatment, will be a key point to actually install DMLs into the real submarine system. Every fiber supplier has investigated this point as well as optical property improvements. In addition to the splicing, dispersion control of IDF is the other very important point, because the sensitivity of dispersion is very high with IDF comparing to SMF. Considering the cost issue is a kind of must due to a recent economical tough situation of telecommunication. As for one approach considering a practical aspect, a new combination of more established fiber type as All Wave fiber plus IDF-45E was also proposed [53].

Table 30. Reported results of a large fiber diameter PSCF with a W-shaped profile at 1550 nm.

	Dispersion [ps/nm/km]	Slope [ps/nm^2/km]	RDS [/nm]	Loss [dB/km]	A_{eff} [μm^2]	PMD [ps/rkm]	Bend(*) [dB/m]
[52]	21.9	0.058	0.0026	0.159	211	0.07	40

(*) Bending loss increase at 20 mm diameter

Table 31. Total optical properties of large fiber diameter SMF [52] plus IDF-45E fiber type [24] at 1550 nm.

Combination	Accumulated Disp$^{(1)}$ [ps/nm]	Disp. Slope [ps/nm^2/km]	Loss [dB/km]	$A_{\mathrm{eff}}{}^{(2)}$ [mm^2]	PMD [ps/rkm]
Large A_{eff} SMF + IDF-45E	731	–0.004	0.186	103.6	0.067

(1) Maximum accumulated dispersion in a 50-km span; (2) equivalent A_{eff}

Table 32. Fabrication results of the ultra-low nonlinearity P-MDF^{150} at 1550 nm [54].

	Dispersion [ps/nm/km]	Slope [ps/nm^2/km]	RDS [/nm]	Loss [dB/km]	A_{eff} [μm^2]	λ_c [nm]	PMD [ps/rkm]	Bend(*) [dB/m]
P150-01	10.2	0.071	0.0070	0.237	146	1595	0.06	3
P150-02	12.3	0.065	0.0053	0.245	157	1588	0.04	9

(*) Bending loss increase at 20 mm diameter

As for MDF, the optical properties of P-MDF$^{\mathrm{EA}}$ plus N-MDF$^{\mathrm{EA}}$ showed a kind of ultimate properties such as accumulated dispersion as low as NZ-DSF, dispersion slope almost 0, an equivalent A_{eff} more than 80 μm^2 and low PMD. The attenuation loss was 0.228 dB/km, but it will be reduced about 0.210 dB/km by using new P-MDF$^{\mathrm{EA}}$ as shown in the Table 29. To explore the further enlargement of A_{eff} with P-MDF or N-MDF is very challenging but interesting. A trial with the same index profile with P-MDF$^{\mathrm{EA}}$ was reported in [54]. An example of simulation results keeping dispersion about 10ps/nm/km is shown in Fig. 44. The simulation results showed that a super

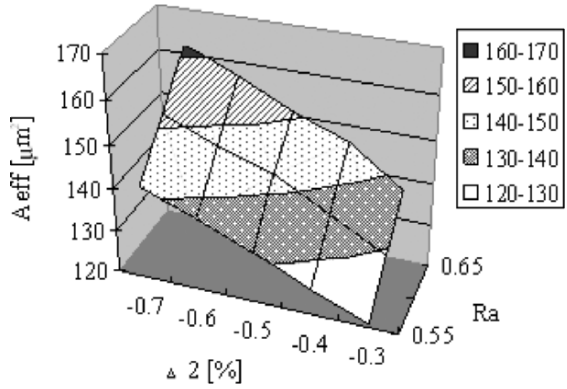

Fig. 44. The simulation results of large $A_{\rm eff}$ P-MDF targeting $A_{\rm eff}$ as 150 μm^2 [54].

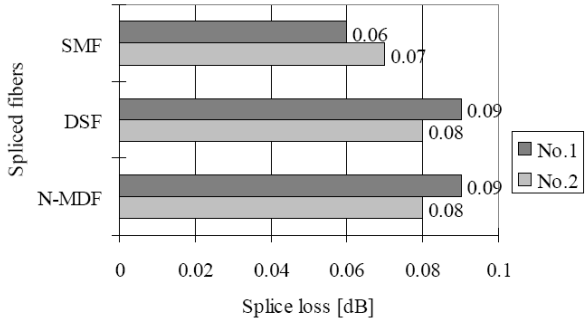

Fig. 45. Splice loss of P-MDF^{150} plus other fibers using MEX splice technique [54].

large $A_{\rm eff}$ about 150 μm^2 could be obtained by shifting λc and bending loss close to almost limitation values. Based on the calculation results, P-MDF with $A_{\rm eff}$ of 150 μm^2 (P-MDF^{150}) was actually fabricated by the VAD method. Fabrication results are shown in the Table 32. As shown in the table, an ultra large $A_{\rm eff}$ as 150 μm^2 was obtained keeping low dispersion around 10 ps/nm/km. The attenuation loss, PMD and every other characteristic were not impaired. A cutoff wavelength became just less than 1530 nm in case of 22-m measurement. As for a sensitivity of P-MDF^{150} for the changes of profile parameters, we have to say it was very high. In other words, the stability of the fiber properties would be one of the biggest problems to be solved in the future. In addition to that, the lower attenuation loss will be required to improve the total performance. However, P-MDF^{150} showed the highest performance in terms of low dispersion and large $A_{\rm eff}$, still keeping fiber diameter as 125 μm.

The splice loss of P-MDF^{150} and the conventional SMF, DSF and N-MDF^{EA} and the total optical properties were investigated and reported [54]. The results were shown in Fig. 45 and Table 33, respectively.

Table 33. Optical properties of various types of transmission lines at 1550 nm assuming a 50-km span and splice loss of 0.1 dB.

Transmission line	Dispersion [ps/nm/km]	Slope [ps/nm^2/ /km]	$A_{\mathrm{eff}}{}^{(1)}$ [mm^2]	A.Disp$^{(2)}$ [ps/nm]	FWM Suppression	Attenuation [dB/km]
Enlarged A_{eff} NZ-DSF	5	0.09	72	250	Not Enough	0.215
Low slope NZ-DSF	5	0.045	55	250	Not Enough	0.215
Ultra low slope NZ-DSF	5	0.02	45	250	Not Enough	0.215
SMF-E+IDF	0	0.005	76	630	Enough	0.205
SMF-E+LL-IDF	0	0.001	71	480	Enough	0.197
LL-SME+IDF	0	0.001	73	680	Enough	0.192
LL-SME+LL-IDF	0	–0.005	67	520	Enough	0.188
P-MDF+N-MDF	0	0.005	62	350	Enough	0.205
P-MDF^{SD}+N-MDF^{SD}	0	0.005	55	260	Enough	0.200
P-MDF^{EA}+N-MDF^{EA}	0	0.002	88	280	Enough	0.230
P-MDF^{150}No.1+N-MDF^{EA}	**0**	**0.008**	**100**	**265**	**Enough**	**0.225**
P-MDF^{150}No.2+N-MDF^{EA}	**0**	**-0.001**	**98**	**289**	**Enough**	**0.227**

(1) Equivalent A_{eff}; (2) maximum accumulated dispersion in a 50-km span

MEX splice technique enables to achieve splice loss lower than 0.1 dB with every fiber connections even for such a large A_{eff} fiber. And as shown in the Table33, P-MDF^{150} plus N-MDF^{EA} showed ultra low dispersion slope lower than 0.01ps/nm^2/km, which is one order lower than conventional NZ-DSFs. Equivalent A_{eff} was such large value as 100μm^2, which is comparable DML with large fiber diameter PSCF plus IDF-45E. The accumulated dispersion in a 50km span was suppressed in a low level, lower than 300 ps/nm. P-MDF^{150} plus N-MDF^{EA} was advantageous for the high-bit-rate transmission from this point of view. The attenuation loss was relatively large as 0.225 dB/km in total including the splice loss. If this characteristic will be improved by fabrication-process optimisation in the future, this transmission line might become one of the ultimate transmission lines. Other than that, a new method (Multimode design Singlemode transmission (MDST) method) for N-MDF improvements was proposed in [55]. In this reference, N-MDF with an ultra large A_{eff} more than 50μm^2 was reported. These results are very encouraging that the further optical improvement might be possible using a well-established silica-based fiber technology.

Finally authors would like to finish this chapter by illustrating the flow of submarine fiber development (Fig. 46). We believe Dispersion Management Line (DML) will play a leading part in a submarine system for a while and be gradually installed into a real submarine system in spite of the recent tough economical situation. And after that, some innovative fiber such as holey fiber might be introduced. Or High nonlinear fiber (HNLF) device might change the optical transmission system and required optical transmission lines drastically in the future. Positive dispersion fibers such as SMF-E or P-MDF might also be installed into a terrestrial system.

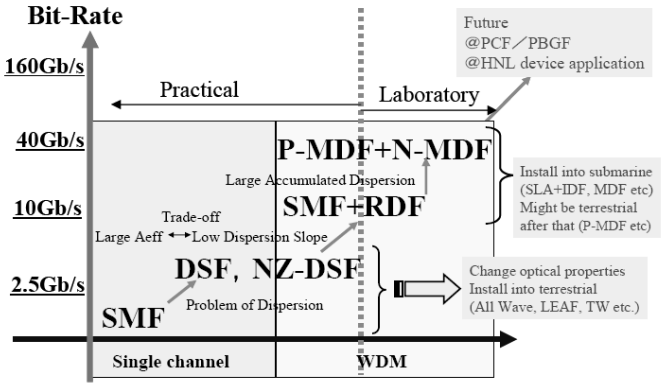

Fig. 46. Submarine transmission fibers development flow chart and some indications of what is happening now and would happen in the future.

References

1. K. Oda, M. Fukutoku, H. Toba, and T. Kominato, "128 channel, 480 km FSK-DD transmission experiment using 0.98 mm pumped erbium-doped fiber amplifiers and tunable gain equalizer" IEE Electron. Lett. **30**, 982–983 (1994).

2. K. Sekine, N. Kikuchi, S. Sasaki, and M. Aoki, "10Gb/s four-channel WDM transmission experiment over 500 km with technique for suppressing four-wave mixing" IEE Electron. Lett. **30**, 1150–1151 (1994).

3. R.B. Kummer, L.R. Dunn, R.E. Fangmann, A.F. Judy, D. Kalish, D.W. Peckham, R.G. Huff, W.A. Reed, A.M. Vengsarkar, K.L. Walker, A.R. Chraplyvy, L. Clark, R. Tkach, and J.J. Thomas, "Fiber design for future high capacity digital transmission" IWCS Proceeding, p. 42 (1995).

4. S. Yoshida, S. Kuwano, and K. Iwashita, "Gain-flattened EDFA with high Al concentration for multistage repeatered WDM transmission" Electron. Lett. **31** (20), 1765–1767 (1995).

5. A.R. Shraplyvy, A.H. Gnuck, R.W. Tkach, and R.M. Derosier, "8 $\times$ 10 Gb/s transmission through 280km of dispersion-managed fiber" IEEE Photon. Technol. Lett. **5**, 1232–1235 (1993).

6. A. Bertaina, S. Bigo, C. Francia, S. Gauchard, J.P. Hamaide, and M.W. Chbat, "Experimental investigation of Dispersion Management for an 8 $\times$ 10 Gb/s WDM transmission system over nonzero dispersion-shifted fiber" IEEE Phton. Technol. Lett. **11**, 1045–1047 (1999).

7. K. Mukasa, Y. Akasaka, Y. Suzuki, and T. Kamiya, " Novel network fiber to manage dispersion at 1.55 μm with combination of 1.3 mm zero dispersion single mode fiber" ECOC'97 Proceeding, Mo3C-127 (1997).

8. M. Onishi, C. Fukuda, Y. Koyano, M. Shigematsu, and H. Kanamori, "Dispersion compensating fiber with a figure of merit of 273 ps/nm/dB and its compact package," OEC'94 Technical Digest, 14B1-3 (1994).

9. Y. Akasaka, R. Sugizaki, A. Umeda, I. Oshima, and K. Kokura, "Dispersion-compensating fiber with W-shaped profile" OFC'95 Technical Digest, ThH3 (1995).

10. Y. Akasaka, R. Sugizaki, and T. Kamiya, "Dispersion-compensating technique of 1300 nm zero-dispersion SMF to get flat dispersion at 1550 nm range" ECOC'95 Proceeding, We.B.2.4 (1995).

11. M. Onishi, H. Kanamori, T. Kato, and M. Nishimura, "Optimization of dispersion-compensating fibers considering self-phase modulation suppression" OFC'96 Technical Digest, ThA2 (1996).

12. R. Sugizaki, Y. Akasaka, S. Arai, K. Furukawa, Y. Suzuki, T. Kamiya, and H. Hondo, "High-reliability dispersion compensator using negative slope DCF" IWCS'96 Proceeding, pp.888–891 (1996).

13. L.G. Nielsen, T. Veng, S.N. Knudsen, C.C. Larsen, and B. Edvold, "New dispersion compensating fiber for simultaneous compensation of dispersion and dispersion slope of non-zero dispersion shifted fibers in C or L band" OFC'00 Technical Digest, TuG6 (2000).

14. R. Sugizaki, K. Mukasa, A.Umeda, and Y. Suzuki, "Dispersion slope compensating fibers for L-Band WDM system using NZ-DSF" OFC'00 Technical Digest, TuG4 (2000).

15. T. Kato, M. Hirano, K. Fukuda, A. Tada, M. Onishi, and M. Nishimura, "Design optimization of dispersion compensating fiber for NZ-DSF considering nonlinearity and packaging performance" OFC'01 Technical Digest, TuS6 (2001).

16. H. Kanamori, H. Tokota, G. Tanaka, M. Watanabe, Y. Ishiguro, I. Yoshida, T. Kakii, S. Itoh, Y. Asano, and S. Tanaka, "Transmission characteristics and reliability of Pure-silica-core single-mode fibers" J. Lightwave Technol. **LT-4** (8), 1144–1150 (1986).

17. M. Murakami, T. Matsuda, H. Maeda, and T. Imai, "Long-haul WDM transmission using higher order fiber dispersion management" J. Lightwave Technol. **18** (9), 1197–1204 (2000).

18. K. Yonenaga, A. Matsuura, S. Kuwahara, M. Yoneyama, Y. Miyamoto, and K. Hagimoto, "Dispersion-compensation-free 40 Gb/s $\times$ 4-channel WDM transmission experiment using zero-dispersion-flattened transmission line" OFC'98 Technical Digest, PD20 (1998).

19. M. Morimoto, I. Kobayashi, H. Hiramatsu, K. Mukasa, R. Sugizaki, Y. Suzuki, and Y. Kamikura, "Development of dispersion compensation fiber cable using Reverse Dispersion Fiber" APCC/OECC'99 Proceeding, C6.8, pp.1590–1593 (1999).

20. M. Morimoto, I. Kobayashi, H. Hiramatsu, K. Mukasa, R. Sugizaki, Y. Suzuki, and Y. Kamikura, "Study on mechanical and optical characteristics of Reverse Dispersion Fiber cable" IWCS'99 Proceeding , Track 2, p. 51 (1999).

21. T. Naito, N. Shimojo, T. Tanaka, H. Nakamoto, M. Doi, T. Ueki, and M. Suyama, "1 Terabit/s WDM transmission over 10,000 km," ECOC'99 Post-deadline papers, PD2-1 (1999).

22. T. Tsuritani, N. Takeda, K. Imai, K. Tanaka, A. Agata, I. Morita, H. Yamauchi, N. Edagawa, and M. Suzuki, "1 Terabit/s (100 $\times$ 10.7 Gbit/s) transoceanic transmission using 30-nm-wide broadband optical repeaters with A_{eff}-enlarged positive dispersion fiber and slope-compensating DCF," ECOC'99, Post-deadline papers, PD2-8 (1999).

23. K. Mukasa, T. Yagi, and K. Kokura, "New type of dispersion management transmission line for long-haul high-capacity transmission" SubOptic'01 Proceeding, T.4.2.4 (2001).

24. S.N. Knudsen, D. W.Peckham, M.O. Pedersen, D. Philen, T. Veng, L.R. Pritchett, and L.G. Nielsen, "New dispersion-slope managed fiber pairs for undersea fiber optic transmission system" SubOptic'01 Proceeding, T.4.2.2 (2001).

25. K. Mukasa, M. Kawasaki, and T. Yagi, "RDF with attenuation as low as 0.205 dB/km" ECOC'03 Proceeding, 4.7.2 (2003).

26. K. Nagayama, M. Kakui, M. Matsui, T. Saitoh, and Y. Chigusa, "Ultra low loss (0.1488 dB/km) pure silica core fiber and extension of transmission distance" Electron. Lett. **38** (20), 1168–1169 (2002).

27. C.D. Poole, R.W. Tkach, A.R. Chraplyvy, and D.A. Fishman, "Fading in lightwave systems due to polarization-mode dispersion" IEEE Photon. Technol. Lett. **3** (1), 68–70 (1991).

28. F. Bruyere, "Impact of first- and second-order PMD in optical digital transmission systems" Opt. Fiber Technol. **2** (3), 269–280 (1996).

29. M.O. Pedersen, S.N. Knudsen, T. Geisler, T. Veng, and L.-G. Nielsen, "New low-loss inverse dispersion fiber for dispersion matched fiber sets," ECOC'02 Proceeding, 5.1.3 (2002).

30. K. Mukasa and T. Yagi, "Dispersion flat and low nonlinear optical link with new type of Reverse Dispersion Fiber (RDF-60)" OFC'01 Technical Digest, TuH7 (2001).

31. H. Sugahara, K. Fukuchi, A. Tanaka, Y. Inada, and T. Ono, "6,050km transmission of 32 $\times$ 42.7 Gb/s DWDM signals using Raman-amplified quadruple-hybrid span configuration" OFC'02 Post-deadline paper, FC6 (2002).

32. S.N. Knudsen and T. Veng, "Large effective area dispersion compensating fiber for cabled compensation of standard single mode fiber," OFC'00 Technical Digest, TuG5 (2000).

33. T. Ito, K. Fukuchi, K. Sekiya, D. Ogasahara, R. Ohhira, and T. Ono,"6.4 Tb/s (160 $\times$ 40 Gb/s)WDM transmission experiment with 0.8 bit/s/Hz spectral efficiency" ECOC'00 Post-deadline papers, PD-1.1 (2000).

34. Y. Kobayashi, K. Kinjo, K. Ishida, T. Sugihara, S. Kajiya, N. Suzuki, and K. Shimizu, "A comparison among PURE-RZ, CS-RZ and SSB-RZ format, in 1 Tbit/s (50 $\times$ 20 Gbit/s, 0.4 nm spacing)WDM transmission over 4,000 km"ECOC'00 Post-deadline papers, PD-1.7 (2000).

35. M. Nakazawa, T. Yamamoto, and K.R. Tamura, "1.28 Tbit/s–70 km OTDM transmission using third-and fourth-order simultaneous dispersion compensation with a phase modulator," ECOC'00 Post-deadline papers, PD-2.6 (2000).

36. I. Yokota, A. Sugiyama, H. Ogiwara, S. Yoshizawa, H. Iwata, H. Isono, T. Tanaka, T. Naito, and M. Suyama "10-Gb/s, 64-ch, WDM 12,000-km transmission experiment using VIPA variable dispersion compensator," OECC'00 Post-deadline papers, PD-1.6 (2000).

37. K. Fukuchi, T. Kasamatsu, M. Morie, R. Ohhira, T. Ito, K. Sekiya, D. Ogasawara, and T. Ono, "10.92-Tb/s (273 $\times$ 40-Gb/s) triple-band/ultra-dense WDM optical-repeatered transmission experiment" OFC'01 Post-deadline Paper, PD24 (2001).

38. K. Shimizu, K. Ishida, K. Kinjo, T. Kobayashi, S. Kajiya, T. Tokura, T. Kogure, K. Motoshima, and T. Mizuochi, "65 $\times$ 22.8 Gb/s WDM transmission over 8,398Km employing symmetrically collided transmission with A_{eff} managed fiber," OFC'02 Technical Digest, WX4 (2002).

39. Y. Zhu, I. Hardcastle, W.S. Lee, C.R.S. Fludger, C. Li, D. Qiao, H. Sun, K.T. Wu, and J. McNicol, "Experimental comparison of dispersion-managed fiber type in a 16-channel, 40-Gb/s, 500-km (6 × 84.5km) Raman-assisted transmission link," OFC'02 Technical Digest, ThX4 (2002).

40. S. Ten, M. Sauer, E. Kolltveit, J. Hurley, D. Dalgoutte, J. Ferner, S. Colby, and D. Witzel, "1.6-Tb/s (40 × 40 Gb/s) transmission over 1200 km of field deployed dispersion managed fiber," OFC'03 Technical Digest, TuS3 (2003).

41. G.C. Gupta, L.L. Wang, O. Mizuhara, R.E. Tench, NN. Dang, P. Tabaddor, and A. Judy, "3.2-Tb/s (40 ch. × 80 Gb/s) transmission with spectral efficiency of 0.8 b/s/Hz over 21 × 100 km of dispersion managed high local dispersion fiber using all-Raman amplified span" IEEE Photon. Technol. Lett. **15** (7), 996–998 (2003).

42. T. Tsuritani, K. Ishida, A. Agata, K .Shimomura, I. Morita, T. Tokura, H. Taga, T. Mizouchi, N. Edagawa, and S. Akiba, "70 GHz-spaced 40 × 42.7 Gb/s Transpacific Transmission over 9400 km using prefiltered CSRZ-DPSK signals, all-Raman repeater, and symmetrically dispersion-managed fiber spans" J. Lightwave Technol. **22** (1), 215–223 (2004).

43. K. Mukasa, T. Yagi, and K. Kokura, "Wide-band dispersion management transmission line with Medial Dispersion Fiber (MDF)," ECOC'00 Proceeding, 2-4-2 (2000).

44. K. Mukasa, T. Yagi, and K. Kokura, "Wide-band transmission line with low-loss Negative Medial Dispersion Fiber (N-MDF)," OECC'01 Technical Digest, THA3 (2001).

45. Y. Inada, T. Ito, K. Mino, R. Yokoyama, Y. Hara, K. Fukuchi, T. Ogata, and Y. Aoki, "Error-free transmission over 6,000 km of 50 × 42.8 Gb/s, FEC-coded CS-RZ WDM signal in EDFA and Medial-Dispersion MDF systems," ECOC'04 Proceeding, Th3.5.4 (2004).

46. K. Mukasa, H. Moridaira, T. Yagi and K. Kokura, "New type of dispersion management transmission line with $\mathrm{MDF}^{\mathrm{SD}}$ for long-haul 40 Gb/s transmission," OFC'02 Technical Digest, TuGG2 (2002).

47. K. Mukasa, T. Yagi, and K. Kokura, "New type of dispersion management line consisted of $\mathrm{MDF}^{\mathrm{EA}}$ with A_{eff} about $90\mu\mathrm{m}^2$ and dispersion slope as low as 0.002 ps/nm^2/km," ECOC'02 Proceeding, 5.1.2 (2002).

48. S. Matsuo, S. Tanigawa, K. Himeno, and K. Harada, "New medium-dispersion fiber with large effective area and low dispersion slope," OFC'02 Technical Digest, WU2 (2002).

49. K. Imamura, K. Mukasa, and T.Yagi "Positive-Medial Dispersion Fiber of ring-core profile with attenuation as low as 0.210 dB/km and A_{eff} about 125 $\mu\mathrm{m}^2$," OFC'04 Technical Digest, TUB6 (2004).

50. K. Tajima, J. Zhou, K. Kurokawa and K. Nakajima, "Low water peak photonic crystal fibres," ECOC'03 Post-deadline papers, Th4.1.6 (2003).

51. B.J. Mangan, L. Farr, A. Langford, P.J. Roberts, D.P. Williams, F. Couny, M. Lawman, M. Mason, S. Coupland, R. Flea, and H. Sabert, "Low loss (1.7 dB/km) hollow core photonic bandgap fiber," OFC'04 Post-deadline papers, PDP24 (2004).

52. M. Tsukitani, M. Matsui, K. Nagayama, and E. Sawada "Ultra low nonlinearity pure-silica-core fiber with an effective area of 211 $\mu\mathrm{m}^2$ and transmission loss of 0.159 dB/km," ECOC'02 Proceeding, 3.2.2 (2002).

53. L.-G. Nielsen, D. Peckham, R. Lingle, and O.A. Levring, "Dispersion managed fibre span optimized for submarine links," SubOptic'04 Proceeding, ThB 1.2 (2004).

54. K. Mukasa, K. Imamura, and T.Yagi "New type of Positive Medial Dispersion Fiber (P-MDF^{150}) with dispersion as 10 ps/nm/km and $A_{\rm eff}$ about 150 μm^2," OFC'03 Technical Digest, TuB1 (2003).

55. K. Mukasa, K. Imamura, and T. Yagi, "Dispersion management transmission line consisted of Medial dispersion fiber (MDF)," ECOC'04 Proceeding, We3.3.3 (2004).

DOI: 10.1007/s10297-005-0060-2
Originally published in J. Opt. Fiber. Commun. Rep. 3, 61–89 (2006)

Dispersion compensating fibers for Raman applications

L. Grüner-Nielsen, Y. Qian, and P. B. Gaarde

OFS Fitel Denmark ApS,
Priorparken 680, DK-2608 Brøndby, Denmark
Email: lgruner@ofsoptics.com

Abstract. Dispersion compensating fibers (DCF) are the most widely used technology for dispersion compensation. A DCF without Raman amplification introduces extra loss in the system, thus increasing the need for gain in the discrete amplifiers and degrading the noise performance. The idea to additionally use the DCF as a Raman gain medium was originally proposed by Hansen et al. in 1998. [1] This was quickly followed by Emori et al., who demonstrated a broadband, loss less DCF using multiple-wavelength Raman pumping. [2] DCF is a good Raman gain medium, due to a relatively high germanium doping level and a small effective area. To get sufficient gain with a reasonable pump power, a discrete Raman amplifier has to contain several kilometers of fiber, adding extra dispersion to the system that must be handled in the overall dispersion management. Dispersion compensating Raman amplifiers integrates two key functions: dispersion compensation and discrete Raman amplification into a single component.

1. Introduction

Compared to EDFA based system, dispersion compensating Raman amplifiers (DCRA) can be easily adjusted and extended to any seamless transmission band, e.g., E-, S-, C-, L-, and/or U-band, [3–8] without extra passive components. This is cost-effective and especially attractive in "all-Raman", ultra broadband, high capacity systems. [9–13,3] In addition, the Raman gain can be simply adjusted by WDM pumps [2,8] or TDM pumps [14,15] to achieve a flat gain spectrum without a high-loss gain-equalizer.

A high-gain DCRA can contribute gain to an "all-Raman" system and reduce the Raman gain in the transmission fibers. [9,10] A transparent DCRA is beneficial for improving the noise performance in repeaters [16] and easy upgrades of transmission lines originally designed without DCF.

Use of DCF for DCRAs raises new requirements for the properties of the DCF including requirements for gain, double Rayleigh scattering, and broadband dispersion compensation.

Section 2 of this paper reviews properties of DCF including basics of dispersion compensation, Raman gain efficiency, and double Rayleigh back scattering (DRB). Section 3 is the central section on DCRAs, reviewing typical amplifier properties and how to cope with impairments such as multi path interference due to DRB and nonlinearities. The final section deals with optimization of DCF for use in DCRA.

2. Properties of Dispersion Compensating Fibers

Dispersion compensating fibers have seen considerable progress over the last several years, and DCFs with dispersion slope matching all common transmission fibers have been demonstrated [17–22] as well as DCFs with improved FOM. [23]

A special type of DCF that has received some recent interest is a DCF supporting more than one mode. The device uses a higher-order mode of the DCF and has mode converters at both ends to convert from the fundamental mode to the higher-order mode at the input and visa versa at the output end. [24–26] The advantage is that the higher-order mode has quite a large effective area on the order 50–70 μm^2. Unfortunately, such fibers have a very low Raman gain efficiency due to the high effective area and because the mode converters have a limited bandwidth. The bandwidth limitation of the mode converters means that normally they will work only for the signal and not for the pump. For that reason, this technology will not be considered further in this paper.

Throughout the paper two types of transmission fibers, standard single mode fiber (SSMF) and TrueWave® Reduced Slope as well as DCF for these two fibers will be used as application examples. For reference, the typical properties for these four fibers are summarized in Table 1.

Table 1. Typical properties for fibers discussed.

Fiber type	Dispersion [ps/nm·km]	RDS [nm^{-1}]	FOM fiber [ps/(nm·dB)]	Effective area [μm^2]	Peak Raman gain efficiency for 1453 nm pump $(W \cdot km)^{-1}$
SSMF	16.5	0.0036	NA	82	0.39
TW-RS	4.5	0.010	NA	52	0.64
DCF for SSMF	–120	0.0036	280	21	2.45
DCF for TW-RS	–160	0.010	270	14	3.50

2.1. Basics of Dispersion Compensation

Because of the non-zero bandwidth of an optical signal, the dispersion leads to pulse broadening due to the different spectral components of the signal having different group delays. For narrowband externally modulated lasers, the bandwidth of the signal is governed by the modulation. Increased modulation speed leads to increased

bandwidth. The tolerable pulse broadening on the other hand decreases with the modulation frequency. Therefore, the dispersion tolerance decreases with the square of the bit rate (B) and linearly with the transmitted length. [27]. The maximum transmission length for dispersion-limited transmission is consequently given as

$$L_{\max} = \frac{K}{B^2 |D|}, \tag{1}$$

where D is the dispersion coefficient of the transmission fiber and K is a constant depending on the details of the transmitter and receiver, modulation format, and allowed penalty. Dispersion values for the most common transmission fibers can be found in Table 2 [28].

Table 2. Typical properties of some commercially available transmission fibers at 1550 nm.

Fiber type	Dispersion [ps/nm km]	Dispersion slope [ps/nm^{2}km]	RDS [nm^{-1}]	Effective area [μm^2]
Standard single mode fiber (SSMF), ITU G652	16.5	0.058	0.0036	82
Non Zero Dispersion Fibers (NZDF) low dispersion, ITU G655				
TrueWave® RS fiber	4.5	0.045	0.010	52
ELEAF* fiber	4.2	0.085	0.020	72
Non Zero Dispersion Fibers (NZDF) medium dispersion, ITU G656				
TrueWave® REACH fiber	7.1	0.042	0.0058	55
TeraLight Ultra* fiber	8	0.052	0.0065	63

*TeraLight is a registered trademark of Alcatel; LEAF is a registered trademark of Corning.

Examples of maximum transmission distances for dispersion limited transmission assuming 1 dB eye-closure penalty and non-return-to-zero (NRZ) modulation format [29] for a conventional SSMF as well as a TrueWave®RS fiber are shown in Table 3.

Table 3. Transmission distances of NRZ signal for 1 dB eye closure penalty due to dispersion.

Bit rate Gbit/s	SSMF km	TW-RS km
2.5	927	3400
10	58	213
40	3.6	13

It is clear from Table 3 that for bit rates of 10 Gbit/s and above; dispersion is a limiting factor and requires compensation.

As illustrated in Fig. 1, the concept of DCF is very simple. A DCF with dispersion opposite to the transmission fiber is inserted after the transmission fiber.

Different configurations for incorporating the DCF into the transmission line are illustrated in Fig. 2.

Also shown in Fig. 2 are different methods for handling the extra loss from the DCF, including use of Raman amplification. For illustration, only counter Raman pumping

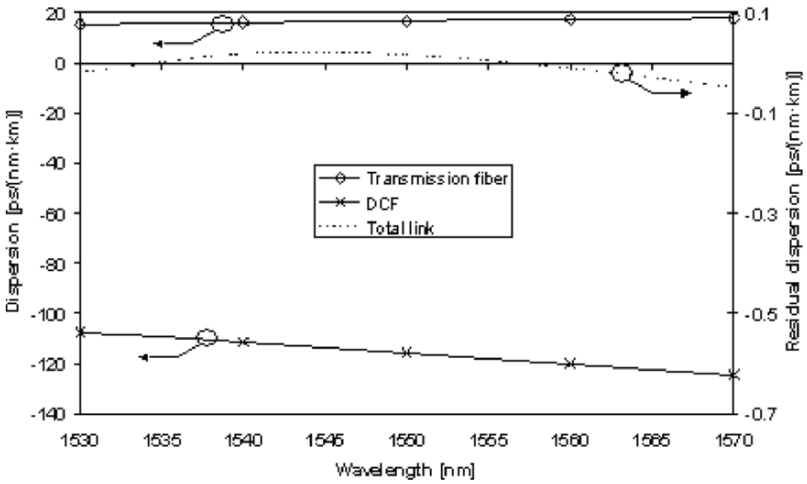

Fig. 1. Principle of dispersion compensation.

is shown but additional co-pumping might be beneficial as discussed in section 3.2.1. In Fig. 2(a), a traditional configuration for an Erbium doped fiber amplified (EDFA) system without any Raman amplification is shown. To overcome the loss from the DCF, the DCF is inserted between the preamplifier and the booster stage in a two stage EDFA. In Fig. 2(b), the DCF is Raman pumped, e.g., to transparency to eliminate the first stage of the EDFA. This configuration might be especially interesting for systems designed for shorter distances, where DCF is not always needed because the same simple single-stage EDFA design can be used regardless of whether or not DCF is needed. In Fig. 2(c), an "all-Raman" system is illustrated. Such systems offer many intriguing advantages. Compared to EDFA systems, amplification in any wavelength band is possible, and very broad, seamless transmission bands can be amplified. Such broadband "all-Raman" systems can be realized with only a few components and are therefore expected to be cost effective. In Fig. 2(d), the DCF is pumped in the traditional two-stage EDFA configuration. Such an arrangement might be used in two situations: to allow for insertion of additional lossy components between the two EDFA stages or to allow use of a DCM with high dispersion (and therefore high loss) to compensate several hundreds kilometers of transmission fiber.

To characterize the loss of an unpumped DCF the Figure of Merit (FOM) is commonly used. The FOM is defined as

$$\mathrm{FOM} = -\frac{D_{\mathrm{DCF}}}{\alpha_{\mathrm{DCF}}},$$

where D_{DCF} is the dispersion coefficient and α_{DCF} is the attenuation coefficient of the DCF. For a passive discrete DCF module equipped with SSMF connectors, the module loss is given as:

$$\alpha_M = \frac{|D_{\mathrm{tot}}|}{\mathrm{FOM}} + 2\alpha_S + 2\alpha_C,$$

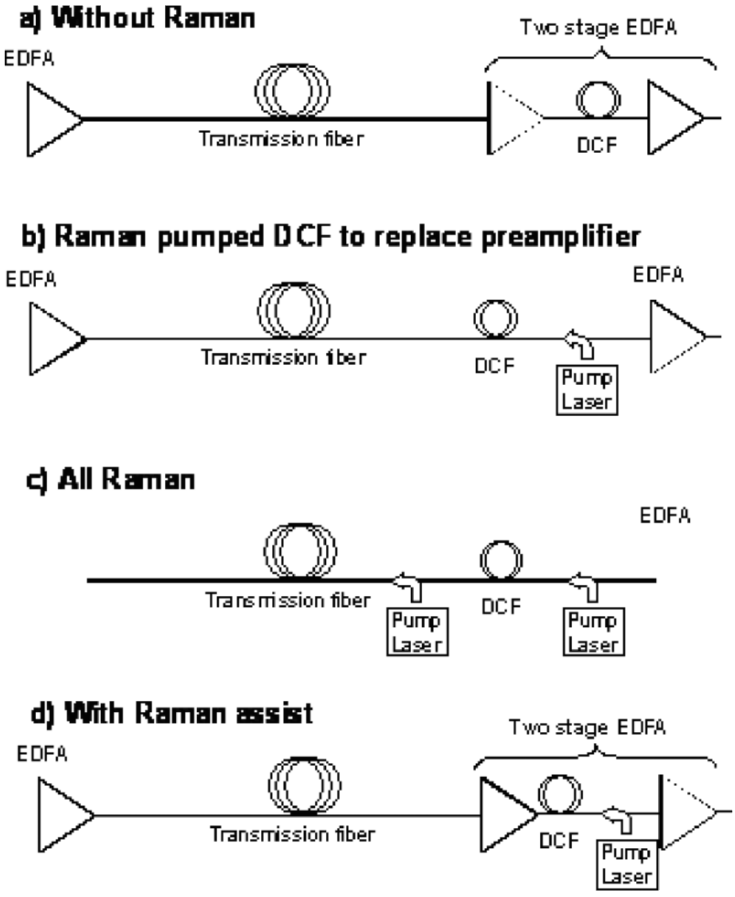

Fig. 2. Examples of DCF placement and loss compensation in different system configurations.

where D_{tot} is the total dispersion of the module, α_s is the splice loss between DCF and SSMF, and α_C is the connector-connector loss. The splice loss depends strongly on the DCF type and splice method. A typical connector-connector loss is 0.1 dB. Optimization of the loss of a passive DCF module is a matter of maximizing FOM and minimizing the splice loss.

If the dispersion is assumed to vary linearly with wavelength, wavelength-independent residual dispersion (D_{res}) (remaining dispersion after dispersion compensation) can be obtained if the dispersion slopes of transmission fiber and DCF are matched. This is obtained if

$$\mathrm{RDS}_{\mathrm{DCF}}(\lambda_0) = \frac{\mathrm{RDS}_{\mathrm{TF}}(\lambda_0)}{\mathrm{DCR}(\lambda_0)}, \tag{2}$$

where $\mathrm{RDS_{TF}}(\lambda_0)$ and $\mathrm{RDS_{DCF}}(\lambda_0)$ are the Relative Dispersion Slope (RDS = ratio of dispersion slope to dispersion) of the transmission fiber and DCF, respectively, at wavelength λ_0, and DCR is the dispersion compensation ratio:

$$\mathrm{DCR}(\lambda) = \frac{D_{\mathrm{TF}}(\lambda)L_{\mathrm{TF}} - D_{\mathrm{res}}}{D_{\mathrm{TF}}(\lambda)L_{\mathrm{TF}}}, \tag{3}$$

where $D_{\mathrm{TF}}(\lambda)$ and $\mathrm{D_{DCF}}(\lambda)$ are the dispersion coefficients of the transmission fiber and DCF versus wavelength λ and L_{TF} and $\mathrm{L_{DCF}}$ are the length of the transmission fiber and DCF, respectively.

Linear dispersion variation versus wavelength is a good approximation for most transmission fibers, when for example the ∼35 nm bandwidth of the C or L band is considered. As will be discussed in section 4, this is not necessarily the case for DCF. Therefore, higher-order terms should be considered. The Relative Dispersion Curvature (RDC) can be defined as:

$$\mathrm{RDC} = \frac{C}{D}, \tag{4}$$

where

$$C = \frac{d^2 D}{d\lambda^2}.$$

RDC is a useful figure for a DCF because, for compensation of a given amount of dispersion, RDC expresses the dispersion curvature obtained from the DCF independent of the dispersion coefficient of the DCF.

2.2. Raman Gain

The Raman scattering effect is named after the Indian physicist C.V. Raman, who in 1928 discovered the effect by studying the scattered light from a liquid illuminated with monochromatic light. Raman scattering was first observed in optical fibers in 1972 by Stolen et al. [30] Raman scattering is a non-linear process, where a pump photon interacts with molecular vibration levels in the scattering medium. Some of the energy from the pump photon is transferred into molecular vibrations (heat) and a new Stokes photon with lower energy is emitted. The energy preservation yields

$$h\upsilon_S = h\upsilon_P - E_{\mathrm{phonon}}, \tag{5}$$

where υ_P and υ_S are the frequency of the pump light and spread Stokes light, respectively, h is Planck's constant, and $\mathrm{E_{phonon}}$ is the phonon energy (the energy transferred to molecular vibrations). In optical fibers, the Stokes photon can propagate co-directionally or counter-directionally to the pump photon.

In the following, the central equations (9) and (16) for modeling of Raman gain will be presented. It will be shown that the influence of the fiber design can be described by one parameter, the Raman gain efficiency, which is again determined by the effective area and doping levels in the fiber. Finally, examples of measured Raman gain efficiency will be shown in Fig. 3.

Raman scattering is a stimulated process, which can be described by [27]

$$\frac{dI_S}{dz} = g_R\left(\upsilon_P, \upsilon_S\right)\ I_P I_S, \tag{6}$$

where I_P and I_S are the intensities of the pump and the Stokes light. $g_R(\upsilon_P,g\upsilon_S)$ is the Raman gain coefficient.

Raman scattering is also a temperature dependent spontaneous process and the intensity of the amplified spontaneous emission, ASE, (I_{ASE}) can be described by [31,32]

$$\frac{dI_{\mathrm{ASE}}}{dz} = 2h\upsilon_{\mathrm{ASE}} \left(1 + \frac{1}{\exp\left(\frac{h(\upsilon_p - \upsilon_{\mathrm{ASE}})}{kT}\right) - 1}\right) g_R\left(\upsilon_P, \upsilon_{\mathrm{ASE}}\right)\ I_P, \tag{7}$$

where k is Boltzmann's constant and T is the absolute temperature.

The Raman gain coefficient g_R depends on the composition of the glass and can vary significantly with the use of different dopants. At a pump wavelength of 1 μm, the 3 dB bandwidth of g_R in pure silica glass is 26 nm with a maximum gain for a Stokes shift of 44 nm. [27] For a germanium doped silica glass, the peak value of the Raman gain coefficient $g_{R,max}$ for a pump wavelength λ_P, can, with good approximation, be calculated from the equation [22,34]

$$g_{R,\max} = \frac{A(1 + BX_{\mathrm{GeO_2}})}{\kappa\lambda_P}. \tag{8}$$

$X_{\mathrm{GeO_2}}$ is the molar concentration of GeO_2, λ_p is the pump wavelength, and κ is a polarization factor, which is equal to 1 when the pump and Stokes light are equally polarized and equal to 2 for random polarization. In the remaining part of this paper random polarization will be assumed. A and B are constants. According to [33] $A = 1.2 \times 10^{-19}$ m/W and $B = 0.08\ \%^{-1}$ for bulk glass. In [34] $B = 0.05\ \%^{-1}$ was found for optical fibers.

For optical fibers Eq. (6) can be rewritten as

$$\frac{dP_S}{dz} = C_R P_P P_S - \alpha_S P_S. \tag{9}$$

P_P and P_S are the pump and signal (Stokes) power, respectively, and α_S is the fiber attenuation coefficient at the signal wavelength. The small contribution from the ASE has been omitted. C_R is the Raman gain efficiency, which is related to the Raman gain coefficient through

$$C_R = \frac{g_{R,f}}{A_{\mathrm{eff},R}}, \tag{10}$$

where $A_{\mathrm{eff},R}$ is the Raman effective area defined as [34,35]

$$A_{\mathrm{eff},R} = \frac{2\pi \int_0^\infty p_P(r) r\, dr \int_0^\infty p_S(r) r\, dr}{\int_0^\infty p_P(r) p_S(r) r\, dr}, \tag{11}$$

where $p_{P,S}(r)$ is the near-field power at radius r of the pump and signal respectively. $g_{R,f}$ is the Raman gain coefficient for the optical fiber given from the overlap integral

$$g_{R,f} = \frac{\int_0^\infty p_P(r) g_R(r) p_S(r) r\, dr}{\int_0^\infty p_P(r) p_S(r) r\, dr}. \tag{12}$$

In contrast to the Raman effective area Eq. (11), the conventional effective area [27] is defined as

$$A_{\text{eff}} = \frac{2\pi \left[\int_0^\infty p(r) r \, dr\right]^2}{\int_0^\infty p(r)^2 r \, dr}. \tag{13}$$

In the case of Gaussian distributions of the near field power $p(r)$, the Raman effective area can be found from the conventional effective areas at the pump and signal wavelength λ_P and λ_S as

$$A_{\text{eff},R} = \frac{A_{\text{eff}}(\lambda_P) + A_{\text{eff}}(\lambda_S)}{2}. \tag{14}$$

The unit of the attenuation in Eq. (9) is m^{-1}.

The relation between attenuation in m^{-1} and dB/km is

$$\alpha_{\text{m}^{-1}} = 2.30 \times 10^{-4} \alpha_{\text{dB/km}}. \tag{15}$$

The differential equation for the pump power evolution with distance is

$$\frac{dP_P}{dz} = -C_R \frac{\upsilon_P}{\upsilon_S} P_S P_P - \alpha_P P_P. \tag{16}$$

The first term on the right-hand side of Eq. (16) can be understood by considering that when no loss is present, the total number of pump and Stokes photon is constant.

The net gain G (in m^{-1}) can be calculated from Eqs. (9) and (16). For an unsaturated amplifier, meaning that we ignore pump depletion (i.e., ignore the first term on the left-hand side of Eq. (16), the net gain is found as

$$G = C_R P_P L_{\text{eff}} - \alpha_S L - \alpha_I. \tag{17}$$

α_I is the insertion loss, i.e., loss from splices, isolator, WDMs, etc., L is the length of the fiber, and L_{eff} is the effective length

$$L_{\text{eff}} = \frac{1 - \exp(-\alpha_P L)}{\alpha_P}. \tag{18}$$

The Raman gain efficiency C_R can be calculated from measurement of the linear Raman on-off gain, $g_{\text{on-off}}$ (ratio of output signal power with pump "on" to that with pump "off"). For unsaturated Raman amplification (when pump depletion can be ignored) the Raman gain efficiency is found from Eq. (17) as

$$C_R = \frac{\ln(g_{\text{on-off}})}{P_p L_{\text{eff}}}. \tag{19}$$

The measured Raman gain efficiency spectra for four different kinds of fibers (Table 1) are illustrated in Fig. 3. The two DCFs have the same GeO_2 doping level of the core of around 17 mole %. The difference in gain can therefore mainly be attributed to the difference in effective areas, which are 14 and 21 μm^2, respectively. The two transmission fibers TrueWave® RS and SSMF have effective areas of 52 μm^2 and 82 μm^2, respectively, and GeO_2 doping levels of the core of 5 and 3.5 mole %. It can be noted that at low germanium doping levels as for SSMF, the Raman gain spectrum reveals two peaks around its maximum. This is due to the Raman nature of silica. Fibers with higher germanium doping concentration show the single-peak around a frequency shift of 13 THz due to the germanium dominating the Raman gain. [36]

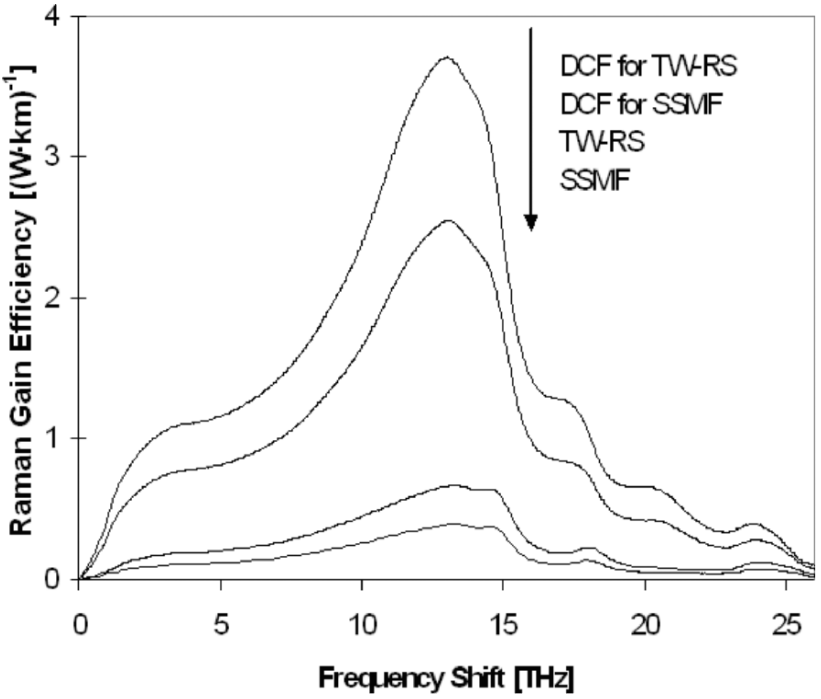

Fig. 3. Measured spectral dependence for Raman gain efficiency pumped at 1453 nm.

2.3. Double Rayleigh Backscattering

Unlike EDFAs with lengths on the order of meters, fibers used for Raman amplification are much longer. Discrete Raman amplifiers have lengths of several to tens of kilometers, while the fiber lengths of distributed Raman amplifiers are tens to hundreds of kilometers. The double Rayleigh backscattering (DRB) [37] is thus more pronounced in Raman amplifiers than in EDFAs. DRB causes a co-propagating, delayed replica of the signal that interferes with the signal and generates noise. This is referred to as multi-path interference (MPI). DRB-induced MPI cross-talk is detrimental to the system performance and is one of the limiting penalties in Raman amplification. [38–41]

The fiber Rayleigh back-scattering coefficient κ is the key parameter to evaluate the DRB-induced MPI. It is defined from

$$\frac{dP_{\mathrm{RBS}}(z)}{dz} = \kappa P_{\mathrm{Signal}}(z), \tag{20}$$

where $P_{\mathrm{RBS}}(z)$ is the Rayleigh back-scattered power and P_{Signal} is the signal power. κ is related to the Rayleigh scattering loss coefficient α_{RS} through the capture fraction B [42,43]

$$\kappa = B\alpha_{\mathrm{RS}}. \tag{21}$$

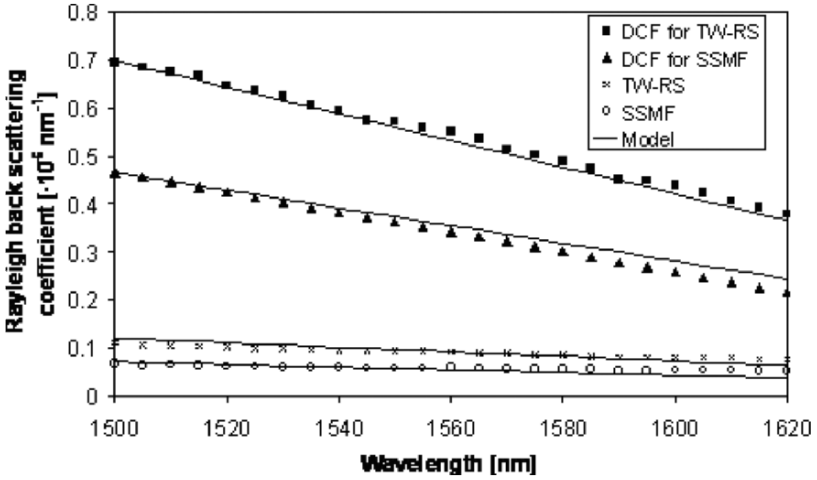

Fig. 4. Measured spectral dependence of the Rayleigh scattering coefficient κ for several fibers.

The capture fraction B has been derived as [44]

$$B = \frac{3}{4k^2n^2} \frac{\int_0^\infty \alpha_{\rm RS}(r)p(r)^2 rdr}{\int_0^\infty \alpha_{\rm RS}p(r)rdr \int_0^\infty p(r)rdr}, \tag{22}$$

where $p(r)$ is the near-field power at radius r, $k = 2\pi/\lambda$, and n is the refractive index.

One can measure the fiber Rayleigh scattering coefficient by using optical time domain reflectometry (OTDR). [45] A more accurate measurement method that additionally allows for easy wavelength scanning is to use a return loss module. [43] The fiber Rayleigh scattering coefficient κ can be calculated from the measured return loss R of the fiber under test:

$$\kappa = \frac{2\alpha R}{\alpha_1^2 \left(1 - e^{-2\alpha L}\right)}. \tag{23}$$

Here, α is the loss of the fiber, α_1 is the loss from the other discrete points including splicing, connector, etc., and L is the length of the fiber.

Measurements of Rayleigh scattering coefficients from this technique are shown in Fig. 4 for the same four fibers as shown in Fig 3. The wavelength range is 1500–1620 nm, covering S+C+L-band, where most of the fiber Raman amplifiers operate presently.

It is observed in Fig. 4 that the variation with wavelength is close to linear. This can be understood from a simple model. If in Eq. (22) it is assumed that $\alpha_{\rm RS}(r)$ is uniform (independent of r), then from Eqs. (13), (21), and (22):

$$\kappa \approx \frac{3\pi\alpha_{\rm RS}}{2\left(\frac{2\pi}{\lambda}\right)^2 n^2 A_{\rm eff}}. \tag{24}$$

Then from [46] the Rayleigh scattering loss α_{RS} is

$$\alpha_{\mathrm{RS}} = \frac{\alpha_0}{\lambda^4}\left(1 + K_{\mathrm{GeO2}} X_{\mathrm{GeO_2}}\right), \tag{25}$$

where α_0 and $\mathrm{K_{GeO2}}$ are constants and $X_{\mathrm{GeO_2}}$is the molar concentration of GeO_2. When Eq. (24) is Taylor expanded in λ and Eq. (25) is used, the following simple model is derived

$$\kappa \approx \frac{K_1\left(1 + K_2 X_{\mathrm{GeO_2}}\right)\left(1 + K_3\lambda\right)}{A_{\mathrm{eff}}}. \tag{26}$$

Figure 4 shows results from this model using best fits of the constants K_1, K_2, and K_3 to the measurement data. A reasonably good agreement is observed.

The measured fiber Raman gain efficiency, attenuation, effective area, and DRB can now be used in Raman amplification simulations using the conventional steady-state model [27], including signal, pump, ASE and DRB noise, etc. [31,37,42]. Such simulations show good agreement with measurements, as demonstrated in section 3 of this paper.

3. Dispersion Compensating Raman Amplifiers

3.1. Amplifier Properties

3.1.1. Raman Characterization Set Up

Raman amplification can be characterized by using the setup shown in Fig. 5(a) [47]. The device under test can, for example, be a bi-directionally pumped DCRA consisting of a DCF as the gain medium, depolarized multi-channel pump source with controlling electronics, and other optical passive components such as coupler, isolator, etc. The input and output signals can be modulated independently by AO modulators at suitable frequency and duty cycle. One can then measure the input and amplified signals using optical spectrum analyzer when the two modulators are in phase. The noises, including ASE and DRB, can be recorded when the two modulators are out of phase. This is referred to as the modified optical time domain extinction method in analogue to EDFA measurement. [47]

A typical measured signal and noise spectra can be seen in Fig. 5(b). The linear Raman net gain (g) is calculated from the measured input (P_{in}) and output signal powers (P_{out}). The interpolated ASE power at the signal wavelength (P_{ASE}), together with the Raman gain, is used to calculate the noise figure (NF), [32] while the DRB power (P_{DRS}) subtracted from the total noise can be used to calculate the MPI:

$$g = \frac{P_{\mathrm{out}}}{P_{\mathrm{in}}}, \tag{27}$$

$$\mathrm{NF} = \frac{1}{g}\left(1 + \frac{2P_{\mathrm{ASE}}}{h\upsilon\Delta f}\right), \tag{28}$$

$$\mathrm{MPI} = \frac{P_{\mathrm{DRS}}}{P_{\mathrm{out}}}, \tag{29}$$

where h is Planck's constant, υ is the frequency of the signal light, and Δf is the bandwidth in which the ASE power is measured.

The MPI due to DRB can also be measured electrically by measuring the laser relative intensity noise (RIN) with an electrical spectrum analyzer. [48] It is worth

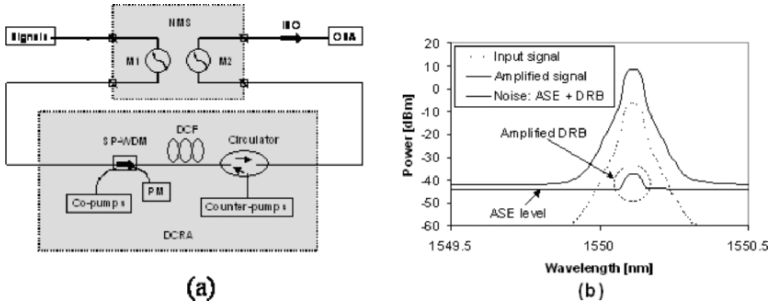

Fig. 5. (a) Schematic of a bi-directionally pumped DCRA in a Raman characterization setup; (b) Typical measured signal and noise (ASE+DRB) spectra. SP-WSM: signal-pump wavelength division multiplexer including a built-in isolator; OSA: optical spectrum analyzer; ISO: isolator; PM: power monitor; NMS: noise measurement system; M1/M2: signal input/output modulator.

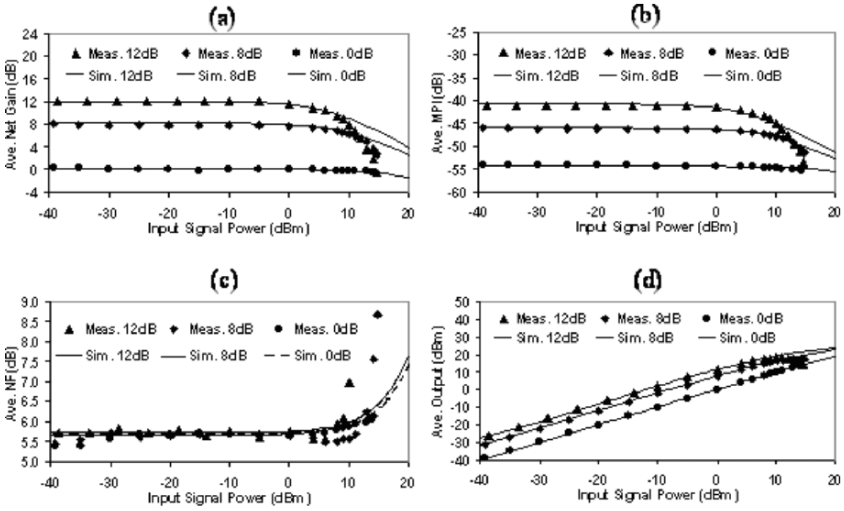

Fig. 6. Measured and simulated average (a) net gain; (b) multi path interference MPI; (c) noise figure NF and (d) output power vs. input signal power for average net gain of 12, 8 or 0 dB. 3.9 km DCF for TW-RS was used. [8]

noting that the optical measurement of MPI gives the worst-case result because all polarizations of both the DRB noise and the signal are included. In the electrical measurement, the MPI is dependent on the degree of polarization of the DRB noise. [49] For unpolarized DRB noise, the electrically measured MPI will be around 3dB lower than the optical measurements. [50]

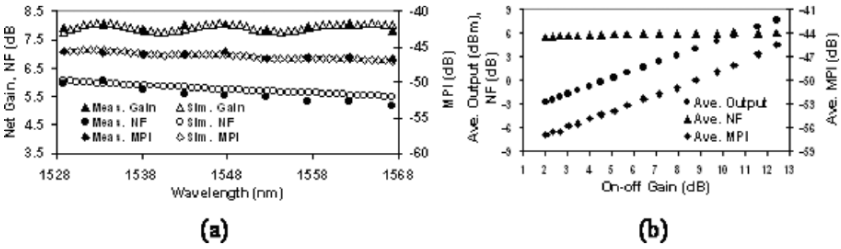

Fig. 7. (a) Measured and simulated net gain, NF, and MPI for optimized 38.4 nm spectral range centered at 1548 nm. (b) Measured average Raman gain, NF, and MPI dependence on Raman pump power with 0 dBm input signal power. [8]

3.1.2. Raman Net Gain, NF, and MPI due to DRB

As an example, measured and simulated net gain, noise figure, MPI, and output power as functions of input signal power are shown in Fig. 6. [8] Good agreement between measurement and simulations is observed. A 3.9-km DCF for dispersion compensation of 90.8 km TW-RS is used in this counter pumped C-band DCRA. The link residual dispersion is within $\pm$ 0.1 ps/km nm from 1528.8 to 1567.2 nm. The average loss of this DCRA in the C-band is around 5 dB without Raman pumping. The saturation effect can be seen from the curves for high signal amplification and the saturation power can be estimated to be 23 dBm in Fig. 5(d), with maximum 589 mW pumping. The NF is independent of the signal level for unsaturated Raman amplification, but will be much higher in the saturation region due to the rapid increase of double Rayleigh backscattered ASE. [42] The deviations of measurements from simulations at high signal level are mainly due to the SBS effect. [42,36] Note that these measurements are performed with only nine channels with 600 GHz spacing, so it can be expected that for real system using 25–100 GHz channel spacing, the signal power per channel will be 6 to 24 times lower for the same amount of total power. In addition, signals are usually coded with bit rate higher than 1 Gbit/s, so the SBS threshold will be drastically higher. Therefore, the SBS effect will not be a serious limitation for Raman amplification in real systems. Spectral broadening or phase modulation of the signal can also be used to eliminate SBS.

Table 4. Pump configuration.

	Total (mW)	1426nm	1438nm	1466nm
Pumps for 12 dB net gain	589	194	194	201
Pumps for 8 dB net gain	451	135	121	195
Pumps for 0 dB net gain	160	52	36	72

Three-wavelength counter pumps, as shown in Table 4, are chosen to achieve optimized flat gain. The measured gain flatness is within $\pm$0.13 dB for 8 dB net gain, close to the simulated flatness of $\pm$0.16 dB, as shown in Fig. 7(a). The average noise figure is 5.6 dB with MPI of $-$46 dB. The measured average net gain, NF, and MPI

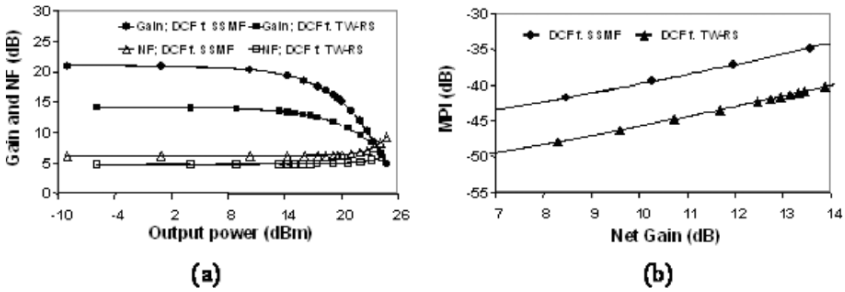

Fig. 8. (a) Simulated Raman net gain and noise figure as functions of output signal power for a total pump power of 660 mW. (b) Simulated MPI due to DRB versus net gain. Fibers are DCF for SSMF and DCF for TW-RS for 80 km SSMF and TW-RS compensation, respectively.

versus pump power is displayed in Fig. 7(b). Raman net gain efficiency can be deduced as 28.5 dB/W. MPI increases about 1 dB for 1 dB gain increase. It should be noted that DRB induced MPI for this DCRA without Raman pumping is very low, only −59 dB. MPI for 0dB net gain is below −54 dB. The NF is less than 6 dB and is nearly independent of the pump power for net gain of several dB.

Different transmission fibers require different DCF. For example, the DCF length will be much longer for compensation of SSMF compared to compensation of NZDF. Figure 8 displays the simulation results of DCFs for compensation of 80 km SSMF and TW-RS, respectively. Three counter propagating pumps with a total pump power of 660 mW are used for amplification in the C-band. The DCF for SSMF is about three times as long as the DCF for TW-RS, due to the much higher dispersion of SSMF compared to TW-RS. Due to the longer length of the DCF for SSMF, it has a higher gain, but the noise figure is 1 dB higher than the DCF for TW-RS. The MPI for the DCF for SSMF is around 5 dB higher than the DCF for TW-RS for the same net gain level again due to the longer length. Thus, from a Raman amplification point of view, the DCF for dispersion compensation of TW-RS will have much lower noise impairment on the transmission system compared with DCF for SSMF.

3.2. Amplifier Configurations

Owing to the relatively long fiber length of Raman amplifiers compared to EDFAs, DRB induced MPI, [38,51,41,52–54] ASE, and fiber nonlinear effects, [55,56] can be major impairments in real systems.

To minimize the noise figure, the signal power excursion should be minimized; thus co-pumping is a promising technique. To minimize the MPI due to DRB, bi-directional pumping and a multi-stage DCRA design with inter-stage isolator [56–59] are preferable. However, to mitigate the nonlinear impairments, the path-averaged signal power should be minimum; so co-pumping would not be the best solution. A DCRA can be optimally designed with respect to both linear and nonlinear impairments by using equations described in [55].

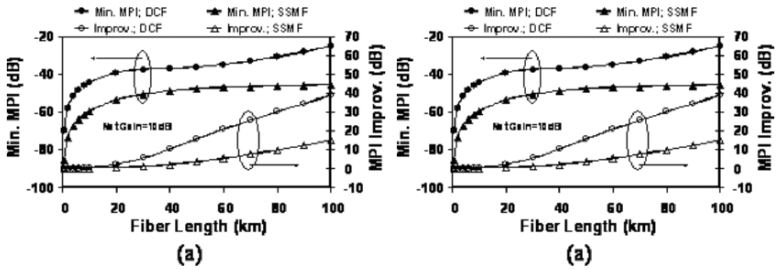

Fig. 9. Simulated minimum MPI and MPI improvement by 50% co-pumping as functions of (a) fiber length with net gain of 10 dB and (b) net gain for small-signal Raman amplification in two different fibers: SSMF and DCF for SSMF.

3.2.1. Linear Impairments

For a DCRA, the MPI comes from DRB of signal and discrete reflections, such as connectors. Both types of MPI result in power penalties in real systems. The penalty for a 10-Gbit/s NRZ signal was in [41] found as

$$\text{Penalty(dB)} = -20\log\left(1 - NR_cQ^2\right), \tag{30}$$

where R_c is the total MPI for a single span from both DRB and reflections measured by an electrical spectrum analyzer. [48] N is the number of amplifier spans. $Q = 6$ for BER=10^{-9}.

To maintain the power penalty within 0.5 dB of $Q = 6$ for transmission over 40 amplifier spans, the cross-talk per fiber span should be kept below -44 dB.

To implement Raman amplification, one can use a co-, counter- or bi-directional pumping configuration. Co-pumped Raman amplifiers suffer from high relative intensity noise transfer from the pump [60,61], but give the lowest noise figure of the three pumping configurations due to high path average power. Recently, pump lasers with very low RIN have become available, so co- or bi-directional pumping has become practical. Counter-pumped Raman amplifiers average the noise fluctuation from the pump, but the gain excursion in the fiber is the maximum, resulting in the largest noise figure. For bi-directional pumping a moderate noise figure can be obtained, with the extra advantage of minimum DRB induced MPI [38,5,55,62] due to minimum gain excursion along the fiber.

The minimum MPI and MPI improvement by using 50% bi-directional pumping can be calculated as illustrated in Fig. 9 for SSMF and DCF for SSMF. The simulation is performed for small-signal amplification using equations in [38]. It can be seen that the MPI improvement is strongly dependent on the fiber length and the Raman net gain. A short length (around 10 km) DCRA benefits much less than long transmission fibers (around 100 km) in distributed RA. This is because the MPI improvement level depends on the gain excursion difference among different pumping configurations. For long transmission fibers, the effective length is much shorter than the fiber length, so there will be a higher gain excursion difference between co- (or counter-) and bi-directional pumped amplifiers. The DCRA with shorter length will exhibit less gain excursion difference because the Raman effective length is close to the fiber length.

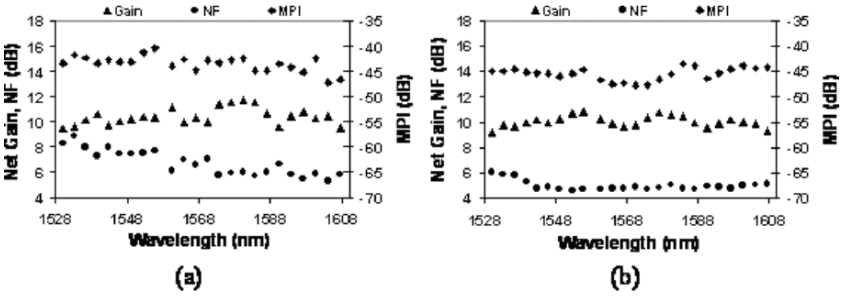

Fig. 10. Measured gain, noise figure, and MPI due to DRB using (a) counter-pumping scheme and (b) bidirectional pumping scheme. [5] The pump configuration is shown in Table 5.

For a 10-dB net gain, the MPI improvement for 17.6 km of DCF for SSMF (for dispersion compensation of 120 km of SSMF) would be around 2 dB while for 100 km of SSMF it could be as high as 15 dB. A DCRA made of 9.5 km of DCF for SSMF (for 60 km SSMF dispersion compensation) exhibits MPI improvement of 0.7 dB with 50% co-pumping at 8 dB net gain. [62]

To improve the NF tilt in broadband DCRAs, it is useful to design a bi-directionally pumped DCRA with co-pumping for the shorter part of the transmission band, but counter-pumping for the longer band. [63,5,4].

A C+L-band DCRA composed of two DCFs was constructed for compensation of 100 km TrueWave®REACH. [5] The Raman gain, NF, and MPI using two different pumping schemes are displayed in Fig. 10, with pumping configurations shown in Table 5.

Table 5. Pump configurations for counter- and bi-directionally pumped C+L-band DCRA. Co-pump is noted as "co" whereas others are all counter-pumped.

Config.	1428nm	1445nm	1467nm	1484nm	1491nm	1507nm	Total
Count. P	297mW	297mW	162mW	41mW	93mW	78mW	967mW
Bi-dir. P	360mW,co	360mW,co	86mW	0mW	138mW	98mW	1042mW

Six pump wavelengths are used in the counter-pumped DCRA. The average net gain is 10.4 dB with flatness of ± 1.2 dB, whereas the average NF is 6.7 dB with flatness of ± 1.8 dB. The average MPI is -43.4 dB.

For the bi-directional pumping case, the co-pumped C-band and counter-pumped L-band are designed as shown in Table 5. The net gain flatness is improved to ± 0.8 dB, whereas the average NF is decreased to 5 dB with improved flatness of ± 0.7 dB. The average MPI is also improved to less than -45 dB. The noise improvement is due to the lower gain excursion along the fiber by using bi-directional pumping.

Another way to improve the MPI performance for DCRAs is to design multi-stage amplifiers with the same type of fibers but different lengths, [57–59] or different types of fibers. The key technique is to use a mid-stage isolator (or circulator) together with couplers to build a bridge for the pump to reach all the stages, but block the signal

back reflections among different stages. The MPI improvement can be as high as 15 dB with an optimized 60%. length proportion for a two-stage discrete RA with 5 km of HNLF [59] The NF degradation due to extra passive components was less than 1 dB in this case.

MPI and NF improvements of 7 and 2 dB, respectively, have been demonstrated by counter-pumping the first stage fiber and using the residual pump to counter-pump the second stage. [56] The first stage fiber length is 36% of the total 6 km of C-DCF (Table 6).

3.2.2. Non-linear Impairments

The non-linear impairments [64,55,65,39,66] in Raman amplification will impose limitations for its application in real systems. These impairments include SBS, intra channel-SRS, self phase modulation (SPM), cross phase modulation (XPM), and four wave mixing (FWM). The last two effects can affect both multi-channel signals and/or multi-channel pumps.

DCF has the general spectral dispersion behavior as shown in Fig. 15, i.e., it will never reach zero dispersion at either pump or signal wavelength. Therefore, FWM will normally not be a consideration in DCRAs.

SBS can be diminished by broadening the signal spectral width or phase modulating the signal.

SRS induced Raman tilt can be compensated by proper adjustment of pump wavelengths and powers for WDM-pumped DCRA.

A DCRA has a higher fiber nonlinear coefficient than transmission fiber, but the DCRA length is generally significantly shorter than that of distributed RA, so their gross nonlinear impairments are comparable.

The nonlinear phase shift φ due to SPM can be calculated from the fiber nonlinear coefficient γ as

$$\varphi = \int_0^L \gamma(z) P_s(z) dz = \gamma P_s(z=0) L_{\text{eff,Raman}}$$

$$L_{\text{eff}}(\text{unpumped}) = \frac{1}{\alpha_s}\left(1 - e^{-\alpha_s L}\right), \tag{31}$$

where γ is assumed to be constant along the fiber length. P_s(z) is the signal power in position z, $L_{\text{eff,Raman}}$ is the nonlinear effective length for a Raman pumped fiber. For an unpumped fiber, the nonlinear effective length is solely dependent on the fiber attenuation at signal wavelength $\alpha_s$and fiber length L, as shown in Eq. (31).

Raman amplification will enhance the nonlinear effect by increasing the nonlinear effective length. The nonlinear enhancement ratio R_{NL} is defined as the ratio of the effective length with Raman amplification to the effective length of the unpumped fiber. [64,55,66] It has the form of

$$R_{\text{NL}} = \frac{\alpha_s}{1 - e^{-\alpha_s L}} \int_0^L G_{\text{net}}(z) dz, \tag{32}$$

which is proportional to the path average net gain/signal power along the fiber.

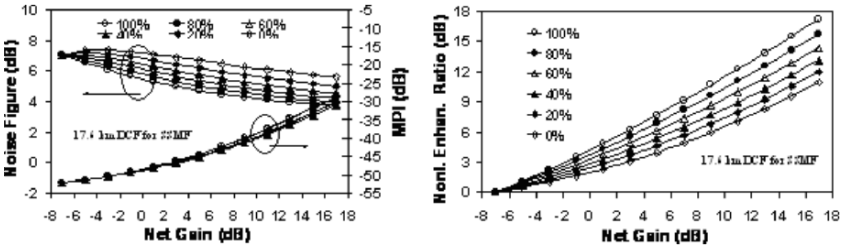

Fig. 11. Simulated (a) noise figure and MPI due to DRB and (b) nonlinear enhancement ratio R_{NL} vs. net gain for various co-pump proportions. 17.6 km of DCF for SSMF is used, and unsaturated amplification is assumed.

The path-average power is maximum for co-pumped RA compared to counter- or bi-directional pumped RA. Thus, the NF is minimum for co-pumped RA but the nonlinear enhancement is at the maximum as shown in Fig. 11. Owing to such trade-offs, careful design for DCRAs is needed. For example, a transparent DCRA made of 17.6 km of DCF for SSMF will have 1.7-dB NF improvement by co-pumping compared to counter-pumping. However, the nonlinear enhancement will be 2.2 dB higher than for counter-pumping. If the nonlinear enhancement is fixed as 3 dB, then the counter-pumping scheme supports Raman amplification to a net gain of 3 dB, whereas co-pumping will only support net gain of –2 dB. To compensate for the nonlinear enhancement due to Raman amplification, the maximum signal input power should be reduced by the same amount as the nonlinear enhancement. Thus, equivalently the co-pumping scheme will reduce the maximum input signal power by 5 dB compared to the counter-pumping scheme for the same nonlinear impairment level. Nonlinear impairments due to Raman amplification will limit the maximum useful signal power in systems.

Owing to the fundamental limitations of Raman amplification with respect to noise and nonlinearity with a certain level of path-average signal power, the optimum design will focus on the minimization of the signal power excursion, signal-to-signal Raman scattering, and temperature dependent noise. [39] EDFAs have at least 3-dB noise figure, so EDFA post amplification will always degrade the noise performance in a Raman based system.

4. Optimizing Dispersion Compensating Fibers for use in Discrete Raman Amplifiers

4.1. Raman Figure of Merit

The fiber Raman net gain $G_{\rm net}$ is the Raman on-off gain minus the fiber loss and other discrete losses, such as splices, couplers, etc. From Eqs. (17) and (18) the net gain for an unsaturated amplifier can be calculated as

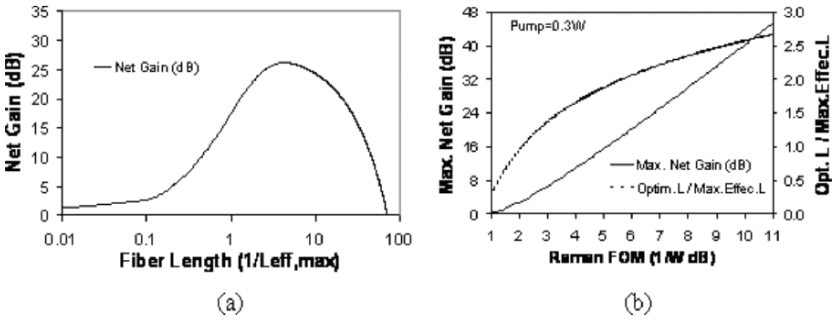

Fig. 12. (a) Calculated Raman net gain versus fiber length normalized by maximum effective length. (b) Calculated maximum net gain and optical length as functions of Raman figure of merit FOM_R.

$$G_{\mathrm{net}} = C_R P_P L_{\mathrm{eff}} - \alpha_S L - \alpha_I,$$
$$L_{\mathrm{eff}} = \frac{1}{\alpha_p}\left(1 - e^{-\alpha_p L}\right) = L_{\mathrm{eff,max}}\left(1 - e^{-\alpha_p L}\right), \tag{33}$$

where α_s and α_p are the fiber losses at the signal and pump wavelengths, respectively, α_I is the sum of the discrete losses, P_P is the pump power, L the fiber length, and $L_{\mathrm{eff,max}} = 1/\alpha_p$ is the maximum effective length.

The dependence of Raman net gain on fiber length is illustrated in Fig. 12(a), using a DCF for SSMF as an example. A maximum net gain at an optimum length L_{opt} is observed.

Using the approximation that the fiber attenuation at signal and pump wavelength is the same $\alpha_s \approx \alpha_p$, the optimum fiber length L_{opt} can be expressed in the form of

$$L_{\mathrm{opt}} \approx L_{\mathrm{eff}}^{\max} \ln\left(\mathrm{FOM}_R P_p\right), \qquad \mathrm{FOM}_R = \frac{C_R}{\alpha_p}. \tag{34}$$

FOM_R is referred to as the Raman figure of merit. [36] The maximum net gain, which is reached using the optimum fiber length, can thus be obtained as

$$G_{\mathrm{net}}^{\max} \approx \mathrm{FOM}_R P_p - 1 - \ln\left(\mathrm{FOM}_R P_p\right) - \alpha_D. \tag{35}$$

This is almost linearly dependent on FOM_R as illustrated in Fig. 12(b). The highest reported FOM_R is 10.3(W^{-1} dB^{-1}). [67]

FOM_R is a strong tool for optimizing fibers for discrete Raman amplifiers, if the length can be chosen freely to equal L_{opt}. Unfortunately, that is not the case for a DCRA where the fiber length has to be adjusted to obtain the required amount of dispersion.

4.2. Optimizing DCF for DCRA

The optimal DCF for a DCRA should fulfill the following requirements:

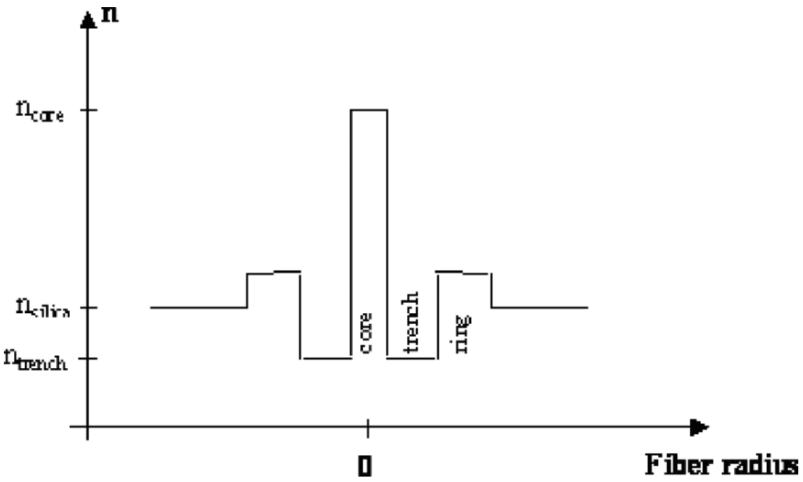

Fig. 13. Triple clad index profile.

1. Dispersion properties:
   a) RDS matching the transmission fiber
   b) Low dispersion curvature (low RDC)
2. High Raman gain efficiency
3. Low loss at pump and signal wavelengths
4. Low Rayleigh backscatter coefficient
5. Optimum length
   a) Long enough to obtain sufficient gain with the available pump power
   b) Short enough to minimize MPI due to DRB

Requirements 2 and 3 can, to some extent, be combined in a requirement of maximizing the Raman FOM$_R$. Lowering the loss (requirement 3) normally also helps to reduce the Rayleigh backscatter coefficient (requirement 4).

The last requirement can often be the most difficult to fulfill. Using standard DCF, the DCF length tends to be too long when compensating long lengths of SSMF, while it tends to be too short when compensating short lengths of NZDF.

DCF with triple cladding index profiles will now be examined. Dual cladding [68] as well as quintuple-cladding profiles [69] can be considered as well, but triple-cladding profiles are sufficient to realize most DCF types. [70,71] The triple cladding index profile (Fig. 13) has a narrow, high delta core surrounded by a deeply depressed cladding followed by a raised ring.

An elegant method for analyzing this type of profile considers the two guiding regions: the core and the cladding separately. [71–73] The propagation characteristics of the combined system can then be obtained by the use of coupled mode theory. A

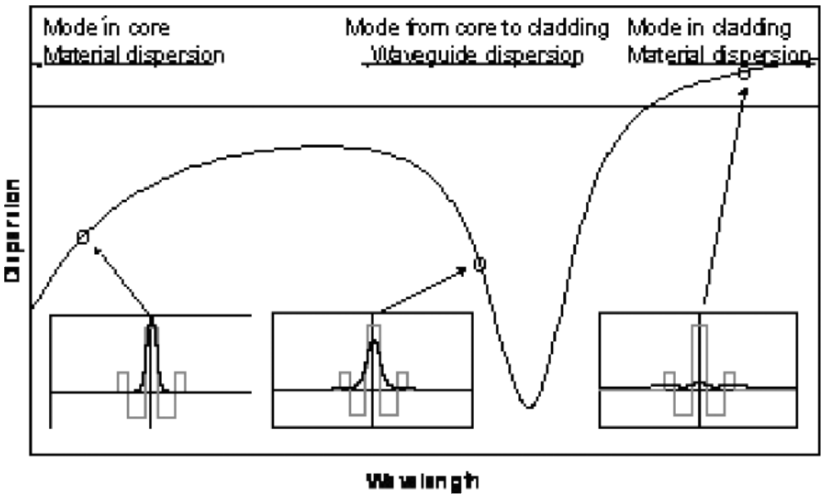

Fig. 14. General dispersion curve in a triple cladding fiber. Insets show mode field evolution.

thorough treatment of fiber design theory is outside the scope of this paper. Here the focus will be on the obtainable properties and design tradeoffs.

Figure 14 shows how the mode field expands with wavelength and the resulting dispersion curve.

As DCF relies on large waveguide dispersion from the expanding mode field, it is important when designing DCF to take micro and macro bend loss into consideration. Generally, it is important to keep the effective index of the mode from becoming too low. One way to maintain a sufficiently high effective index is to increase the index of the core or the ring. However, increasing the index can only be done to a certain limit before the fiber will start to support higher order modes. Guidance of higher order modes should be avoided because the higher order modes can interfere with the fundamental mode, leading to modal noise from MPI. [74] As emphasized in [74] it is important to distinguish MPI due to interference between different modes from the MPI from double Rayleigh scattering treated earlier in this paper. Both penalties and measurement should be treated differently. Another drawback of increasing especially the core index is increased loss due to higher GeO_2 doping and anomalous loss. [46,75] A benefit from increasing the core index is increased Raman gain efficiency due to the higher GeO_2 doping. A further draw back is increased Rayleigh backscatter coefficient. DCF design is therefore a balance between the wanted dispersion properties, macro bend loss, micro bend loss, and higher order mode cut off wavelength as well as Raman properties.

Figure 15 shows an expanded view, of the region of interest for DCF, of the general dispersion curve from Fig. 14. The generic curve has an inflection point where the curvature changes from negative to positive. Three interesting operating points can be identified:

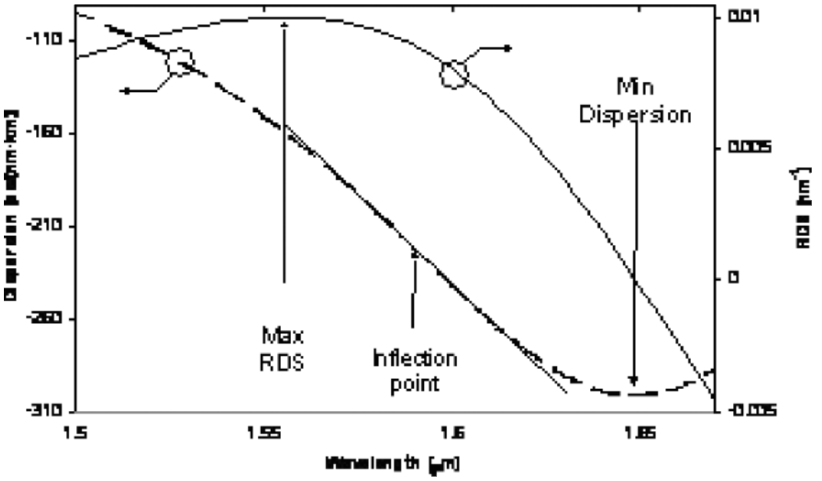

Fig. 15. General shape of dispersion versus wavelength for DCF.

1. The operating wavelength range is below the inflection point. Here RDS can be maximized.
2. The inflection point is in the center of the operating wavelength range. This will give minimum curvature.
3. The operating wavelength range is above the inflection point. This will give the most negative dispersion, maximizing the FOM.

It can be shown [76,71] that even when DCF are designed for operation at the inflection point, which might not be possible for the very high RDS fibers due to macro bend loss, the usable bandwidth is inversely proportional to the RDS. An example of broadband compensation of low RDS fibers like SSMF and TrueWave®REACH (Table 2) are shown in Fig. 16. [5] DCFs having their inflection point in the middle of the operating range at 1570 nm are used. Record bandwidth of 165 nm with a residual dispersion of ± 0.18 ps/(nm km) was reported by Gorlier et al. using optimized DCF for a NZDF with a RDS of 0.0035 nm^{-1}. [77]

Such broad compensation bandwidth DCFs have an exciting potential for Raman amplifiers due to the possibility for very broadband amplification. Such DCF can actually only be fully utilized in "all-Raman" systems, as illustrated in Fig. 17.

In the traditional system using EDFAs, the bands have to be split and one DCF is usually required for each band. In an "all-Raman" systems, the same DCF is used to cover the entire system bandwidth for both dispersion compensation and as gain medium. [4,5] A much simpler configuration is obtained and no channels are lost between the bands.

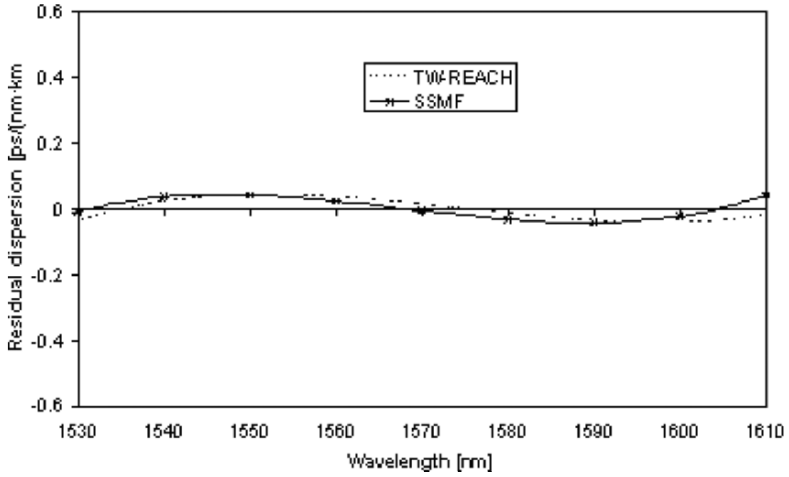

Fig. 16. Residual dispersion for SSMF and TW-REACH compensated corresponding broadband DCF.

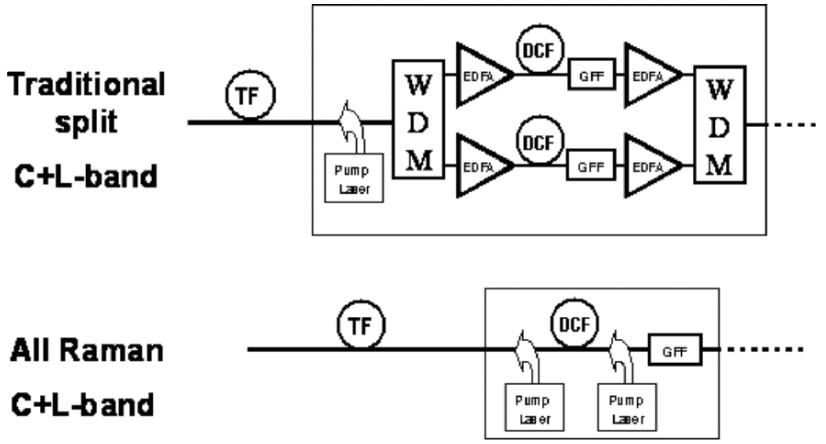

Fig. 17. Advantage of "all-Raman" C+L band transmission.

4.2.1. Example: Optimized DCF for DCRA for TW-RS Fibers

As an example, optimization of DCF for compensation of dispersion and dispersion slope of TrueWave®RS in the L-band will be considered. A conventional DCF (C-DCF) will be compared with two fibers R-DCF-1 and R-DCF-2 with the same RDS but with improved Raman gain properties. The typical values for the three fibers are listed in Table 6:

Table 6. Measured fiber properties.

Fiber type	C-DCF	R-DCF-1	R-DCF-2
Attenuation @1585 nm [dB/km]	0.57	0.34	0.42
Dispersion @1585 nm [ps/(nm·km)]	-111	-71	-78
RDS @1585 nm [nm^{-1}]	0.0065	0.0060	0.0067
RDC @1585 nm [nm^{-2}]	$5.9{\cdot}10^{-5}$	$1.7{\cdot}10^{-5}$	$6.1{\cdot}10^{-5}$
Effective area @1580 nm [μm^2]	15.6	21.0	15.5
Raman gain efficiency, pump@1453 nm [$W^{-1}km^{-1}$]	3.6	2.1	3.2
Raman FOM, pump@1453 [$W^{-1}dB^{-1}$]	4.4	5.4	5.8
Rayleigh backscattering coefficient [$10^{-6}m^{-1}$]	0.59	0.31	0.49

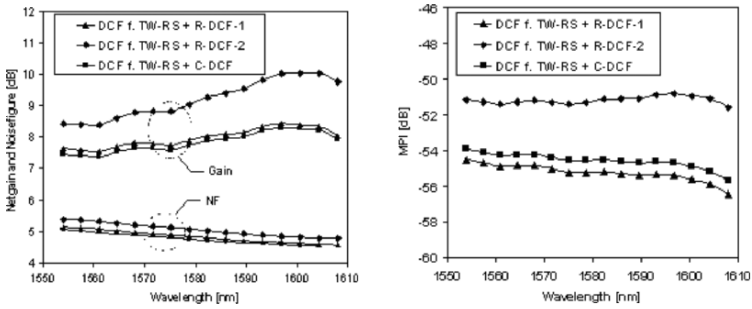

Fig. 18. Simulated net gain, noise figure and DRB MPI in DCRA for compensation of 50 km of TW-RS transmission fiber keeping the pump power constant.

The dispersion of the new fibers is lower than that of C-DCF. Thereby the length of fiber needed for compensating a certain amount of dispersion is increased, resulting in a longer gain medium for Raman amplification. The Rayleigh backscattering, resulting in MPI, is lower and the Raman FOM is higher for both R-DCF fibers making them better suited for Raman amplification, whereas the RDS is almost the same for all three fiber types.

Modules for compensating 50 km of TW-RS in the L-band have been simulated. They consist of DCF for TW-RS C-band (Table 1) in combination with C-DCF or R-DCF-1 or R-DCF-2. Simulations with realistic system parameters have been performed on these modules and are shown in Fig. 18. It is seen that with R-DCF-2 an improvement in the gain of up to 1.6 dB can be obtained whereas with R-DCF-1 there is a slight improvement in both gain and MPI.

5. Summary

Dispersion compensating fiber (DCF) is generally a good Raman gain medium, making DCF well suited for combining dispersion compensation and amplification into one component, the dispersion compensating Raman amplifier (DCRA). In this paper, the

basic properties of DCF have been presented with special emphasis on Raman gain properties. The two central parameters to describe Raman properties, the Raman gain efficiency and the Rayleigh back scattering coefficient, are presented and are both shown to depend mainly on GeO_2 doping level and effective area. It has been shown that DCRAs can be realized with high gain for moderate pump power, low noise figure, and low multi path interference (MPI) due to double Rayleigh back scattering (DRB).

Due to the relatively short length, bi-directional pumping of a DCRA using the same wavelengths for both co- and counter-pumping is not as appealing to reduce MPI and noise figure (NF) as for distributed Raman amplification. For broadband DCRAs, however, it is attractive to have the shorter pump wavelength(s) co-propagating and the longer pump wavelength(s) counter-propagating relative to the signals to improve noise figure and MPI.

Use of DCF for DCRAs leads to new requirements, raising the need for new fiber designs optimized for this application. For example, it can be useful to optimize the DCF, so the required DCF length is not too short in a DCRA compensating a short length of low dispersion NZDF or, conversely, not too long in a DCRA compensating long lengths of high dispersion SSMF.

Acknowledgement

The author would like to thank Bera Pálsdóttir from OFS Denmark and Lynn Nelson from OFS Laboratories, Somerset, NJ for invaluable help in preparing this paper.

References

1. P.B. Hansen, G. Jacobovitz-Veselka, L. Grüner-Nielsen, A.J. Stentz, Raman amplification for loss compensation in dispersion compensating fibre modules,; Electron. Lett., **34** (11), 1136–1137 (1998).
2. Y. Emori, Y. Akasaka, S. Namiki, Broadband lossless DCF using Raman amplification pumped by multichannel WDM laser diodes, Electron. Lett., **34** (22), 2145–2146 (1998).
3. T. Tanaka, K. Torii, M. Yuki, H. Nakamoto, T. Naito, I. Yokota, 200-nm bandwidth WDM transmission around 1.55 μm using distributed Raman amplifier, Proceedings of ECOC'02, paper PD4.6, 2002.
4. T. Miyamoto, T. Tsuzaki, T. Okuno, M. Kakui, M. Hirano, M. Onishi, M. Shigematsu; Raman amplification over 100 nm bandwidth with dispersion and dispersion slope compensation for conventional single mode fiber, Proceedings of OFC'02, paper TuJ7, 2002.
5. L. Grüner-Nielsen, Y. Qian, B. Pálsdóttir, Y. Qian, P.B. Gaarde, S. Dyrbøl, T. Veng, R. Boncek, R. Lingle, Module for simultaneous C+L-band dispersion compensation and Raman amplification, OFC'02, paper TuJ6, 2002.
6. D.A. Chestnut, C.J.S. de Matos, P.C. Reeves-Hall, J. R. Taylor, Co- and counter-propagating second-order-pumped lumped fiber Raman amplifiers, Proceedings of OFC'02, paper ThB2, 2002.
7. J. Bromage, H.J. Thiele, L.E. Nelson, Raman amplification in the S-band, Proceedings of OFC'02, paper ThB3, 2002.

8. Y. Qian, Carsten G. Jørgensen, P. B. Gaarde, B. Pálsdóttir, B. Edvold, C-band discrete Raman amplification with simultaneous dispersion and dispersion-slope compensation for NZDF, Proceedings of OAA'02, paper OWB2, 2002.
9. A.H. Gnauck, G. Raybon, S. Chandrasekhar, J. Leuthold et al., 2.5 Tb/s (64x42.7 Gb/s) Transmission Over 40 × 100 km NZDSF Using RZ-DPSK Format and all-Raman-Amplified Spans, OFC'02, paper FC2, 2002.
10. B. Zhu, C. Doerr, P. Gaarde, L. E. Nelson, S. Stulz, L. Stulz, L. Gruner-Nielsen, Broad bandwidth seamless transmission of 3.56 Tbit/s over 40 ×x 100 km of NZDF fibre using CSRZ-DPSK format, Opt. Lett., **39** (21), 1528–1530 (2003).
11. B. Zhu, L. Leng, A.H. Gnauck, M.O. Pedersen, D. Peckham, L.E. Nelson, S. Stulz, S. Kado, L. Grüner-Nielsen, R.L. Lingle, Jr., S. Knudsen, JU. Leuholdt, C. Doerr, S. Chandrasekhar, G. Baynham, P. Gaarde, Y. Emori, S. Namiki, Transmission of 3.2 Tb/s (80 × 42.7 Gbit/s) over 5200 km of UltraWave fiber with 100 km dispersion-managed spans using RZ_DPSK format, Proceedings of ECOC 2001, paper PD4.2, 2002.
12. C. Rasmussen, S. Dey, F. Liu, J. Bennike, B. Mikkelsen, P. Mamyshev, M. Kimmitt, K. Springer, D. Gapontsev, V. Ivshin, Transmission of 40 × 42.7 Gbit/s over 5200 km Ultra-Wave fiber with terrestrial 100 km spans using turn-key ETDM transmitter and receiver, Proceedings of ECOC 2002, paper PD4.4, 2002.
13. D.F. Grosz, A. Agarwal, S. Banerjee, A.P. Kung, D.N. Maywar, A. Gurecich, T.H. Wood, C.R. Lima, B. Faer, J. Black, C. Hwu, 5.12 Tb/s (128 × 42.7 Gb/s) Transmission with 0.8 bit/s/Hz spectral efficinecy over 1280 km of standard single-mode fiber using all-Raman amplification and strong signal filtering, ECOC'02, paper PD4.3, 2002.
14. L.F. Mollenauer, Dispersion managed solitons for ultra long distance, Terabit WDM, Proceedings of OFC'00, Tutorial 5, 2000.
15. P.J. Winzer, K. Sherman, M. Zirngibl, Experimental demonstration of time-division multiplexed Raman pumping, Proceedings of OFC'02, paper WB5, 2002.
16. G. Charlet, W. Idler, R. Dischler, J.-C. Antona, P. Tran, S. Bigo, 3.2 Tbit/s (80'42.7 Gb/s) C-band transmission over 9'100 km of TeraLightTM fiber with 50 GHz channel spacing; Proceedings of OAA'02, PD1, 2002,
17. A.J. Antos, D.K. Smith, Design and Characterization of Dispersion Compensating Fiber Based on the LP01 Mode, J. Lightwave Technol., **12** (10), 1739–1745 (1994).
18. L. Grüner-Nielsen, S.N. Knudsen, B. Edvold, T. Veng, D. Magnussen, C.C. Larsen, H. Damsgaard, Dispersion compensating fibers, Opt. Fiber Technol., **6**, 164–180 (2000).
19. T. Kato, Design optimisation of dispersion compensating fiber for NZ-DSF considering nonlinearity and packaging performance, Proceedings of OFC2001, paper TuS6, 2001.
20. M.J. Li, Recent Progress In Fiber Dispersion Compensators; Proceedings of ECOC 2001, paper Th.M.1.1, 2001.
21. M. Wandel, P. Kristensen, T. Veng, Y. Qian, Q. Le, L. Grüner-Nielsen, Dispersion compensating fibers for non-zero dispersion fibers, Technical Digest of OFC'2002 paper WU1, 2002.
22. L. Grüner-Nielsen, B. Edvold, Status and future promises for dispersion-compensating fibers,; Proceedings of ECOC'02, paper 6.1.1, 2002.
23. M. Wandel, T. Veng, Q. Le N.T., L. Grüner-Nielsen, Dispersion compensating fibre with a high figure of merit; Proceedings of ECOC'01, paper PD.A.1.4, 2001.
24. C.D. Poole, J.M. Wiesenfeld, D.J. DiGiovanni, A.M. Vengsarkar, Optical Fiber-Based Dispersion Compensation Using Higher Order Modes Near Cut-off, J. Lightwave Technol., **12** (10), 1746–1758 (1994).

25. A.H. Gnauck, L.D. Garrett, Y. Danziger, U. Levy, M. Tur, Dispersion and dispersion-slope compensation of NZDSF over the entire C band using higher-order-mode fibre, Electron. Lett., **36**, 1946 (2000).

26. S. Ramachandran, B. Mikkelsen, L.C. Cowsar, M.F. Yan, G. Raybon, L. Boivin, M. Fishteyn, W.A. Reed, P. Wisk, D. Brownlow, L. Gruner-Nielsen, All-Fiber, Grating-based, Higher-order-mode Dispersion Compensator for Broadband Compensation and 1000-km Transmission at 40-Gb/s, Photon. Technol. Lett., **13** (6), 632–634 (2001).

27. G.P. Agrawal, *Nonlinear Fiber Optics* (Academic Press, San Diego, CA, 2001).

28. P. Nouchi, P. Sillard, L.A. de Montmorillon, New transmission fibers for future networks, in Proceedings of ECOC'2004, paper Th3.3.1.

29. L. Nelson, B. Zhu, *Raman Amplifiers for Telecommunications.* (Springer-Verlag, New York, 2004), chapter 19.

30. R.H. Stolen, E.P. Ippen, A.R. Tynes, Raman gain in glass optical waveguide, Appl. Phys. Lett., **22**, 62–64 (1972).

31. H. Kidorf, K. Rottwitt, M. Nissov, M. Ma, E. Rabarijaona, Pump Interactions in a 100-nm Bandwidth Raman amplifier, IEEE Photon. Technol. Lett., **11**, 5 (1999).

32. C.R.S. Fludger, *Raman Amplifiers for Telecommunications* (Springer-Verlag, New York, 2004), chapter 4.

33. S.T. Davey, D.L. Williams, B.J. Ainslie, W.J.M. Rothwell, B. Wakefield, Optical gain spectrum of GeO_2-SiO_2 Raman fibre amplifiers, IEE Proceedings, **136**, Pt. J, 6 (1989).

34. K. Rottwitt, J. Bromage, A.J. Stentz, L. Leng, M. Lines, H. Schmith, Scaling of the Raman gain coefficient: Applications to germanosilicate fibers, J. Lightwave Technol., **21** (7), 1652 (2003).

35. R.H. Stolen, *Raman Amplifiers for Telecommunications* (Springer-Verlag, New York, 2004), chapter 2.

36. Y. Qian, J.H. Povlsen, S.N. Knudsen, L. Grüner-Nielsen, Fiber Raman amplifications with single-mode fibers, Trends in Optics and Photonics Series TOPS, Vol. 44, pp. 128–134, 2000.

37. P.B. Hansen, L. Eskildsen, A. J. Stentz, T. A. Strasser, J. Judkins, J.J. DeMarco, R. Pedrazzani, D. J. DiGiovanni, Rayleigh scattering limitations in distributed Raman pre-amplifiers, IEEE Photon. Tech. Lett., **10** (1), 159–161 (1998).

38. M. Nissov, K. Rottwitt, H.D. Kidorf, M.X. Ma, Rayleigh crosstalk in long cascadedes of distributed unsaturated Raman amplifiers, Electron. Lett., **35** (12), 997–998 (1999).

39. V.E. Perlin, H.G. Winful, On trade-off between noise and nonlinearity in WDM systems with distributed Raman amplification, Proceedings of OFC'02, paper WB1, 2002.

40. A. Artamonov, V. Smokovdin, M. Kleshov, S.A.E. Lewis, S. V. Chernikov, Enhancement of double Rayleigh scattering by pump intensity noise in fiber Raman amplifier, Proceedings of OFC'02, paper WB6, 2002.

41. C.H. Kim, J. Bromage, R.M. Jopson, Reflection-induced penalty in Raman amplified systems, IEEE Photon. Techn. Lett., **14**, 4 (2002).

42. Y. Qian, J.H. Povlsen, S.N. Knudsen, L. Grüner-Nielsen, Fiber Raman amplifications with dispersion compensating fibers, Trends in Optics and Photonics Series TOPS, Vol. 44, pp. 36–43, 2000.

43. P.B. Gaarde, Y. Qian, S. N. Knudsen, B. Pálsdóttir, Predicting MPI in Raman optical amplifiers by measuring the Rayleigh backscattering coefficient, Proceedings of SOFM'02, 2002.

44. A. Hartog and M. Gold, On the Theory of Backscattering in Single-Mode Optical Fibers, J. Lightwave Technol., **LT-2** (2), 76–82 (1984).

45. A.F. Judy, An OTDR based combined end-reflection and backscatter measurement, SOFM, pp. 19–22, 1992.

46. M. Ohashi, K. Shiraki, K. Tajima, Optical Loss Property of Silca-Based Single-Mode Fibers, J. Lightwave Technol., **10** (5), 539–543 (1992).

47. S.A.E. Lewis, S.V. Chernikov, J.R. Taylor, Characterization of double Rayleigh scatter noise in Raman amplifiers, IEEE Photon. Technol. Lett., **12**, 528–530 (2000).

48. C.R.S. Fludger, R.J. Mears, Electrical measurements of multipath interference in distributed Raman amplifiers, J. Lightwave Technol., **19** (4), 536 (2001).

49. M.O. van Deventer, Polarization properties of Rayleigh backscattering in single-mode fibers, J. Lightwave Technol., **11**, 1895–1899 (1993).

50. V. Smokovdin, S.A.E. Lewis, S.V. Chernikov, Direct comparison of electrical and optical measurements of double Rayleigh scatter noise, ECOC'02, paper S3.5, 2002.

51. S. Burtsev, W. Pelouch, P. Gavrilovic, Multi-path interference noise in multi-span transmission links using lumped Raman amplifiers, Proceedings of OFC'02, paper TuR4, 2002.

52. J. Bromage, L.E. Nelson, C.H. Kim, P.J. Winzner, F-J. Essiambre, R.M. Jopson, Relative impact of multiple-path interference and amplified spontaneous emission noise on optical receiver performance, Proceedings of OFC'02, paper TuR3, 2002.

53. A. Artamonov, V. Smokovdin, M. Kleshov, S.A.E. Lewis, S.V. Chernikov, Enhancement of double Rayleigh scattering by pump intensity noise in fiber Raman amplifier, Proceedings of OFC'02, paper WB6, 2002.

54. P. Parolari, L. Marazzi, L. Bernardini, M. Martinelli, Double Rayleigh backscatter noise measurements in discrete and distributed Raman amplifiers; Proceedings of OAA'02, paper OWA3, 2002.

55. R. Essiambre, P. Winzer, J. Bromage, C. H. Kim, Design of bidirectionally pumped fiber amplifiers generating double Rayleigh backscattering, IEEE Phonton. Techon. Lett., **14** (7), 914–916 (2002).

56. H.J. Thiele, J. Bromage, L. Nielsen, Impact of discrete Raman amplifier architecture on nonlinear impairments, Proceedings of ECOC'02, paper 7.0.2, 2002.

57. A.J. Stenz, S.G. Grubb, C.E. Headley, J.R. Simponson, T. Strasser, N. Park, Raman amplifier with improved system performance, Proc. of OFC'96, paper TuD3, 1996.

58. D. Hamoir, J. Boniort, L. Gasca, D. Bayart, Optimized, two-stage architecture for Raman amplifiers, Proc. of OAA'00, paper OMD8, 2000.

59. T. Tsuzaki, T. Miyamoto, T. Okuno, M. Kakui, M. Hirano, M. Onishi, M. Shigematsu, Impact of double Rayleigh backscattering in discrete fiber Raman amplifiers employing highly nonlinear fiber, Proceedings of OAA'02, paper OWA2, 2002.

60. C.R.S. Fludger, V. Handerek,d R. J. Mears, Pump to signal RIN transfer in Raman fibre amplifiers, J. Lightwave Technol., **19** (8), 11400-1148 (2001).

61. M.D. Mermelstein, C. Headley, J.-C. Bouteiller, RIN transfer analysis in pump depletion regime for Raman fibre amplifiers, Electron. Lett., **38** (9), 403–405 (2002).

62. Y. Qian, S. Dyrbøl, J.S. Andersen, P.B. Gaarde, C.G.Jørgensen, B. Pálsdóttir, L. Grüner-Nielsen, Bi-directionally pumped discrete Raman amplifier with optimized dispersion compensation for non-shifted transmission fibre, Proceedings of ECOC'02, paper 6.4.1, 2002.

63. S. Kado, Y. Emori, S. Namiki, Gain and noise tilt control in multi-wavelength bi-directionally pumped Raman amplifier, Proceedings of OFC'02, paper TuJ4, 2002.

64. A.F. Evans, J. Grochocinski, A. Rahman, Corey Reynolds, Michael Vasilyev, Distributed Amplification: How Raman gain impacts other fiber nonlinearities, Proceedings of OFC'01, paper MA7, 2001.

65. J. Bromage, P.J. Winzner, L.E. Nelson, C.J. McKinstrie, Raman-enhanced pump-signal four-wave mixing in bidirectionally-pumped Raman amplifiers; Proceedings of OAA'02, paper OWA5, 2002.

66. Q. Le N.T., C.G.Jørgensen, L. G Grüner-Nielsen, B. Pálsdóttir, Enhancement of Nonlinear response of a highly nonlinear fibre due to Raman amplification, Proceedings of ECOC'02, 2002.

67. T. Okuno, T. Tsuzaki, H. Hirano, T. Miyamoto, M. Kakui, M. Onishi, Y, Nakai, M. Nishimura, Nonlinear-fiber-based discrete Raman amplifier with sufficiently suppressed degradation of WDM signal quality, Proceedings of OAA'1, paper OTuB5, 2001.

68. T. Wang, Y. Cao, J. Luo, Dispersion compensation fiber working in U band, in Proceedings of OFC'2003, Paper MF2.

69. J.U. Jeon, H.K. Seo, Y.T. Lee, Wide-band High Negative Dispersion-Flattened Fiber, in Proceedings of ECOC'2002, Paper P1.35.

70. J. Rathje, M. Andersen, L. Grüner-Nielsen, Dispersion Compensating fiber for identical compensation in the S,C and L band, in Proceedings of OFC'2003, Paper FK6.

71. P. Kristensen, Design of dispersion compensating fiber, in Proceedings of ECOC'2004, Paper 3.3.1.

72. V.M. Schneider, J. A. West, Analysis of wideband dispesion slope compensating optical fibres by supermode theory, Electron. Lett., **38** (7), 306–307 (2002).

73. J.L. Auguste, J.M. Blondy, J. Maury, J. Marcou, B. Dussardier, G. Monnom, R. Jindal, K. Thyagarajan, B.P. Pal, Conception, realization, and characterization of a very high negative chromatic dispersion fiber, Opt. Fiber Technol., **8**, 89–105 (2002).

74. S. Ramachandran, J. Nicholson, P. Kristensen, S. Ghalmi and M. Yan, Measurement of multi-path interference in the coherent cross-talk regime, in Procedings of OFC'2003, paper TuK6.

75. M.E. Lines, W.A. Reed, D.J. DiGiovanni, J.R.Hamblin, Explanation of anomalous loss in high delta singlemode fibres, Electron. Lett., **35** (12), 1009–1010 (1999).

76. J. Rathje, L. Grüner-Nielsen, Relationship between Relative Dispersion Slope of a transmission fiber and the usable bandwidth after dispersion compensating, in Proceedings of ECOC'2002, paper P1.23.

77. A. Gorlier, P. Sillard, F. Beaumont, L.-A. de Montmorillon, L. Fleury, Ph. Guénot, A. Bertaina, P. Nouchi, Optimized NZDF-based link for wide-band seamless terrestrial transmissions, in Proceedings of OFC'2002, paper ThGG7.

DOI: 10.1007/s10297-006-0076-2
Originally published in J. Opt. Fiber. Commun. Rep. 4, 173–213 (2007)

Modeling dispersion in optical fibers: applications to dispersion tailoring and dispersion compensation

K. Thyagarajan and B.P. Pal

Physics Department, Indian Institute of Technology Delhi
New Delhi 110016 India

Abstract. The phenomenon of temporal pulse dispersion, which is a key characteristic of an optical fiber communication system is described from the first principles. Beginning with the basics of dispersion in a bulk medium, these concepts are then applied to propagation of a pulse in an optical fiber. Details of modeling dispersion are then described in the context of dispersion tailoring and dispersion compensation with a view to form the foundation for subsequent chapters on dispersion compensation that follow in this report. Basic physics behind the design target for dispersion compensating fibers is discussed, which should be useful to fiber designers.

1. Introduction

Over the last two decades millions of kilometers of optical fibers have been laid all over the world in order to meet the ever increasing demand for higher and higher transmission bandwidth primarily driven by the growth in the Internet and data traffic. These increased demands are being met either through high bit rates (10–40 Gbps) and/or increased number of wavelength channels using wavelength division multiplexing (WDM). Increased bit rate however implies transmission of narrower optical pulses, which results in severe signal impairments due to higher amount of chromatic dispersion with propagation through the fiber, which may lead to intersymbol interference and loss of information and hence increased bit error rates (BER). Increasing the number of wavelength channels implies an increase in total transmitted power and also reduced spacing between adjacent channels—both of which lead to an enhanced sensitivity to certain optical nonlinear effects detrimental to clean transmission of signal. These detrimental effects could be substantially reduced by suitably tailoring the chro-

matic dispersion characteristics of an optical fiber, which forms topic of our discussion in this paper.

Chromatic dispersion has indeed been a major cause of worry to system designers especially at high bit transmission rates. By mid-1980s, single-mode fiber-based optical trunk networks showed a steady increase in transmission bit rate. Optical channel OC-48 rate, which corresponds to a transmission rate of ≈ 2.5 Gbps, became an industry standard for signal transmission over the 1310- nm-optimized single-mode fibers, which were christened by International Telecommunications Union (ITU) as G.652 fibers. Although in principle very high transmission bit rate was achieved at 1310 nm due to coincidence of this wavelength with the characteristic zero-dispersion wavelength (see definition in later sections) of silica fibers, maximum link length/repeater spacing was however limited by transmission loss (~ 0.34 dB/km at this wavelength) in these systems. Thus it became evident that it would be of advantage to shift the operating wavelength to the 1550-nm lowest loss window, where the loss is about 40% less. However, commercial introduction of next generation systems based on exploitation of the 1550-nm lowest loss window had to wait for few more years. This was mainly because conventional G.652 type fibers optimized for transmission at the 1310-nm window exhibited excessive chromatic dispersion $\sim +17$ ps/(km-nm) at 1550 nm. It was realized that this limitation on repeater spacing of 1550-nm-based systems could be overcome if the fiber designs could be so tailored to shift zero-dispersion wavelength to coincide with this wavelength so as to realize dispersion shifted fibers (DSF), which were given the generic classification as G.653 fibers by the ITU.

During the 1980s till about mid-1990s, commercially available optical system speed had doubled every 2.4 years [1]. Indeed, optical fibers have now penetrated virtually all segments of telecommunication networks—be it under-sea, long haul, junction, or access. Commercial introduction of erbium doped fiber amplifiers (EDFA) in mid-1990s and the emergence of the Internet revolution around the same time coupled with deregulation of the telecommunication sector from Government controls, have substantially contributed to this unprecedented growth in data traffic. Systems, which were operating at 2.5 Gb/s required capacity upgrades to 10 Gb/s or to even 40 Gb/s in certain sectors in order to absorb this enormous demand in bandwidth [2]. Emergence of dense wavelength division multiplexing (DWDM) technology, involving simultaneous transmission of at least 4 wavelengths in the 1550-nm low-loss wavelength window through one single-mode fiber has resulted in an enormous increase in available bandwidth for high-speed telecommunication and data transfer. DWDM systems with simultaneous transmission of 80 wavelength channels spanning 80-nm bandwidth across the C- and L-bands of fiber amplifiers are commercially available! The resulting high optical signal power level encountered by a fiber along with the demands for i) tighter channel spacing, and ii) longer signal reach have brought to the foray the criticality of interplay between nonlinear propagation effects and chromatic dispersion in a fiber communication system. In order to address these issues a variety of newer dispersion-tailored fibers for signal transmission and optical networking were proposed and developed by different groups around late 1990s, which were generically referred to as G.655 non-zero dispersion shifted fibers (NZ-DSF) [3–5]. The need to deploy such advanced fibers became so imminent that ITU-T Committee had to evolve new standards for G.655 fibers [ITU-T G.655]. As per ITU recommendations, G.655 fibers should exhibit finite dispersion (characterized through dispersion coefficient D, see section 3) $2 \leq D$ (ps/(km-nm)) ≤ 6 in the 1550-nm band in order to detune the

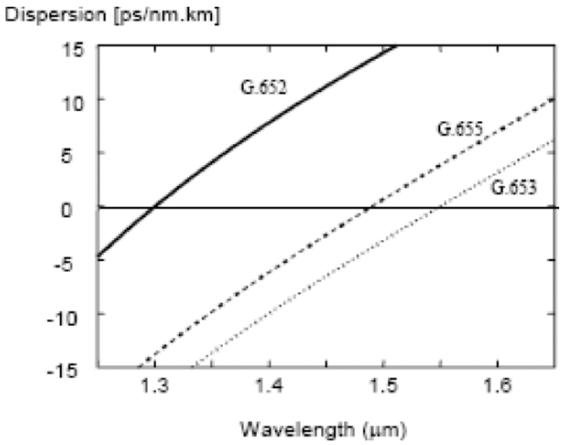

Fig. 1. Typical dispersion spectra of different types of standard signal transmission fibers.

phase matching condition required for detrimental nonlinear propagation effects like four-wave mixing (FWM) and cross-phase modulation (XPM) to take place during multi-channel transmission. ITU arrived at the above range for D by assuming a channel spacing of 100 GHz or more. For smaller channel spacing like 50 or 25 GHz, it turned out that the above range for D is insufficient to suppress potential nonlinear effects unless i) the power per channel is reduced substantially and ii) number of amplifiers is limited. Unfortunately these steps would amount to a decrease in the repeater spacing(s), which would be counterproductive since this would defeat the very purpose for which G.655 fibers were proposed [6]. In order to overcome this disadvantage of an NZDSF, a more advanced version of NZDSF as a transmission fiber has been proposed [7] for super-DWDM, which has been christened by ITU as advanced-NZDSF (A-NZDSF)/G.655b fibers. As per ITU recommendation, upper limit on D for an A-NZDSF should be 10 ps/(km-nm) at the longer wavelength edge of the C-band, i.e., at 1565 nm [8]. In view of its reduced sensitivity to detrimental nonlinear effects, it can accommodate transmission of as many as 160 channels of 10 Gb/s at 25 GHz channel spacing within the C-band alone and also offers ease in deployment of 40 Gb/s systems [8]. Another attractive feature of A-NZDSF is that it can be used to transmit signals in the S-band as well, for which gain-shifted thulium doped fiber amplifiers (TDFA) [9], EDFAs [10] and Raman fiber amplifiers (RFA) [11] have emerged as attractive options. Figure 1 shows typical dispersion spectra for few sample ITU-standard single-mode transmission fibers. These include the standard single mode fiber (G.652), dispersion shifted fiber (G.653) and non-zero dispersion shifted fiber (G.655). Note that each fiber type is characterized by different dispersion and dispersion slopes (variation of dispersion with wavelength).

Since dispersion leads to spilling of a signal pulse into the adjacent time slot of a bit, dispersion would lead to intersymbol interference. Hence the accumulated dispersion in the fiber needs to be compensated before detection and this can be achieved in the optical domain by the use of different dispersion compensation devices such

as dispersion compensating gratings (DCG) [12], Mach-Zehnder interferometer in a planar waveguide form [13], dispersion compensating fibers (DCF) [14], mid system spectral inversion [15], arrayed waveguides [16], etc. These devices optically compensate for accumulated dispersion in an optical fiber link and thus greatly improve the performance of the system.

In sections 2–5, we will discuss the basic phenomenon of dispersion in bulk dielectric media and in an optical fiber and the concept of optical dispersion compensation. This will be followed by a discussion in section 6 on tailoring dispersion compensation characteristics of a dispersion compensating fiber including some recent fiber designs to achieve very large negative dispersion coefficient. Finally in the concluding sections, we would briefly discuss issues related to nonlinear effects vis à vis dispersion compensation.

2. Propagation Through a Bulk Dielectric Medium

Consider the propagation of a plane electromagnetic wave of frequency ω through a dielectric medium characterized by a refractive index $n(\omega)$. We can write for the electric field of the plane wave as

$$E(z,t) = E_0 \exp[i(\omega t - kz)], \tag{1}$$

where E_0 represents the amplitude of the wave and $k(\omega)$ represents the propagation constant of the wave and is given by

$$k(\omega) = \frac{\omega}{c} n(\omega). \tag{2}$$

2.1. Phase and Group Velocity

The phase velocity of the wave described by Eq. (1), which determines the velocity of propagation of the phase front, is given by

$$v_p = \frac{\omega}{k} = \frac{c}{n(\omega)}. \tag{3}$$

Let us consider the propagation of an optical temporal pulse through this medium. At the plane $z = 0$, let the optical pulse be described by

$$E(z=0,t) = E_0 f(t) \exp[i\omega_0 t], \tag{4}$$

where $f(t)$ represents the pulse envelope and ω_0 is the carrier frequency. The pulse envelope can take on different shapes such as Gaussian, super-Gaussian, rectangular etc.

It is well known that by using the Fourier transform relationship a pulse can be described as a superposition of different frequency components. The Fourier transform of the pulse described by Eq. (4) is given by

$$\tilde{E}(z=0,\omega) = \int_{-\infty}^{+\infty} E(z=0,t) \exp[-i\omega t] dt. \tag{5}$$

Similarly we can write for the inverse Fourier transform of the above equation as

$$E(z=0,t)=\frac{1}{2\pi}\int_{-\infty}^{+\infty}\tilde{E}(z=0,\omega)\exp[i\omega t]d\omega. \tag{6}$$

The above equation implies that the input pulse can be decomposed into different monochromatic waves at different frequencies and the complex amplitude of the component frequency ω is given by $\tilde{E}(z=0,\omega)$.

In a linear medium, each frequency component propagates independently and at any plane z, the resultant pulse shape can be obtained by superposition of these waves with appropriate phases. Since k represents the propagation constant of the wave at frequency ω, each frequency component within the integral in Eq. (6) will suffer a phase shift of kz and hence the pulse at z will be given by

$$E(z,t)=\frac{1}{2\pi}\int_{-\infty}^{+\infty}\tilde{E}(z=0,\omega)\exp[i(\omega t-kz)]d\omega. \tag{7}$$

It is understood that k is a function of ω.

Usually the duration of the optical pulse is much longer than the time period of the optical carrier wave and hence there would be thousands of cycles of oscillation of the carrier wave electric field within the pulse. Thus the Fourier spectrum given by Eq. (5) is expected to be sharply peaked around the center frequency ω_0. For example, if we consider transmission at 10 Gb/s, the pulse widths are about 100 ps and the corresponding spectral width of its Fourier spectrum would be about 10^{10} s^{-1}, which is much smaller than the typical optical frequency of 10^{15} s^{-1}. Hence we can make a Taylor series expansion of $k(\omega)$ about $\omega=\omega_0$ and write

$$k(\omega)=k(\omega_0)+(\omega-\omega_0)\frac{dk}{d\omega}+\frac{(\omega-\omega_0)^2}{2}\frac{d^2k}{d\omega^2}+\frac{(\omega-\omega_0)^3}{6}\frac{d^3k}{d\omega^3}\cdots, \tag{8}$$

where the differentials are evaluated at the frequency $\omega=\omega_0$ and we have retained terms up to the third order.

If we retain only the first two terms in Eq. (8) and substitute for k in Eq. (7), we get

$$E(z,t)=\left[\frac{1}{2\pi}\int_{-\infty}^{+\infty}\tilde{E}(z=0,\Omega)\exp[i\,(t-z/v_g)\,\Omega]d\Omega\right]\exp[i\{\omega_0 t-k(\omega_0)z\}], \tag{9}$$

where $\Omega=\omega-\omega_0$ and

$$v_g=\left(\frac{dk}{d\omega}\right)^{-1}. \tag{10}$$

Comparing the term within the square bracket in Eq. (9) with Eq. (6) we see that it is nothing but $E(z=0,t-\frac{z}{v_g})$. Hence Eq. (9) may be rewritten as

$$E(z,t)=E\left(z=0,t-\frac{z}{v_g}\right)\exp[i\{\omega_0 t-k(\omega_0)z\}]. \tag{11}$$

Thus by retaining only the first two terms in Eq. (8) we find that the pulse envelope remains the same as it was at $z=0$; the center of the pulse just gets shifted through a distance $v_g t$. Hence the quantity v_g [as given by Eq. (10)] represents the velocity of the center of the pulse and is referred to as the *group velocity* of the pulse.

For free space $k=\omega/c$ and $v_g=c=v_p$. Thus in the case of free space the phase and group velocities are equal and such a medium is referred to as dispersion-free.

2.2. *Group Velocity Dispersion (GVD)*

In the case of a medium, for which k is not a linear function of ω, the medium is said to be dispersive. For a dispersive medium, using Eqs. (2) and (10), we obtain

$$\frac{1}{v_g} = \frac{1}{c}\left[n(\omega) + \omega\frac{dn}{d\omega}\right]. \tag{12}$$

By expressing ω in terms of wavelength in free space λ_0, we can rewrite Eq. (12) as

$$\frac{1}{v_g} = \frac{1}{c}\left[n(\lambda_0) - \lambda_0\frac{dn}{d\lambda_0}\right]. \tag{13}$$

The quantity

$$N_g = n(\lambda_0) - \lambda_0\frac{dn}{d\lambda_0} \tag{14}$$

is also referred to as the group index; it determines the group velocity of the pulse just like refractive index (n) which determines the phase velocity.

2.3. *Material Dispersion*

Concept of Zero Material Dispersion

The time delay suffered by a pulse in traveling through a length L of the medium is given by

$$\tau(\lambda_0) = \frac{L}{v_g} = \frac{L}{c}\left[n(\lambda_0) - \lambda_0\frac{dn}{d\lambda_0}\right]. \tag{15}$$

If the source is characterized by a spectral width $\Delta\lambda_0$, then each wavelength component within $\Delta\lambda_0$ travels with a different group velocity resulting in pulse broadening. This broadening is given by

$$\Delta\tau = \frac{d\tau}{d\lambda_0}\Delta\lambda_0 = -\frac{L}{c}\lambda_0\frac{d^2n}{d\lambda_0^2}\Delta\lambda_0, \tag{16}$$

which is known as the *material dispersion*. From Eq. (16), dispersion of the pulse can be quantified through

$$\frac{d\tau}{d\lambda_0} = -\frac{L}{c}\lambda_0\frac{d^2n}{d\lambda_0^2} \tag{17}$$

and is expressed in units of picoseconds per nanometer (ps/nm). The dispersion coefficient (D) of the medium representing the dispersion per unit length of the medium is defined through

$$D_m = \frac{1}{L}\frac{d\tau}{d\lambda_0} = -\frac{\lambda_0}{c}\frac{d^2n}{d\lambda_0^2}. \tag{18}$$

This is referred to as the material dispersion coefficient and is usually expressed in units of ps/(km-nm).

Figure 2 shows the spectral variation of $d^2n/d\lambda_0^2$ for pure silica. It could be seen that at the wavelength of 1280 nm, referred to as the zero material dispersion wavelength, $d^2n/d\lambda_0^2 = 0$. At this wavelength pulses will suffer negligible dispersion as they propagate through pure silica. Below this wavelength, $d^2n/d\lambda_0^2$ is positive

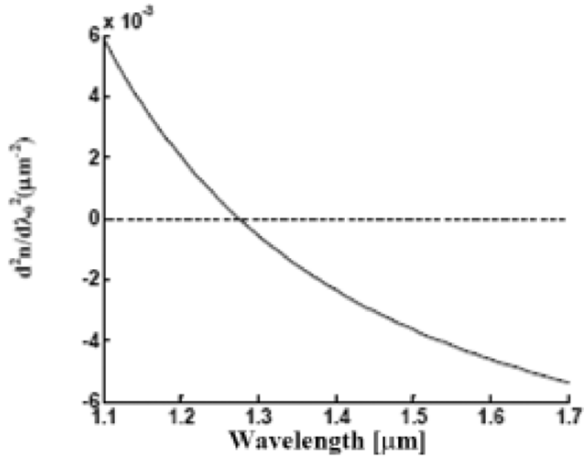

Fig. 2. Variation of $d^2n/d\lambda_0^2$ (proportional to material dispersion parameter) with wavelength for pure silica.

while above this wavelength $d^2n/d\lambda_0^2$ is negative. The former wavelength region is referred to as *normal* group velocity dispersion region while the latter wavelength region is known as *anomalous* group velocity dispersion region. Note that the pulse disperses in both the regions; in the normal dispersion regime, longer wavelength components of the pulse travel faster than shorter wavelength components while the converse is true for the anomalous dispersion region.

For pure silica at $\lambda_0 \sim$1300 nm, $d^2n/d\lambda_0^2 \approx -0.00055\ \mu\text{m}^{-2}$ and the corresponding material dispersion is about 2.38 ps/(km-nm). Thus if the spectral width of the source is assumed to be 0.1 nm and the pulse propagates through 1 km length of the medium, then the pulse dispersion would be 0.238 ps. Similarly at 1550 nm, $d^2n/d\lambda_0^2 \approx -0.004\ \mu\text{m}^{-2}$, which would imply a material dispersion of about 21 ps/(km-nm).

Broadening of a Gaussian Pulse Due to Material Dispersion

We now consider propagation of a Gaussian pulse described by the following expression [17]:

$$E(z=0,t) = E_0 e^{-t^2/2\tau_0^2} \exp(i\omega_0 t). \tag{19}$$

Such a pulse is referred to as a Fourier transform limited pulse. The quantity ω_0 represents the carrier frequency of the pulse and τ_0 determines the pulse width. The instantaneous frequency of the pulse given by Eq. (19) is independent of time and such a pulse is also referred to as an unchirped pulse.

Using Eq. (19) in Eq. (5), we can evaluate the Fourier spectrum $\tilde{E}(z=0,\omega)$. Substituting this Fourier spectrum in Eq. (7) and using the expansion (retaining terms up to the second differential) given by Eq. (8) and carrying out the integration we obtain (see e.g., [17])

$$E(z,t) = \frac{E_0}{(\tau(z)/\tau_0)^{1/2}} \exp\left[-\frac{\{t - z/v_g)^2}{2\tau^2(z)}\right] \exp[i(\Phi(z,t) - k_0 z)], \tag{20}$$

where $k_0 = 2\pi/\lambda_0$,

$$\Phi(z,t) = \omega_0 t + \kappa\left(t - \frac{z}{v_g}\right)^2 - \frac{1}{2}\tan^{-1}\left(\frac{\sigma z}{\tau_0^2}\right), \tag{21}$$

$$\kappa = \frac{\sigma z}{2\tau_0^4}\left(1 + \frac{\sigma^2 z^2}{\tau_0^4}\right)^{-1}, \tag{22}$$

$$\sigma = \frac{d^2k}{d\omega^2}\bigg|_{\omega=\omega_0} = \frac{\lambda_0^3}{2\pi c^2}\frac{d^2n}{d\lambda_0^2}, \tag{23}$$

and

$$\tau^2(z) = \tau_0^2\left(1 + \frac{\sigma^2 z^2}{\tau_0^4}\right). \tag{24}$$

Equation (20) shows that center of the pulse travels with a velocity v_g and the pulse remains Gaussian as it propagates; the pulse width at any value of z is given by $\tau(z)$.

From Eq. (24) we note that the input pulse width, which was τ_0 at $z = 0$ becomes $\sqrt{2}\tau_0$ after propagating through a length

$$L_D = \frac{\tau_0^2}{|\sigma|} \tag{25}$$

of the dispersive medium. This length is referred to as the *dispersion length* and is a characteristic length, which is often used to describe dispersive effects of a medium. Smaller the dispersion, longer is this length.

We can define pulse broadening by $\Delta\tau$ as being given by

$$\Delta\tau = \left[\tau^2(z) - \tau_0^2\right]^{1/2} = \frac{z}{\tau_0}\left|\frac{d^2k}{d\omega^2}\right|. \tag{26}$$

Using Eq. (2) for $k(\omega)$ and the fact that the spectral width of a pulse of duration τ_0 is approximately given by $\Delta\omega \sim 2/\tau_0$, we can show that the pulse broadening described by Eq. (26) is indeed consistent with Eq. (16).

We also note from Eq. (21) that the phase Φ of the output pulse is not linearly proportional to time; this implies that the instantaneous frequency of the pulse varies with time within the pulse. Such a pulse is referred to as a chirped pulse. The instantaneous frequency of the output pulse is given by

$$\omega(t) = \frac{d\Phi}{dt} = \omega_0 + 2\kappa\left(t - \frac{z}{v_g}\right). \tag{27}$$

The center of the pulse is defined by $t = z/v_g$ and the leading and trailing edges of the pulse correspond to $t < z/v_g$ and $t > z/v_g$, respectively. In the normal dispersion region $d^2n/d\lambda_0^2$ is positive, thereby implying a positive κ. Hence in the normal dispersion region, the leading edge of the pulse will be down-shifted (often referred to in the literature as *red-shifted*) in frequency while the trailing edge will be up-shifted (also referred to as *blue-shifted*) in frequency with respect to the center

frequency ω_0. The converse is true for the anomalous dispersion region where $d^2n/d\lambda_0^2$ is negative. Hence as the pulse broadens with propagation it also gets *chirped*. It is important to note that since we are studying pulse propagation in the linear regime, the spectral width of the pulse remains the same as it propagates (neglecting any spectral dependence of attenuation); temporal broadening is accompanied by chirping of the pulse.

Figure 3 shows the electric field variation of a Gaussian pulse as it propagates through a dispersive medium in the normal and anomalous group velocity regions. Notice the broadening of the pulse and the resultant chirping in both normal as well as the anomalous dispersion regimes.

3. Propagation of a Gaussian Optical Pulse Through an Optical Fiber

Until now we have not incorporated any fiber-specific characteristic in the above analysis. We now consider the propagation of the fundamental mode at a frequency ω through a single-mode optical fiber. We can write for the electric field of the mode as

$$E(z,t) = E_0 F(x,y,\omega)\exp[i(\omega t - \beta z)], \tag{28}$$

where E_0 represents the amplitude of the wave, β represents the propagation constant of the mode and $F(x,y,\omega)$ represents the transverse modal field distribution of the fundamental mode. In general the field distribution of the mode depends on the frequency; however if the spectral width of the pulse is small compared to the center frequency as is usually the case, then we can neglect the frequency dependence of F.

3.1. Phase and Group Velocity

If $n_{\text{eff}}(\omega)$ represents the effective index of the fundamental mode then,

$$\beta = \frac{\omega}{c} n_{\text{eff}}(\omega). \tag{29}$$

The phase velocity of the mode, which determines the velocity of propagation of its phase front, is given by

$$v_p = \frac{\omega}{\beta} = \frac{c}{n_{\text{eff}}(\omega)}. \tag{30}$$

The analysis presented in section 2 for a medium can be directly applied to the case of an optical fiber by replacing k by β and n by n_{eff}. Thus in the case of an optical fiber the modal group velocity v_g would be described by

$$\frac{1}{v_g} = \frac{d\beta}{d\omega} = \frac{1}{c}\left[n_{\text{eff}}(\lambda_0) - \lambda_0 \frac{dn_{\text{eff}}}{d\lambda_0}\right]. \tag{31}$$

3.2. Group Velocity Dispersion (GVD)

In the case of an optical fiber, σ [see Eq. (23)] is defined by

$$\sigma = \frac{d^2\beta}{d\omega^2}\Big|_{\omega=\omega_0} = \frac{\lambda_0^3}{2\pi c^2}\frac{d^2 n_{\text{eff}}}{d\lambda_0^2} = -\frac{\lambda_0^2}{2\pi c} D, \tag{32}$$

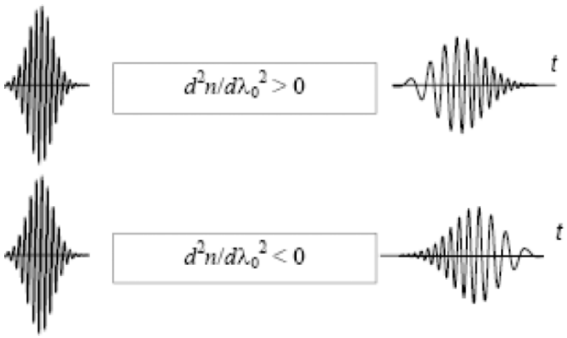

Fig. 3. Broadening of a Gaussian temporal pulse due to propagation through a dispersive medium showing broadening as well as chirping. Note that the chirping is opposite in sign in the normal and anomalous dispersion regions.

where the dispersion coefficient D is given by

$$D = \frac{1}{L}\frac{d\tau}{d\lambda_0} = -\frac{\lambda_0}{c}\frac{d^2 n_{\text{eff}}}{d\lambda_0^2}. \tag{33}$$

The corresponding dispersion length [see Eq. (25)] is defined by

$$L_D = \frac{\tau_0^2}{|\sigma|} = \frac{\tau_0^2}{|d^2\beta/d\omega^2|}. \tag{34}$$

For propagation in an infinitely extended medium, $n_{\text{eff}} = n$, the refractive index of the medium and the corresponding dispersion reduces to what was already described as material dispersion above.

3.3. Material and Waveguide Dispersion

In the case of an optical fiber, the effective index n_{eff} of its mode depends on the core and cladding refractive indices as well as the waveguide parameters (refractive index profile shape and radii of various regions). Hence n_{eff} would vary with wavelength even if the core and cladding media were assumed to be dispersion-less (i.e., the refractive indices of core and cladding are assumed to be independent of wavelength). This dependence of effective index on wavelength is due to the waveguidance mechanism and is referred to as waveguide dispersion. Waveguide dispersion can be understood from the fact that the effective index of the mode depends on the fraction of power in the core and the cladding at a particular wavelength. As the wavelength changes, this fraction also changes. Thus even if the refractive indices of the core and the cladding are assumed to be independent of wavelength, the effective index will change with wavelength. It is this dependence of $n_{\text{eff}}(\lambda_0)$ that leads to waveguide dispersion.

Thus the total dispersion in the case of an optical fiber can be attributed to two types of dispersion namely material dispersion and waveguide dispersion. Indeed it

can be shown that the total dispersion coefficient is given by the following sum to a good accuracy [18]

$$D = D_m + D_w, \tag{35}$$

where D_m and D_w correspond to material and waveguide contributions respectively. The material contribution is given by Eq. (18) while the waveguide contribution for a step-index fiber is given by (e.g., [17])

$$D_w = -\frac{n_2 \Delta}{c\lambda_0}\left(V\frac{d^2(bV)}{dV^2}\right), \tag{36}$$

where V is the normalized waveguide parameter defined by

$$V = \frac{2\pi}{\lambda_0} a\sqrt{(n_1^2 - n_2^2)} \tag{37}$$

and b represents the normalized propagation constant of the mode:

$$b = \frac{n_{\text{eff}}^2 - n_2^2}{n_1^2 - n_2^2} \tag{38}$$

with n_1 and n_2 being the refractive indices of core and cladding. In the single-mode regime, the quantity within the bracket in Eq. (36) is usually positive; hence the waveguide dispersion is negative. Since the sign of material dispersion depends on the operating wavelength region, it is possible that the two effects namely, material and waveguide dispersions cancel each other at a certain wavelength. Such a wavelength, which is a very important parameter of single-mode fibers, is referred to as the *zero-dispersion wavelength* (λ_{ZD}).

3.4. Positive and Negative GVD

Figure 4 shows the variation of material, waveguide, and total dispersions for a standard single-mode fiber (G.652 fiber). Such fibers characterized with a λ_{ZD} near about 1310 nm are the most widely used fibers in the world. Figure 5 shows similar curves for a dispersion-shifted fiber (G.653) wherein zero total dispersion occurs at a wavelength close to 1550 nm, where silica fibers exhibit lowest transmission loss. The shift in the zero dispersion wavelength is achieved by appropriately tailoring the refractive index profile of the fiber in order to modify the waveguide dispersion contribution to the total dispersion and hence the dispersion spectrum of a fiber. For example, as could be seen from Fig. 5 that through appropriate tailoring of the refractive index profile of the fiber, if the magnitude for D_w (which is negative) could be made larger in magnitude, then the net sum of D_w and D_m could be made to cancel at a longer wavelength to tune λ_{ZD} and hence tailor overall dispersion characteristics such as approximately constant dispersion over a range of wavelengths (dispersion flattened fibers), very large negative dispersion coefficients with appropriate dispersion slope (dispersion compensating fibers—see section 5), etc. Figure 6 shows schematic diagrams of different dispersion-tailored refractive index profiles,which yield different dispersion spectra.

Negative values of D correspond to normal GVD regime while positive values of D correspond to anomalous GVD. The chirp in the dispersed pulses is of opposite sign in the two cases. An unchirped pulse will undergo broadening in both the normal and anomalous dispersion regimes. Figure 7 shows the broadening of a Gaussian pulse with propagation through a G.652 fiber.

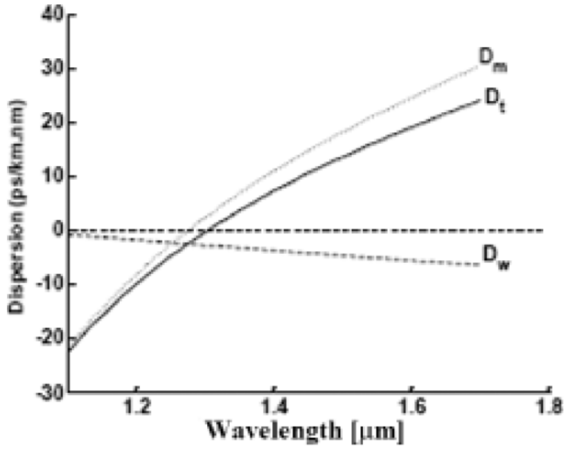

Fig. 4. Variation of material dispersion coefficient (D_m), waveguide dispersion coefficient (D_w) and total dispersion coefficient (D_t) for a G.652 type fiber. Notice that total dispersion becomes zero at a wavelength close to 1310 nm and the dispersion is anomalous in the 1550-nm region.

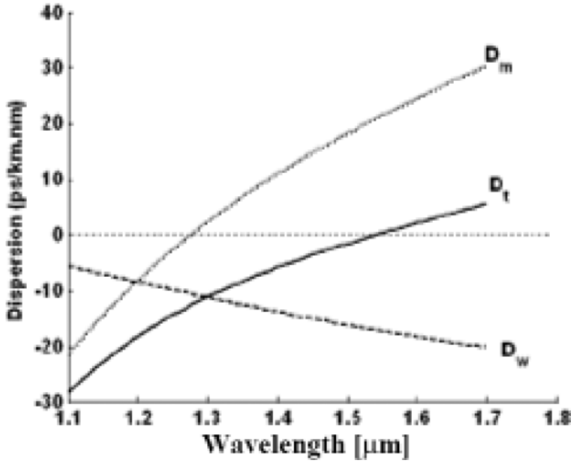

Fig. 5. Variation of material dispersion (D_m), waveguide dispersion (D_w) and total dispersion (D_t) for a G.653 type fiber. Notice that due to larger D_w (in magnitude) the total dispersion becomes zero at a wavelength in the 1550-nm region.

3.5. Optimum Input Pulse Width

Looking at Eq. (24) we see that the output pulse width $\tau(z)$ increases both as τ_0 becomes very large or very small. Thus for a given value of $z = L$, there must be an

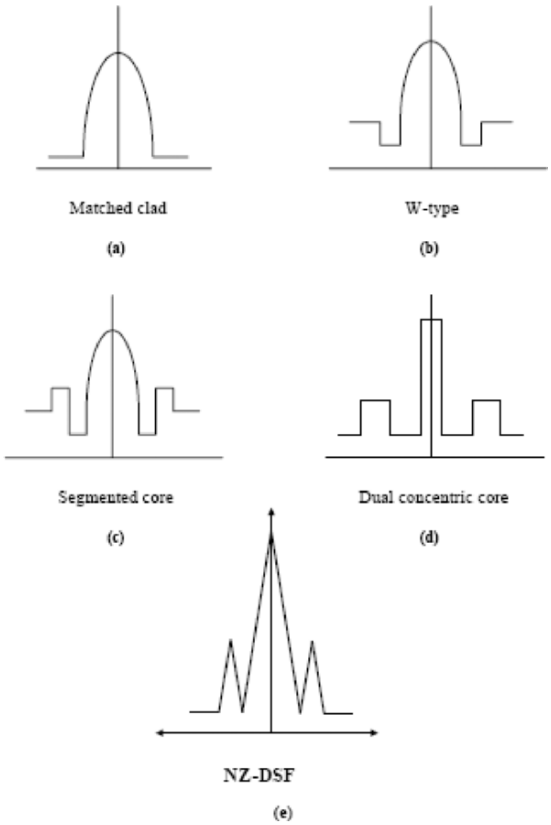

Fig. 6. Schematic diagram showing different refractive index profiles used to tailor the dispersion characteristics of optical fibers. Using such profiles, it is possible to have zero dispersion in the 1550-nm region (dispersion shifted fibers), very small dispersion over an extended region of wavelengths (dispersion flattened fibers), large negative dispersion values (dispersion compensating fibers), non-zero dispersion shifted fiber (NZ-DSF), and so on.

optimum input pulse width for which the output pulse width has a minimum value. Indeed this can be easily obtained from Eq. (24). The optimum input pulse width is given by $\tau_0^{\text{opt}} = \sqrt{\sigma L}$. For this value of optimum input pulse width, the pulse width of the output pulse is

$$\tau = \sqrt{2\sigma L}. \tag{39}$$

3.6. Propagation of Chirped Pulses Through an Optical Fiber

In section 2.3 we considered the incidence of an unchirped Gaussian pulse in which the instantaneous frequency was constant. We saw that such an input pulse always gets broadened and develops a chirp with propagation. This happens irrespective of

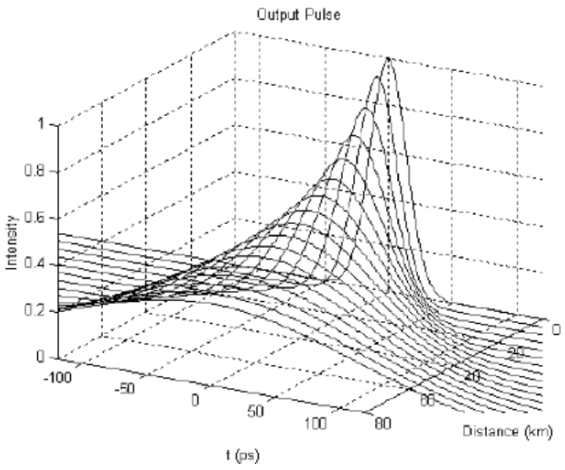

Fig. 7. Illustration of broadening of a Gaussian temporal pulse at 1550 nm as it propagates through a G.652 fiber.

whether we are operating in the normal or anomalous dispersion region of the fiber. We now consider the incidence of a chirped Gaussian pulse described by

$$E(z=0,t) = E_0 \exp\left[-\frac{t^2}{2\tau^2}(1+ig)\right] e^{i\omega_0 t}, \tag{40}$$

where g is known as the chirp parameter; for $g < 0$, the frequency increases from the leading edge of the pulse to the trailing edge and this is referred to as up-chirp. On the other hand for $g > 0$, the instantaneous frequency decreases from the leading edge to the trailing edge and corresponds to down-chirp. The expression for the output pulse after propagating through a distance z in the fiber can be obtained from the earlier expression by replacing τ_0^2 by $\tau^2/(1+ig)$. From the expression so obtained we can evaluate the variation of pulse width with z, which comes out to be

$$\tilde{\tau}^2 = \tau^2 \left[\left(1 - \frac{\sigma g z}{\tau^2}\right)^2 + \frac{\sigma^2 z^2}{\tau^4}\right]. \tag{41}$$

For an unchirped incident pulse $g = 0$ and Eq. (41) is identical to Eq. (24) with the pulse width increasing monotonically. Similarly if $\sigma g < 0$, then again the pulse width increases monotonically. This will happen either if $\sigma > 0$ and $g < 0$ or $\sigma < 0$ and $g > 0$. The former case corresponds to normal dispersion and an up-chirped pulse and the latter case corresponds to anomalous dispersion and a down-chirped pulse. Nevertheless in both these cases the pulse will broaden as it propagates along the fiber.

The interesting case is when $\sigma g > 0$. In such a case the pulse width first reduces and then increases. This would correspond to either $\sigma > 0$ with $g > 0$ or $\sigma < 0$ with $g < 0$. The former case corresponds to normal dispersion and down-chirped pulse and the latter case to anomalous dispersion and up-chirped pulse. It can be shown that in this case, the minimum pulse width occurs for

$$z = \frac{g}{(1+g^2)}\frac{\tau^2}{\sigma}. \tag{42}$$

At this distance the pulse acquires the minimum pulse width of

$$\tilde{\tau} = \frac{\tau}{(1+g^2)^{1/2}}. \tag{43}$$

It can thus be seen that when appropriately chirped pulses propagate through an optical fiber, the pulses can get compressed until they attain a minimum width after which they again begin to broaden. This technique can be used to extend the dispersion-limited distance L_D in an optical fiber communication system; this is referred to as pre-chirping.

Directly modulated lasers are chirped due to the changes in refractive index brought about by the injection of electrons and holes in the gain region of the semiconductor laser during pulsing; the pulses are characterized by $g > 0$. Standard SMF operating in the 1550-nm band have anomalous dispersion and hence are characterized by $\sigma < 0$. Hence when directly modulated pulses are launched into standard SMFs operating at 1550 nm, it corresponds to $\sigma g < 0$ and hence the pulse disperses faster than the case without chirping. Typically the maximum distance for a 2-dB dispersion penalty in G.652 fiber is about 100 km. On the other hand, it is possible to use the chirp for reducing dispersive effects by using fibers with $\sigma > 0$, i.e., with fibers having normal dispersion at the operating wavelength. Indeed special fiber designs have been developed which have normal dispersion in the 1550-nm region and hence can be used with chirped directly modulated lasers for extended propagation distances without suffering from dispersive effects. Such fibers could be very interesting especially in metro networks [19].

3.7. Higher Order Dispersion

It appears that when an optical fiber is operated at the zero dispersion wavelength, the pulses will not suffer any dispersion at all. In fact zero dispersion only signifies that the second order dispersive effects are absent. In this case the next higher order dispersion namely third order dispersion characterized by $d^3\beta/d\omega^3$ will become the dominating term in determining the dispersion. Thus in the absence of second order dispersion, we can write for dispersion suffered by a pulse as

$$\Delta\tau = L\Delta\left(\frac{1}{v_g}\right) = L\frac{(\Delta\omega)^2}{2}\frac{d^3\beta}{d\omega^3}. \tag{44}$$

The above equation can be expressed in terms of variation of D with wavelength through

$$\Delta\tau = \frac{L(\Delta\lambda_0)^2}{2}S, \tag{45}$$

where $S = dD/d\lambda_0$ represents the dispersion slope at zero dispersion wavelength and is measured in units of ps/(km-nm^2). Third order dispersion becomes important when operating close to the zero-dispersion wavelength. In the presence of only third order dispersion, the pulse does not remain symmetric. Figure 8 shows simulation results of pulse broadening due to third-order dispersion in a fiber at the zero-dispersion wavelength clearly showing asymmetric distortion. Table 1 lists values of D and S for some standard fibers at 1550 nm.

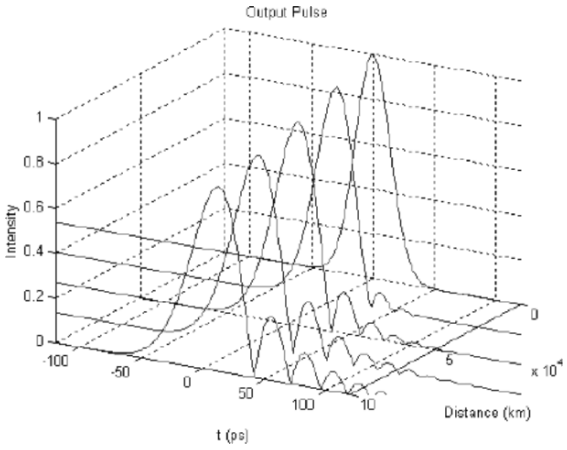

Fig. 8. Pulse broadening due to third order dispersion when the operating wavelength corresponds to zero dispersion wavelength. Note that the broadening is asymmetric unlike the broadening due to second order effects.

Table 1. (After [20].) Values of dispersion and dispersion slope for some standard fibers.

Fiber type	D (ps/(km-nm))	S (ps/km nm^2)
Standard SMF (G.652)	17	0.058
LEAF (Corning)	4.2	0.085
Truewave-Reduced slope (OFS)	4.5	0.045
TeraLight (Alcatel)	8.0	0.057

3.8. Maximum Bit Rate

As pulses disperse with propagation, they start to spill into the adjacent slots, which would result in interference between adjacent bits, and which in turn will lead to inter symbol interference and hence increased bit error rates (see Fig. 9). Apart from this, since the energy in the pulse gets reduced within the time slot, the corresponding signal to noise ratio (SNR) will decrease. One can offset this by increasing the power in the pulses. This additional power requirement is termed as dispersion power penalty. Increased dispersion would imply increased power penalty.

In order to get an estimate of the power penalty due to dispersion we first introduce a more general definition of pulse width in terms of root mean square (rms) width. This is especially useful for pulse shapes other than Gaussian. The rms width is defined by

$$\tau_{\rm rms} = \sqrt{\langle t^2\rangle - \langle t\rangle^2}, \tag{46}$$

where

$$\langle t^n\rangle = \frac{\int_{-\infty}^{\infty} t^n |E(z,t)|^2 dt}{\int_{-\infty}^{\infty} |E(z,t)|^2 dt}. \tag{47}$$

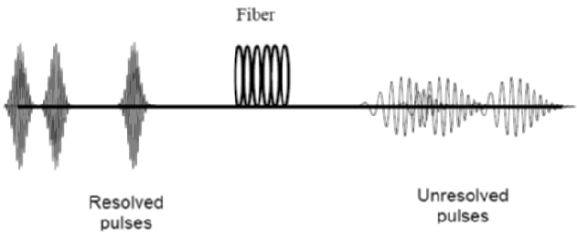

Fig. 9. Schematic illustrating dispersion and resulting intersymbol interference leading to errors in detecting bits at the receiver end.

For a Gaussian pulse, the rms width $\tau_{\rm rms}$ is related to the pulse width τ [as defined by Eq. (19)] by $\tau_{\rm rms} = \tau/\sqrt{2}$. For a communication system working at a bit rate of B bits per second, the bit period is $1/B$ s. In order to keep the interference between adjacent bits below a specified level, the rms width of the dispersed pulse needs to be kept below a certain fraction ϵ of the bit period B. Thus we obtain the following equation for maximum allowed rms pulse width τ of the dispersed pulse as

$$\tau_{\rm rms} = \frac{\tau}{\sqrt{2}} < \frac{\epsilon}{B}, \tag{48}$$

which implies

$$B\tau < \sqrt{2}\epsilon. \tag{49}$$

Using the optimum value for τ as obtained in section 3 we can rewrite Eq. (49) as

$$B^2 DL < \frac{2\pi c}{\lambda_0^2}\epsilon^2, \tag{50}$$

where we have used Eqs. (48), (32) and (39). For a 2-dB power penalty, $\epsilon \sim 0.491$ (see e.g., [21]). At the wavelength of 1550 nm, we can write Eq. (46) as

$$B^2 DL < 1.9 \times 10^5 \ {\rm Gb}^2{\rm ps/nm}, \tag{51}$$

where B is measured in Gbps, D in ps/(km-nm) and L in km.

Table 2 gives the maximum allowed dispersion for different bit rates for a dispersion power penalty of 2 dB. Knowing the dispersion coefficient, the maximum possible distance can be easily calculated for a given bit rate (in Gbps) from the above inequality.

It may be appropriate to mention here that precise values for dispersion tolerance in a given link depends on several factors like nature of modulaton format, receiver bandwidth, whether forward error correction is included in transmission, etc. Nevetheless, Table 2 is a good guideline to get an initial estimate for system design purpose.

4. Modeling and Tailoring of Dispersion

In order to estimate the dispersion of a given optical fiber, we need to obtain the spectral dependence of the propagation constant β or the effective index of the mode.

Table 2. Maximum allowed dispersion for different bit rates for a dispersion power penalty of 2 dB.

Bit rate (Gbps)	Maximum allowed dispersion (ps/nm)
2.5	30400
10	1900
40	118

Since fibers in general (including dispersion compensating fibers) are characterized by complex refractive index profiles with multiple cores and claddings and with possibly graded refractive index regions, it is important to have methods to analyze the dispersion characteristics of such fibers. Since most designs have circular cylindrical symmetry, i.e., the refractive index profile $n(r)$ is a function of the cylindrical radial coordinate r only (and independent of the azimuthal coordinate ϕ) , the problem reduces to solving the radial part of the wave equation given by (see e.g., [17])

$$r^2\frac{d^2R}{dr^2} + r\frac{dR}{dr} + \{[k_0^2n^2(r) - \beta^2]r^2 - l^2\}R = 0, \tag{52}$$

where $R(r)$ is the radial part of the electric field distribution and β is the propagation constant of the mode. The azimuthal ϕ dependence is assumed to be of the form

$$\exp[-il\phi]; \quad l = 0, \pm1, \pm2, \ldots; \tag{53}$$

radially symmetric modes correspond to $l = 0$.

If the fiber profile could be broken down into discrete regions of constant refractive indices [e.g., as shown in Fig. 6(d)], then in each region of constant refractive index, the solution $R(r)$ can be described in terms of Bessel functions (see e.g., [17]); the solution is given by

$$R(r) = A_pJ_0(\kappa_pr) + B_pY_0(\kappa_pr) \tag{54}$$

in regions for which the effective index (n_{eff}) is smaller than the refractive index (n_p) of that region and by

$$R(r) = A_qK_0(\gamma_qr) + B_qI_0(\gamma_qr) \tag{55}$$

in regions for which the effective index is greater than the refractive index (n_q) of that region. Here

$$\kappa_p^2 = k_0^2(n_p^2 - n_{\text{eff}}^2) \quad \text{and} \quad \gamma_q^2 = k_0^2(n_{\text{eff}}^2 - n_q^2) \tag{56}$$

and A_p, B_p, A_q and B_q are constants. Applying boundary conditions at each interface and using the fact that the solutions should not diverge at $r = 0$ and at $r = \infty$, an eigenvalue equation can be obtained whose solution would give us the propagation constant β of the propagating mode. Knowing the value of the propagation constant one can then obtain the field distribution, the effective mode area (designated as A_{eff} in the literature) and the dispersion values; A_{eff} is essentially a measure of the cross sectional area of the fundamental mode [22]. This technique directly yields the total dispersion including material and waveguide dispersion.

Since the boundary conditions relate the fields in different regions, the relationship between the constants A_p and B_p in different regions can be written in the form of a matrix equation. The constants in the first region (denoted by subscript 1) and the last region (denoted by subscript N) would then be connected by a product of 2×2 matrices:

$$\begin{pmatrix} A_N \\ B_N \end{pmatrix} = \begin{pmatrix} S_{11} & S_{12} \\ S_{21} & S_{22} \end{pmatrix} \begin{pmatrix} A_1 \\ B_1 \end{pmatrix}, \tag{57}$$

where S_{11}, S_{12}, etc. are the elements of the product matrix. Since the fields should not diverge at $r = 0$ and at $r = \infty$ we have

$$B_1 = 0 \quad \text{and} \quad B_N = 0, \tag{58}$$

implying

$$S_{21} = 0, \tag{59}$$

which represents the eigenvalue equation. This equation can be solved by any standard numerical technique (e.g., [23]) to obtain the effective index of the mode. Once the effective index of the mode is obtained, Eqs. (54) and (55) can be used to obtain the transverse modal field distributions and hence other parameters such as the effective mode area, etc. The spectral variation of n_{eff} can be used to evaluate the second order dispersion, dispersion slope and higher order dispersion of the fiber mode. It should be noted that since dispersion calculation involves estimation of the second derivative of the effective index, the numerical solution needs to be very accurate.

If the fiber has graded refractive index variation in any region, then this can be approximated by a series of steps and the above mentioned technique can then be utilized to obtain the propagation characteristics. Thus, from design point of view dispersion tailoring essentially boils down to a solution of the second order differential equation [Eq. (52)]. As a sample, we have described here outline of a matrix method [23], which was developed in our Fiber Optics Group. One could as well use any other numerical method to yield dispersion spectra. Precise dispersion tailoring involves extensive numerical simulations as to sensitivity of dispersion spectra as well as magnitude of D to variations in profile parameters, e.g., core-cladding index difference, core diameter, separation between multiple cores or claddings (in case of segmented refractive index profiles depth and width of claddings) etc. Having said this, most important fact is that by appropriate design of the transverse refractive index profile, it is possible to achieve positive or negative dispersion at any chosen wavelength greater than 1270 nm. It is using such design principles that one can achieve dispersion shifted fiber, non-zero dispersion shifted fiber, etc. These designs essentially alter the waveguide dispersion component of the mode which together with the material dispersion permits one to achieve specific dispersion characteristics.

5. Concept of Dispersion Compensation

Historically initial efforts on system upgrades to take advantage of the availability of EDFA had centered on exploiting the already installed base of millions of kilometers of G.652 fibers, whose design was optimized to function as the transmission fiber in the wavelength region around 1310 nm. Sound economic considerations favored this route to be the most natural choice. However, it is apparent from Fig. 4 that if a G.652 fiber

were operated in the EDFA band, at the 1550-nm wavelength region it would typically induce a dispersion of about 17 ps/(km-nm) to the signals. At 2.5 Gb/s bit rate, and assuming externally modulated lasers, we can estimate from Table 2 that the maximum distance of propagation to be about 1800 km which was easily acceptable to system designers. If, however, bit rate were scaled up 4 times to 10 Gb/s, the maximum distance would be reduced by a factor of 16 to $\sim$ 110 km only! In other words, D that could be tolerated at 10 Gb/s would be only 1 ps/(km-nm), if the maximum distance were taken to be $\sim$1800 km (i.e., same as @ 2.5 Gbps). Realization of this immediately triggered a great deal of R&D efforts to develop some dispersion compensating schemes, which could be integrated into such high speed fiber optic links so that net dispersion of the link could be maintained within tolerable limits. Three major state-of-the-art fiber-based technologies available as options for dispersion management are: dispersion compensating fibers (DCF) [14,25–33], chirped fiber Bragg gratings (CFBG) [12,34–36], and high-order-mode (HOM) fiber [37–43].

As discussed earlier, a Fourier transform limited pulse undergoes temporal broadening as it propagates along a single-mode optical fiber due to chromatic dispersion effects. In an optical communication system this broadening will lead to overlap of adjacent pulses, which in turn will result in errors in detection. In order to keep the bit error rate below a specified value (typically 10^{-12} to 10^{-15}), optical pulses cannot be allowed to spill beyond certain limits into adjacent time slots. One of the methods to overcome this effect is to use regenerators based on optoelectronic conversion, i.e., the incoming optical pulses are converted into electrical pulses by a detector and after electronic processing for retiming and reshaping, these electrical pulses are reconverted into optical pulses using a transmitter. Although this is quite straightforward, this scheme has certain disadvantages. In a DWDM system each wavelength channel would need a separate regenerator. The electronic regenerator would need to be replaced whenever any up gradation in terms of higher bit rate is to be carried out. Optical dispersion compensating schemes which compensate the dispersion in the optical domain itself are very attractive as they do not involve any optical to electrical conversion. We restrict our discussion here to dispersion compensating fibers.

Optical dispersion compensators work in the optical domain itself without converting the optical signals into electronic signals. As we have discussed earlier, optical pulses broaden as they travel along an optical fiber due to the variation of group velocity with wavelength. Thus in the anomalous dispersion region (wavelengths longer than the zero dispersion wavelength) longer wavelength components of an optical pulse travel slower than shorter wavelength components leading to broadening, i.e, the group delay increases with increase in wavelength. The leading edge of the pulse would have higher frequency compared to the trailing edge. If the broadened pulses are passed through an optical device in which the group delay decreases with increase in wavelength, i.e, the device exhibits normal dispersion with longer wavelengths traveling faster than shorter wavelengths, then it should be possible to compensate for the accumulated dispersion in the fiber. Dispersion compensating fibers (DCF) are specially designed fibers with an appropriate refractive index profile such that they have normal dispersion at the wavelength of operation. Figure 10 shows the working principle of a DCF; the pulse broadens and gets chirped as it propagates along a given span through transmission fiber. As the broadened pulse propagates through the DCF, which is characterized with a negative dispersion coefficient, it undergoes recompression. Depending on the magnitude of dispersion coefficient, an appropriate length of

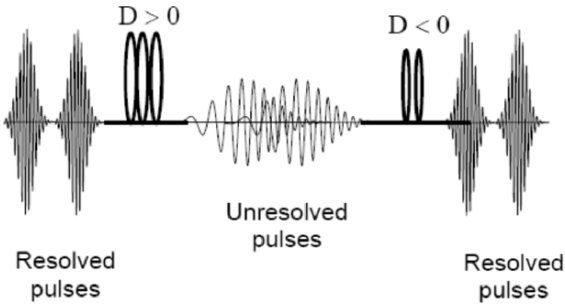

Fig. 10. Principle of dispersion compensation. When the pulse propagates through the link fiber operating in the anomalous dispersion region, the output pulse is broadened and chirped due to $D > 0$. If the dispersion-compensating device has normal dispersion, i.e., $D < 0$, then it can compensate for the dispersion of the propagating pulse induced by the transmission fiber.

the DCF would be able to compensate for accumulated dispersion over a span of the given fiber. It may be mentioned that the compensation can be exact when nonlinear effects are negligible; however, in the presence of nonlinearity and attenuation, this compensation is only approximate.

Since the dispersion coefficient of the transmission fiber is usually positive, any dispersion compensating fiber should have high negative dispersion coefficient, dispersion slope matching with the fiber for which it is designed, low propagation and bend losses (because a DCF is usually co-located with a fiber amplifier in the form of a spool) and relatively large mode effective area to have reduced nonlinear effects. Design trade offs to meet some of these requirements are necessary, e.g., large dispersion coefficients are usually characterized by small mode effective areas and hence large nonlinear effects. Design optimization involves modification of the transverse refractive index profile of the fiber to achieve the desired characteristics by choosing multiple cores and claddings in the fiber.

The dispersion characteristic of an optical fiber is determined by the wavelength dependence of the effective index of the mode [see Eq. (33)]. Since dispersion is related to the second derivative of the mode effective index, any deviation from linearity of the effective index variation with wavelength would lead to dispersion. The sign of the dispersion would in turn depend on the curvature of the effective index variation. The effective index in turn depends on the distribution of the modal power among the various regions of the fiber, such as core and cladding. As the wavelength changes, the distribution of the power among the various refractive index regions of the fiber changes and this leads to a variation of the effective index. To obtain a large dispersion, the objective would then be to look at refractive index profiles wherein the modal power distribution changes rapidly and nonlinearly with wavelength. Such changes can be expected in fibers with multiple cores and claddings with appropriate refractive indices and widths. The modal power distribution at any wavelength also determines the bend loss of the mode as well as the nonlinear effect suffered by the mode.

There exist primarily three types of refractive index profiles which have evolved in the literature namely, the matched clad [see Fig. 6(a)], depressed clad or W-type [see Fig. 6(b)] and segmented core with multiple cores/claddings [see Fig.6 (c)–(e)]. By an appropriate choice of the refractive indices of the core and the diameter, the zero dispersion wavelength of the matched clad design can be shifted to wavelengths longer than the long wavelength edge of an amplifier band and thus the fiber would have negative dispersion at the operating wavelength within the amplifier band. This is discussed in the next section. The W-type fiber can achieve negative dispersion values but is usually characterized by small mode effective areas. By suitable optimization, the dispersion of the segmented core designs can be made very large and negative. By choosing multiple cores/claddings, as the wavelength changes, the changes in the modal power distribution leads to characteristic changes in the mode effective index and hence large dispersion values.

5.1. Conventional Single Wavelength DCFs

Conventional single wavelength DCFs have large negative dispersion at one operating wavelength and hence can be used to compensate for dispersion at one chosen wavelength. However, they cannot be used for compensating dispersion over a band of wavelengths such as in DWDM systems.

If $D_T(\lambda_n)$ and L_T represent the dispersion coefficient and length of the transmission fiber and $D_c(\lambda_n)$ and L_c represent the corresponding quantities of the DCF, then for achieving zero net dispersion at a chosen wavelength λ_n we must have

$$D_T(\lambda_n)L_T + D_c(\lambda_n)L_c = 0. \tag{60}$$

Hence for given values of $D_T(\lambda_n)$, L_T and $D_c(\lambda_n)$, the length of the DCF required would be

$$L_c = -\frac{D_T(\lambda_n)}{D_c(\lambda_n)}L_T, \tag{61}$$

showing that $D_c(\lambda_n)$ and $D_T(\lambda_n)$ should have opposite signs. Also larger the value of $D_c(\lambda_n)$ the smaller would be the length of the required DCF.

Since material dispersion coefficient D_m is positive in the EDFA wavelength window, the primary design task for a DCF designer thus involves generating a negative D_w of sufficiently high magnitude so that the net sum of $D_m + D_w$ is negative at the amplifier window. If the dispersion properties of the fiber could be so tailored that D_w far exceeds D_m, then by virtue of Eq. (61) one would require a relatively short L_c. Typical example of the refractive index profile of such a fiber is shown in the schematic diagram Fig. 6 (b) and typical dispersion spectrum of one such sample fiber is displayed in Fig. 11. Negative waveguide dispersion is achievable by choosing the refractive index profile of the fiber in a manner so that at the wavelengths of interest the propagating mode is weakly guided with a large fraction of its modal power rapidly spreading into the cladding layer for a small variation in wavelength. This implies that the modal spot size varies rapidly with small variations in wavelength. The key to achieve this is to design a narrow width high refractive index contrast (Δ) fiber core. In fact the first generation DCFs indeed relied on this basic concept. The first generation DCFs were targeted to compensate dispersion in G.652 fibers at a single wavelength; these were characterized with a $D \sim -50$ to -100 ps/(km-nm) and a positive dispersion slope

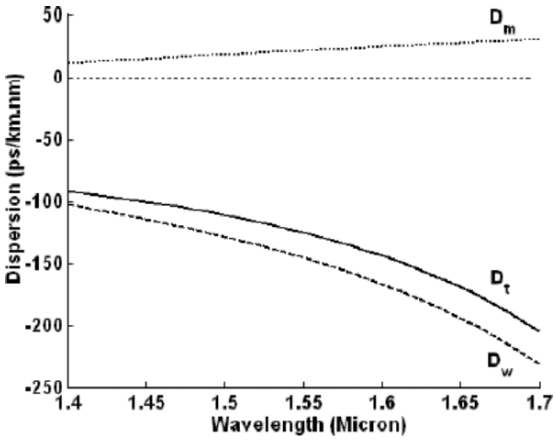

Fig. 11. Variation of material dispersion coefficient (D_m), waveguide dispersion coefficient (D_w) and total dispersion coefficient (D_t) of a typical dispersion compensating fiber having a refractive index profile shown in Fig. 6 (b).

[44,45]. Owing to high Δ (typically $\geq 2\%$) and narrow mode confinement, such a DCF necessarily involved relatively large insertion loss, and also higher sensitivity to bend-induced loss. In view of this feature, a DCF designer is required to compromise between generating a high negative D coefficient and low attenuation coefficient, α_c. In order to simultaneously account for these two characteristics of a DCF, an important composite parameter has evolved in the literature known as Figure of Merit, FOM, which is defined through

$$\text{FOM} = -\frac{D_c}{\alpha_c} \tag{62}$$

and expressed in ps/(nm-dB). Total attenuation and dispersion in a dispersion compensated link would be given by

$$\alpha = \alpha_T L_T + \alpha_c L_c, \tag{63}$$

$$D = D_T L_T + D_c L_c, \tag{64}$$

where subscripts T and c stand for transmission and dispersion compensating fibers, respectively. One can derive from Eqs. (62)–(64), that for $D = 0$,

$$\alpha = \left(\alpha_T + \frac{D_T}{\text{FOM}}\right) L_T, \tag{65}$$

which shows that any increase in total link attenuation is due to FOM alone; thus, larger FOM is, smaller would be incremental attenuation in the link due to insertion of the DCF. Therefore, an efficient DCF would be one whose D_w in magnitude far exceeds D_m and at the same time who's FOM is relatively large. A schematic plot for D vs λ for a first generation DCF along with that for a conventional single-mode transmission fiber is shown in Fig. 12.

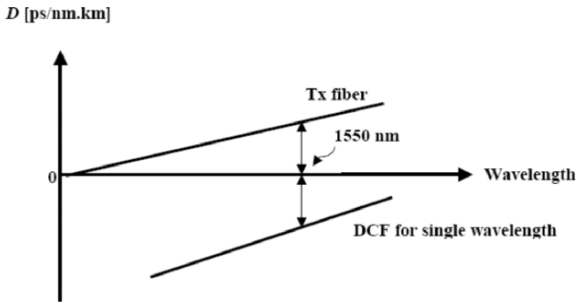

Fig. 12. Schematic illustrating D vs λ for a first generation DCF relative to that of a G.652 fiber; notice that the DCF compensates for dispersion perfectly only at a single wavelength.

5.2. Dispersion Slope Compensating Fiber (DSCF) for Broadband Dispersion Compensation

It is obvious from Fig. 12 that the DCF would compensate dispersion of the transmission fiber only at a single wavelength (say λ_n) whereas DWDM links, which are of maximum current interest, involve simultaneous transmission of several wavelengths. This requires a broadband DCF, which could compensate for signal impairments due to chromatic dispersion at multiple wavelengths in a DWDM stream. The key to achieve this in a DCF involves design of a DCF, with not only a negative D but also whose dispersion slope is negative. Thus if we consider a channel at a wavelength λ_n, then the accumulated dispersion for this channel after propagating through the transmission fiber and the DCF would be

$$\tilde{D}(\lambda_n) = D_T(\lambda_n)L_T + D_c(\lambda_n)L_c. \tag{66}$$

Assuming the channels λ_n and λ_{n+1} to be close to each other, we can make a Taylor series expansion of $D_T(\lambda_{n+1})$ and $D_c(\lambda_{n+1})$ around λ_n and show that for zero net dispersion at the nearby wavelength λ_{n+1}, we must have

$$\mathrm{RDS} = \frac{S_T}{D_T} = \frac{S_c}{D_c}, \tag{67}$$

where RDS stands for relative dispersion slope (expressed in nm^{-1}) and

$$S_T = \frac{dD_T}{d\lambda_0}\Big|_{\lambda_0=\lambda_n}, \qquad S_c = \frac{dD_c}{d\lambda_0}\Big|_{\lambda_0=\lambda_n} \tag{68}$$

represent the dispersion slope of the transmission fiber and the DCF evaluated at the wavelength λ_n. Thus for the DCF to compensate dispersion simultaneously for multiple wavelengths, the transmission fiber and the DCF should have the same value of RDS thereby, implying that the dispersion slope compensating ratio (DSCR), i.e., the ratio of $(\mathrm{RDS})_c$ to $(\mathrm{RDS})_T$ should ideally be unity. A DCF, which satisfies this condition should function as a dispersion compensator for all the wavelength channels in a DWDM link and hence such DCFs are referred to as broadband DCFs or more

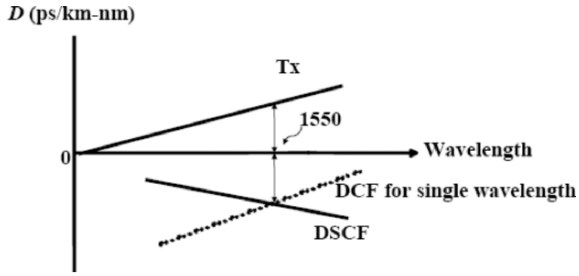

Fig. 13. Schematic illustrating D vs λ for a DSCF relative to a single wavelength DCF and to that of a G.652 fiber.

commonly as dispersion slope compensating fibers (DSCF). A schematic for the dispersion spectrum of such a DSCF alongwith its counterpart single-wavelength DCF is shown in Fig. 13. Any differences in the value of RDS between the transmission fiber and the DCF would result in under- or over- compensation of dispersion leading to increased BERs at those channels. Usually a DSCF designer targets to match values of the RDS for the two fibers at the median wavelength of a particular amplification band e.g. for C-band the median wavelength is 1545 nm while for L-band it is 1590 nm. In principle this is sufficient to achieve dispersion slope compensation across the entire gain spectrum of a specific amplifier because dispersion spectrum of the transmission fiber is approximately linear within a specific amplification band. However, other considerations e.g. countenance of nonlinear optical effects through large mode effective area, reduced sensitivity to bend loss etc often demand a compromise between 100% dispersion slope compensation and largest achievable A_{eff}. In many situations a DCF designer targets $< 100\%$ (e.g., about 60%) dispersion slope compensation and maximize A_{eff}. In such situations, S may not match for wavelengths at the edges of a particular amplifier band (see Fig. 14). It was shown that @ 10 Gb/s signal transmission rate a slope mismatch (i.e., $\Delta S/S$) of 20% is tolerable while the corresponding figure is barely 1% @ 40 Gb/s [46]. Smaller the dispersion slope of the transmission fiber, relatively easier becomes the design for corresponding DSCF. In Table 3 we list typical values of RDS at 1550 nm of some commonly used transmission fibers.

Table 3. Typical RDS values of different standard transmission fibers @ 1550 nm.

Fiber type	RDS (nm^{-1})
G.652	0.0034
TrueWave-RS™	0.01
TeraLight™	0.0073
LEAF™	0.0202

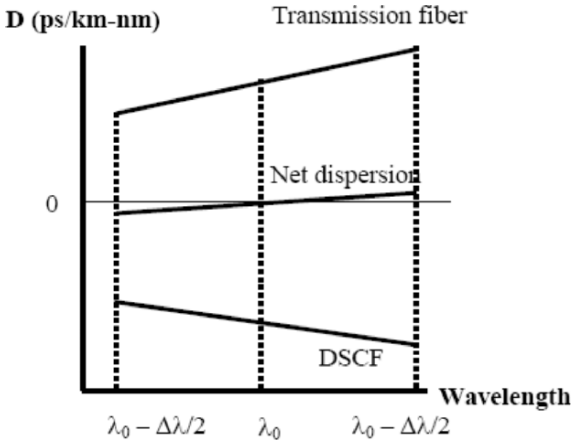

Fig. 14. Schematic illustrating under- (for wavelengths longer than λ_0) and over-compensation (for wavelengths shorter than λ_0) of dispersion slope due to mismatch of slopes between transmission fiber and DCF. (Adapted from [46].)

In place of RDS, sometimes the inverse of RDS is also used in the literature to quantify the measure of slope compensation. This quantity is referred to as κ and is expressed in unit of nm.[1]

6. Dispersion Compensating Fibers

We saw in the previous section that a DCF should have a large negative dispersion value and should have matching dispersion slope but of opposite sign to achieve dispersion compensation over a band of wavelengths for use in a WDM system. Apart from this the fiber should also have low bend losses, large mode effective area and reduced splice loss to tranmission fibers.

The key to realization of negative S lies in introducing more than one cladding layers in the refractive index profile of the DCF, typically a coaxial depressed index cladding/moat region immediately surrounding the central core and/or a raised index region away from the core. These additional features in the refractive index profile offer a greater degree of freedom to a DSCF designer with regard to simultaneous optimization of different fiber characteristics. Some of these DSCF designs are shown in Fig. 15. In [29] some results in terms of sensitivity of D to variations in profile parameters of triple-clad DSCF designs were presented. For example, for generating a large negative D what is required is a large Δ for the central core, which reduces RDS and also results in excessive loss due to higher Rayleigh scattering. Reduced core diameter reduces negative D and also enhances sensitivity to bend-induced loss. Deeper the trench/moat cladding region surrounding the core, smaller would be the

[1] Powerform™ DCM® marketed by Avanex Corporation, NY

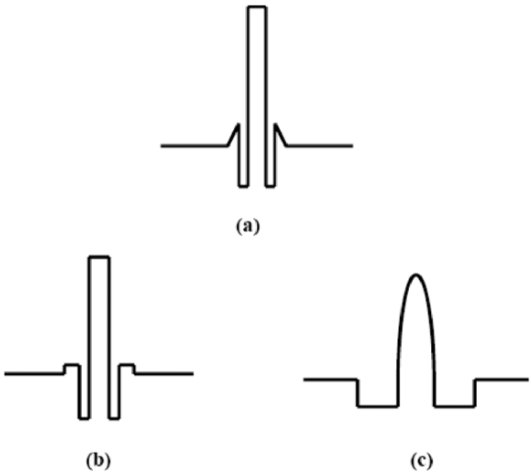

Fig. 15. Schematics representing samples of typical refractive index profiles of few commercially available DSCFs: a) Corning, b) Lucent, and c) Fujikura. The common noticeable features in all these profiles are that there is a depressed index cladding/moat region around the central high index core surrounded by a small Δ ring. Precise values of widths and index values for different segments in the index profile are not available in open literature.

magnitude of negative D. Further, RDS increases with decrease in core diameter for a trench width above a certain value. For each individual designs one has to undertake a parametric study and optimize through a systematic approach in terms of low loss-sensitivity to bending, negative dispersion slope for broadband compensation, and also low sensitivity to nonlinear optical effects through maximization of A_{eff}. Sensitivity to bend loss is important because a DCF is normally co-located with an EDFA in the form of a spool. Further, since a DCF's core dimension and Δ are very different from that of the transmission fiber, it is important to account for splice loss between the transmission fiber and a DCF while estimating its insertion loss, and hence its FOM [47]. Due to the multiple index layers involved in a DSCF and hence the potential inter-diffusivity between different index layers, it is rarely possible to theoretically estimate precise loss figures for a DSCF except for a notional value estimable on the assumption of perfect step index layers. Thus it is always advisable to make an actual measurement on a fabricated DSCF in order to get a realistic value of FOM.

With regard to profile optimization, there is no straightforward recipe for this optimization procedure because trade off(s) between different optical properties and propagation effects is involved. A detailed opto-geometric parametric study for individual refractive index profile is required to be made to arrive at the optimum values of various index profile parameters after trends in variations of different properties due to variations in profile parameters are established. The bottom line in any such fiber design optimization exercise would be to realize low insertion loss, low bend-induced loss, large negative dispersion with appropriate negative slope for slope compensation, large effective area to reduce sensitivity to optical nonlinear effects and low polariza-

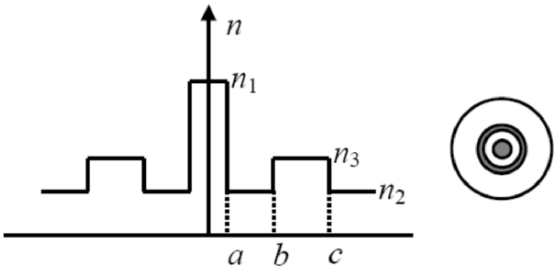

Fig. 16. The refractive index profile of a dual concentric core DCF fiber design. Also shown is the transverse section of the fiber showing the two concentric cores.

tion mode dispersion. Apart from the various designs for DSCFs shown in Fig. 15, other designs with dual concentric cores [Fig. 16] with extremely large dispersion values have also been demonstrated (see next section and [48,49]). Detailed study on such coaxial dual-core DCF design is given in the next section.

We shall also see in section 7 that when fibers with low chromatic dispersion are used in a DWDM system then due to nonlinear interactions, there could be a strong cross talk between various wavelength channels. The efficiency of such nonlinear interaction depends on the dispersion coefficient of the fiber with maximum efficiency close to zero-dispersion wavelengths and this effect reduces cross talk with increase in the dispersion coefficient. Thus to minimize nonlinear interactions, it is necessary to have a non-zero value of dispersion coefficient. DCFs are fibers, which have a D opposite to that of the span fiber. If the DCFs are placed in a spool at the optical repeater site, then although the optical pulses are propagating through a long span of fiber, no actual distance in terms of the actual link is being covered. In order to have both low overall dispersion (to have small BER) and a large local dispersion (to reduce nonlinear effects), dispersion flattened fiber technology or dispersion managed fiber link has been developed wherein the fiber span consists of a certain number of alternate segments of positive and negative dispersion fibers so as to give low overall dispersion. Dispersion versus length curve of a dispersion managed link mimicks a saw-tooth curve. These DCFs are referred to as reverse or inverse dispersion fibers, which are used with the transmission fibers almost in the length ratio of 1:1 in segments, meaning thereby that their D and S are similar in magnitude to that of the transmission fiber except for the signs [50,51]. Thus for the reverse dispersion fiber used in [50], its D and S were -16 ps/(km-nm) and -0.05 ps/(km-nm^2). Losses in such DCFs are usually low ($\sim$ that of the transmission fibers) as compared to DCFs characterized with high negative D. Such dispersion managed fiber spans have been used to transmit terabits of information over an undersea link [52].

6.1. Dual Concentric Core DCFs

As discussed earlier, the chromatic dispersion of an optical fiber can be tailored primarily through appropriate waveguide dispersion, which depends on the fiber refractive

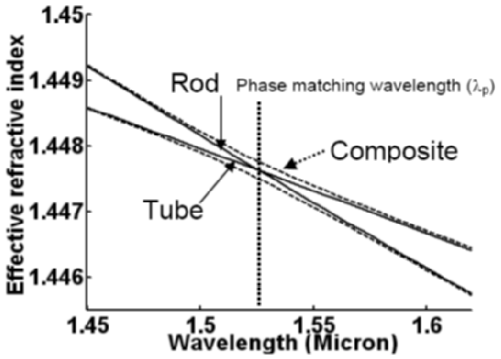

Fig. 17. Variation of the effective indices of the modes of a dual core DCF fiber with solid curves representing that due to the inner core (rod fiber) and the outer core (tube fiber). The two curves cross each other at the phase matching wavelength (λ_p), which for the parameters chosen is 1525.5 nm. The dashed lines represent the effective index variations with wavelength of the two fundamental normal modes of the composite dual core fiber.

index profile. There are many fiber designs to achieve large negative dispersion required for DCFs. In this section we will discuss a design consisting of a dual concentric core design to achieve extremely large dispersion values.

Basic Physics

Figure 16 shows the refractive index profile of a dual concentric core fiber design. It consists of a central high index core surrounded by a concentric second core of smaller index increase with an intermediate matched cladding layer in between. The dual concentric core fiber is like a directional coupler with the two interacting waveguides being a fiber with the inner core only and a fiber with the outer core only. If the two waveguides are chosen to be significantly non-identical, the dispersion curves of the individual modes of the inner and outer core will be different. At some chosen design wavelength they can be made to have the same propagation constant (phase matched) and in such a case, the normal modes of the coaxial fiber (which are a linear combination of the individual modes of the two cores) will undergo rapid changes in effective indices as well as modal field distributions while passing through the phase matching wavelength. Figure 17 shows a typical variation of the effective indices of the fundamental and the first azimuthally symmetric modes showing the rapid variation of the effective indices of the normal modes around the phase matching wavelength. The figure corresponds to the following parameters: $n_1 = 1.47299$, $n_3 = n_4 = 1.444388$ (pure silica) and $n_2 = 1.44871$ at 1550 nm, $a = 1$ μm, $b = 9$ μm and $c = 16.32$ μm. For wavelengths much below the phase matching wavelength, the effective index of the fundamental mode of the composite fiber is very close to that of the inner core and for wavelengths much larger than the phase matching wavelength, the effective index of the fundamental mode would be very close to that of the outer core mode. Typical distribution of modal power for three different wavelengths around the phase matching

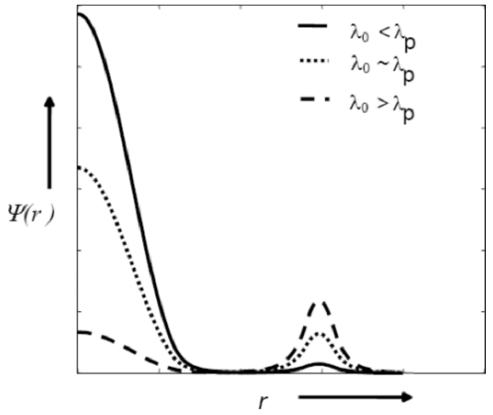

Fig. 18. Modal field distribution illustrating variation in extent of the field with wavelength relative to the phase matching wavelength.

wavelength (λ_p) are shown in Fig. 18. Thus around the phase matching wavelength, the effective index variation with wavelength is far from linear and this leads to a very large value for the dispersion coefficient for this normal mode [48,49,53] leading to applications in dispersion compensating fibers. The specific variation of the effective index of the normal mode leads to a significant shift of the field distribution of the mode from being concentrated around the inner core to being concentrated in the outer core. Interestingly, this modal evolution with wavelength has been exploited to realize important functional features of other fiber devices for achieving inherently gain flattened erbium doped fiber amplifiers or fiber Raman amplifiers (see e.g., [54–57]).

Dispersion in Dual Concentric Core Fibers

Figure 19 shows the variation of dispersion with wavelength for a typical dual concentric core fiber design with the phase matching wavelength chosen to be close to 1550 nm [48]. It can be seen that dispersion values of less than -5000 ps/(km-nm) is indeed possible around the phase matching wavelength (λ_p). The wavelength at which such large negative dispersion is feasible can be changed by appropriate modifications of the refractive index profile parameters of the fiber. Figures 20 and 21 show an experimentally realized dual core DCF refractive index profile and its dispersion spectrum, respectively having peak negative D as large as -1800 ps/(km-nm) [49]. The peak value of dispersion and the wavelength range across which the dispersion is large and negative depend on the spacing between the inner and outer cores. Thus if the cores are brought closer together, their interaction increases leading to a reduction in the magnitude of dispersion with a corresponding increase in the bandwidth. Thus dual concentric core fibers can also be appropriately designed for application in WDM systems [58]. This route has been pursued to achieve broadband dispersion compensation in G.652 fibers in the S-, C-, and L-bands to achieve a DSCF [59].

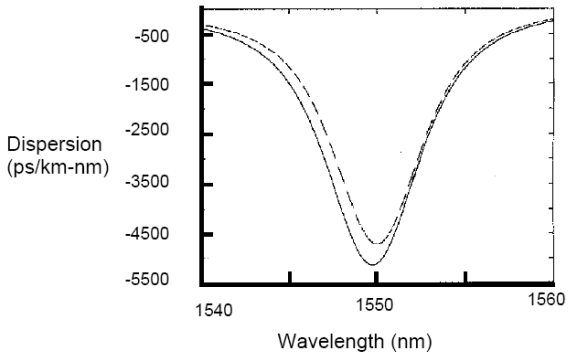

Fig. 19. Spectral variation of dispersion of the fundamental mode for a dual concentric core fiber having a phase matching wavelength close to 1550 nm. Solid and dashed curves correspond respectively to step and parabolic refractive index variations in the cores. Note the very large negative value of dispersion around the phase matching wavelength. (After [48]).

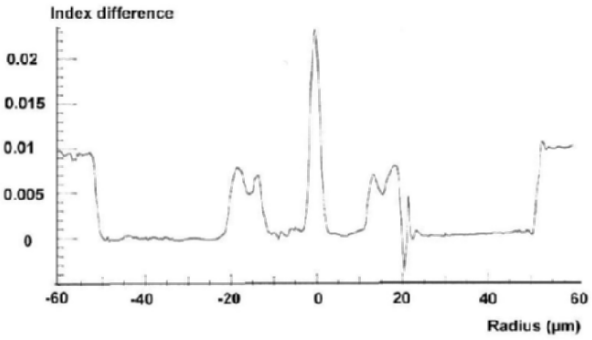

Fig. 20. Measured refractive index profile of a fabricated dual-core DCF preform. (After [49]).

Owing to the presence of the outer ring, the fiber supports higher order modes. However, experiments have shown that the primary mode that propagates after some length of the fiber is the fundamental super mode, whose field distribution varies significantly with wavelength and which is the mode that exhibits the large dispersion [53]. The field distribution at the output of the fiber exhibits the characteristic changes in the fundamental modal distribution with wavelength. The absence of the higher order mode is explained by the much higher losses suffered by the higher order modes primarily by coupling to leaky modes. Tolerance of the dispersion value and minimum dispersion wavelength on the optogeometric parameters of the dual concentric core fiber have been studied [53]. Both the minimum value of dispersion and the wavelength of minimum value depend critically on the fiber parameters. However, the sensitivity can be significantly reduced by increasing the interaction between the inner core and

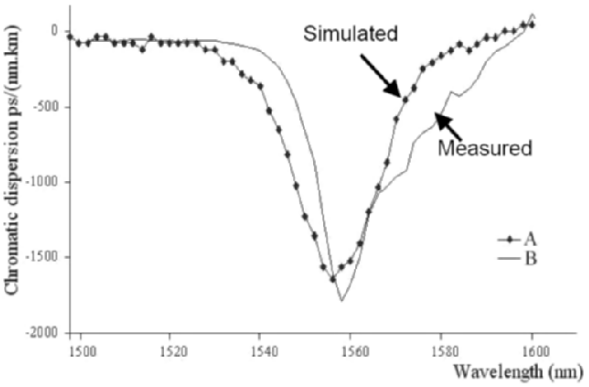

Fig. 21. Experimentally measured spectral variation of dispersion in a dual concentric core fiber and comparison with results from simulation. (After [49]).

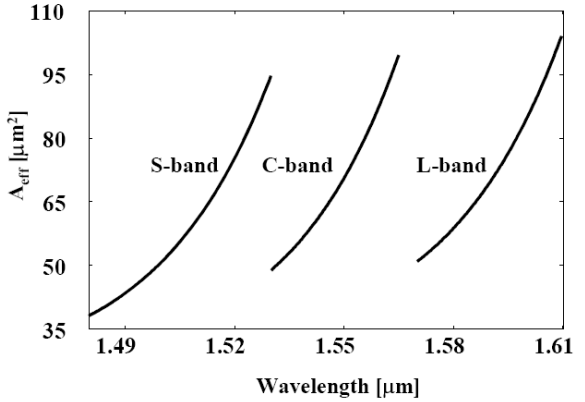

Fig. 22. Variation in mode effective area with wavelength of the dual core DSCFs designed for S-, C-, and L-bands. (After [58]).

the outer ring which would of course reduce the dispersion value. In spite of the reduction in the dispersion such fibers are expected to have significantly large negative dispersion. The concept of achieving large negative dispersion using the dual core design has also been exploited to realize large negative dispersion in photonic crystal fibers [60–62].

Some of the other commercially available broadband DSCFs essentially realized through segmented core profiles (see Fig. 15) are characterized with a mode effective area A_{eff} (see section 7 for its definition), which typically range between 15 to 25 μm^2, and which make them susceptible to nonlinear effects unless care is taken to reduce launched power (1 dBm per channel) into the fiber. In contrast, the ones based on

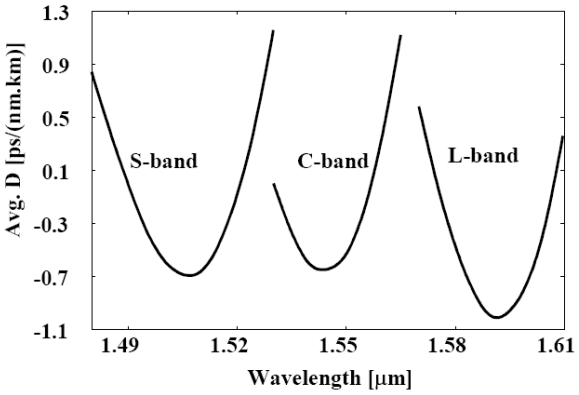

Fig. 23. Net average residual dispersion of about 100 km of G.652 fiber joined with the designed dual-core DSCFs (in approximately 10:1 ratio) in the S-, C- and L-bands (after [58]).

dual core DSCFs could be designed to attain A_{eff}, which are comparable to that of the G.652 fiber (see Fig. 22). The net residual dispersion spectra of a 100-km-long G.652 fiber link along with so designed DSCFs (approximately in 10:1 ratio) at each of the amplifier band are shown in Fig. 23. It could be seen that residual average dispersion is well within $\pm$ 1 ps/(km-nm) within all the three fiber amplifier bands. Other estimated performance parameters of the designed DSCFs are shown in Table 4 [59].

Table 4. Key features of designed DCFs meeting G.652 fibers for various amplifier bands.

Wavelength (nm)	κ (nm)	α (dB/km)	FOM [ps/(dB nm)]	α_b^* (dB)
1500 (S-band)	178	0.242	771	0.022
1550 (C-band)	369	0.207	941	0.095
1509 (L-band)	294	0.193	837	0.002

* For a single turn bend-diameter of 32 mm.

Figures 24 (a) and (b) show residual dispersion spectra for standard G.655 fibers when joined with the designed DSCFs in the C- and L-bands, again designed through dual core DCF route to achieve broadband dispersion compensation for signal transmission in standard NZ-DSF based fiber links [63]. In Table 5 we display other estimated performance parameters of these dual-core design basic DSCFs [63].

Asymmetric Twin Core Fiber Design

In the dual concentric core design, the two cores that are interacting are concentric. The same principle of achieving large dispersion by choosing the effective index variation around the phase matching wavelength in a directional coupler can be achieved by using an asymmetric twin core (ATC) fiber design shown in Fig. 25. An ATC fiber

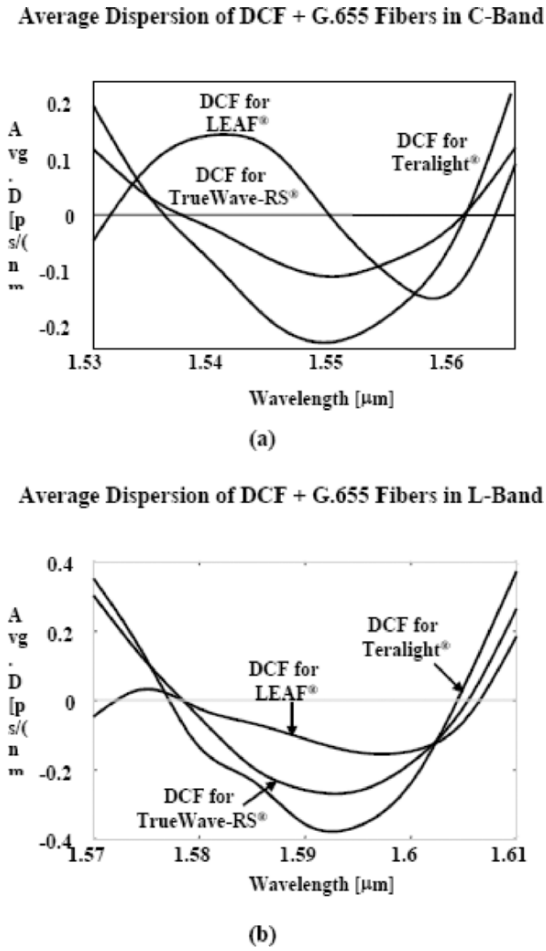

Fig. 24. Net average residual dispersion of about 100 km of standard G.655 fibers joined with the appropriately designed dual-core DSCFs (approximately 10 km in length in each case) in the a) C-band and b) L-band (after [63]).

consists of two parallel, non-identical cores and finds applications as wavelength filters, couplers etc [64,65]. The two cores, each supporting a single mode, can be designed to have the same propagation constant at a chosen wavelength—the phase matching wavelength (PMW). In terms of supermodes, this structure supports one even and one odd supermode, having typical spectral variation of effective indices similar to that shown in Fig. 17 for a dual concentric core. Just like the dual concentric core design, far away from the PMW, the effective indices of the two normal modes are very close to those of the individual modes and as the wavelength sweeps across the phase matching wavelength, the effective index varies in a highly nonlinear fashion leading to large

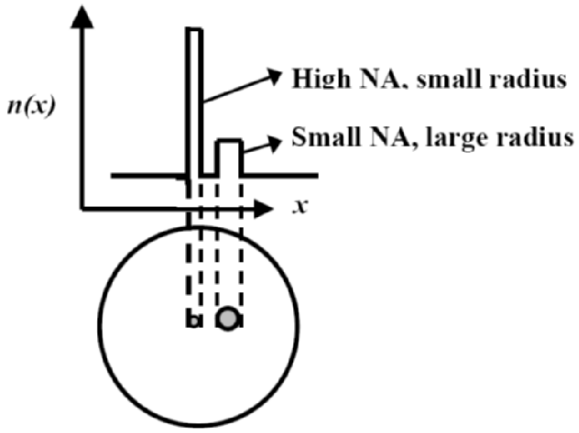

Fig. 25. Schematic illustrating asymmetric twin core fiber design as a DCF.

negative dispersion coefficient (-230 to -330) ps/(km-nm) for the even supermode, so that the fiber can act as a dispersion compensating fiber. In view of the special design of this fiber, the variation in the Raman gain coefficient of the fiber can be compensated by a wavelength dependence of the A_{eff}. Thus such a fiber can also act as a broadband, lossless dispersion-compensating module (DCM) [66].

Table 5. Key features of designed DCFs matching standard NZ-DSFs for various amplifier bands.

DCF For	D [ps/(km-nm)]	κ (nm)	A_{eff} (μm^2)	ω_p^+ (μm)	α (dB/km)	FOM [ps/(nm-dB)]	α_b^* (dB)
LEAF @ 1550 nm	-264	30.33	41.8	3.34	0.212	1248	2.54×10^{-2}
LEAF @ 1590 nm	-172	59.13	43.63	3.47	0.195	885	4.28×10^{-3}
TWRS @ 1550 nm	-173	100.63	49.92	3.68	0.227	760	2.35×10^{-6}
TWRS @ 1590 nm	-173	133.44	61.4	4.02	0.203	851	1.89×10^{-6}
TeraLight @ 1550 nm	-187	118.68	49.99	3.51	0.214	873	6.51×10^{-3}
TeraLight @ 1590 nm	-150	156.74	57.77	3.92	0.195	771	1.4×10^{-2}

$^+$ Petermann spot size; * Bend loss for a single turn of 16 mm.

7. Nonlinear Effects and DCF

Even moderate optical powers can produce significant intensities of light within an optical fiber; under these circumstances the response of the fiber becomes nonlinear. One of the manifestations of this optical nonlinearity is the intensity dependent modal effective index given by the following equation [67,68]:

$$\beta_{\text{NL}} = \beta + \frac{\omega n_2}{c A_{\text{eff}}} P, \tag{69}$$

where β is the propagation constant of the mode in the absence of nonlinearity, $\beta_{\rm NL}$ is the propagation constant in the presence of nonlinearity, n_2 is a constant characteristic of the fiber ($\sim 3.2 \times 10^{-20}$ m^2/W for silica), P is the optical power in the propagating mode, ω is the frequency of the wave and $A_{\rm eff}$ is the effective modal area defined by [22,67]

$$A_{\rm eff} = \frac{\left[\int_0^\infty \int_0^{2\pi} \Psi^2(r) r \, dr \, d\phi\right]^2}{\int_0^\infty \int_0^{2\pi} \Psi^4(r) r \, dr \, d\phi}. \tag{70}$$

It can be shown that $A_{\rm eff} = \pi w_0^2$ under the Gaussian approximation for the fundamental modal field, where $2w_0$ is the mode field diameter.

The intensity dependent propagation constant (or effective index) leads to self phase modulation (SPM) of the wave that induces chirping within the pulse. This happens since the peak of the pulse with a larger power will propagate with a slower speed as compared to the wings of the pulse, which have smaller powers. Since n_2 is positive in silica fibers, SPM leads to an increase in frequency with time; this corresponds to up-chirp and a negative value of g in Eq. (40). In the absence of dispersive effects, the pulse width remains the same. It is well known that a chirped pulse of certain duration has a larger spectral width as compared to an unchirped pulse of the same duration. Thus SPM leads to spectral broadening of the pulse. Stronger the nonlinearity and longer the propagation length, the greater will be the spectral broadening.

In the presence of dispersion, the chirping caused due to SPM will interact with dispersion and lead to a different pulse evolution. Since SPM leads to negative value of the chirp parameter g, if the dispersion is positive ($\sigma < 0$) then the pulse will suffer reduced dispersion as compared to the case when there was no nonlinearity. Thus the dispersion suffered by a pulse while propagating through a G.652 fiber at a wavelength around 1550 nm (corresponding to $\sigma < 0$), will be smaller for higher power pulses than for lower power pulses. This implies that the dispersion compensation required at the end of the span will be different for pulse powers having SPM and this fact needs to be incorporated during system design.

Another factor that needs to be kept in mind is that due to attenuation in the fiber, the pulse power keeps dropping with propagation and hence the local contribution from nonlinear effects will reduce as the length of the fiber increases. In order to take this aspect into account, we define an effective length of the fiber by

$$L_{\rm eff} = \frac{1 - e^{-\alpha L}}{\alpha}, \tag{71}$$

where α is the attenuation coefficient. For $\alpha L \gg 1$, $L_{\rm eff} = 1/\alpha$, and for $\alpha L \ll 1$, $L_{\rm eff} \approx L$, the fiber length.

From Eq. (69) it follows that smaller the effective mode area, stronger will be the nonlinear effects. Standard G.652 SMFs have typically an effective area of about 75 $\sim$ 80 μm^2, at the median operating wavelength within an amplifier band while the corresponding figure for commercially available typical DCFs is 15 $\sim$ 25 μm^2. Hence the sensitivity to nonlinear effects of a signal pulse while propagating through DCFs is much higher than during propagation through the transmission fiber. The difference in nonlinear coefficient and dispersion between the transmission fiber and the DCF implies that the precise location of the DCF in the link becomes an important factor. Thus in a linear system (in the absence of nonlinearity) one could have post- or pre-compensation, i.e., the DCF could be placed either after or at the beginning of the link.

The output pulse would be the same in both cases. On the other hand in the presence of nonlinearity, the response of the system is not the same. A significant amount of work has been carried out on optimization of a dispersion compensated link in terms of the fraction of pre- and post compensation that needs to be employed (see e.g., [69,70]).

8. Conclusions

In this paper we have discussed the basic physics behind dispersion in bulk media and in optical fibers. Dispersion causes intersymbol interference among the bits in a fiber optic communication link and it is very important to overcome dispersion effects to achieve high bandwidth communication systems. At the same time it is necessary to have a finite non zero value of dispersion in the optical fiber to overcome nonlinear effects. This has led to the development of different types of dispersion tailored fibers with various dispersion characteristics. The accumulated dispersion can be compensated using DCFs which are specially designed fibers. Major emphasis in this chapter has been on discussing design issues to realize efficient DCFs. Optical amplifiers coupled with DCFs have revolutionized optical fiber communication systems in recently years and have made possible the realization of multi terabit systems.

Acknowledgment

The authors wish to thank the Editor, Sidhharth Ramachandran for his invitation and giving us the opportunity to contribute this paper. We wish to thank our graduate students Charu Kakkar, Sonali Dasgupta and Kamna Pande for their assistance in the preparation of the manuscript. Authors also like to thank their spouses Raji and Subrata for their patience and understanding.

References

1. Jopson B and Gnauck A, (June 1995), “Dispersion compensation for optical fiber systems”, IEEE Communications Mag, pp. 96–102.
2. Ghatak A and Pal BP, (2002), “Progress in Fiber Optics for Telecommunication”, in the book International Trends in Applied Optics, Ed. A. Guenther, SPIE, Washington, pp. 359–388.
3. Chraplyvy AR, Tkach RW, and KL Walker, (1994), “Optical Fiber for Wavelength Division Multiplexing”, U.S. Patent 5,327,516 (issued July 5, 1994).
4. Peckham DW, Judy AF, and Kummer RB, (1998), “Reduced dispersion slope, non-zero dispersion fiber”, in Proceedings of 24th European Conference on Optical Communication ECOC’98 (Madrid, 1998), pp. 139–140.
5. Liu Y, Mattingly WB, Smith DK, Lacy CE, Cline JA, and De Liso EM, (1998), “Design and fabrication of locally dispersion-flattened large effective area fibers”, in Proceedings of 24th European Conference on Optical Communication ECOC’98 (Madrid, 1998), pp. 37–38.
6. Ryan J, Special report “ITU G.655 adopts higher dispersion for DWDM”, (2001), Lightwave, Vol. 18, no. 10.

7. Frignac Y and Bigo S, (2000), "Numerical optimization of residual dispersion in dispersion managed systems at 40 Gb/s", in Proceedings of Optical Fiber Communications Conference OFC2000 (Baltimore, 2000), pp. 48–50.
8. Danziger Y and Askegard D, (2001), "High-order-mode fiber—an innovative approach to chromatic dispersion management that enables optical networking in long-haul high-speed transmission systems", Opt. Networks Mag., Vol. 2, pp. 40–50.
9. Sakamoto T, (2001), "S-band fiber optic amplifiers", in Proceedings of Optical Fiber Communications Conference OFC'01 (Anaheim, Calif., 2001), paper TuQ1.
10. Thyagarajan K and Charu Kakkar, (2004) S-band single stage EDFA with 25 dB gain using distributed ASE suppression, IEEE Photon. Tech. Lett. **16**, 2448–2450.
11. Rottwitt K and Stenz AJ, (2002), "Raman amplification in lightwave communications systems", in *Optical fiber Telecommunications, Vol. IVA*, I.P. Kaminow and T. Li, eds. (Academic, San Diego, 2002), pp. 213–257.
12. Ouellette F, (1987), "Dispersion cancellation using linearly chirped Bragg grating filters in optical waveguides", Opt. Lett. **12**, 847–849.
13. Takiguchi K, Okamoto K, and Moriwaki K, (1994), "Dispersion compensation using a planar ligthwave circuit optical equalizer", IEEE Photon. Tech. Lett. **6**, 561–564.
14. Antos AJ and Smith DK, (1994), "Design and characterization of dispersion compensating fiber based on LP01 mode", IEEE J. Lightwave Technol. **LT-12**, 1739–1745.
15. Gnauck AH, Jopson RM, Iannone PP, and Derosier RM, (1994), "Transmission of two wavelength multiplexed 10 Gb/s channels over 560 km of dispersive fiber", Electron. Lett., **30**, 727–728.
16. Tsuda H, Okamoto K, Ishi T, Nagnuma K, Inoue Y, Takenouchi H, and Kusukowa T, (1999), "Second and third order dispersion compensator using a high resolution arrayed waveguide grating", IEEE Photon. Tech. Lett. **11**, 569.
17. Ghatak A and Thyagarajan K, (1998), *Introduction to Fiber Optics* (Cambridge University Press, UK).
18. Marcuse D, (1979), "Interdependence of waveguide and material dispersion", App. Opt. **18**, 2930–2932.
19. Tomkos I, Chowdhury D, Conradi J, Culverhouse D, Ennser K, Giroux C, Hallock B, Kennedy T, Kruse A, Kumar S, Lascar N, Roudas I, Sharma M, Voldhanel RS, Wang CC, (2001), "Demonstration of negative dispersion fibers for DWDM metropolitan area networks", IEEE J. Selected Top. Quant. Electron. **7**, 439–460.
20. Li MJ, (2001), "Recent progress in fiber dispersion compensators", Proc ECOC 2001, Amsterdam, Paper ThM1.1, Vol. 4, pp 486-489.
21. Ramaswami R and Sivarajan KN, (1998), *Optical networks: a practical perspective* (Morgan Kaufmann, San Francisco).
22. Agrawal GP, (2001), *Nonlinear Fiber Optics*, 3rd Edition (Academic Press, San Diego).
23. Thyagarajan K, Supriya Diggavi, Anju Taneja and Ghatak AK, (1991), "A simple numerical technique for the analysis of cylindrically symmetric refractive index profile optical fibers", Appl. Opt. **30**, 3877.
24. Pal BP, Kumar A and Ghatak AK, (1981), "Predicting dispersion minimum in step index monomode fiber: comparison of the theoretical approaches", J. Opt. Commun. **2**, 505–507.
25. Akasaka Y, Suguzaki R, and Kamiya T, (1995), "Dispersion Compensating Technique of 1300 nm Zero-dispersion SM Fiber to get Flat Dispersion at 1550 nm Range", in Digest of European Conference on Optical Communication (1995), paper We.B.2.4.

26. Hawtoff DW, Berkey GE, and Antos AJ, (1996), "High Figure of Merit Dispersion Compensating Fiber", in Technical Digest Optical Fiber Communication Conference (San Jose, 1996), Post-deadline paper PD6 (1996).

27. Vengsarkar AM, Miller AE, and Reed WA, (1993), "Highly efficient single-mode fiber for broadband dispersion compensation", in Proceedings of Optical Fiber Communications Conference OFC'93 (San Jose, 1993), pp. 56–59.

28. Grüner-Nielsen L, Knudsen SN, Veng T, Edvold B, and Larsen CC, (1999),"Design and Manufacture of Dispersion Compensating Fiber for Simultaneous Compensation of Dispersion and Dispersion Slope", Tech. Dig. OFC'99, Paper WM13, pp. 232–234.

29. Grüner-Nielsen L, Knudsen SN, Kristensen P, Veng T, Edvold B, and Magnussen T, (2000), "Dispersion Compensating Fibers and Perspectives for Future Developments", Proc. Europ. Conf. Opt. Comm. ECOC'2000, Vol. 1, pp. 91–94.

30. Grüner-Nielsen L, Knudsen SN, Edvold B, Veng T, Edvold B, Magnussen T, Larsen CC, and Daamsgard H, (2000), "Dispersion Compensating Fibers", Opt. Fib. Tech. **6**, 164–180.

31. Knudsen SN, Pedersen MØ, and Grüner-Nielsen L, (2000), "Optimization of Dispersion Compensating Fibers for Cabled Long-haul Applications", Electron Lett. **36**, 2067–2068.

32. Srikant V, (2001) "Broadband dispersion and dispersion slope compensation in high bit rate and ultra long haul systems", in Technical Digest Optical Fiber Communication Conference (Anaheim, 2001), paper TuH1.

33. Mukasa K, Akasaka Y, Suzuki Y, and Kamiya T, (1997), "Novel network fiber to manage dispersion at 1.55 μm with combination of 1.33 μm zero dispersion single-mode fiber", Proc. Europ. Conf. Opt. Comm. ECOC'97, pp. 127–130.

34. Winful HG, (1985), "Pulse compression in optical fibers", Appl. Phys. Lett. **46**, 527–529.

35. Eggleton BJ, Stephens T, Krug PA, Dhosi G, Brodzeli Z, and Ouellette F, "Dispersion compensation over 100 km at 10 Gb/s using a fiber grating in transmission", in Technical Digest Optical Fiber Communication Conference (San Jose, 1996), Post-deadline paper PD5 (1996).

36. Pal BP, (2000), "All-fiber guided wave components", in *Electromagnetic fields in unconventional structures and materials*, Eds. O.N. Singh and A. Lakhtakia (John Wiley, New York), pp. 359–432.

37. Poole CD, Weisenfeld JM, and Giovanni DJ, (1993), "Elliptical-core dual-mode fiber dispersion compensator", IEEE Photon. Tech. Lett. **5**, 194–197.

38. Poole CD, Weisenfeld JM, DiGiovanni DJ, and Vengsarkar AM, (1994), "Optical fiber-based dispersion compensation using higher order modes near cutoff", IEEE J. Lightwave Technol. **12**, 1746–1758.

39. Tur M, Herman E, and Danziger Y, (2001), "Nonlinear properties of dispersion management modules employing high-order mode fibers", in Technical Digest Optical Fiber Communication Conference (Anaheim, 2001), paper TuS5.

40. Ramachandran S, Mikkelsen B, Cowsar LC, Yan MF, Raybon G, Boivin L, Fishteyn M, Reed WA, Wisk P, Brownlow D, Huff RG and Gruner-Nielsen L, (2000), "All-fiber, grating-based, higher-order-mode dispersion compensator for broadband compensation and 1000-km transmission at 40 Gb/s", Proc. European Conf. Optical Comm., PD-2.5.

41. Ramachandran S, Mikkelsen B, Cowsar LC, Yan MF, Raybon G, Boivin L, Fishteyn M, Reed WA, Wisk P, Brownlow D, Huff RG and Gruner-Nielsen L, (2001), "All-fiber, grating-based, higher-order-mode dispersion compensator for broadband compensation and 1000-km transmission at 40 Gb/s", IEEE Photon. Tech. Lett. **13**, 632–634.

42. Ramachandran S, Ghalmi S, Chandrasekhar S, Ryazansky I, Yan M, Dimarcello F, Reed W, and Wisk P, (2003), "Wavelength-continuous broadband adjustable dispersion compensator using higher order mode fibers and switchable fiber-gratings", IEEE Photon. Tech. Lett. **15**, 727–729.

43. Gnauck AH, Garrett LD, Danziger Y, Levy U, and Tur M, (2000), "Dispersion and dispersion-slope compensation of NZDSF over the entire C band using higher order mode fibre", Electron. Lett. **36**, 1946–1947.

44. Izadpanah H, Lin C, Gimlett H, Johnson H, Way W, and Kaiser P, (1992), "Dispersion compensation for upgrading interoffice networks built with 1310 nm optimized SMFs using an equalizer fiber, EDFAs, and 1310/1550 nm WDM", Tech Digest Optical Fiber Communication Conference, Post-deadline paper PD15, pp. 371–373.

45. Onishi M, Koyana Y, Shigematsu M, Kanamori H, and Nishimura M, (1994), "Dipsersion compensating fiber with a high figure of merit of 250 ps/nm.dB", Electron. Lett. **30**, 161–163.

46. Uchida N, (2002), "Development and future prospect of optical fiber technologies", IEICE Trans. Electron. **E85 C**, 868–880.

47. Tewari R, Basu M, and Acharya HN, (1998), "Modified figure of merit for dispersion compensated optical fibers", Opt. Commun. **155**, 260–262.

48. Thyagarajan K, Varshney RK, Palai P, Ghatak AK, and Goyal IC, (1996), "A novel design of a dispersion compensating fiber", IEEE Photon. Tech. Lett. **8**, 1510–1512.

49. Auguste JL, Jindal R, Blondy JM, Clapeau M, Marcou J, Dussardier B, Monnom G, Ostrowsky DB, Pal BP and Thyagarajan K, (2000), "−1800 ps/km-nm chromatic dispersion at 1.55 μm in a dual concentric core fiber", Electron. Lett. **36**, 1689–1691.

50. Mukasa K, Akasaka Y, Suzuki Y, and Kimaya T, (1997), "Novel network fiber to manage dispersion at 1.55 μm with combination of 1.3 μm zero-dispersion single-mode fiber", in Proc. 23rd European Conference on Opt. Commn. (ECOC'1997), Edinburgh, Session MO3C, pp. 127–130.

51. Nakazima K and Ohashi M, (2002), "Design considerations for inverse dispersion fiber", IEICE Trans. Electron. **E85-C**(4), 896–902.

52. Bakshi B, Manna M, Mohs G, Kovsh DI, Lynch RL, Va M, Golovchenko EA, Patterson WW, Anderson WT, Corbett P, Jiang S, Sanders MM, Li H, Harvey GT, Lucero A, and Abbott, SM, (2004), "First dispersion flattened transpacific undersea system: From design to trabits/s field trial", IEEE J. Lightwave Technol., 233.

53. Auguste J-L, Blondy JM, Maury J, Marcou J, Dussardier B, Monnom G, Jindal R, Thyagarajan K, and Pal BP, (2002), "Conception, realization, and characterization of a very high negative chromatic dispersion fiber", Opt. Fib. Technol. **8**, 89–105.

54. Thyagarajan K and Kaur Jagneet, (2000), "A Novel Design of an Intrinsically gain Flattened Erbium doped fiber", Opt. Commun. **183**, 407.

55. Thyagarajan K and Anand J Kaur, (2003), "Intrinsically gain-flattened staircase profile erbium doped fiber amplifier", Opt. Commun. **222**, 227–233.

56. Thyagarajan K and Kakkar Charu, (2003), "Fiber design for broadband, gain flattened Raman fiber amplifier", IEEE Photon. Tech. Lett. **15**, 1701–1703

57. Thyagarajan K and Kakkar Charu, (2004), "Novel fiber design for flat gain Raman amplification using single pump and dispersion compensation in S-band", IEEE J. Lightwave Technol. **22**, 2279–2286.

58. Palai P, Varshney RK, and Thyagarajan K, (2001), "A dispersion flattening dispersion compensating fiber design for broadband dispersion compensation", Fib. Int. Opt. **20**, 21–27.

59. Pal BP and Pande K, (2002), "Optimization of a dual-core dispersion slope compensating fiber for DWDM transmission in the 1480-1610 nm band through G.652 single-mode fibers", Opt. Comm. **201**, 335–344.

60. Huttunen, A and Torma P, (2005), "Optimization of dual core and microstructure fiber geometries for dispersion compensation and large mode area", Opt. Express **13**, 627–635.

61. Jiang Y, Howley B, Shi Z, Zhou Q, Chen RT, Chen M, Brost G and Lee C, (2005), "Dispersion-enhanced photonic crystal fiber array for a true time delay structured X-band phased array antenna", IEEE Photonics Technol. Lett. **17**, 187–189.

62. Ni Y, Zhang L, An L, Peng J and Fan C, (2004), "Dual core photonic crystal fiber for dispersion compensation", IEEE Photonics Technol. Lett. **16**, 1516–1518.

63. Pande K and Pal BP, (2003), "Design optimization of a dual-core dispersion compensating fiber with high figure of merit and a large effective area for dense wavelength division multiplexed transmission through standard G.655 fibers", Appl. Opt. **42**, 3785–3791.

64. Tjugiarto T, Peng GD, and Chu PL, (1993), "Bandpass filtering effect in tapered asymmetrical twin-core optical fibers", Electron. Lett. **29**, 1077–1078.

65. Ortega B and Dong L, (1999), "Selective fused couplers consisting of a mismatched twin-core fiber and a standard optical fiber", IEEE J. Lightwave Technol. **17**, 123–128.

66. Kakkar Charu and Thyagarajan K, (2005), "Broadband, lossless DCF utilizing flat-gain Raman amplification in asymmetrical twin-core fiber", Appl. Opt. **44**, 2396–2401.

67. Thyagarajan K, (2003), "Linear and nonlinear propagation effects in optical fibers", in *Optical Solitons: Theoretical and Experimental challenges*, K Porsezian and V Kuriakose (Eds.), Lecture Notes in Physics, Vol. 613 (Springer-Verlag, Heidelberg).

68. Thyagarajan K and Ghatak A, (2004), "Nonlinear optics" in *Encyclopaedia of Modern Optics*, B. Guenther, L. Bayvel and D. Steel (Eds.), (Elsevier, UK).

69. Palai P and Thyagarajan K, (1997), "Effect of self phase modulation on a dispersion compensated link employing a dispersion compensating fiber", Opt. Commun. **143**, 203–208.

70. Naito T, Terahara T, Shimojoh N, Yorita T, Chikama T, and Suyama M, (2000), "Pre and post dispersion compensation in WDM transmission system, IEICE Trans. Commun. **E83-B**, 1409–1416.

DOI: 10.1007/s10297-006-0070-8
Originally published in J. Opt. Fiber. Commun. Rep. 3, 159–220 (2006)

Static and tunable dispersion management with higher order mode fibers

Siddharth Ramachandran and Man F. Yan

OFS Laboratories, Murray Hill, NJ 07974, USA
Email: sidr@ieee.org

Abstract. Few mode fibers have recently attracted a lot of attention, because of the prospect of enhanced design flexibility, unique modal properties, and the existence of several simultaneous light-paths in them. After the pioneering experiments by Craig Poole from Bell Labs in 1993, an application that faded away but saw a re-emergence in 2000–2003 was higher order mode dispersion compensation. In this scheme, mode converters are used to selectively propagate the signal in a higher order mode of a few-mode fiber.

Demonstrations over the last few years have shown that this novel technology can provide several benefits over the conventional dispersion compensating fiber, such as lower nonlinearity, higher dispersions, potentially lower loss, and most interestingly, a format to realize tunable dispersion compensation devices. It also has attendant trade-offs arising from the need to manage modal interference, and a complex architecture that may make it more costly. This talk will review the physics and technology of the higher order mode dispersion compensator and discuss its future directions.

1. Introduction

Common to several fiber-devices is the single mode fiber (SMF). Two ubiquitous devices on this platform are the erbium doped fiber amplifier (EDFA) and the dispersion compensating fiber [1,2] (DCF). They have together enabled repeater-less wavelength division multiplexed (WDM) transmission as the preferred means of optical communications. The SMF is a natural choice for fiber-devices, because it is compatible with the rest of the transmission line, and propagates only one mode, thereby avoiding mode coupling, differential modal properties and related problems of a multimode fiber.

However, in the process, the SMF also eliminates a unique attribute of fibers—the ability to simultaneously co-propagate different modes with specifically tailored

properties for each mode. This paper will describe one such device, the higher order mode (HOM) dispersion compensator, where the signal is intentionally forced to propagate in a mode other than the fundamental mode of a fiber. This schematic opens up the design space for fiber devices, which enables performance superior to DCF, in some cases. It also has some unique attributes, which open up an application space (tunability) that was hitherto the domain of compact bulk-optic, waveguide or grating devices.

1.1. Dispersion Compensation Requirements

1.1.1. Static Dispersion

There are several designs of transmission fibers deployed in a network today, but they share three common dispersive characteristics. In the operational window of 1530–1650 nm of a communications system, their dispersion is nominally positive, and has a positive slope. It is also linear as a function of wavelength. Thus, for broadband dispersion compensation the dispersion compensation module (DCM) should simultaneously match the dispersion as well as dispersion-slope. This can be succinctly stated in terms of the dispersive properties of a DCM as [3]:

$$\begin{aligned} &\tfrac{D'}{D} = \mathrm{RDS}_{\mathrm{comp}} = \mathrm{RDS}_{\mathrm{trans}}, \\ &\mathrm{RDC}_{\mathrm{comp}} = \tfrac{D''}{D} \to 0, \end{aligned} \tag{1}$$

where D is dispersion, the primes indicate derivates with respect to wavelength, RDS stands for "relative dispersion slope," and RDC stands for "relative dispersion curvature." The subscripts "trans" and "comp" stand for the transmission fiber (or link) and compensating device, respectively. The additional constrain of zero RDC is added because while transmission fibers are linear in dispersion versus wavelength, dispersive fibers can in fact be highly nonlinear.

1.1.2. Tunable Dispersion

Long-haul, high-speed transmission links are designed with tight tolerances on their dispersion maps. Statistical variations in the dispersion of transmission fibers, amplifier-hut spacings or ambient conditions can lead to significant transmission penalties. One way to address this problem is by introducing tunable dispersion compensators (TDC) that can provide either dynamic or set-able control. Dynamic control is needed to offset dispersion variations due to environmental changes. Alternatively, set-able dispersion control can address variations in network link-design arising from manufacturing variations in transmission fiber spans or the distance between amplifier huts. A broadband means for set-able dispersion control also facilitates link-design by allowing the prospect of "mixing and matching" different fiber types to realize a transmission span. Any TDC would have to provide dispersion granularity small enough to cover the dispersion tolerance range of a system. Dispersion tolerance is inversely proportional to bit rate, and falls from roughly 1000 ps/nm for 10 Gb/s signals to 40-60 ps/nm for 40 Gb/s data.

Most common TDC technologies exploit the frequency dependent phase response of an optical filter. Examples include planar waveguide-based devices such as ring

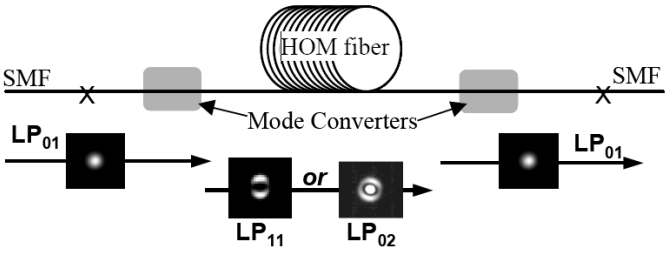

Fig. 1. Schematic of Higher order mode Dispersion compensating module (HOM-DCM). Fundamental LP_{01} mode enters and exits device. Mode converters transform mode between LP_{02} and HOM (e.g. LP_{11}, LP_{02}). Operation requires HOM fiber, mode converters, and robust assembly technique.

resonators [4] and waveguide-gratings [5], free-space devices such as tunable etalons [6] and virtually imaged phase arrays (VIPA) [7], and chirped fiber-Bragg gratings (CFBG) [8,9]. While such devices offer an attractive means to manage dispersion variations in an optical link, they do not possess the versatility, bandwidth, bit-rate or bit-format transparency, and low loss characteristics of their widely deployed static counterpart; namely, the DCF.

1.2. Device Schematic; Component Requirements

A schematic layout for a HOM dispersion-compensating module, the HOM-DCM, is shown in Fig. 1. It illustrates that the device comprises a mode converter at the input and output, respectively, between a suitably designed HOM fiber. The mode converter transforms the incoming signal in the fundamental mode (LP_{01}—Gaussian profile—only mode supported in SMFs) into a HOM, such as the azimuthally symmetric LP_{02} mode, or the anti-symmetric LP_{11} mode. An extension of this schematic, for tunable dispersion compensators, comprises repeating this structure several times in series, and will be the focus of Section 6. There are three essential issues to consider, in constructing a HOM-DCM:

1. The HOM fiber design, for its dispersive characteristics (Section 2).
2. The mode converter: its design, characteristics and performance (Section 3).
3. Assembly technique and fiber design to minimize mode mixing (Section 4).

1.3. Outline

First, we will describe the generic characteristics of different modes in a fiber, with its dispersive properties as the focus. Section 2 will start with providing some physical intuition for dispersive fiber design, and follow that with an analytical theory for a simple fiber waveguide, in order to elucidate the dispersive operation of modes. The treatment will make extensive use of dimensionless parameters to provide a general

framework for modal properties. This section concludes with a discussion of the required design constraints for HOM fibers, and specialized techniques to characterize their dispersion.

Section 3 will exclusively focus on the mode converter—its design as well as performance. Both static as well as dynamic mode converters will be discussed, since both are relevant for different HOM-fiber-based dispersion compensators. The focus will be on fiber gratings as mode converters, because they have proven to be the lowest loss mode-converting technology, to date.

Section 4 will discuss multi-path-interference—noise due to inter-modal interference. This is a key distinction between fiber-devices based on SMF and HOMs. Ultimately, this is an impairment that should be managed by minimizing energy in any mode but the desired one. However, it is also a relatively less-studied topic. While interference noise has been studied in detail for other systems, the vast majority of those systems involve the interference of incoherent signals. The interference suffered by HOM devices is coherent, on the other hand. Hence, this section will describe the range of issues related to it—starting from techniques to measure it, to techniques for minimizing it, in addition to the impact this noise phenomenon has on a real communications system.

Section 5 will then discuss device performance of dispersion compensators made with this technology. Illustrative examples of static dispersion compensators will be provided in Section 5,and the DCF will appear as a benchmark, often, in this section. This section will also give an opportunity to compare the intuitive and theoretical predictions made about HOMs in Section 2, with data from real devices. Section 5 will conclude with systems demonstrations highlighting one of the advantageous attributes of HOM-DCMs—the large effective area of signal propagation that leads to diminished nonlinear-distortions.

Section 6 will describe a tunable dispersion compensator, uniquely enabled by few moded fibers. The section will include illustrations of device as well as systems demonstrations, and will describe some key distinctions between it and the widely studied optical-filter-based TDCs.

Section 7 offers a summary of the HOM fiber device platform, and some thoughts on future evolutions and applications of this technology.

2. Dispersion Engineering of Fiber Eigenmodes

2.1. Physical Intuition Behind Dispersive Modes

Since the wave equations and boundary conditions governing modal properties in optics are analogous to the equations of motion governing the wavefunction of a particle in a box in quantum mechanics, important physical insight can be gained from quantum mechanical analogies. The typical refractive index profile of a dispersive fiber is akin to a potential distribution with three discrete segments—a core and a ring that have index greater than silica, which act as attractive wells for light, and a down-doped trench, which acts as a barrier. The indices and thicknesses of these three regions govern the "rate", as a function of wavelength, with which the mode transitions from residing primarily in the core, to "escaping" to the ring. The propagation constant β, of a mode can be expressed in terms of the mode-field as well as refractive index profile as

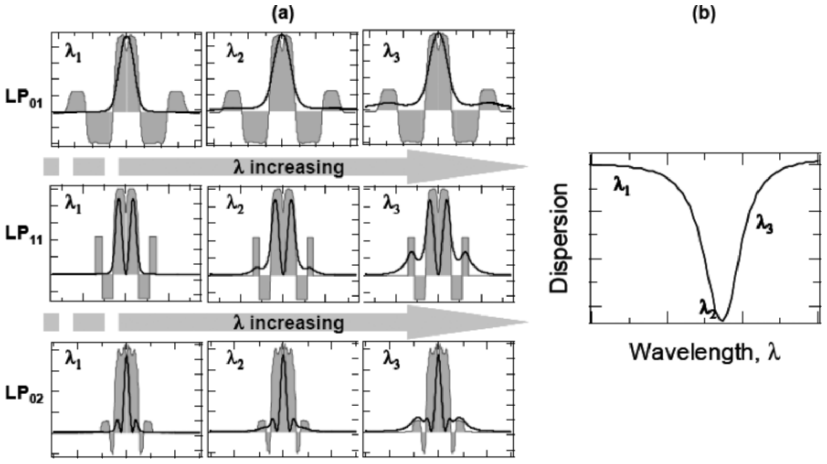

Fig. 2. Canonical refractive index profiles for dispersive LP_{01}, LP_{11}, and LP_{02} modes (grey), and intensity profiles for respective modes (solid lines) at spectral positions relative to the dispersion curve shown in (b). Fiber profiles for each mode scaled to same core size. Thus, radial extent as a fraction of core size for each is the same. As λ increases, dispersive modes rapidly transfer power to the ring. LP_{01}: entire mode expands. HOMs: only sidelobes expand. Hence, HOMs are more dispersive while being tightly guided. Sidelobes also increase design flexibility, because only part of the mode has to expand.

$$\beta^2(\lambda) \leq \left(\frac{2\pi}{\lambda}\right)^2 \iint n^2(r,\lambda)\,|E(r,\lambda)|^2 dA, \tag{2}$$

where r is the radial coordinate, λ is the free-space wavelength of light, $E(r,\lambda)$ is the mode field distribution, $n(r,\lambda)$ is the refractive index profile of the fiber, and $\int\int dA$ signifies an integration across the cross-section of the fiber. Equation (2) shows that the propagation constant of a mode is bounded by the average refractive index of the region in which light exists, weighted by the local intensity profile. Combining this concept with the intuition for designing fibers with specific mode profiles at various wavelengths, yields the general recipe for tailoring the refractive index profiles of a fiber to obtain desired values for $\beta(\lambda)$, and by extension, all its wavelength dependent derivates given by

$$v_g = -\frac{2\pi c}{\lambda^2}\left(\frac{d\beta}{d\lambda}\right)^{-1};\; D = \frac{d}{d\lambda}\left(\frac{1}{v_g}\right), \tag{3}$$

where v_g is the group velocity of a lightwave signal, and D is dispersion.

Figure 2(a) shows the canonical refractive index profiles of fibers that are dispersive in the LP_{01}, LP_{11} and LP_{02} modes respectively, at wavelengths λ_1, λ_2 and λ_3. All 3 fiber-designs lead to similar dispersive characteristics, as shown in Fig. 2(b). The 3 fiber-designs of Fig. 2(a) have different core sizes but the lateral dimensions in the plot have been normalized to the core sizes of the respective fibers. Hence, transition rates of the mode profiles can be compared in relation to the core size. A signature

of a dispersive mode is fast (with respect to wavelength) transition of power from the core to lower index rings. Since light travels faster in lower index regions, the group velocity of a mode increases with wavelength, leading to negative waveguide dispersion [see Eq. (3)]. When the mode is well guided, this effect is small, but as it transitions, say from a core to the cladding or another high index ring, the dispersion becomes large and negative. Finally, after this transition, the mode may either be cutoff, or resume well-guided behavior in the ring. Figure 2(b) plots the typical behavior of dispersion versus wavelength for modes in a fiber, and illustrates this transition from small, to large negative, and back to small dispersion values. For the LP_{01} mode, this transition happens by expanding the entire, roughly Gaussian mode. This concept has been used to make highly dispersive (–1800 ps/nm-km) dispersive fibers [10], while practical designs that are low loss have achieved dispersion values of roughly –300 ps/nm-km [11]. On the other hand, HOMs can affect this transition by radially outward movement of only some of their sidelobes. This physical distinction translates into differences in dispersive behavior for different modes of a fiber.

The presence of sidelobes, and thus the ability to obtain dispersive behavior by only moving a fraction of the energy to the rings, indicates that for similar core-index values, HOMs will be more dispersive than the LP_{01} mode. Note from Fig. 2(a), that the HOMs are better confined (for spectral ranges with comparable dispersion), than the LP_{01} mode. This suggests that for similar dispersion values, HOMs are better guided and hence experience lower bend or radiation losses. Finally, HOMs provide a larger effective area A_{eff}, for signal propagation because they occupy a larger modal area compared to the LP_{01} mode (not obvious from Fig. 2 because the radial dimension is scaled). We will now test these intuitive assertions with a simple analytic formulation for modal properties in step index waveguides.

2.2. *Dispersive Properties of Guided Modes*

An elegant theoretical motivation for using HOMs for dispersion compensation was provided by Poole and coworkers [12]. Simple analytical solutions for the dispersive properties of any guided mode can be obtained for step index fibers that comprise only a core and a cladding [13]. In the following treatment, dispersion, RDS, A_{eff} and fractional power in the core, are compared for different modes. All quantities are expressed in terms of normalized or dimensionless terms that do not explicitly depend on core size. Hence, they allow comparing modal properties of different fibers, where each one is optimized for dispersive behavior of a specific mode. This analysis considers only waveguide dispersion, and neglects material dispersion, which is small for highly dispersive waveguides. The propagation constant, β, defined in Eq. (2) can be recast as

$$\beta = kn_{\text{eff}} = kn_{\text{cl}}\left(\frac{1+\Delta W^2}{V^2}\right), \tag{4}$$

where $k = 2\pi/\lambda$ is the free-space propagation constant; n_{eff} is the effective index of the modes; n_{cl} is the index of the cladding, $\Delta = (n_{\text{co}} - n_{\text{cl}})/n_{\text{cl}}$ is the relative difference between the core (n_{co}) and cladding indices; and V is the normalized frequency, related to the core radius a, by

$$V = ka(n_{\text{co}}^2 - n_{\text{cl}}^2) \approx kan_{\text{cl}}\sqrt{2\Delta}. \tag{5}$$

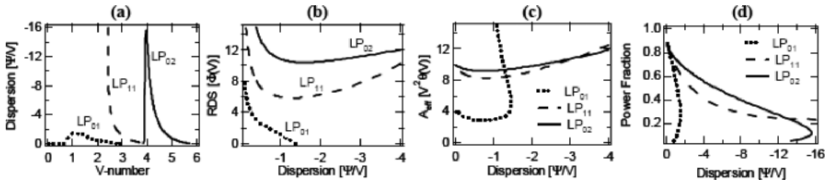

Fig. 3. Dimensionless modal properties normalized for core size, for matched clad fiber. (a) Normalized dispersion vs. V-number. HOMs are significantly more dispersive, (b) RDS vs. dispersion. LP_{01} can achieve wider range, but HOMs more suitable for high RDS, (c) A_{eff} vs. dispersion. HOMs have larger area for comparable dispersion, (d) Power fraction in core vs. dispersion. For large dispersion, HOMs have higher power in core, implying lower bend losses.

The waveguide parameter W, is determined by the characteristic equation which expresses the boundary conditions of the mode field at the core-cladding interface by

$$U\frac{J_{l-1}(U)}{J_l(U)} = -W\frac{K_{l-1}(W)}{K_l(W)}, \tag{6}$$

where $J_l(U)$ and $K_l(W)$ are Bessels functions of the first and second kind, respectively, and U, W are related to V by

$$V^2 = U^2 + W^2. \tag{7}$$

The chromatic dispersion values of different fiber modes are given as

$$D = \frac{d}{d\lambda}\left[\frac{1}{c}\frac{d\beta}{d\lambda}\right] = \frac{n_{\mathrm{cl}}\Delta}{c\lambda}\frac{\Psi(V)}{V}, \tag{8}$$

where $\Psi(V)$ is a dimensionless function given as

$$\Psi(V) = V^2\frac{d^2}{dV^2}\left(\frac{U^2}{V^2}\right). \tag{9}$$

Equation (8) allows analyzing the dispersive properties of different modes with the normalized parameter $\Psi(V)/V$, which is independent of core size. Figure 3(a) plots Ψ/V as a function of V, for the LP_{01}, LP_{11} and LP_{02} modes. Note that the x-axis is the normalized frequency V, and hence small x-axis values on this plot correspond to large wavelength—the x-axis in Fig. 2(b). For dispersion compensation, negative dispersion as well as dispersion slope is required, which corresponds to the regions where Ψ/V is negative with a downward slope on this plot. This plot shows that for a given Δ, the dispersion magnitude of HOMs is several times larger than that for the LP_{01} mode, confirming the intuitive arguments of Section 2.1 that HOMs are more dispersive.

For practical dispersion compensation applications, the dispersive device should not only have large negative dispersion, but it must also match the dispersion slope of the transmission fiber. As described in Section 1.1.1, this is satisfied by matching the RDS of the transmission fiber and DCF. The RDS can be restated as

$$\mathrm{RDS} = -\frac{1}{\lambda}\frac{V}{\Psi(V)}\frac{d\Psi}{dV} = -\frac{1}{\lambda}\Phi(V). \tag{10}$$

The dimensionless RDS $\Phi(V)$, is plotted for the first 3 modes as a function of normalized dispersion Ψ/V in Fig. 3(b). While the LP_{01} mode is much less dispersive than the HOMs, it can achieve a much larger range of RDS values. This plot shows that low RDS fibers may be more easily designed for the LP_{01} mode, while the HOM is better suited for large RDS values—in fact for the more desirable case of large dispersion fibers, the RDS of HOMs increases. While the LP_{01} mode can also achieve large RDS values, the curve is steeper for high RDS, indicating that the fiber will have larger dispersion curvature (RDC, which should be minimized), and may be more sensitive (rapid changes in a parameter indicate that the mode would be susceptible to dimensional perturbations).

The effective areas A_{eff} of guided modes is given by

$$A_{\mathrm{eff}} = 2\pi\frac{\left[\int_0^\infty E^2 r dr\right]^2}{\int_0^\infty E^4 r dr} = 2\pi a^2\frac{\left[\int_0^1 \frac{J_l^2(Ux)}{J_l^2(U)}xdx + \int_1^\infty \frac{K_l^2(Wx)}{K_l^2(W)}xdx\right]^2}{\left[\int_0^1 \frac{J_l^4(Ux)}{J_l^4(U)}xdx + \int_1^\infty \frac{K_l^4(Wx)}{K_l^4(W)}xdx\right]} = \frac{\lambda^2 V^2\theta(V)}{4\pi n_o^2\Delta}. \tag{11}$$

Figure 3(c) is a plot of dimensionless effective area $V^2{\cdot}\theta(V)$, as a function of normalized dispersion Ψ/V. In the dispersive regime, A_{eff} is significantly larger for HOMs in comparison to the LP_{01} mode. Thus, HOM-based devices are less susceptible to nonlinear distortions, as will be demonstrated in Section 5.5. Figure 3(c) shows that the LP_{01} does attain significantly larger A_{eff} values, but in this regime, the dispersion magnitude decreases [denoted by λ_3 in the dispersion plot of Fig. 2(b)]. This yields negative RDS, and hence is not useful for dispersion compensation. In addition, the mode also becomes lossy and unstable, as will be shown below.

Dispersive modes are by definition, not strongly guided by a waveguide core, and are susceptible to bend and radiation losses. A useful proxy for bend losses is the fraction of power in the core—more power in the core implies less power reaches the protective, high-index, polymer jacket of a fiber, whereupon it is radiated. For a weakly guiding fiber, the fractional power in the core, P_{core}, can be given as a dimensionless parameter:

$$\frac{P_{\mathrm{core}}}{P_{\mathrm{total}}} = 1 - \frac{U}{V}\frac{dU}{dV}. \tag{12}$$

Figure 3(d) is a plot of modal power fraction, as a function of normalized dispersion Ψ/V. This plot shows that for large dispersion values, the fractional power in the core is much higher for the HOMs, indicating that for high dispersion values, they would be less lossy. As we will see in Section 5, complex waveguide designs indicate that dispersive LP_{01} fibers can also be made with low bend loss, and the above analysis is strictly true only for step-index waveguides. Nevertheless, the larger Δs needed for LP_{01}-fibers makes them susceptible to higher scattering losses and shear stress losses [14], since these loss values scale with Δ of a fiber.

The manufacturability or sensitivity of dispersive fibers can be deduced from Eq. (8), and expressed in terms of relative changes in dispersion δD, as a function relative changes in core index $\delta\Delta$, and core radius δa, as

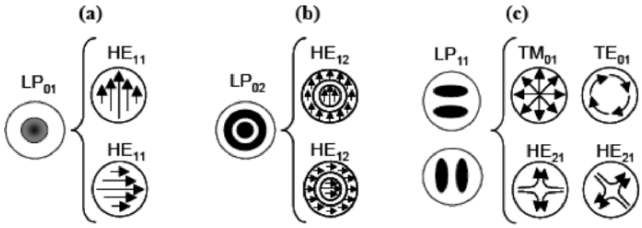

Fig. 4. Scalar (left) and vector (right) representations of the LP_{01} (a), LP_{02} (b), and LP_{11} (c) modes. Even LP_{0m} modes comprise degenerate linearly polarized pairs of vector modes. Odd LP_{1m} modes not pure modes. Comprise 4 almost degenerate vector modes, with slightly different β. For oval fiber, true solution for odd eigenmodes resemble scalar LP_{11} pair.

$$\frac{\delta D}{D_o} = \frac{\delta \Delta}{2\Delta_o} - \frac{\delta a}{a_o}. \tag{13}$$

Since the HOM requires a larger nominal core radius a, we expect a smaller change in dispersion for random fluctuations in fiber dimensions (δa). Thus, a dispersive HOM is less sensitive to fiber diameter variations. However, HOMs would be more sensitive to core index variation $\delta\Delta$s since they require smaller core Δs. Fiber diameter fluctuations are usually harder to control than preform index variations, and hence HOMs would be more stable with respect to manufacturing variations, in comparison to DCFs of comparable dispersion values.

The comparisons made above are agnostic to dimensions of a fiber, because none of parameters were explicitly dependent on core size, a. This is important because different modes are dispersive for different core dimensions. However, normalized dispersion as well as A_{eff} was explicitly dependent on Δ. Since Δs, being bounded by manufacturing constraints, are similar for different dispersive fibers, previous comparisons independent of Δ accurately represent the available fiber design space.. While advanced manufacturing capabilities and numerical design tools today facilitate much more complex waveguides (as opposed to matched clad structures considered here), the comparison between properties of different modes should show similar trends.

2.3. HOM Choice and Design Criteria

While HOMs appear attractive, the other important question to ask is, *which* HOM is appropriate? The first demonstration of dispersive fibers operating in a HOM used an LP_{11} mode with dispersion values of –200 to –700 ps/nm-km [12,15]. This seems like a good choice for an HOM, since it yields the benefits of highly dispersive modes, without introducing too many guided modes, which may cause modal mixing problems (noise due to mode mixing is described in Section 4). However, there are some inherent problems with the LP_{11} mode.

Solutions to the scalar wave equation yield the eigenmodes LP_{01}, LP_{11} or LP_{02}. However, the rigorous vector solution reveals [16] that while the even LP_{0m} modes comprise two strictly degenerate, orthogonally polarized modes, the LP_{11} mode comprises 4 almost degenerate modes—TE_{01}, HE_{21}even, HE_{21}odd, and TM_{01}. Figures

4(a) and (b) illustrate the scalar as well as vector representations of the even, LP_{01} and LP_{02} modes, respectively. Figure 4(c) shows the field distributions for the two orientations of the scalar LP_{11} mode, as well as its 4 distinct vector mode counterparts. The propagation constants for the vector modes comprising the LP_{11} mode are slightly different. This is expected, since the TE mode has electric field tangential to the waveguide boundary [Fig. 4(c)], while the field of the TM mode is normally incident. Since the phase shift at an index-boundary depends on the incidence-angle of the E-field vector, the propagation constants for TE_{01} and TM_{01} will differ. The pair of HE_{21} modes are mixtures of normally and tangentially incident electric field vectors on a waveguide boundary, and thus have identical propagation constants.

The difference in propagation constants between modes of the LP_{11} triplet increases with modal power at index boundaries [17]. Since by definition a dispersive mode has a lot of power in the transition regions, the propagation constants are vastly separated. Thus, the propagation constant, and hence dispersion of this mode, will depend on the state of polarization (SOP) of light in the waveguide, leading to severe polarization mode dispersion (PMD) problems. The other problem is that while the modes in the LP_{11} quartet are separated enough to lead to PMD, they are not sufficiently separated to avoid mode mixing between them.

Poole and coworkers had attempted to address these problems with two modifications. One was by intentionally making oval fibers, in which case the eigenmodes are no longer the vector quartet shown in Fig. 4(c), but look similar to the scalar profiles on that plot (they still have different propagations for different SOPs). The advantage is that the propagation constants for the different orientations of the LP_{11} mode [see Fig. 4(c)] are vastly separated, and bending the fiber in one direction preferentially radiates the LP_{11} mode of one orientation [18]. This effectively decreases the well-guided (low loss) modes to 3—the LP_{01}, and the LP_{11} of one orientation and two SOPs, hence decreasing modal mixing [19]. The second was to control the SOP entering the device and/or use a polarization-rotating mirror to "double-pass" the signal through the fiber so as to average the polarization response [12,19].

Both these solutions pose significant barriers for realizing a practical device. Spooling a fiber so that one of the elliptical axes line up with the spooling axis is very complex and not amenable to a manufacturing setup. The use of polarization controllers or polarization rotating mirrors immediately requires dynamic feedback control to ensure optimal device operation. This is infeasible for a passive device.

Hence, future work with HOM-DCMs migrated to the LP_{02} mode. Several design criteria need to be satisfied to enable a practical module. Obviously, the dispersion and dispersion-slope for the LP_{02} mode should be tailored such that the RDS of this mode matches that of the variety of transmission fibers, as indicated in Section 1.1.1. Section 5 discusses experimental results and characteristics of HOM fibers, and we will show that the high-dispersion, low-loss attributes of the LP_{02} mode have enabled fabricating fibers with record high figures of merit (FOM = dispersion/loss). There are two other important design objectives for LP_{02} fibers.

The few moded nature of HOM fibers makes them susceptible to mode mixing (see Section 4). Mode mixing is due to detuned resonant coupling induced by random perturbations, between co-propagating modes in a fiber, and its efficiency is inversely proportional to the difference in propagation constants between the modes. Thus, any LP_{02} dispersive fiber design must ensure that guided modes other than the dominant

mode are sufficiently separated in n_{eff} or β. Indeed, one of the arguments against the LP_{11} mode was the presence of 3 closely spaced modes (in β).

The other design objective primarily concerns fiber-gratings used as mode converters (to be described in Section 3). A preferred mode converter for the HOM-DCM is a fiber grating induced in a fiber *similar* to the dispersive HOM fiber. As will be shown in Section 3, very broad bandwidth mode converters can be obtained in HOM fibers at the wavelength where the group velocities of the LP_{01} and LP_{02} modes match—a condition called the turn-around-point (TAP) for reasons to be elucidated in Section 3. Hence, HOM fibers for grating mode converters should be designed so that their LP_{02} mode profiles are similar to the main HOM fiber used for dispersion (so the signal efficiently transmits between the two fibers), and should simultaneously possess a TAP in the spectral range of interest for the device.

2.4. Measurement of HOM Dispersion

To characterize fibers, either during design cycles, or for building DCMs with precise lengths of fiber (dispersion values), its dispersion can be measured by the widely used radio frequency (RF) phase-shift technique [20]. While this is readily applicable for DCFs, measuring HOM dispersion would require assembling full modules, which comprises strong mode converters (Section 3), as well as careful assembly (Section 4). In the absence of the above precautions, a commercial test-set would measure the *effective* dispersion of a mixture of randomly coupled modes. Hence, techniques to accurately measure HOM dispersion without full module assembly have been developed, and are described here.

2.4.1. Spectral Interferometry

Spectral interferometry is a well-known technique to measure dispersion, and commercial test-sets are now available for measuring the dispersion of WDM components [21]. Typically, for HOM fibers, a simple splice with SMF excites both the LP_{01} and LP_{02} modes, and hence a single HOM fiber is an in-built two-path interferometer, as shown by Menashe et al [22]. Thus, for an HOM fiber with energy $|E_0|^2$ in one mode, and energy $\eta|E_0|^2$ in the other, interference leads to an output P_{out} given by

$$P_{\text{out}} \propto 2\eta^2 |E_0|^2 \cos\left(\frac{2\pi}{\lambda}\Delta n_{\text{eff}}(\lambda) L\right), \tag{14}$$

where $\Delta n_{\text{eff}}(\lambda)$ is the difference in effective index between the LP_{01} and LP_{02} modes, L is the length of HOM fiber, and λ is wavelength. The fringe spacing $\Delta\lambda$, of this oscillatory spectrum is related to the difference in group-index between the two modes Δn_g, given by

$$\Delta\lambda = \frac{\lambda^2}{\Delta n_g(\lambda) L}. \tag{15}$$

Since $D = d(1/v_g)/d\lambda$ and $n_g = c/v_g$, where c is the speed of light and v_g is the group velocity of a mode, the fringe spacing yields the dispersion *difference* between the two modes. In addition, the LP_{01} dispersion can be easily measured by the conventional phase-shift technique, when the mode-strippers are employed to

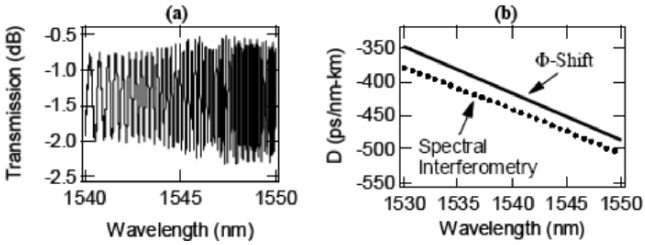

Fig. 5. (a) Interference fringes between LP_{01} and LP_{021} in a 10-m long HOM fiber. Fringe spacing changes dramatically with wavelength. (b) Dispersion deduced from spectral interferometry and direct phase shift measurement – 4–8% error.

radiate all HOMs. Thus, the LP_{02} dispersion is obtained from spectral interferometry complemented by conventional measurement of the LP_{01} mode.

Figure 5(a) shows a typical interference spectrum for a 10-m-long HOM fiber, measured with a tunable laser with 3 pm tuning resolution. Signal processing and appropriate windowing techniques enable obtaining a Fourier peak of local fringes as a function of wavelength, which is then used to deduce dispersion using Eq. (15). Figure 5(b) shows a plot of LP_{02} dispersion measured by this technique, and is compared with a phase shift measurement on a fully assembled module with 2 km of HOM fiber. Errors of 4–8% are primarily because the 10-m HOM fiber section may not be representative of the 2-km spool. Thus, the drawback of this technique is that device length fibers cannot be measured, though the advantage is the very simple and quick measurement, which enables quickly characterizing fibers during design cycles.

2.4.2. RF Modulation Measurements

Phase noise in laser sources can be coupled to intensity noise in an interferometer. The frequency response of P_{out} in Eq. (14) can be obtained from its Fourier transform as [23]:

$$P(f) \propto \frac{\Delta f}{f^2 + \Delta f^2} \left\{ 1 + e^{-4\pi\,\Delta f\,\tau} - 2\,e^{-2\pi\,\Delta f\,\tau}\,\cos\left(2\pi f \tau\right) \right\}, \qquad (16)$$

where Δf is the source linewidth, f is the radio frequency (RF), and τ is the relative group delay per unit length, between the LP_{01} and LP_{02} modes. This is related to dispersive parameters by $\tau = \Delta n_g / c$, where the relationship of Δn_g with differential dispersion was outlined in the previous section (2.4.1). $P(f)$ in Eq. (16) can be measured by an electrical spectrum analyser (ESA) recording the photocurrent of detector at the HOM fiber output. Measuring the period of the frequency spectrum yields τ, and when the measurement is repeated over lasers at different wavelengths, the differential dispersion can be obtained [24].

The measurement setup comprises a bank of DFB lasers multiplexed on to a fiber, which is connected to a 3-dB mode coupler (easily obtained with long period grating

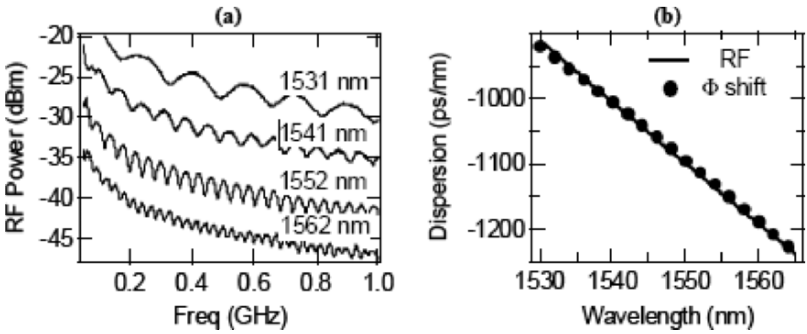

Fig. 6. RF measurement of intensity modulation over 2-km-long HOM fiber. (a) RF spectra at different DFB λ's—fringe spacing $\propto 1/\tau$. (b) Deduced dispersion. $< 0.5\%$ error with respect to phase-shift reference.

described in Section 3). This is followed by the HOM fiber under test whose output is mapped on to an SMF, connected to a photodetector and ESA. Figure 6(a) shows typical ESA spectra obtained at different wavelengths, clearly showing the oscillatory behavior, related to group delay τ. Figure 6(b) shows the dispersion measured over a 5.25-km spool of HOM fiber (circles). Also shown is the reference, RF phase-shift measurement made on a module made from this fiber (solid line)—errors of the order of only 0.5% occur [25]. As in the case of spectral interferometry, only the differential dispersion can be obtained by this technique, and an independent measurement of the LP_{01} mode is required. In fact, this technique is in principle identical to spectral interferometry. The distinction is that fringes smaller than 100 fm can be measured now, thus enabling measurements on device-length fiber with negligible errors.

2.4.3. Gated Pulse Measurements

Direct instantaneous frequency measurements [26] (DIFM) excite a device under test with a short pulse, large bandwidth source, following which the waveform is detected by either by a fast sampling scope (to measure its temporal intensity pattern) or an optical spectrum analyser (OSA-to deduce its spectral response), after passing through an interferometer of delay T. The setup is shown in Fig. 7(a). Simultaneous measurement of the temporal and spectral interferograms yield dispersion of the device, because the time varying part of the output I_3 can be shown to be

$$I_3 = I_1 \left[\Omega(t - T/2)\right] 2\pi\Omega'(t - T/2) \exp\left[-iT\Omega(t - T/2)\right] + \text{c.c.}, \qquad (17)$$

where I_1 is the input intensity [see Fig. 7(a)], Ω is the instantaneous frequency of the electric field, defined as the inverse function of the modal group delay τ by $\Omega[\tau(\omega)] = \omega$, where ω is frequency. Equation (17) shows that measuring the temporal interference patterns yields the phase $T\Omega(t - \tau/2)$ up to an arbitrary constant $T\omega_0$. Further, a spectral interferogram will yield one of the constants T, so that group delay can be

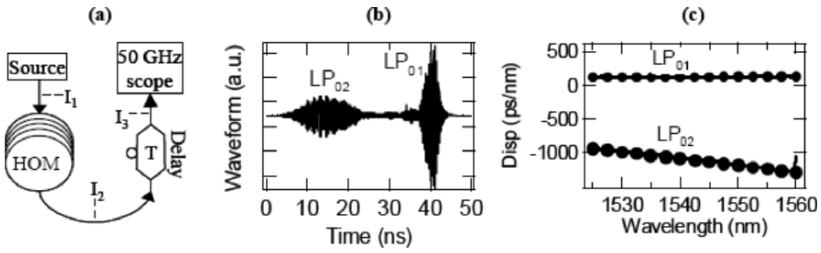

Fig. 7. (a) DIFM measurement setup. Measures temporal and spectral interference. (b) Sample temporal interference—LP_{01} and LP_{02} fringes separated by modal group delay. (c) Dispersion of both modes measured with DIFM (circles) and phase shft technique (line). DIFM yields $\sim$ 0.5% accuracy.

determined up to an arbitrary constant. The important attribute of this experimental technique is that the temporal interference patterns for a two-moded structure (such as HOM fibers) would be distinct for the two modes, because the different group-delays for the LP_{01} and LP_{02} mode ensure the signals in the two modes do not temporally coincide at the output. This is illustrated in Fig. 7(b) which shows a temporal waveform for a 5.99-km-long HOM fiber excited by a 40-nm wide pulsed source centered at 1540nm—note that two distinct interference patterns are obtained for the two modes. Figure 7(c) shows the dispersion deduced from the measurement shown in Fig. 7(b)—both the LP_{01} as well as LP_{02} dispersions are obtained. The markers show experimental results from this measurement, while the solid lines show the results of a reference measurement with the RF phase-shift technique. Dispersion values ranging from +130 ps/nm to –1200ps/nm can be easily measured, and measurement accuracy is very high (errors $\sim$ 0.5%) [27].

This technique can measure dispersions of long lengths of fiber, as with the RF measurement technique (Section 2.4.2), but has the added advantage of measuring both modes simultaneously, obviating the need for a reference measurement. However, the setup and measurement are more complex than the previous two techniques.

2.5. Summary

A physically intuitive picture of dispersive behavior for different spatial modes in a fiber was presented. It suggested that HOMs of fibers are attractive candidates for use in dispersion compensation, because they possess several favourable attributes. This was further investigated with a simple analytical formulation, which enabled studying modal properties of interest, such as dispersion, RDS, A_{eff} and loss, for waveguides that would either guide a dispersive LP_{01}, LP_{11} or LP_{02} mode. These comparisons showed that HOMs are in principle, more dispersive for lower loss, and have a larger A_{eff} for signal propagation. All these properties are important pluses for dispersion compensation applications. The range of RDS values that can be attained by the LP_{01} mode is larger, while HOMs appear to be more stable for high RDS values. Hence, for applications requiring high RDS, HOMs may be more suitable while for low RDS applications, the LP_{01} mode may be a better solution. These conclusions address

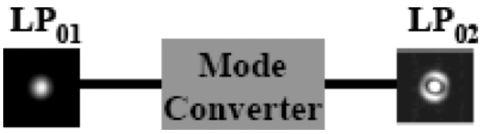

Fig. 8. Schematic illustration of a mode conversion device. Converts the fundamental mode into a HOM, or vice-versa. Should offer high extinction as well as be low loss.

only the modal behavior, and operation in HOMs requires other considerations that will be addressed in the following sections. Next, we considered the choice of HOM suitable for device applications, and presented arguments for the use of the first even HOM—the LP_{02} mode, as opposed to the first HOM—the LP_{11} mode, which was used to first demonstrate this technology. Finally, we described specialized dispersion measurement techniques that are needed to measure the dispersion of HOMs, since conventional measurements are suited only for the LP_{01} mode.

3. The Mode Converter

Of critical importance in enabling devices that operate in a HOM of a fiber, is the ability to shuffle light between the LP_{01} mode and HOMs. The schematic representation of such a device is illustrated in Fig. 8, which shows the LP_{01} mode converted to the the LP_{02} mode. A device that performs this function should obviously be low loss, low cost and compact, so as to be deployed in a practical subsystem. In addition, the fact that a HOM-based device inherently possesses several possible modes of propagation, minimizing inter-modal interference (described in greater detail in Section 4) requires that a substantial fraction of light propagate in only one, well-defined spatial-mode of the fiber. Thus, the device should not only convert light into the desired mode with high efficiency, it should also minimize scattering into other modes. It may seem that a device with high efficiency (low loss) would naturally satisfy the latter, high-extinction, constraint. However, Section 4 will show that the levels of mode-extinction have to be substantially higher than those deduced by measuring insertion loss. Typically, mode-extinction should be greater than 20 dB—that is, after mode conversion, the amount of light in *all* other modes should be less than 1% of the energy in the LP_{02} mode. If the insertion loss of the device were entirely accounted for by the amount of light *not* converted from the LP_{01} to the LP_{02} mode, 20-dB mode extinction would imply a device loss of only 0.04 dB. Nevertheless, insertion losses of up to 0.1 dB would be tolerable in a practical system, since that value is similar to typical splice losses and loss-values for additive components such as WDMs and couplers. Hence, the mode converter may indeed lose energy to modes other than the desired HOM, as long as they are lost to lossy or radiative modes, or are absorbed by the glass or its dopants. Moreover, these attributes should be satisfied over a broad wavelength range, typically between 40 and 100 nm (so as to cover the C-, L-, or both bands).

Spatial mode converters can be broadly classified into two classes—the transverse and longitudinal transformers. Holographic plates and phase-sensitive elements are

examples of transverse spatial transformers. A common application for these is in converting the aspheric beam output of a semiconductor laser diode, into a circularly symmetric pattern to efficiently couple with single mode fibers. Such mode converters typically act in free-space, and in the context of the present application, require coupling light out of an SMF input pigtail, on to the mode converting plate, whose output is then coupled into an HOM fiber.

Alternatively, longitudinal transformation (mode conversion) can be achieved within the HOM fiber itself, by use of in-fiber gratings that resonantly couple two co-propagating modes in the fiber. This schematic is attractive because the HOM device then comprises a concatenation (splices) of different fiber types, and the low cost, high-reliability, and small form-factor attributes of fiber devices can be realized. Indeed, the first demonstration of HOM fibers as dispersion compensators used fiber-gratings [15]. Long-period fiber gratings (LPG), with grating periods ranging from 50–500 μm, were first demonstrated as mode coupling elements by Shaw and coworkers [28] and were extensively applied to spectral shaping applications by Vengsarkar and coworkers [29]. LPGs are essentially periodic perturbations induced in a fiber, with a period that matches the beat period between two modes. The perturbations may either be periodic microbends induced on the surface of the fiber, or periodic longitudinal changes in the refractive index of the core of the fiber. This latter technique is especially attractive, because refractive index changes can be easily written into a fiber by exposure to UV light, and this enables a device platform that is highly reliable, low cost and small in size. This section will describe the physics of operation of LPGs, and show how they are very attractive candidates for the critical mode-converting functionality of HOM-DCMs.

3.1. Long-Period Fiber Gratings: Principle of Operation

The coupling behavior of LPGs can be characterized by a phase matching relationship given by [30]:

$$\delta(\lambda) = \frac{1}{2}\left(\Delta\beta(\lambda) - \frac{2\pi}{\Lambda}\right), \tag{18}$$

where δ is a detuning parameter, Λ is the grating period and $\Delta\beta$ is the difference in propagation constants between the two modes (which is a function of wavelength, λ). As a general rule, maximum mode coupling occurs at the resonant wavelength λ_{res}, where the $\delta = 0$ condition (the resonance condition) is satisfied. An intuitive picture of the spectral dependence of LPG couplers can be obtained by considering the phase matching curve (PMC) of a fiber, which is a plot of the grating period with respect to wavelength at resonance [i.e., a plot of Λ vs. λ_{res} when $\delta = 0$, in Eq. (18)], shown in Fig. 9(a). Figure 9(b) shows the corresponding grating spectrum obtained, for the residual light in the LP_{01} mode, after the HOM is stripped out. In this spectrum, the energy in the LP_{01} mode is –27 dB below the baseline, at resonance. Hence, the mode extinction value is the same, and the coupling efficiency into the HOM is $1–10^{-27/10} = 0.998$, or 99.8%. The coupling magnitude decreases monotonically, at wavelengths away from λ_{res}, that is, as δ departs from 0, in the PMC. Moreover, the bandwidth of the spectrum in Fig. 9(b) is strongly coupled to the gradient of the PMC, in Fig. 9(a). The slope of the PMC ($d\Lambda/d\lambda$), and the bandwidth of the corresponding spectrum $\Delta\lambda_{\mathrm{bandwidth}}$, respectively, are given by

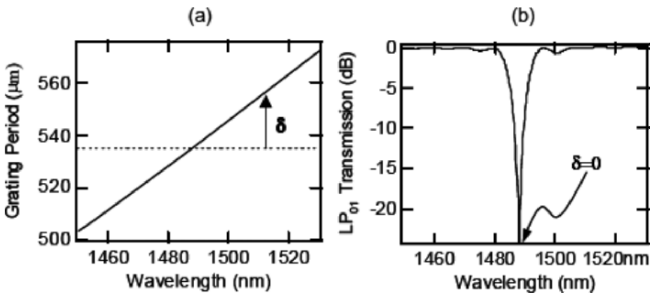

Fig. 9. (a) Phase matching curve (plot of Λ vs. λ when $\delta = 0$). Dashed line represents grating period. (b) Maximum coupling at $\delta = 0$, decreases as δ departs from 0.

$$\frac{d\Lambda}{d\lambda_{res}} = -2\pi \frac{\Delta\beta'}{\Delta\beta^2}, \tag{19}$$

$$\Delta\lambda_{\text{bandwidth}} \propto \frac{1}{\Delta\beta'}, \tag{20}$$

where $\Delta\beta'$ is the slope with respect to wavelength, of the difference in the propagation constants between the two modes, and all other terms have been defined earlier. Thus, the bandwidth of the resonance decreases as the quantity$\Delta\beta'$, and correspondingly the slope of the PMC, increases. The quantity $\Delta\beta'$ is proportional to the difference in group-delays between the two modes, and Eqs. (19) and (20) can be understood in the following physically intuitive manner: At the resonant wavelength, the phases of the two modes are matched by the grating vector, yielding the condition $\delta = 0$ in Eq. (18), and maximal coupling. The strength of the resonance away from this wavelength is governed by the rate of de-phasing between the two modes, which is governed by the next higher-order Taylor term in the expansion of the propagation constant, namely the group delay.

More generally, the spectral response of an LPG is governed by the spectral evolution of the detuning parameter δ. Since the wavelength dependent quantities in δ are the propagation constants of modes in a fiber, an LPG spectrum is strongly coupled to the dispersive nature of the fiber itself. Equation (18) may be re-written as a Taylor expansion about the resonant wavelength, λ_{res}:

$$\delta(\lambda) = \frac{1}{2}\left(\Delta\beta'(\lambda_{\text{res}})\Delta\lambda + \frac{\Delta\beta''(\lambda_{\text{res}})}{2!}\Delta\lambda^2 + \frac{\Delta\beta'''(\lambda_{\text{res}})}{3!}\Delta\lambda^3 + \ldots\right), \tag{21}$$

where the primes represent derivatives with respect to wavelength, and $\Delta\lambda$ is the difference between the wavelength of interest and the resonant wavelength. These derivatives are related to physically relevant parameters: $\Delta\beta' \sim -\Delta\tau$, the differential group delay, $\Delta\beta'' \sim \Delta D$, the differential dispersion, and $\Delta\beta''' \sim \Delta D'$, the differential dispersion slope, etc. Thus, the spectrum of an LPG may be precisely tailored by adjusting well-known fiber-design parameters, means of whose control was described in Section 2.

This provides an additional degree of freedom in the ability to obtain phase matching that is not available in conventional bulk optic diffraction gratings. Fully exploiting

the intimate connection between fiber design parameters and LPG spectra enables a variety of passive and active (tunable, switchable) mode conversion devices, as is described in the following sections.

3.2. LPGs in Dispersion Tailored Few-Mode Fibers: Broadband Mode Converters

The concept of broadband mode-conversion was first demonstrated by Poole *et al* [31], in a fiber designed to support the LP_{01} and LP_{11} modes with identical group delays at a predetermined wavelength. Note from Eq. (20), that the bandwidth$\Delta\lambda$, of an LPG is inversely proportional to the difference in group-delays $\Delta\beta'$, and thus a fiber with identical group delays would be expected to yield very large bandwidths. Periodic microbends, used to couple between the fundamental mode and an LP_{11} mode in the fiber used by Poole et al. [12], yielded strong mode conversion ($>$ 10 dB) over a bandwidth as large as 74 nm. The few mode fiber with identical group velocities was designed by operating the LP_{11} mode, close to cutoff.

The operation principle for such fibers is illustrated in Fig. 10, which shows the mode profiles of the fundamental as well as the LP_{02} mode at two different wavelengths. At a short wavelength $\lambda = \lambda_1$, when the LP_{01} and LP_{02} modes are well guided and reside predominantly in the core of the fiber [Fig. 10(a), left], the ray picture [Fig. 10(a), right] for waveguides accurately predicts that the group delay, $[-\beta'(LP_{02})] > [-\beta'(LP_{01})]$, since the LP_{02} mode travels at steeper bounce angles compared to the LP_{01} mode. At a longer wavelength $\lambda = \lambda_2$, most of the energy of the LP_{02} mode resides in the low-index ring [Fig. 10(b)], and the mode picture is better suited to gain an intuitive understanding of mode propagation. As the wavelength of operation is increased, the power fraction of the LP_{02} mode in the low-index ring increases, and its group velocity approaches that of light residing primarily in the ring (which is higher than that of the core, since it has a lower index of refraction compared to the core). Now, $[-\beta'(LP_{02})] < [-\beta'(LP_{01})]$—the LP_{01} mode continues to be well-guided and thus no significant change is expected for $\beta'(LP_{01})$. Hence, at an intermediate wavelength $\lambda_1 < \lambda_T < \lambda_2$, the group delays of the two modes match, as shown in Fig. 10(c).

Thus, $\Delta\beta'$changes sign and this implies that the slope of the phase matching relationship [Eq. (19)] changes polarity. The result is a turn-around point (TAP) in the PMC, as shown in Fig. 11(a). Following the intuitive rule from Section 3.1, inspection immediately reveals that large bandwidths are attainable if the grating period (shown by the horizontal dashed line) is chosen to couple at the TAP. This is because the dashed line representing the grating period does not depart from the PMC over a large wavelength range. In other words, the resonance condition $\delta = 0$, is satisfied over a larger wavelength range.

The fiber design criteria are, as mentioned earlier, quite similar to those described in Section 2 for designing fibers with specific dispersive properties. Thus, the design and manufacture of fibers required for mode-conversion follow the same recipes as those outlined in Section 2.

Figure 11(b) shows the spectrum of light in the LP_{01} mode after the LP_{02} mode has been stripped out, for a 1-cm-long LPG in a fiber with a TAP at 1540 nm. The grating period for coupling at the TAP of this fiber is 120.2 μm—at this period the resonance of the phase matching curve is satisfied at two distinct wavelengths because of the existence of a TAP, as shown in Fig. 11(a). The resultant spectrum yields more

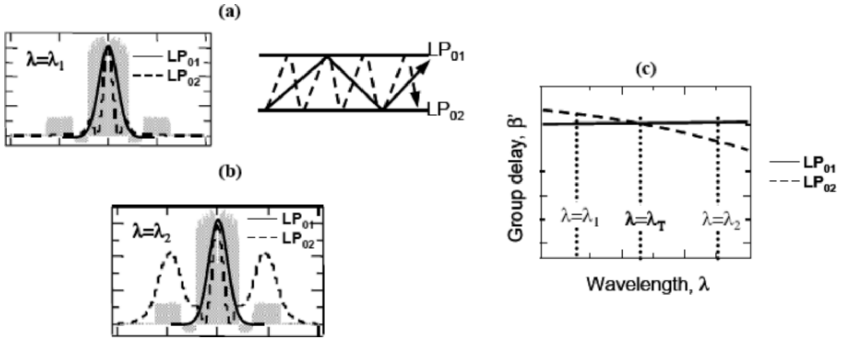

Fig. 10. Dependence of modal delay on mode profile. Grey background is the refractive index profile. (a) Mode profiles at short $\lambda = \lambda_1$ (left), corresponding ray picture (right), (b) Mode profiles at long $\lambda = \lambda_2$; LP_{02} travels in lower index regions, (c) modal delay for LP_{01} and LP_{02}; Equal modal delays at intermediate wavelength $\lambda = \lambda_T$.

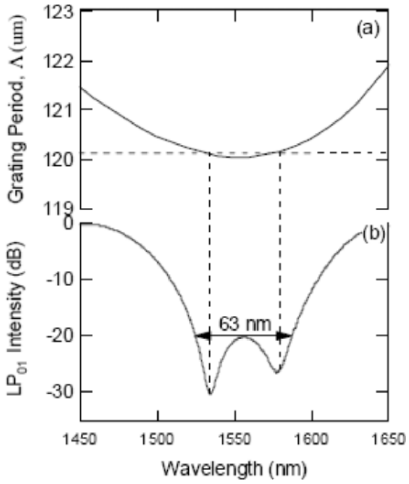

Fig. 11. (a) Simulation: Grating phase matching curve in dispersion tailored fibers. Large bandwidths obtained at TAP (b) Experiment: Resultant TAP LPG spectrum. Peak coupling $>$ 30 dB More than 20 dB (99%) coupling over 63 nm. Horizontal dashed line indicates the grating period, and shows the correspondence between the PMC and the grating spectrum obtained.

than 99% mode-conversion over a wavelength range of 63 nm [32]. In comparison, the 20-dB bandwidth of conventional LPGs is only $\sim$ 1 nm.

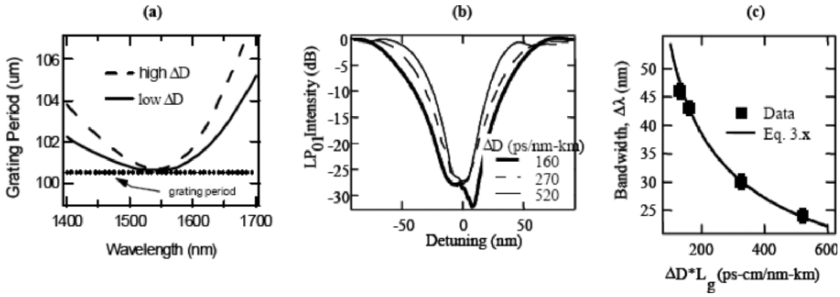

Fig. 12. Control of the LPG spectra by fiber design. (a) PMCs for fibers with low and high ΔD. Higher curvature at TAP for high ΔD fiber. (b) Experimental spectra show that the 20-dB bandwidth increases as ΔD of the fiber decreases. (c) Grating bandwidth vs. $\Delta D^* L_g$. Experimental data shows an excellent match with theory [Eq. (22)].

3.3. Bandwidth Control by Fiber Design

The bandwidth of TAP-LPGs cannot be determined from Eq. (20), since the difference in modal group-delays $\Delta\beta'$, is zero at the TAP wavelength. Expanding $\Delta\beta$ as a Taylor expansion [Eq. (21)] and retaining the next higher-order term (the next higher- order term is the modal dispersion, $D \sim d^2\beta/d\lambda^2$), the 20-dB bandwidth of TAP gratings can be obtained as [32]:

$$\Delta\lambda \propto \frac{\lambda_{\text{res}}}{\sqrt{\Delta D L_g}}, \tag{22}$$

where ΔD is the difference in dispersion between the two modes, and L_g is the length of the grating. As is expected, when the first-order term in the Taylor expansion of β is zero ($\delta\beta' = 0$, identical group delays), the next order term, differential dispersion $\delta\beta''$, plays a role in determining the bandwidth of the resonance. Just as the gradient of the PMC was related to the difference in group-delays $\delta\beta'$, the curvature of the PMC is controlled by the differential dispersion. This is shown in Fig. 12(a), which plots the PMCs for a fiber with a low differential dispersion ΔD at the TAP, and one with a high ΔD, respectively. As is evident, the curvature of the PMC at the TAP is lower for the fiber with lower ΔD. Following the insight gained in Section 3.1, it may be inferred that the PMC with lower curvature at the TAP (lower ΔD), will yield a broader LPG bandwidth. This is because the condition $\delta = 0$ is satisfied or nearly satisfied over a larger wavelength range for such a fiber. Indeed, this is also predicted by Eq. (22). This concept is illustrated with gratings in several fibers with different differential dispersion values (ΔD) at the TAP. Figure 12(b) is a comparison of the spectra of TAP-LPG written in fibers with ΔDs of $\sim$ 160, 270 and 520 ps/nm-km respectively [32]. As expected, fibers with larger differential dispersion show narrower resonances.

Equation (22) indicates that the bandwidth of TAP gratings is inversely proportional to $\sqrt{\Delta D L_g}$. Figure 12(c) shows the experimental and theoretical dependence of the 20-dB grating bandwidth with respect to the parameter $\Delta D^* L_g$. The excellent

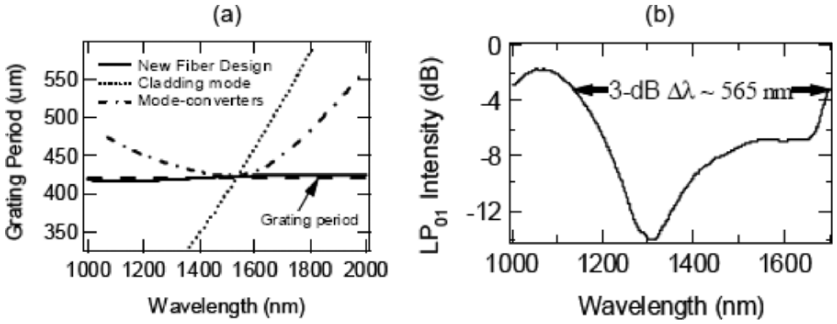

Fig. 13. (a) Grating phase matching curve (PMC) for various fibers. PMC of few-mode fiber design shown in Fig. 7 is almost invariant with wavelength. Implies phase matching is wavelength insensitive over a large spectral range. (b) Microbend grating spectrum in novel few-mode fiber. Grating length = 1 cm. Record 3-dB bandwidth (565 nm) due to flat PMC shown in (a). Spectrally flat coupling in 1550-nm region extends over 110 nm.

match between the prediction and the data indicates that Eq. (22) accurately describes the behavior of LPG spectra in dispersion tailored fibers.

This concept can be extended to unique fiber designs in which several orders in the Taylor expansion of $\delta\beta$, as shown in Eq. (21), can be matched. This is illustrated with a few-mode fiber that was designed and fabricated to yield identical group-delays, dispersions and dispersion-slopes for the LP_{01} and LP_{11} modes. This implies that several Taylor terms of Eq. (21) representing detuning δ, are negligible in value. Thus, δ remains close to zero over a large wavelength range, and phase matching is maintained over this enhanced wavelength range.

The corresponding PMC for this fiber is shown in Fig. 13(a). Also shown for comparison, are PMCs for conventional LPGs (denoted as "Cladding Mode," since they couple core to cladding modes), as well as the TAP-LPGs described in the previous sections (denoted as "Mode Converters"). The PMC is essentially flat throughout a spectral range spanning an octave. As is evident, the line representing the grating period is coincident with the PMC over the whole spectral-range. Hence, gratings coupling the LP_{01} and LP_{11} modes of this fiber would be expected to be not only broadband, but also spectrally insensitive to coupling efficiency.

Figure 13(b) shows the spectrum of a 1-cm-long microbend grating induced in this fiber (microbends, rather than UV index change are used as the perturbation in this example, because they are more efficient for coupling between symmetric (LP_{01}) and anti-symmetric (LP_{11}) modes). The 3-dB spectral width is a record value of 565 nm, and since the dispersive parameters are especially well matched in the 1500-nm range (and hence the PMC is especially flat), the coupling is also spectrally flat there. The flat spectral region extends over more than 100 nm [33].

3.4. Novel Tuning Effects: In-Fiber Switches

Tuning mechanisms for conventional LPGs comprise either changing the grating period by strain, or shifting the PMC by some mechanism that alters the dispersive

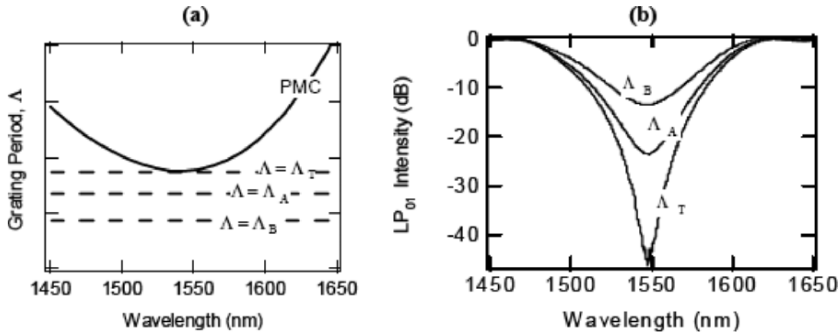

Fig. 14. Novel detuning effects in TAP-LPGs. (a) Typical PMC for few mode fibers. Horizontal dashed lines represent grating periods at and away from TAP, (b) Resultant spectra. Coupling efficiency decreases as grating period departs from TAP-period Λ_T. No phase matching at any λ for grating periods Λ_A, Λ_B. Hence diminished resonance with same shape.

properties of one or both the modes that are coupled through the grating. These mechanisms include the thermo-optic effect (induced by temperature-induced changes of the waveguide properties), stress-optic effect (pressure induced refractive index changes), electro-optic effect or any other effect that essentially changes the refractive index profile of the fiber. This leads to changes in the propagation constants of one or both modes, as is evident from Eq. (2) in Section 2.1, which in turn shifts the PMC [as is clear from Eq. 18)]. Correspondingly, the wavelength at which the line representing the grating period intersects the PMC shifts [see Fig. 8(a)], moving the entire LPG spectrum to be centered at the shifted resonant wavelength. Strain directly changes the grating period [and thus the position of the grating line in Fig. 8(a)] to shift the resonant wavelength. In either case, the tuning mechanism does not dramatically change the gradient of the PMC, and thus tuning results in reproduction of an identical spectrum at a new resonant wavelength. Such tuning effects have resulted in a variety of tunable devices comprising conventional LPGs [34–36]. On the other hand, tuning TAP-LPGs results in amplitude changes rather than wavelength shifts, due to characteristics unique to their PMCs.

Figure 14(a) shows the now-familiar PMC of TAP-LPGs, along with 3 horizontal dashed lines representing grating periods Λ_T, Λ_A, and Λ_B, where Λ_T corresponds to grating-coupling at the TAP, and the two other grating periods lie in regions where they do not intersect the PMC at any wavelength. The phase matching condition of Eq. (18) may be recast in terms of this PMC as

$$\delta = \pi \left(\frac{1}{\Lambda_{\mathrm{TAP}}\left(\lambda\right)} - \frac{1}{\Lambda} \right), \tag{23}$$

where Λ_{TAP} is the grating period *required* for resonance along the PMC [i.e., the plot of the curve shown in Fig. 14(a)], and Λ is the actual LPG period, taking values Λ_T, Λ_A, and Λ_B, shown in Fig. 14(a). The corresponding spectra obtained at these periods are shown in Fig. 14(b). For $\Lambda = \Lambda_T$, coupling occurs at the TAP, and the familiar broadband resonance, is obtained. However, for a grating with $\Lambda = \Lambda_A$ and

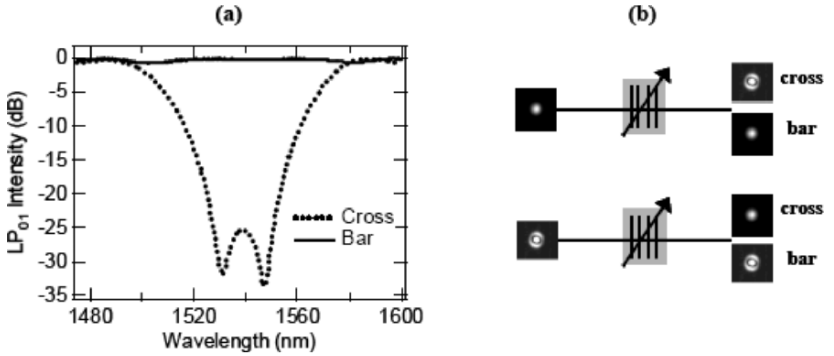

Fig. 15. 2×2 switches with TAP-LPGs. (a) Spectrum of switch showing strong (cross state) or no (bar state) mode conversion, (b) Near field images of the modal input and output in the cross and bar states.

$\Lambda = \Lambda_B$, no resonance occurs because the grating period does not intersect the PMC at any wavelength. In terms of Eq. (23), this represents a condition where $\delta \neq 0$ for any wavelength. In this case, the spectrum somewhat resembles that of a TAP resonance, but with diminished coupling strength. Moreover, the coupling efficiency for the grating with $\Lambda = \Lambda_B$ is weaker than that for the grating with $\Lambda = \Lambda_A$, since δ is larger in magnitude throughout the spectral range. Thus, the coupling efficiency for TAP-LPGs decreases roughly monotonically, as the grating period departs from the TAP grating period Λ_{TAP}, while maintaining its spectral shape.

This novel amplitude-tuning mechanism can be applied for assembling 2-state switches instead of continuous modulators. Toggling the LPG between a state that represents coupling at the TAP and another that yields identically zero coupling over a broad bandwidth, yields 2×2 switches [37], as shown in Fig. 15. Figure 15(a) shows the spectrum of the switch in the cross and bar states, respectively. Since LPGs are reciprocal devices, input light in either mode can be switched to an output, again in either mode, simply by switching the LPG between the cross and bar states, as the experimentally measured mode images in Fig. 15(b) show. The switching action can be induced by packaging the LPG in a stainless steel package, which when heated, applies a strain as well as a temperature-shift in the PMC. Thus, only moderate temperatures are required for the switching action—switching these LPGs from the cross to the bar states involved changing the temperature on the packages between 50 and 120°C.

3.5. Other Grating Characteristics

3.5.1. Insertion Loss

To measure the low insertion loss of TAP-LPGs, 7 gratings were spliced in series, as shown in Fig. 16(a). The input and output LPGs are operated in the "cross" state, while the intermediate 5 LPGs are in the "bar" state. Hence, input and output are in the LP_{01} mode, which is easier to measure accurately. Figure 16(b) shows the transmitted

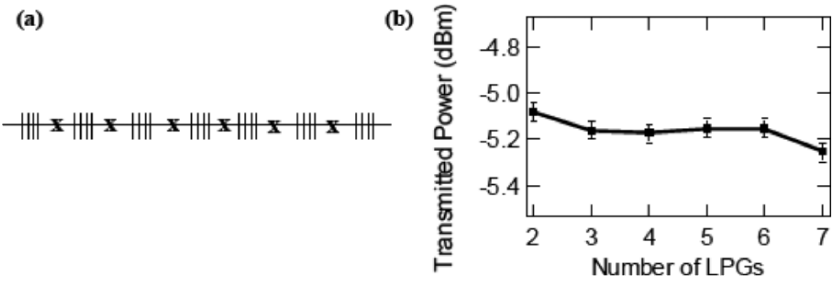

Fig. 16. (a) Series of concatenated TAP-LPGs to measure insertion loss. Input and output grating in "cross" state, intermediate LPGs in "bar" state. (b) Transmitted power measured by cutback. LPGs replaced with HOM fiber to normalize for splice loss. TAP-LPG loss $\sim 0.034 \pm 0.04$ dB.

intensity for a cut-back measurement, where LPGs were successively removed from this series, but replaced by a similar, bare HOM fiber, to normalize for splice loss. The loss for 5 LPGs in the series was 0.17 dB, indicating an insertion loss of 0.034 dB per LPG. The plot also shows the measurement uncertainty ($\pm$0.04 dB), which is comparable to the loss per grating. Hence, we conclude that insertion losses for TAP-LPGs are significantly lower than 0.1 dB.

3.5.2. Stability and Polarization Sensitivity

The grating periods for LPGs are of the order of 100s of microns, and thus can be written by low-cost lithographic processes. Nevertheless, conventional LPG devices, which couple the LP_{01} mode with a cladding mode, have not been considered to be cost-effective because they are sensitive to ambient conditions, and also exhibit high polarization dependent losses (PDL).

TAP-LPGs, described in this section, and considered for mode converting applications, differ from conventional LPGs in two important respects. The conventional LPG is primarily a band rejection filter, and hence the operand of interest is the amount of LP_{01} light attenuated. Stability considerations thus require that this number be held constant, with respect to temperature, stress and other ambient variations over time. In contrast, the TAP-LPG is primarily a mode converter, and as was noted in the beginning of this section, the primary consideration is mode conversion efficiency and mode-extinction levels. For these applications, only the mode conversion efficiency levels need to be stabilized with respect to environmental variations and fabrication errors. The extinction ratio just needs to be maintained over a prescribed, threshold value (20 dB). This condition is significantly easier to meet.

The second distinction is related to the fiber. Conventional LPGs are written in SMF, and couple the signal to a cladding mode. Since a cladding mode is sensitive to the ambient (the glass air interface of a uncoated fiber defines the waveguide for the cladding modes), the LPGs are also sensitive to ambient conditions. In addition, the two modes coupled by conventional LPGs (core and cladding mode) will exhibit different levels of sensitivities to perturbations such as ovality, diameter fluctuations

etc. TAP-LPGs, in contrast, couple two core guide modes. Therefore, small perturbations in either the grating period, or fiber manufacturing conditions, affect both modes in approximately the same manner. Since, LPG coupling is sensitive only to the difference in the propagation constants, perturbations on both modes will not result in any change of the LPG response. Many of the problems regularly encountered with conventional LPGs—polarization dependence, sensitivity to small diameter fluctuations and changes in UV induced index Δn_{UV}, and extreme sensitivity to stress and strain—are either diminished or non-existent, for TAP-LPGs.

This stability is illustrated by considering the polarization response of a TAP-LPG. The simplest way to obtain a value for PDL is by measuring the variation in output intensity of the LP_{02} mode with respect to variations in the input polarization state. In such measurements, no changes have been detected within the measurement accuracy of typical external-cavity lasers and photo-detectors (measurement accuracy ~ 0.02 dB), indicating that TAP-LPGs have negligible PDL. Substantially higher accuracy can be achieved by measuring the amount of residual fundamental mode in the fiber after the LP_{02} mode is stripped out—for a sufficiently strong LPG, a miniscule amount of the fundamental mode would remain, and small changes in its intensity would result in large variations on a log (dB) scale (indeed, as we discussed above, it is this sensitivity to the residual levels of the fundamental mode that make an LPG operating in the conventional, band-attenuation schematic, highly sensitive). Figure 17(a) shows the grating spectra for a very strong TAP LPG—the peak coupling efficiency is ~ 45 dB, with a 40-dB bandwidth of 10 nm and 20 dB bandwidth of 43 nm. Strong LPGs require large UV-induced index changes Δn_{UV}, and the polarization dependence of gratings increases with Δn_{UV}. The inset shows the spectra of two orthogonal polarizations corresponding to the largest deviations in grating strength. Figure 17(b) shows the spectral response of the LP_{02} mode calculated from the data in Fig. 17(a). The spectrum is shown on a linear scale because small deviations from unity are more visible thus. Even then, the two spectra are barely distinguishable. Variations in input polarization caused the coupling efficiency to range from 99.9960% to 99.9996%, corresponding to a negligible change for applications in optical communications systems. The 20-dB bandwidth also shows a negligible change of ~ 0.2 nm [38].

3.5.3. Thermal Response and Packaging

The stability arguments from the last section also indicate that TAP-LPGs are significantly less sensitive to ambient temperature variations. They can maintain a 20-dB mode conversion bandwidth of 60 nm or more, over a $30^{\circ}\mathrm{C}$ temperature range. This does not suffice for devices deployed in optical networks where the typical operating temperature range is 60–$80^{\circ}\mathrm{C}$. This can be achieved in TAP-LPGs by employing packaging techniques that are commonly used for commercially deployed grating devices [39].

Section 3.4 illustrated that strain and temperature serve to modulate the amplitude of TAP-LPG resonances. Thus, a package that releases strain with increasing temperature will enable a thermally insensitive grating-response. The schematic of the packages used with TAP-LPGs is shown in Fig. 18(a). The package comprises two distinct materials with low and high coefficients of thermal expansion (CTE), respectively, which when assembled in the manner shown in Fig. 18(a), result in a package that has a negative CTE. Figure 18(b) shows the spectra of a TAP-LPG packaged with

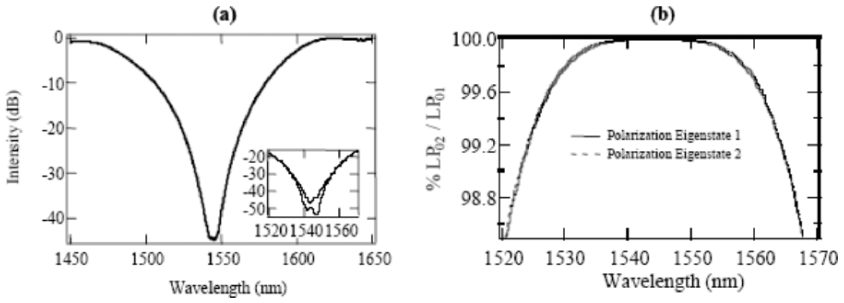

Fig. 17. Polarization dependence of TAP LPG. (a) Spectrum for a strong mode converter; inset shows polarization dependent response of the residual fundamental mode. (b) Polarization response of the LP_{02} mode, deduced from data in (a). Spectra barely distinguishable. Peak coupling changes by 0.0002 dB, 20 dB bandwidth changes by 0.2 nm.

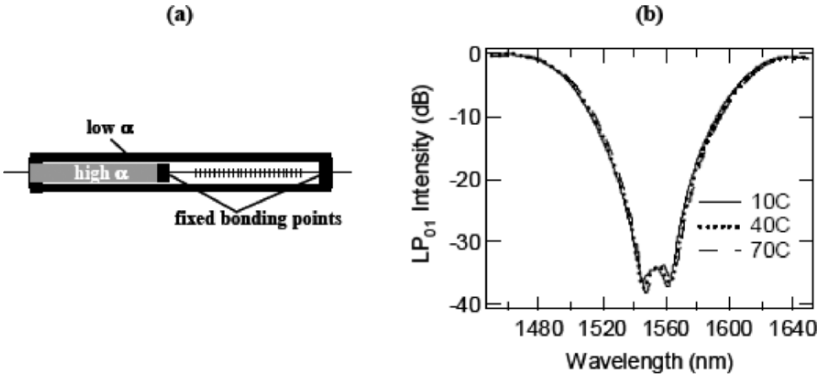

Fig. 18. TAP-LPG packaging for athermal response. (a) Athermal package schematic. Two materials with different CTEs yields negative CTE for composite structure. (b) Resultant temperature dependent spectra for TAP-LPG. No change in spectrum from 10–70°C.

the appropriate negative CTE, as a function of temperature. As is evident, the spectra are indistinguishable over a 60°C range, demonstrating that athermal packages offer an attractive means to obtain temperature insensitive performance from TAP-LPGs.

3.6. Summary

This section has described the critical role a mode converter plays in building HOM-based dispersion compensators. In-fiber LPGs, which allow building strictly all-fiber HOM devices with its attendant advantages, possess several desirable characteristics when a HOM fiber with the appropriate TAP condition is used. The several attractive

attributes of TAP-LPGs are listed below, and form the basis for their deployment in HOM-based devices described in Sections 5 and 6.

- Very low insertion losses ($\ll 0.1$ dB).
- Extinction ratios of up to 45 dB. 20-dB bandwidths ranging from 30 to 110 nm.
- Mode conversion efficiencies higher than 99% over spectral ranges of interest.
- Can realize *tunable/switchable* as well as static mode converters.
- Substantially more stable, lower PDL and higher fabrication tolerance compared to conventional LPGs.
- Appropriate packaging can extend the operating temperature range to more than 150°C.

4. Module Assembly and Combating Modal Interference

Having described the attributes of the critical components in HOM-DCMs, namely the few mode fiber and the mode converter, we turn our attention to the means to assemble and characterize such modules. The most important distinction between these devices and the vast majority of conventional fiber devices, is that the fiber can support multiple modes of propagation for the signal, though as in the case of single mode fiber devices, the desire is to propagate the signal in only one well-defined mode. There are two impairments that must be managed in fibers supporting multiple modes—differential group delay (DGD) and intermodal interference, also called multi-path interference (MPI).

DGD is the relative difference in group-delays (GD), for portions of the signal travelling in different co-propagating modes of a fiber. This is an important consideration in multimode fiber links used for LANs and the Ethernet [40]. DGD can cause a well-defined input pulse to arrive as several temporally separated pulses at the output, because traversal times (GDs) for light in different modes may be distinct. This is not a significant problem in HOM devices, because there is only one dominant mode of propagation.

MPI occurs when the dominant signal, in its preferred path, interferes with a highly attenuated replica, which travels in a different path. This can lead to two problems. Interference obviously leads to wavelength dependent changes in transmitted light, which yields a device that introduces spectral ripples in a communications band. More debilitating is the fact that an interferometer output depends on the relative phases between the interfering arms, and phase noise in transmitters will thus be converted into intensity noise, which directly impacts the performance of an optical communications system. Such a system is equivalent to the concatenation of several parallel and serial interferometers, and the output power P_{out}, of the device can be given by

$$P_{\mathrm{out}} = |E_0|^2 \left| 1 + \sum_{i}^{N} \eta_i e^{\Phi_i} \hat{p}_i \right|^2, \tag{24}$$

where N is the number of random mode coupling events, η_i are their mode coupling efficiencies, Φ_i are the phases of light in the parasitic modes relative to the dominant

mode, p_i are their unit vectors representing their states of polarization (SOP). In systems where MPI is of concern, the fraction of energy in parasitic modes is usually very low (that is, η is small), and hence only terms of the order η^2 are dominant in Eq. (24). Equation (24) indicates that the probability distribution function of power fluctuations, and hence the systems impact of MPI will depend both on the number of events N, as well as their efficiency η. However, MPI has been described by a "composite" parasitic mode level, defining the total amount of light in undesired modes interfering with the signal. Hence, a generalized quantity η^2, is used to characterize the level of MPI. A device MPI of –22 dB typically yields a 1-dB bit-error-rate (BER) penalty, but much lower values of MPI are required in a practical application, because of the need to concatenate many such devices in series. Since devices such as dispersion-compensators are typically installed at every amplifier-stage (spaced by 50–200 km), long haul ($\sim$1000–3000 km) or ultra-long-haul ($\sim$6000–20000 km) links comprise 10 to 200 devices in series. Hence, MPI requirements for individual devices range between –30 and –50 dB so that concatenation adds negligible additional systems penalty [41].

Since MPI depends on the phase difference between two light-paths, and interference itself is a coherent phenomenon, the signature and impact of MPI critically depends on the ratio of the coherence time of the signal to the effective path delay. In addition, the effect could be induced by several discrete instances of unintended coupling to parasitic light-paths, or it may occur in a distributed fashion throughout the fiber. Hence, MPI is also defined by the number of interfering arms. This is illustrated in Fig. 19, which shows the different regimes of MPI, and typical devices and systems that are susceptible to them. MPI has been extensively studied for double Rayleigh backscattering (DRB) in Raman amplification [42] schemes ($N \rightarrow \infty$) and discrete reflections arising from multiple connectors in a transmission line [43]. Another class of MPI impairments occurs in WDM nodes [44] as well as HOM-DCMs, where the signal and replica interfere discretely and coherently. The fourth form of MPI, arising from coherent but distributed coupling, is especially relevant to HOM-DCMs, since they may be susceptible to random, in-fiber mode coupling between the desired LP_{02} mode and other modes. This section will describe the means to characterize the coherent distributed as well as discrete MPI that needs to be managed for practical deployment of HOM-DCMs.

4.1. Impact of Module Assembly on Discrete Coherent MPI

The detailed schematic of a HOM-DCM is shown in Fig. 20. The desired, dominant mode of propagation is shown in thick arrows. Mode coupling instances due to various discontinuities and perturbations can potentially introduce parasitic modes, which are represented by the thin arrows. The spool of fiber may randomly couple light between the LP_{02} mode and other parasitic modes (shown by thin, curved arrows), because of random perturbations such as microbends within the spool or fiber-diameter fluctuations. On the other hand, the potential for discrete, deterministic mode coupling instances include:

1. Splices between the SMF pigtail and the HOM fiber used to fabricate the TAP-LPG mode converters.
2. Incomplete/insufficient mode conversion by the TAP-LPGs.
3. Splices between HOM fibers in the spool and the LPG fiber.

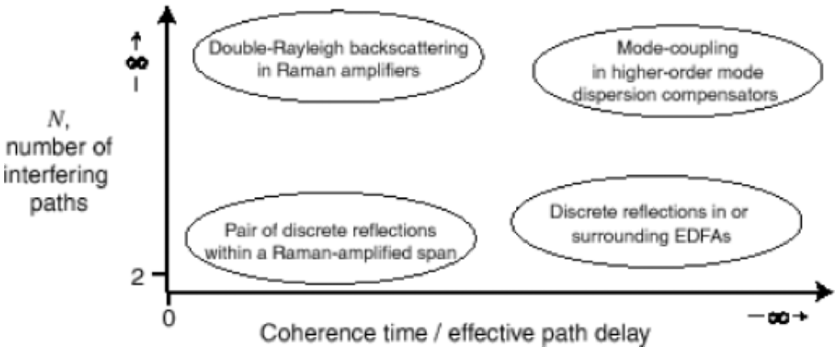

Fig. 19. Examples of MPI plotted versus the number of paths and the ratio of coherence time to path-delay. Reprinted from Bromage et al. [41].

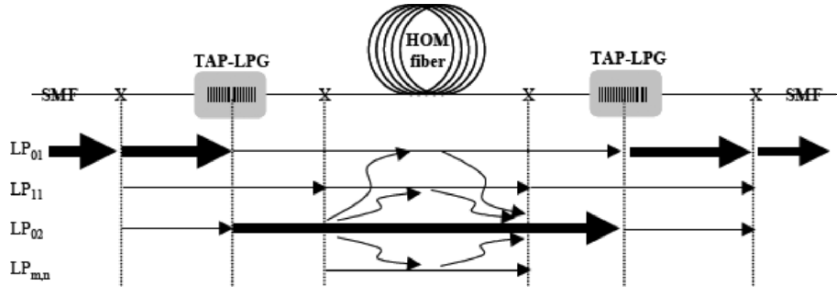

Fig. 20. Detailed schematic of HOM-DCM. Dominant mode of propagation shown with thick arrows. Splices and connections may be a source for discrete coherent MPI (straight, thin arrows), whereas spool may lead to distributed, coherent MPI (curved, thin arrows). Hence, fiber design + assembly technique important for low MPI HOM devices.

The discrete mode coupling events can be analysed separately, by testing modules comprising only two mode coupling events. The resultant interference is similar to that analyzed in Section 2.4.1 [Eq. (14)], where the spectral dependence of the interference fringes yielded dispersion of the LP_{02} mode. The maximum power excursion of those interference fringes is related to the ratio of the powers in the two arms. Hence, MPI η^2 due to the discrete coupling events can be obtained from

$$\eta^2 = \left(\frac{10^{\mathrm{ptp}}/20 - 1}{10^{\mathrm{ptp}}/20 + 1} \right)^2, \tag{25}$$

where ptp is the peak-to-peak amplitude (in dB) of the interference spectrum.

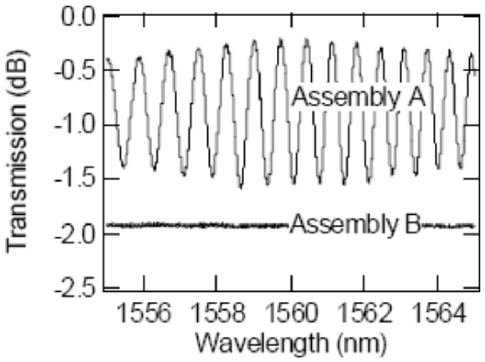

Fig. 21. Interference spectra showing SMF-HOM fiber pigtail connection optimisation. Standard splices cause interference ripples yielding ~ -23 dB MPI. Optimized connections yield excellent performance (MPI~ -57 dB, $\sim 0.1\%$ coupling to undesired modes). Spectra are vertically offset for clarity.

4.1.1. Pigtail connection MPI

MPI due to connections and splices to SMF pigtails is measured by simply connecting a standard SMF at the in/output of a short segment of HOM fiber identical to that used for the TAP-LPGs, and measuring its wavelength dependent transmission spectrum. Figure 21 shows spectra for two different conditions. Assembly A comprises a conventional splice, with parameters commonly used to splice SMF, and yields $\eta^2 = -23$ dB, indicating that each connection transfers approximately –23/2 dB, or $\sim 7.5\%$ of the fundamental mode energy into the LP_{02} mode. This is an unacceptable level of MPI. Consequently, a specialized splice + mode-stripping assembly is commonly employed. This condition is shown in plot B, which indicates that $\eta^2 < -57$ dB, that is, coupling to parasitic modes at each splice is roughly 0.1%, thus significantly surpassing the required mode suppression levels.

4.1.2. Incomplete Mode Conversion by TAP-LPGs

As emphasized in Section 3, the mode converter has to offer not only low insertion loss, but also high mode extinction. The MPI arising from mode converters is easily ascertained by considering its spectrum—since the typical measurement technique for LPG mode converters is to measure the residual LP_{01} light after the converted LP_{02} light is stripped out (as described in Section 3.1), the parasitic mode excitation level is directly obtained from the LPG spectrum. Hence, satisfying the –40 dB MPI requirements for HOM systems, requires that each mode converter offer at least 40/2 = 20-dB mode-conversion. Indeed, an important characteristic of TAP-LPGs, as described in Sections 3.2 and 3.3, was the 20-dB bandwidth. Thus, in reference to Fig. 11, TAP-LPGs enable MPI < -40 dB over at least 63 nm, and as seen from the LPG illustrated in Fig. 17, MPI values as low as $-45 \times 2 = -90$ dB can be obtained.

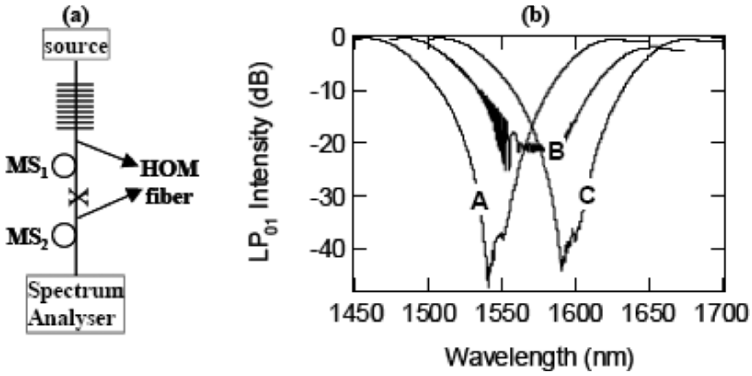

Fig. 22. (a) Schematic of HOM-HOM splice MPI measurement. MS = Mode Stripper. (b) Mode converter spectra: A with $MS_1 + MS_2$; B and C with MS_2 only. Unoptimized splice yields 53 dB MPI (plot B). Optimized connection yields < -90 dB MPI (plot C). Spectra horizontally offset for clarity.

4.1.3. Splices Between HOM Fibers

As the schematic in Fig. 20 shows, module assembly requires splices between LPG fiber and the HOM fiber, *such that* the LP_{02} mode is transmitted with low loss and MPI. This can be measured indirectly, by measuring the spectrum of the mode converter, as explained with reference to Fig. 22. The schematic in Fig. 22(a) shows the spectrum of LPG fiber spliced to the HOM fiber, with and without a mode-stripper (MS_1) employed on the LPG fiber. When a mode stripper is present, the spectrum of just the LPG is obtained, as shown in plot A of Fig. 22(b). This is because only the tightly bound residual LP_{01} mode passes through the splice. However, when the mode stripper is removed, the splice predominantly passes the LP_{02} mode. Now, an imperfect connection will scatter some of this light into the LP_{01} mode of the HOM fiber, which will interfere with the residual LP_{01} light that was not mode-converted by the LPG. This results in an interference pattern superimposed on the LPG spectrum [Fig. 22(b), plot B]. In addition, the level of mode conversion offered by the LPG also appears to be apparently reduced—this is because the mode conversion level was measured by recording the residual LP_{01} light, whose intensity has now increased because of the additional LP_{01} light from the splice. The MPI due to this imperfect splice must be quantified by both the mode extinction level of the spectrum, as well as the peak-to-peak amplitude of the superimposed fringes. In plot B, the ripple amplitude is ~ 5 dB, yielding a relative energy ratio of –5.5 dB. The MPI due to the splice is deduced by subtracting this amount from the average extinction value of the spectrum (–21 dB, in the case of plot B). Hence, the additional parasitic mode excitation level due to the HOM-HOM splice is ~ 26.5 dB, and the resultant MPI due to two such splices would be –53 dB. This is may be enough for many practical applications, but can lead to problems if multiple splices are required (a device requiring several HOM-HOM connections is described in section 6). Hence, this splice must be optimized—plot C of Fig. 22(c) shows the LPG spectrum with an optimized HOM-HOM splice. Indeed,

this spectrum is barely distinguishable from that of the original LPG, and the MPI resulting from this splice is < -90 dB.

4.2. Characterization of Distributed Coherent MPI

Perturbations in a HOM fiber spool, such as microbends and fiber diameter fluctuations, can lead to coupling between modes. Hence, the fiber spool can be a source of MPI. Since this can occur in a continuous fashion throughout the spool, and the path lengths are usually shorter than the coherence lengths of distributed feedback lasers used as sources, this leads to distributed, coherent MPI. This is an impairment unique to HOM fiber devices. Assuming that the mode coupling occurs primarily between the LP_{02} mode and one other parasitic mode, and further assuming that this system can be modelled as a two-port interferometer, with an *effective* length and MPI level η^2, the output power $P_{\rm out}$ may be deduced from Eq. (24) as

$$P_{\rm out} \propto 2\eta^2 \left|E_0\right|^2 \cos\left(\Delta\phi\right), \tag{26}$$

where $\Delta\phi$ is the relative phase between the two arms, given by

$$\Delta\phi \propto \frac{\Delta n_{\rm eff}\left(\lambda, t\right) L(t)}{\lambda} + \tilde{\phi}(t), \tag{27}$$

where $\Delta n_{\rm eff}$ is the effective index difference between the two modes in which the signal propagates, L is the length of fiber, λ is wavelength of the signal, and $\tilde{\phi}\left(t\right)$ is the laser phase noise. Typically, index and length would change due to environmental fluctuations such as temperature, and thus will have long time scales (seconds to minutes), while phase noise of a laser source would fluctuate on a time scale roughly equal to the reciprocal of its bandwidth ($\sim$ MHz). In this section, we will introduce several measurement techniques to capture this noise phenomenon, and address their advantages and drawbacks.

4.2.1. Swept Wavelength Measurement

It may seem that measuring peak-to-peak amplitudes of interference spectra, as employed to measure mode extinction of discrete connections in Sections 4.1.1 and 4.1.3, may yield MPI due to distributed mode coupling. However, for a 2-km length of HOM fiber, typical group-delay values between the LP_{01} and LP_{02} modes is 10–30 ns at 1550 nm, which translates to a fringe spacing of 0.5 pm. This is an order of magnitude smaller than the resolution of the state of the art of spectral measurement capabilities. The corresponding fringe spacing between LP_{02} and another mode may be larger, and this value would obviously vary with fiber design and length of fiber used, but it would still be of the same order of magnitude. Thus, interference due to mode coupling in the spool may not be resolvable simply by measuring an interference spectrum. Moreover, there would also be no clear, sinusoidally varying spectrum even if a measurement technique with sufficient resolution existed, because of the distributed nature of coupling. Nevertheless, a spectral measurement would be expected to yield a noisy spectrum, corresponding to spectrally random occurrences of interference extrema. Taylor et al proposed statistically sampling these extrema to measure MPI [45]. The technique entailed sweeping a tunable external cavity laser (ECL) across the C-band,

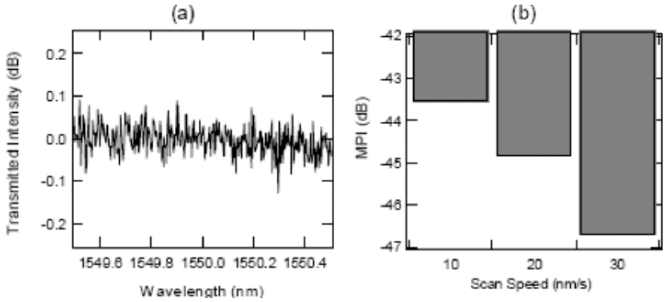

Fig. 23. Swept wavelength-scanning technique for measuring MPI. (a) Typical scan at 20 nm/s: Predicts lower (better) MPI than reference (b) Measured MPI for different scan speeds. Result dependent on scan speed.

with a fast detector at the module output recording transmitted intensity as a function of wavelength. Since the signal and replica possess the same degree of polarisability (they are coherent replicas), the MPI can be deduced from Eq. (26) as

$$\eta^2 = \frac{1}{2}\left(\frac{\sigma}{P_{\mathrm{av}}}\right)^2, \tag{28}$$

where σ is the standard deviation of the transmitted intensity fluctuation, and P_{av} is the average power.

Figure 23(a) shows a typical swept wavelength measurement. The scan speed was set to 20 nm/s. This yields an MPI of –45 dB, according to Eq. (26). Figure 23(b) shows the MPI deduced from measurements made at different scan speeds on the same module, and illustrates the drawback of this measurement technique. The finite response time of the detector and the sweep speed of the ECL define an effective bandwidth of the system. Higher sweep speeds lead to lower resolution bandwidths, leading to a measurement that underestimates the MPI of the system. The highest value of MPI measured by this technique (–43.5 dB) for this module, is still lower than that yielded by an alternate measurement technique, to be described later. This highlights the fact that distributed MPI measurements should be made with care, and the measurement technique should be mentioned along with measured values.

4.2.2. RIN Measurement Using Electrical Spectrum

Intensity noise can also be analysed in the frequency domain. This is the most extensively employed technique to measure MPI due to Rayleigh scattering in Raman amplifiers [41,42], since it is most suitable to measure noise at high modulation frequencies. Thus, fast noise due to laser phase noise is best recorded by this technique. The relative intensity noise (RIN) due to MPI is the Fourier transform of the autocorrelation of Eq. (26). For coherent interference when the fields are in quadrature, the RIN is approximately [46]:

$$\mathrm{RIN}_{\mathrm{MPI}}(f) = \frac{16}{\pi}\eta^2 \Delta\upsilon\tau^2 \mathrm{sinc}^2(f\tau), \tag{29}$$

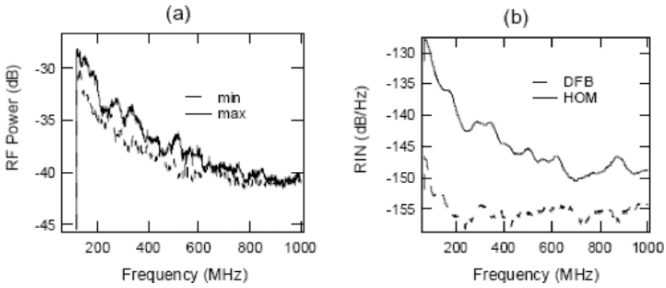

Fig. 24. MPI Measurement with an ESA. (a) RF power vs. Frequency. Spectrum shifts in/out of quadrature. Averaging introduces +/– 2-dB uncertainty in MPI (b) RIN vs. Frequency. Measured MPI ~ -48 dB. Measures > 70 MHz noise. Slow drift filtered out.

where f is the RF frequency, and all other quantities are as defined earlier. Integrating the RIN, measured with an electrical spectrum analyser, therefore yields η^2, the MPI.

Figure 24(a) is a plot of the RF power spectrum of the same HOM-DCM module used for the swept wavelength measurements, measured with a commercial electrical spectrum analyser (ESA). A DFB laser ($\Delta\nu = 2.5$ MHz) was used, and the input power into the ESA was limited to –1 dBm. The spectrum clearly shows the characteristic nulls observed in interferometers in which the two arms are coherent. In addition, changing the input polarization state changes the visibility of the interference spectrum, which indicates that the two arms of the interferometer are not depolarized. Also, note that the interferometer drifts in and out of quadrature on a time scale of several seconds to minutes, changing the RF power (and therefore measured MPI), by 4 dB. Thus, it is expected that this measurement technique will introduce errors in measured MPI of approximately +/–2 dB.

Figure 24(b) is a plot of the electrical RIN spectrum (which is twice in dB scale, of the optical RIN) obtained from an averaged RF spectrum of Fig. 24(a). Also shown is the RIN spectrum, for the DFB laser alone. The MPI was obtained by integrating the RIN spectrum from 70 MHz to 1 GHz, as this range captured most of the distinguishing features of the HOM. Subtracting this value from the RIN for the DFB laser alone yields $\mathrm{RIN}_{\mathrm{MPI}}$, which is related to MPI η^2, by Eq. (29). The MPI for the HOM-DCM was deduced to be –48 dB, 5 dB lower than the value obtained from the swept wavelength measurement.

The discrepancy is not accounted for by the uncertainty in the measurement technique alone, since that is only +/–2 dB. This is resolved by considering the time scales of fluctuations in coherent distributed interferometers. As noted earlier, such interferometers can exhibit slow (sec. to min. timescale) as well as fast (μs to ps timescale) fluctuations. However, the ESA cannot measure RIN below 100 kHz. Thus, this technique samples only high frequency noise, and may not be suitable to measure noise from devices that exhibit a large frequency spread in their noise spectrum. Nevertheless, it gives a measure of fast noise due to MPI in HOM devices, which lead to deterministic systems penalties, as will be described in Section 4.3.

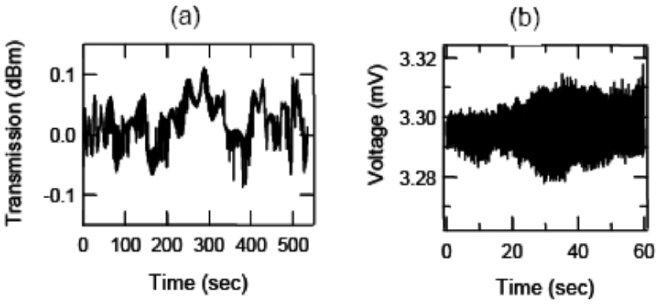

Fig. 25. Temporal fluctuation of transmitted intensity. (a) Power meter (20 ms response) catches slow fading; MPI ~ -39 dB; (b) Measurement with fast photodetector (1us response) yields MPI ~ -49 dB; slow variations filtered out.

4.2.3. Direct Temporal Transmission Fluctuation

Another means to deduce MPI is to measure the intensity fluctuations over time directly with a photodetector [47]. The primary distinction from other measurement techniques is that the fluctuations are recorded over time scales of minutes. Figure 25 shows the variation in transmitted intensity for a 20-ms and 1-μs response-time detector, respectively. Assuming that the long recording time ensures sampling all states of the interferometer, the peak-to-peak (ptp) power swing yields MPI from Eq. (25) (Section 4.1). The detector with the slowest response over the longest scan time yields the highest MPI, –39 dB [Fig. 25(a)]. Note that the most dramatic changes occur in a "bursty" fashion, presumably because the multitudes of interferometers in the HOM fiber align to yield large power extinctions, only sporadically. The measured MPI decreases monotonically, as the detector response time (and correspondingly, the scan time) is shortened. With a detector with 1-μs response time, the measured MPI is –49 dB [Fig. 25(b)], which is similar to the value obtained from the RIN measurements. This is consistent with the fact that both the RIN measurements as well as the direct intensity measurements with a fast detector, sample only fast variations. The source bandwidth is a critical parameter to ascertain while measuring MPI by this technique. We have found that when the source bandwidth is increased from 2.5 to 100 MHz, the MPI drops by more than 15 dB. Since DFB lasers are the sources of choice in long haul communications systems, using a DFB laser for the MPI measurements yields the most relevant MPI values [48].

It is now clear that MPI measurements on HOM fiber devices yield two distinct values, depending on the time scale of the measurement itself. It appears that MPI related to slow (ms-sec) variations is significantly higher than that due to fast variations, and Section 4.3 will explore the systems implications of these two distinct noise sources.

Fiber MPI Characterization. Recall that in Section 2.3 design constraints for fibers required that the effective index difference between the LP_{02} and other modes be large. As mentioned then, this constraint helps minimizing random coupling from/to

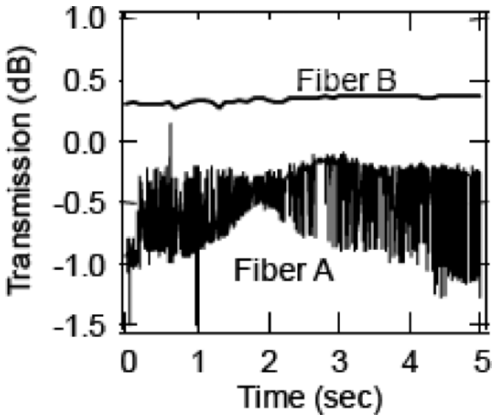

Fig. 26. Temporal intensity fluctuation measurement of coherent distributed MPI in HOM fibers. Fiber A guides several modes, while fiber B is optimized for MPI performance. Transmission spectra vertically offset for clarity.

the LP_{02} mode, and thus reduces coherent, distributed MPI. That assertion can now be tested, with the tools to measure MPI described in the previous sections. As an example, two HOM fibers are chosen. Fiber A guides the LP_{03} and LP_{21} mode, in addition to the LP_{01}, LP_{11}, and LP_{02} modes. Fiber B does not guide the LP_{03} mode, and the smallest effective index separation is between the LP_{02} and LP_{21} mode, with a value of $\Delta n_{\text{eff}} \sim 1.25 \times 10^{-3}$.

Direct temporal intensity variation measurements on both fibers, are shown in Fig. 26. The measurements were conducted on modules with strong mode converters and optimized discrete connections, and hence truly measure the effect of the fiber alone. Fiber A yields significantly higher MPI than fiber B (–25 dB as opposed to –43 dB). This confirms the design rules laid out in Section 2.3, which prescribe a minimum value for effective index separations between the LP_{02} mode and other guided modes in a HOM fiber.

4.3. Systems Impact of MPI in HOMs

Extensive studies have been conducted [42,43] to evaluate the systems impact of MPI arising from incoherent interference, such as discrete reflections from connectors and DRB from Raman amplifiers. Phase difference between the light-paths is a random variable in the incoherent case, and is uniformly distributed in $[2\pi]$. This simplifies the analysis of MPI, and deterministic systems penalties can be obtained. In that sense, the impact of MPI is similar to that of noise due to amplified spontaneous emission (ASE) in amplifiers, and leads to deterministic systems penalties. Zheng et al. [49] have made similar assertions with respect to coherent distributed MPI in HOMs. However, note that a characteristic signature of MPI in HOMs is the slow, bursty evolution of transmitted power, as shown in Fig. 25(a). This has more in common with slow

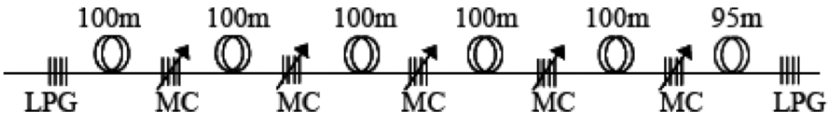

Fig. 27. HOM MPI emulator schematic. Input and output LPGs convert LP_{01} light into LP_{02} and vice versa. Intermediate 5 MCs can be tuned to yield desired mode coupling. Delay between interfering arms emulated by ∼100 m of HOM fiber.

fading due to polarization mode dispersion (PMD), another impairment due to mode coupling between co-propagating modes. The problem of MPI in HOMs is as recent as the advent of the devices themselves, and thus has not been studied in nearly as much detail as PMD. The following experiments describe some of the first in emulating and understanding the systems impact of this.

4.3.1. MPI Emulator Schematic and Characterization

Distributed mode coupling can be emulated with a device comprising a series of concatenated mode converters (MC) that provide desired amounts of mode coupling in a distributed fashion, as shown in Fig. 27. The MCs are tunable TAP-LPGs, described in Section 3.4 (see Fig. 14) whose mode coupling efficiencies η, can be tuned from –30 dB (0.1%) to 0 dB (100%) The input and output of the device comprise strong static gratings, like those described in Section 3.2, providing –40-dB mode-conversion ($\eta \sim 0.01\%$). HOM fiber segments of ∼100 m are added between each MC to yield modal delays similar to those encountered in HOM-DCMs (10–20 ns) [50].

Interference results from light coupled by any pair of MCs in the series. As mentioned in the introduction of this section, interference terms arising from coupling due to more than one pair of MCs will be 2–3 orders of magnitude lower, and thus can be neglected. Thus, for N coupling events, $N(N-1)/2$ interference terms will result [43], as is clear from Eq. (24). The emulator comprises $N = 5$ MCs, leading to 20 mode coupling events. Liu et al. [51] showed that $M > 10$ is a good approximation for $M \to \infty$, from a systems penalty perspective. Hence, the HOM emulator with 20 discrete mode-coupling events is expected to closely resemble distributed mode coupling in a HOM fiber. Table 1 shows the variety of mode coupling states used for each of the 5 MCs in this emulator. The emulator is then characterized by the series of letters (A through E) denoting the state of each of the MCs.

Table 1. Mode coupling efficiency levels for MC state designations.

	A	**B**	**C**	**D**	**E**	**0**
η (dB)	−12.5	−15	−17	−20	−25	−30

Figures 28(a) and (b) show the MPI measured by two different techniques to capture the slow (see Section 4.2.3) as well as fast noise (see Section 4.2.2) contributions

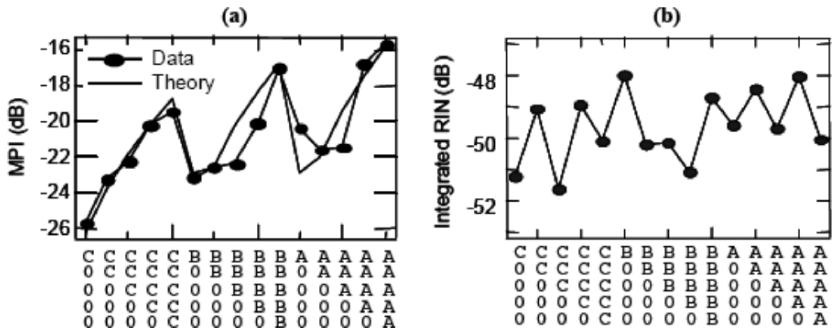

Fig. 28. MPI for various emulator states. (a) Slow noise measured with power meter. Fits well with Eq. (24). (b) MHz noise measured with RF spectrum analyzer—small, and no correlation with MPI state.

of the emulator. The expected MPI for any given emulator switch state (determined by a series of letters denoting the mode coupling efficiency of each of the MCs, as shown in Table 1) is deduced from Eq. (24). Figure 28(a), which shows MPI deduced from measuring slow power fluctuations (Section 4.2.3), shows an excellent match between data and theory. However, MPI contributions from fast fluctuations (Ssection 4.2.2) have no correlation with the emulator switch (MPI) state [Fig. 28(b)]. Fast fluctuations are caused by laser phase noise, and will be sensitive to the amplitude of the replica with the largest relative delay. This value is held constant, since the total length of the fiber does not change between switch states.

4.3.2. Systems Evaluations of Emulator

10.6-Gb/sec NRZ data at a signal wavelength of 1545 nm with a PRBS of $2^{31}-1$ is transmitted through the HOM emulator, and detected by an optically pre-amplified receiver with adaptive threshold control. For such a system, a device yielding incoherent interference resulting in fast noise, will lead to deterministic power penalties given by [51]

$$P(dB) = -10\log\left\{1 - Q^2(\eta_1\eta_2)\frac{1+r}{\left(1-\sqrt{r}\right)^2}\right\}, \tag{30}$$

where $Q \sim 6$ for a BER of 10^{-9}, $\eta_1\eta_2$ is the MPI, and $r = 0.05$ is the extinction ratio of our transmitter.

For each MPI state of the emulator, the BER was measured in 1-sec intervals over a 1-min period, at a variety of average received power levels (Fig. 29). The BER slowly drifts by almost an order of magnitude during the measurement. It is interesting to note that the BER drift is of identical timescale as that of the slow power fluctuations described in Section 4.2.3.

Since one manifestation of coherent MPI is slow power fluctuations, some of the drift seen here could conceivably be due to drifts in received power. This is investigated in further detail by recording the BER as a function of instantaneous received power, as

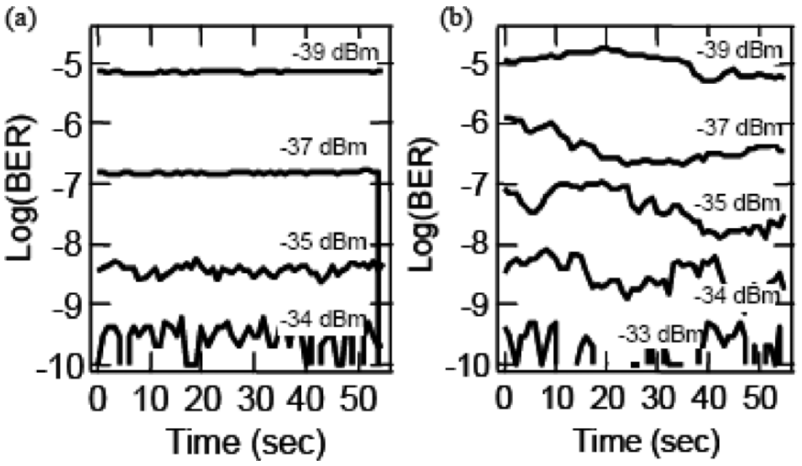

Fig. 29. BER vs time for different average received powers (a) back-to-back (b) Emulator MPI = –22 dB; Order $\sim 10\times$ slow BER fluctuations.

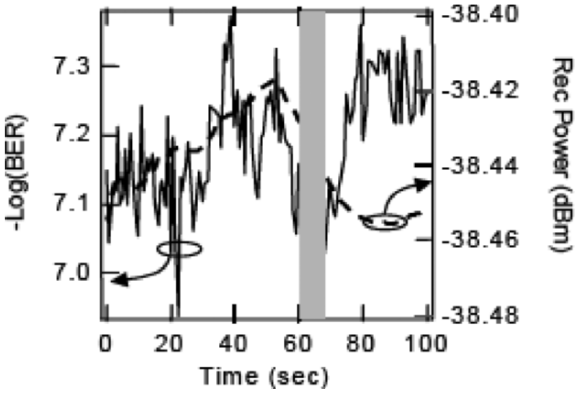

Fig. 30. Correlation between power swings and change in BER. BER increases when received power swings between maximum and minimum value—highlighted in grey shaded region of plot.

shown in Fig. 30. No obvious correlation is evident between received power and BER. However, the BER degrades at instances when the received power "swings" by a large value. Thus, while received power and BER do not correlate, the BER degradation is found to closely track large power swings. This is consistent with the fact that large power swings represent the complex interferometer going from in-quadrature to out-

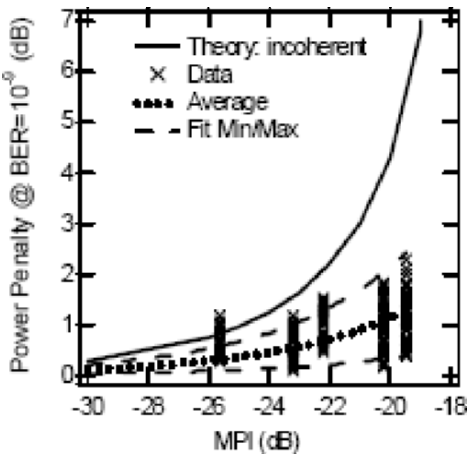

Fig. 31. Power Penalty vs. emulator MPI. Minimum distortions are virtually penalty free. Average penalty lower than penalty from incoherent MPI. Spread in penalties increases with MPI.

of-quadrature or vice-versa, and these are the instances when an interferometer is most sensitive to phase fluctuations.

Figure 31 shows the power penalty at a BER of 10^{-9} culled from all the systems tests conducted on the emulator, plotted as function of the MPI state of the emulator. The spread in power penalties increases for larger MPI. Also shown in Fig. 31 are four lines: theoretical prediction from Eq. (30), a fit through the average, minimum and maximum power penalties for the variety of MPI states, respectively.

As is evident near penalty-free operation is obtained for at least some length of time, for *any* MPI value of the emulator. This is understood by considering the contributions of fast and slow noise. Figure 28(b) showed that the distortions due to fast fluctuations are virtually negligible (MPI ~ -50 dB). Thus, the slow power fluctuations essentially determine the BER, and long dwell-times at constant-power states of the complex interferometer result in penalty-free operation. Another interesting aspect of the data shown in Fig. 31 is that the average as well as peak penalties scale at a significantly slower rate with MPI, than in the case of incoherent interference resulting in fast fluctuations [Eq. (30)]. The average penalty shows expected behavior, since slow fluctuations may be slow enough to be partially filtered out by the 50-kHz high-pass filter comprising the receiver. The maximum penalties are also smaller than in Eq. (30)— this may be because power swings of the complex interferometer (resulting in maximum penalties) may be rare occurrences, requiring longer sampling times [52].

4.4. Summary

HOMs may potentially suffer from MPI due to their few-moded nature, and this section described the two predominant sources of intermodal interference, namely discrete and distributed coherent interference. The discrete mode coupling problems are relatively

to easy to identify/isolate, and when in-fiber gratings are used as mode converters, they are relatively easy to minimize. The assembly technique plays an important role in this.

Random mode coupling in the HOM fiber leads to MPI in the distributed coherent regime. It possesses two distinct time scales of distortions, 1–10s of seconds, and few microseconds. The most widely used technique to measure incoherent MPI, using RIN measurements from an ESA, may not capture an important noise mechanism in these devices. The worst measured MPI values (and hence, presumably the values that capture all relevant noise phenomena) in HOMs is obtained from a long timescale, direct transmitted power measurement.

In addition, the systems impact of these noise phenomena also shows clear distinctions from MPI in the incoherent regime. The average power penalty from this kind of MPI is lower than penalties due to similar levels of MPI from incoherent crosstalk, though the spread in power penalties is significantly larger. The slow nature of BER swings may open up the possibility of utilizing adaptive control (of the throughput power or input SOP) as a means to manage this impairment. However, it is important to note that only preliminary studies of the systems impact of MPI in HOM fibers exist, and a clearer understanding may follow as this technology matures.

5. Static Dispersion Compensators

To recap from Section 1, a DCM should offer dispersion compensation over the entire spectral range of interest. This implies that the dispersion of the span and that of the module must be of equal magnitude and opposite sign. In addition, the RDS and RDC of the span and module should also match. Typically, the transmission fiber span has practically no curvature. Hence, the RDC of the DCM should be close to zero.

This section will provide some examples of static dispersion compensators built with HOM fiber technology, and their performance-metrics, in terms of loss, polarization mode dispersion (PMD), Raman gain coefficient, MPI etc. Representative systems tests, comparing an HOM module with a DCF module with similar characteristics, will be described to evaluate HOM-DCMs with respect to the benchmark technology (DCF). It is important to note that the module characteristics shown in this section are not theoretical predictions, but are measured on fibers that can be used for practical deployment. That is, their profile sensitivity is such that several km of the fibers from the same preform had similar characteristics, and the preform profiles could be duplicated with relative ease in the laboratory environment. In addition, the fibers and designs deemed practical also satisfy several other performance metrics such as low values for loss (attenuation as well as bend induced), MPI, and PMD, among others. Hence, this section enables comparing the theoretical possibilities described in Section 2, with what has been achieved to date.

5.1. Dispersion and Slope Compensation

Following the description in Section 2.2 on the design flexibility for dispersion engineering available with HOMs, it would be expected that fibers with high dispersion or dispersion slope should be achievable. Figure 32(b) shows the dispersion as well

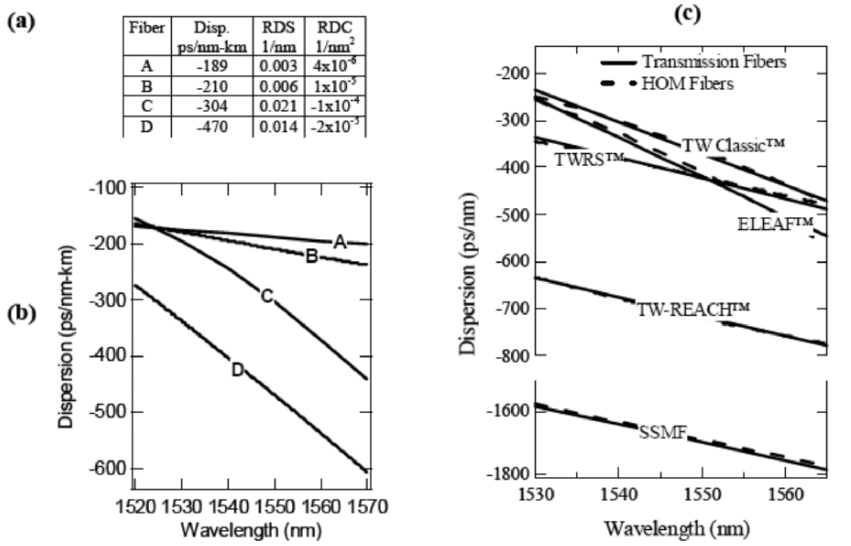

Fig. 32. (a) Table showing representative dispersive values attained by HOM fibers operating in the LP_{02} mode. Very high dispersion and RDS, and very low RDC feasible. (b) Dispersion vs. wavelength for fibers listed in (a). (c) Dispersion vs. wavelength plot of 100-km transmission fiber span requirements, and the corresponding curves of HOM fibers designed for compensating them.

as RDS for the LP_{02} mode for a variety of representative HOM fibers. It shows that dispersion values ranging from ~ -150 ps/nm-km to as large as ~ -500 ps/nm-km are readily achievable [53], [54]. Highly dispersive fibers are very attractive because they offer three attendant benefits arising from the shorter lengths of fiber needed in a module, namely, lower cost, lower nonlinear distortion, and potentially lower loss (if the fiber attenuation is not drastically compromized on account of it being highly dispersive). The lower loss and nonlinearity aspects of HOM fibers will be discussed in the following sections.

Figure 32(a) (table) shows the dispersion, RDS and RDC values for the fibers shown in Fig. 32(b). The RDS values range from 0.003/nm to 0.0021/nm, which cover the range of transmission fibers currently deployed. An interesting aspect of the HOM fibers is its dispersion curvature. Normally, the curvature increases with the magnitude of dispersion. However, it appears that near-linear dispersive behavior is feasible with HOMs even when the dispersion is large in magnitude (for fiber with $D = -470$ ps/nm-km, RDC is only 2×10^{-5}). There does appear to be a weak correlation between RDS and the magnitude of RDC in these fibers. DCFs with such high dispersions would be expected to have high curvature [55], and the preferred approach for conventional technology is a (potentially more complex) combination module that splices a series of different DCF types to obtain low RDC [56].

Figure 32(c) shows the characteristics of HOM fibers that are designed for matching the specific dispersion requirements of a range of transmission fibers commercially

deployed around the world. The solid lines of the plot show the amount of dispersion *required*, as a function of wavelength, for a typical 100-km transmission fiber span. The different fibers are denoted by their trademark names. The dashed lines show the dispersive characteristics of HOM, and given that the entire range of desired RDS is feasible with these fibers, the dashed lines are shown to overlap very well with the solid lines.

5.2. Fiber and Module Loss

Module loss directly impacts systems performance by adding ASE noise. The metric commonly used to quantify this impairment is the figure of merit (FOM), defined as

$$\text{FOM} = \left| \frac{D}{\alpha} \right|, \tag{31}$$

where α is the loss of fiber, in dB/km, and D is its dispersion (hence FOM has the rather non-physically-intuitive units of ps/dB-nm). The FOM is a useful parameter, because it allows scaling loss with dispersion, and hence compare the relative value of transmission fibers for systems designers—a transmission fiber with large required dispersion compensation would automatically require more lossy compensators. Currently, DCF-based DCMs for compensating NZDSF have module losses of $\sim$2–4 dB, and the best reported value of FOM is $\sim$ 459 dB-nm/ps [57]. Typically, DCF has a propagation loss of 0.4–0.6 dB/km, and hence techniques to increase FOM typically involve increasing the dispersion of the waveguide design.

HOM fibers offer some new possibilities [58], since their waveguide-dispersion is inherently larger in magnitude than that of the LP_{01} mode (see Section 2). For a practical HOM-DCM module, the HOM fiber as well as the mode-converters and connections should be low loss. As described in Section 3, the use of long-period fiber gratings, enables very low loss mode conversion (insertion losses $\ll 0.1$ dB). The other two aspects governing loss—the fiber loss, and connection losses are described below.

5.2.1. Fiber Figure of Merit

The FOM for HOM fibers is measured by conventional techniques (optical time domain reflectometry—OTDR, or cut-back), but it additionally involves first connecting the fiber to a strong mode converter so that the measurand is the LP_{02} mode. Figure 33(a) (table) shows representative measurements for some fibers (see right-hand side columns denoting LP_{02} properties). As in the case of DCF, propagation losses range between 0.4 and 0.6 dB/km, but the ability to obtain high dispersion values enables FOMs as high as 734 ps/nm-dB, which is a record at the time of this writing, for dispersive fibers operating in any mode.

5.2.2. Splices Between HOM Fibers

Splices between HOM fibers used for the mode converter, and that used for the dispersive medium, may lead to discrete MPI as well as loss. Module assembly techniques described in Section 4.1.3 (see Fig. 22) indicate that MPI can be arbitrarily minimized.

(a)

Fiber	LP_{01} properties		LP_{02} properties		
	A_{eff} (μm^2)	Pigtail splice loss (dB)	D (ps/nm-km)	α (dB/km)	FOM (ps/dB-nm)
A	48	0.26	169	0.42	402
B	43	0.31	189	0.406	466
C	45	0.34	470	0.64	734

(b)

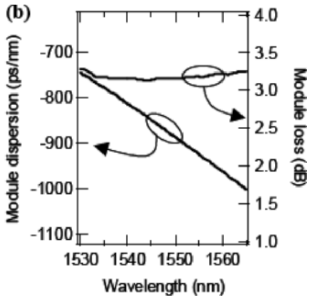

Fig. 33. (a) Summary of LP_{01} and LP_{02} properties for HOM fibers with different magnitudes of dispersion. Important parameters for HOM module loss are LP_{01} Aeff and LP_{02} propagation loss—both show no correlation to LP_{02} dispersion => high design flexibility, (b) Low loss dual-span TWRS compensator with –886 ps/nm dispersion has only 3.16 dB loss at 1550 nm—may enable future systems requiring large dispersion magnitudes.

On the other hand, early investigations of HOM-HOM fiber splice losses revealed values as high as 0.35 dB. Advanced splice optimization techniques have since shown that this splice loss can be reduced to $\ll$ 0.1 dB, while achieving the –60 to –90 dB MPI levels described in Section 4.1.3. This is expected, since the LPG fiber was designed (see Section 2.3) to yield an LP_{02} mode profile similar to that of the dispersive HOM fiber.

5.2.3. Splices Between HOM and Pigtail Fibers

The splice between the pigtail connector and the HOM fiber couples between two non-dispersive, well-guided LP_{01} modes. In contrast, DCFs couple the light from the pigtail fiber directly into the dispersive mode. The latter case has the potential to (a) increase splice/connection losses, (b) cause large wavelength dependence at the connection (since the dispersive mode is by definition rapidly changing in shape and size with wavelength), or (c) limit the design space in light of the former two constraints. While specialized splicing techniques reduce the impact of this impairment, the greatest impact may be on the design freedom—DCFs with dispersion greater than 300 ps/nm-km have not proven to be suitable for practical modules.

While the LP_{02} mode is highly dispersive, the LP_{01} mode of the HOM fiber has dispersion and mode field diameter (MFD) comparable to that of single-mode transmission fibers. The left hand side of the table in Fig. 33(a) shows the A_{eff} and splice loss for HOM fibers with different dispersion values for the LP_{02}mode. Note that the splice loss does not vary significantly for fibers with dramatically different dispersion magnitudes. This is expected, since the LP_{01}mode of the HOM fibers has A_{eff} that is mostly independent of their LP_{02} dispersion value.

The ability to design HOM fibers without splice/connection loss constraints and the inherently large FOM for such fibers enables building low loss compensators. Losses for HOM-DCMs built with LPG-base converters for 100-km NZDSF spans are approximately 2–2.5 dB, but the impact of their inherently higher FOM becomes

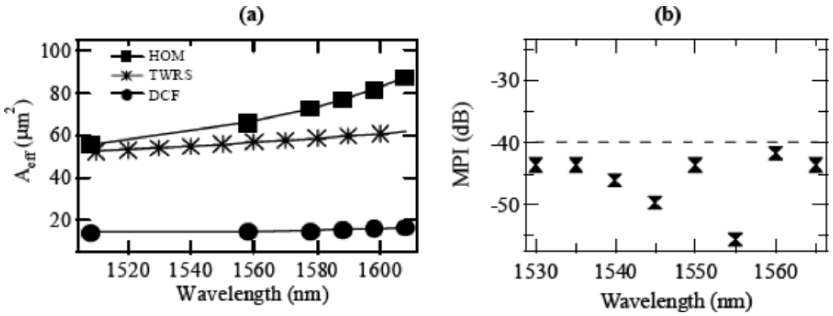

Fig. 34. (a) Effective area for HOM fibers, in comparison to DCFs and transmission fibers. Larger than DCF by 4–5×. (b) MPI over C-band, for typical HOM module. MPI measured by temporal intensity measurement technique (Section 4.3), which yields the highest values of MPI. MPI < -40 dB readily achieved by HOM technology now.

apparent for modules requiring large dispersion. Figure 33(b) shows a plot of the dispersion as well as insertion loss (splices, mode converters and fiber, included) in the C-band for a module that compensates for dispersion of a 200-km TWRS^{TM} span. At 1550 nm, a module providing –886 ps/nm dispersion has an insertion loss of only 3.16 dB. This module was made with unoptimized HOM-HOM fiber splices, which have subsequently been shown to be much lower. Thus, applying the splice optimization techniques for HOM-HOM fiber connections (see Section 5.2.2) module losses as low as 2.6 dB may be realized for this module.

5.3. Effective Area and MPI

The two most distinguishing features between HOM fibers and DCF are their effective areas and the potential for modal noise. DCF has A_{eff} ranging from 15–20 μm^2, and this is approximately 4–6 times smaller than that of transmission fiber. Even though the length of fiber used is substantially lesser than the transmission span itself, the small A_{eff} often leads to debilitating nonlinear distortions. Hence, Forghieri et al. [59] proposed an alternate FOM for DCF that includes the impact of nonlinearities. They noted that increasing both the A_{eff} and the dispersion per unit length mitigate nonlinear distortions. Both these quantities are bounded in DCFs, for reasons elucidated earlier, and it is unclear what process developments will fundamentally change the level of nonlinear distortions caused by DCFs.

HOMs, on the other hand, are inherently more dispersive and propagate with larger A_{eff} [see Fig. 34(a)], thus satisfying both parameters of interest in reducing nonlinear distortions. A_{eff} for dispersive HOM fibers are typically similar to that of transmission fibers (i.e., they are 4–5 times larger than DCF), and their dispersion per unit length is 50–100% larger than DCF. The impact of this has been demonstrations of larger transmission distances in comparison to identical systems operating with DCFs. Some representative systems experiments reinforcing this attribute will be described in Section 5.5.

Modal interference or MPI is the other distinguishing feature. DCFs, because of their single-moded nature, do not suffer from this impairment, though they may be susceptible to incoherent MPI when they are Raman-pumped. Section 4 gave a detailed description of MPI in HOMs, and presented arguments for the utility of the direct temporal intensity fluctuation measurement technique as a standard for measuring and quoting MPI values. Hence, the data shown here is based on that measurement technique. Figure 34(b) shows some representative MPI measurements made on modules constructed with TAP-LPGs and HOM fibers depicted in Figs. 32 and 33. MPI values lower than –42 dB are readily achieved over the spectral ranges of interest.

Several publications on HOM-DCMs quote MPI < -40 dB today, but do not mention the technique used to measure it. As described in Section 4, there are several techniques to measure MPI, and the actual measured value depends on the measurement technique. Nevertheless, given that the primary cause of MPI is random mode mixing in the HOM fiber, it is reasonable to assume that HOM technology can readily achieve MPI < -40 dB.

Perhaps the best proof of the adequacy of MPI levels in HOM-DCMs lies in successful systems demonstrations. Section 5.5 will describe experiments where 40 Gb/s transmission distances of 1700 km have been achieved with 12 concatenated HOM-DCMs whose MPI is shown in Fig. 34(b). Garrett et al. [60] have transmitted 10 Gb/s signals over 6000-km-long transmission experiments using 60 concatenated HOMs. The authors claim their modules have MPI ~ -41 dB though they do not specify the measurement technique. In addition, the authors claim their transmission distance was primarily limited by OSNR degradation, apparently confirming that MPI was not a problem.

5.4. Other Characteristics

Several other properties are important to assess the viability of a technology. All fibers can suffer from non-circularity induced from manufacturing errors. This results in polarization mode dispersion (PMD). In DCFs, the typical values for first order PMD are approximately 0.07 ps/$\sqrt{}$km. However, this number is strongly dependent on the diameter of the spool and other packaging parameters. Earliest demonstrations of HOM-DCMs revealed PMD values as high as 6 ps/$\sqrt{}$km [61], but developmental efforts have brought this number down to 0.4 ps/$\sqrt{}$km, with the best measured numbers for spooled and packaged modules being around 0.32 ps/$\sqrt{}$km. It is highly likely that large-scale production will provide the level of process control to actually take this number down to the levels of the state of the art for DCF. Thus, in this respect, HOM fibers and DCF appear to be similar.

Polarization dependent loss (PDL) is practically nonexistent for DCFs. For HOM-DCMs, PDL primarily arises from the PDL of the mode converters. As shown in Section 3.5 (Fig. 18), long-period fiber gratings are especially suited for this application, because the measured PDL for them is $\sim 10^{-4}$ dB (as described in that section, residual LP_{01} light had to be measured to deduce this value because no measurement system can measure such low values of power fluctuations). The measured PDL values in LPG-based HOM-DCMs are less than 0.1 dB. The majority of this arises from MPI. Since the polarization evolution is different for different modes, changing the input SOP can take an interferometer from constructive to destructive interference state,

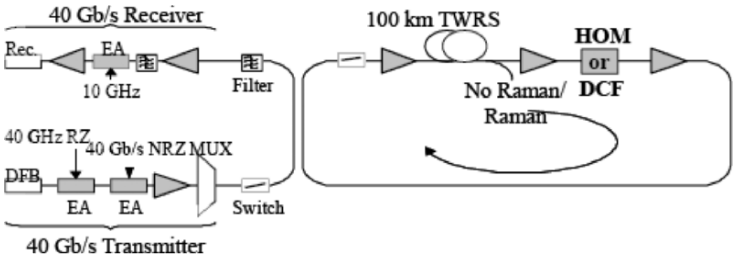

Fig. 35. Systems setup for evaluating HOM and DCF modules for nonlinearity in DCMs. 40 GB/s modulator drives transmitter at 1552.6. Signal fed into recirculating loop comprising 100 km of TWRS fiber and a DCM at the mid-stage of an EDFA to simulate multiple-span transmission. Set up allows for counterpumping transmission fiber for $\sim$ 15 dB Raman gain.

which is the essence of intensity noise due to MPI. Thus, a module with low MPI and PDL-free LPGs ensures PDL-free performance.

The small A_{eff} in DCFs, which can potentially cause nonlinear distortions, has a spin-off benefit as a high Raman gain medium. Raman amplification in DCFs, where pumping the DCF at a wavelength that is one Stokes-shift lower than 1550 nm, yields broadband gain [62]. HOM-DCMs, on the other hand, are not very efficient Raman gain elements because they have large A_{eff} (similar or larger than transmission fiber). A comparison of DCF and HOM-DCM of similar attributes (~ -420 ps/nm dispersion, slope matched for TWRS$^{\text{TM}}$, $\sim$3 dB loss) was obtained by counter-pumping the modules with 1455 nm light, and measuring a 1550-nm CW signal. For the HOM-DCMs with TAP-LPG mode converters, no mode conversion occurs at 1455 nm, and thus the pump light travels in the LP_{01} mode, while the signal travels in the LP_{02} mode. This decreases the power overlap between the pump and signal to 71% of the expected value if both the signal and pump were travelling in the LP_{02} mode. We found that the Raman gain coefficients for the HOM-DCM were a factor of 6 lower than those for the DCF, confirming that HOM-DCMs are not well suited for Raman amplification.

5.5. Systems Tests and Evaluations: Nonlinearity Impact

Provided MPI is sufficiently managed (as previous descriptions suggest they have been), HOM-DCMs offer a unique attribute, namely the potential for a low nonlinearity device (in contrast to DCFs) due to the large A_{eff} for signal propagation. This assertion has been tested in several ways described below.

Tur and coworkers have measured the level of stimulated Brillouin scattering [63] as well as cross-phase modulation [64] in HOM-DCMs and DCFs, and found that (after normalizing for differences in characteristics between the two modules, such as dispersion, loss, length of fiber, etc.) the HOM modules had 5 dB higher input power threshold for the same level of nonlinear signal.

Direct comparisons of DCFs and HOM-DCMs have been conducted in transmission systems, with a 40 Gb/sec systems test bed illustrated in Fig. 35 [65], [66]. In these experiments, the objective was to compare the nonlinearity accumulation in HOMs and

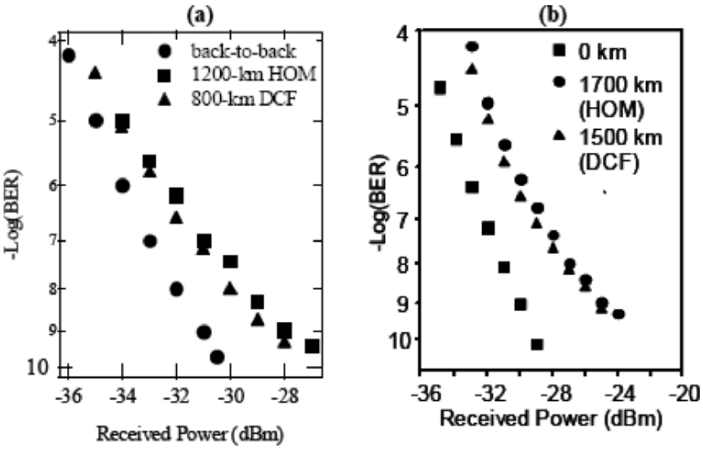

Fig. 36. 40 Gb/s single channel transmission experiments on 100-km TWRS in recirculating loop with HOM and DCF under identical conditions, to evaluate their relative performance. (a) 2 ps RZ pulses at 1550 nm; EDFA only. Input power into HOM could be increased by 10 dB compared to DCF, without incurring nonlinearities. Lead to 50% increase in transmission distance with HOM. (b) EDFA + 15 dB distributed Raman gain, 8 ps RZ pulses at 1552.6 nm. Amplifier NF improved by 1 dB when HOM was used, because up to 5 dB higher power could be introduced into HOM compared to DCF.

DCFs due to the vastly dissimilar A_{eff}, and hence similar modules were chosen. Both had dispersion of ~ -420 ps/nm, the RDS was similar though immaterial because this was a single channel experiment, the HOM module loss was 3 dB, while that of the DCF was $\sim$ 3.7 dB. Additionally the HOM-DCM had low MPI (–44 dB), but PMD was 5 times higher than in DCF. Thus, while the DCF loss was slightly higher, leading to the possibility of biasing the results against DCF, the HOM module had significantly higher PMD, which would impact its performance.

5.5.1. Long Distance Transmission

1550-nm light with pulse widths of $\sim$2 ps, corresponding to a 10% duty cycle, were sent through a span with no Raman gain and compensated for dispersion with a HOM or DCF, to evaluate the maximum feasible transmission distance before a bit-error-rate (BER) floor occurred above a BER value of 10^{-9}. Figure 36(a) shows BER curves after 12 spans of transmission (1200 km) when the HOM-DCM was used. In addition, the BER power penalty was only 1 dB after 1000 km of transmission [67]. In contrast, similar experiments with the DCF yielded 800 km of maximum achievable distance. Achieving the longer distance of transmission required raising the input power into the HOM-DCM to 4 dBm. The DCF performance would degrade rapidly for input power levels over –0.5 dBm, but the HOM could tolerate input power levels up to 9.5 dBm before any observable onset of nonlinear distortions.

5.5.2. Improved Amplifier Noise Figure

When the same span described above was Raman pumped, longer distance transmission was (obviously) feasible with either DCF or HOM. However, it is expected that in systems with high Raman gain, higher input power capabilities of DCMs will become more important because signal OSNR is roughly determined by the lowest power level of the span, and that condition may now occur within the DCM. Although only single-channel transmission was conducted, a WDM multiplexer with 100 GHz channel spacing was used at the transmitter output to ensure that the 40-Gb/s RZ signal was compatible with a 100-Ghz channel spacing. The duty cycle of the 40-Gb/s RZ signal with a PRBS of 2^{31-1}, was 30% at the output of the WDM multiplexer (yielding a pulse-width of 8 ps). Signal transmission with a BER $< 10^{-9}$ was achieved over 1700 km with the HOM-DCM as the compensator [68] [Fig. 36(b)]. The optimum launch power into the transmission fiber was found to be 0 dBm, whereas the launch power into the HOM could be varied between 0 and +5 dBm without changing the transmission performance. A similar experiment with DCF as a compensator yielded 1500-km transmission, where the input power into the DCF had to be limited to –3 dBm. The attendant increase in transmission distance arises from a lower amplifier noise figure when the HOM-DCM is used. This was directly confirmed by measuring this parameter—the optical signal to noise ratio (OSNR) degradation due to the DCF was approximately 1 dB, while no OSNR degradation was observed due to the HOM-DCM.

In the systems tests described here, we find that for "standard" 8-ps pulse at 40 Gb/sec, systems margins gains of 1 dB can be achieved, which translates into a 12% increase in transmission distances. On the other hand, short (2-ps) pulses, can be transmitted for roughly 50% longer distances when HOM-DCMs are used in place of DCFs. This is consistent with the fact that shorter pulses have higher peak powers, making them more susceptible to nonlinear distortions. Hence, we find that the larger A_{eff} of HOMs can offer a distinct advantage over DCF, and this contrast becomes more apparent as the pulse width decreases (or bit-rate increases).

5.6. Summary

The capability of attaining large dispersion with low loss, as theoretically posited in Section 2, is confirmed for HOM fibers—fibers with record FOMs $>$ 700 ps/nm-dB have been achieved. In addition, the properties of the LP_{01} mode in HOM fibers are de-linked with those of the dispersive modes, and hence HOMs can be designed to be highly dispersive without sacrificing splice efficiencies. However, losses for modules providing moderate levels of dispersion (as required for NZDSFs) are only marginally lower in HOM-DCMs compared to DCFs, even though the demonstrated FOMs in HOM fibers are 60% higher than in DCFs. This situation may change as and when systems require large amounts of signal chirping, as is proposed for future 160 Gb/sec communications systems [69]. Several other fiber-related parameters, such as PMD, PDL etc, also have similar, low values, for both HOMs and DCFs.

There are important distinctions. MPI was a concern for HOM-DCMs. Many studies over the past few years show that this may be a manageable impairment, and MPI < -40 dB is readily achieved. However, it remains to be seen if this number

would degrade during prolonged field tests, or if it translates into a higher module cost due to the need for additional tests and qualifications.

The other distinction is A_{eff}. Since HOM-DCMs have 4–5 times larger A_{eff} in comparison to DCF, they are less susceptible to nonlinear distortions. This translates into lower amplifier noise figures and higher OSNRs. Straight comparisons in a transmission test bed have shown that this feature has allowed 12% larger transmission distances for 8-ps long pulses, and up to 50% longer distances for 2-ps long pulses. This points towards the fact that the large A_{eff} of HOMs will become increasingly beneficial as systems migrate to higher bit rates.

6. Tunable/Adjustable Dispersion Compensators

This section will describe a unique attribute of HOM fibers, namely its inherent ability to guide more than one mode with different group delays and dispersion, and a unique device effect (adjustable dispersive devices [70]) that can exploit it. The resultant device enables a wavelength-continuous, broadband, tunable dispersion compensator.

6.1. Modal Path Diversity: Device Schematic

Since a HOM fiber inherently guides several modes, many different optical paths exist for the signal, though the dispersion compensator utilizes only the LP_{02} mode as the preferred path. As described in Section 2, different modes will induce different amounts of group delay and dispersion to the mode. Hence, if light can be shuffled at will between the modes, several optical paths, and therefore dispersion values, can be obtained from the device. This is illustrated in Fig. 37(a), which shows the familiar schematic of a HOM-DCM with 2×2 switches at the input and output, respectively, instead of strong, static mode converters. Also shown are near-field images of the LP_{01} and LP_{02} modes—the two modes between which the 2×2 switch can shuffle light. When the two switches are the "bar" states, light passes through the device in the LP_{01} mode, and dispersion is just the dispersion of the LP_{01} of the HOM fiber. As described in Sections 2.4 and 5.2.2, the LP_{01} mode in HOM fibers is a strongly guided negligibly dispersive mode, whose dispersion is approximately the small, positive value for material dispersion. On the other hand, if both the switches are in the "cross" state, light travels in the LP_{02} mode of the HOM fiber, as is the case of the static HOM-DCM described in Section 5. Figure 37(b) shows the dispersion for the device operated in both the states, and it is immediately apparent that the dispersion can be changed by a large amount with appropriate 2×2 switches.

Figure 37(c) shows the schematic for an adjustable dispersion compensator built with this concept. The device comprises N segments of HOM fiber connected by $N+1$ tunable TAP-LPGs. Recall from Section 3.4 (Fig. 16) that the unique, strength-tuning action of TAP-LPGs enables realizing 2×2 switches between the LP_{01} and LP_{02} modes. Hence, the multiple switches shown in this schematic can be realized with LPGs in heat- or strain-tunable housing that provides the switching action. Since each fiber-segment can support two modes, it follows that this device can be switched between 2^N states. Furthermore, if the lengths of HOM fiber are arranged in a binary progression, such that $L_N = 2^{N-1}L$, the effective path length of the signal in each

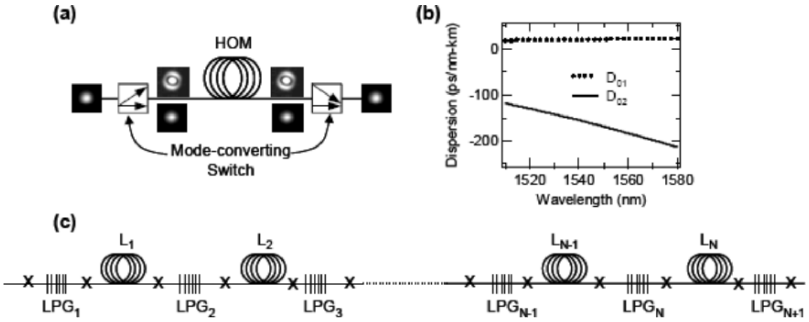

Fig. 37. (a) HOM compensator with 2×2 switches instead of static mode converters to exploit the modal path diversity. (b) Dispersion for the LP_{01} and LP_{02} modes in a HOM fiber. Signal experiences different dispersion in different modes (c) Schematic of AHOM. N HOM-fiber spans connected by $N + 1$ TAP-LPG based 2×2 switches (Section 3.4). Binary length progression of Li enables tunable optical path lengths with constant spacing.

mode is equally spaced. Hence, for a given dispersion difference $D_{01} - D_{02}$ between the two modes, such a device yields

$$\begin{aligned} &\Delta D = (D_{01} - D_{02})\, L_1, \\ &\mathrm{TR} = \Delta D \tfrac{N(N-1)}{2} \\ &\Rightarrow \Delta D = \tfrac{\mathrm{TR}}{2^N - 1}, \end{aligned} \tag{32}$$

where ΔD is the smallest dispersion step size, which defines the granularity of the adjustable HOM (AHOM), L_1 is the length of the smallest segment of HOM fiber, and TR is the (dispersion) tuning range. This illustrates an important attribute of this device:

– Step size is determined by the first segment length
– Tuning range is determined by number of segments (or number of LPGs)
– Bandwidth is determined by TAP-LPG characteristics.

Thus, the three important characteristics of this TDC are governed by independent variables, in contrast to all other TDCs which inherently possess bandwidth-versus-tuning-range tradeoffs. Since the dispersion is provided by the fiber itself, the device is broadband and wavelength continuous [70].

6.2. Device Characteristics

Again, the critical component for realizing the AHOM is the switchable mode converter, for which the tunable TAP-LPG is an ideal candidate. The negligible loss and all fiber nature of the TAP-LPG are especially important here, because multiple switches are needed throughout the device. The characteristics of the LPG switch were shown in Fig. 15. Since this is a linear reciprocal device, the mode conversion efficiency as well as mode extinction level is the same in the "bar" as well as "cross" states. For the

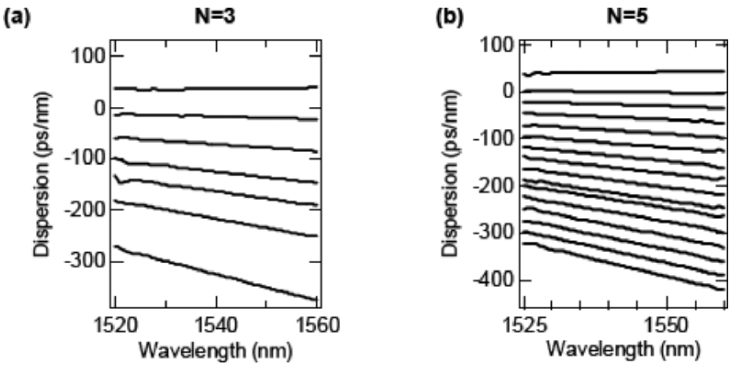

Fig. 38. Dispersion tuning measurements on AHOM. (a) three-segment AHOM yields $\Delta D \sim 58$ ps/nm; (b) five-segment AHOM yields $\Delta D \sim 14$ ps/nm. ΔD controlled by number of segments N, and tuning range controlled by total fiber length.

examples shown below, the LPG switches are 3-cm-long UV-induced LPGs that were bonded in a stainless tube wrapped with resistive heating wires. Heating the package thus imparts both temperature as well as strain changes on the LPG. The tuning is calibrated to yield two distinct states corresponding to strong mode conversion and no mode conversion, respectively.

6.2.1. Dispersion and Slope Tuning; Scalability

Figure 38 shows experimental measurements of dispersion tuning characteristics for AHOMs with different number of segments, N in Eq. (32). The HOM fiber used here has a dispersion of +21 ps/nm-km for the LP_{01} mode and –210 ps/nm-km for the LP_{02} mode. For the device shown in Fig. 38(a) with number of segments, $N = 3$, the total length of fiber is approximately 1750 m, yielding a dispersion step size of 58 ps/nm. When the number of segments is increased to five, the dispersion step size falls to $\sim$ 14 ps/nm (total length of fiber in this case was slightly different—1937 m). AHOMs of up to six segments, with $\Delta D \sim 7$ ps/nm have been demonstrated [71]. This high granularity, and the ability to scale it even further should make these devices applicable even for 160 Gb/sec applications, since the device has no passband limitations and should work for any signal bandwidth. This flexibility must be balanced with increases in loss and MPI of the device, as may occur as the number of segments is increased. This is addressed in Section 6.2.2.

6.2.2. Loss and MPI

Loss investigations of the tunable gratings were already described in Section 3.5.1, where the experimental schematic was similar to that of the AHOM. With insertion losses well below 0.1 dB, adding a large number of switchable MCs should not affect the AHOM loss. However, the AHOM also requires multiple splices. As was argued in

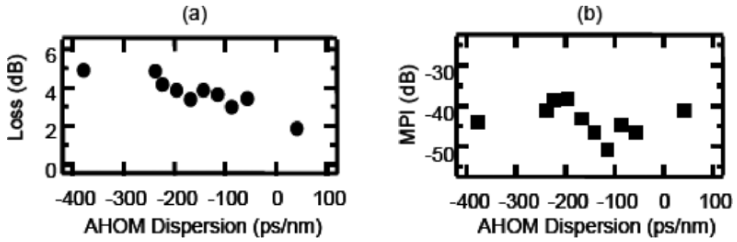

Fig. 39. Loss (a), and MPI (b) of AHOM with $N = 5$ segments. Average loss $\sim$ 3.7 dB. Loss contribution primarily from unoptimized splices. MPI from combination of mode converter and fiber. Worst MPI ~ -39 dB; Still allows 25 concatenated devices in a system for $<$ 1-dB BER penalty.

Section 5.2.2, many initial device demonstrations were made with unoptimized splices between identical HOM fibers. These splices add roughly 0.35 dB of loss, which can quickly add up to a large splice loss for AHOMs with large number of segments. Following that, additional investigations have shown that splice losses are $\sim$ 0.05 dB, which would enable constructing AHOMs with as many as 10 segments (20 splices) with only 1 dB additional loss. Figure 39(a) shows the insertion loss for an AHOM with five segments, as a function of its tuned dispersion value, constructed with unoptimized HOM fiber splices. Even so, an average device loss of 3.7 dB represents one of the lowest values among colourless TDCs reported to date.

As with static compensators, the sources for MPI are the fiber, incomplete mode extinction from the mode converter, and splices. Mode conversion in the fiber obviously remains the same as in earlier discussions. Splices, when optimized for MPI, can yield parasitic mode extinctions down to –90 dB, and hence multiple splices should not be a problem from this perspective. The influence of multiple mode converters can be analysed by Eq. (24) and the related discussion in Section 4.3.1, where an MPI emulator was built with a schematic very similar to the AHOM. We had found that the scaling of MPI with number of discrete mode coupling instances could be predicted fairly accurately. Thus, ignoring the (small) effect of in-fiber mode coupling and splices, an N-segment AHOM with switches that yield mode extinction η:

$$\mathrm{MPI} = \frac{N(N-1)}{2}\eta^2. \tag{33}$$

Hence, MPI was increase monotonically with the number of segments in the AHOM. For an AHOM with five segments, and hence six switches with mode extinctions, $\eta \sim$ –30 dB, the MPI of the device should be ~ -48 dB. This number underestimates the practical case, because fiber and splice MPIs are not included, and mode conversion efficiencies can be lower. Measurements of MPI on an AHOM with five segments is shown in Fig. 39(b), where the average MPI (–44 dB) is slightly higher than that predicted above.

Nevertheless, all these MPI values are small enough so that no BER penalty should arise out of a single span transmission experiment. Filter based TDCs are normally considered successful as long as they yield less than 1 dB BER penalty for a *single*

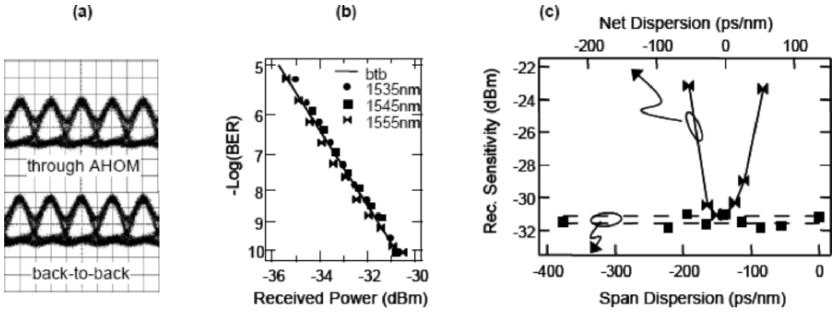

Fig. 40. (a) 40 Gb/s CSRZ eye diagrams for span with = 377 ps/nm and AHOM at –378 ps/nm at 1545 nm (b) BER curves for 40 Gb/s CSRZ – penalty free operation at wavelengths across C-band. (c) Squares (w.r.t. bottom axis) show received power for BER = 10^{-9}, for different fiber spans + AHOM states. Penalty-free operation over tuning range, within measurement uncertainty (dashed lines). Diamonds (top axis) show received power for BER = 10^{-9} vs. residual dispersion as AHOM was tuned. Rapid rise in penalty shows dispersion tolerance for this system.

device. The highest value of MPI measured for the AHOM is ~ -39 dB, which still allows concatenating approximately 25 devices in series for a 1-dB BER penalty.

6.3. Systems Test

The AHOM with five segments was used to test the performance of these TDCs [37]. 40 Gb/sec carrier-suppressed RZ signals were transmitted through a span comprising TWRS™ and TW-Reach™ fibers (span dispersion $\sim$ +377 ps/nm at 1545 nm). The device switch state was adjusted to yield –378 ps/nm at 1545 nm. The open eye in Fig. 40(a) qualitatively confirms the distortion-free, dispersion–compensating capability of the device. To quantify this, BER measurements were conducted for the same span at 1535, 1545 and 1555 nm, respectively. Figure 40(b) shows that the BER curves at all three wavelengths essentially overlap with the back-to-back measurement, indicating that the device is broadband, and offers penalty-free performance.

The dispersion-tuning characteristic of the device was tested by measuring receiver sensitivities at a BER of 10^{-9} for 1545-nm signals. Several different transmission fiber spans (comprising combinations of TWRS™ and TW-REACH™ fibers) with different lengths were assembled, and the adjustable HOM-DCM was tuned to the appropriate values to yield the closest match in dispersion. Figure 40(c) shows the receiver sensitivity for the different spans (with different dispersion values) compensated by the TDC tuned to the corresponding optimal state. The two horizontal dashed-lines show back-to-back receiver sensitivities from two separate measurements, indicating 0.4-dB measurement uncertainty. As is evident from Fig. 40(c), penalty-free transmission (within the measurement error) is achieved for switch states spanning the entire tuning range of the TDC. Figure 40(c) also shows the effect of residual dispersion on receiver sensitivity. The TW-REACH span had dispersion = +139 ps/nm, and the AHOM was switched in 14 ps/nm steps around a state with –141 ps/nm dispersion.

The symmetric departure from penalty-free transmission indicates that the AHOM has roughly constant step-size. Since the power-penalty increases by only 0.3 dB for the first detuning steps, an AHOM with five segments suffices for fine-tuning dispersion of 40 Gb/s CSRZ signals.

6.4. Summary

A tunable dispersion device that is uniquely enabled by the modal path diversity afforded by few moded fibers was described in Section 6. Unlike DCFs or static HOM compensators described in Section 5, this device shares the application space addressed by the variety of tunable optical filters used to make TDCs.

Dispersion tuning ranges can be made arbitrarily large, and step sizes down to 7 ps/nm have been demonstrated. The loss and MPI of this device is higher than those of static HOM compensators or DCF, but the values are lower than corresponding values for optical filter based TDCs. The significant distinction from other TDCs is that this device is simultaneously broadband and wavelength-continuous. Thus, it is not constrained to operation at specific bit-rates, bit-formats or channel spacings. Furthermore, there are no inherent trade-offs between tuning range and bandwidth, as is the case for other TDCs. Thus, they combine the advantages of tunability available from other TDCs, with the universally transparent characteristics of static DCFs.

There *is* a trade-off between the granularity of dispersion tuning and the MPI of the device, but we find that while the MPI may rise slightly above the –40 dB levels required of DCF and static HOM compensators, this application may be more tolerant to MPI. This is because the stringent MPI requirement for the static compensators arises from the fact that several devices (more than 40 in an ultra-long haul link) may have to be concatenated in series. On the other hand TDCs are usually used only once at the receiver, but the MPI levels of the AHOM indicate that up to 25 of these may be concatenated in series, before accumulating significant noise (BER penalty $>$ 1 dB).

One aspect in which optical filter based TDCs perform better than the AHOM, is that the AHOM tuning occurs in discrete steps, and is fully blocking *when* the switching action in occurring. Hence, these devices may be more suitable for set-able applications rather than dynamic ones.

This device enables the prospect of deploying TDCs in-line in a transmission link, as well as at the receiver, a degree of freedom that has not been currently explored by network architects. In addition, this concept can be extended to a schematic where HOM fibers of different slopes are used, which can potentially lead to independent tuning of dispersion as well as dispersion slope.

7. Summary and Conclusions

7.1. Summary of Device Characteristics

In this paper, we discussed the application of higher order modes of a fiber for dispersion compensation. The application space of static as well as tunable dispersion compensation has been addressed by several technologies, especially in the late 1990s and early 2000s as investment in optical communications ballooned. As of today, the DCF, operating in the fundamental mode, remains the most widely deployed device.

Among the alternative candidates, HOM-DCMs have shown the greatest promise as drop-in replacements, because they share a very important attribute with DCF—the dispersion is wavelength-continuous, and the device has very low loss. Probably the best indication of their superiority compared to several alternatives, is the way noise for various devices has been treated. Alternative technologies such as fiber Bragg grating (tunable or static), etalons, ring resonators have all concentrated on minimizing the primary source of noise for them—group delay ripple (GDR). Today, successful implementations of these technologies advertize GDR low enough for BER power penalties of $\sim 0.5 - 1$ dB. On the other hand, HOM-DCMs have strived to (and successfully) achieve MPI levels of –45 dB, which means that they will yield an additional BER power penalty of 0.5 dB after 50 devices concatenated in series (obviously, the impact of just one module is not measurable). Thus, clearly HOMs are unique among alternative technologies, in striving to and achieving performance metrics comparable with DCF.

Table 2. Comparisons of important attributes for DCFs and HOM-DCMS.

Attribute	**DCF**	**HOM DCM**
Technology	Dispersive fibers	Dispersive fibers + Mode converters
Bandwidth	Broad (C+L-band); More possible	63 nm demonstrated; 110 nm feasible C+L possible
RDS compensation	All possible	All possible
Effective area (OSNR impact)	15 – 20 μm^2 (1–3 dB)	50 – 80 μm^2 (Negligible)
Tunability	Feasible with external MEMs switches. Granularity $\propto N$, *number of segments* Loss/segment $>$ 1.3 dB Splices & connections/segment=2	Inherent two-path device. In fiber switches Granularity $\propto N$, *number of segments* Loss/segment $\sim$ 0.04 – 0.1 dB Splices & connections/segment = 1
Insertion loss	FOM up to 459 ps/nm-dB Low loss modules possible	FOM up to 734 ps/nm-dB Low loss with LPG mode converters
MPI	~ -55 dB	< -42 dB; –44 – 45 dB average
Raman amplification	Efficient	Weak
PMD	~ 0.1 ps/$\sqrt{}$km	~ 0.32 ps/$\sqrt{}$km (lesser fiber needed)
PDL	~ 0.016 dB	< 0.1 dB (limited by MPI)

However, "comparable to DCF" is clearly not enough to displace an entrenched technology. Indeed attention to HOMs increased as requirements for compensating high RDS fibers arose. It appeared that HOMs were uniquely positioned for this, since they are better suited for high RDS designs, as elucidated in Section 2. The first systems demonstration of LP_{02} DCMs was with high RDS fibers, for which suitable DCF modules did not exist. However, subsequent improvements in DCF have shown that it can achieve the range of RDS required of currently deployed transmission fibers. The other consideration is loss, or FOM. Indeed, as theory posited, practical HOM fibers with FOMs 60% larger than in DCF have been demonstrated. In addition, mode converters required by HOM-DCM add practically no additional loss if realized with long-period fiber gratings. Thus, HOM technology appears to be a better candidate than

DCF for low loss applications. However, for current network requirements, DCF loss may be "adequate," though this could change, as we will discuss in the next section.

There are two key advantages of HOMs compared to DCFs. Systems demonstrations have clearly shown improvements of amplifier noise figures and the attendant ability to transmit signal over longer distances with HOMs. This is because nonlinear distortions are negligible with large A_{eff} HOMs, as opposed to DCFs, where the signal must transmit through very small A_{eff}. The other distinction is that the inherent modal path diversity in HOM fibers can be exploited to build adjustable dispersive devices. The device essentially acts like a DCF whose dispersion value can be changed with very fine granularity. This device thus provides several desirable attributes of TDCs along with the low loss, universally applicable attributes of static HOMs or DCFs. Table 2 summarizes the key distinctions between DCFs and HOMs.

The other consideration is cost. HOM-DCMs need less fiber because the fiber is more dispersive, which means they would be more cost-effective than DCF. However, the need for additional components (mode converters) and the need for specialized assembly would make HOM-DCMs more expensive than DCFs. It would be difficult to predict which of these two competing factors will be more important, but the existence of such trade-offs indicate that performance, in niche applications or more demanding future optical networks, will potentially be the primary driver for the commercial success of HOM-DCMs.

7.2. Future Directions for HOM Technology

The inherent ability to obtain higher dispersions and lower losses would become a significant benefit for systems that require large dispersions. Transmission fibers have undergone several iterative design cycles, and it is unlikely that a future transmission fiber will have larger magnitudes of dispersion. On the other hand, schematics for migrating to 160 Gb/s or higher bit rates have proposed the use of very large amounts of pre- or post chirps on signals. These and any other applications that require large amounts of dispersion will benefit from using HOM-DCMs.

Nonlinear distortions are significantly reduced in HOM-DCMs, as several transmission experiments have shown. An interesting aspect of the experiments described in Section 5.5, is that while signals with 8-ps pulse widths transmit 12% longer in a system comprising HOMs instead of DCFs, 2-ps long pulses can travel 50% longer distances. This is because the peak power of a pulse increases as its pulse width increases, which in turn makes it more susceptible to nonlinear distortions. Thus, systems migrating to higher bit rates will also benefit from deploying HOM-DCMs.

The adjustable HOM described in Section 6 is a unique device whose functionality is not covered by any alternative technology to date. A fully optimized transmission system will obviously benefit from the ability to adjust the dispersion of the compensating device at several amplifier huts, and hence this device offers the means to alter network management.

Finally, dispersion management with fiber devices is finding several non-telecom applications. Emerging applications for high power fiber lasers demand high dispersion, low loss, and very low susceptibility to nonlinear distortions. In this application space, it is already clear that DCF would not be able to meet the extreme power handling capabilities required of the dispersive device, and hence several investigations involve the use of hollow core, photonic crystal fibers with very low nonlinearities.

While HOMs would have higher nonlinearities than hollow core fibers, the technology platform is significantly more mature, and it is conceivable that several pulse compression schemes for high-power and ultra-fast lasers and amplifiers will benefit from using HOM fibers [72,73].

Acknowledgments

Much of the work presented in this paper was a result of extensive theoretical and experimental collaborations with several researchers at OFS Laboratories and Bell Laboratories. We would like to thank Samir Ghalmi, Patrick Wisk, Zhiyong Wang, Eric Monberg, Frank Dimarcello, Jeffrey Nicholson and Jim Fleming for critical fabrication and characterization support. In addition, we would like to thank Lawrence Cowsar for much of the initial simulation support while developing HOM fibers. We are grateful to Benny Mikkelsen, Sethumadhavan Chandrasekhar and Gregory Raybon for performing several systems experiments over the course of these investigations. Finally, we would like to acknowledge the invaluable technical as well as strategic advice and support of several people in our organization, such as David DiGiovanni, Poul Kristensen and William Reed.

References

1. A.M. Vengsarkar, A.E. Miller and W.A. Reed, "Highly efficient single-mode fiber for broadband dispersion compensation," Proc. Opt. Fiber Commun. – 1993, pp. 56–59.
2. A.J. Antos and D.K. Smith, "Design and characterization of dispersion compensating fiber based on LP01 mode," IEEE J. Lightwave Technol. **12**, 1739–1745 (1994).
3. L. Gruner-Nielsen, S.N. Knudsen, B. Edvold, T. Veng, D. Magnussen, C.C. Larsen and H. Damsgaard, "Dispersion compensating fibers," Opt. Fiber Technol. **6**, 49–60 (2000).
4. C.K. Madsen, "Integrated waveguide allpass filter tunable dispersion compensators," Proc. Opt. Fiber Conf.2002, TuT-1.
5. C.R. Doerr, L.W. Stultz, S. Chandrasekhar, L. Buhl and R. Pafchek, "Multichannel integrated tunable dispersion compensator employing thermooptic lens," Proc. Opt. Fiber Conf. 2002, FA6.
6. L. M. Lunardi, D.J. Moss, S. Chandrasekhar and L.L. Buhl, "An etalon-based tunable dispersion compensator (TDC) Device for 40-gbit/s applications," Proc. European Conf. Opt. Commun. 2002, 5.4.6
7. M. Shirasaki and S. Cao, "Compensation of chromatic dispersion and dispersion slope using a virtually imaged phased array," Proc. Opt. Fiber Conf. 2001, TuS-1.
8. B.J. Eggleton, A. Ahuja, P.S. Westbrook, J.A. Rogers, P. Kuo, T.N. Nielsen and B. Mikkelsen, "Integrated Tunable Fiber Gratings for Dispersion Management in High-Bit Rate Systems," J. Lightwave Technol. **18**, 1419 (2000).
9. X-J. Cai, K.-M. Feng, A.E. Willner, V. Grubsky, D.S. Starodubov and J. Feinberg, "Simultaneous Tunable Dispersion Compensation of Many WDM Channels Using a Sampled Nonlinearly Chirped Fiber Bragg Grating," IEEE Photon. Technol. Lett. **11**, 1455 (1999).
10. J.-L. Auguste, R. Jindal, J.-M. Blondy, M. Claeau, J. Marcou, B. Dussardier, G. Monnom, D.B. Ostrowsky, B.P. Pal and K. Thyagarajan, "–1800 ps/(nm.km) chromatic dispersion at 1.55 μm in dual concentric core fibre," Electron. Lett. **36**, 1689–1691 (2000).

11. L. Gruner-Nielsen and B. Edvold, "Status and future promises for dispersion compensating fibres," Proc. European Conf. Opt. Commun. – 2002, 6.1.1.

12. C.D. Poole, J.M. Weisenfeld, D.J. DiGiovanni and A.M. Vengsarkar, " Optical fiber-based dispersion compensation using higher order modes near cutoff," J. Lightwave Technol. **12**, 1746–1758 (1994).

13. A.W. Snyder and J.D. Love, *Optical Waveguide Theory* (London, U.K.: Chapman & Hall, 1983).

14. M.E. Lines, W.A. Reed, D.J. Di Giovanni and J.R. Hamblin, "Explanation of anomalous loss in high delta singlemode fibres," Electron. Lett. **35**, 1009–1010 (1999).

15. C.D. Poole, J.M. Wiesenfeld, A.R. McCormick and K.T. Nelson, "Broadband dispersion compensation by using the higher-order spatial mode in a two-mode fiber," Opt. Lett. **17**, 985–987 (1992).

16. S. Golowich and S. Ramachandran, "On the polarisation dependence of microbend fiber gratings: Relation to fiber design," Opt. Express **13**, 6879 (2005).

17. S. Ramachandran, M.F. Yan, S. Golowich, E. Monberg, F.V. Dimarcello, J. Fleming, S. Ghalmi and P. Wisk, "A novel fiber design for polarisation insensitive microbend gratings," Proc. European Conf. Opt. Commun. – 2004, paper No. Th2.3.2.

18. C.D. Poole and S.-C. Wang, "Bend-induced loss for the higher-order spatial mode in a dual-mode fiber," Opt. Lett., **18**, 1712–1714 (1993).

19. C.D. Poole, J.M. Weisenfeld and D.J. DiGiovanni, "Elliptical-core dual mode fiber dispersion compensator," IEEE Photonics Technol. Lett. **5**, 194–196 (1993).

20. *Fiber Optic Test and Measurement*, edited by Dennis Derickson (Prentice Hall PTR, 1998).

21. M. Froggatt, "Interferometric measurement of dispersion in optical components," Proc. Opt. Fiber Commun. – 2002, paper No. WK1.

22. D. Menashe, M. Tur and Y. Danziger, "Interferometric technique for measuring dispersion of higher order modes in optical fibers," Electron. Lett. **37**, 1439–1440 (2001).

23. R.W. Tkach and A.R. Chraplyvy, "Phase noise and linewidth in an InGaAsP DFB laser," J. Lightwave Technol. **4**, 1711–1716 (1986).

24. J.W. Nicholson, S. Ramachandran, S. Ghalmi, E. Monberg, F. DiMarcello, M. Yan, P. Wisk and J. Fleming, "Characterization of dispersion in higher order mode fibers using electrical spectrum measurements," Proc. Opt. Fibers Commun. – 2003, Paper No. FK8.

25. J.W. Nicholson, S. Ramachandran, S. Ghalmi, E. Monberg, F. DiMarcello, M. Yan, P. Wisk and J. Fleming, "Electrical spectrum measurements of dispersion in higher order mode fibers," IEEE Photon. Technol. Lett. **15**, 831 (May 2003).

26. C. Dorrer, "Chromatic dispersion characterization by direct instantaneous frequency measurement," Opt. Lett. **29**, 204–206 (2004).

27. C. Dorrer and S. Ramachandran, "Self-referencing dispersion characterization of multimode structures using direct instantaneous frequency measurement," IEEE Photon. Technol. Lett. **16**, 1700–1702 (2004).

28. W.V. Sorin, B.Y. Kim and H.J. Shaw, "Highly selective evanescent modal filter for two-mode optical fibers," Opt. Lett., 581–583 (1986).

29. A.M. Vengsarkar, P.L. Lemaire, J.B. Judkins, V. Bhatia, T. Erdogan and J.E. Sipe, "Long-period fiber gratings as band rejection filters," J. Lightwave Technol. **14**, 58–65 (1996).

30. T. Erdogan, "Fiber grating spectra," J. Lightwave Technol. **15**, 1277–1294 (1997).

31. C.D. Pool, C.D. Townsend and K.T. Nelson, "Helical-grating two-mode fiber spatial-mode coupler," J. Lightwave Technol. **9**, 598–604 (1991).

32. S. Ramachandran, Z. Wang and M.F. Yan, "Bandwidth control of long-period grating-based mode converters in few-mode fibers," Opt. Lett. **27**, 698–700 (2002).

33. S. Ramachandran, M. Yan, E. Monberg, F. Dimarcello, P. Wisk and S. Ghalmi, "Record bandwidth microbend gratings for spectrally flat variable optical attenuators," IEEE Photon. Technol. Lett. **15**, 1561–1563 (2003).

34. A. Abramov, A. Hale, R.S. Windeler and T.A. Strasser, "Widely tunable long-period fibre gratings," Electron. Lett. **35**, 81–82 (1999).

35. S. Ramachandran, S. Ghalmi, Z. Wang and M. Yan, "Band-Selection Filters using Concatenated Long-Period Gratings in Few-mode Fibers," Opt. Lett. **27**, 1678–1680 (2002).

36. Z. Wang and S. Ramachandran, "Ultrasensitive long-period fiber gratings for broadband modulators and sensors," Opt. Lett. **28**, 2458–2460 (2003).

37. S. Ramachandran, S. Ghalmi, S. Chandrasekhar, I. Ryazansky, M.F. Yan, F. Dimarcello, W. Reed and P. Wisk, "Wavelength-continuous broadband adjustable dispersion compensator using higher order mode fibers and switchable fiber-gratings," Proc. European Conf. Opt. Commun., paper No. PD-2.6.

38. S. Ramachandran, M. Yan, L. Cowsar, A. Carra, P. Wisk, R. Huff and D. Peckham, "Large bandwidth, highly efficient mode coupling using long-period gratings in dispersion tailored fibers," Proc. Opt. Fiber Commun. – 2001, MC2.

39. W.W. Morey and W.L. Glomb, "Incorporated Bragg filter temperature compensated optical wavelength device," U.S. Patent 5,042,898, 1991.

40. L. Raddatz, I.H. White, D.G. Cunningham, and M.C. Nowell, "Increasing the bandwidth-distance product of multimode fiber using offset launch," Electron. Lett **33**, 232–233 (1997).

41. J. Bromage, P.J.Winzer and R.-J.Essiambre, "Multiple Path Interference and its Impact on System Design," in *Raman Amplifiers for Telecommunications*, edited by M.N. Islam (Springer-Verlag, New York, 2004).

42. C.R.S. Fludger and R.J. Mears, "Electrical measurements of multipath interference in distributed Raman amplifiers," J. Lightwave Technol. **19**, 536 (2001).

43. J.L. Gimlett and N.K. Cheung, "Effects of phase-to-intensity noise conversion by multiple reflections on gigabit-per-second DFB laser transmission systems," J. Lightwave Technol. **7**, 888 (1989).

44. C.X. Yu, W-k Wang and S.D. Brorson, "System degradation due to multipath coherent crosstalk in WDM network nodes," J. Lightwave Technol. **16**, 1380 (1998).

45. M.G. Taylor, D. Craig, H.P. Sardesai, A. Khot, W. Zheng, "Measurement of system penalty due to multipath interference," Proc. ECOC-2002, paper No. 3.1.7.

46. J.L. Gimlett and N.K. Cheung, "Effects of phase-to-intensity noise conversion by multiple reflections on gigabit-per-second DFB laser transmission systems," J. Lightwave Technol. **7**, 888 (1989).

47. S. Ramachandran, J.W. Nicholson, P. Kristensen, S. Ghalmi and M.F. Yan, "Measurement of multi-path interference in the coherent cross-talk regime," Proc. Opt. Fibers Commun. 2003, Paper No. TuK6.

48. S. Ramachandran, J.W. Nicholson, S. Ghalmi and M.F. Yan, "Measurement of Multipath Interference in the Coherent Crosstalk Regime," IEEE Photon. Technol. Lett. **15**, 1171–1173 (2003).

49. W. Zheng, H.P. Sardesai, M.G. Taylor, D.L. Craig, J. Fowlkes and J.R. Simpson, "Measurement and system impact of multipath interference from dispersion compensating modules," IEEE Trans. Instr. Meas. **53**, 15–22 (2004).

50. S. Ramachandran, S. Ghalmi, S. Chandrasekhar and L.L. Buhl, "Evolution and systems impact of MPI in HOM fiber devices," Proc. European Conf. Opt. Commun. – 2003, Paper No. 4.7.5.

51. F. Liu, C.J. Rasmussen and R.J.S. Pedersen, "Experimental Verification of a New Model Describing the Influence of Incomplete Signal Extinction Ratio on the Sensitivity Degradation Due to Multiple Interferometric Crosstalk," IEEE Photon. Technol. Lett., 137–139 (1999).

52. S. Ramachandran, S. Ghalmi, J. Bromage, S. Chandrasekhar and L.L. Buhl, "Evolution and systems impact of coherent distributed multi-path interference," IEEE Photon. Technol. Lett. **17**, 238–240 (2005).

53. Siddharth Ramachandran, "Higher-Order-Mode Dispersion Compensation for Broadband Dispersion and Non-linearity Management in Transmission Systems," Proc. Opt. Fiber Commun. – 2002, Paper No. WU-5.

54. O. Raz, R. Rotman, Y. Danziger and M. Tur, "Implementation of Photonic True Time Delay Using High-Order-Mode Dispersion Compensating Fibers," IEEE Photon. Technol. Lett. **16**, 1367–1369 (2004).

55. M. Wandel, P. Kristensen, T. Veng, Y. Qian, Q. Le and L. Gruner-Nielsen, "Dispersion compensating fibers for non-zero dispersion fibers," Proc. OFC-2002, paper No. WU1 2002.

56. L.V. Jørgensen, J.S. Andersen, S. Primdahl, M.N. Andersen and B. Edvold, "Next generation dispersion compensating modules for 40 Gbit/s systems," Proc. NFOEC-2002, pp.1171–1182 (2002).

57. M. Wandel, T. Veng, N.T. Quang Le, L. Gruner-Nielsen, "Dispersion compensating fibre with a high figure of merti," Proc. European Conf. Opt. Commun., PD-2.5.

58. Siddharth Ramachandran, "Dispersion management with few mode fibers," Proc. Optoelectronics & Commun. Conf. – 2003, Shanghai, China.

59. F. Forghieri, R.W. Tkach and A.R. Chraplyvy, "Dispersion Compensating Fiber: Is There Merit in the Figure of Merit?," IEEE Photon. Technol. Lett. **9**, 970–972 (1997).

60. L.D. Garrett, M. Eiselt, J. Wiesenfeld, R. Tkach, D. Menashe, U. Levy, Y. Danziger and M. Tur, "ULH DWDM transmission with HOM-based dispersion compensation," Proc. ECOC-2003, Paper No. We 4.P.98.

61. A.H. Gnauck, L.D. Garrett, Y. Danziger, U. Levy and M. Tur, "Dispersion and dispersion-slope compensation of NZDSF over the entire C band using higher order mode fibre," Electron. Lett. **36**, 1946–1947 (2000).

62. P.B. Hansen, G. Jacobovitz-Veselka, L. Grüner-Nielsen and A.J. Stentz, "Raman amplification for loss compensation in dispersion compensating fibre modules," Electron. Lett. **34**, 1136–1137 (1998).

63. M. Tur, E. Herman, A. Kozhekin and Y. Danziger, "Stimulated Brillouin scattering in high-order-mode fibers employed in dispersion management modules," IEEE Photon. Technol. Lett. **14**, 1282–1284 (2002).

64. M. Tur, E. Herman and Y. Danziger, " Nonlinear properties of dispersion management modules employing high-order mode fibers," Proc. Opt. Fiber Commun. – 2001, paper No. TuS5.

65. S. Ramachandran, B. Mikkelsen, L.C. Cowsar, M.F. Yan, G. Raybon, L. Boivin, M. Fishteyn, W.A. Reed, P. Wisk, D. Brownlow, R.G. Huff and L. Gruner-Nielsen, "All-fiber, grating-based, higher-order-mode dispersion compensator for broadband compensation and 1000-km transmission at 40 Gb/s", Proc. European Conf. Opt. Commun. – 2000, PD-2.5.

66. S. Ramachandran, G. Raybon, B. Mikkelsen, M.F. Yan, L.C. Cowsar and R-J. Essiambre "1700-km Transmission at 40-Gb/s with 100 km Amplifier-Spacing Enabled by Higher-Order-Mode Dispersion-Compensation," Proc. European Conf. Opt. Commun., WeF-2.2, 2001.

67. S. Ramachandran, B. Mikkelsen, L.C. Cowsar, M.F. Yan, G. Raybon, L. Boivin, M. Fishteyn, W.A. Reed, P. Wisk, D. Brownlow, R.G. Huff and L. Gruner-Nielsen, "All-fiber, grating-based, higher-order-mode dispersion compensator for broadband compensation and 1000-km transmission at 40 Gb/s", IEEE Photon. Technol. Lett. **13**, 632–634 (2001).

68. S. Ramachandran, G. Raybon, B. Mikkelsen, M.F. Yan, L. Cowsar and R-J. Essiambre, "1700-km Transmission at 40-Gb/s with 100-km Amplifier-Spacing Enabled by Higher-Order-Mode Dispersion-Compensation," Electron. Lett. **37**, 1352–1354 (2001).

69. B. Konrad, A. Hodzic and K. Petermann, "Dispersion Compensation Schemes For 160 Gb/S Tdm-Transmission Over SSMF And NZDSF," Proc. ECOC-2002, paper No. Tu.L.2.4.

70. S. Ramachandran, S. Ghalmi, S. Chandrasekhar, I. Ryazansky, M. Yan, F. Dimarcello, W. Reed and P. Wisk, "Tunable dispersion compensators utilizing higher order mode fibers," IEEE Photon. Technol. Lett. **15**, 727–729 (2003).

71. S. Ghalmi, S. Ramachandran, I. Ryazansky, M.F. Yan and F.V. Dimarcello, "On the Scalability of Adjustable High-Order Mode Fiber Dispersion Compensators," Proc. Opt. Fiber Commun. Conference – 2003, paper No. FK7.

72. S. Ramachandran, J.W. Nicholson, S. Ghalmi, M.F. Yan, P. Wisk, E. Monberg and F.V. Dimarcello, "Light propagation with ultra-large modal areas in optical fibers," Opt. Lett. **31**, 1797 (2006).

73. S. Ramachandran, S. Ghalmi, J.W. Nicholson, M.F. Yan, P. Wisk, E. Monberg and F.V. Dimarcello, "Anomalous Dispersion in a Solid, Silica-based Fiber," Opt. Lett. **31**, 2532 (2006).

DOI: 10.1007/s10297-007-0081-0
Originally published in J. Opt. Fiber. Commun. Rep. 4, 110–172 (2007)

High-order mode based dispersion compensating modules using spatial mode conversion

M. Tur[1], D. Menashe[2], Y. Japha[3], and Y. Danziger[4]

[1] School of Electrical Engineering, Tel-Aviv University, Tel-Aviv, Israel 69978
Email: tur@eng.tau.ac.il
[2] RED-C Optical Networks, Atidim Tech. Park, Bldg 3, Tel-Aviv, Israel
[3] Department of Physics, Ben-Gurion University of the Negev, Beer-Sheva, Israel 84150
[4] Email: yochay_danziger@yahoo.com

Abstract. High-Order Mode Dispersion Compensating Modules (HOM-DCM) using spatial optical transformations for mode conversion are reviewed. It is shown that mode transformers using this technology can be designed to transform the LP_{01} mode of SMF fibers to the LP_{02} mode of specially designed dispersion compensating High-Order Mode Fiber (HOMF), with typical insertion loss of $\sim$1 dB, and typical extinction ratio to other modes less than -20 dB. The HOMF itself can provide high negative dispersion [typically in the range of 400–600 ps/(nm km)], and high negative dispersion slope, allowing efficient compensation of all types of transmission fiber. Combining two mode transformers with HOMF and possibly trim fiber for fine-tuning, results, for example, in a HOM-DCM that compensates 100 km LEAF® fiber, with Insertion loss < 3.5 dB, and Multi-Path Interference (MPI) < -36 dB. MPI phenomena in HOM-DCMs is characterized, and shown to comprise both coherent and incoherent parts, and to result from both the mode transformers and fiber coupling within the HOMF. MPI values of < -36 dB have been shown to allow error free transmission of 10 Gb/s signals over up to 6000 km. Finally, a number of applications well suited to the properties of HOM-DCMs are reviewed.

1. Introduction

In 1994, Craig Poole and coworkers [1–2], as well as others [3], pointed out that High-Order Modes (HOM) in optical fibers, such as LP_{11}, LP_{02}, etc. [4], could be advantageously used for chromatic dispersion compensation. Motivated by the high *negative* dispersion of such modes near their respective cutoffs, as well as by the negative slope of the obtained dispersion (with respect to wavelength), Poole et al.

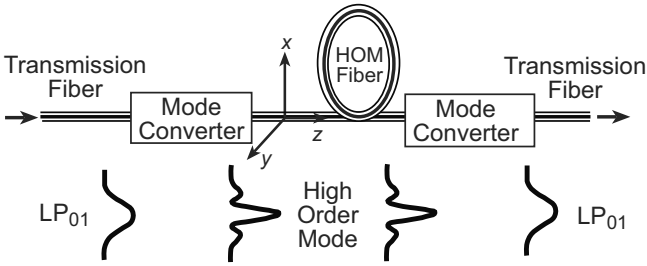

Fig. 1. A High-Order Mode based dispersion compensator. Light propagating in the LP_{01} mode of the transmission fiber is converted to a highly (negative) dispersive high-order mode of a few mode fiber. Finally, the output mode converter sends the light back to the transmission fiber in the form of an LP_{01} mode.

have proposed and demonstrated a HOM-based dispersion compensator for SMF28 fiber.

The device, Fig. 1, comprised of a slightly elliptical fiber, carrying the LP_{11} mode, and two broadband mode converters to efficiently transfer the LP_{01} light from the input SMF28 single-mode fiber into the LP_{11} negative dispersion mode, and back into the LP_{01} mode of the output SMF28 fiber. With negative dispersion values as high as -770 ps/(nm km) @ 1555 nm (as compared with ~ -90 ps/(nm km) for regular single-mode Dispersion Compensating Fibers (DCF) [5]), a close to ten-fold saving in fiber length could be achieved with only a relatively small excess loss due to the mode transformers. Poole's reported experimental work has revealed the potential of the technology, although the demonstrated implementation fell short of meeting some key industry requirements (e.g., the use of a slightly elliptical fiber, carrying the LP_{11} mode, could not guarantee polarization insensitivity).

Theoretically, high-order modes introduce a new degree of freedom for dispersion management. They can be designed to have dispersion curves that can match many transmission fibers, including the many Non-Zero-Dispersion-Shifted-Fibers (NZDSF), which were introduced in the last 10 years. The high negative dispersion of HOM fibers (HOMFs) requires much less fiber to achieve a given total dispersion (in ps/nm), resulting in significantly lower loss for the final product. High-order modes are also characterized by large effective areas (50–80 μm^2), much larger than those of dispersion compensating fibers (DCF), which use the LP_{01} mode ($\sim$20 μm^2). While recent advances in basic mode DCF have led to higher values of dispersion and dispersion slope, even comparable to HOMF, these have been achieved at the expense of an even further reduction in effective area, typically to about 15 μm^2 [20]. Thus, HOM based dispersion compensators have the potential to be much more immune to optical nonlinear effects, which are to be minimized to ensure successful high channel count WDM, and high capacity 40 Gbs transmission.

In practice, however, a series of obstacles must be overcome before all these advantages can be utilized. The most challenging one is the transformation process between the dispersion compensating HOM and the LP_{01} mode of the transmission

fiber. First, this modal transformation has to be very efficient in order to minimize the device insertion loss. But the HOM dispersion compensating fiber is not single-mode, and even if the transformation efficiency is very high, some input optical power may be coupled by the input mode converter to other modes of the HOM fiber (HOMF), including to the always-existing lowest order LP_{01} mode. Mode coupling in the HOMF and/or a non-ideal output mode converter will generate in the *output* transmission fiber multiple electromagnetic fields, which traversed the device via different modes (i.e., different optical paths), resulting in Multiple Path Interference (MPI) (see section 4). Eventually, HOM dispersion compensators are to serve as important building blocks in high performance fiber-optic communication systems, and the above mentioned MPI is the most dominant contribution to system penalty associated with the HOM technology.

A spatial mode of an optical fiber is a solution of Maxwell equations, subject to boundary conditions, having the form [4]

$$\mathbf{E}(x,y,z,t) = \mathbf{E}_0(x,y)\exp(i\beta z)\exp(-i\omega t);$$
$$\mathbf{H} = \mathbf{H}_0(x,y)\exp(i\beta z)\exp(-i\omega t). \quad (1)$$

Here, $\mathbf{E}$ and $\mathbf{H}$ are the vector electromagnetic fields, t is the time and ω is the optical (angular) frequency, z is a coordinate along the fiber length, while x and y are the transverse spatial coordinates, see Fig. 1, $\mathbf{E}_0(x,y)$ and $\mathbf{H}_0(x,y)$describe the z-independent mode transverse shape, and finally, β is the propagation constant. Modes differ from each other in their transverse field distributions $\mathbf{E}_0(x,y)$, $\mathbf{H}_0(x,y)$and propagation constant β.

In the so-called weakly guiding approximation, modes in cylindrically symmetric fibers are classified using the LP_{mn} designation [6] , where LP stands for "linearly polarized", m represents the azimuthal symmetry of the mode, and n the radial distribution. Figure 2 shows typical spatial distributions of the electromagnetic *field* (not intensity) of the modes, most relevant to the design of HOMF for dispersion compensation. The basic mode LP_{01}, exclusively used for high bit-rate transmission, is cylindrically symmetric, and its radial distribution is approximately Gaussian. The LP_{02}, and LP_{03} modes are also cylindrically symmetric, however their radial distribution has one and two zero-amplitude rings, respectively, i.e. points where the electric field changes sign. The LP_{11} and LP_{21} modes are not cylindrically symmetric, having two and four lobes respectively. Besides their different spatial distributions, modes are further characterized by the their effective index n_{eff}, or alternatively by the propagation constant $\beta = kn_{\mathrm{eff}}$, where $k\,(=\omega/c)$ is the vacuum wave-number (c is light velocity in vacuum). Since $n_{\mathrm{core}} > n_{\mathrm{eff}} > n_{\mathrm{clad}}$, where n_{core} and n_{clad} are respectively, the refractive indices of the fiber core and cladding, the larger n_{eff} the more guided and stable the mode. Figure 3 shows the n_{eff} values for a typical HOM fiber to be discussed in section 3.

LP_{01}has the highest n_{eff}, with n_{eff} decreasing according to the following typical order LP_{11}, LP_{21}, LP_{02}, LP_{12}, LP_{03}, LP_{22}. The number of guided modes in the fiber is equal to the number of modes for which $n_{\mathrm{eff}} > n_{\mathrm{clad}}$, where n_{clad} is the index of the fiber cladding material (typically undoped Silica, with n_{clad} = 1.444 @ 1550 nm).

The vast majority of fibers in commercial use today may be divided into two distinct categories: single and multi-mode fibers [4]. In single mode fibers, only the LP_{01} is guided for wavelengths exceeding a cutoff value. On the other hand, a multi-mode fiber (MMF) supports a multitude of guided modes, with the signal propagating

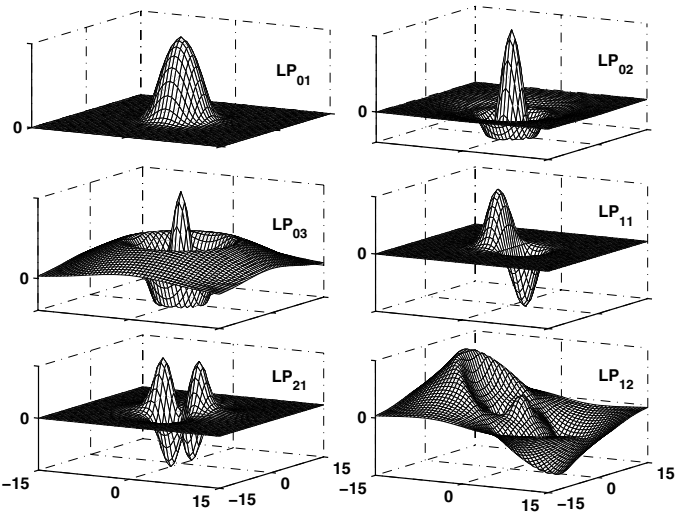

Fig. 2. Typical spatial *field* distribution of selected modes of a HOM fiber.

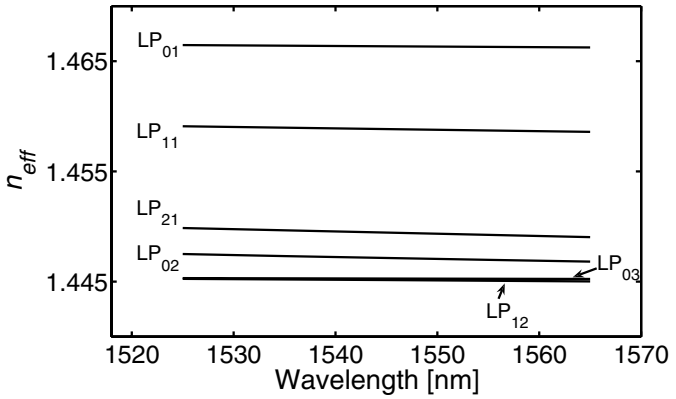

Fig. 3. Typical n_{eff} values for the modes of Fig. 2 (Δ_1=0.027, see section 3).

simultaneously in all (or in some cases a subset) of the modes. The term HOMF used here refers to a subclass of the multimode family, also being referred to as few-mode fibers [7]. These fibers are designed to support a limited number of guided modes (typically less than ten), with the signal designated to propagate in a pre-selected *single* high-order mode.

To selectively couple the input LP_{01} to the HOMF LP_{11} mode and back, Poole et al. have used grating coupling to introduce longitudinal periodic perturbations in the core region of the fiber with a spatial period matched to the intermodal beat length

$L_B = 2\pi/(|\beta_{01} - \beta_{11})$ (β_{01} and β_{11} are the propagation constants of the LP_{01} and LP_{11} modes, respectively). This grating method has been further perfected in recent years by Ramachandran et al. [8–9]. Recently, another method for mode conversion using hollow fibers has also been proposed [10].

In 1998 one of the authors of this paper (Y. D.) proposed to replace the *one-dimensional* selectivity of β matching by a *two-dimensional* mechanism, where the spatial shape, $\mathbf{E}_0(x, y)$, $\mathbf{H}_0(x, y)$ of the transmission fiber LP_{01} mode is transformed by a two-dimensional spatial filter into the precise $\mathbf{E}_0(x, y)$, $\mathbf{H}_0(x, y)$ field distribution of the desired high-order mode and *vice versa*. Reshaping laser beams by diffractive optical elements has been a known practice for years, but only lately it was utilized for modal transformation [11]. In this paper we demonstrate how mode transformers (MOXes) based on spatial wavefront transformation, combined with appropriately designed HOMF, can achieve:

– Broadband, continuous and full (including slope) compensation over the transmission band of wavelengths (e.g., the C (1525–1565 nm) or L (1570–1610 nm) bands
– Low insertion loss
– Low polarization mode dispersion (PMD) and polarization dependent loss (PDL) [6]
– High tolerance to optical power
– Low return loss
– Low MPI
– Compact size and full compatibility with Telcordia requirements from a passive device

Higher-Order-Mode Dispersion Compensation Modules (HOM-DCMs) based on this technology have been developed and built by LaserComm, Inc. to meet all the stringent requirements of modern and future high performance fiber optic telecommunication systems.

Paper structure: section 2 describes the design and construction of a *spatial* mode transformer. The trade-off considerations in the design of the HOM fiber itself are discussed in section 3, while MPI is the subject of section 4. The overall performance of the integrated HOM-DCM is presented in section 5 along with numerous potential applications, and its success in various field experiments.

2. Spatial Mode Transformer (MOX)

2.1. General

Mode transformation is needed in order to transfer the signal in the incoming single-mode transmission fiber into a higher order transverse mode of the dispersion compensating fiber. An inverse mode transformation is then invoked to transfer the signal back into the single-mode output transmission fiber. The transmission fiber is usually a single-mode fiber (SMF), with a Gaussian shape transverse mode, LP_{01}, while the HOMF is a few mode fiber, supporting a high-order spatial transverse mode, designed

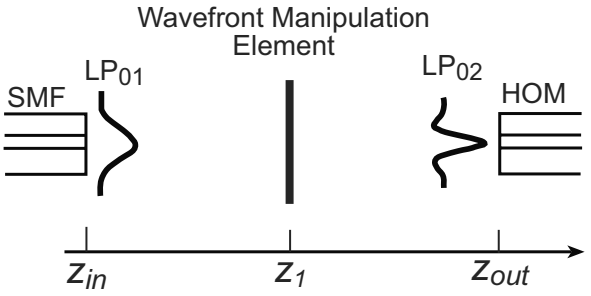

Fig. 4. Transformation from the Gaussian LP_{01} mode of an SMF to the LP_{02} mode of a HOM fiber.

to have a prescribed high negative dispersion curve. For a variety of reasons to be discussed in section 3, we chose to work with the cylindrically symmetric *non-degenerate* LP_{02} high-order mode, whose schematic field distribution, $E_{02}(x, y)$, is shown in Fig. 2 (in the weakly guiding approximation [4], the polarization is uniform across the (x, y) plane and its value will be that of the incident LP_{01} wave). Note that unlike LP_{01}, $E_{02}(x, y)$ for LP_{02} has a cylindrically symmetric π radians phase shift around its central lobe. As discussed above, the challenge in designing a good spatial mode transformer is twofold: (a) to transfer a maximum fraction of the energy of the input mode into the desired output mode, i.e., to have a minimum insertion loss; (b) to minimize excitation of other guided modes in the HOM fiber in order to prevent undesired interference effects at the HOM-DCM output fiber (MPI, see section 4). This challenge should be successfully met over a broad spectrum of wavelengths and environmental conditions.

2.1.1. Principles of Spatial Mode Transformation

Spatial mode transformation is based on wavefront manipulation using specially designed optical elements and free-space propagation. Since the input fiber modes are weakly guided and the optical beams will be seen to have only small to moderate divergence/convergence angles, we may assume that for incoming linearly polarized light, all optical beams in free space will share the same polarization, with the electric field component along the polarization axis described by a *scalar* complex function of the form

$$E(x, y, z, t) = f(x, y, z) \exp(-i\omega t). \tag{2}$$

Using scalar diffraction theory [12,13], free space propagation of the electric field from plane z_1 to plane z_2 is governed by

$$f(x, y, z_2) = \iint dx'dy'G(x - x', y - y', z_2 - z_1)f(x', y', z_1), \tag{3}$$

where the Green's function $G(\cdot)$ in the Fresnel approximation is given by [12]

$$G(x-x', y-y', z-z') = \frac{i}{\lambda\,|z-z'|}\exp\left(-i\frac{\pi}{\lambda\,|z-z'|}[(x-x')^2+(y-y')^2]\right), \tag{4}$$

The field at any given distance z, $f(x,y,z) = \sqrt{I(x,y,z)}\exp\left(i\varphi(x,y,z)\right)$ has intensity profile $I(x,y,z)$ and phase $\varphi(x,y,z)$. Through theory and/or measurements we know the fields of the input and output modes at $z = z_{\rm in}$ and $z = z_{\rm out}$, respectively, Fig. 4. Using Eq. (3) we can forward propagate $f(x,y,z_{\rm in})$ of the input mode to get its value $f(x,y,z_1^-)$, just before the assumingly relatively thin transforming element, and reverse propagate $f(x,y,z_{\rm out})$ of the output mode to just after the transforming element to produce the wavefront $f(x,y,z_1^+)$, that will converge to $f(x,y,z_{\rm out})$ through free space propagation. Successful mode conversion can be achieved by placing an optical element at $z = z_1$, having a complex transfer function

$$H(x,y) = T(x,y)\exp\left(i\Phi(x,y)\right) = |H(x,y)|\exp\left(i\Phi(x,y)\right), \tag{5}$$

such that

$$f(x,y,z_1^+) \propto H(x,y)f(x,y,z_1^-). \tag{6}$$

Thus, up to a constant of proportionality, i.e., allowing for some spatially uniform insertion loss, the mode of the left-hand fiber is spatially matched to that of the right-hand one, as required. In practice, however, this approach is problematic: while the $\exp\left(i\Phi(x,y)\right)$ part of $H(x,y)$ of Eq. (6) could be implemented using a *phase-only* optical element, which can be made today to high precision [14] , absorptive masks, performing the wavefront transformation prescribed by $|H(x,y)|$, are more difficult to manufacture. Moreover, the use of an absorptive element may entail considerable insertion loss.

An alternative approach is to use an optical system, comprising two phase-only thin elements at z_1 and z_2, Fig.5, combined with free space propagation between the z_1 and z_2 planes to convert the phase variations imposed at z_1 to intensity variations at z_2. In fact, it may be shown [15] that for a suitable choice of distances, $z_1 - z_{\rm in}$, $z_2 - z_1$ and $z_{\rm out} - z_2$, any wavefront transformation between the planes $z_{\rm in}$ and $z_{\rm out}$ can be implemented by phase-only wavefront manipulation at z_1 and z_2. The required phase elements can be designed using a phase retrieval algorithm, described in section 2.2.3.

2.1.2. The Need for Collimation

The proposed mode transformer must also possess significant optical (focusing) power, since it must collect the diverging beam, emanating from the left-hand fiber and transform it into an appropriately modified converging beam into the right-hand fiber. For easy implementation, and to keep the phase elements as *thin* and *shallow* as possible, it is preferable to assign the required optical power to collimating and focusing lenses, L1 and L2 in Fig. 6. Although quite a few other mode transformer architectures can be also envisaged, in the following we concentrate on the architecture of Fig. 6, and in particular on the $\mathrm{LP}_{01} \rightarrow \mathrm{LP}_{02}$ transformation.

2.1.3. Efficiency of the Spatial Transformation

Starting with the normalized field $f_{01}(x,y,z_{\rm in})$ of the LP_{01} mode at $z = z_{\rm in}$, the output of the optical system of the input MOX of Fig. 6 is a transformed field $f_{\rm trans}(x,y,z_{\rm out})$

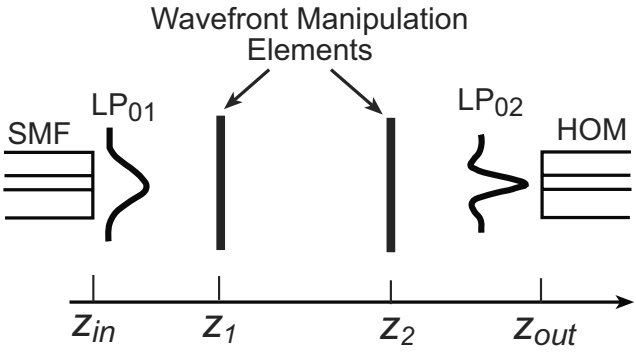

Fig. 5. Same as Fig. 4 but with two thin phase elements to execute the required mode transformation.

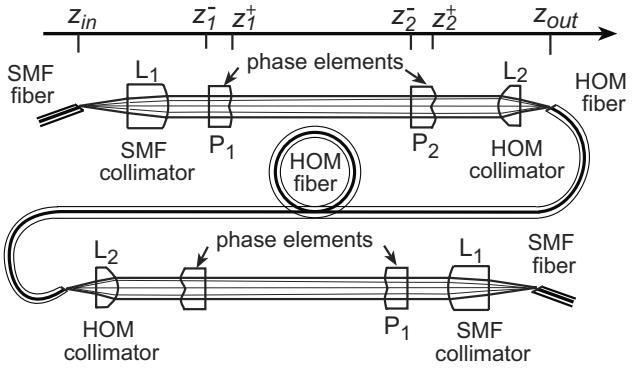

Fig. 6. Typical architecture of a HOM-DCM with both input and output MOXes to be discussed below. Ray tracing shows how intensity is spread into a central lobe and outer ring near the P2 phase elements. The SMF-28 fiber ends are cut at an angle of 8°, and consequently, the fiber mechanical axis forms an angle of ∼3.6° with the MOX optical axis, see section 2.2.1.

at the input facet of the HOM fiber (inside the fiber so that reflection losses are taken into account). The fraction of power coupled into a specific fiber mode LP_{mn}, having a normalized mode field $f_{mn}(x, y)$ is given by $|A_{mn}|^2$, where the amplitude A_{mn} can be evaluated from the overlap integral

$$A_{mn} = \int dxdy f^*_{mn}(x, y) f_{\mathrm{trans}}(x, y, z_{\mathrm{out}}). \tag{7}$$

The MOX is designed to perform ideal transformation at the design wavelength λ_0, which is typically at the center of the transmission band. For this wavelength, $|A_{mn}|^2$

should be unity for the desired mode (excluding losses in the optical system), and zero for all other modes. However, the transformation is not ideal at wavelengths away from the central wavelength λ_0, and in addition, imperfections in the MOX manufacturing cause the transfer of power into some undesired modes.

2.1.4. Definitions

The insertion loss of an $\mathrm{LP}_{01} \rightarrow \mathrm{LP}_{02}$ MOX is defined as

$$\text{Insertion Loss(IL)} = -10 \log_{10} |A_{02}|^2 \ , \tag{8}$$

The extinction ratio (ER) of the undesired mode LP_{mn} ($(m, n) \neq (0, 2)$) is defined as

$$\mathrm{ER}_{mn} = 10 \log_{10} \left[\left| \frac{A_{mn}}{A_{02}} \right|^2 \right] . \tag{9}$$

Obviously, a high *efficiency* MOX is characterized by an insertion loss of close to zero dB and extinction ratio approaching $-\infty$ dB, over the full wavelength band of operation.

The *broadband* efficiency of the transformation is limited by two main factors:

– The chromatic aberrations of the optical system, caused by either material dispersion of the elements or wavelength-dependent diffractive effects.

– The wavelength dependence of the wavefronts $f_{01}(x, y, z_{\mathrm{in}})$ and $f_{02}(x, y, z_{\mathrm{out}})$ of the LP_{01} mode of the transmission fiber and LP_{02} mode of the HOM fiber, respectively.

One would expect the diffractive effects in the optical elements to present an obstacle to broadband operation. However, this problem can be minimized by using smooth phase elements with mostly refractive nature, in the sense that they do not have the 2π phase jumps typical of regular diffractive elements [13]. Material dispersion in the optical elements is important but in principle can be compensated for using conventional achromatization techniques [13].

The main limitation is then modal shape dispersion of the HOM fiber. While the wavelength dependence of the incoming LP_{01} modal shape $f_{01}(x, y, z_{\mathrm{in}})$ can be shown to be insignificantly small, the whole idea of choosing a high-order mode was because of its high group velocity dispersion, see section 3. It is to be expected, therefore, that $f_{02}(x, y, z_{\mathrm{out}})$ might also have considerable wavelength dependence, posing significant limitations to the transformation efficiency. However, it turns out that for dispersion values in the range of practical interest, about 200–600 ps/nm/km, the rate of change of the HOMF mode shape is still small enough to allow efficient and broadband spatial mode transformation. To illustrate this point consider an achromatic optical system designed for ideal transformation at $\lambda = 1550$ nm, with wavelength-independent $f_{01}(x, y, z_{\mathrm{in}})$. The insertion loss of the desired mode and the extinction ratio for the undesired modes are then obtained from an overlap integral of the desired mode function $f_{02}(x, y, z_{\mathrm{out}})|_{\lambda_0}$ at $\lambda_w = 1550$ nm (since this is the incident wavefront at the entrance of the HOM fiber) with the corresponding modes of the HOM fiber at the other wavelengths. These quantities are shown in Figs. 7 and 8 for the transformation to the mode LP_{02}, as well as to the undesired modes LP_{01} and LP_{03} for a typical

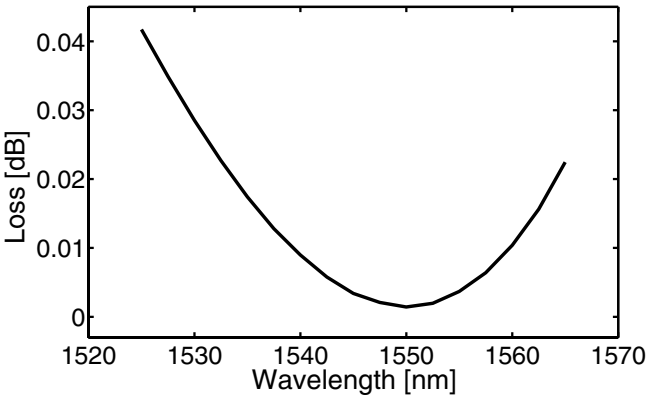

Fig. 7. LP_{02} loss over the C-band for a typical HOM fiber due to the spectral dependence of the transverse shape of the LP_{02} mode.

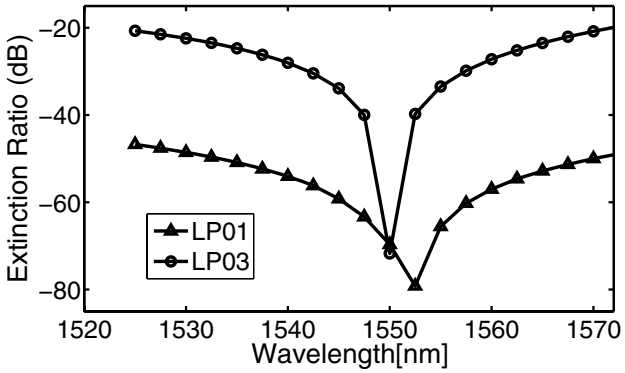

Fig. 8. Extinction ratio for the LP_{01} and LP_{03} modes over the C-band for a typical HOM fiber due to spectral dependence of the transverse shape of the LP_{02} mode.

dispersion compensating HOMF of section 3 (Dispersion for this fiber at 1555 nm is -230 ps/(nm km) and dispersion slope is –3.5ps/(nm^2 km)). It is clearly seen that IL does not deteriorate by more than 0.07 dB over the whole C band, while the ER of LP_{01} is at most -40 dB per MOX. The ER for LP_{03} is worse but not so important for properly designed HOMF, since this mode can be removed by fiber bending (see section 3.4.2.2). Finally, in principle it is possible though difficult, to intentionally design some chromatic aberration into the optical elements to somewhat compensate for the wavelength dependence of the HOMF modal shapes.

2.2. *Details of the MOX Architecture*

Here we give a more detailed description of the MOX architecture of Fig. 6.

2.2.1. The Fiber Ends

The fiber ends are mounted into a ferrule, and to reduce back-reflections, cleaved and polished at an angle of 8° (for the SMF-28). Due to Snell's law of refraction, the beam coming out of the fiber creates an angle of 11.6°with the polished face, so that the mechanical axes of both ferrules have to be adjusted to deviate from the MOX optical axis by 3.6°. The tilt angles for the HOMF, as well as the resulting back-reflections will be discussed in section 2.3.4.

2.2.2. The Collimators

The SMF collimator lens L1, Fig. 6, is designed to transform the diverging LP_{01} output of the transmission fiber into a collimated beam, while on the HOM fiber side, the purpose of lens L2 is to refocus the beam into the HOMF. Conversely, for the LP_{02} $\rightarrow LP_{01}$ MOX, L2 collimates the beam emanating from the HOMF, while L1 refocuses it into the transmission fiber. When a propagating mode exits the fiber into free space, the beam starts to diverge. The distribution of angles from a given mode (the angular power spectrum) is given by the following Fourier transform over the transverse mode function $f(x, y)$:

$$g(\theta, \varphi) \propto \left| \iint dxdy \exp\left(i \frac{2\pi}{\lambda} \sin\theta (x \cos\varphi + y \sin\varphi \right) f(x, y) \right|^2 , \qquad (10)$$

where θ and φ are spherical angles in free space in the *xyz* coordinate system of Fig. 1. The numerical aperture of a beam is defined [13] as the width of the angular spectrum distribution, or more precisely: the sine of an angle θ_{NA} such that a specified fraction (e.g., $1/e^2$ or 99%) of beam power is contained in a cone, having an opening angle of $2\theta_{\mathrm{NA}}$. Owing to their dissimilar modal fields, the NA's of LP_{01} and LP_{02} are quite different, with that of the LP_{02} significantly larger (ranging between 0.36 and 0.42) than that of LP_{01} (NA = 0.155).

The focal length of a lens dedicated for the collimation of a beam with a given NA into a collimated beam with diameter D is given by

$$f = \frac{D}{2\mathrm{NA}}. \qquad (11)$$

To ease environmental stability, all MOX dimensions should be chosen as small as possible but large enough so that the manufacturing resolution of the phase elements enables the capturing of all the spatial details needed for a precise spatial transformation. This includes the diameter D of the collimated beam. Typically, D can be of the order of a few millimeters. Since fairly little beam divergence occurs between L1 and L2 (Typically, the length of an assembled MOX is a few centimeters), L2 can also be of diameter D, but due to the different NA's, its focal length is shorter than that of L1 by the NA's ratio. Clearly, L1 and especially L2 are high NA lenses and should be manufactured to high standards of accuracy.

2.2.3. The Phase Elements

The phase elements play the most important role in the spatial mode transformation. As described above, a pair of phase elements is needed to perform the transformation. The first phase element P1 adds a phase to the input beam such that the free-space propagation through the air gap to the face of the second phase element P2 creates an intensity profile, matching the intensity profile of the desired output beam at the side of the HOM fiber. The second phase element P2 adds another phase such that the intensity and phase of the resulting field matches the intensity and phase of the desired HOM fiber mode, when focused onto the end-face of the HOM fiber.

Phase elements can be manufactured using transparent dielectric disks with position- dependent thickness, or 'height'. A dielectric element with refractive index n and a curved surface of height $h(x, y)$ adds an optical phase

$$\Phi(x, y) = \frac{2\pi}{\lambda}(n-1)h(x, y) \tag{12}$$

to an incident beam of light (n is the refractive index of the material from which the phase elements are made).

An iterative algorithm for the design of the phase elements is based on the phase retrieval algorithm, known also by the "pendulum" or "ping-pong" algorithm [15]. The design of phase elements P1 and P2 starts after their locations, z_1 and z_2, have been selected (based on various mechanical and optical criteria), and comprises the following steps:

1. Based on the wavefront of the LP_{01} mode at the input SMF end face, $f_{01}(x, y, z_{\text{in}})$, and the detailed design and focal distance of the collimating lens, L1 (see Fig. 5 and the upper part of Fig. 6) calculate the collimated field $f_{01}(x, y, z_1^-) = \left|f_{01}(x, y, z_1^-)\right| \exp[i\phi_{01}(x, y)]$ incident on P1 at $z = z_1^-$ (The subscript 01 is used to emphasize that both the amplitude and phase of this field are determined by the mode shape of the input fiber and they will *not* change during the iterations). Similarly, by reverse-propagating the LP_{02} wavefront, $f_{02}(x, y, z_{\text{out}})$ from the HOM end face, through the focusing lens, L2, and to $z = z_2^+$, we obtain the collimated target field $f_{02}(x, y, z_2^+)$, which should leave P2 at $z = z_2^+$ in order to perfectly excite LP_{02} at the input of the HOM fiber. Again, both the amplitude and phase of this wavefront, $f_{02}(x, y, z_2^+) = \left|f_{02}(x, y, z_2^+)\right| \exp[i\phi_{02}(x, y)]$, will not change during the iterations.
2. Start an iterative process by first setting the optical phase added by P1 to be $\Phi_{P1}(x, y) \equiv 0$.
3. Add the phase $\Phi_{P1}(x, y)$ to the field $f_{01}(x, y, z_1^-)$ to obtain a forward propagating wavefront $f_{\rightarrow}(x, y, z_1^+) = f_{01}(x, y, z_1^-) \exp[i\Phi_{P1}(x, y)]$ at the output of P1.
4. Use the Fresnel formula, Eq. (3), to propagate the field $f_{\rightarrow}(x, y, z_1^+)$ from z_1^+ to z_2^- and obtain the field distribution at the input of P2, $f_{\rightarrow}(x, y, z_2^-)$, whose phase is $\phi(x, y, z_2^-)$, i.e., $f_{\rightarrow}(x, y, z_2^-) = \left|f_{\rightarrow}(x, y, z_2^-)\right| \exp[i\phi(x, y, z_2^-)]$.
5. Define the phase to be added by P2 to be $\Phi_{P2}(x, y) = \phi_{02}(x, y) - \phi(x, y, z_2^-)$s which is the difference between the spatial phases of wavefronts before and after P2. By the very definition of $\Phi_{P2}(x, y)$, the field emerging from P2 matches the correct field $f_{02}(x, y, z_2^+)$ in phase, but its amplitude: $\left|f_{\rightarrow}(x, y, z_2^+)\right| = \left|f_{\rightarrow}(x, y, z_2^-)\right|$ does not necessarily equal that of the target field $f_{02}(x, y, z_2^+)$! To correct for that we proceed with a backward iteration:

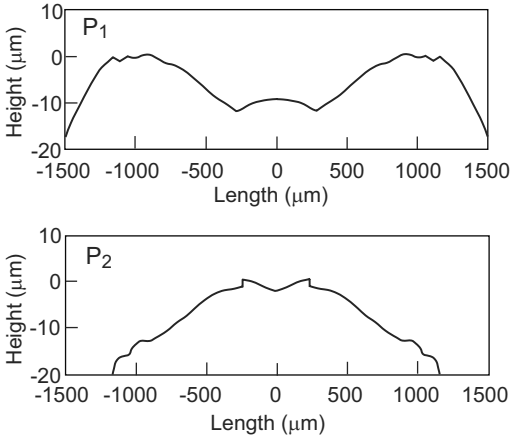

Fig. 9. Sections through the center of the surface heights of the phase elements P1 and P2.

6. Impose the amplitude of $f_{02}(x, y, z_2^+)$ on the field at $z = z_2^-$ by subtracting $\Phi_{P2}(x, y)$ from the collimated HOM field $f_{02}(x, y, z_2^+)$ to obtain a new estimate for the field at $z = z_2^-$: $f_{\leftarrow}(x, y, z_2^-) = f_{02}(x, y, z_2^+) \exp[-i\Phi_{P2}(x, y)]$ (note the backward arrow subscript).
7. Reversepropagate this field from z_2^- to z_1^+ and obtain the field distribution $f_{\leftarrow}(x, y, z_1^+) = \left|f_{\leftarrow}(x, y, z_1^+)\right| \exp[i\phi(x, y, z_1^+)]$.
8. Assign a new value to $\Phi_{P1}(x, y)$, using $\Phi_{P1}(x, y) = \phi(x, y, z_1^+) - \phi_{01}(x, y)$. Again, we have matched the phase of the calculated field with that of the known input field $f_{01}(x, y, z_1^-)$, but the amplitude of $f_{01}(x, y, z_1^-)$ may not match that of the calculated field $\left|f_{\leftarrow}(x, y, z_1^-)\right| = \left|f_{\leftarrow}(x, y, z_1^+)\right|$. Therefore,
9. Using the updated $\Phi_{P1}(x, y)$, go back to step 3 and iterate until $\Phi_{P1}(x, y)$ and $\Phi_{P2}(x, y)$ converge to stable values.
10. Determine the surface heights of phase elements P1 and P2 from the phases $\Phi_{P1}(x, y)$ and $\Phi_{P2}(x, y)$ using Eq. (12).

The procedure may result in surface heights with sub-micron spatial detail (in the $\{x, y\}$ plane). However, a spatial smoothing procedure is recommended in each step of this algorithm, see section 2.2.4.

The phase $\Phi(x, y)$ is defined up to an integer multiple of 2π, so that one may use either a continuous function or a piecewise continuous function with 2π phase jumps. The first option is much more favorable for broad spectral response, since discontinuous optical elements have significant chromatic aberrations [13]. For a transformation between the cylindrically symmetric modes LP_{01} and LP_{02}, cylindrically symmetric phase elements are used. Such phase elements may be manufactured by relatively cheap diamond turning techniques. The curved surfaces of P1 and P2 face each other, such that the transformation is done in the air gap between them.

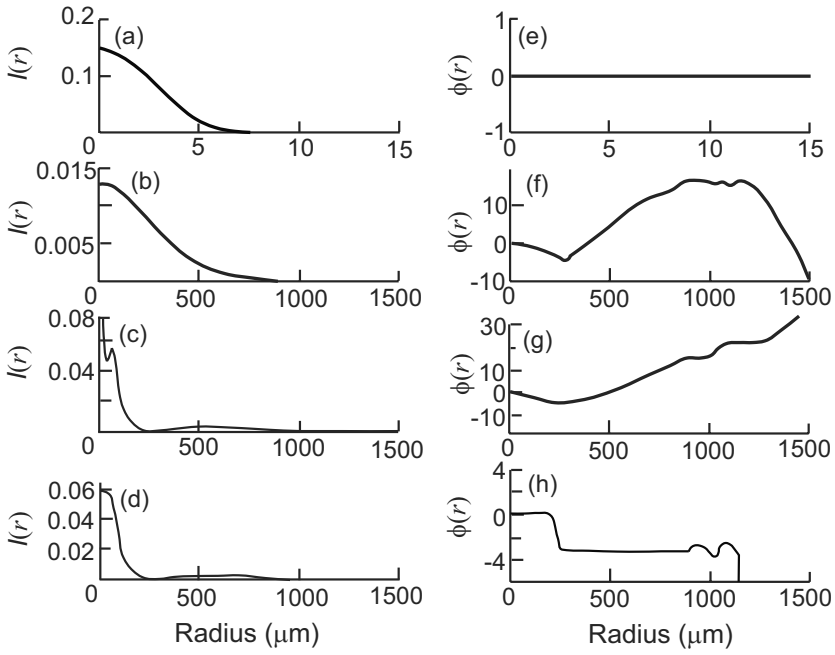

Fig. 10. Radial shape of the field at some planes along the MOX. The intensity (left, arbitrary units) and the phase (right, radians) of the field are shown (from top to bottom) at the SMF fiber end [(a) and (e)], after phase element P1 [(b) and (f)], just before phase element P2 [(c) and (g)] and after P2 [(d) and (h)]. The field diameter after collimation grows by a factor of about 100. After P2 the phase of the field assumes a π phase jump at about $r = 200\ \mu$m. The absolute value of the phase here is not important.

Figure 9 shows the surface height of the phase elements P1 and P2 of a typical MOX at a section through their centers. The role of phase element P1 may be understood in terms of geometrical optics. It consists of a central convex part, which resembles a lens. This convex part is responsible for focusing the central part of the incident Gaussian-shaped beam to the central lobe of the soon-to-become LP_{02} mode. The outer ring of P1 transforms the outer part of the incident beam into the outer ring of the LP_{02} mode. Free space propagation between P1 and P2 generates the required intensity pattern at P2, as well as some phase distribution. P2 contributes the final phase correction, and in particular, it introduces a sharp phase step ofπ radians between the inner and outer parts of the element to faithfully reproduce the negative outskirts of the LP_{02} mode of the HOM fiber. For a $LP_{02} \rightarrow LP_{01}$ MOX, the π phase shift flips the sign of the negative part of the LP_{02} mode, such that the lobe and ring parts have the same sign, as dictated by the Gaussian shape of the LP_{01} mode. Again, the central part of P2 maps the central LP_{02} lobe into the central part of the Gaussian LP_{01}, and P2 outer part focuses the ring part of LP_{02} into the outer part of the Gaussian. An example of the evolution of the field along the axis of the MOX is given in Fig. 10.

2.2.4. Design Considerations

2.2.4.1. Surface Smoothness

The accuracy of the transformation at the design wavelength is limited by how accurately the designed surface, $h(x, y)$, can be manufactured. Conventional and relatively low cost manufacturing techniques, such as diamond turning, have transverse resolutions of the order of 30-40 μm. Thus, the designed $h(x, y)$ should always be smoothed to comply with the available manufacturable resolution. A smoothed design also offers low sensitivity to alignment and collimation imperfections, wavelength dependence and environmental conditions. On the other hand, a too-smoothed surface may hurt the accuracy of the required wavefront transformation, resulting in lower MOX efficiency in terms of both IL and ER. In practice, a balance can be achieved between sufficient broadband accuracy and stable and robust performance.

2.2.4.2. Transformation Distance

The transformation distance $|z_2 - z_1|$ should be large enough so that the phase variation introduced by P1 will have enough distance to translate into the desired intensity of the target beam. However, it should be kept short enough to minimize chromatic and thermal effects. An optimum distance may be achieved by consecutive applications of the design algorithm with different trial distances.

2.3. MOX Imperfections

The performance of the MOX may be characterized by its insertion loss and its extinction ratio, as well as by its PMD (polarization mode dispersion), PDL (polarization dependent loss), return loss and stability of performance over the required spectral band under industry standard environmental conditions. As discussed in section 2.1.3, wavelength dependence of the mode shape puts a theoretical upper limit on the broadband MOX performance. However, in practice, most of the insertion loss and leakage of power into undesired modes is caused by alignment errors and imperfections in manufacturing, as well as by temperature effects.

2.3.1. Chromatic Aberrations of the Optical System

The use of optical elements without discontinuous jumps minimizes their chromatic dependence. The main contribution of the optical components to the wavelength dependence of MOX performance is then due to chromatic aberrations caused by material dispersion of the optical elements, having relatively high optical power, namely, the lenses. The change in the focal length, f, of a thin lens with refractive index n, may be approximated by

$$\frac{\partial f}{\partial \lambda} \approx \frac{f}{n-1}\frac{\partial n}{\partial \lambda}. \tag{13}$$

For typical numbers of $\partial n/\partial \lambda = -0.01$ μm^{-1}, n=1.5 and $f \sim$3 mm, we obtain $\delta f \approx \pm 1.5$ μm over the C transmission band. Figures 11 and 12 show the loss and extinction ratio for modes LP_{01} and LP_{03} as a function of the defocusing length δf at the HOM fiber end.

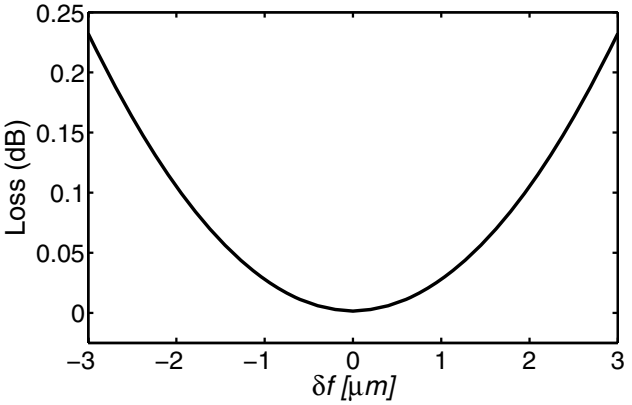

Fig. 11. Insertion loss as a function of defocusing at the HOMF side.

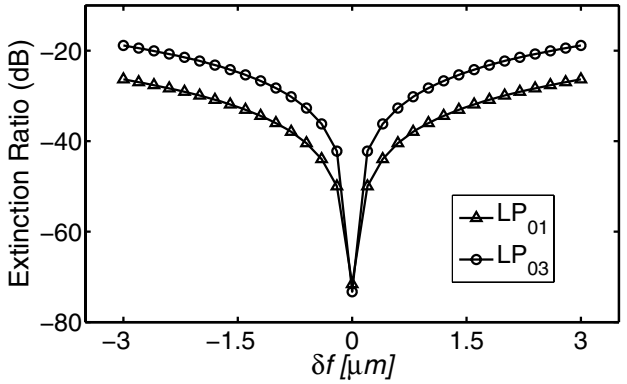

Fig. 12. Extinction ratio as a function of defocusing at the HOMF side.

The sensitivity of the transformation to defocus at the SMF end is much smaller. However, a combination of defocus at the SMF and the HOM ends may be used to compensate for aberrations during MOX assembly, as described in section 2.4.2.

The overall wavelength dependence of the loss and extinction ratio of the MOX is shown in Figs. 13 and 14. The plotted curves represent the results of a theoretical simulation that takes into account the combined effects of the fiber modal shape dispersion and the chromatic aberrations of all optical elements. We see that the effect of the chromatic aberrations is of the same order of magnitude as the effect of the modal shape dispersion, cf., Figs. 7 and 8.

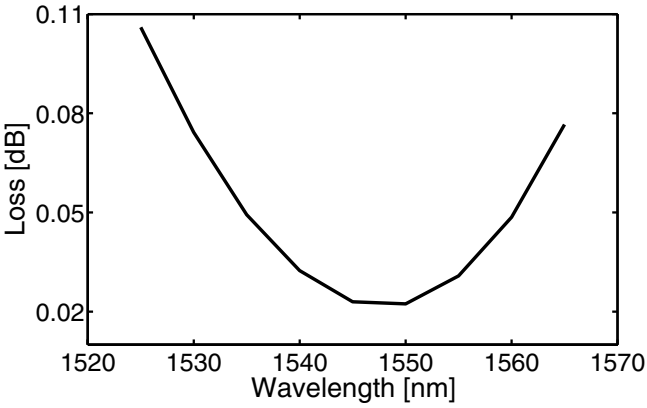

Fig. 13. Theoretical loss of the MOX as a function of wavelength in the C band.

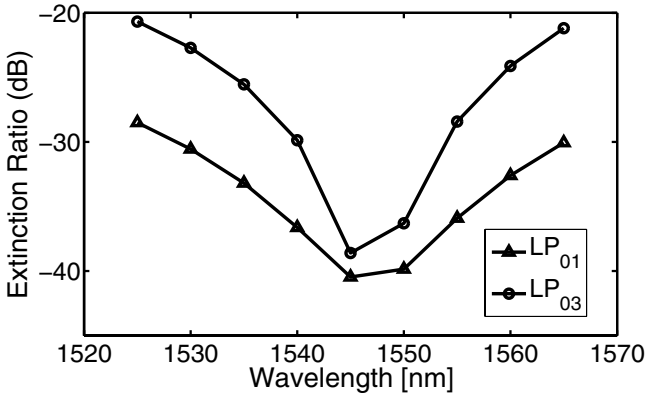

Fig. 14. Theoretical wavelength dependence of the extinction ratio for the modes LP_{01} and LP_{03}.

2.3.2. Achromatic Aberrations of the Optical System

Achromatic aberrations of the optical system may be caused either by manufacturing-induced imperfections of the optical elements and fiber ends, or by imperfections in the manual or automated assembly of the MOX. The aberrations may be divided into a few groups:

Cylindrically symmetric aberrations, such as defocus or spherical aberrations: This kind of aberrations is responsible for the excitation of cylindrically symmetric fiber modes, such as LP_{01}, LP_{03} etc. These aberrations can be partially compensated for by the movement of the fiber end along the lens axis. An example of the effect of defocus on the loss and ER of the MOX is shown in Figs. 11 and 12, respectively.

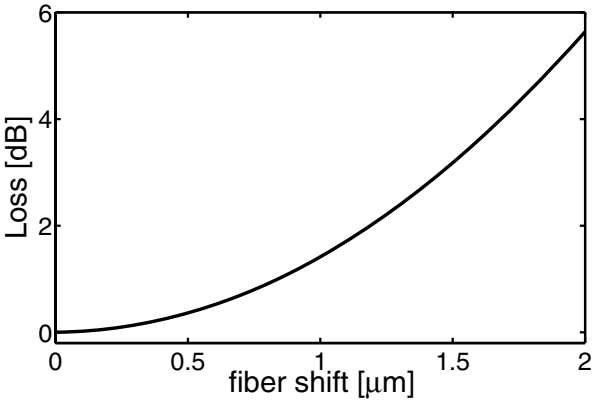

Fig. 15. Theoretically calculated insertion loss of the MOX due to a transverse shift of the HOM fiber end from its center position.

Antisymmetric aberrations, such as tilt or coma, which are antisymmetric about the x or y axes: These aberrations cause the excitation of antisymmetric modes, such as LP_{11}. They may be partially compensated for by moving the fiber end perpendicular to the optical axis. Examples of the effect of a transverse shift on the insertion loss and on the excitation of higher order modes, other than the LP_{02} mode, are shown in Figs. 15 and 16.

Elliptical aberrations such as astigmatism, where the phase is symmetric about the x and y-axis but not cylindrically symmetric: Such aberrations cause the excitation of modes such as LP_{21}. Usually, this kind of aberration is difficult to compensate during assembly and should be avoided.

The main *practical* cause of aberrations is due to imperfect manufacturing of the phase elements. Very careful collimation and alignment of the optical elements is needed in order to partially compensate for these aberrations. If the process of assembly is not done very carefully, then the main cause of additional aberrations may be tilts and shifts of optical elements. Automated assembly processes can alleviate most of these problems, producing MOXes of the required quality.

2.3.3. Combination of Chromatic and Achromatic Aberrations: The Appearance of Wavelength Dependent Loss

As discussed above, the main chromatic aberration is a wavelength dependent defocus. If a defocus exists in the system at the central wavelength then this defocus adds to the chromatic defocus to create wavelength dependent loss (WDL). An example of the appearance of WDL for a system with defocus is shown in Fig.17.

WDL can be minimized to below 0.1 dB over the C-band. However, by playing with the MOX collimation (changing the defocus) one can choose a specific wavelength slope of the loss of a MOX to compensate for other sources of WDL in the DMD (fiber WDL, temperature dependent WDL).

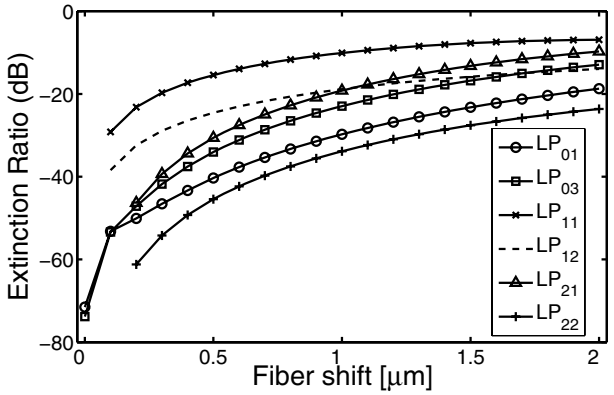

Fig. 16. Theoretically calculated extinction ratios of some guided modes (excluding) LP_{02}, caused by a transverse shift of the HOM fiber end from its center position.

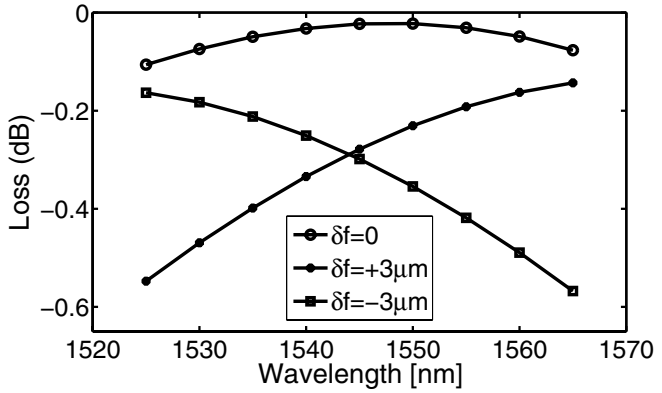

Fig. 17. Wavelength dependent loss (WDL) of the MOX caused by a longitudinal shift $df = \pm 3$ μm of the HOM fiber tip with respect to the optimal focus point.

2.3.4. Insertion and Return Losses Due to Surface Reflections and Scattering

The main source for return loss in the typical MOX architecture of Fig. 6 could be back-reflections at the fiber ends due to refractive index mismatch. Unless cleaved at an angle, each fiber end reflects about $\sim$3.3% (=[(1.444-1)/(1.444+1)]^2) of the incident light, or –15 dB. Light hitting the fiber end from within the fiber (e.g., at the MOX input), returns with a tilted wavefront, whose overlap with the fiber backward propagating mode is very small (< -60 dB of return loss for an SMF with 8 degrees tilt). Conversely, light rays incident on the fiber tilted end face at the focus of a converging beam (e.g., following L2 in the upper part of Fig. 6), return into the focusing lens with angles outside the numerical aperture cone of a properly designed lens, again ensuring small

back reflection. For both processes to succeed, the tilt angle must increase with the fiber numerical aperture (NA). For SMF fibers, the preferred angle is 8 degrees. Due to the larger NA (0.36–0.42) of the LP_{02} mode, to achieve back-reflection performance similar to that of SMF, tilt angles in excess of 16 degrees should be used, at the expense of unacceptable levels of polarization dependent loss (PDL). Angles around 10 degrees were adopted as a compromise, resulting in return loss values approaching –30 dB.

Tilting the fiber end faces will not prevent back-reflections from the free space optical elements in the MOX to contribute to its return loss performance. In the typical architecture shown in Fig. 6 there are an additional eight surfaces of optical elements. They must have high-quality antireflective coating and be properly aligned to ensure low insertion and reflection losses.

2.3.5. Temperature Effects

When the MOX is properly designed mechanically, temperature affects the system mainly through a defocus created at the fiber collimators. The following effects occur when the system is heated:

- Expansion of the lenses, leading to increase of the focal length.
- Change of the refractive index of the lenses, leading to either increase or decrease of the focal length, depending on the properties of the glass.
- Expansion of the metal holders of the collimators, which may compensate for the increase of the focal length.

These processes in combination cause an effective change of the focus position of the collimators, and may result in temperature dependent loss (TDL) and wavelength dependent loss (WDL). Athermal design of the MOX can be achieved by proper choice of materials for the lenses and metal holders, so that the different temperature effects will compensate one another. Deterioration of the quality of phase transformation due to a change in the refractive index and expansion of the phase elements is negligible when compared with the defocusing effect.

2.4. Actual Performance of the MOX

Experimentally, one usually characterizes a pair of MOXes, having a very short piece of HOM fiber between them. Such experimental data will be presented in Sections 4 and 5. However, to satisfy the inquisitive reader we conclude this section with the most important characteristics of manufactured MOXes:

- MOX insertion loss lies in the range of 0.8–1.25 dB.
- Wavelength dependent loss (WDL) can be minimized to below 0.1 dB over the C-band.
- Back reflection from the MOX below –28 dB.
- No PMD (a few fsec at most).
- Insignificant PDL if fiber angles do not exceed $\sim 10^{\circ}$.
- High power tolerance (no damage at 30 dBm).

Table 1. Maximum MOX extinction ratios over the C-Band for the three relevant modes. Best values refer to results obtained in a controlled laboratory environment, whereas typical values refer to volume production.

	Extinction ratio (dB)	
Mode	Best	Typical
LP_{01}	-26	-22
LP_{11}	< -30	-24
LP_{21}	< -35	< -30

– Size: a cylinder of diameter $\sim$1 cm and length of 6 cm.

As for individual extinction ratios, these were measured using a novel technique to be described in section 3.4.2.3, and the results are summarized in Table 1. Note that modes LP_{03} and LP_{12} can be easily removed using attenuation loops, see section 3.4.2.2, and therefore are of much less practical importance.

3. High-Order Mode Fibers for Dispersion Compensation

Having developed high-quality spatial mode transformers, it is our task now to show that HOM fibers (HOMF) can be designed to achieve the required dispersion properties (i.e., dispersion coefficient and dispersion slope coefficient), to compensate all modern transmission fibers, without sacrificing other importing properties, such as effective area. Combining the specially designed HOMF with the mode transformation technology of section 2, it has been possible to develop improved DCMs for use in modern high capacity optical transmission systems.

In this section we focus on the design and implementation of such HOMF. In section 3.1 we describe the selection criteria for the mode to be used for the purpose of dispersion compensation. In section 3.2 we discuss whether and how the mode transformation technology affects the design of the HOMF. In section 3.3 we discuss the required dispersion characteristics of the HOMF, while in section 3.4 we consider the design of the HOMF refractive index profile to achieve these characteristics. Finally, in section 3.5 we discuss the addition of a *trim* fiber to fine-tune the dispersion characteristics of the HOM-DCM.

3.1. Which High-Order Mode?

A key issue in the design of HOMF is which higher order mode the signal is to propagate in. Since our goal is dispersion compensation, one would naturally tend to choose the mode that gives the most desirable dispersion characteristics. However, it turns out that other design issues limit the choice of modes.

The most important amongst these issues is multi-path interference (MPI), which was mentioned in the introduction to this paper and will further be considered in section 4 below. Generally speaking, in order to limit MPI, one should limit the number of guided modes, and thus the possible interference paths in the HOMF. This means that

the signal should propagate in the lowest order mode that still provides the required dispersion characteristics. For example, see Fig. 3, if we were to select the LP_{11} mode as the propagation mode, then it would be possible to design a fiber with only two guided modes (LP_{01}, LP_{11}). On the other hand, if we were to select the LP_{03} mode there would have to be at least six guided modes (LP_{01}, LP_{11}, LP_{02}, LP_{21}, LP_{12}, LP_{03}), and almost certainly some others as well. This means that even if the LP_{03} mode were to exhibit particularly attractive dispersion properties, the increased MPI due to MOX coupling to other modes would be very prohibitive.

A second important consideration is polarization dependent behavior, and particularly polarization mode dispersion (PMD). Modes that are not cylindrically symmetric are by their nature more susceptible to polarization effects, and thus may have much larger PMD than cylindrically symmetric modes. Since PMD is a key design issue for DCMs, this effectively restricts the selection of modes to those with cylindrical symmetry, i.e., LP_{on}.

The preceding discussion basically means that the LP_{02} mode is the logical choice for the propagation mode in HOMFs for HOM-DCMs. In fact, we will see that with proper fiber design this mode also provides the required dispersion properties for most applications, and is thus well suited for the task. Therefore, for the remainder of this paper we will consider only HOMFs where LP_{02} is the designated propagation mode.

3.2. Interdependence of MOX and Fiber

As discussed in section 2, for HOMF to be useful it needs to be accompanied by mode transformers (MOXes) at the input and output of the HOM-DCM. An important practical issue is whether and how the two basic components of the HOM-DCM, HOMF and MOXes, are interrelated, and how the design of each depends on the other. From the discussion of spatial mode transformation technology in section 2 it is clear that the mode transformers need to be designed specifically for a given HOMF. More importantly however, it was also shown that in principle the design methodology is powerful enough to handle almost *any* HOMF. This indicates that the two problems can be separated, i.e., the HOMF can be designed and implemented independently, and then the mode transformers may be designed in the second stage.

Nevertheless, there are still two issues related to spatial mode transformation that do influence the design of HOMF. The first is the necessity to keep the spatial distribution of the high-order mode relatively constant over the transmission band, so as to maintain low insertion loss and high extinction ratio of the MOXes for all wavelengths. Since wavelength-dependent steep changes in spatial distribution go hand in hand with steep changes in the effective index, which in turn means large dispersion, it would appear that high dispersion HOMF and spatial mode transformation may not well suite each other. However, it turns out that for dispersion values in the range of practical interest, about 200–600 ps/nm/km, the rate of change of the mode shape is still small enough to allow efficient and broadband spatial mode transformation (see section 2.1.4). A second, equally important issue is the necessity to design the HOMF such that the LP_{03} mode is as close to cutoff as possible, or preferably not guided at all. The reason for this is that typical spatial mode transformers only provide high extinction ratio between LP_{02} and LP_{03} at the center of the band, whereas towards the band edges the extinction ratio deteriorates sharply, see Fig. 8. This means that in order to maintain sufficiently low MPI across the band, it is necessary for the LP_{03}

mode to be below or very close to cutoff (in the latter case special attenuation loops may be used to effectively kill the LP_{03} mode, see section 3.4.2.2)

3.3. Required Dispersion Characteristics of the HOMF

Clearly, the main requirement of a HOM-DCM is to provide accurate broadband dispersion compensation. Therefore, the most important characteristics of the HOMF are its dispersion characteristics, or more specifically the dispersion characteristics of the propagation mode of the HOMF, in our case, the LP_{02} mode. For the sake of brevity, we shall often use the term "dispersion of the HOMF" while actually meaning the dispersion of the LP_{02} mode of the HOMF

3.3.1. Simultaneous Slope and Dispersion Matching

To achieve linear distortionless transmission, the dispersion curve of the HOM-DCM should be a negative mirror of the dispersion curve of the transmission span to be compensated. Since the dispersion curve of all types of transmission fiber is very well approximated by a linear curve within a given transmission band, the dispersion curve of a transmission span of length L (in units of ps/nm) may be written as

$$D_{\mathrm{span}}(\lambda) = D(\lambda_0)\cdot L + S(\lambda_0)L(\lambda-\lambda_0) = D(\lambda_0)L\left(1+\frac{S(\lambda_0)}{D(\lambda_0)}(\lambda-\lambda_0)\right), \tag{14}$$

where λ_0 is some wavelength within the band (e.g., 1550 nm for the C-band), and $D(\lambda_0)$ and $S(\lambda_0)$ are the dispersion coefficient and dispersion slope coefficient of the transmission fiber at λ_0. Equation (14) shows that the dispersion curve may be characterized by: (1) The total dispersion given by $D_{\mathrm{span}} = D(\lambda_0)L$; (2) The ratio $S(\lambda_0)/D(\lambda_0)$, which does not depend on the length L, and therefore is a characteristic of the type of transmission fiber. This second quantity is often denoted as the RDS of the fiber [16], while the inverse quantity $D(\lambda_0)/S(\lambda_0)$ is denoted as κ [17]. Alternatively, an equivalent quantity can be defined, referred to as the Projected Zero Dispersion wavelength (PZD) [18],

$$\mathrm{PZD}\,(\lambda_0) = \lambda_0 - \frac{D(\lambda_0)}{S(\lambda_0)} = \lambda_0 - \frac{1}{\mathrm{RDS}} = \lambda_0 - \kappa. \tag{15}$$

The physical meaning of the PZD(λ_0), Fig. 18, is the wavelength for which the *linear approximation* of the fiber dispersion curve at wavelength λ_0 crosses the zero dispersion axis. An advantage of using the PZD is that for linear and quasi-linear dispersion curves the value of PZD does not depend on center wavelength λ_0, in contrast to κ and RDS. Table 2 enumerates the *dispersion properties* of common transmission fibers in the C and L bands.

Thus, to compensate the (assumingly linear) dispersion of a transmission fiber, having dispersion of $D_{\mathrm{span}}\,@\,\lambda_0$ and an RDS value $\mathrm{RDS_{TF}}$, the HOMF needs to fulfill the following two conditions:

$$\mathrm{RDS_{HOMF}}\,(\lambda_0) = \mathrm{RDS_{TF}}\,(\lambda_0)\,, \tag{16}$$

$$D_{\mathrm{HOMF}}(\lambda_0)L_{\mathrm{HOMF}} = -D_{\mathrm{span}}(\lambda_0), \tag{17}$$

Table 2. Nominal Dispersion, Dispersion slope, RDS, κ and PZD for a number of common transmission fibers in the C and L bands. The dispersion is calculated at 1550 nm for the C-Band, and 1590 nm for the L-Band. eLEAF, Truewave and Teralight are trademarks of Corning, Inc., OFS Fitel L.L.C. Inc., and Alcatel Corporation, respectively.

Fiber type	Band	Dispersion (ps/nm/km)	Slope (ps/nm^2/km)	RDS (nm^{-1})	κ (nm)	PZD (nm)
SMF-28	C	17	0.057	0.0035	291	1261
	L	19	0.057	0.0030	331	1261
TrueWave-RS®	C	4.4	0.045	0.010	98	1452
	L	6.2	0.045	0.0072	138	1452
eLEAF®	C	4.2	0.087	0.020	49	1501
	L	7.6	0.087	0.011	89	1501
TeraLight®	C	8	0.057	0.071	140	1410
	L	10.3	0.057	0.0056	180	1410

where $\mathrm{RDS}_{\mathrm{HOMF}}(\lambda_0)$ is the RDS of the HOMF at λ_0, $D_{\mathrm{HOMF}}(\lambda_0)$ is the dispersion coefficient, and L_{HOMF} is the length of the HOMF.

Clearly, the larger the absolute value of $D_{\mathrm{HOMF}}(\lambda_0)$, the less HOMF we need, which leads to a reduction in insertion loss of the HOM-DCM. In this context one can use the so-called Figure of Merit (FOM) introduced to characterize single mode DCF, and defined as the ratio of the fiber dispersion coefficient to the attenuation coefficient. The higher the FOM, the lower the resulting module loss of the DCM. For early DCFs, with dispersion in the range 90–120 ps/(nm km) and attenuation of 0.4–0.5 dB/km, The FOM was in the range of 200–300 ps/(nm km dB). Recent improvements in DCF design and manufacturing have led to FOM values nearing 500 [19].

For practical implementations of HOMF it is quite feasible to achieve dispersion values up to 600 ps/(nm km), with attenuation in the range 0.45–0.6 dB, resulting in FOM up to $\sim$1000 ps/(nm km dB). While such high FOM potentially enables HOM-DCMs with very low module loss, one still has to account for the extra loss of the two MOXes, typically about 2 dB. This means that for DCMs compensating 80–100 km of transmission fiber, the high HOMF FOM does not translate into a significant improvement in module loss compared to state of the art DCF. However, for applications such as multi-span compensation (see section 5.3.1), where more negative dispersion fiber is required, the high HOMF FOM can be used to good advantage. The high HOMF FOM also results in savings in cost and packaging space.

3.3.2. Third-Order Dispersion (TOD)

While the dispersion curve of the transmission fiber can be considered linear, the HOMF dispersion curve quite often displays significant deviations from linearity within the transmission band. This nonlinearity of the dispersion curve is often referred to as third-order dispersion (TOD), or dispersion curvature, and is especially relevant when the dispersion coefficient and/or the dispersion slope coefficient have large negative values.

For a dispersion curve that deviates significantly from linearity over the transmission band, specifying the dispersion and RDS at λ_0 is only partially useful, and does

not tell us anything about the overall behavior of the curve. Specifically, we would like to introduce an *average* RDS that represents the curve as a whole over the transmission band, and also introduce a measure for the deviation of the curve from linearity. To achieve both goals we introduce a linear fit to the dispersion curve such that *the maximum deviation of the actual curve from the linear fit within the transmission band* is minimized. This is different from the usual least mean squared (LMS) fit, since we aim to minimize the *maximum* deviation, and not the *average* deviation. An example of such a fit and the deviation from linearity is shown in Fig. 18.

Using the linear fit (LF), conditions (3.3) and (3.4) may be rewritten as

$$\mathrm{RDS}_{\mathrm{HOMF-LF}} = \mathrm{RDS}_{\mathrm{TF}}\left(\lambda_0\right), \tag{18}$$

$$L_{\mathrm{HOMF}} D_{\mathrm{HOMF-LF}}\left(\lambda_0\right) = -D_{\mathrm{span}}\left(\lambda_0\right), \tag{19}$$

where $\mathrm{RDS}_{\mathrm{HOMF-LF}}$ and $D_{\mathrm{HOMF-LF}}\left(\lambda_0\right)$ refer to the linear fit. Then the residual dispersion (RD) of the transmission span + HOM-DCM is given by

$$\begin{aligned} \mathrm{RD}\left(\lambda\right) &= D_{\mathrm{span}}\left(\lambda\right) - L_{\mathrm{HOMF}} D_{\mathrm{HOMF}}\left(\lambda\right) \\ &= L_{\mathrm{HOMF}}\left[D_{\mathrm{HOMF-LF}}\left(\lambda\right) - D_{\mathrm{HOMF}}\left(\lambda\right)\right], \end{aligned} \tag{20}$$

where $\left[D_{\mathrm{HOMF-LF}}\left(\lambda\right) - D_{\mathrm{HOMF}}\left(\lambda\right)\right]$ is the deviation of the HOMF dispersion curve from linearity, as in Fig. 18. Since the objective is to minimize $\mathrm{RD}(\lambda)$ over the transmission band, i.e., to minimize $\max\limits_{\lambda\in\mathrm{Band}} RD\left(\lambda\right)$, the advantage of using this type of linear fit becomes clear: Any other linear fit would *by definition* lead to higher residual dispersion at some wavelength, whereas here the *maximum* residual dispersion is minimized over the whole transmission band. It also provides us with an important *measure* of the deviation from linearity. To make this measure independent of HOMF length, we may use Eqs (19) and (20) to write

$$\max_{\lambda\in\mathrm{Band}} RD\left(\lambda\right) = D_{\mathrm{span}}\left(\lambda_0\right) \frac{\max\limits_{\lambda\in\mathrm{Band}}\left[D_{\mathrm{HOMF-LF}}\left(\lambda\right) - D_{\mathrm{HOMF}}\left(\lambda\right)\right]}{D_{\mathrm{HOMF-LF}}\left(\lambda_0\right)}. \tag{21}$$

We now define the third order dispersion (TOD) of the HOMF as

$$TOD = 100\,\frac{\max\limits_{\lambda\in\mathrm{Band}}\left[D_{\mathrm{HOMF-LF}}\left(\lambda\right) - D_{\mathrm{HOMF}}\left(\lambda\right)\right]}{D_{\mathrm{HOMF-LF}}\left(\lambda_0\right)}, \tag{22}$$

i.e., the maximum deviation from the linear fit as a percentage of $D_{\mathrm{HOMF-LF}}\left(\lambda_0\right)$. Thus

$$\max_{\lambda\in\mathrm{Band}} RD\left(\lambda\right) = D_{\mathrm{span}}\left(\lambda_0\right)\mathrm{TOD}_{\mathrm{HOMF}}/100, \tag{23}$$

which means that TOD of the HOMF is a direct measure of the *maximum residual dispersion over the transmission band.*

To summarize, we may say the HOMF should ideally satisfy three conditions:

- Largest negative dispersion coefficient possible (to minimize HOMF length)
- Correct RDS as defined by Eq. (18) (broadband compensation).
- Smallest TOD possible (to minimize residual dispersion).

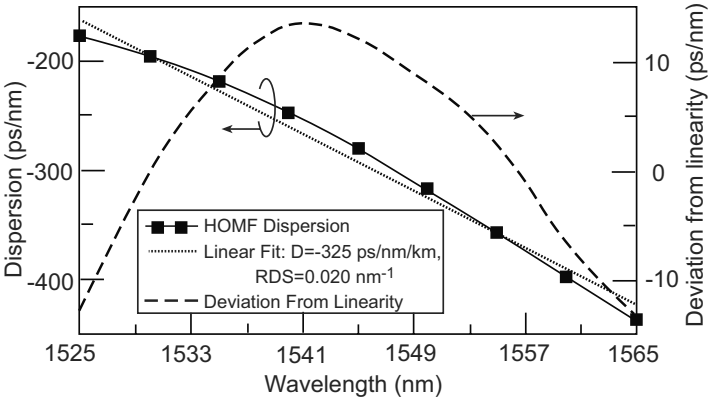

Fig. 18. Measured dispersion curve, linear fit, and the difference between the two (i.e., deviation from linearity) for a sample HOMF.

3.4. HOMF Refractive Index Profile Design

In this section we discuss the design of the refractive index profile of the HOMF. As a concrete example we concentrate on the compensation of Corning eLEAF® transmission fiber, which according to Table 2 has a high RDS value of 0.02 nm^{-1}. Such a high RDS is difficult to achieve using conventional DCF without resorting to very low effective area (typically about 15 μm^2 [20], highlighting the advantage of HOM-DCMs. It should be stressed, however, that the design principles discussed below equally apply to HOMF for any type of transmission fiber.

3.4.1. Basic Three Zone Profile and Dispersion Curve

The physics behind the three-zone profile used for DCF is well known within the context of single mode DCF, which is designed to have high negative dispersion in the basic LP_{01} mode. However, the same arguments apply just as well to higher order modes.

Figure 19 shows a typical three-zone profile of a HOMF used for dispersion compensation. The profile includes an inner core region with high relative refractive index (in this case $\Delta_1 = 1.47 - 1.444 = 0.026$), a depressed index region, and an outer core region. To understand the mechanism for the high negative dispersion of the LP_{02} mode, Fig. 20(a) shows the mode intensity distribution at 1550 and 1650 nm. As can be seen, the LP_{02} mode undergoes a sharp transformation from being mainly concentrated within the inner core region, to being mainly concentrated in the outer core region. This, and the accompanying change in effective index, leads to the sharp negative dispersion of the mode in this wavelength region, as clearly illustrated in Fig. 20(b).

Figure 21 shows a zoom-in of the dispersion curve to the region of interest for dispersion compensation. The general shape is shown in Fig. 21(a), and is common

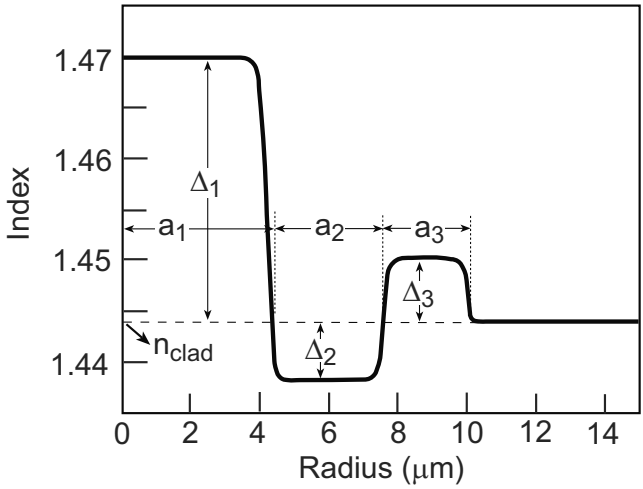

Fig. 19. Typical three zone profile of a HOMF for dispersion compensation. Δ_1, Δ_3 and Δ_3 are the relative (to the clad) indices of the zones, while a_1, a_2 and a_3 are the zone widths.

to all three-zone profiles of the type shown in Fig. 19 (and indeed to other profiles used for dispersion compensation). At shorter wavelengths the curve is concave, then passes through a zero-curvature point (in this case at about 1570 nm), after which it becomes convex and reaches a minima. By changing the various profile parameters, one can control the curve parameters, such as position along the wavelength axis, and the value of the minimum dispersion. Through such manipulations, to be discussed in more detail in section 3.4.3, one can achieve the desired dispersion characteristics within the transmission band of interest.

Figure 21(b) shows the dispersion curve in the C-band, together with a linear fit as described in section 3.3.2. On the basis of the linear fit, we see that the dispersion at 1550 nm is –376 ps/nm/km, and the RDS is 0.02 nm^{-1}. Thus, if we consider an 80-km eLEAF® span, we would need only 0.9 km of HOMF to achieve full dispersion and dispersion slope compensation of the span. These impressive dispersion characteristics have been achieved while maintaining a large mode effective area, which is 51 μm^2 at 1550 nm, and above 44 μm^2 over the entire C-band, as shown in Fig. 22. While recent single mode DCF designs have achieved comparable dispersion slope characteristics [20], the corresponding effective area is typically $\sim$15 μm^2, over three times smaller than the HOMF. Furthermore, the HOMF fiber profile itself is quite standard and easily manufactured. While the inner core index is high compared to standard SMF transmission fiber, it is comparable to regular DCF fiber, and can easily be achieved using standard manufacturing processes. The inner core radius is over 4 μm, much larger than DCF, and comparable to SMF, which further simplifies manufacturing. The measured dispersion curve of a fiber manufactured according to a profile similar to Fig. 19 is shown in Fig. 18, showing similar characteristics to the simulated curve.

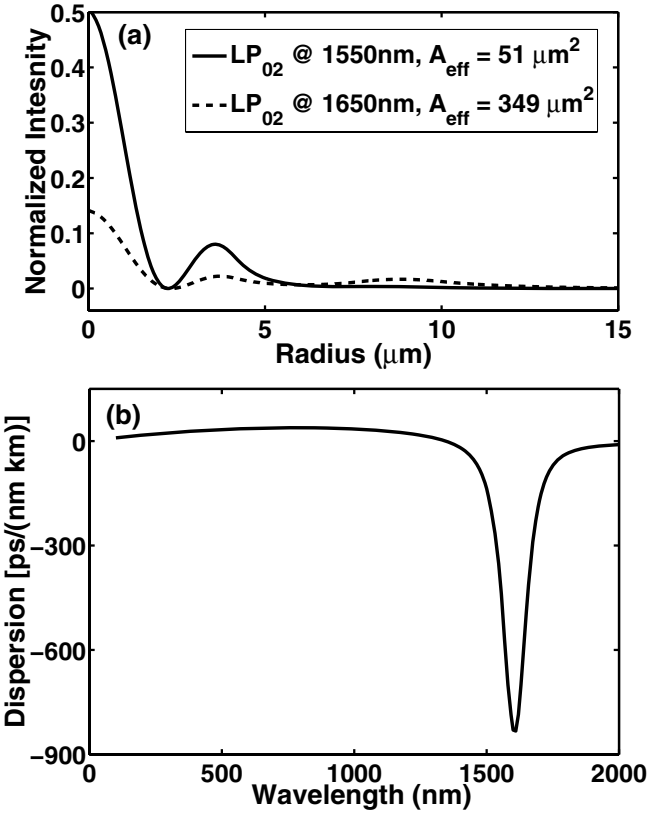

Fig. 20. (a) LP_{02} mode intensity distribution at two different wavelengths, for the profile shown in Fig. 19. The effective area (A_{eff}) of the mode at the two wavelengths is given in the figure legends. (b) The associated *waveguide* dispersion curve (i.e., without material dispersion) showing the sharp transition in the region of the C-Band.

However, while the linear fit to the dispersion curve has ideal characteristics for dispersion compensation, the actual dispersion curve itself suffers from a non-negligible deviation from linearity, as is clearly visible from the curvature of the curve in Fig. 21(b). The corresponding TOD value, as defined in section 3.3.2, is 4.3%, meaning that for an 80-km span the resulting maximum residual dispersion after compensation will be about 15 ps/nm. For long haul links up to 1000 km this is probably not an issue, however, for ultra-long-haul links of 2000 km and above, the total accumulated residual dispersion will exceed 400 ps/nm, which is already sufficient to incur a non-negligible transmission penalty at 10 Gb/s.

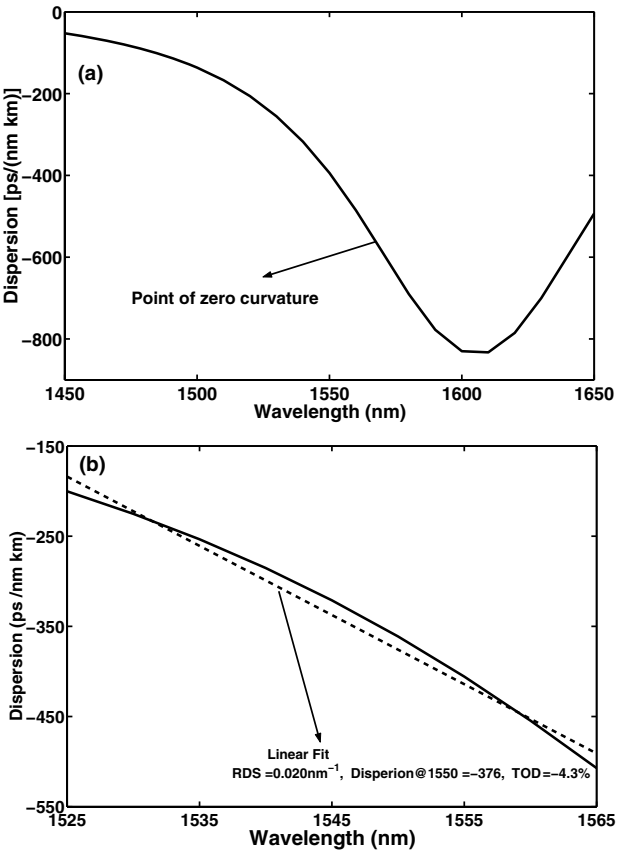

Fig. 21. Zoom-in of the LP_{02} mode dispersion for the profile shown in Fig. 19. (a) within the wavelength range 1450–1650. (b) within the C-band, together with the linear fit.

3.4.1.1. Relation Between TOD and RDS

Ideally, we would like to reduce the TOD while still maintaining the *RDS value* dictated by the transmission fiber to be compensated. While this is possible to some extent, it usually involves trade-offs with other important fiber properties, such as the n_{eff} of LP_{02} to be discussed in section 3.4.2 below. In practice, the TOD is strongly related to the RDS of the fiber, so that a meaningful reduction in TOD can only be achieved at the expense of reducing the RDS of the HOMF. This relation is to be expected, since higher RDS means higher dispersion slope (relative to dispersion), i.e., stronger dependence of the dispersion on wavelength. Since the dispersion curve is in any case strongly non-linear [Fig 21(a)], this results in higher TOD. In section 3.5 we will show that even if the RDS of the HOMF is not strictly the same as that of the transmission fiber, one can still obtain accurate broadband compensation using an additional trim

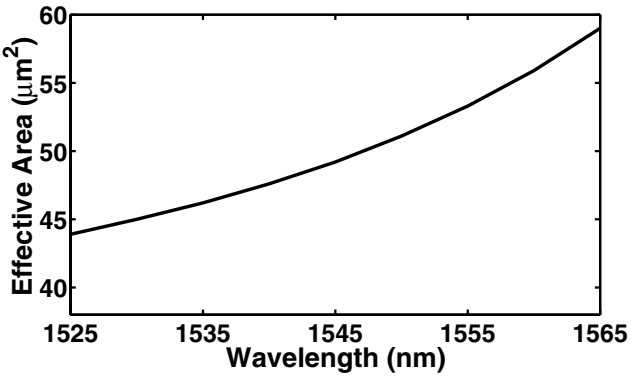

Fig. 22. Effective area as a function of wavelength for the profile of Fig. 19

fiber. This allows us some freedom in choosing the RDS of the HOMF in order to optimize other parameters, such as the TOD.

To illustrate this we have slightly altered the profile of Fig. 19 by decreasing the parameter a_2, the width of the 2nd profile zone, which as discussed in section 3.4.3.2 below, leads to a reduction in RDS. The resulting dispersion curves and deviation from linear fit for a reduction of 10% and 25% in a_2 are shown in Fig. 23, along with the original dispersion curve of Fig. 19. At an RDS value of 0.017 nm^{-1}, the TOD is reduced by more than half to 2.1%, whereas at an RDS value of 0.011 nm^{-1} it is reduced by an order of magnitude to 0.4%. The extremely low TOD in the latter case results directly from the fact that the zero curvature point of the dispersion curve occurs within the C-band near 1545 nm.

It is important to stress that the issue of TOD is not unique to HOM-DCF, but is also relevant to high RDS single mode DCF fiber. For example, Wandel and co-workers [20] present data for two high RDS DCFs. The first has RDS of 0.018 nm^{-1} and TOD above 5%, while the second has RDS of 0.01 nm^{-1}, and TOD of 0.4%. These reported TOD values are similar to those given in Fig. 23 for HOM-DCMs with comparible values of RDS.

Figure 23 also illustrates the relation between RDS and dispersion, or alternately between RDS and FOM. The lower the RDS, the easier it is to achieve high dispersion values, and thus high FOM values, while still maintaining other important profile characteristics discussed in the next section.

3.4.2. Other Important Characteristics of the Profile

The refractive index profile determines not only the dispersion characteristics, but also other properties of the HOMF, that can affect the performance of transmission systems. In this section we consider the more important of these properties, and how they are affected by the profile design.

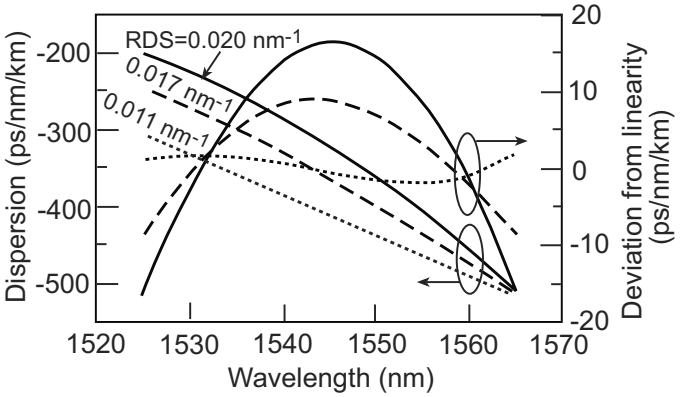

Fig. 23. Dispersion curves and deviation from linear fit for three different profiles: (a) Solid curves—The profile of Fig. 19, with linear fit parameters: RDS = 0.020 nm^{-1}, $D = -376$ ps/nm/km, TOD = 4.3%; (b) Dashed curves—The profile of Fig 19 with a_2 reduced by 10%, with linear fit parameters: RDS = 0.017 nm^1, $D = -405$ ps/nm/km, TOD = 2.1%; (c) Dotted curves—The profile of Fig 19 with a_2 reduced by 25%, with linear fit parameters: RDS = 0.011 nm^{-1}, $D = -429$ ps/nm/km, TOD = 0.4%.

3.4.2.1. Attenuation Coefficient and Effective Mode Cutoff

A mode is guided as long as its effective index is above the cladding index (typically 1.444 in the C-Band). Using this formal definition, the cutoff of the LP_{02} mode of the profile of Fig. 19 is beyond 2000 nm. However, long before the formal cutoff is reached, the attenuation of the mode due to micro- and macro-bending [21] becomes so large as to render it unguided for all practical purposes.

One typically finds that the mode attenuation coefficient increases sharply when the effective index reaches a certain critical threshold, which depends on the fiber profile, the manufacturing process, and the fiber spooling conditions (which strongly affect micro-bending). The reason for this is that beyond this threshold, the mode extends away from the fiber core, and is more sensitive to various perturbations of the fiber profile, such as bending (both micro- and macro-).

The critical effective index in turn defines a critical wavelength, λ_c, which we call the *effective cutoff wavelength* of the mode (as opposed to the formal cutoff wavelength discussed above). In Fig. 24 we show the spectral dependence of the LP_{02} attenuation coefficient of a fiber manufactured according to a profile similar to that of Fig. 19. One can clearly observe the onset of effective cutoff at about 1575 nm.

When designing the fiber profile, it is crucial to ensure that λ_c lies beyond the end of the transmission band. Since λ_c also depends on manufacturing conditions and on spooling, it is necessary to empirically determine the critical effective index for a given set of conditions. Once known, the profile may be designed so that the maximum effective index within the transmission band is above the critical effective index. We have determined that for a wide range of manufacturing and spooling conditions, the critical effective index for the LP_{02} mode is in the range 1.4455–1.4460 (assuming

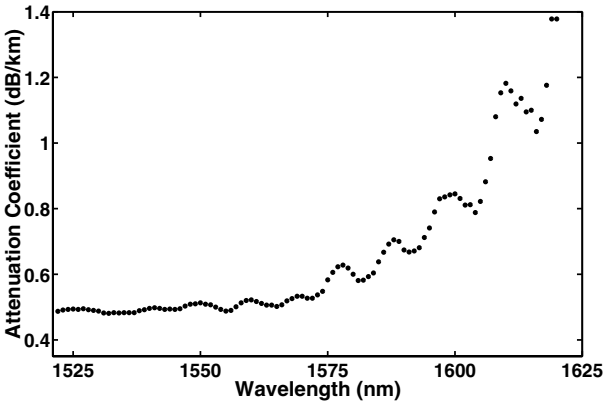

Fig. 24. LP_{02} attenuation coefficient of a fiber manufactured according to a profile similar to that of Fig. 19.

n_{clad} = 1.444). For the profile of Fig. 19 the effective index at 1565 nm is 1.4460, in accordance with the fact that λ_c lies beyond the C-Band (e.g., Fig. 24).

λ_c not only affects the mode attenuation coefficient, but also other fiber properties, notably polarization mode dispersion (PMD). Below λ_c, PMD has a weak spectral dependence, and is mainly determined by manufacturing and spooling conditions. Near λ_c, PMD takes on a stronger spectral dependence, and increases sharply beyond λ_c. The reason for this, as with the increase in attenuation, is that above λ_c the mode extends away from the fiber core, and becomes increasingly sensitive to perturations such as bending which break the fiber cylindrical symmetry. Practically speaking, the increased PMD means that even if the rise in attenuation due to effective cutoff can be tolerated, one should still design the profile to ensure that λ_c is beyond the transmission band.

Finally, Fig. 24 also illustrates the typical achievable attenuation coefficient for well-designed and manufactured HOMF, which is in the range 0.45–0.6 dB/km. This is similar to that of DCF with comparable dispersion characteristics [19].

3.4.2.2. Number of Guided Modes

As discussed in section 3.1, a major concern in the design of HOMF is the number of guided modes supported by the fiber, with more guided modes resulting in higher MPI of the HOM-DCM (All modes are excited, even if to a small extent, by the wave incident on the HOMF tip [see overlap integral of Eq. (7)]. If they are guided, they contribute to MPI, otherwise, they just represent tolerable loss). The profile of Fig. 19 supports six guided modes, whose effective indices in the C-Band are listed in Table 3. While the exact values can change, the number and order of modes as listed in the table is typical to most profiles.

In particular, the three modes more guided than the LP_{02} mode, i.e., LP_{01}, LP_{11}, and LP_{21}, are expected to be present in most HOMF profiles designed to use the LP_{02}

mode. Therefore, one should always account for the presence of these three modes, for example, in the context of mode coupling to be discussed in section 3.4.2.3.

On the other hand, there is some freedom regarding the two modes that are less guided than the LP_{02} mode, i.e., LP_{03} and LP_{12}. Using appropriate design, the effective indices of these modes may be decreased, and they may even be made to be non-guided, i.e., with effective indices below 1.4440. As discussed in section 3.2, this is particularly important with regards to LP_{03} due to MOX design issues. Even if the LP_{03} and LP_{12} modes are formally guided, i.e., their effective index is above 1.4440, they may be strongly attenuated using special *attenuation loops* in the HOMF just after the input MOX, and just before the output MOX. These loops work on the principle that the macro-bending loss of a mode is strongly dependant on the effective index. For a step index fiber it has been shown that the macro-bending loss, α, associated with a loop of curvature radius R satisfies [22]

$$\alpha \propto \frac{1}{\sqrt{R}} \exp\left[-\frac{2}{3}\frac{\left(n_{\text{eff}} - n_{\text{clad}}\right)^{3/2}}{n_{\text{eff}}^2} k \cdot R\right] \equiv \frac{1}{\sqrt{R}} \exp\left(-\frac{R}{R_c}\right), \qquad (24)$$

where n_{clad} is the cladding index, and k the free space wavevector. Thus it is natural to define a critical radius R_c, such that loops with radius $R < R_c$ strongly attenuate the mode. In Table 3 we also list the critical radius for each mode at the beginning and end of the C-Band. This shows us that if we introduce attenuation loops of radius R $\sim$ 2cm, these loops should strongly attenuate the LP_{03} and LP_{21} mode, while only having a minor effect on the LP_{02} mode. Clearly, the smaller n_{eff} of LP_{03}, the easier it is to attenuate the mode. In practice we have found it desirable to keep the LP_{03} mode effective index below 1.4445 across the entire transmission band. Table 3 shows that the profile of Fig. 19 does not strictly satisfy this requirement. On the other handthe altered profile with RDS = 0.017 nm^{-1} (Fig. 23) does, with virtually no change to n_{eff} of the LP_{02} mode.

Table 3. Guided modes of the profile of Fig. 19, their effective indices, and critical bending radii [according to Eq. (24)].

	Effective index		Critical Bending radius R_c (mm)	
Mode	at 1525 nm	at 1565 nm	at 1525 nm	at 1565 nm
LP_{01}	1.4653	1.4651	0.3	0.3
LP_{11}	1.4582	1.4577	0.5	0.5
LP_{21}	1.4492	1.4484	2.0	2.6
LP_{02}	1.4467	1.4460	5.4	8.5
LP_{03}	1.4447	1.4445	41.0	67.9
LP_{12}	1.4446	1.4445	51.7	67.9

3.4.2.3. Mode Coupling

Mode coupling refers to transfer of optical power between modes propagating along the fiber. Power transferred from a guided mode to a non-guided mode results in loss, since the power in the non-guided mode dissipates along the fiber. However, power transferred to another guided mode continues to propagate, and at a later stage (either

further along the HOMF, or at the output MOX) can recombine with the main signal and lead to MPI. The precise relation between mode coupling and MPI will be discussed in section 4.4.2, whereas here we discuss mode coupling in general, and how it is affected by the fiber profile design.

Mode coupling occurs due to random perturbations of the refractive index profile along the fiber. These may results from manufacturing imperfections, or external causes such as stress and micro-bending [21]. Since the perturbations are random, the mode coupling is *incoherent*, as opposed to coherent mode coupling that occurs due to a systematic perturbation along the fiber (e.g., Bragg gratings). Thus, the power transfer rate between modes is constant, and independent of position along the fiber, allowing one to define a mode-coupling coefficient between any two modes denoting the power transfer rate. For example, a mode coupling coefficient of 0.01 km^{-1} between the LP_{02} mode and the LP_{01} mode means that every km, 1% of the LP_{02} power is transferred to the LP_{21} mode, and *vice versa*.

A detailed discussion of the mode-coupling coefficient is beyond the scope of this paper, and can be found, for example, in [23–25]. Furthermore, the details of any theory depend strongly on the types of perturbations and their statistics, data that is very difficult to extract experimentally from a fiber. Having said that, there are a few general observations that can be made about the factors that determine the mode-coupling coefficients:

– A given type of perturbation will have a specific symmetry, and thus only couple between certain modes [23]. For example, micro-bending will only couple between modes whose azimuthal numbers (m in the LP_{mn} notation) differ by unity, such as LP_{02} and LP_{11}, but not modes with the same azimuthal symmetry, such as LP_{02} and LP_{01}. Similarly, elliptic perturbations (i.e., perturbations that distort the cylindrical symmetry of the fiber), will couple between LP_{02} and LP_{21}, but again not between modes with the same azimuthal symmetry. For a given set of manufacturing and spooling conditions one typically finds that there are one or two dominant perturbations, and these determine the modes that couple most strongly to each other.
– As a general rule, the larger the difference in propagation constants of two modes [$\Delta\beta = \beta_1 - \beta_2 = k(n_{\text{eff},1} - n_{\text{eff},2})$], the smaller the mode coupling between them. However, the decrease in mode coupling occurs only for $\Delta\beta$ larger than the inverse of the typical length scale of the perturbation causing the coupling. For smaller $\Delta\beta$, the dependence on $\Delta\beta$ is weak, since the perturbation length scale is in any case much smaller than the phase walk-off (i.e., $\Delta\beta^{-1}$) between the two modes.
– Fibers whose profiles exhibit sharp features are more sensitive to perturbations along the fiber, and have higher mode coupling coefficients. Quantitatively, this is related to the profile derivative dn/dr, r being the radial coordinate. Referring to Fig. 19, it is clear that the larger the value of Δ_1, the sharper the transition between the first and second zones of the profile, and the larger is dn/dr at the boundary between two zones. The same applies to the magnitude of Δ_2 and Δ_3. However, since Δ_1 is typically much larger, it usually has the dominant effect. Thus, an important conclusion is that the higher Δ_1, the stronger the mode coupling.

In order to measure the mode-coupling coefficient we use a high resolution reflectometer [26] in a setup shown schematically in the left-hand side of Fig. 25. The output

pulse of the reflectometer enters the MOX via the circulator and is then transformed primarily to the LP_{02} mode of the HOMF. As the pulse propagates along the HOMF, part of it is coupled to other modes, having different group velocities. The entire signal is then coupled from the HOMF back to an SMF fiber using a splice with a known lateral offset, and then, via the circulator back into the reflectometer. The lateral offset of the splice is necessary so that optical power carried by the LP_{11} and LP_{21} modes of the HOMF couples to the SMF and is thus able to reach the reflectometer. A sample reflectometer trace is shown in the right-hand side of Fig. 25, and consists of discrete peaks in between which there is a continuous signal. The discrete peaks correspond to power coupled to the different modes by the input MOX, and can be identified by comparing their position to the simulated group velocity of the fiber modes. As should be expected, the strongest peak corresponds to the LP_{02} mode. The continuum between the peaks represents power that was coupled from the LP_{02} mode to other modes at various points along the fiber.

Referring to Fig. 25 as an example, one can observe the following:

- The continuum between the LP_{01} peak and the LP_{02} peak is due to coupling from LP_{02} to LP_{01}.
- The continuum between the LP_{02} peak and the LP_{11} is due to coupling from LP_{02} to both LP_{11} and LP_{21}
- The continuum between the LP_{11} peak and the LP_{21} peak is due to coupling from LP_{02} to LP_{21}

By integrating these three continuums, comparing to the integrated LP_{02} power, and correcting for the HOMF-SMF coupling for each mode due to the lateral splice offset (these correction factors were calculated and verified experimentally), it is possible to derive the mode coupling coefficients between the LP_{02} mode and the three other modes. A variation of this technique can also be also used to derive the MOX extinction ratios, as for example listed in Table 1.

As discussed in the previous section, at least three other modes besides the LP_{02} mode are present in a typical HOMF: LP_{01}, LP_{11}, and LP_{21}. Thus, the three most important coupling coefficients for the design of HOMFs are between the LP_{02} mode and these three modes. We have measured these coupling coefficients for a wide range of fibers manufactured under different conditions, and have found the general behavior shown in Table 4. Thus, the $LP_{02} - LP_{21}$ coupling is one to two orders of magnitude stronger than the $LP_{02} - LP_{01}$ coupling, with $LP_{02} - LP_{11}$ coupling somewhere in the middle. This order also corresponds to the decreasing order of Δn_{eff} (i.e., of $\Delta\beta$), as discussed above. However, caution should be exercised in concluding that $\Delta\beta$ has a critical impact on mode coupling, since the three types of coupling correspond to different perturbation symmetries. Thus, it is quite possible that a certain type of perturbation is dominant in the fibers, e.g., elliptical perturbations, and this is the main factor determining the order of the coupling strengths. In fact, for a given type of coupling, e.g., LP_{02}–LP_{21}, we have found no correlation between $\Delta\beta$ and the coupling strength, thus lending support to this possibility.

A key question remains as to which profile parameters affect the mode coupling strength. This is particularly relevant to LP_{02}–LP_{21} coupling, which is by far the dominant mechanism. As discussed above, one would expect the core relative index Δ_1 to influence the coupling strength, since higher Δ_1 leads to higher profile derivatives at

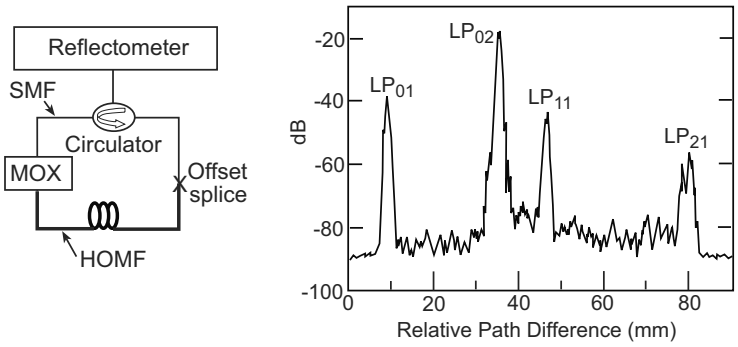

Fig. 25. Schematic representation of the mode coupling measurement setup (left), and sample output trace of the Reflectometer (right).

the boundary between the first and second profile zones. This is indeed apparent from Fig. 26, which shows the measured LP_{02}–LP_{21} coupling coefficient for a number of fibers having different values of Δ_1. Besides the issue of profile derivatives, it is well known that high levels of Germanium doping lead to increased Rayleigh scattering in fibers, and a similar mechanism may also be responsible for increasing the mode coupling (over and above the increase due to higher profile derivatives).

Table 4. Typical range of measured coupling coefficients between the LP_{02} mode and three other modes.

Between modes	Typical value of Δn_{eff}	Coupling coefficient (km^{-1})	
		Range	Typical
LP_{02} – LP_{01}	0.019	0.0001 – 0.001	0.0002
LP_{02} – LP_{11}	0.012	0.001 – 0.005	0.002
LP_{02} – LP_{21}	0.003	0.005 – 0.02	0.007

3.4.3. Profile Design Degrees of Freedom

The preceding sections presented the basic three-zone profile of the HOMF, together with the dispersion curve and other fiber properties. Here we consider the main degrees of freedom that allow one to control these properties.

3.4.3.1. Controlling the Dispersion Through Profile Scaling

As with the simple step index fiber [27] a scaling relation exists between the dimensions of the fiber profile and the wavelength. Specifically, scaling the fiber radius by a factor α (i.e., the parameters a_1, a_2 and a_3 in Fig. 19 are multiplied by α), results in a change in waveguide dispersion according to

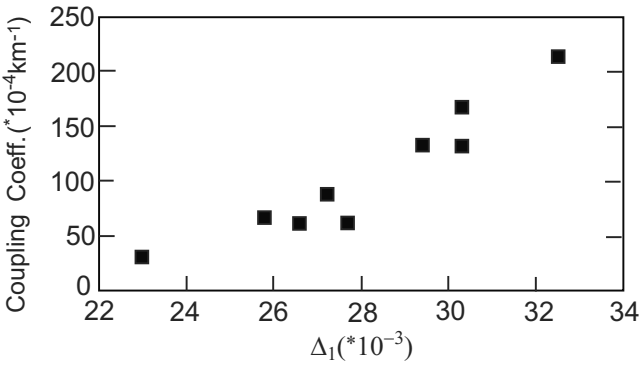

Fig. 26. Correlation between measured LP_{02}-LP_{21} coupling coefficient and the core relative index Δ_1.

$$\tilde{D}_{\mathrm{WG}}(\lambda) = \frac{1}{\alpha} D_{\mathrm{WG}} \left(\frac{\lambda}{\alpha} \right). \tag{25}$$

Here $\tilde{D}_{\mathrm{WG}}(\lambda)$ is the waveguide dispersion of the scaled fiber, whereas $D_{\mathrm{WG}}(\lambda)$ is that of the original fiber. Equation (25) is easily derived from the wave equation of the fiber and the definition of waveguide dispersion. The total dispersion, including also material dispersion, does not strictly satisfy Eq. (25), however, for the high dispersion fibers discussed here, waveguide dispersion is by far the dominant contribution. The physical meaning of Eq. (25) is that scaling the fiber radius shifts the dispersion curve on the wavelength axis, as illustrated in Fig. 27 for the profile of Fig. 19. Thus, contracting/expanding the profile shifts the dispersion curve to shorter/longer wavelengths, having the effect of changing the dispersion at a given wavelength. For example, Fig. 27 shows that the dispersion at 1550 nm changes from –200 ps/nm/km to –750 ps/nm/km for a scaling range of only 4%.

Besides being an important design tool for achieving the required dispersion at a given wavelength, scaling also has an important practical aspect: When drawing a fiber during manufacturing, the outer diameter of the fiber, as well as all other transverse dimensions, may be altered by altering the drawing conditions. This results in scaling of the fiber profile, and allows fine-tuning of the dispersion during manufacturing.

3.4.3.2. Controlling the RDS

A given dispersion curve is characterized by the value of the dispersion and dispersion slope at each point along the curve. Scaling the profile shifts the dispersion curve along the wavelength axis, thus changing the dispersion for a given wavelength. However, for each value of dispersion, the slope, and hence the RDS, is predetermined by the shape of the curve. Thus, to achieve a different RDS for the same dispersion, the dispersion curve should be *altered*, as opposed to just shifting it along the wavelength axis. This basically means altering the depth of the dispersion minima, which can be achieved by changing the parameters of the second profile zone, i.e., the depressed index region.

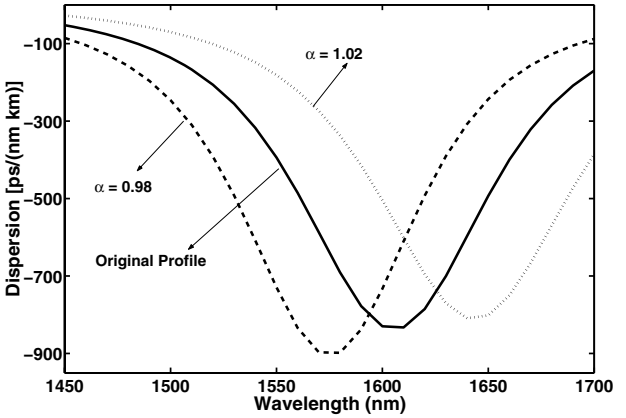

Fig. 27. The effect of the fiber scaling on the dispersion curve. The dispersion curve of the profile of Fig. 19 is displayed together with dispersion curves of the same profile where the radius is multiplied by a factor α.

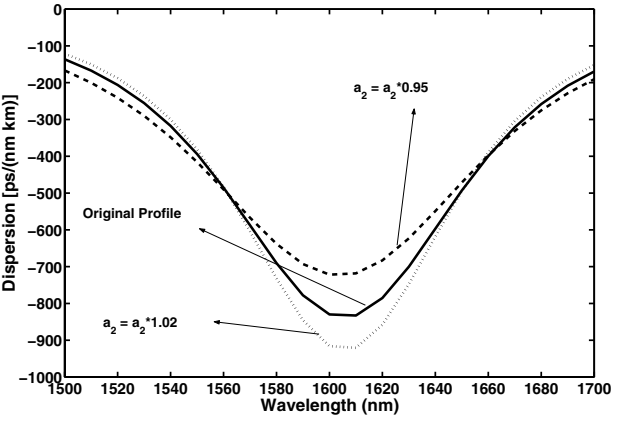

Fig. 28. The effect of a_2, the width of the second profile zone, on the dispersion curve. The dispersion curve of the profile of Fig. 19 is displayed together with dispersion curves for the same profile where a_2 is decreased by 5% and increased by 2%.

The deeper or wider this region, the deeper the dispersion minimum, and *vice versa*. Figure 28 shows the effect of a_2, the width of the second profile zone, on the dispersion curve, while a similar effect can be achieved by changing Δ_2, the depth of the zone.

The deeper the dispersion curve, the higher the achievable slope for a given dispersion, and the higher the RDS. For example, scaling the three curves shown in Fig. 28 to the same dispersion, results in RDS values from 0.017 nm^{-1} for the shallowest

curve, to 0.022 nm^{-1} for the deepest curve. Another example can be seen in Fig. 23, where a reduction in a_2 leads to a significant decrease in RDS, with only minor change in the dispersion.

3.4.3.3. Controlling the Mode Effective Indices

As discussed in section 3.4.2.1, it is crucial to maintain high n_{eff} of LP_{02} in order to avoid effective cutoff occurring within the transmission band. In the previous two sections we saw how to modify the profile to achieve the desired dispersion and RDS. However, these modifications also alter n_{eff} of LP_{02}, with higher dispersion and RDS usually meaning lower n_{eff}. Thus, we would like to independently control n_{eff} so as to satisfy all three requirements simultaneously. This can be achieved through the core relative refractive index Δ_1: The higher Δ_1, the higher n_{eff} of all modes, including LP_{02}. This is easily understood since n_{eff} is nothing but a form of weighted average of the refractive index profile [27]. Increasing Δ_1 not only increases n_{eff}, but also changes the dispersion and RDS, which can then be altered using the methods of the previous sections. The important point is that we may achieve the same dispersion and RDS, but with a higher n_{eff} for the LP_{02} mode, thus providing independent control of the three parameters.

However, there are two problems with this approach: Fig. 26 shows that increasing Δ_1 above 0.28 leads to prohibitively high mode coupling (see also section 4.4.2), and should therefore be avoided. This limit on Δ_1 effectively limits the range of dispersion and RDS that may be achieved while still maintaining acceptably high n_{eff}.

The second problem is that n_{eff} of LP_{03} mode also increases with Δ_1. To overcome this we take advantage of the different intensity distributions of the two modes, as shown in Fig. 29. We see that most of the LP_{02} mode power is concentrated in the first and second profile zones, whereas most of the LP_{03} mode power is concentrated in the third profile zone. This allows us to achieve a degree of independent control of the n_{eff} of the two modes. For example, the relative index of the third zone, Δ_3, has a much larger impact on the n_{eff} of the LP_{03} mode than on that of the LP_{02} mode. Thus, by decreasing Δ_3 and then slightly increasing Δ_1, one can achieve the net effect of decreasing n_{eff} of LP_{03} while maintaining the n_{eff} of LP_{02}.

3.5. Trim Fiber and HOM-DCM Design Options

Up till now we have implicitly assumed that the only fiber within the HOM-DCM is the HOMF. Thus, the target dispersion and RDS of the HOMF are dictated by those of the HOM-DCM itself, as discussed in section 3.3. However, it has been noted before in the context of single mode DCF [28], that for applications where broadband dispersion compensation is critical, i.e., when it is necessary to simultaneously and accurately compensate for both slope and dispersion, it can be advantageous to use an additional fiber within the HOM-DCM, which we refer to as *trim* fiber. One of the advantages of trim fibers has to do with manufacturing tolerances. Naturally, it is impossible to manufacture HOMF exactly according to design specifications, and therefore it is necessary to specify manufacturing tolerances, namely, a range of dispersion and RDS values around the nominal design values. Any deviation of the actual dispersion coefficient from the design value may easily be compensated for by altering the length of the HOMF used in the HOM-DCM. However, deviations of the actual RDS from

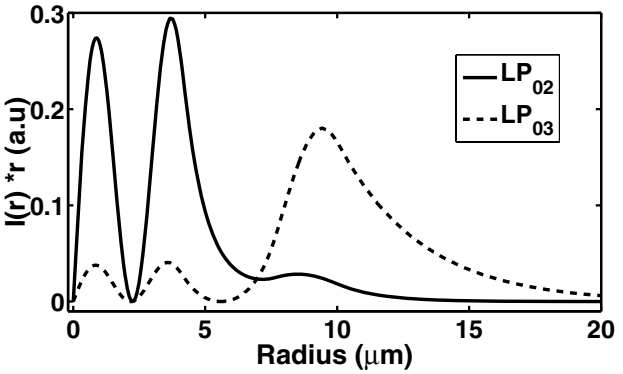

Fig. 29. $I(r) \cdot r$ corresponding to the LP_{02} and LP_{03} modes of the profile of Fig. 19 at 1550 nm, $I(r)$ being the modal intensity distribution.

the design value cannot be compensated for, and this results in a HOM-DCM with inaccurate dispersion properties. A trim fiber allows one to fine-tune the dispersion properties of the DCM to achieve accurate dispersion and RDS simultaneously.

Given the dispersion and dispersion slope coefficients of the HOMF, $D_{\mathrm{HOMF}}(\lambda_0)$ and S_{HOMF}, and the dispersion and dispersion slope coefficients of the trim fiber, $D_{\mathrm{Trim}}(\lambda_0)$ and S_{Trim}, it is easy to show that the lengths of HOMF and trim fiber required to achieve accurate dispersion compensation must satisfy the following equations:

$$D_{\mathrm{HOMF}}\left(\lambda_0\right) L_{\mathrm{HOMF}} + D_{\mathrm{Trim}}\left(\lambda_0\right) L_{\mathrm{Trim}} = D_{\mathrm{span}}\left(\lambda_0\right), \tag{26}$$

$$S_{\mathrm{HOMF}} L_{\mathrm{HOMF}} + S_{\mathrm{Trim}} L_{\mathrm{Trim}} = S_{\mathrm{span}}. \tag{27}$$

Note that the dispersion slope coefficients referred to in Eq. (27) are defined in the same manner as described in section 3.3.2, i.e., they do not represent the actual slope at λ_0, but rather the slope of the linear fit to the dispersion curves. Clearly, in order for Eqs. (26) and (27) to have physically meaningful solutions, i.e., for L_{HOMF} and L_{Trim} to both be positive, the dispersion characteristics of the trim fiber and HOMF must satisfy certain conditions. This just means that only certain types of trim fiber may be used in conjunction with given HOMF.

A good example for the use of trim fiber concerns HOM-DCMs designed to compensate eLEAF® transmission fiber, which has an RDS value of 0.020 nm^{-1}. If we design the RDS of the HOMF to be less than 0.020 nm^{-1}, say 0.018 $\mathrm{nm}^{-1}$with a manufacturing tolerance of ± 0.002 nm^{-1}, then it is easy to show that regular SMF fiber may be used as a trim fiber. The closer the RDS of the HOMF is to 0.020 nm^{-1}, the less trim fiber is required to achieve accurate dispersion compensation. However, even if the RDS of the HOMF is at the other end of the manufacturing tolerance range, i.e., 0.061 nm^{-1}, it is still possible to achieve accurate compensation by using the correct amount of trim fiber according to Eqs. (25) and (26).

Besides allowing relaxed manufacturing tolerances for the HOMF, trim fiber also allows additional freedom in the actual *design* of the HOMF. The main motivation for

this is that even if we are able to manufacture HOMF with RDS close to that required, there is still the issue of TOD. Considering the example of a HOM-DCM for eLEAF® transmission fiber: we saw in section 3.4.1.1 that by reducing the RDS of the HOMF, we may significantly reduce the TOD as well. Thus, it may be desirable to purposely design the HOMF with lower RDS, relying on the SMF trim fiber to accurately provide the required dispersion compensation. This entails now a new trade-off, this time between TOD and the insertion loss of the HOM-DCM. The higher the RDS of the HOMF, the higher the TOD, but the less trim fiber needed, meaning less insertion loss. Conversely, the lower the RDS of the HOMF, the lower the TOD, but the more trim fiber is needed, increasing the insertion loss. To illustrate this trade-off, Table 5 shows three different design options for a C-band HOM-DCM for 80 km of eLEAF® transmission fiber, based on the three HOMF designs corresponding to Fig. 23. To calculate the insertion loss, we have assumed that each MOX contributes 1.25 dB, the attenuation coefficient of the HOMF is 0.5 dB/km, and the attenuation coefficient of the SMF fiber is 0.22 dB/km, all at 1550 nm. The module maximum residual dispersion is given by Eq. (23), and is the maximum residual dispersion over the C-Band of the HOM-DCM + transmission fiber.

Of the three options, option C is not particularly realistic from a packaging point of view, due to the large amount of trim fiber required. This just illustrates that while trim fiber allows us some freedom in choosing the RDS of the HOMF, it is still highly desirable to be as close to the target transmission fiber RDS as possible. The choice between options A and B (or similar ones), depends on the type of application being considered. For example, in links below 1000 km the accumulated residual dispersion for option A is less than 200 ps/nm, which is easily tolerated. Thus, the reduced insertion loss of the HOM-DCM for option A may be used to simplify the link design and reduce costs. Conversely, for links above 2000 km the accumulated residual of option A may be prohibitive, thus making option B more favorable.

Table 5. Different design options for a HOM-DCM for 80 km of eLEAF® transmission fiber, based on the three HOMF designs corresponding to Fig. 23.

Parameter	Option A	Option B	Option C
HOMF Dispersion (ps/nm/km)	−375	−405	−430
HOMF RDS (nm^{-1})	0.020	0.017	0.011
HOMF TOD (%)	4.3	2.1	0.4
HOMF Length (km)	0.9	1.1	1.7
SMF trim fiber length (km)	0	5.6	24.1
Maximum Residual Dispersion (ps/nm)	15	9	3
Module Insertion loss (dB)	2.9	4.3	8.7

3.6. Summary

In this section we have discussed the requirements for HOMF to be used in HOM-DCMs, and how to design refractive index profiles to meet these requirements. Using these design methods it is possible to achieve the high negative dispersion and dispersion slope necessary to compensate for most transmission fibers, without paying

the price of a small effective area. Furthermore, it is possible to ensure that the LP_{02} mode is well guided, with attenuation of the same order as regular DCF, about 0.5 dB/km, while at the same time keeping mode coupling and the number of unwanted modes, and hence MPI (see section 4 below), at acceptable levels. Finally, we have shown how the addition of a trim fiber to the HOM-DCM allows us to fine-tune the dispersion characteristics, as well as providing additional freedom in the design of the HOMF (which can be used to reduce the TOD).

4. Multi-Path Interference (MPI)

While HOM-DCMs have much to offer in terms of dispersion characteristics, low insertion loss, and low non-linear effects, multi-path interference (MPI) remains a major concern that must be addressed. In this section we characterize MPI in HOM-DCMs, and discuss the system level impact of the effect.

4.1. Introduction

MPI refers to the interference of an optical signal with a replica of itself (which we will call a "satellite signal") that has traversed a different path in the system. The classical example of MPI is multiple back reflections that create delayed replicas of the signal [29]. Such back reflections may be due to discontinuities in the systems (e.g., connectors and splices), or continuous Rayleigh backscattering, which is particularly relevant in system employing Raman amplification [30]. In HOM-DCMs, MPI results directly from the existence of additional modes within the HOMF besides the signal LP_{02} mode. A satellite is created when a portion of the signal couples to one of the additional modes, and then couples back to the main signal at a later stage. Such coupling can either occur within the MOXes, or along the HOMF itself due to mode coupling, as shown schematically in Fig. 30.

In general one can differentiate between two types of satellites, to be discussed in more detail in section 4.4: A *discrete* satellite is created when the coupling to the additional mode occurs at the input MOX, and the coupling back to the signal occurs at the output MOX. We use the term discrete since only one such satellite can exist for each mode within the HOMF, and both coupling events occur at distinct discrete points within the HOM-DCM. Conversely, mode coupling in the HOMF give rise to a *continuum* of small satellites, since coupling can occur at any point along the fiber (similar to Rayleigh scattering). In section 4.4 we show that due to the high efficiency of current MOX technology, discrete satellites make a relatively minor contribution to the total MPI. This means that the significant part of MPI in HOM-DCMs consists of a continuum of small satellites, which as we shall see below has important practical implications.

4.2. Definition of MPI

Consider a CW field input to a HOM-DCM exhibiting MPI. At the output of the system the optical field may be written as

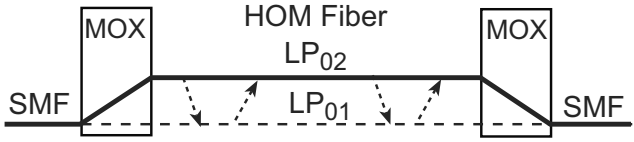

Fig. 30. Illustration of coupling between the main signal and an additional mode (e.g., LP_{01}). This coupling can occur within the MOXes, or along the HOMF.

$$\mathbf{E}(t) \propto \sqrt{P_0}\Bigg[\mathbf{p}_s \exp\left[j(\omega t + \varphi(t))\right] + \sum_i \mathbf{p}_i \sqrt{\varepsilon_i} \exp\left[j(\omega t + \varphi(t - \Delta\tau_i) + \Delta\psi_i(t))\right]\Bigg], \tag{28}$$

where P_0 is the average optical power, ω is optical frequency, $\mathbf{p}_s$ is the polarization of the main signal, $\varphi(t)$ represents laser phase noise, and $\mathbf{p}_i$, ε_i, $\Delta\tau_i$, $\Delta\psi_i(t)$ are respectively, the polarization, relative power, accumulated group delay difference and accumulated phase difference of satellite i. The summation is over all satellites created in the module, and in the case of a continuous source of MPI, should be replaced with an appropriate integral.

The optical power (averaged over a few optical cycles) detected at the output is then given by

$$P(t) = P_0\left[1 + 2\sum_i \sqrt{\varepsilon_i} \cos\left[\Delta\theta_i\,(t)\right] \cos\left[\varphi(t) - \varphi(t - \Delta\tau_i) - \Delta\psi_i\,(t)\right]\right], \tag{29}$$

where $\Delta\theta_i(t)$ is the relative angle between $\mathbf{p}_s$ and $\mathbf{p}_i$, and we have kept only the interference terms between the signal and the satellites, ignoring second order interactions. While $\Delta\theta_i(t)$ and $\Delta\psi_i(t)$ have relatively slow environmentally-governed time scales, the dynamics of $\varphi(t) - \varphi(t - \Delta\tau_i)$ are determined by the laser linewidth (a few MHz). The interference terms cause the power to fluctuate over time, with a standard deviation (over an infinitely long time) given by [31]

$$\sigma^2 = P_0^2 \sum_i \varepsilon_i, \tag{30}$$

where we have assumed no temporal correlation between the various satellites. Since the system impact of MPI is directly related to the standard deviation of power fluctuations, a convenient and useful definition of MPI is just sum of the satellite relative powers,

$$\mathrm{MPI} \equiv \sum_i \varepsilon_i. \tag{31}$$

The probability distribution function (PDF) of the power fluctuations approaches a Gaussian form as the number of satellites increases [31]. This has important implications for the system impact of MPI, and as we shall see further on, is the relevant case for MPI in HOM-DCMs.

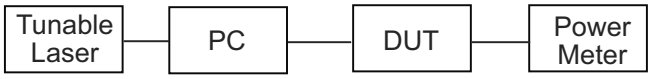

Fig. 31. MPI measurement setup. PC = Polarization controller, DUT = Device Under Test.

4.3. Measurement of MPI

In order to fully characterize the MPI of a device or system, it is necessary to have a standardized and reproducible measurement method. Referring to Eqs. (29)–(31), it is clear that by generating a full sample of phases $\{\Delta\psi_i(t)\}$ and polarization fluctuations$\{\Delta\theta_i(t)\}$, and measuring the resulting standard deviation of the output power fluctuations, one can directly measure the MPI.

To implement this we use the wavelength scanning method, also described in [32]. The measurement setup simply consists of a high coherence tunable laser [typically an external cavity laser (ECL), with a linewidth of a few kHz and $\sim$1pm spectral resolution], a polarization controller, and a power meter, as shown in Fig. 31. The method involves measuring the power for a range of wavelengths and polarization states, and calculating the average P_{avg} and standard deviation σ of the resulting measurement sample. From Eqs. (30 and (31), the MPI is then given by

$$\text{MPI} = \frac{\sigma^2}{P_{\text{avg}}^2}. \tag{32}$$

To gain further insight into this method we note that due to the use of a highly coherent laser, the laser phase noise difference $\Delta\varphi\,(\Delta\tau) \equiv \varphi(t) - \varphi(t - \Delta\tau)$ is identically zero. Thus, for a given wavelength and polarization state, the power remains constant over a long time (typically longer than 1 s), and can be accurately measured by a power meter with a long integration time. When the wavelength is changed, the path phase differences $\Delta\psi_i$ appearing in Eq. (28) changes in the following manner:

$$\Delta\psi_i\,(\lambda + \delta\lambda) = \Delta\psi_i(\lambda) + \frac{d}{d\lambda}\left[\frac{2\pi}{\lambda}\Delta L_{\text{opt},i}\right]\delta\lambda = \Delta\psi_i(\lambda) + \frac{2\pi c\Delta\tau_i}{\lambda^2}\delta\lambda, \tag{33}$$

where c is the vacuum speed of light, and $\Delta L_{\text{opt},i}$ and $\Delta\tau_i$ are, respectively, the optical path difference and group delay difference between satellite i and the signal. As long as $\Delta\tau_i > 1$ ns, which is the relevant case for HOM-DCMs (see Table 6 below), the quantity $c\Delta\tau_i/\lambda^2$ is larger than 0.1 pm^{-1}. Thus, by changing the wavelength by more than 10 pm we induce a phase difference larger than 2π, and effectively randomize the phase. By scanning a few hundred wavelengths within a narrow 1nm widow we can therefore generate a large random sample of phases for the various satellites. Similarly, by scanning a number of polarization states, the polarization angles $\Delta\theta_i$ may also be sampled, thus creating a representative sample of power fluctuations.

The wavelength scanning method can efficiently be implemented using a swept wavelength system that allows one to rapidly scan the entire C-band with a 1-pm resolution, and a number of different input polarization states. Then, by separating

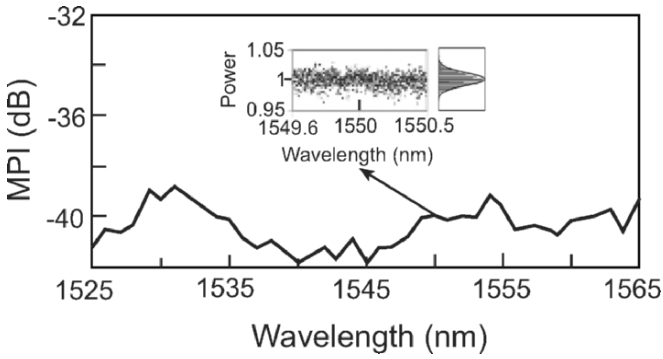

Fig. 32. MPI Measurement of a HOM-DCM for 100 km eLEAF compensation. Inset: 1300-point sample (and probability distribution) used for MPI measurement at 1550 nm.

the C-band into 1 nm windows, and calculating the MPI for each window, one can obtain the spectral dependence of the MPI with a 1-nm resolution. When using a swept wavelength system, care should be taken that the sweep rate is low enough so that the wavelength does not change significantly during the integration time of the detector. This can lead to an artificial reduction of the measured MPI, as discussed in [32].

Figure 32 shows results for a wavelength scanning MPI measurement of a HOM-DCM designed to compensate for 100 km of eLEAF transmission fiber. The inset of the figure shows the raw data (power as a function of wavelength, with four polarization states for each wavelength) used to calculate the MPI at 1550 nm. Also shown is the probability distribution function of the power fluctuations, which is well approximated by a Gaussian distribution, as noted above.

For a more detailed review of different aspects of MPI measurement in HOMF, see the work of Ramachandran and co-workers [32].

4.4. Sources of MPI in HOM-DCMs

In this section we discuss in more detail the various sources of MPI, and their relative contribution to the total MPI

4.4.1. Discrete Satellites

A discrete satellite is created when part of the signal energy is coupled to a HOMF mode other than the LP_{02} mode at the input MOX, propagates along the HOMF, and then is coupled back to the signal at the output MOX. By definition, only a single discrete satellite can exist for each guided mode within the HOMF (assuming all polarization states of the same mode are degenerate). As discussed in section 3.4.2.2, there are typically six guided modes within the HOMF: $LP_{01}, LP_{11}, LP_{21}, LP_{02}, LP_{12}$ and LP_{03}. The latter two modes are less guided than the LP_{02} mode, which means

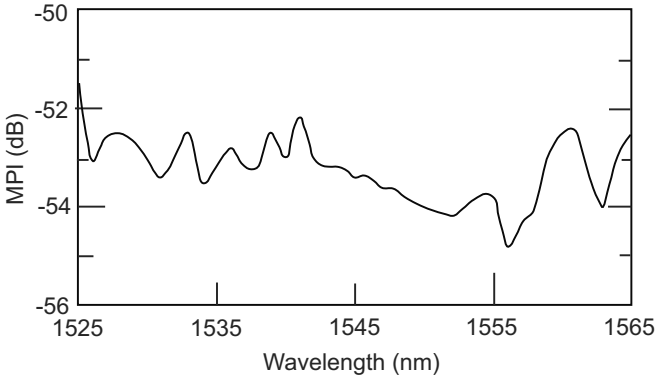

Fig. 33. MPI measurement of a "short" HOM-DCM, containing only 100 m of HOMF.

the HOMF can be designed to maximize the attenuation of these modes (if necessary with the aid of special attenuation loops, section 3.4.2.2) Therefore, in the context of discrete satellites we need only consider the three modes LP_{01}, LP_{11} and LP_{21},

If we designate the MOX extinction ratio with respect to mode i as η_i, then the power of the discrete satellite associated with this mode, relative to the power of the LP_{02} mode, is just η_i^2, where we have assumed that the input and output MOXes have the same extinction ratios (on average, this is a reasonable assumption). In Table 1 of section 2 we summarized results for the extinction ratios of the above three mode. This table shows that for a typical MOX the highest satellite power (usually that of LP_{01}) is about –45 dB, however, in the best case it can be as low as –52 dB.

The combined MPI from all three discrete satellites is then given by

$$\mathrm{MPI}_{\mathrm{discrete}} = \eta_{01}^2 + \eta_{11}^2 + \eta_{21}^2. \tag{34}$$

This value can be measured by constructing a HOM-DCM with a short ($\sim$100 m) length of HOM fiber. The short length of fiber means that mode coupling in the fiber is negligible, so the entire MPI of the HOM–DCM comes from discrete satellites. Fig. 33 shows an example of such a measurement over the C-Band, where it can be seen that the total MPI is below –51 dB over the entire band. This result is consistent with the best case values of the extinction ratios given in Table 1.

4.4.2. Continuous Satellites

Continuous satellites are created when coupling of the signal to an additional mode, and/or coupling back to the signal occurs due to mode coupling along the HOMF (See section 3.4.2.3 for a detailed discussion of mode coupling). Therefore, for each guided mode i(excluding the LP_{02} mode) in the HOMF, we identify three alternative processes for the creation of continuous satellites:

1. At the input MOX, power is coupled to the *i*th mode, and then part of this power is coupled back to the LP_{02} mode due to mode coupling along the HOMF.

2. As the signal propagates along the LP_{02} mode, power is coupled to the *i*th mode due to mode coupling, and then part of this is coupled back to the signal at the output MOX.
3. As the signal propagates along the LP_{02} mode, power is coupled to the *i*th mode due to mode coupling, and then is coupled back to the LP_{02} mode also due to mode coupling.

We refer to the first two processes as first order mode coupling, since each satellite created involves only a single mode-coupling event. Practically, these two processes are identical, and it is simple to show that the total satellite energy created by each is given by

$$\eta_i \int_0^L \kappa_i dx = \eta_i \kappa_i L, \tag{35}$$

where η_i is the MOX extinction ratio defined above, κ_i is the mode coupling coefficient between the LP_{02} mode and mode i as defined in section 3.4.2.3, and L is the HOMF length. We see that first order mode coupling can be reduced by improving the MOX extinction ratio η_i, and in theory can be eliminated entirely using ideal MOXes.

This is not the case for the third process, which we refer to as second order mode coupling. This process does not involve the MOXes at all, and occurs solely due to mode coupling. The total satellite power due to this process is given by

$$\int_0^L \kappa_i dx \int_x^L \kappa_i dy = \frac{1}{2} (\kappa_i L)^2, \tag{36}$$

i.e., it is quadratic in both the coupling coefficient and the fiber length. Since the process does not involve the MOXes, it cannot be reduced by improving MOX quality, and will exist even for ideal MOXes. Clearly one can consider higher order processes that involve more than two mode-coupling events. However, as long as $\kappa_i L \ll 1$, their contributions will be negligible compared to second order mode coupling.

As in section 4.4.1, we assume that the $LP_{03}$and LP_{12} modes have high attenuation coefficients, so that we need only consider the LP_{01}, LP_{11}, and LP_{21} modes. From Table 4 in section 3.4.2.3 we see that the mode-coupling coefficient between LP_{02} and LP_{01} is typically much lower than the other two mode coupling coefficients, which leaves only 1st and 2nd order mode coupling involving LP_{11} and LP_{21}. Fig. 34 shows the (calculated) MPI due to 1st and 2nd order mode coupling involving these two modes, as a function of HOMF length. As can be seen from the figure, LP_{21} 2nd order coupling dominates for most relevant fiber lengths, although for lengths below 1.5 km the combined effect of LP_{11} and LP_{21} 1st order coupling can be greater.

4.4.3. Combined Contribution

Combining the various contributions discussed in sections 4.4.1 and 4.4.2, the total MPI may be written as

$$\mathrm{MPI} = \sum_{i=01,11,21} \left(\eta_i^2 + 2\eta_i \kappa_i L + \frac{1}{2} (\kappa_i L)^2 \right), \tag{37}$$

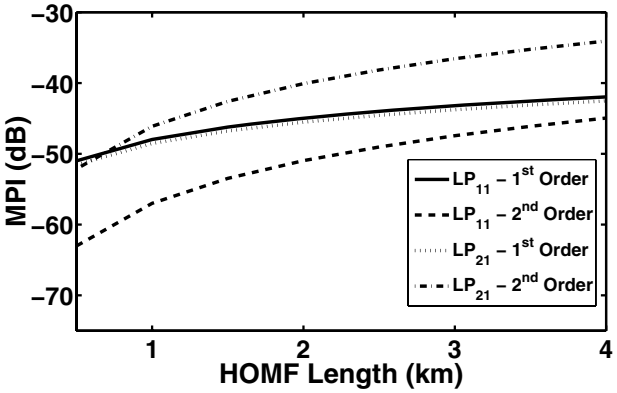

Fig. 34. MPI due to 1st and 2nd order mode coupling as a function of HOMF length. Typical MOX extinction ratios (Table 1) and mode coupling coefficients (Table 4) have been used in the calculation.

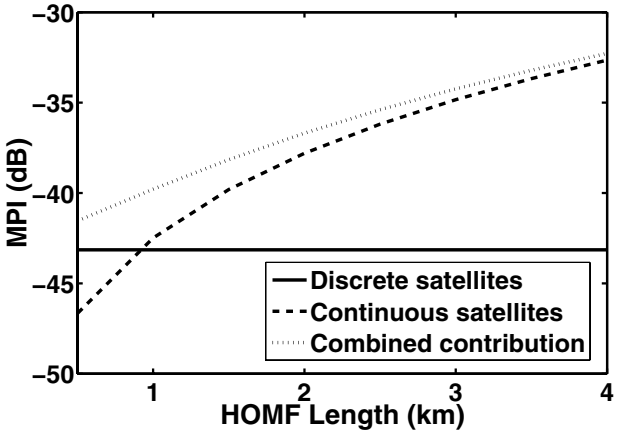

Fig. 35. MPI as a function of HOMF length from discrete and continuous satellites, and combined contribution.

where the η_i^2 terms represent discrete satellites, and all other terms represent continuous satellites. Figure 35 shows the relative contribution of discrete and continuous satellites to the total MPI for typical values of the various parameters. We see that for HOMF lengths of 1 km and above, the contribution from continuous satellites dominates the total MPI, while that of the discrete satellites becomes more and more negligible.

4.5. Coherent and Incoherent MPI, and System Impact

An important issue when considering the system impact of MPI is the time-scale of the power fluctuations. This is governed by the laser coherence time, τ_{coh}, which determines whether the MPI is coherent or incoherent [32–33]. If for a given satellite i, its relative delay with respect to that of the LP_{02} mode, $\Delta\tau_i$ (see Eq. (28) satisfies $\Delta\tau_i \ll \tau_{\mathrm{coh}}$, then the interference term due to that satellite is *coherent*, and will fluctuate with a time scale typical of the environmental changes in the system (usually a few seconds). On the other hand, if $\tau_{\mathrm{coh}} \ll \Delta\tau_i$, the interference term is *incoherent*, and will fluctuate with a timescale of the laser phase noise, i.e., τ_{coh}.

Since the laser sources used in long haul communication system typically have a linewidth, $\Delta\nu$, of a few MHz, τ_{coh} is usually in the range of 30–100 ns. Table 6 lists typical group delay values (per km HOMF) for the profile family discussed in section 3.4.1 (these values can be measured using a reflectometer setup as described in section 3.4.2.3). As the table shows us, $\Delta\tau_i <\sim \tau_{\mathrm{coh}}$, which means that MPI in HOM-DCMs can include both coherent and incoherent contributions, with the relative importance of each depending on the laser linewidth as well as the wavelength.

Table 6. Relative group delay per km between the LP_{02} mode and three other modes for the fiber profile family discussed in section 3.4.1. The range of group delay values corresponds to different wavelengths within the C-Band.

Mode	$\Delta\tau$ (ns/km)
LP_{01}	0–10
LP_{11}	5–20
LP_{21}	15–30

The system impact of coherent and incoherent MPI has been extensively studied both theoretically and experimentally [29–31,34–36]. In particular Ramachandran and co-workers [34], have studied the system impact of coherent distributed MPI, which is characteristic of HOM-DCMs.

When applying these results, the following should be remembered:

– The MPI as measured by the method described in section 4.3 is the total of coherent and incoherent MPI, and can thus be viewed as an upper limit for either contribution. For a discussion of separate measurement of coherent MPI in HOM-DCMs, see [32].

– The number of satellites contributing to MPI is large (see section 4.4), meaning that the distribution of power fluctuations due to MPI can be considered as Gaussian (see also Fig 32). This is particularly true when a number of HOM-DCMs are cascaded along a link. The Gaussian power distribution simplifies the theoretical analysis of MPI system impact, as well as the statistical treatment of coherent MPI power fluctuations [37].

4.6. Summary

MPI in HOM-DCMs is a relatively complex phenomenon, with multiple discrete and continuous sources and different timescales. In the preceding section we have discussed

various aspects of the phenomenon, and characterized the nature of MPI in HOM-DCMs.

The MPI values of manufacturing grade HOM-DCMs are typically in the region of –36 to –40 dB. Various system tests to be described in section 5 have shown that these values are sufficiently low to allow virtually unimpaired ultra-long-haul transmission, in one case up to 6000k @ 10 Gb/s.

5. Applications of HOM-DCMs

In this section we consider the application of HOM-DCMs in modern optical networks. Specifically, we will show that despite the issue of MPI, HOM-DCMs can provide an excellent solution for dispersion management in many important cases.

5.1. Accurate Broadband Compensation

The widespread deployment in recent years of NZDSF has emphasized the need for a suitable broadband dispersion management solution that accounts for the large negative dispersion slope of these transmission fibers. In section 3.4 we showed how HOMF may be designed with the appropriate RDS for eLEAF® compensation, while maintaining a high effective area to minimize non-linear effects. Furthermore, in section 3.5, we discussed the option of adding a trim fiber to the HOM-DCM to fine-tune the dispersion and dispersion slope for accurate broadband compensation. While the discussion in section 3 focused on the design of HOMF for C-Band eLEAF® compensation, the same principles apply to the design of HOMF for other types of fiber and other transmission bands.

5.1.1. C-Band eLEAF® Compensation

Figure 36 shows the dispersion, MPI and insertion loss characteristics of a typical manufacturing grade HOM-DCM for compensation of 100 km eLEAF® transmission fiber. The maximum residual dispersion in the designed transmission band is 12 ps/nm, while the maximum MPI and insertion loss are –37.5 and 2.1 dB, respectively. Note that the insertion loss for this particular module is very low, due the fact that the insertion loss of the MOX'es is close to their ideal limit of about 0.8 dB/Mox (see section 2). Typically, the insertion loss for such a module would be in the range of 2.5–3.5 dB. Note also the very stable performance over a wide temperature range. The PMD of this particular module is 0.47 ps, which is more than sufficient for most applications.

The use of HOM-DCMs for C-Band eLEAF® compensation has been demonstrated in a number of 40G [38,39] and 10G [40] system experiments. In the latter, successful transmission was achieved over 2800 km, demonstrating that despite the issue of MPI, HOM-DCMs are an attractive solution even in ultra-long-haul (ULH) systems.

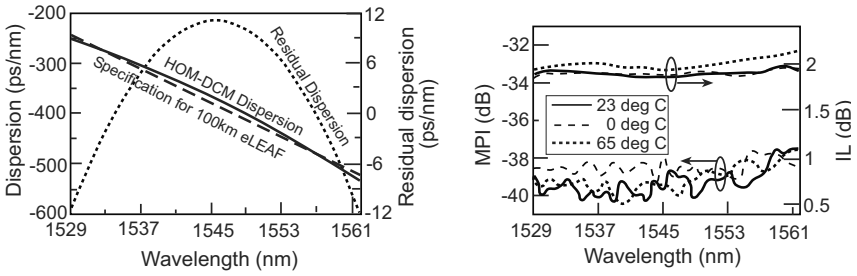

Fig. 36. Dispersion characteristics (left), and temperature dependent MPI and Insertion Loss (right) of a typical manufacturing grade HOM-DCM designed and built to compensate 100 km eLEAF® transmission fiber in the wavelength band 1529–1562 nm. The PMD of the HOM-DCM is 0.47 ps.

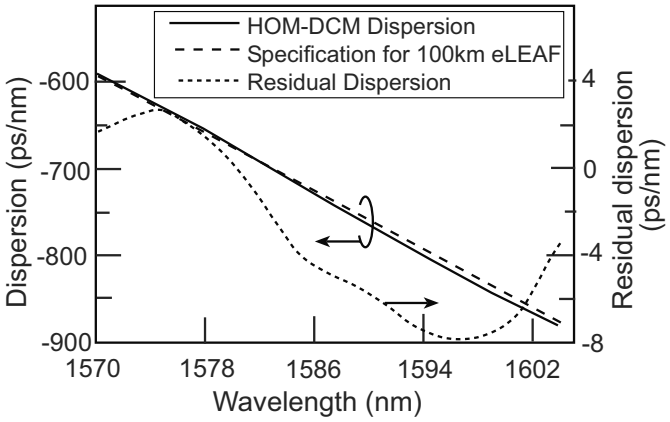

Fig. 37. Dispersion characteristics of a typical manufacturing grade HOM-DCM designed to compensate 100 km eLEAF® transmission fiber in the wavelength band 1570–1605 nm.

5.1.2. L-Band eLEAF® Compensation

The specified dispersion of eLEAF® transmission fiber at the center of the L-Band (1590 nm) is 7.6 ps/nm/km, while the dispersion slope is 0.085 ps/nm^2/km. On the one hand, this means that more HOMF is needed than in the C-Band in order to account for the larger dispersion. On the other hand, the RDS is lower than for the C-Band case, meaning that it's easier to achieve low TOD, and thus, low residual dispersion (see section 3.4.1.1).

This is illustrated in Fig. 37, which shows the dispersion curve of a manufacturing grade HOM-DCM designed to compensate for 100 km of eLEAF® transmission fiber in the wavelength band 1570–1605 nm. While the residual dispersion of the module is

8 ps/nm, it could easily be reduced to 5 ps/nm by fine-tuning the trim fiber within the module. Not only is the TOD much less than for a C-Band module ($\sim$1% compared to $\sim$3%), but the absolute residual dispersion is also less. The insertion loss of the module is 3.9 dB, which is more than a typical C-Band module due to the need for more HOMF. The maximum MPI of the module is –36 dB, which is about 2 dB worse than typically achieved values of more recent manufacturing series.

The above module together with others similar modules have been tested in a rigorous transmission test over 6000 km [41]. Despite the relatively high MPI of these modules, the results clearly show that MPI was not a limiting factor in the system. This illustrates once again that HOM-DCMs can be used in ultra-long-haul systems, and see also [42].

5.1.3. Other Transmission Fibers

In recent years, a new class of NZDSF fibers has been introduced, with the purpose to improve dispersion characteristics with respect to minimization of intra- and inter-channel non-linear effects, especially in high channel count WDM systems. The first such fiber to be introduced was Teralight® by Alcatel, and more recently True-wave reach® by OFS-Fitel [43], as well as others [44]. These fibers share common characteristics in that the dispersion at 1550 nm is typically 6–10 ps/nm/km, higher than previous generation NZDSF, but still significantly lower than SMF, while the RDS is typically in the range of 0.005-0.008 nm^{-1}, lower than previous generation NZDSF, but higher than SMF.

HOM-DCMs can also be manufactured to provide broadband compensation for these new NZDSFs, as well as for regular SMF fiber. A recent 2700-km, 40-Gb/s transmission test by Bissessur and co-workers [45] demonstrates the use of HOM-DCM for Teralight® compensation.

5.2. Reduced Nonlinear Penalty

As discussed previously, a key advantage of HOM-DCMs over conventional DCF is that the attractive dispersion properties of the HOMF can be achieved while maintaining a large modal effective area, typically above 50 μm^2 (compared to 20 μm^2 or less for DCF [46]). This, together with the small amount of HOMF in each device (below 3 km for most applications), significantly reduce the non-linear system penalty associated with HOM-DCMs.

A number of different tests [48–50] have directly demonstrated the increased power handling capabilities of HOM-DCMs over conventional DCF. With respect to cross phase modulation [47], it has been shown [48] that HOM-DCMs can tolerate almost 8 dB more power than commercially available DCF (with the same amount of dispersion). Furthermore, it was shown [49] that the HOM-DCM threshold to Brillouin scattering [47] is higher than 20 dBm, while that of commercially available DCF is as low 5 dBm. A system level test [50], also described in section 5.2.1 below, shows that HOM-DCMs can tolerate up to 13 dB more power for the same level of system penalty.

The increased power handling capability of HOM-DCMs is particularly important in high capacity systems, where non-linear effects tend to play a crucial role. This was

first demonstrated for 40 Gb/s systems in a 1700-km transmission experiment using standard 100 km spans, and HOM-DCMs based on Bragg grating mode transformers [51]. Additionally, Killey and co-workers [39] have demonstrated how the improved power handling capabilities of HOM-DCMs can be utilized to minimize the overall non-linear penalty of 40 Gb/s systems. More recently, Bissessur and co-workers [45] have also utilized the power handling capability of HOM-DCMs in a novel 2700-km, 40-Gb/s test employing only single stage EDFA amplification. High density (25 and 50 GHz channel spacing) DWDM systems can also benefit from the reduced non-linear penalty of HOM-DCMs, as demonstrated by Meyer and co-workers [40] in a 2800-km, 25-GHz channel spacing, 10-Gb/s DWDM transmission experiment.

While the power handling capability of HOM-DCMs is most useful in next-generation high capacity systems, it can also be advantageous in current generation 10 Gb/s systems. Specifically, by optimizing the amplifier design to account for the properties of the HOM-DCMs placed at mid-stage, it is possible to improve the overall noise figure of the amplifier. This is briefly discussed in section 5.2.2 below.

5.2.1. System Level Comparison Between DCF and HOM-DCM

In this section we describe a system level test [50] designed to directly compare the power handling capabilities of HOM-DCMs and conventional DCF. Since the test involves only single channel transmission, inter-channel effects such as four-wave mixing and cross phase modulation [47] are not included. Furthermore Brillouin scattering is purposefully suppressed using phase dithering of the transmitter, leaving self-phase modulation as the main effect that is tested in the experiment.

The main components of the experimental setup are shown in Fig. 38. A 2^{23}–1 NRZ 10 Gb/s PRBS is transmitted through 80 km of SMF transmission fiber at a constant launch power of –4 dBm to minimize non-linear effects within the fiber. On the other hand, using Amp1 and Att1, the launch power into the DCM may be varied between –5 to +25 dBm. By varying the attenuation of Att2 and Att3, it is possible to change the OSNR (measured by the OSA) at the input to the receiver, while maintaining a constant receiver input power. The experimental procedure is as follows: For each value of launch power into the DCM, the OSNR at the receiver is changed until a specified BER is achieved. Since higher launch power means a larger non-linear penalty, it is necessary to increase the OSNR in order to maintain a fixed BER. The amount by which the OSNR must be increased quantifies the penalty.

Both the HOM-DCM and the commercially available DCF used in the experiment were designed to compensate the dispersion of 80 km SMF transmission fiber. Figure 39 shows the OSNR required to maintain a BER of 10^{-9} for different levels of DCM input power. The OSNR is given relative to the required OSNR at –5 dBm input power (i.e., negligible non-linear effects within the DCM). The results clearly illustrate that the HOM-DCM can tolerate up to 13 dB more input power for the same level of OSNR penalty, compared to the conventional DCF. This conclusion is further supported by the recorded eye diagrams, shown in the insets of Fig. 39. For the conventional DCF, the bit pattern exhibits clearly noticeable distortions for an input power of 13 dBm, whereas no such distortions can be seen for an input power of 21 dBm launched into the HOM-DCF.

It should be noted that the exact power tolerance advantage of HOM-DCMs over conventional DCF depends on the application. The more fiber (both HOMF and con-

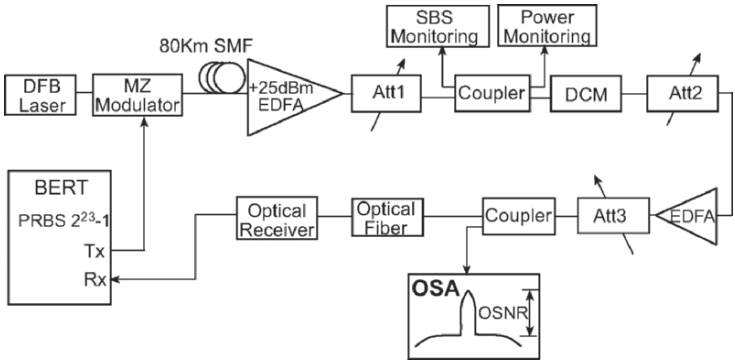

Fig. 38. Experimental setup used to compare the power handling capabilities of HOM-DCMs and conventional DCF.

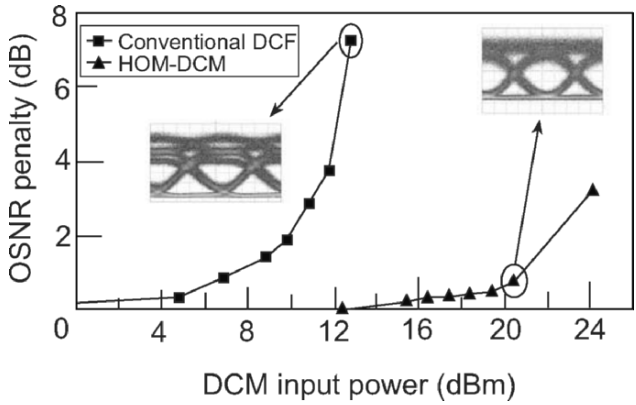

Fig. 39. The experimental results. Insets: transmitted eye diagrams corresponding to the marked input power.

ventional DCF) within the DCM, the larger the advantage of HOM-DCMs. Thus, systems using SMF transmission fiber will typically benefit more from HOM-DCMs (with respect to power tolerance) than systems employing NZDSF transmission fiber.

5.2.2. Using HOM-DCM to Optimize Amplifier Design

As illustrated in Fig. 40, in most conventional system designs DCMs are placed at the mid-stage of in-line amplifiers in each span. Current amplifier designs need to take into account the properties of conventional DCF, namely the low power tolerance and

relatively high loss. The low power tolerance of the DCF means that the output power of the first amplification stage, the pre-amplifier, is restricted, which means that less of the total gain of the amplifier is assigned to the pre-amplifier, and more to the second amplification stage, the booster. The relatively high loss of the DCF also needs to be accounted for, since most amplifiers are optimized to work with a given *fixed* mid-stage loss. Thus, even if one uses a HOM-DCM with lower loss, it is often necessary to insert an attenuator to increase the total loss to that for which the amplifier is optimized.

The noise figure of a two-stage amplifier is given by (using linear quantities, not dB) [52]

$$\mathrm{NF} = \mathrm{NF}_{\mathrm{pre}} + \frac{\mathrm{NF}_{\mathrm{boost}}}{G_{\mathrm{pre}} T_{\mathrm{mid}}}, \tag{38}$$

where $\mathrm{NF}_{pre/boost}$ is the noise figure of the pre/booster amplification stage, G_{pre} is the gain of the pre-amplifier, and T_{mid} is the transmittance at the mid-stage. Assuming $\mathrm{NF}_{\mathrm{pre}}$ and $\mathrm{NF}_{\mathrm{boost}}$ remain constant, then one immediately sees that by increasing G_{pre} and T_{mid} (i.e., decreasing the mid-stage loss), it is possible to achieve an improvement in the noise figure of the amplifier as a whole.

By using a HOM-DCM for dispersion compensation, one may achieve both these goals, as illustrated in Fig. 40. Since the HOM-DCM can tolerate significantly more input power, G_{pre} may be increased, and in practice ceases to be limited by the HOM-DCM (it may be limited by available pump power and other factors). Furthermore, the reduced loss of the HOM-DCM allows the amplifier to be optimized for a much lower mid-stage loss, resulting in an increase of T_{mid} and a consequential decrease in the amplifier noise figure.

Clearly, the above arguments present a highly simplified picture, while amplifier design is a complex issue, far beyond the scope of this section. However, a detailed analysis supports the basic picture, and it can be shown that a 0.5–1 dB improvement in noise figure is obtainable using designs optimized for HOM-DCMs. This was demonstrated by the 40 Gb/s transmission test performed by Ramachandran and co-workers [51], where the improved amplifier noise figure was key to the ability to transmit over 1700 km using 100 km spans.

5.3. Additional Applications

In this section we describe additional applications of HOM-DCMs, which serve as examples as to how the advantages of the technology can open up new and advanced possibilities for system design. An example of this is a novel method for achieving tunable dispersion compensation using fiber based mode conversion and HOM fiber [53]. Other applications are described in more detail below.

5.3.1. HOM-DCMs for Multiple Span Compensation

One of the unique advantages of HOM-DCMs is the high figure of merit (FOM) of the HOMF, typically in the range of 800–1000 ps/nm/dB. However, this advantage is somewhat offset by the overhead loss of the MOXes, typically 0.7-1.3 dB/MOX. If for example we consider a HOM-DCM designed to compensate for 100 km eLEAF® transmission fiber, then the module loss will be 2.5–3.5 dB, with only ∼0.7 dB due to the HOMF, and the rest due to the MOXes. On the other hand, a HOM-DCM designed

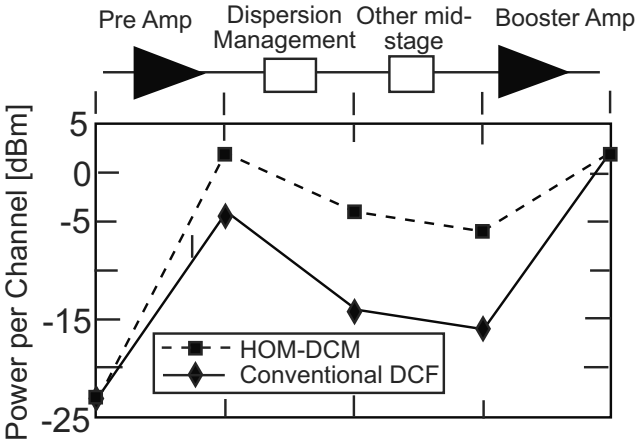

Fig. 40. Typical structure of a two-stage amplifier with mid-stage dispersion compensation. The solid line represents a typical EDFA design based on the relatively high loss and low power tolerance of conventional DCF, while the dashed line represent a possible improved design taking advantage of the HOM-DCM low loss and high power tolerance. The displayed power levels are for illustration purposes only.

to compensate for 200 km of eLEAF® will have 3.5–4.5 dB loss, since the MOX overhead remains changed. Thus, the longer the transmission span being compensated for, the more beneficial is the use of the high FOM HOMF, as illustrated in Fig. 41. This opens up an interesting possibility of using a single HOM-DCM to compensate for multiple spans [54], instead of using a single DCM in each span. This could potentially reduce system costs, since it would enable simpler, possibly single-stage amplifiers in the spans that do not include DCMs.

A potential limitation to this scheme is the MPI of the HOM-DCMs, as shown in Fig. 41. From this figure we see that a HOM-DCM for 400 km spans is expected to have 8 dB worse MPI than a corresponding HOM-DCM designed for 100 km spans. If on the other hand we were to concatenate four 100-km HOM-DCMs, then the MPI would be 6 dB worse than for a single 100-km HOM-DCM (see section 4.6.1). The extra 2 dB for the 400-km HOM-DCM results from the quadratic dependence of mode coupling on HOMF length, as discussed in section 4.4.2. For a 200-km HOM-DCM this is not an issue, since the MPI is expected to be similar to that of two 100-km HOM-DCMs (i.e., 3 dB worse).

Figure 42 shows insertion loss and MPI of a manufacturing grade HOM-DCM for compensation of 200 km eLEAF® spans. The maximum MPI of this module is –37.5 dB within the designed transmission band, which is better than the nominal –35 dB predicted in Fig. 41.

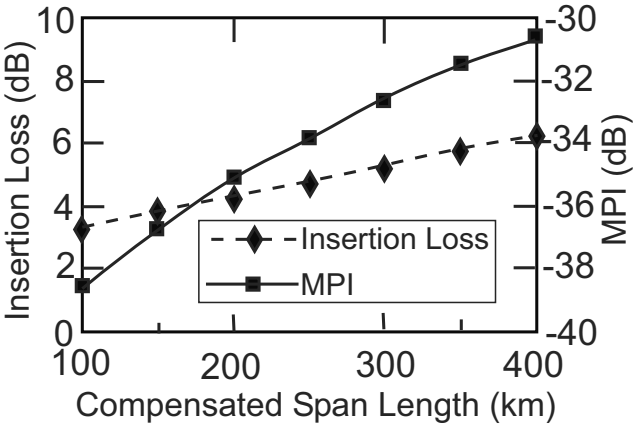

Fig. 41. Simulated MPI and Insertion loss of a HOM-DCM for compensation of eLEAF® fiber, as a function of compensated span length.

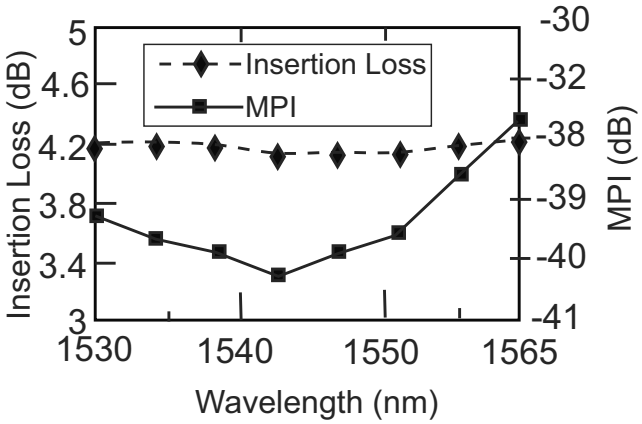

Fig. 42. Insertion loss and MPI of a manufacturing grade HOM-DCM for 200 km span eLEAF® compensation.

5.3.2. 160 GHz In-Channel Slope Compensation

Dispersion slope compensation is usually considered in the context of broadband WDM dispersion compensation. By achieving dispersion slope matching, one guarantees that if a single WDM channel is compensated for, the all other channels in the transmission band will also be compensated for. However, as bit rates grow, dispersion slope

compensation also becomes important in the context of a *single* channel. If one has a residual uncompensated slope of δS at the receiver, then a non-negligible system penalty will be encountered if

$$\delta S \Delta\lambda^2 \sim \tau_{\mathrm{bit}}, \tag{39}$$

where $\Delta\lambda$ is the modulation-dictated spectral width of the channel, and $\tau_{\mathrm{bit}} \sim \lambda^2/(c\Delta\lambda)$ is the time-slot of a single bit. Thus, in order to avoid significant penalty, the residual slope should satisfy

$$\delta S < \frac{\lambda^2}{c\Delta\lambda^3}. \tag{40}$$

The cubic dependence on $\Delta\lambda$ means that a 160-Gb/s channel is ∼4000 times more sensitive to residual slope than a 10-Gb/s channel, and ∼60 times more sensitive than a 40-Gb/s channel. Specifically, a 160-Gb/s C-Band channel can tolerate up to ∼2 ps/nm^2 residual slope. If one considers a 1000-km SMF link with total slope of 57 ps/nm^2, then this means that the slope compensation must be accurate to within better than 4%.

The ability to design HOMF with high dispersion slope opens up the possibility of producing specialized HOM-DCMs dedicated to dispersion slope compensation. The dispersion curve of such a module is shown Fig. 43, which shows that the dispersion at 1550 nm is close to zero, while the dispersion slope is 1.33 ps/nm^2. The HOM-DCM was constructed using ∼150m of HOMF with $D = -470$ ps/nm/km and $S = -10.2$ ps/nm^2/km, and ∼4.3 km of SMF fiber.

Fatome and co-workers [55] have demonstrated the usefulness of such a module in a 160-Gb/s transmission experiment over 900 km. In the absence of the HOM-DCM Slope compensator, it is estimated that the transmission distance would be reduced to ∼100 km.

5.3.3. Microwave Photonics True Time Delay Using HOM-DCM

Modern RF imaging systems are required to exhibit improved resolution, wider angular scans and bandwidths exceeding 10% of the RF carrier frequency. These requirements have led to the development of photonic True Time Delay (TTD) technology for beam steering/forming in phased array radars, as well as in other applications [56]. Soref [57] has suggested the use of chromatic dispersion in optical fibers to produce wavelength-dependent delay through $\Delta\tau = DL\Delta\lambda$, where $\Delta\tau$ is the relative delay between two wavelengths, separated by $\Delta\lambda$, D is the fiber dispersion coefficient, and L is the fiber length. A major problem with this method is the temperature drift of the RF phase, which is a direct consequence of the temperature dependence of the *optical* length of the fiber $d(n_{\mathrm{eff}}L)/dT$ (n_{eff} is the effective refractive index of the propagating mode). Since this thermal sensitivity is proportional to L, maximizing the fiber dispersion, D, will minimize the fiber length L and its associated $d(n_{\mathrm{eff}}L)/dT$.

Having a much higher dispersion coefficient, HOM-DCM have indeed been proven [58] to successfully implement photonic true time delay using much shorter fiber than equivalent DCF implementations, resulting in a three fold lower temperature dependence of the total delay. A possible issue of concern with HOM-DCMs is the effect of MPI on the transmitted RF signal. However, since to prevent walk-off [59],

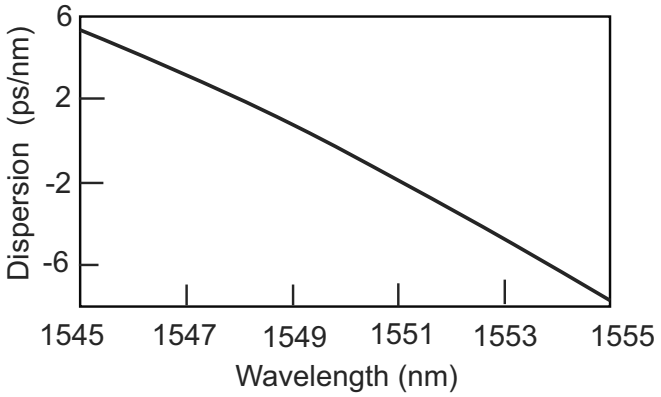

Fig. 43. Dispersion curve of a HOM-DCM dedicated to dispersion slope compensation. The module has close to zero dispersion @ 1550 nm, with a slope of 1.33 ps/nm^2.

the total dispersion in such applications is ∼100 ps/nm/km (for GHz applications), the length of HOMF is typically 200-300m, which means that mode coupling (see section 4. 4.2) is negligible. Thus, MPI values better than –40 dB can be achieved, resulting in negligible impact on the RF signal [58].

6. Summary

In this paper we have described in detail higher-order mode dispersion compensating modules (HOM-DCMs) based on spatial mode transformation technology. The combination of highly efficient spatial mode transformers (MOXes), together with carefully designed high-order mode fibers (HOMF), provides accurate broadband dispersion compensation, high power tolerance, and low insertion loss. While multi-path interference (MPI) remains a concern in HOM-DCMs, numerous system tests have demonstrated that currently achievable levels of MPI are sufficiently low to allow ultra-long-haul transmission.

The above properties make HOM-DCMs an attractive alternative in many applications in modern optical communications. Systems employing NZDSF transmission fiber especially benefit from HOM-DCMs, since it is relatively difficult to achieve broadband dispersion compensation using conventional DCF. The high power tolerance of HOM-DCMs provides important advantages in next generation high capacity systems, and can also be utilized in current generation systems to improve in-line amplifier performance. Other advanced applications, such as multi-span compensation, in-channel slope compensation for 160 Gb/s systems, and microwave Photonics, also benefit from the unique combination of HOM-DCM advantages.

Acknowledgement

The technological developments described in this paper, and their transformation into a manufacturable and field tested product, are the direct result of the dedication and talent of the entire LaserComm team.

References

1. C.D. Poole, J.M. Wiesenfeld, A.R. McCormick, and K.T. Nelson, "Broadband dispersion compensation by using high-order spatial mode in a two-mode fiber", Opt. Lett. **17**, 985–987 (1992).
2. C.D. Poole, J.M. Wiesenfeld, D.J. DiGiovanni, and A.M. Vengsarkar, "Optical fiber-based dispersion compensation using higher order modes near cutoff ", J. Lightwave Technol. **12**, 1745–1758 (1994).
3. M. Eguchi, M. Koshiba, and Y. Tsuji, "Dispersion compensation based on dual-mode optical fiber with inhomogeneous profile core", J. Lightwave Technol. **14**, 2387 (1996).
4. J.A. Buck, *Fundamentals of optical fibers* (John Wiley, 1995).
5. A.H. Gnauck and R.M. Jopson, "Dispersion compensation for optical fiber sytems", in *Optical fiber Telelcommunications*, IIIA (Academic Press, 1997).
6. G.P. Agrawal, *Fiber-optic communication systems* (Wiley-Interscience, 1997).
7. H.G. Park and B.Y. Kim, "Intermodal coupler using permanently photoinduced grating in two-mode optical fibre", Electron. Lett. **25**, 797–799 (1989).
8. S. Ramachandran, B. Mikkelsen, L.C. Cowsar, M.F. Yan, G. Raybon, L. Boivin, M. Fishteyn, W.A. Reed, P. Wisk, D. Brownlow, R.G. Huff, and L. Gruner-Nielsen, "All-fiber grating-based higher order mode dispersion compensator for broad-band compensation and 1000-km transmission at 40 Gb/s", IEEE Photon. Technol. Lett. **13**, 632–634 (2001).
9. S. Ramachandran, Z. Wang, and M. Yan, "Bandwidth control of long-period grating-based mode converters in few-mode fibers", Opt. Lett. **27**, 698 (2002).
10. S. Choi, W. Shin, and K. Oh, "Higher-order-mode dispersion compensation technique based on mode converter using hollow optical fiber", in Proc. Optical Fiber Communication Conference 2002, pp. 177–178.
11. R. Oron, Y. Danziger, N. Davidson, A.A. Friesem, and E. Hasman, "Transverse Mode Selection with Phase Elements", Conference on Lasers and Electro-Optics Europe (CLEO/Europe), p. 365, September 1998.
12. J.W. Goodman, *Introduction to Fourier Optics*, 2nd ed. (McGraw Hill, 1996).
13. M. Born and E. Wolf, *Principles of Optics*, 7th ed. (Cambridge University Press, 1999).
14. J. Bengtsson and M. Johansson, "Fan-out diffractive optical elements designed for increased fabrication tolerances to linear relief depth errors", Appl. Opt. **41**, 281–289 (2002).
15. R.G. Dorsch, A.W. Lohmann, and S. Sinzinger, "Fresnel ping-pong algorithm for 2-plane computer-generated hologram display", Appl. Opt. **33**, 869–875 (1994).
16. L. Gruner-Nielsen, S.N. Knudsen, B. Edvold, T. Veng, D. Magnussen, C.C. Larsen, and H. Damsgaard, "Dispersion Compensating Fibers", Opt. Fiber Technol. **6**, 164–180 (2000).
17. M.J. Li, "Recent progress in fiber dispersion compensators", Paper Th.M.1.1., ECOC 2001, Amsterdam.

18. U. Levy and M. Tur, "Projected Zero Dispersion—A Concept for Link Design", Tech. Digest of NFOEC 2002, p. 1527.
19. M. Wandel, T. Veng, Q. Le, and L. Grüner-Nielsen, "Dispersion compensating fibre with a high figure of merit", Proceedings of 2001 European Conference on Optical Communications, Paper PD.A.1.4.
20. M. Wandel, P. Kristensen, T. Veng, Y. Qian, Q. Le, and L. Grüner-Nielsen, "Dispersion compensating fibers for non-zero dispersion fibers", OFC 2002, Paper WU1.
21. Allan W. Snyder and John D. Love, *Optical Waveguide Theory* (Kluwer Academic, 1983).
22. D. Marcuse, "Bend loss of slab and fiber modes computed with diffraction theory", IEEE J. Quantum Electron. **29**, 2957–2961 (1993).
23. D. Marcuse, "Microdeformation losses of single-mode fibers", Appl. Opt. **23**, 1082 (1984).
24. A. Bjarklev, "Microdeformation losses of single-mode fibers with step-index profiles", J. Lightwave Technol. **4**, 341 (1986).
25. C.B. Probst, A. Bjarklev, and S.B. Andreasen, "Experimental verification of microbending theory using mode coupling to discrete cladding modes", J. Lightwave Technol. **7**, 55 (1989).
26. D Derickson, *Fiber Optic test and measurement* (Prentice-Hall, New Jersey, 1998).
27. J.A. Buck, *Fundamentals of optical fibers* (Wiley, New York, 1995).
28. L. Gruner-Nielsen, Yujun Qian, B. Palsdottir, P.B. Gaarde, S. Dyrbol, and T. Veng, "Module for simultaneous C+L-band dispersion compensation and Raman amplification", Optical Fiber Communication Conference (OFC), TuJ6, Anaheim, California (2002)
29. J.L. Gimlet and N.K. Chaung, "Effects of phase to intensity noise generated by multiple reflection on Gigabit per second DFB laser transmission systems", J. Lightwave Technol. **7**, 888 (1989).
30. S. Burtsev, W. Pelouch, and P. Gavrilovic, "Multi-path interference noise in multi-span transmission links using lumped Raman amplifiers", Optical Fiber Communication Conference and Exhibit (OFC), TuR4, Anaheim, California (2002).
31. P.J. Legg, M. Tur, and I. Andonovic, "Solution paths to limit interferometric noise induced performance degredation in ASK/Direct detection lightwave networks", J. Lightwave Technol. **14**, 1943 (1996).
32. S. Ramachandran, J.W. Nicholson, S. Ghalmi, and M. F. Yan, "Measurement of multipath interference in the coherent crosstalk regime", IEEE Photon. Technol. Lett. **15**, 1171–1173 (August 2003).
33. Y. Shen, K. Lu, and W. Gu, "Coherent and incoherent crosstalk in WDM optical networks", J. Lightwave Technol. **17**, 756 (1999).
34. S. Ramachandran, S. Ghalmi, J. Bromage, S. Chandrasekhar, and L.L. Buhl, "Evolution and Systems Impact of Coherent Distributed Multipath Interference", IEEE Photon. Technol. Lett. **17**, 238 (2005).
35. H. Takahashi, O. Kazuhiro, and T. Hiromu, "Impact of crosstalk in an arrayed waveguide multiplexer on NxN Optical Interconnection", J. Lightwave Technol. **14**, 1097 (1996).
36. C.X. Yu, W. Wang, and S.D.Brorson, "System degredation due to multipath coherent crosstalk in WDM network nodes", J. Lightwave Technol. **16**, 1380 (1998).
37. S.D. Dods and A.J. Lowery, "Temporal Statistics of Crosstalk-Induced Errors in WDM Optical Networks", NFOEC 2001, Session C5, pp. 876–879 (2001).
38. A.H. Gnauck, L.D. Garrett, Y. Danziger, U. Levy, and M. Tur, 'Dispersion and dispersion-slope compensation of NZDSF over the entire C band using higher-order-mode fibre', Electron. Lett. **35** (23), 1946–1947 (2000).

39. R.I. Killey, V. Mikhailov, S. Appathurai, and P. Bayvel, "Investigation of Nonlinear Distortion in 40-Gb/s Transmission With Higher Order Mode Fiber Dispersion Compensators", J. Lightwave Technol. **20**, 2282 (2002).

40. C. Meyer, S. Lobo S, D. Le Guen, F. Merlaud, L. Billès, and T. Georges, "High spectral efficiency wideband terrestrial ULH RZ transmission over LEAF® with realistic industrial margins", paper 1.1.2, ECOC 2002.

41. L.D. Garrett, M. Eiselt, J. Weisenfeld, R. Tkach, D. Menashe, U. Levy, Y. Danziger, and M. Tur, "ULH DWDM Transmission with HOM-Based Dispersion Compensation", The 29th European Conference on Optical Communication (ECOC), Rimini, Italy, September 2003.

42. L.D. Garrett, M.H. Eiselt, J.M. Weisenfeld, M.R. Young, and R. Tkach, "Bidirectional ULH transmission of 160-gb/s full-duplex capacity over 5000 km in a fully bidirectional recirculating loop", IEEE Photon. Technol. Lett. **16**, 1757–1759 (2004).

43. B. Zhu, L. Leng, L.E. Nelson, L. Gruner-Nielsen,Y. Qian, J. Bromage, S. Stulz, S. Kado, Y. Emori, S. Namiki, P. Gaarde, A. Judy, B. Palsdottir, and R.L. Lingle Jr., "3.2Tb/s (80 /spl times/ 42.7 Gb/s) transmission over 20 /spl times/ 100 km of non-zero dispersion fiber with simultaneous C + L-band dispersion compensation", paper FC8, Optical Fiber Communication Conference and Exhibit, (OFC), 2002.

44. K. Mukasa, H. Moridaira, T. Yagi, and K. Kokura, "New type of dispersion management transmission line with $\mathrm{MDF}^{\mathrm{SD}}$ for long-haul 40 GB/s transmission", paper ThGG2, Optical Fiber Communication Conference (OFC), Anaheim, California, 2002.

45. H. Bissessur, A. Hugbart, C. Bastide, S. Gauchard, and S. Ruggeri, "Transmission of 32 $\times$ 43 Gb/s over 27 $\times$ 100 km of TeraLight fiber with low-cost EDFA amplification", Paper ThE3, Optical Fiber Communication Conference (OFC), Los Angeles, California, 2004.

46. F. Forghieri, R.W. Tkach, and A.R. Chraplyvy, in "*Optical Fiber Telecommunications*, IIIA", edited by I.P. Kaminow and T.L. Koch, pp. 196–264 (Academic Press, 1997).

47. G.P. Agrawal, *Non-Linear Fiber Optics*, 2nd ed. (Academic Press, 1997).

48. M. Tur, E. Herman, and Y. Danziger, "Nonlinear properties of dispersion management modules employing high-order mode fibers", Optical Fiber Communication Conference and Exhibit (OFC), TuS5-1-TuS5-3, (2001.

49. M. Tur, E. Herman, A. Kozhekin, and Y. Danziger, "Stimulated Brillouin Scattering in High-Order Mode Fibers Employed in Dispersion Management Modules", IEEE Photon. Technol. Lett. **14**, 1282–1284 (2002).

50. O. Mor, B. Moav, A. Ben-Dor, M. Tur, S. Steinblatt, U. Levy, and D. Menashe, "Reduced nonlinearities in high order mode dispersion compensation modules", The 7th European/French-Israeli Symposium on Nonlinear and Quantum Optics (EURISNO/FRISNO), Les Houches, France, February 2003.

51. S. Ramachandran, G. Raybon, B. Mikkelsen, A. Yan, L. Cowsar, and R.J. Essiambre, "1700 km transmission at 40 Gbit/s with 100 km amplifier spacing enabled by higher-order-mode dispersion compensation", Electron. Lett. **37**, 1352–1354 (2001).

52. E. Desurvire, *Erbium-doped fiber amplifiers: principles and applications* (Wiley, 1994).

53. S. Ramachandran, S. Ghalmi, S. Chandrasekhar, I. Ryazansky, M. F. Yan, F. V. Dimarcello, W. A. Reed, and P. Wisk, "Tunable Dispersion Compensators Utilizing Higher Order Mode Fibers", IEEE Photon. Technol. Lett. **15**, 727 (2003).

54. S. Ghalmi, S. Ramachandran, E. Monberg, Z. Wang, M. Yan, F. Dimarcello, W. Reed, P. Wisk, and J. Fleming, "Multiple Span Dispersion Compensation Using All-Fiber Higher Order Mode Dispersion Compensators", The 28th European Conference on Optical Communication (ECOC), Paper P1.33, Copenhagen, Denmark, September, 2002.

55. J. Fatome, S. Pitois, P. Tchofo Dinda, and G. Millot, "Experimental demonstration of 160-GHz densely dispersion-managed soliton transmission in a single channel over 896 km of commercial fibers", Opt. Express **11**, 1553–1558 (2003).

56. H. Zmuda and E.N. Toughlian, *Photonic Aspects of Modern RADAR* (Artech House, 1994).

57. R. Soref, "Optical dispersion technique for time-delay beam steering", Appl. Opt. **31**, 7395–7397 (1992).

58. O. Raz, R. Rotman, Y. Danziger, and M. Tur, "Implementation of Photonic True Time Delay Using High-Order-Mode Dispersion Compensating Fibers", IEEE Photon. Technol. Lett. **16**, 1367–1369 (May 2004).

59. J.L. Corral, J. Marti, and J.M. Fuster, "General Expressions for IM/DD Dispersive Analog Optical Links With External Modulation or Optical Up-Conversion in a Mach-Zehnder Electrooptical Modulator", IEEE Trans. Microwave Theory Technol. **49**, 1958–1975 (2001).

DOI: 10.1007/s10297-005-0058-9
Originally published in J. Opt. Fiber. Commun. Rep. 2, 435–461 (2005)

Control of dispersion in photonic crystal fibers

P.J. Roberts[1,2], B.J. Mangan[1], H. Sabert[1], F. Couny[1,2], T.A. Birks[2], J.C. Knight[2] and P.St.J. Russell[2]

[1] Blaze Photonics, University of Bath Campus
Claverton Down, Bath BA2 7AY, UK
[2] University of Bath, Claverton Down, Bath BA2 7AY, UK

Abstract. Photonic crystal fibers (PCFs) exploit the large index difference between air and glass to achieve modal properties unattainable by conventional fiber techniques.

1. Introduction

The photonic crystal fibers (PCF) geometry comprises an array of parallel air holes, generally in a triangular lattice arrangement, running down the length of the fiber. The fibers fall into two distinct classes: those with a solid core which guide by a modified form of total internal reflection, and those with an air core which guide by means of a photonic band gap of the holey cladding. The guidance mechanism of the first type of PCF, an example of which is shown in Fig. 1(a), is analogous to the guidance in conventional MCVD fibers, with the index of the holey cladding region being a particular weighted average of the material indices in this region. The band gap PCFs guide by a less familiar mechanism, with the arrangement of air holes in the cladding causing a gap to open in the modal spectrum of the cladding over a range of effective index values. Figure 1(b) shows a typical fabricated hollow core fiber that operates over a 200 nm wavelength range centered at 1550 nm.

The two classes of PCF have very different mode dispersion, loss and nonlinearity properties. Both classes can nevertheless be used as the basis of dispersion compensating fiber (DCF). The solid core variety has been more extensively explored and developed in a DCF context, and most of the discussion of the current paper will concentrate on this geometry. The emergent technology of hollow core band gap PCF nevertheless provides the potential for achieving compact high quality DCF, or even for eliminating the need for dispersion compensation altogether if used as transmission fiber. A section will be devoted to a discussion of this type of fiber.

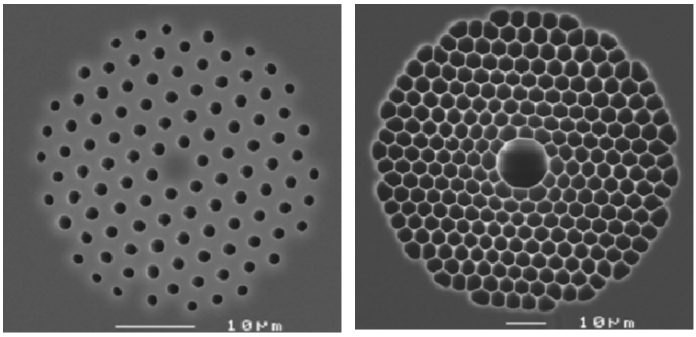

Fig. 1. A SEM of (a) a typical solid core PCF (BlazePhotonics SC-5.0-1040) and (b) a typical hollow core band gap PCF (BlazePhotonics HC-1550-02).

The dispersion of a guided mode in a solid core PCF can be considered as being due (a) to the material dispersion (since most of the light resides in glass), (b) the confining waveguide effect and (c) the dispersion in the effective index of the cladding region. Strong confinement to a small core region can be achieved with use of a cladding with a large air filling fraction. The resulting high waveguide dispersion can act to cancel even the large negative dispersion of silica glass that exists at visible wavelengths. [1,2] By tailoring the hole spacing and air filling fraction in the cladding, the wavelength at which the dispersion passes through zero can be tuned to a required wavelength. This has been exploited to enhance nonlinear phenomena, a particularly striking example of which is supercontinuum generation, whereby the short high intensity pulses are broadened into a spectrum which can extend over more than an octave. [3,4]

For larger cores, the guided mode dispersion is primarily a consequence of the material dispersion and the cladding index dispersion. For small holes in the archetypal PCF geometry, such as the fiber shown in Fig. 1(a), the effective index of the cladding approaches the index of silica as the wavelength is reduced in such a way that the fiber remains single mode guiding at all wavelengths. [5,6] For this to occur, the diameter of the holes must be less than about 0.42 of the hole spacing Λ.

Exploiting different holes sizes within the cladding region enables a spatial variation in the effective index of the cladding to be realized. [7–12] This opens up the possibility of achieving a highly modified dispersion in the same way as can be achieved by using a modulated index profile in the cladding of conventional MCVD fibers. [13–15] In particular, the "W"-profile and the dual concentric core profile used in conventional MCVD fiber DCFs have PCF analogues in which a radial variation in hole size is imposed. The mechanism of achieving large dispersion by exploiting an anti-crossing of the fundamental mode and a second ring-like mode can be applied to both fiber forms.

High bit rate communication places stringent constraints on the polarization mode dispersion (PMD) and multi-path interference (MPI) that can be tolerated from a dispersion compensating module. Conventional fiber development has taken great steps to minimize these effects. Particularly notable is the advances is achieving a regular and even doping concentration with a close to circular core and the spinning of the

fiber during its draw so as to further reduce the PMD. To compete with MCVD fibers in a communications context, PCF fabrication must of course address these same issues. The microstructure within a PCF imposes new problems for the fiber draw due to the natural tendency of the holes to collapse under surface tension. The holes are prevented from collapsing by applying gas pressure during the draw, but it possible for small fluctuations to grow due to an inherent instability in the process.

To be compatible with current transmission fiber, low loss interfaces must exist between PCF and MCVD fiber forms. The constraint that multi path interference (MPI) imposes on these interfaces in a high bit rate communication system is particularly stringent. Recent advances in adiabatic transforms between standard fiber and PCF, using for example a ferrule, suggests that this might become achievable even for connection to small core PCF forms.

Although PCFs have been around for less than ten years, it is worthwhile at this time to assess their potential for deployment as DCF and compare their properties with current DCF technology. The paper is organized as follows: Section 2 describes how dispersion in PCFs can be modeled and introduces the effective index model for solid core PCFs. Section 3 gives details of the design space available for achieving a negative dispersion characteristic slope-matched to commercial transmission fiber using concentric cores. Section 4 gives an overview of other solid core PCF geometries that could be used for dispersion compensation. Section 5 presents experimental results for a fabricated PCF that shows more (negative) than -1000ps/nm/km dispersion at 1550 nm and is dispersion slope-matched to SMF-28 with a low dispersion curvature. Section 6 discusses the constraints that PMD and MPI impose on the incorporation of a PCF-based compensator in a communication system. Section 7 discusses the prospects for using band gap fibers for dispersion compensation and also considers the implications for dispersion management of using hollow core fiber as transmission fiber. Section 8 draws some conclusions and considers future directions for PCF-based dispersion compensation.

2. Modeling Dispersion in PCFs

2.1. Analogies with Step Index Fibers—The Effective Index Model

Solid core PCFs guide by a modified form of total internal reflection and can often be modeled sufficiently accurately by use of an effective index model. Considering first the archetypal PCF geometry exemplified by the fiber in Fig. 1(a), a single effective index for the cladding region is required for such a model, as well as a size to ascribe to the silica core region. From fitting to the results of rigorous calculations, it has been found [16,17] that taking the effective index of the cladding to be its cut-off index n_{cut} and considering the core to be a circular region of diameter 1.24Λ provides a remarkably accurate description of the modal properties of these solid core PCFs. Here Λ is the distance between the centers of nearest neighbor holes.

The cladding cut-off index n_{cut} can be calculated by a number of different approaches. An accurate yet quick numerical method is to calculate the index of the fundamental space filling mode of the cladding using a band structure code such as a plane wave approach. The fundamental space filling mode is the mode of highest

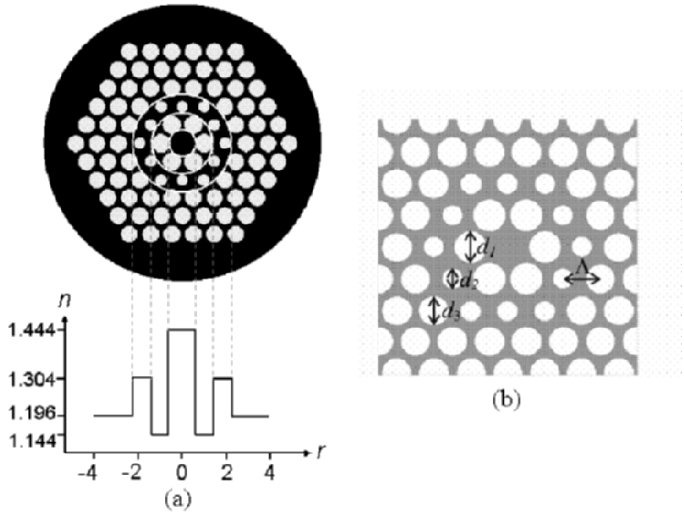

Fig. 2. (a) A solid core PCF design for dispersion compensation, together with its effective index representation that is of a dual concentric core form. The example shown has a pitch $\Lambda = 1.0\mu$m and hole diameters d_1=0.926Λ, $d_2 = 0.619\Lambda$, $d_3 = 0.804\Lambda$ as defined in Fig. 2(b). The effective index variation in the cladding of such a small core and high air filling fraction fiber is many times larger than could be achieved by MCVD technology.

effective index at the Γ-point of the crystal cladding Brillouin Zone and its index coincides with the cladding cut-off index $n_{\rm cut}$.

Solid core PCFs with a radially modulated hole size, such as the design shown in Fig. 2, can also be modeled approximately using an effective index model. The cladding is divided up into annular regions as shown schematically in Fig. 2, with the area of the jth ring from the center being given by $3\sqrt{3}j\Lambda^2$. The effective index of the jth ring containing holes of diameter d_j can be taken to be the index of the fundamental space filling mode for a triangular lattice arrangement of holes with pitch Λ and hole diameter d_j.

Despite the apparent crudity of the effective index model for the geometry of Fig. 2, it provides a reasonable estimate of the hole sizes and pitch required to achieve a particular dispersion characteristic with minimal computational effort. It also provides an important conceptual framework since it maps the problem onto a form familiar to designers of conventional MCVD fiber DCFs.

To obtain more precise design parameters for solid core fibers, or to adequately model band gap fibers, more accurate analysis is required, a few schemes for which are cited below.

2.2. *Rigorous Numerical Approaches*

A variety of numerical schemes are available for modeling the dispersion properties of PCFs, most of which have come across from electronic band structure calculations.

The most extensively used approach is based on a plane wave expansion of both the dielectric distribution and the electromagnetic fields within the fiber. The core and a sufficient region of the cladding are included within the supercell over which the Fourier expansions take place. Plane wave schemes operate by finding modes either at a fixed frequency ω, [18] or alternatively at a fixed longitudinal wavevector component β. [19] The fixed ω methods are more suitable since they allow material dispersion to be naturally included, but are slightly more complex to code.

Other numerical approaches that are appropriate for the PCF geometry include a localized basis expansion technique, [20] the finite difference time domain method, [21] finite element [22] and boundary element [23] schemes, and the multipole method. [24] The multipole approach is only appropriate to arrangements of circular holes, but is particularly efficient for mode calculations unless a very large number of holes are required to confine the light. This method is employed in the next section to explore the DCF design space.

3. Solid Core PCF Dispersion Compensators with Concentric Cores

3.1. An Example Small Core PCF Dispersion Compensator

For dispersion compensation of standard commercial fiber such as Corning SMF-28, a negative dispersion D and negative dispersion slope $dD/d\lambda$ are required. The relative dispersion slope RDS $= (dD/d\lambda)/D$ should match as closely as possible that of the fiber being compensated (RDS = 0.0036 nm^{-1} for SMF-28) if multiple wavelength compensation is needed. Since the dispersion curvature of standard transmission fiber is small over the communication bands, this quality should also be reflected in the dispersion compensating fiber if broadband and high bit-rate signal transfer is envisaged.

To achieve the required dispersion properties, a mode anti-crossing event between the fundamental LP_{01}-like mode of the PCF and a mode associated with a ring of relatively small holes (the second ring of the fiber in Fig. 2) can be exploited. Anti-crossing in the wavelength (λ) – effective mode index (n) plane can occur whenever the trajectories of two modes of a waveguide come close together. If interaction between the modes is not forbidden due to a symmetry incompatibility, the modes interact such that the two mode branches of the waveguide repel each other and an anti-crossing is formed. Close to the anti-crossing point, the curvature of the trajectories is large which implies a high dispersion value.

Figure 3(a) shows as an example of a mode anti-crossing for a small core and large air filling fraction DCF, with a pitch Λ of just 1.0 μm, circular holes of diameter d_1 = 0.926Λ in the first ring, d_2 = 0.619Λ in the second ring, the remaining holes having diameter d_3 = 0.804Λ. The fiber is the example shown schematically in Fig. 2 with its effective index representation. The high curvature in the mode indices around the anti-crossing signifies a high dispersion, with the upper branch giving the negative dispersion characteristic shown in Fig. 3(b). The RDS of the upper branch is 0.0038 nm^{-1}, which is close to matching the value for SMF-28.

Figure 4(a) shows the mode field intensity profile of the upper branch at a wavelength of 1.55 μm. Near the center of the core the profile is close to Gaussian, but the intensity levels out somewhat at the ring of smaller holes. Figure 4(b) shows the azimuthally averaged intensity profile as a function of the distance r from the center

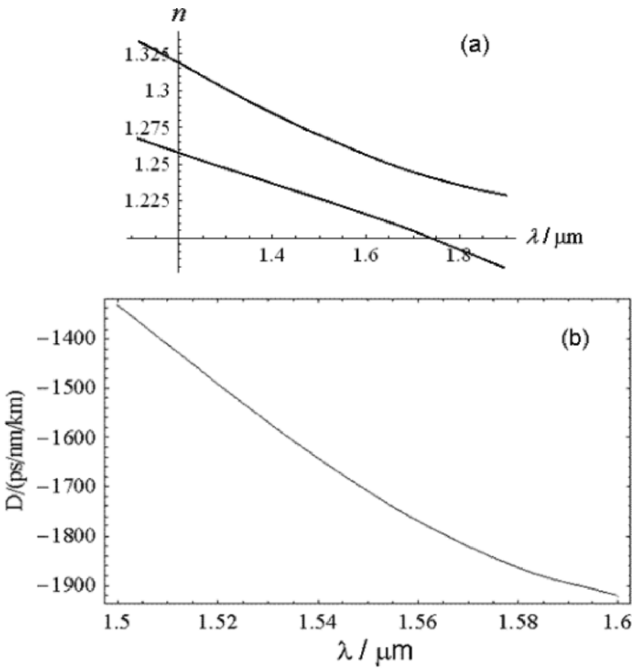

Fig. 3. The mode indices of the LP_{01}-like and ring-like modes are plotted as a function of wavelength λ in (a) for the small core PCF dispersion compensator shown schematically in Fig. 2. The mode interaction causes an avoided crossing with an associated high curvature. The resulting dispersion of the upper (LP_{01}-like over the plotted wavelength range) branch is shown in (b).

of the core, for wavelengths λ = 1.5, 1.55 and 1.6 μm. Within the C-band the field of the mode in the upper branch is not excessively distorted by hybridization with the competing mode associated with the annular ring of smaller holes; the field intensity in this ring is at least 18 dB below the intensity at the mode center and the shape overlap with a conventional LP_{01} fiber mode is above 90%.

Despite mode dispersion being directly linked to a wavelength dependence of the mode shape, Fig. 4(b) shows that the high dispersion of the example DCF appears not to be accompanied by a large wavelength dependence of the field distribution. This is because of the large index difference between silica and air: a small shift of the field from air to silica produces a sizeable change in the mode index.

3.2. The Mode Area vs. Dispersion Trade-Off

In achieving a negative dispersion with a particular relative dispersion slope (RDS), there remains some design freedom. In particular, the effective mode area of the device can be varied over a wide range whilst maintaining suitable dispersion characteristics. The most important driver for the mode area is the nearest neighbor hole spacing Λ,

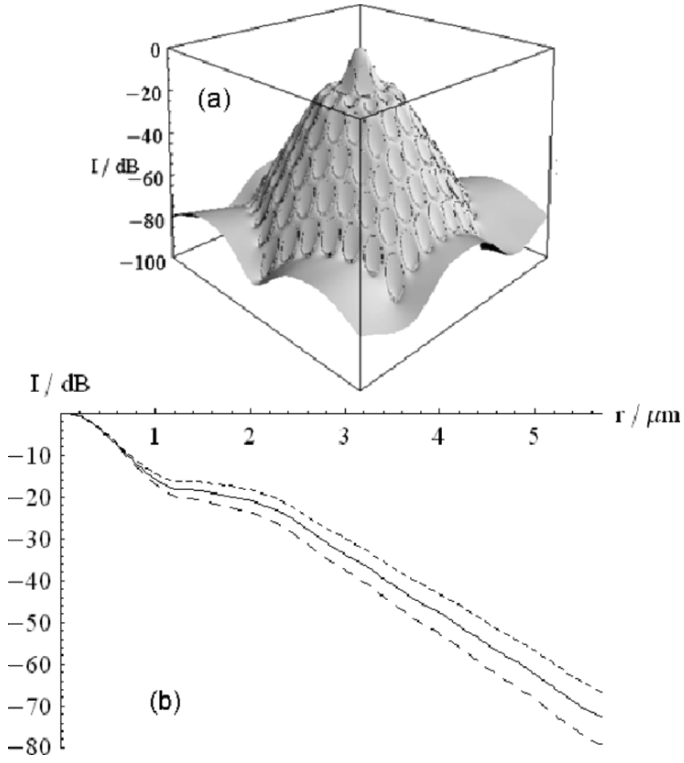

Fig. 4. The mode field intensity distribution at λ = 1.55 μm for the DCF depicted in Fig. 2 is shown in (a). The azimuthally averaged mode intensity distribution is shown in (b) as a function of the distance r from the center of the core at wavelengths λ = 1.5 μm (long dashed curve), λ = 1.55 μm (continuous curve) and λ = 1.6 μm (short dashed curve).

with the mode area expected to increase with Λ. Sets of hole sizes can be found at a chosen hole spacing which give the wanted dispersion characteristic. The discussion will henceforth be restricted to designs with the type of geometry depicted in figure 2, which is determined by three hole sizes d_1, d_2 and d_3, as well as the pitch Λ.

An automatic optimization scheme was adopted to find the highest negative dispersion obtainable for the chosen geometry at the central operation wavelength λ_c = 1.55 μm, as a function of an imposed Λ. Constraints are enforced to ensure the RDS at λ_c is equal to that of a target transmission fiber, such SMF-28, to within a tolerance and also to ensure the dispersion curvature is not too high. A standard simplex algorithm was employed for the optimization, which did not allow for rigid constraints to be imposed. Instead soft constraints were in-built into the cost function $Z\left(d_1, d_2, d_3\right)$ that was minimized. The chosen functional form of $Z\left(d_1, d_2, d_3\right)$ was

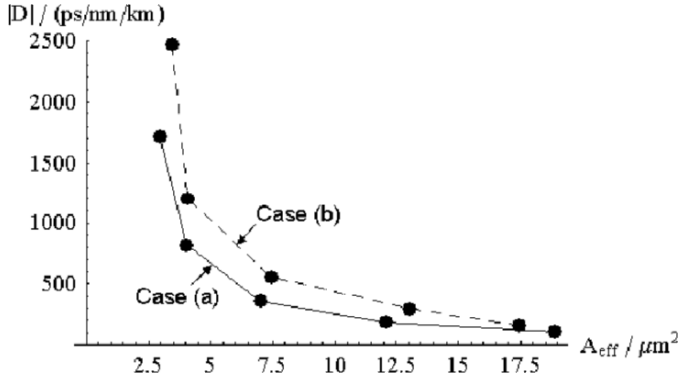

Fig. 5. The dispersion obtained for the DCF designs which are slope-matched to SMF-28, plotted as a function of the mode effective area for the two optimization schemes.

$$Z\left(d_1, d_2, d_3\right) = D + |D| \left\{ a \exp\left[\mu \left| \frac{1}{D}\frac{dD}{d\lambda} - \mathrm{RDS}_t \right| \right] + b \exp\left[\nu \left| \frac{1}{D}\frac{d^2D}{d\lambda^2} \right| \right] \right\}, \tag{1}$$

where the dispersion D, the RDS $(= D^{-1}dD/d\lambda)$ and the relative dispersion curvature $(D^{-1}d^2D/d\lambda^2)$ are evaluated at λ_c, and a, b, μ and v are positive-valued parameters which determine the "softness" of the constraints. RDS_t is the relative dispersion slope of the transmission fiber to be compensated.

Figure 5 shows the dispersion value obtained by this procedure plotted as a function of the effective mode area A_{eff}, for a target RDS of $\mathrm{RDS}_t = 0.0036\ \mathrm{nm}^{-1}$ appropriate to SMF-28, and two choices of the parameters a, b, μ and v. The case (a) is for $a = 0.02$, $b = 0.02$, $\mu = 4.0\ \mu$m and $\nu = 0.05\ \mu\mathrm{m}^2$ and case (b) is for $a = 0.02$, $b = 0.02$, $\mu = 4.0\ \mu$m and$\nu = 0.025\ \mu\mathrm{m}^2$. The two cases differ only in the stringency on the dispersion curvature: choice (a) maintains a straighter dispersion characteristic that can match better the dispersion shape of SMF-28 over a wide wavelength band. The straightness of the dispersion curve also affects the sensitivity to the geometrical parameters of the fiber, with a higher curvature indicating a higher sensitivity. Hence maintaining a straighter dispersion characteristic yields a design that is more tolerant to fabrication uncertainties. Both case (a) and case (b) yield designs with RDS values within 10% if the target value RDS_t.

From Fig. 5 it is apparent that the dispersion of the optimized designs decreases with increasing mode area. An important figure of merit (FOM) that assesses the nonlinearity of the DCF can be defined by

$$\eta_{\mathrm{NL}} = A_{\mathrm{eff}}\ |D|\,, \tag{2}$$

a larger value of η_{NL} indicating that higher power can be handled before nonlinear effects become prohibitive. Figure 6a shows the nonlinear figure of merit as a function of mode area A_{eff} for case (a) above, from which it is apparent that the dependence is weak, with η_{NL} decreasing by just a factor of two as the effective mode area is

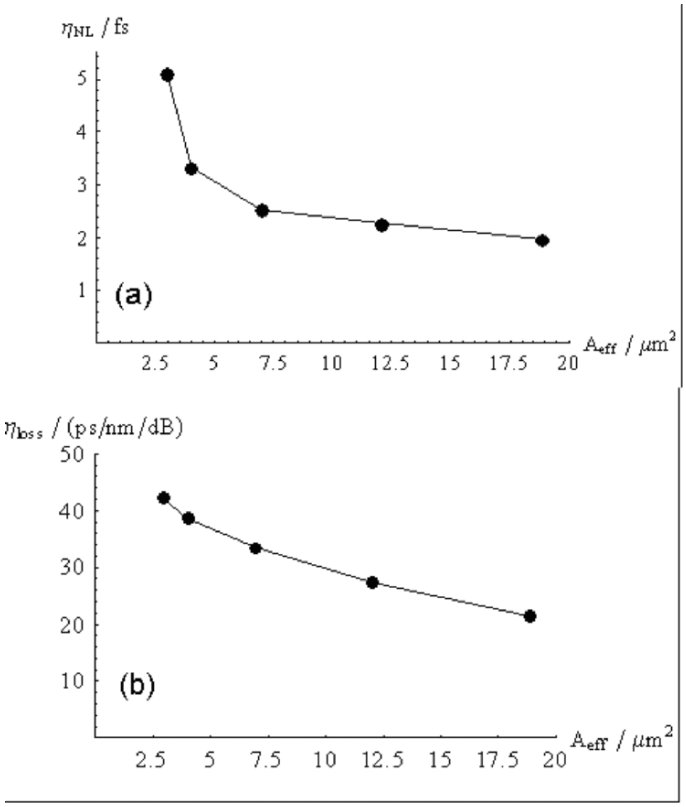

Fig. 6. The (a) nonlinear and (b) loss figure of merits for case (a) DCF designs. The nonlinear figure of merit is comparable to that of a commercial high quality dual concentric core DCF, but the loss figure of merit is inferior by a factor of around ten.

increased from 3 to 20 μm. Hence from a power tolerance standpoint, a small core fiber having an effective mode area of 3 μm^2 actually performs slightly better than a fiber with a mode area of 20μm^2. The smaller mode area is more than balanced by an increase in dispersion that reduces the length of DCF required to compensate a given length of transmission fiber. The nonlinear FOM for a high quality commercially available DCF is around 3.5 fs, which is very similar to the value for the PCF-based compensator.

A second important figure of merit relates to the loss of the compensating fibers. Loss in PCFs is due to bulk Rayleigh scattering and absorption of the glass material (just as in standard fiber), roughness at the hole interfaces and impurity scattering and absorption both at the hole interfaces and within the glass. The roughness scattering loss increases in strength as the normalised field intensity at the interfaces increases. The relative strength of interface scattering can be assessed using the parameter F [25,26] defined by

$$F = \left(\frac{\varepsilon_0}{\mu_0}\right)^{1/2} \frac{\oint_{\text{hole perimeters}} ds\, |\mathbf{E}|^2}{\int_{\text{x-section}} dS\ (\mathbf{E} \wedge \mathbf{H}^*) \cdot \hat{\mathbf{z}}}, \tag{3}$$

where $\mathbf{E}$ and $\mathbf{H}$ are the electric and magnetic fields being guided by the fiber. The fields in the numerator integrand are evaluated on the air side of the interfaces. Rayleigh scattering loss at the interfaces can be shown to be accurately governed by the factor F. Even for longer-scale forms of surface roughness, the factor F is found to qualitatively provide a relative measure of the scattering loss that can be expected. [26] In typical fabricated PCFs, the interface roughness scattering loss around a wavelength of 1.55 μm can be estimated using

$$\gamma_{\text{rough}} \Big/ \text{dB km}^{-1} \approx 20\, F \Big/ \mu\text{m}^{-1}. \tag{4}$$

Interface roughness scattering dominates over bulk Rayleigh scattering at this wavelength when F is greater than about 0.01 μm^{-1}.

A loss figure of merit for the DCF can be defined by

$$\eta_{\text{loss}} = D/\text{loss}. \tag{5}$$

This figure of merit increases as the loss of the DCF required for compensating a fixed length of transmission fiber decreases. Figure 6(b) shows η_{loss} for the PCF dispersion compensator, designed according to case (a) defined above, where the loss was assumed to be dominated by interface roughness scattering and to be determined by Eq. (4). The loss FOM for a high quality MCVD DCF is around 450 ps/nm/dB, [27] a factor of about ten higher than for the PCF compensator. It is clear that at current hole interface roughness levels, the incurred scattering loss provides a severe limitation to the loss FOM of solid core PCF-based DCFs of the current design.

The hole size to pitch ratios d_1/Λ, d_2/Λ and d_3/Λ which were found by the optimization procedure for case (a) are shown in Fig. 7 as a function of the imposed pitch Λ. The ratios all monotonically decrease with increasing Λ, the diameter d_3 of the holes which define the outer cladding region approaching 0.31Λ at Λ = 2.0μm. The decrease in these ratios explains why the effective area increases more rapidly than with the square of Λ. All the designs require several rings of the outer cladding material to sufficiently confine the light. The total number of rings of holes required to achieve lower than 1 dB/km leakage loss over the C-band increases from 9 for the Λ = 1.0μm design to 13 for the Λ = 2.0μm design.

The designs with smaller mode area do support modes other than the "fundamental" modes associated with the central core and the high index ring. These modes can, however, be rendered lossy by choosing the number of cladding rings to be just sufficient to guide the fundamental central core mode with adequately low leakage loss over the operational bandwidth. In this way the impact of the higher order modes on multi path interference (MPI) is minimized.

The separation in mode effective index between the two anti-crossing mode braches for the Λ = 1μm design is maintained at a value of at least 0.03, as can be inferred from Fig. 3. This separation does decrease as the mode size increases, but even for the design with mode area close to 20 μm^2, the mode interaction is strong enough for it to remain at a value above 0.0025 over the C-band. This in conjunction with the relatively small mode areas of the fibers implies that macro- and micro- bend induced coupling between the modes small for the devices unless extremely tight bends are attempted.

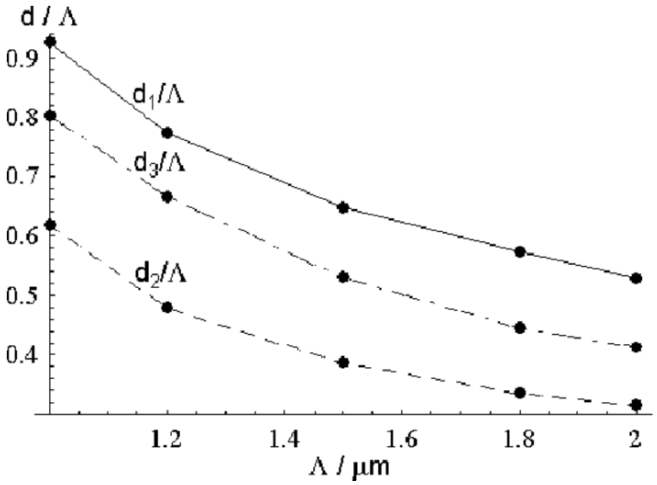

Fig. 7. The normalized hole diameters plotted as a function of the imposed pitch Λ for the SMF-28 DCFs designed according to case (a).

Over the explored mode area range, the amount of the ring-like mode that is admixed to the LP_{01}-like core mode within the C-band is broadly similar for all the designs found with same set of optimization parameters. Likewise the wavelength dependence of the field intensity is similar over the C-band for each design, although the larger pitch designs have less modal power residing within the air holes. These properties are exemplified in Fig. 4 for the 1-μm pitch design.

3.3. Sensitivity to Geometrical Perturbations

To be manufacturable, it is essential that the compensator designs do not show undue sensitivity to the fiber parameters. Current fabrication tolerances with regard to hole spacing and hole sizes lie in the region of 1% at feature sizes appropriate to the compensator designs. The impact this has on the dispersion characteristic will determine the yield that can be expected. The precise value of the dispersion figure attained for a fabricated DCF is not important, as long as it is large and negative, since the fiber can be cut to the length required to compensate the transmission fiber at the central operating wavelength. The RDS and curvature sensitivities then dictate the yield for achieving acceptable values for these parameters.

Figure 8 shows the change of dispersion and RDS produced by 1% changes in the pitch and hole sizes for three designs from case (a) in section 3.2. The geometric changes are amplified by a factor of order 10; this is not surprising, since the high sensitivity to wavelength implied by large dispersion is closely associated with high sensitivity to all other parameters.

The sensitivity is indeed found to increase for designs that possess higher dispersion and dispersion curvature. For example, sensitivities for case (b) of section 3.2 are

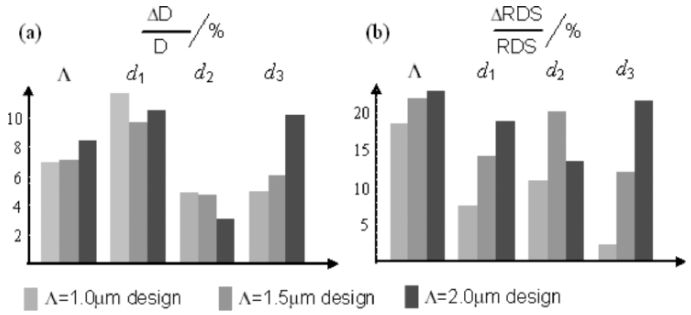

Fig. 8. Sensitivities of (a) the dispersion and (b) RDS of case (a) DCF designs to changes in the fiber parameters. The magnitude of the relative change in these quantities is shown for 1% changes in each of the parameters Λ, d_1, d_2 and d_3.

found to be about twice those for case (a), so that attempting to fabricate a design of higher dispersion figure of merit will adversely affect the yield.

3.4. Compensating Fibers with Large Relative Dispersion Slope

Achieving multi-wavelength dispersion compensation of high RDS transmission fibers, such as large-effective-area-fiber (LEAF) that has an RDS figure of about 0.02 nm^{-1} at a wavelength of 1.55 μm, is more difficult than for standard SMF-28. At a large negative dispersion, the very high dispersion slope needed for a DCF that compensates high RDS fibers is more difficult to maintain over a sizeable wavelength range such as the C-band and the sensitivity to fiber parameters is increased.

A design at $\Lambda = 1.5\mu$m which shows the correct dispersion properties for LEAF compensation is shown in Fig. 9. The structure has hole sizes $d_1 = 0.821\Lambda$, $d_2 = 0.452\Lambda$, $d_3 = 0.590\Lambda$ and was obtained using the case (a) minimization procedure of section 3.2. The dispersion value at a wavelength of 1550 nm is around -1420ps/nm/km, which is somewhat higher than the design in section 3.2 for the SMF-28 compensator at the same mode area ($A_{eff} = 4.5\ \mu m^2$). Although the curvature is low at 1550 nm, it rapidly increases beyond the C-band, and the dispersion slope actually becomes positive above a wavelength of about 1580 nm. The sensitivity of the dispersion characteristic to hole sizes and pitch is increased by around a factor of 3 compared to the SMF-28 compensator designs, which is a consequence of the LP_{01}-like mode and the companion ring-like mode coming closer together in effective index in order to achieve the required dispersion characteristic.

Figure 10(a) shows the field intensity distribution for the LEAF compensator at a wavelength of 1550 nm. A comparison with Fig. 4(a) shows that the amount of the outer ring-like mode that admixes with the central core mode is increased for the LEAF compensator, so that the mode is more distorted from a conventional LP_{01} shape than its SMF-28 compensating counterpart. Figure 10(b) shows the azimuthally averaged intensity distribution at wavelengths λ = 1500, 1550 and 1600 nm for the LEAF compensator design. The wavelength dependence of the mode shape is much increased compared to the SMF-28 compensator, c.f., Fig. 4(b).

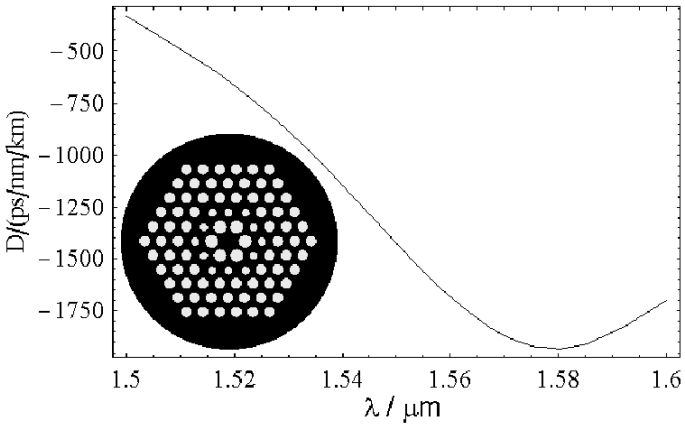

Fig. 9. The dispersion of a LEAF compensating DCF. The fiber, shown schematically in the insert, has pitch $\Lambda = 1.5$ μm and hole sizes $d_1 = 0.821\Lambda$, $d_2 = 0.452\Lambda$ and $d_3 = 0.590\Lambda$. Large negative dispersion is achieved throughout the C-band (1532–1568 nm), but sensitivity to fiber parameters is high. The dispersion curvature and RDS are compromised towards the upper C-band edge.

The two mode branches for the LEAF compensating fiber come closer together within the communication band than they do for the SMF-28 compensating fiber of the same mode area. The separation in index for the fiber of Fig. 9 is nevertheless always at least 0.002 over the C-band, corresponding to a beat-length of less than 1mm. This should be small enough to ensure micro- and macro- bend coupling between the modes is minimal.

4. Other Solid Core PCF Dispersion Compensator Designs

4.1. Small Core PCFs

The design strategy developed above exploits an anti-crossing between the central core mode and a subsidiary ring-like mode. Other designs do exist for achieving high negative dispersion values. The simplest is to use a very small core in a conventional PCF geometry. [1] Such fibers show a dispersion dependence on wavelength that rises to pass through zero, attains a maximum value, and then decreases to pass through zero again. For very small cores, the second zero-GVD crossing wavelength can be significantly smaller than the C-band range and a large negative dispersion with negative slope can be attained around 1550 nm. The problem with this design is its very high loss which is associated with roughness scattering at the hole interfaces, the difficulty of fabricating fibers with sub-micron hole sizes and spacing and in interfacing to standard fiber.

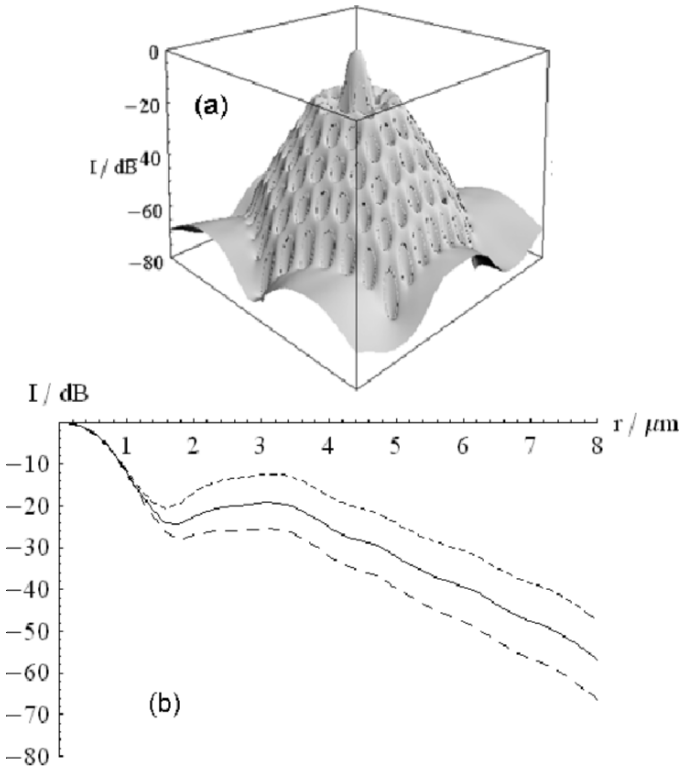

Fig. 10. The mode field intensity distribution at $\lambda = 1.55\ \mu$m for LEAF compensating fiber is shown in (a). The azimuthally averaged mode intensity distribution is shown in (b) as a function of the distance r from the center of the core at wavelengths $\lambda = 1.5\ \mu$m (long dashed curve), $\lambda = 1.55\ \mu$m (continuous curve) and $\lambda = 1.6\mu$m (short dashed curve). The hump at the position of the outer core and the wavelength dependence of the profile is much increased compared to the SMF-28 compensator.

4.2. Operation Near Cut-Off

A mode that is operated close to its cut-off wavelength necessarily shows high dispersion since the degree of confinement is a sensitive function of wavelength. A PCF design in which the holes surrounding the solid core are larger than the outer holes can show such a cut-off in the fundamental (LP_{01}-like) mode, but achieving the correct RDS is not straightforward. Higher order modes (HOMs), which naturally tend to show higher dispersion than the fundamental (LP_{01}-like) mode, can be used as a basis for dispersion compensation. This has been demonstrated with conventional MCVD fibers, [28-30] and the dispersion can be enhanced by operation close to cut-off. The dual concentric core configuration is also appropriate for achieving a large negative dispersion of a chosen HOM with a suitable dispersion slope. A challenge for these

HOM-based compensators is to achieve high efficiency mode transitions between the fundamental mode of transmission fiber and the HOM of the DCF, without incurring unacceptable levels of MPI.

4.3. Other Dual Concentric Core PCF Compensator Designs

A different form of dual concentric core PCF compensator has been proposed [10] which incorporates just two hole sizes. The geometry is the archetypal PCF geometry, comprising a triangular arrangement of air holes surrounding a solid silica core, but the holes around a single ring centered at the solid core are smaller than the others so as to define the outer core region. The authors suggest that incorporation of three airhole layers between the inner and outer cores is optimal for achieving high negative dispersion with acceptable tolerance to structural parameter variations. A dispersion figure of -2200 ps/nm/km was calculated for their structure, but no slope matching to transmission fiber was attempted.

Another dual-core PCF dispersion compensator has been considered in [11]. The geometry comprises the archetypal PCF geometry, but the core is divided into two by incorporation of a ring of 6 much smaller holes. Very large negative dispersions (as high as -18000 ps/nm/km) were calculated for the structure, but over a very narrow wavelength range and with extremely high sensitivity to structural parameter. Fabrication of fibers with very different hole sizes is difficult due to the need to balance surface tension forces.

4.4. Doped Core PCF Compensator

A hybrid design, which incorporates a doped core within a graphite crystal arrangement of air holes, has recently been proposed as a means of realizing the dual concentric core geometry. [12] This design has the advantage of requiring just one hole size to be incorporated within the fiber, and dispersions close to those achieved for the 3 hole size geometry in section 3.2 have been predicted at an RDS matched to SMF-28. The mode area at a given dispersion value is comparable to that achieved with the 3 hole size structure, since both geometries are describable by an effective index model with similar effective index profiles. A disadvantage of the doped core design is that high concentrations of Ge (or other index increasing dopant) are required, which can significantly increase the nonlinearity at a given mode effective area. The structure is nevertheless a good candidate for achieving a high loss figure of merit.

5. Fabricated Example of a Dispersion Compensating PCF

Silica photonic crystal fibers are generally fabricated using a stack and draw technique. A set of capillary tubes of equal outer diameter is stacked in a triangular lattice arrangement. A solid silica tube that will become the guiding core is incorporated at the center of the stack. The inner diameter of the tubes in the stack depends on the distance from the central core in a manner that parallels the hole size variation required in the final fiber. The stack, which typically has a cross sectional diameter of around 30 mm, is then drawn down in a furnace to a cane with a diameter of order 2 mm. The

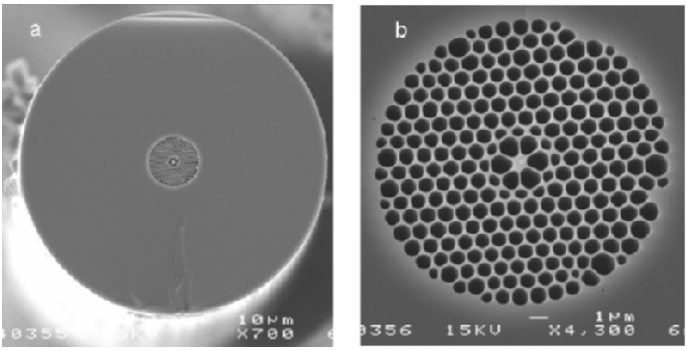

Fig. 11. SEMs taken at two magnifications of a fabricated DCF, which is slope matched to SMF-28. The outer diameter of the fiber is 105 μm and the core is less than a micron across. The structure is intentionally birefringent.

cane is inserted within a capillary jacket tube and the assembly is then drawn to fiber. Water and impurity reduction techniques are employed during the process just as in conventional MCVD fiber production.

As a demonstration of the high dispersion values that can be achieved for a slope-matched DCF using PCF technology, small core fibers have been fabricated based on the design strategy described in section 3.2. [31] Figure 11 shows SEMs of one such fiber with a core diameter of just 1 μm. The holes close to the core are deformed somewhat from being circular, and this does affect the dispersion characteristic of the fiber. The hole deformations can easily be taken into account, using for example a plane wave method, to design a fiber with a particular target RDS. Such studies show that the attainable dispersion at a target relative dispersion slope is not significantly compromised. The sensitivity to small perturbations are also found not to adversely affected by the inner-hole shape deformations.

The fiber shown in Fig. 11 was fabricated to be polarization maintaining: two of the six holes that surround the core are smaller than the other four. Several fibers showing similar dispersion and RDS characteristics were also fabricated without intentional birefringence being imposed. Despite the attempt to fabricate polarization independent fibers, small perturbation are found to persist down the length of a fabricated fiber which result in a differential group delay (DGD) of several ns/km in fibers with such a small core. Since significant birefringence is inevitable, it was decided to enhance the polarization maintaining properties by deliberately increasing the polarization mode splitting, but not to such an extent that the spatial distribution of the fields becomes strongly perturbed. The motivation for exploring PM compensating fibers will be discussed in more detail in section 6.

Figure 12 shows the measured dispersion of the two polarization states associated with the fundamental (LP_{01}-like) spatial mode. The dispersion of one of the polarized states is around -1210 ps/nm/km at a wavelength of 1550 nm and shows a near linear dispersion characteristic over the measured wavelength range with an RDS of 0.004 nm^{-1}, which is within 15% of the figure for SMF-28. The effective mode area of the fiber is calculated to be just 2.0 μm^2, so that the nonlinear FOM is 2.4 fs, a value 1.5

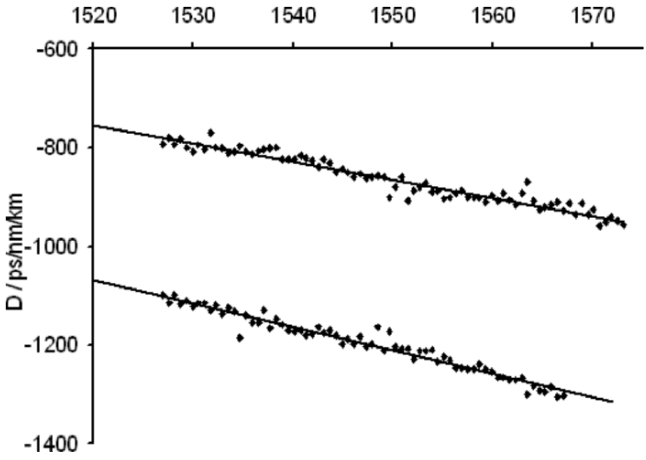

Fig. 12. Measured dispersion of both polarization modes of the fabricated birefringent DCF. The more dispersive mode gives RDS = 0.004 nm^{-1}, which is close to the value for SMF-28. The dispersion of this mode at 1550 nm is −1211 ps/nm/km.

times smaller than for a highest quality commercial DCF. The mode profile, which was calculated directly from a SEM image of the fabricated fiber, is shown in Fig. 13. It is seen that the field penetrates some way into the holey region, with the intensity having decayed only by about 5 dB from its central peak value as it enters the first ring of holes.

Owing to the small size of the core and the high air filling fraction in the cladding of the fabricated fiber, the birefringence level imparted by the relatively small geometrical breaking of six-fold symmetry is substantial. The splitting in effective index of the polarization states is found to be around 0.009 within the C-band, and the differential group delay was measured to be 45 ns/km. The difference in the dispersion levels of the two polarization channels is also sizeable at about 200 ps/nm/km, as can be inferred from Fig. 12.

The loss of the fabricated fiber is high, at around 100 dB/km, which can mostly be attributed to the very high hole interface fields associated with such a small core fiber. The loss FOM is around 25 times lower than for a high performance commercial DCF.

6. PMD and MPI Properties of Solid Core PCF Compensators

6.1. Current PMD Levels of PCF

In a communication system it is generally required to ensure that any inline components operate as far as possible in a polarization independent manner. Arbitrary and time-varying states of polarization pass through the system and pulse spreading or splitting due to PMD or residual birefringence must be maintained at very low levels in high

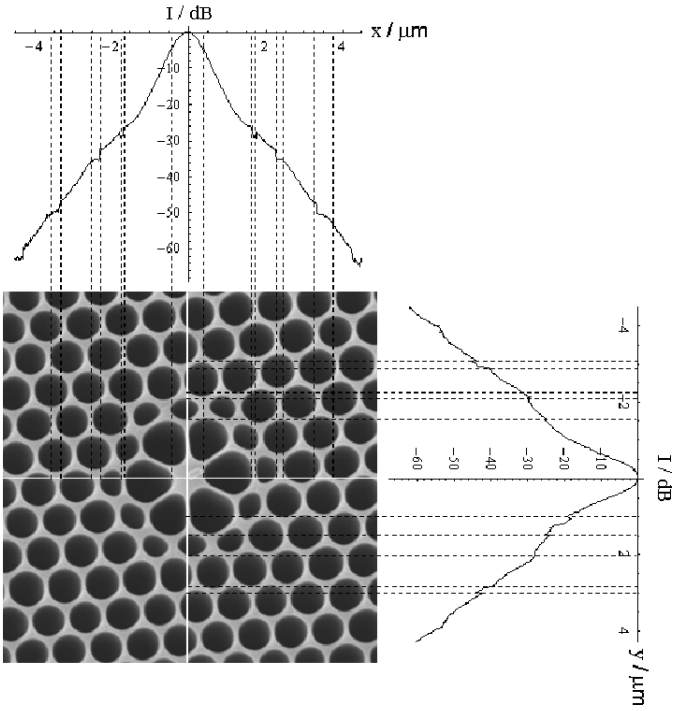

Fig. 13. The mode intensity for one polarization state of the fabricated fiber at a wavelength of 1.55 μm, calculated directly from the SEM image. The intensity profiles are shown along the white horizontal and vertical lines that pass through the center of the fiber core. The intensity has dropped by only 5 dB from its peak value as it enters the fist ring of holes, so hole interface scattering loss is high.

bit rate communication. As an example, the PMD level for 10 GB/s single channel communication over 1000 km must be maintained below about 100 ps over the span length. A span of this length will comprise many components, including around 15 transmission line and amplifier stages and a similar number of dispersion compensating units. If of order 100 separate components are needed, assuming the polarization evolves in a stochastic manner so that PMD over the span increases roughly with the square root of the number of components, one can estimate that a maximum of about a picosecond of PMD can be tolerated for each DCF unit. This is a stringent requirement for PCF-based compensators to achieve. Current commercially available DCF has reached PMD levels as low as 0.5 ps for a unit designed to compensate 80 km of SMF-28, but such low levels are currently far from being achievable with PCF at a mode size compatible with attaining a suitable dispersion characteristic for dispersion compensation.

Unintentional form birefringence in PCFs causes the fibers to show substantial PMD. A Monte-Carlo simulation has been performed in which the hole sizes suffer

from random variations which are maintained along the length of the fiber. Each hole is assumed statistically independent of the others and its diameter is drawn from a Gaussian distribution centered at the hole diameter for the target non birefringent DCF structure. The differential group delay that is incurred by just 1% fluctuations about the six-fold target structure is around 3 ns/km at an effective area of 3 μm^2 and is about 100 ps/km at an effective area of 20 μm^2. If hole sizes are maintained along the length of fiber, this implies the PMD (or rather the differential group delay) figure for the PCF-based DCF will be at least two orders of magnitude higher than the acceptable level for use in a high bit-rate communication system.

In practice some variation of hole diameter with length will occur which will lessen the birefringence level to some degree. Random coupling between the polarization states leads to a diffusive evolution of the polarization state which is characterized by a length scale L_{corr} for state de-correlation and signaled by a square root dependence of PMD on the fiber length. Fabricated PCFs with mode areas of 20 μm^2 or less tend to have large values of L_{corr} so that the lessening of pulse spreading or splitting due to random polarization coupling is minimal. It appears that the variations of the individual hole sizes along the length of the fiber are correlated so that the direction of the axis of polarization is maintained; the dominant variation is typically just a congruent scaling of the entire cross section. The correlation length could be substantially reduced by spinning the fiber as it is drawn, which would significantly reduce the level of PMD. This technique, familiar in conventional MCVD fiber fabrication, has just begum to be developed for PCF, with initial results showing a twenty-fold decrease in the level of PMD for a large mode area fiber. [32] Achieving PMD reduction for the smaller mode area DCF fibers presents a considerably greater challenge.

6.2. Schemes to Combat PMD and Their Impact on MPI

Since PMD constraints are not met by current non polarization preserving solid core PCF-based dispersion compensating fibers, schemes which involve PM compensators have been explored. Since the DCF is required to deal with arbitrary input polarization, just a single pass through a length of PM fiber will not suffice. One scheme to achieve polarization independent characteristics is to splice a length of PM fiber to the same length of identical fiber that has been rotated so that its fast axis is 90 degrees to the fast axis of the first fiber. This is shown schematically in figure 14a. The challenge for such a scheme is to achieve a high efficiency transfer at the splice between the fast and slow polarization states. The highly stringent limitation on multi-path-interference (MPI) in a communication system [33] appears very difficult to meet: the splice must not give rise to a reflected pulse of power greater than about -30 dB to be acceptable. Beyond the MPI issue, maintaining the cancellation of the differential group delay to the required level over a range of wavelengths such as the C-band, as well as a range of operating temperatures, is also found to be difficult. The demands on the polarization maintenance are also high: the polarization extinction ratio (PER) level needs to be maintained at better than about 30 dB over the length of the DCF.

Alternative schemes in which a circulator or Faraday rotators are used in conjunction with a PM fiber have also been considered and are shown schematically in Figs. 14(b)–(d). The set up in Fig. 14(b) ensures the components of an arbitrary incident polarization state propagate in one polarization state of the fiber in one pass through the fiber and in the other fiber polarization state in the other pass. In the schemes shown in

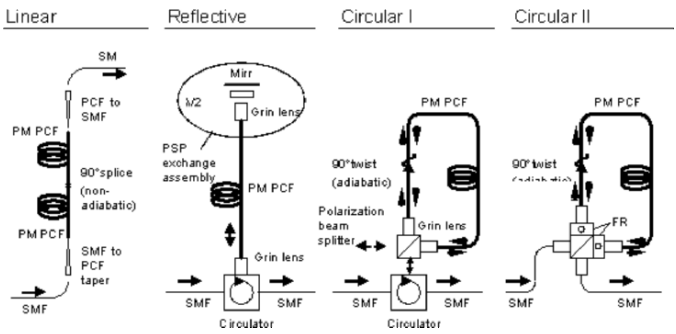

Fig. 14. Candidate schemes to enable the use of a PM compensating fiber in a transmission system.

Figs. 14(c) and 14(d), only one polarization state of the fiber is employed independent of the input polarization. The alternative designs, at the expense of added complexity, act to remove the need for a highly efficient splice and also reduce or eliminate any impact from PMD. Unfortunately, they can be shown to suffer from unacceptable levels of MPI. Even if the efficiency of the polarizing beam splitters is high enough, first order backscattering within the fiber will contribute to the MPI signal. This will be many times higher than the level of second order backscattering which is relevant to a standard DCF setup involving just a single pass through the fiber. For a DCF compensating about 80 km of transmission fiber, one can estimate the level of MPI noise due to first order Rayleigh backscatter to be of order -30 dB relative to the main signal, which is about 30 dB higher than an acceptable figure.

Despite the restrictions imposed by MPI on the use of a PM DCF in a communication system, PM designs are useful to obtain compression or pre-chirp of pulses emitted from a laser source which are subsequently transmitted through a dispersive element such as a fiber. This provided the motivation for developing the fiber described in section 5.

6.3. Other Causes of MPI

Random signal fluctuations induced by MPI can build up over long transmission distances and severely hamper high bit rate communication. For this reason, each constituent of the transmission system should not introduce MPI noise above about -60 dB compared to the main signal intensity. The MPI can be incurred at transitions between different elements in the transmission system, as well as within distributed components such as the transmission fiber itself and dispersion compensating fiber. Although the use of adiabatic mode transformations can at least in principal solve the interfacing problem, scattering events within a fiber provide an intrinsic source of MPI.

For a single pass through a fiber, two scattering events are required to cause the interference in the forward propagating signal mode. Within a single mode transmission fiber such as SMF-28, the dominant MPI contribution comes from double Rayleigh scattering. The first scattering event causes a reflection of a small fraction of the signal

into the backward propagating guided mode and the second reflects a fraction of this power back into the forward propagating mode.

In the DCF, other pathways exist for the creation of MPI within the fiber. Scattering into the ring-like mode, followed by scattering back into the forward propagating LP_{01}-like signal mode, can give a larger contribution to MPI than the double reflection events described above. Although the ring-like mode is lossier than the LP_{01}-like mode, it nevertheless survives typically over several meters so that a large range of temporal delays in the MPI signal can result. Higher order modes of the DCF, which are rendered lossy due to scattering processes and leakage loss, also contribute to the MPI. A detailed exploration of the MPI has not been attempted, but it is estimated that the contribution from the solid core PCF-based DCF in a conventional single pass setup will be similar to that from the transmission fiber it compensates. The estimate is based on considering double scattering events which result in light re-entering the forward propagating signal mode. Fortunately, the capture probability from scattering at the hole interfaces is substantially reduced due to the relatively low normalized intensity of the signal mode at these positions. Since the magnitude of the dispersion of the DCF is many times that of the transmission fiber, the amount of loss due to distributed scattering along the DCF is far smaller than that in the transmission fiber it compensates. These two favorable properties act to cancel the effect of the much enhanced NA associated with the small core DCF (the cross section for double Rayleigh scattering from within the core is roughly proportional to the fourth power of the NA).

As discussed in the previous subsection, the PMD mitigating schemes involving a circulator or Faraday rotator are subject to very high levels of MPI from single scattering events.

7. Prospects for Hollow Core Photonic Crystal Fiber

7.1. Dispersion Compensation Using HCPCF

Whereas solid core PCF compensating fibers behave in a very similar way to conventional MCVD fiber DCFs, the prospect of using band gap fibers opens new possibilities in dispersion management. In contrast to solid core transmission fibers in which material dispersion dominates, the dispersion in hollow core photonic crystal fiber (HCPCF) is due to the waveguide geometry. The dispersion notionally breaks down into two components: that associated with the wavelength dependence of the confining properties of the band gap cladding and that which arises as a natural consequence of confinement. The former component increases as the band gap edges are approached and the field penetrates progressively further into the cladding, whereas the latter component is shown even by a metallic waveguide that allows no penetration of the field into the cladding.

The dispersion of a typical hollow core photonic crystal fiber (HCPCF) is shown in Fig. 15 together with its loss. The shape of the dispersion curve is very characteristic of band gap guidance, with large negative dispersion shown towards the short wavelength side of the band gap and large positive dispersion shown at the high wavelength end: this behavior is a fundamental consequence of a Kramers-Kronig relation operating in the presence of a gap in the density of states. Superimposed on this dispersion is an overall positive shift of around 80 ps/nm/km which may be ascribed to the mode

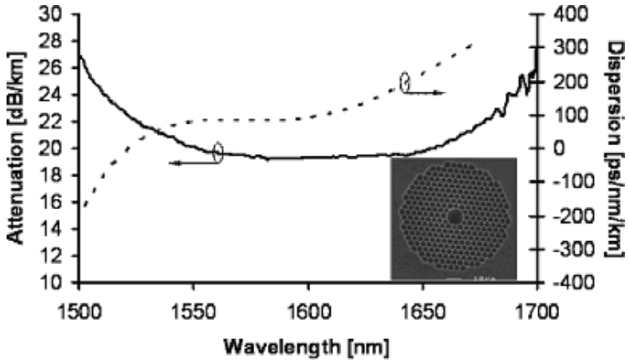

Fig. 15. The dispersion and loss of a typical fabricated HCPCF with a core formed from the omission of seven capillaries (BlazePhotonics fiber HC-1550-02).

confinement effect, although this figure is around three times the dispersion shown by a metallic waveguide with the same core area.

The large negative dispersion close to the short wavelength band gap edge can be used for pre or post-compensation of short pulses from a laser source. [34–37] For the example fiber of Fig. 15, a dispersion of -100 ps/nm/km is associated with just a 25% increase in loss compared to its minimum value of 18 dB/km, whereas a dispersion of -200 ps/nm/km is attained at the expense of a 40% increase in loss. The slope of the dispersion curve is unfortunately positive at such negative dispersion values. To be of use in most communication systems, some degree of RDS matching to the transmission fiber is necessary.

The dispersion properties within the band gap can be altered from the form exemplified in Fig. 15 if an anti anti-crossing occurs between the LP_{01}-like mode and another mode. Such events can occur due to occurrence of modes in the band gap that are associated with the core surround. They are signaled by very rapid and large changes in dispersion and loss. To be able to controllably tune the dispersion and its slope over a sizeable wavelength range such as the C-band and not incur too much of a loss penalty, it is necessary to employ an anti-crossing of the LP_{01} mode with a more air-like mode, perhaps associated with a secondary core situated outside the central air core. The design philosophy then parallels the one used for solid core DCFs.

To incorporate HCPCF for dispersion compensation within a system that uses conventional solid core transmission fiber, low reflection and low loss interfacing solutions will need to be developed. This provides a significant challenge in itself since the mode index of an air guided mode is close to (and just below) unity, whereas the mode index for the solid core fiber is close to the index of silica.

7.2. HCPCF as Transmission Fiber: Is Dispersion Compensation Necessary?

There is a much publicized conjecture that hollow core fibers will reach loss levels below those of conventional fiber and be used directly as transmission fiber. As well as

achieving low loss, it is necessary for the fiber to show sufficiently low levels of PMD and MPI. Whereas the loss levels are rapidly being reduced, with the current reported record standing at 1.7 dB/km, [38] little attention has been paid to PMD and MPI. To achieve the necessary PMD levels, the precision in the manufacturing process will need to be improved and it is likely that the fiber will need to be spun during the fiber draw. MPI also presents a problem, since several long-lived modes other than the one carrying the signal exist within the band gap in current HCPCFs.

If HCPCFs can satisfy the loss, PMD and MPI criteria for use as transmission fiber, there exists the potential for dispensing with dispersion compensating units altogether. This is because the nonlinear coefficient of these fibers can be a thousand times lower than that of a solid fiber, [37] which implies that a much lower dispersion can be tolerated at a fixed power level before nonlinear effects become prohibitive. It remains to design a HCPCF fiber that maintains a low dispersion over an appreciable wavelength window.

8. Conclusions and Future Prospects for PCF-Based Dispersion Compensation

Photonic crystal fibers (PCFs) can be tailored to show a negative dispersion that is slope-matched to transmission fiber such as SMF-28. The large index step between silica and air can be exploited to achieve very large dispersion values whilst maintaining an acceptable tolerance of the dispersion characteristic to the structural parameters of the fiber. The dispersion level achievable at a practical sensitivity level is inextricably linked to the mode area: the smaller the mode area, the larger the dispersion that can be attained. As a consequence, the nonlinearity figure of merit of the fiber for compensating a given length of transmission fiber is only very weakly dependent upon mode area. The loss figure of merit also shows a relatively weak dependence upon mode area, but is currently inferior to this figure for commercial DCFs based on MCVD fiber technology.

Dispersion compensators based on solid core PCFs can be approximately described using an effective index model. This model maps the complex PCF geometry to a radially dependent refractive index profile analogous to the index distributions used in MCVD DCFs. For mode areas greater than about $15\mu m^2$, the index variation inferred from the model is at a level attainable by glass doping technology. This implies that the dispersion characteristics and design constraints of PCF-based DCFs with such mode areas can be expected to be very similar to those of established MCVD DCFs.

In order to compete with MCVD fiber technology in a communication system, DCFs based on solid core PCFs must overcome two main hurdles. The first is loss, which appears to be governed mainly by the roughness at the hole interfaces and the extent to which this can be reduced is at present unclear. A solid-core PCF-based dispersion compensator with a mode area of around 20 μm^2 is expected to show a loss of around 5 dB/km, which is several times higher than the 0.6 dB/km of a commercially available DCF with a similar mode area. The second obstacle to overcome is that of polarization mode dispersion (PMD). This effect becomes more severe as mode area decreases, but even at a mode area of around $20\mu m^2$ is currently at a level that is unacceptable in long haul high bit-rate communication systems. To reduce the figure to an acceptable level will require a substantial increase in the geometrical precision of the fabrication process, and it is likely that the fiber will need to be spun during the

drawing process. Schemes which involve using a polarization maintaining PCF-based DCF can be explored, but to be able to handle an arbitrary input polarization state, they require complicated elements to be introduced which cause unwanted multi-path-interference (MPI) effects.

Although solid-core PCF-based DCFs are currently outperformed by conventional DCFs in a communication system context, they do offer a simple, compact means of achieving pulse compression or pre-chirp in some optical set-ups. Here the high degree of polarization maintenance possible in Hi-Birefringence PCF fibers can be exploited if the polarization direction of the output from a laser is aligned with the polarization axis of the fiber. The highly dispersive fiber forms also find application as highly compact True Time-Delay lines [39] in which pulses centered at slightly different wavelengths become temporally separated.

The use of hollow core photonic crystal fiber (HCPCF) as transmission fiber offers the exciting possibility of eliminating the need for dispersion compensation. Since the nonlinearity of these fibers is much lower than in solid core fibers, operation at low dispersion values can be tolerated. The challenge in the development for HCPCF transmission fibers is to achieve loss figures comparable or better than standard fiber, whilst maintaining an acceptably low level of PMD and MPI. It is also required to design and fabricate a fiber that shows a low dispersion over a significant waveband. None of these goals has yet been demonstrated.

Large negative dispersion can be obtained using HCPCF, making it a candidate for use as DCF. Indeed, this characteristic has been used for compression and pre-compensation of high power laser pulses. To be appropriate for dispersion compensation in a multi-channel communication system, some degree of slope matching to the transmission fiber is necessary. This might be achieved by exploiting an anti-crossing event, just as in solid core DCFs. A detailed exploration of the dispersion compensating possibilities of the hollow core fibers has yet to be carried out.

Acknowledgments

Most of the content of this paper is based on work done by the R&D team of Blaze Photonics. The authors would particularly like to thank L. Farr, D. Williams and M. Mason

References

1. T.A. Birks, D.Mogilevtsev, J.C. Knight and P.St.J. Russell, Dispersion compensation using single-material fibers, IEEE Photon. Technol. Lett., **11**, 674 (1999).
2. J.C. Knight, J. Arriaga, T.A. Birks, A. Ortigosa-Blanch, W.J. Wadsworth, and P.St.J. Russell, Anomalous dispersion in photonic crystal fiber, IEEE Phot. Technol. Lett., **12**, 807 (2000).
3. J.K. Ranka, R.S. Windeler, and A.J. Stentz, Visible continuum generation in air-silica microstructure optical fibers with anomalous dispersion at 800 nm, Opt. Lett., **25**, 25 (2000).
4. S. Coen, A.H.L. Chau, R. Leonhardt, J.D. Harvey, J.C. Knight, W.J. Wadsworth, and P.St.J. Russell, White-light supercontinuum generation with 60-ps pump pulses in a photonic crystal fiber, Opt. Lett., **26**, 1356 (2001).

5. J.C. Knight, T.A. Birks, P.St.J. Russell, and D.M. Atkin, All-silica single-mode optical fiber with photonic crystal cladding, Opt. Lett., **21**, 1547 (1996).
6. T.A. Birks, J.C. Knight, and P.St.J. Russell, Endlessly single-mode photonic crystal fiber, Opt. Lett., **13**, 961 (1997).
7. F. Poli, A. Cucinotta, S. Selleri, and L. Vincetti, Characterisation of microstructured optical fibers for wideband dispersion compensation, J. Opt. Soc. Am. A **20**, 1958 (2003).
8. F. Poli, A. Cucinotta, S. Selleri and A.H. Bouk, Tailoring of flattened dispersion in highly nonlinear photonic crystal fibers, IEEE Photon. Technol. Lett., **16**, 1065 (2004).
9. L.P. Sheng, W.P. Huang, G.X. Chen, and S.S. Jian, Design and optimization of photonic crystal fibers for broad-band dispersion compensation, IEEE Phot. Techn. Lett., **15**, 540 (2003).
10. F. Gerome, J.-L. Auguste and J.-M. Blondy, Design of dispersion-compensating fibers based on dual-concentric-core photonic crystal fiber, Opt. Lett., **29**, 2725 (2004).
11. Y. Ni, L. Zhang, L. An, J. Peng, and C. Fan, Dual-core photonic crystal fiber for dispersion compensation, IEEE Photon. Technol. Lett., **16**, 1516 (2004).
12. B. Zsigri, J. Laegsgaard, and A. Bjarklev, A novel photonic crystal fiber design for dispersion compensation, J. Opt. A: Pure Appl. Opt., **6**, 717 (2004).
13. A.J. Antos and D.K. Smith, Design and characterization of dispersion compensating fiber based on LP_{01} mode, IEEE J. Lightwave Technol., **12**, 1739 (1994).
14. L. Grüner-Nielsen, S.N. Knudsen, T. Veng, B. Edvold, and C.C. Larsen, Design and Manufacture of Dispersion Compensating Fiber for Simultaneous Compensation of Dispersion and Dispersion Slope,' Tech. Dig. OFC'99, Paper WM13, p. 232, 1999.
15. L. Grüner-Nielsen, S.N. Knudsen, P. Kristensen, T. Veng, B. Edvold , and T. Magnussen, Dispersion Compensating Fibers and Perspectives for Future Developments, Proc. Europ. Conf. Opt. Comm. ECOC'2000, Vol. 1, p. 91, 2000.
16. A. Birks, D.Mogilevtsev, J.C. Knight, P.St.J. Russell, J. Broeng, P.J. Roberts, J.A. West, D.C. Allan, and J.C. Fajardo, The analogy between photonic crystal fibers and step index fibers, in Optical Fiber Communication Conference, OSA Technical Digest, Optical Soc. of America, Wash. DC, p. 114, 1999.
17. J.C. Knight, T.A. Birks, P.St.J. Russell and J.P. deSandro, Properties of photonic crystal fiber and the effective index model, J. Opt. Soc. Am. A **15**, 748 (1998).
18. J.M. Pottage, D.M. Bird, T.D. Hedley, T.A. Birks, J.C. Knight, P.St.J. Russell, and P.J. Roberts, Robust photonic band gaps for hollow core guidance in PCF made from high index glass, Opt. Express, **1**, 285 (2003).
19. S.G. Johnson and J.D. Joannopoulos, Block-iterative frequency-domain methods for Maxwell's equations in a planewave basis, Opt. Express, **8**, 173 (2001).
20. D. Mogilevtsev, T.A. Birks, and P.St.J. Russell, Localized function method for modeling defect modes in 2-D photonic crystals, J. Lightwave Technol., **17**, 2078 (1999).
21. R. Ghosh, A. Kumar, J.P. Meunier, and E.. Marin, Modal Characteristics of Few-mode Silica-Based Photonic Crystal Fibers, Opt. Quant. Electron., **32**, 963 (2000).
22. S. Guenneau, A. Nicolet, F. Zolla, and S. Lasquellec, Modeling of photonic crystal optical fibers with finite elements, IEEE Trans. Magn. (USA), **38**, 1261 (2002).
23. N. Guan; S. Habu, S.K. Takenaga, K. Himeno, and A. Wada, Boundary element method for analysis of holey optical fibers J. Lightwave Technol., **21**, 1787 (2003).

24. T.P. White, B.T. Kuhlmey, R.C. McPhedran, D. Maystre, G. Renversez, C.M. de Sterke and L.C. Botten, Multipole method for microstructured optical fibers: 1. Formulation, J. Opt. Soc. Am. B, **19**, 2322 (2002).

25. L. Farr, J.C. Knight, B.J. Mangan, and P.J. Roberts, 'Low loss photonic crystal fiber, European Conference on Optical Communication (ECOC 2002), Copenhagen Denmark, postdeadline paper PD13, 2002.

26. P.J. Roberts, F. Couny, H. Sabert, B.J. Mangan, D.P. Williams, L. Farr, M.W. Mason, A. Tomlinson, T.A. Birks, J.C. Knight, and P.St.J. Russell, Ultimate low loss of hollow-core photonic crystal fibers, Opt. Express, **13**, 236 (2005).

27. M. Wandel, T. Veng, Q. Le, and L. Grüner-Nielsen; Dispersion compensating fiber with a high figure of merit, Proceedings of 2001 European Conference on Optical Communications, Paper PD.A.1.4, 2001.

28. C.D. Poole, J.M. Wiesenfeld, A.R. McCormick, and K.T. Nelson, Broadband dispersion compensation by using high-order spatial mode in a two-mode fiber, Opt. Lett., **17**, 985 (1992).

29. C.D. Poole, J.M. Wiesenfeld, D.J. DiGiovanni, and A.M. Vengsarkar, Optical fiber-based dispersion compensation using higher order modes near cutoff, J.l Lightwave Technol., **12**, 1745 (1994).

30. S. Ramachandran, B. Mikkelsen, L.C. Cowsar, M.F. Yan, G. Raybon, L. Boivin, M. Fishteyn, W.A. Reed, P. Wisk, D. Brownlow, and R.G. Huff, L. Gruner-Nielsen, All-fiber grating-based higher order mode dispersion compensator for broad-band compensation and 1000-km transmission at 40 Gb/s, IEEE Phot. Techn. Lett., **13**, 632 (2001).

31. B.J. Mangan, F. Couny, L. Farr, A. Langford, P.J. Roberts, D.P. Williams, M. Banham, M.W. Mason, D.F. Murphy, E.A.M. Brown, H. Sabert, T.A. Birks, J.C. Knight, and P.St.J. Russell, Slope-matched dispersion-compensating photonic crystal fiber, Technical Digest Conference on Lasers and Electro-Optics, CLEO'04, San Francisco, California, U.S.A., May 2004, post-deadline paper CPDD3, 2004.

32. M. Fuochi, J.R. Hayes, K Furusawa, W. Belardi, J.C. Baggett, T.M. Munro, and D.J. Richardson, Polarization mode dispersion reduction in spun large mode area silica holey fibers, Opt. Express, **12**, 1972–77 (2004).

33. J.L. Gimlet and N.K. Chaung, Effects of phase to intensity noise generated by multiple reflection on Gigabit per second DFB laser transmission systems, J. Lightwave Technol., **7**, 888 (1989).

34. C.J.S. de Matos, J.R. Taylor, T.P. Hansen, K.P. Hansen and J. Broeng, All-fiber chirped pulse amplification using highly dispersive air-core photonic bandgap fiber, Opt. Express, **11**, 2832 (2003).

35. H. Lim and F.W. Wise, Control of dispersion in a femtosecond ytterbium laser by use of hollow-core photonic bandgap fiber, Opt. Express, **12**, 2231 (2004).

36. W. Gobel, A. Nimmerjahn, and F. Helmchen, Distortion-free delivery of nanojoule femtosecond pulses from a Ti:sapphire laser through a hollow-core photonic crystal fiber, Opt. Lett., **29**, 1285 (2004).

37. G. Humbert, J.C. Knight, G. Bouwmans, P.St.J. Russell, D.P. Williams, P.J. Roberts and B.J. Mangan 2004, Hollow core photonic crystal fibers for beam delivery, Opt. Express, **12**, 1477 (2004).

38. B.J. Mangan, L. Farr, A. Langford, P.J. Roberts, D.P. Williams, F. Couny, M. Lawman, M. Mason, S. Coupland, R. Flea, and H. Sabert, Low loss (1.7 dB/km) hollow core photonic bandgap fiber, OFC 2004, postdeadline paper #24, 2004.

39. Y. Jiang, B. Howley, Z. Shi, Q. Zhou, R.T. Chen, M.Y. Chen, G. Brost, and C. Lee, Dispersion-enhanced photonic crystal fiber array for a true time-delay structured X-band phased array antenna, IEEE Photon. Technol. Lett., **17**, 187 (2005).

DOI: 10.1007/s10297-005-0055-z
Originally published in J. Opt. Fiber. Commun. Rep. 2, 397–434 (2005)

Broadband fiber Bragg gratings for dispersion management

James F. Brennan III

Raydiance, Inc., 2602 Challenger Tech Ct., Suite 240, Orlando, FL 32826
Email: jbrennan@raydiance-inc.com

Abstract. This paper provides an overview and technology update of a dispersion management component made from chirped fiber Bragg gratings. The history and technology of fiber Bragg gratings (FBGs) have been extensively covered in several excellent review articles, [1–6] book chapters, [7] and books. [8,9] We give a brief overview of fiber Bragg grating technology in this section and then focus on the details concerned with construction and performance of dispersion management devices in optical communications systems with a single broadband long-length grating used in reflection. Sampled chirped grating are sometimes referred to as broadband devices, but they actually have a narrow bandwidth of operation that is periodically repeated across a given spectral range. Although these periodic devices have shown promise as dispersion management devices in communications systems, they will not be discussed in this paper.

1. Introduction

Much advancement in fiber grating technology has been made since 1978, when K. O. Hill and his colleagues first observed a photoinduced grating in a germanium-doped optical fiber. [10] In less than 20 years, gratings evolved from being laboratory curiosities to critical building blocks in the world's communications infrastructure. A fiber Bragg grating is a spectrally selective reflector that is inscribed into the core of an optical fiber. One can imagine that the grating behaves similar to a thin-film stack that has been fabricated into the fiber core. As with thin film stacks, fiber gratings reflect light within a narrow band of wavelengths and transmit wavelengths outside that band. The reflected wavelengths are determined by the spacing of the regions of alternating refractive index to be twice the period of the index perturbation multiplied by the refractive index. For example, a grating reflecting light of 1550 nm wavelength would have an index period of $\sim$0.532 μm. A typical FBG is a few millimeters in length and

thus has thousands of these index perturbations. This chapter deals with 'long-length' gratings that are several centimeters to meters in length and have millions of index gradations.

Fiber gratings offer several advantages over competing optical filter technologies, including all-fiber geometry, low insertion loss, high extinction ratios, and high reliability. Numerous physical parameters of the grating may be varied during grating inscription, including induced index change, length, apodization, and period chirp. By varying these parameters, gratings with desired spectral characteristics can be made that have, for instance, very wide or very narrow bandwidths, extremely sharp spectral features, and specialized dispersive characteristics. Gratings can be 'chirped' to reflect different wavelengths at different locations by varying the grating period along the device length, and they can be 'apodized' to shape their spectral response by varying the fringe visibility and phasing along the device length.

The index perturbations that compose the fiber grating are induced in the core of an optical fiber via the phenomena of photosensitivity. When certain glass is exposed to radiation at high power levels, the refractive index of the glass changes in proportion roughly to the radiation dose delivered to that area of the glass. By placing a fiber into an interferogram where the light intensity varies sinusoidally along the length of the fiber, one can record the varying light intensity pattern into the fiber and make a fiber grating. With the fiber's protective polymer coating removed, the writing beam is directed through the side of an optical fiber and is absorbed in the core of the fiber. The wavelength of light is chosen so that it will propagate freely through the fiber cladding and induce a refractive index perturbation in the fiber core. Typically $\sim$240 nm light is used to alter the index of germanium-doped glass, which is present in the fiber core but not in the cladding. Often a fiber is saturated with molecular hydrogen before UV-exposure to increase its photosensitivity.

Numerous methods of creating fiber gratings have been developed. Conventional techniques involve placing an optical fiber in a three-dimensional light fringe pattern, typically an interferogram created by interfering two coherent UV beams or a Talbot image made by launching light through a transmission diffraction grating. Often the interferogram method is referred to as the 'holographic' method and the Talbot image method as the 'phase mask' method. A fiber is placed in the fringe pattern, and the fiber photosensitivity causes the pattern to be recorded as a perturbation to the refractive index in the fiber core. After the fringe pattern is inscribed into the fiber, that portion of the fiber is heated to a few hundred degrees Celsius to stabilize the induced index changes and anneal the structure. Some of the induced photosensitivity is lost during this annealing process, so proper grating designs must account for this index loss. After annealing, the fiber is re-coated and is ready to be packaged.

Fiber grating solutions for dispersion management in optical telecommunication systems have been pursued for many years. In principle, these devices have ideal characteristics compared with conventional fiber-based solutions, but manufacturing difficulties, product performance and value, and market conditions have hindered the implementation of these devices in current commercial telecommunications systems. Many of the anticipated advantages of these devices over conventional fiber-based devices have been negated by engineering solutions, at least for current 10 Gb/s speed systems [e.g., 11]. The deployment of faster speed systems that run at higher peak powers may awaken commercial interest in these devices.

Most fiber grating solutions involve very short lengths of fiber, on the order of a meter or less in length, to accomplish what other solutions do with several kilometers of fiber. Because of this, optical nonlinear interactions in grating-based dispersion compensation modules are considered to be non-existent, the pulse transit time in the device is significantly reduced, and optical insertion losses are generally lower. However, since grating-based devices were introduced to the commercial 10-Gb/s market several years after conventional fiber solutions, grating-based devices, or any other alternative technology, are required to be drop-in replacements in existing multi-stage optical amplifiers, where the advantages of gratings over standard dispersion compensating fiber (DCF) solutions are negligible. Grating-based dispersion management technology is immature compared to fiber approaches and mass-manufactured grating components have yet to consistently reach the system performance of the entrenched DCF solution.

Dispersion management solutions must occupy as little volume as possible since rack space is scarce in most system designs. Fiber grating approaches are much smaller than those with transmission fiber since comparatively very little fiber is needed to accomplish the same job, but even this advantage is diminished with current DCF solutions in 80 μm fiber, which allows for a tremendously reduced DCF package volume. The cost of a grating approach is also, to date, not substantially lower than that of DCF. Many people hoped that since so little specialty fiber was involved in making grating devices that material costs would be significantly cheaper than fiber solutions. Yet the increased handling, complex process steps, and other component costs, such as the optical circulator, needed to make grating-based modules resulted in devices similar in price to DCF.

Although current market conditions look bleak, the advantages that grating solutions offer cannot be overlooked. Gratings can be fabricated with complex dispersion profiles to solve system design challenges that other technologies cannot address, a few of which will be detailed in section 5. The desirability of grating modules over conventional techniques will likely change as grating technology matures, market conditions force component and system designs to change, and higher speed and power systems are deployed. Mass manufacturing of grating based devices will result in reduced costs. The pulse transit time in the grating-modules is much shorter, allowing for less complex and faster control of the optical amplifier dynamics, and an integrated amplier/grating solution will be much smaller than current modularized solutions.

Optical system designers have wanted to use chirped fiber Bragg gratings as dispersion compensators since they were first proposed over a decade ago. [12] In this approach, the grating period is chirped to reflect lagging wavelengths before faster wavelengths, which must travel further into the grating before they are reflected, as shown in Fig. 1. An optical circulator is used to separate the input of the device from the output. A chirped grating module recompresses a data pulse that has been corrupted by chromatic dispersion, and optical communications system performance is enhanced. A longer grating yields a greater compression factor and a wider bandwidth device. Long-length gratings are also desirable for use in distributed sensor systems, [13] optical pulse stretching and recompression, [14] pattern generation and recognition in code-division multiple access systems, [15] optical pulse shaping, [16] nonlinear optical switching, [17] and numerous other applications.

Adaptation by optical system designers of dispersion compensation gratings (DCGs) has been slowed by technical difficulties. Historically the principal chal-

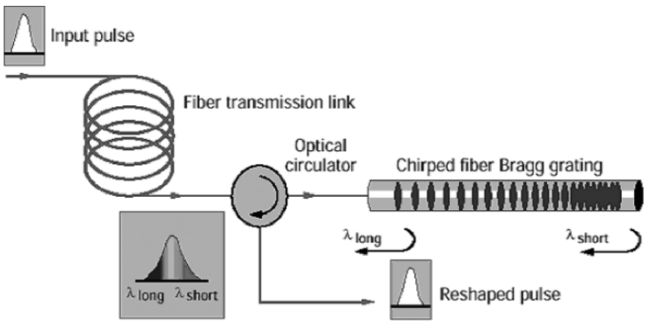

Fig. 1. Functional diagram of a chirped fiber grating used for dispersion compensation.

lenge has been to maintain grating pitch accuracy to very high precision along the device length. Fabrication errors cause inaccuracies in grating dispersion characteristics, commonly referred to as group delay ripple (GDR), which distort the phase of signals reflected from the devices and thereby degrade the performance of a communications system. Grating fabrication technology has advanced considerably over the past several years and impressive laboratory demonstrations have shown that quality devices can be fabricated. Translating that laboratory success to readily manufacturable and cost-effective components is still a challenge.

Extreme mechanical tolerances must be maintained to manufacture quality long length gratings. As mentioned, fabrication errors in chirped gratings create ripples in the group delay performance and thus inaccuracies in the dispersion correction. The amplitude of the ripple has been used as a metric for determining chirped grating quality, and early work by optical communications system designers surmised that the amplitude of these ripples must be less than $\sim$40 ps peak-to-peak for a DCG to be useful as dispersion compensators in 10 Gb/s systems. A ripple amplitude this small can be caused by many fabrication imperfections, such as a 20 % variation in the grating UV-induced index change, a $\sim$0.3 % dimensional change in a fiber core, or a $\sim$4 pm error in grating pitch. Given the silicon-oxygen inter-atomic spacing in glass is $\sim$160 pm, many scientists thought that holding these tolerances during grating inscription was not possible.

Since the early days of chirped grating development, many advances have occurred in fabrication technology and in understanding their system performance. As will be discussed, the GDR amplitude multiplied by its periodicity, which is proportional to the phase ripple, was found to be most indicative of device performance in optical telecommunications systems. By significantly decreasing the ripple frequency, performance degradation was also decreased. With these advances, many other issues with DCG manufacture could be addressed, such as thermal management, mechanical reliability, and packaging. In section 5, we show that quality chirped grating modules have been made that cover full communications bands and work well in 10 Gb/s telecommunications system.

The remainder of this chapter is organized as follows. In section 2, an overview of long length grating fabrication and design is detailed. Section 3 focuses on packaging issues with these gratings and their thermal management. Section 4 details measurements and specification issues encountered when designing these devices into communication systems. Finally, a few specific applications highlighting strengths of this technology over other approaches are presented in Section V.

2. Long Length Grating Fabrication

This section focuses on challenges encountered when making the chirped fiber grating that is built into a dispersion compensation module. Later sections in this chapter discuss how these devices are packaged, characterized, and used in communications systems. The first part of this section gives a brief history and overview of long-length grating writing methods, the second part discusses how the grating profile must be shaped to compensate for internal losses in the grating structure, and the third part details causes of grating imperfections and how they affect its dispersion characteristics.

2.1. Grating Inscription

A chirped grating module recompresses a data pulse by reflecting lagging wavelengths before faster wavelengths that must travel further into the grating before being reflected, as shown in Fig. 1. With this approach, a longer grating yields a greater compression factor and a wider bandwidth device. Early researchers quickly ascertained that conventional grating fabrication techniques limited many grating designs. The length of a grating was limited to the diameter of the laser beam with the holographic method or the length of a phase mask, which could be made to only a few centimeters in length. Apodization and chirping were also difficult to perform with conventional fabrication techniques. Spectral shaping of the grating reflection profile, or apodization, was typically accomplished by exposing the same length of fiber to two different optical beam configurations, by using specially crafted phase masks, or by dithering a component of the fabrication system as the grating was being written. Chirped gratings were fabricated typically with custom phase masks that had a varying periodicity. If one desired to change these parameters of a grating, one would need new optics and phase masks, which were difficult to acquire and delayed device development. These techniques were not transferable to a manufacturing environment where operating wavelengths and dispersion characteristics differ between customers.

Initial attempts to fabricate chirped gratings relied on methods where the fiber and interferogram were held stationary during the exposure process. Williams et al. introduced a technique where a fiber core was scanned two times during the fabrication of a chirped grating. [18] In the first scan, a standard 5-cm uniform (unchirped) phase mask was placed close to the fiber and a UV laser beam was scanned across the mask to write a long single wavelength grating. In the second scan, the phase mask was removed and the laser beam was scanned across the grating as the beam intensity varied to alter the fiber refractive index and chirp the device. Others researchers chirped gratings by scanning once over a uniform phase mask and then altered the fiber properties before

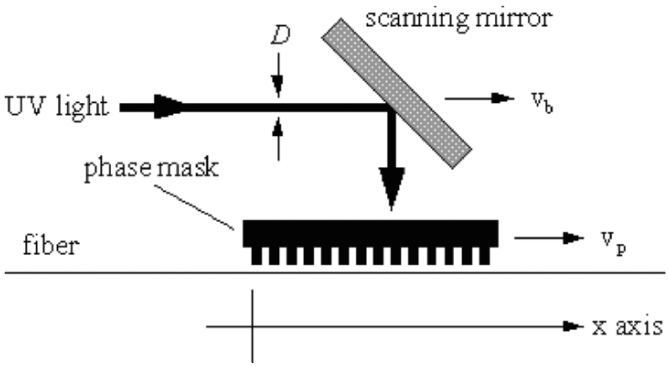

Fig. 2. Experimental configuration used by Cole et al. to vary the chirp of a grating during fabrication.

or after grating inscription, such as by tapering the fiber diameter [19] or applying strain and thermal gradients. [19–23]

Fabricating gratings longer than a phase mask was also very challenging. Kashyap et al. developed a method of concatenating individual chirped fiber gratings by irradiating fiber sections between adjacent gratings with UV radiation to tune the optical phase between sections. [24] In one implementation, they concatenated thirteen 10-cm-long chirped phase masks, each with a sequential start and finish wavelength, to create a phase continuous 130-cm-long grating. [25] Building upon this work, Rourke et al. obviated the UV-trimming step by using the fiber fluorescence magnitude during UV-irradiation to align each new phase mask with the previously inscribed fiber grating. [26] Although these methods generated meter-long fiber gratings, they required highly specialized phase masks to be fabricated for each new grating design. These approaches were not developed past the proof-of-principle stage and thus never produced broadband DCGs useful for telecommunications systems.

2.1.1. Arbitrary Chirps

To arbitrarily vary the chirp of a fiber grating during inscription, Cole et al. introduced a method to fabricate chirped gratings where a laser beam is scanned across a uniform phase mask with a fiber behind it. [27] As the beam is scanned, the fiber or phase mask is moved at a much slower velocity than the beam scan with a piezo-electric transducer, as detailed in Fig. 2. A simple analysis helps illustrate this approach. Assuming the fiber is stationary and that x is the distance along the fiber length, the light intensity, I, that may be delivered to this fiber through a phase mask of period 2Λ moving at velocity v_p in the positive x-axis direction may be expressed as

$$I(x) = I_0 \sin^2 \left[\frac{\pi}{\Lambda} (x - v_p t) \right]. \tag{1}$$

The fluence Φ delivered to a fiber through this phase mask by a flat-top laser beam of width D and intensity I as it is translated across the phase mask at velocity v_b is

$$\Phi(x) \propto \int_{x/v_b}^{x+D/v_b} I_0 \sin^2\left[\frac{\pi}{\Lambda}(x - v_p t)\right] dt$$
$$\propto \frac{I_0}{2} \int_{x/v_b}^{x+D/v_b} \left[1 - \cos\left(\frac{2\pi}{\Lambda}(x - v_p t)\right)\right] dt, \quad (2)$$

which reduces to

$$\Phi(x) \propto \frac{I_0}{2}\frac{D}{v_b}\left\{1 - \text{sinc}\left(\frac{\pi}{\Lambda}\frac{v_p}{v_b}D\right)\cos\left[\frac{2\pi}{\Lambda}(1 - \frac{v_p}{v_b})x - \frac{\pi}{\Lambda}\frac{v_p}{v_b}D\right]\right\}, \quad (3)$$

where $\text{sinc}(z) = \sin(z)/z$. The factor $(1 - \frac{v_p}{v_b})$ in the cosine function changes the pitch of the grating from that made by a stationary phase mask. If $v_p \ll v_b$, then

$$1 - \frac{v_p}{v_b} \approx \left(1 + \frac{v_p}{v_b}\right)^{-1}$$

via a Taylor series expansion, changing the fiber grating pitch by $\sim \Lambda\frac{v_p}{v_b}$. Thus for a shift of $\sim$1 nm, the mask must move at only $\sim$0.1 % of the beam scanning speed. Larger wavelength shifts decrease the grating strength, since the grating fringe visibility is reduced when the interference pattern formed by the mask moves too quickly across the fiber. If the phase mask moves too fast relative to the beam movement, $v_p \geq \frac{\Lambda v_b}{D}$, no appreciable grating fringe visibility is recorded into the fiber.

2.1.2. Direct-Write Methods

Scores of sophisticated methods for fabricating long-length fiber gratings have been developed, but direct-write methods have produced the highest quality chirped gratings to date. In these techniques, the fiber is generally in constant motion relative to the interferogram as the grating is written. The grating is written essentially a fringe at a time and much flexibility in the phasing and strength of each grating section can be obtained.

To arbitrarily vary the apodization and the chirp, as well as overcome some length limitations, Stubbe et al. introduced a technique that stitches small gratings together to fabricate a phase-continuous long-length grating. [28, 29] A small grating is written, the fiber is translated by a grating period along the interferogram with a high-precision air-bearing linear stage, and then the fiber is irradiated again. Stubbe used a pulsed dye laser and synchronized the movement and pulsing of the laser to create chirps and apodize a grating of up to 50 cm in length. Since Stubbe's announcement, a number of other approaches that built upon his technique have been demonstrated for writing long continuous gratings with complex profiles. For example, Ibsen et al. modulated the intensity of a CW laser with an acousto-optic modulator. In this technique, the fiber is also translated by a precision linear stage, but the interpolated output of the encoder that monitors the position of the translational stage was used to control the modulation of the writing beam to create pulses that are precisely timed with respect to the scanning. [30] A chirped and apodized grating could be written into the fiber simply by programming that function into the computer that controls fabrication system.

To increase the placement accuracy of the grating fringes and remove length limitations, Brennan et al. introduced a method where the fiber is treated as the recording medium of an analog signal, analogous to magnetic tape recording where a magnetic

medium is translated at a controlled velocity past a magnetic circuit writing head. [31,32] An advantage of this technique is that it is a velocity-controlled approach that does not require position information for feedback and thus is not limited by the throw of available high-precision motion staging. Constant velocity can be maintained to a degree that exceeds available position measurements by increasing the mechanical inertia of the motion system to mechanically low-pass filter interpolator errors. Previous direct-write methods relied on measuring with extreme accuracy the position of a fiber relative to an interferogram to stitch gratings together. The accuracy of these location measurements is limited by the motion stage encoder – usually interferometer based, which is susceptible to several degradations, such as interpolator inaccuracies, noise in edge detection electronic circuitry, and random fluctuations in received interpolator-laser light. [33]

A simple analysis illustrates some of the advantages and disadvantages of the velocity-controlled approach. The fiber is translated at a velocity v past a stationary phase mask through which propagates a laser beam that is time-modulated at radial frequency ω, which be expressed as

$$\begin{aligned}\Phi(x) &\propto \int_{x/v}^{x+D/v} I_0 \sin^2\frac{\omega}{2}t \sin^2\left[\frac{\pi}{\Lambda}(x-vt)\right] dt \\ &\propto \frac{I_0}{4}\int_{x/v}^{x+D/v} (1-\cos\omega t)\left(1-\cos\left[\frac{2\pi}{\Lambda}(x-vt)\right]\right) dt. \end{aligned} \tag{4}$$

The integral reduces to yield

$$\begin{aligned}\Phi(x) \propto \frac{I_0}{4}\frac{D}{v}\Bigg\{1 &- \operatorname{sinc}\left[\frac{2\pi}{\Lambda}D\right] - \operatorname{sinc}\left(\frac{\omega}{v}D\right)\cos\left[\frac{\omega}{v}x+\frac{\omega}{v}D\right] \\ &- \frac{1}{2}\operatorname{sinc}\left[D\left(\frac{2\pi}{\Lambda}\pm\frac{\omega}{v}\right)\right]\cos\left[\pm\frac{\omega}{v}x - D\left(\frac{2\pi}{\Lambda}\pm\frac{\omega}{v}\right)\right]\Bigg\}. \end{aligned} \tag{5}$$

The first and second terms within the curly brackets in Eq. (5) are equivalent to Eq. (3) if $v_p = v_b$ and the same time-average light intensity is used. The third term indicates that if one can make the laser beam smaller than the desired fiber grating pitch, then a phase mask is not needed, which is useful for making long-period gratings but is impractical for short-period grating fabrication. [34]

If the diameter of the beam is much larger than the period of the phase mask, then Eq. (5) reduces to

$$\Phi(x) \approx \frac{I_0}{4}\frac{D}{v}\left\{1 - \frac{1}{2}\operatorname{sinc}\left[D\left(\frac{2\pi}{\Lambda}\pm\frac{\omega}{v}\right)\right]\cos\left[\pm\frac{\omega}{v}x - D\left(\frac{2\pi}{\Lambda}\pm\frac{\omega}{v}\right)\right]\right\}. \tag{6}$$

The second term in Eq. (6) (which is actually two terms) contains a tuning parameter $(\frac{2\pi}{\Lambda}\pm\frac{\omega}{v})$ whereby if $\frac{f}{v}\approx\Lambda$ (where $\omega = 2\pi f$), then

$$\Phi(x) \approx \frac{I_0}{4}\frac{D}{v}\left\{1 - \frac{1}{2}\cos\left[\frac{\omega}{v}x\right]\right\}. \tag{7}$$

This result is significant since one can manufacture a chirped FBG by slightly detuning the frequency of the light amplitude modulation or changing the velocity of the fiber. Note that a small uniform phase mask (say 1 inch o.d.) of an appropriate period could be used to make very long gratings that are chirped over a very wide wavelength range.

As the frequency of the light modulation or the velocity of the fiber is changed, the tuning parameter in the sinc function in Eq. (6) will increase from zero and cause the amplitude of the cosine-function spatial-modulation to decrease. If these control parameters are changed too much, no usable fringe visibility will be written into the fiber. This amplitude decrease is proportional to the diameter of the laser beam, which can be focused to make wide wavelength chirps possible. Also note the amplitude of the fringes in Eq. (7) is only half that of the total index perturbation. Different modulation formats, such as clipped sine waves, can increase this ratio.

Another, perhaps more intuitive, method to analyze the constant-velocity approach is to realize that the fringe visibility that is recorded into the fiber is actually the beam shape convolved with the desired grating profile. The beam profile is performing a moving average of the modulated signal across the grating length. The analysis leading to Eq. (6) assumed a flat-top writing beam and the resulting sinc-function is the Fourier transform of that beam. A Gaussian beam can be handled in an analogous manner to obtain

$$\Phi(x) \propto e^{-\left[W\left(\frac{2\pi}{\Lambda}-\frac{\omega}{v}\right)\right]^2} \cos\left[\frac{\omega}{v}x + W\left(\frac{2\pi}{\Lambda}-\frac{\omega}{v}\right)\right]. \tag{8}$$

The constant-velocity method of manufacturing gratings requires motion stages and intensity modulators of high precision. Acceptable deviations in the fiber grating pitch ($\delta\Lambda$) due to jitter in this equipment can be determined by modeling the stage velocity as $v = v_0 \pm \delta v$ and the modulator frequency as $f = f_0 \pm \delta f$, where δv and δf are the respective jitter terms. The fiber grating pitch would be

$$\Lambda \pm \delta\Lambda \approx \frac{v_0 \pm \delta v}{f_0 \pm \delta f} \approx \frac{v_0}{f_0}\left(1 \pm \frac{\delta v}{v_0} \pm \frac{\delta f}{f_0}\right), \tag{9}$$

resulting in deviations in the FBG resonance wavelength due to equipment jitter on the order of

$$\frac{\delta\lambda}{\lambda_B} \approx \frac{\delta v}{v_0} \quad \text{or} \quad \frac{\delta f}{f_0}. \tag{10}$$

The velocity of the motion stage and the frequency of the modulator must vary <1 ppm to achieve >1 pm phase accuracy in the telecommunications C-band wavelength range. Scanning velocities are typically $\sim$1 mm/s when manufacturing gratings, so a motion stage with <0.001 μm/s precision and a $\sim$2 KHz modulation with <2 mHz flutter is needed.

The light intensity can be modulated at high precision ($\sim 10^{-9}$) with standard acousto-optic modulators and quartz crystal oscillators. To translate the fiber with $\sim$1 ppm (10^{-6}) velocity precision, the fiber is placed in a helical groove on a spool that is mounted to a rotary spindle, as shown in Fig. 3. The spindle is rotated at a constant velocity, and a large flywheel is used to regulate the speed. The groove on the spool is like a thread on a screw. As the spindle turns, a linear stage is used to track the laser beam on the fiber, in a manner analogous to cutting threads on a lathe. Gratings that are tens of meters long have been fabricated with this method. [31] To meet the tolerances needed to fabricate gratings, the spool diameters are trued to <10 millionths of an inch (250 nm) precision.

The grating results discussed throughout the chapter have been manufactured with this velocity-controlled fabrication method. The approach by Ibsen et al. has also been highly successful in creating quality chirped gratings. [30]

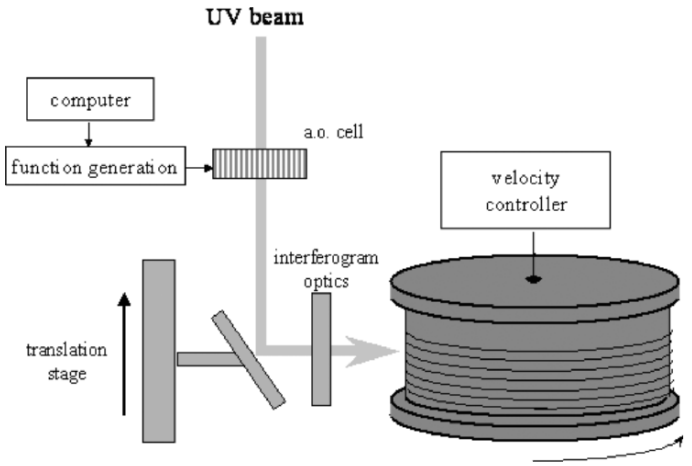

Fig. 3. Experimental configuration used by Brennan et al. to fabricate long-length fiber gratings.

2.2. Spectral Shaping

This part of the paper will discuss factors that one needs to consider when designing long-length fiber gratings. The total time delay available for pulse stretching/compression in a grating is fixed by the length of the grating at $\sim$1 ns per 10 cm of FBG length—the time its takes light to double-pass the fiber length, so the grating length is readily calculated with the desired grating bandwidth and dispersion. Many modeling studies have been reported where the shaping, or apodization, of a grating is varied to reduce the group delay ripple of the device. [35,36] In practice, the dominant contribution to group delay ripple is caused by fabrication imperfections and not improper apodization of the device, as discussed in the section 2.3.

In general, system designers want the insertion loss of a dispersion management solution to be constant across the full system bandwidth to ease the system design [e.g., 37]. The grating fringe visibility will decrease as the grating is chirped if the fringe smoothing is not counteracted, as illustarted in Eqs. (6) and (8). Increasing the amplitude of the write beam modulation at the bandwidth edges counteracts the decrease in fringe visibility, but the optical losses inside the grating must also be included in the grating shaping to flatten the insertion loss across the grating bandwidth. Longer gratings provide more time delay, but typically have greater optical loss, especially if they are very wide in bandwidth. The optical losses in a long length fiber Bragg grating may be divided into three groups: fixed loss, length-dependent loss, and bandwidth-dependent loss. [38] These losses will be individually discussed.

2.2.1. Length Dependent Loss

The optical loss at a given wavelength due to absorption and scattering depends on the length in the grating traversed during the pulse roundtrip, making the length-dependent loss a function of the device bandwidth and dispersion. As discussed, fiber gratings are

written by exposing optical fiber to UV radiation to induce refractive index changes in the fiber core, but this radiation exposure also increases the optical loss in the fiber, especially when the fiber is saturated with H_2 to increase its photosensitivity. [39, 40] The magnitude of this loss is wavelength-dependent and strongly influenced by the chemical dopants used to manufacture the fiber. Usually this loss is negligible in a typical grating of a few millimeters in length, but when the grating is meters long, this effect cannot be ignored.

Here we present a study of these losses in the 1550-nm range and identify certain common fiber components, such as Boron, GeOH & SiOH, as causing high loss after grating inscription. As expected, deuterating fiber to increase its photosensitivity, instead of hydrogenating it, reduces the hydride loss significantly, [41] and boron must be avoided in the fiber manufacture. With these changes, the radiation induced losses are not a major portion of the loss for $\sim$1-m-long gratings in the 1550 nm wavelength range, but longer gratings need to consider this issue. The UV-induced loss at shorter wavelengths, such as $\sim$980 nm, is substantially larger than that at 1550 nm and needs to be addressed when devices are fabricated in those wavelength regions. As presented below, the radiation-induced loss that a fiber incurs during grating fabrication depends on many factors, such as fiber doping, thermal history, and specific process steps. We present this study to illustrate this variability, but emphasize that the precise loss values that a fiber may have should be studied within the context of the specific fabrication process used.

Example study of radiation induced loss in fibers. [42] The optical loss in the 700 to 1700 nm wavelength range for two classes of optical fibers used in the fabrication of fiber Bragg gratings were investigated. Greater than ten-meter lengths of fiber were exposed with 244 nm wavelength light under conditions similar to those used in grating fabrication. Fibers were saturated with H_2 by placing them in a hydrogen rich environment at 60°C and 2000 psi for three days. The optical loss magnitude is reported as a function of each process step used in grating manufacture. Particular attention was given to the optical attenuation in the 700 to 900 nm wavelength region where Ge-H losses dominate and the 1390 to 1700 nm wavelength range where the vibration overtones of SiOH, GeOH, and hydroxyls of boron and phosphorus dominate. [41,43,44]

Two types of silica optical fibers were investigated: a standard $\sim$9 % GeO_2 core fiber (Fiber #1) and another similar fiber with boron-codoping (Fiber #2). Optical loss spectra are given in Fig. 4, which were taken before and after hydrogen doping, after hot acid stripping of the fiber buffer at 180°C for 2 minutes, UV exposure in the 40 to 900 mJ/cm^2 range, high temperature annealing at 300°C for 10 minutes, and low temperature bake at 80°C for two days. After hydrogen loading, Fiber #1 has absorption bands due to germanium and silica hydrides that increase optical attenuation in the 1390 nm spectral range to 0.02 dB/m, while Fiber #2 experiences an increase to $\sim$0.3 dB/m in the same wavelength range and exhibits additional absorptions near 1650 nm associated with hydroxyls of boron. The loss also increased in Fiber #2 to $\sim$0.5 dB/m as a result of acid stripping, whereas no increase was observed for Fiber #1. The optical losses in both fibers varied considerably as the various grating process steps completed, as illustrated in the figure.

In another experiment, hydrogen-loaded Fiber #2 was exposed to radiation and then loss measurements were taken at room temperature over 21 days. The optical loss

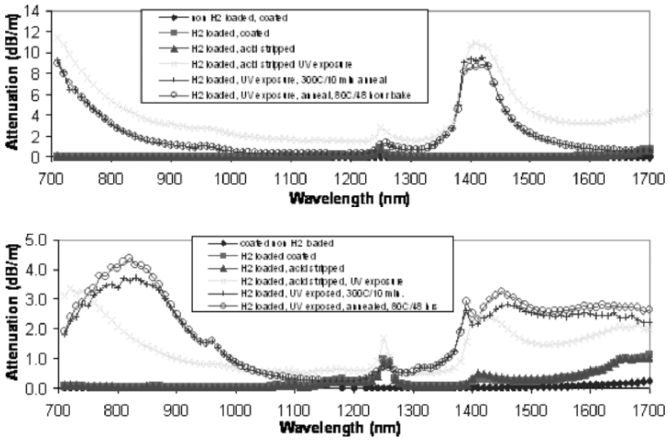

Fig. 4. Optical loss spectra of standard (top) and boron-doped (bottom) germanosilicate fibers after experiencing various process steps used in fiber grating production.

doubled over this time and approached values experienced when the fibers were baked at low temperatures for two days. The reactivity of H_2 in both fibers indicates that reactive sites are formed during UV-exposure and persist at low temperature.

The dominant contribution to the optical absorption for Fiber #1 in the 1550 nm range results from vibrational overtones of Ge- and SiOH at $\sim$1390 nm. [41,43,44] Overtones of BOH also occur in this wavelength range and can be seen in the transmission spectra of Fiber #2. This optical loss is significantly reduced in the 1550-nm region by using deuterium, which shifts the OH absorptions to longer wavelength by $\sim$500 nm. Deuterium does not reduce the loss in the shorter wavelength ranges ($<$ 1300 nm), since this absorption is due to electronic transitions and renders isotope substitution ineffective.

2.2.2. Bandwidth Dependent Loss

Ideally a grating would couple light from the forward-propagating core mode into only the backward-propagating core mode. However, gratings also often meet the phase-matching condition to couple light into backward-propagating cladding modes at wavelengths that are shorter than the fundamental grating wavelength. [45,46] Since energy that is coupled into these cladding modes is lost, a single-wavelength (unchirped) grating is lossy at wavelengths that are shorter than the fundamental. The wavelength separation between the core-to-core and core-to-clad couplings typically ranges from $\sim$1 nm to $\sim$10 nm, depending on the specific optical fiber waveguide design [e.g., 47].

When a grating is widely chirped, the cladding-mode coupling produced by a grating section operating at one wavelength may create loss at another wavelength within the device. [48] This loss will accumulate as a function of grating bandwidth once the cladding-mode coupling overlaps with the grating operating bandwidth, as shown in Fig. 5. In the figure, the onset of cladding mode coupling occurs spectrally at $\sim$1.5

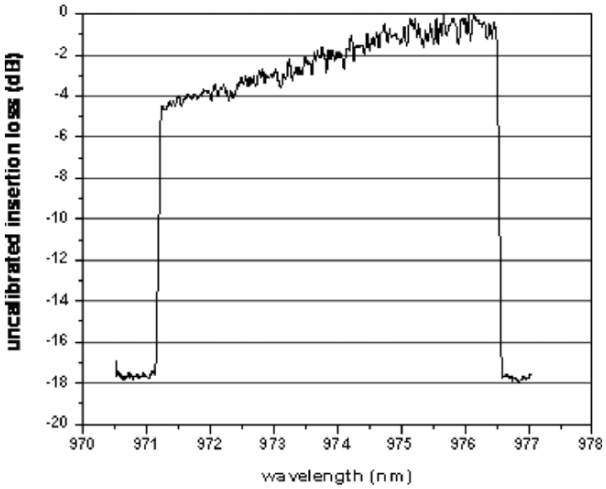

Fig. 5. Reflection spectrum from a chirped fiber grating where the cladding mode coupling loss is evident at wavelengths shorter than ∼975 nm.

nm away from the central reflection and then proceeds at ∼1 dB/nm. The magnitude of this loss is proportional to the square of the strength of the index modulation of the grating, so proper grating designs reduce this bandwidth dependent loss considerably. [45,49,50] To illustrate and exaggerate the cladding mode loss, the grating in Fig. 5 was written with >20 dB rejection in transmission. This loss reaches a maximum value and becomes bandwidth independent, since cladding-mode coupling efficiency decreases as the wavelength from that of the grating fundamental increases. Precise analytical models have been developed that model the cladding mode coupling in a chirped gratings for given grating strengths. [49,50]

As discussed, cladding-mode coupling causes a distributed loss that increases with the grating bandwidth when light is launched into the long wavelength end. When light is launched into the shorter wavelength end, the grating reflects a given wavelength before cladding mode coupling occurs. Pulse compression with anomalous dispersion could be achieved by launching into the short wavelength end of the chirped grating, but unfortunately most communication system links require normal dispersion in their dispersion management modules.

2.2.3. Fixed Loss

Fixed losses in a grating-based dispersion compensation module include circulator and splice losses. At 1550 nm wavelength operation, circulators are readily available with ∼0.75 dB loss per pass, which gives ∼1.5 dB total circulator loss in the DCG module. Splicing routines can be optimized to yield less than ∼0.1 dB per splice, even

when coupling dissimilar specialty fibers. The splice between the circulator and the grating in the DCG module is double-passed to give $\sim<$0.2 dB loss. A conservative manufacturing specification for the total splice loss would be $<$ 0.5 dB.

2.2.4. Total Insertion Loss

The total insertion loss IL that an FBG must account for by spectral shaping may then be expressed as

$$\mathrm{IL} = \alpha + \gamma c D B W + \varsigma(BW - \Delta\lambda)u[BW - \Delta\lambda], \tag{11}$$

where α, γ, and ζ are the fixed, length-dependent, and bandwidth-dependent loss parameters, respectively; D is the dispersion; c is the speed of light double-passed in the fiber (10^{-4} m/ps); and BW is the bandwidth of the FBG. The unit step, u[], equals zero when $(BW - \Delta\lambda p) < 0$ and 1 otherwise. The cladding-mode loss caused by a given grating section begins $\Delta\lambda$ from its primary Bragg reflection. The actual values for these variables will vary tremendously with the fiber, grating design, and operating wavelength.

During grating fabrication, the strength of the grating is varied along its length to minimize insertion loss variation across its bandwidth. [50] When a broadband grating is fabricated, the strength of the grating on the long wavelength side is reduced typically to reject $<$ 3 dB in transmission, which minimizes cladding mode coupling. Depending on the fiber design and the grating coupling strength, the cladding mode coupling can be negligible and $>$50 nm bandwidth devices can be obtained. An obvious drawback is that these gratings have an additional $>$3 dB of insertion loss, since the grating reflection strength is reduced, making full band devices with $>$6 dB of total insertion loss. This tradeoff is made for broadband devices where the grating strength is reduced to minimize cladding mode coupling, but this strength reduction diminishes the magnitude of the reflected light. The grating design must also account for the annealing process step. Since annealing reduces the grating strength by a certain amount, this reduction in grating strength must be carefully factored into the initial grating shaping. [51]

2.3. Grating Imperfections

This part of the paper covers some of the causes of grating imperfections. A given grating fabrication system and process generally has unique causes of grating defects. Many factors can perturb a fabrication system in its local environment, such as low-frequency acoustic and floor vibrations, mechanical resonances in optical mounting hardware, and turbulence in the laser cooling water and pressurized air for the motion stages. We have constructed similar long-length grating fabrication facilities in the same building, but obtained vastly different performances from them initially because the local disturbances affecting them were different. Here we relay some general experiences that may be informative or useful to the reader.

The errors in a grating can be classified as localized, noise-related, or periodic. Localized defects occur when a part of the grating deviates from ideal due to a disturbance that occurred when that portion of the grating was being written. A common problem was that residue from the fiber buffer was still on the fiber. Although hot acid

can be used to strip the fiber, it was nearly impossible to prevent sporadic films of dissolved buffer from re-adhering to the fiber. This thin coating film was nearly imperceptible to the grating fabricator, but it affected the light absorption and geometric properties of the fiber enough to significantly disturb the grating inscription where it was located. Another localized perturbation arose when particulates lodged between the writing spool and the fiber, which caused the fiber core at that location to be at a larger radius on the rotating spool than the rest of the fiber, and thus the grating was written at an unwanted wavelength at that location. This problem can be overcome by running streams of filtered gas between the fiber and the spool during the fiber loading process, but locating the fabrication system in a clean room could have also minimized this problem.

Noise in the fabrication system causes grating fringes throughout the device to be distributed away from their ideal desired location in a random manner. [52] One noise source was due to the turbulence of the laser cooling water shaking the optical beam train, which was readily solved by mounting the laser on a platform separate from the writing optics. Random beam movements at the fiber were minimized by enclosing the beam train and by installing an active beam alignment system that used a quad-photocell receptor and piezo-electric actuated mirrors. Turbulence in the compressed air that levitates the translation stages was also a problem and was overcome by installing large compressed air reservoirs to supply the system. Air-bearing horizontal translation stages are also prone to randomly 'hopping' by several nanometers in the vertical direction, which jars the optical beam train. Electrical noise in the motion stage control electronics can also contribute to random errors in a grating. The velocity-controlled approach to writing gratings is less prone to this error source, since the mechanical inertia of the system can filter the electrical noise, but lower electrical noise is always desirable.

Perhaps the most pernicious and challenging cause of grating errors is low-frequency periodic disturbances. [53] Periodic errors in a grating cause the grating to have sidebands, as detailed below, and if these perturbations are at a low frequency (<10 Hz in our system), the sidebands are separated spectrally from the main grating by only tens of picometers in wavelength. [54] We have found that these sidebands are the major cause of ripple in our chirped gratings. Periodic disturbances are sometimes easy to locate, such as an optical mount resonating at a few tens of Hertz. Levitated optical benches can isolate a fabrication system from most ground-based disturbances, but generally table isolation is marginal when vibrations are below a few Hertz. An active levitation system further minimizes these errors.

2.3.1. Analysis of Periodic Errors [55]

Periodic perturbations in the fiber grating pitch form spectral sidebands that compromise the performance of chirped gratings. These sidebands create spatial etalons in a grating, which cause phase and amplitude perturbations in chirped gratings across the bandwidth of a reflected signal. The sideband model has been used successfully to explain a host of commonly observed chirped grating features. [53] Here we use this model to derive a simple equation that provides an intuitive understanding of phase ripples.

In this model, we represent the grating response as the sum of two parts. The first part is the idealized response of the grating, referred to as the "bulk" property

of the grating, which is commonly calculated with coupled mode equations. [7] The second part of the response is caused by small perturbations to the desired grating. By assuming these perturbations and the resultant sidebands are small, we decouple the bulk properties of a grating from the perturbations and then use the sideband model to calculate the fine structure of the phase and amplitude ripple. This model treats the perturbations to the grating as simple optical etalons with localized reflections. [35] If the etalons are shorter in length than an effective interaction length for a given wavelength in a chirped grating, [56] then the reflection is distributed over a length larger than the etalon spacing, and this model does not apply. In most cases, the rapid variations in phase in a grating are caused by etalons that are much larger than the effective interaction length of the device. We have obtained reasonable agreement between this model and coupled-mode simulations that include periodic disturbances in the grating pitch. [55]

Consider the index profile of a fiber grating with nominal refractive index n_0. The refractive index pattern in a grating may be described as

$$n(z) = n_0 + \frac{\Delta n(z)}{2}\left[1 + m(z)\right]\cos\left[p(z)z + \phi(z)\right], \tag{12}$$

where $m(z)$ is an amplitude perturbation of the refractive index, and $\phi(z)$ is a perturbation of the grating period $\Lambda(z) = 2\pi p(z)$. A grating of period Λ_0 reflects light of wavelength $\lambda_0 = 2n_0\Lambda_0$, and a linearly chirped grating has a position dependent period characterized as $\Lambda(z) = \Lambda_0 + C_0 z$. The desired grating profile has been expressed with $\Delta n(z)$ being the apodization profile and $p(z) \approx p_0(1 - C_0 z/\Lambda_0)$ being the chirp profile. As mentioned, we refer to these as "bulk" grating properties, considered here to be varying spatially with much slower rates than the nominal grating frequency p_0. We also assume that the grating bandwidth is much smaller than the center wavelength ($C_0 z \ll \Lambda_0$).

The creation of sidebands is illustrated by rewriting Eq. (12) with the spatial Fourier components of each perturbation as

$$\begin{aligned} m(z) &= \int \left[W\cos gz + X\sin gz\right] dg \\ \phi(z) &= \int \left[Y\cos gz + Z\sin gz\right] dg \end{aligned} \tag{13}$$

where the amplitudes of the perturbation W, X, Y and Z are functions of the spatial frequency g. In the limit that m and ϕ are $<<1$, $n(z)$ may be rewritten as

$$n(z) = n_0 + \frac{\Delta n}{2}\mathrm{Re}\left[e^{ipz} + \frac{1}{2}\int\left(N^+(g)e^{i(p+g)z} + N^-(g)e^{i(p-g)z}\right)dg\right], \tag{14}$$

where $N^{\pm} \equiv W \mp iX + iY \pm Z$. Spectrally distinct periodicities are present with periods $2\pi/p$, $2\pi/(p+g)$ and $2\pi/(p-g)$, which form the main band and sidebands of the grating, where the spectral separation of the side bands from the main band is $\Delta\lambda \approx \pm\lambda_0 g/p$ when $g \ll p$. All three bands are identical in their bulk phase and amplitude response functions, $p(z)$ and $\Delta n(z)$, but differ in scaling and wavelength offsets.

When periodic disturbances create sidebands, a given location along a grating length can reflect multiple distinct wavelengths. When the grating is chirped, a particular wavelength will then be resonant at a different locations z in the grating and thus etalons are formed. The reflected electric field has four contributions that are of

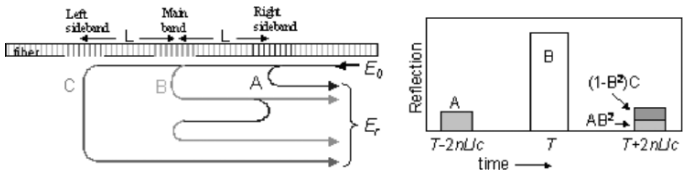

Fig. 6. Diagram of reflections to first order in sideband strength. Light enters from the right (E_0) and is reflected from the grating at various points. The highlighted regions of the fiber grating A,B,C represent the near sideband, main band, and far sideband respectively, for a particular wavelength. (right) Time domain representation of a single pulse after reflection from the band structure, showing early and late echoes.

first order in sideband reflectivity or larger, as shown in Fig. 6. In the time domain, an incoming pulse will produce both early and late echoes according to the travel time. The reflected electric field can be expressed with the four reflections as

$$E_r(k,t) = AE_0(t-\tau) + BE_0(t) + [-AB^2 + C(1-B^2)]E_0(t+\tau) + \cdots \\ + O(A^2, B^2, AB)\}e^{i\varphi}, \tag{15}$$

where

$$A \equiv f\left[\mathrm{Re}\left(N^+(g)\right)\Delta n(k - g/2n_0)/4\right], \\ B \equiv f\left[\Delta n(k)/2\right], \\ C \equiv f\left[\mathrm{Re}\left(N^-(g)\right)\Delta n(k + g/2n_0)/4\right]. \tag{16}$$

The phase $\exp\, i(\omega t - kx)$has been dropped; k is the wavenumber; φ is the ideal phase response; and $\tau = 2n_0L/c$ is the optical propagation delay due to the path length L between the bands. The period chirp determines the path length for each reflection as $L = \Delta\lambda/2n_0C_0 \approx \lambda_0 g/2n_0 pC_0$. The field reflection coefficients for each band, A, B, and C, are a function f of the index contrast $\Delta n(k)$ in Eq. (14), where a change of variable has been used $\Delta n\,(z \to \pi/n_0C_0k)$. The function f [] is difficult to calculate analytically and is normally found numerically, but the reflection magnitudes are not needed to estimate ripple parameters. The negative sign in front of the third term in Eq. (15) is needed because that term reflects at A from the opposite side as the first term.

Assuming that E_0 is coherent, $A, C \ll 1$, and $E_0(k, t \pm \tau) = E_0 \exp(\pm i\phi)$ with $\phi = 2k\, n_0 L$, one can solve Eq. (15) for the intensity I and phase α of the reflected field as

$$I = E_r^* E_r \approx \left[B^2 + 2B(A+C)(1-B^2)\cos(\phi)\right] E_0^2, \tag{17}$$

$$\alpha = \tan^{-1}\frac{\mathrm{Im}\,(E_r)}{\mathrm{Re}\,(E_r)} \approx \varphi - \left(1+B^2\right)\frac{A}{B}\sin(\phi) + \frac{C}{B}\left(1-B^2\right)\sin(\phi). \tag{18}$$

The group delay may be calculated as $c^{-1}(\partial\alpha/\partial k)$, and the group delay ripple, $\Delta\tau$, as a departure from the ideal group delay $c^{-1}(\partial\varphi/\partial k)$ yielding

$$\Delta\tau = \frac{2nL}{c}\left[-(1+B^2)\frac{A}{B} + (1-B^2)\frac{C}{B}\right]\cos\left(2knL\right). \tag{19}$$

The phase ripple is taken as the terms in Eq. (18) perturbing the ideal phase φ. The bulk properties of the grating are determined by the reflectivity B and phase φ of the main band. There is a cutoff period associated with phase ripple stemming from the spectral overlap of A, B and C and the minimum ripple period in Eq. (19) is caused by the longest etalon supported by the grating, or simply when L equals the grating length. This model has been shown to agree well with numerical simulations that use couple-mode theory when the main band is strong ($B > 0.95$). For strong sidebands, the weak perturbation approximation begins to fail and additional terms are needed in Eq. (15) to restore accuracy. [55]

3. Mechanical Integrity and Packaging

Optical components must pass rigorous mechanical tests that are stipulated by organizations, such as Telcordia and the International Telecommunications Union, which specify and recommend testing that manufactured modules must pass before being deployed [e.g., 57, 58]. The more stringent examinations involve thermal testing from –40°C to 80°C and vibration tests where the module is shaken vigorously for extended periods of time. The modules must still operate within specification after being subjected to these examinations. This section focuses on challenges encountered when building long-length fiber grating into dispersion compensation modules. The first part of this section briefly details a fiber protection scheme that we developed to ensure that the fiber grating remains mechanically robust, and the second part discusses thermal packaging that allows the devices to operate over extreme temperature gradients.

Much theoretical and experimental work has been done to understand the optical performance of these long gratings, but little attention has been given to maintaining their mechanical integrity. Little published work exists on these topics for long-length gratings, so we focus on our approaches to solving these issues. References to other work are given when appropriate.

3.1. Write-Through Coatings [59]

In standard FBG production, the protective coating on a fiber must be removed before a grating can be written, after which the fiber is immediately recoated to preserve its mechanical strength. These process steps of stripping and recoating a fiber are time-consuming and tedious, which requires skilled operators, and the bare fiber is prone to damage during grating inscription, reducing production yields. These problems are exacerbated when long lengths of fiber are stripped, handled, and recoated.

Several solutions have been proposed to eliminate these process steps. Most involve writing gratings through specialized, UV-transparent polymeric fiber coatings. [60–62] Writing gratings through a fiber coating may be a solution for short length grating production, but a write-through coating must meet demanding physical and optical requirements to be used in long-length grating production. [63] We developed a process to deposit a diamond-like film (DLF) onto a fiber that is UV-transparent and maintains the mechanical integrity of the fiber close to that of pristine fiber. By depositing a thin film on the fiber ($\sim$1–5 μm thick), fiber geometry, such as concentricity and diameter, is preserved to the degree necessary to produce long gratings. Diamond-like films can also withstand the temperatures that are used to anneal fiber gratings.

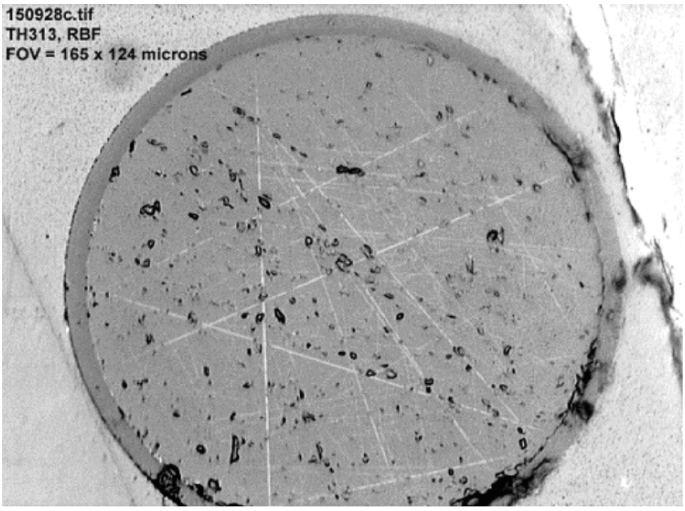

Fig. 7. Photomicrograph of a diamond-like film encapsulated fiber.

Carbon films contain substantially two types of carbon-carbon bonds: trigonal graphite bonds (sp^2) and tetrahedral diamond bonds (sp^3). Diamond is composed almost entirely of tetrahedral bonds; DLF, approximately 50 to 90 % tetrahedral bonds; and graphite, nearly all trigonal bonds. One can manipulate the crystallinity and nature of the bonding of the carbon network to affect the physical and chemical properties of a diamond-like film. Diamond is crystalline and essentially pure carbon, whereas DLF is amorphous and can contain a substantial amount of additional components. [64]

The composition of DLFs can be tailored so that they have desirable diamond-like optical and mechanical properties, such as extreme hardness (1000 to 2000 kg/mm^2 Vickers). Diamond's optical bandgap is 5.56 eV ($\sim$223 nm) and is therefore transmissive in the ultraviolet, but the polycrystalline structure of diamond films causes light scattering from grain boundaries. DLFs are amorphous and don't suffer from light scattering at grain boundaries. The carbon-carbon double bonding that is prevalent in DLF causes undesirable optical absorption below $\sim$500 nm. We have found that incorporating silicon and oxygen atoms into the amorphous diamond-like carbon film during the deposition process alters this absorption. For example, DLFs of 1 μm thick were deposited on quartz slides as the oxygen flow rate during deposition was varied, and the optical transmissions through these slides were measured. Tauc plots were calculated from data, and the band gap was seen to change with oxygen content from $\sim$4.1 to $\sim$4.8 eV. [59] A 1-μm-thick layer of DLF can be $\sim$98 % transmissive at 244 nm.

To deposit DLF onto fibers, a capacitively-coupled reactor system is used that has two electrodes in a plasma reaction chamber. During DLF deposition, the chamber is partially evacuated, and power at radio frequencies is applied to one of the electrodes. A carbon-containing source is introduced between the electrodes to form plasma comprising reactive species in proximity to the electrodes, and to also form an ion sheath

proximate to one electrode. A fiber handling apparatus strips the fiber of its acrylate coating with a continuous-flow acid bath before it enters the reaction chamber and draws it through the reactive ion sheath at a controlled speed. A uniform thickness film of $\sim$2 μm can be deposited onto the fiber, as shown in the micrograph in Fig. 7. The variations in film thickness along the fiber were immeasurable with our equipment; we estimate them to be $<$10 nm. Most failure mechanisms in long length grating manufacture due to this film, either in surface quality, optical transparency, or mechanical strength, could ultimately be traced to the transition zone between the fiber acid strip station and the deposition chamber. This problem can be addressed by utilizing liquid bearings that seal the vacuum chamber from the environment and prevent the bare fiber from impacting hard surfaces.

The mechanical properties of DLF- encapsulated fibers were compared with those of acrylate-coated fibers and uncoated fibers. The DLF-encapsulated fibers were insensitive to handling, such as by wiping the fibers between fingers or wrapping them on mandrels. In contrast, stripped fibers easily broke under such handling. The Weibull parameters of these fibers are the same as that of pristine acrylate-coated fibers, even when 0.5 m gauge lengths were tested. [65]

To ensure long-term reliability, the gratings are recoated with standard fiber acrylate coatings, which have glass transition temperatures below the lowest operating temperature of the device. We refined the recoat process to avoid defects, voids, and thickness variations in the recoat to avoid unwanted localized strain gradients, which become apparent during temperature cycling. The DLF coating must be removed before the fiber can be cleaved and spliced, which is accomplished by thermally shocking the film on the fiber end by heating it to $>$450°C and then letting in cool rapidly to room temperature. The resulting stripped fiber can then be handled as any other fiber.

An uncoated standard fiber cannot be wrapped around the spool used to write long gratings and retain its mechanical integrity, but gratings in the DLF-encapsulated fiber can withstand 200 kpsi proof testing. The optical and mechanical properties of this film allowed fabrication of long length fiber gratings that worked well as dispersion compensators in optical communications systems. [65]

3.2. Thermal Stabilization [66]

Fiber Bragg gratings are excellent temperature sensors, which raises concerns about the thermal stability of DCGs during operation. [67] The center wavelength of an uncompensated grating will shift at $\sim$0.01 nm/$^\circ$C for standard fiber, which is unacceptable for many applications, so several researchers have designed packages to minimize this wavelength shift [e.g., 68]. Since direct-write methods can produce gratings with very wide bandwidths, a shift in the center wavelength of a grating will not change significantly the dispersion of a low dispersion-slope DCG, but a thermal gradient along the length of a grating will affect its dispersion. If a grating experiences a thermal gradient along its length, then one end of the grating will shift in wavelength more than the other. For example, if a 10°C temperature gradient is experienced across a 1-nm bandwidth grating, the bandwidth of the device will change to $\sim$1.1 nm and cause roughly a 10% change in device dispersion. Investigators have exploited this effect to produce tunable DCGs by imposing thermal gradients along the grating length via resistive heating. [69]

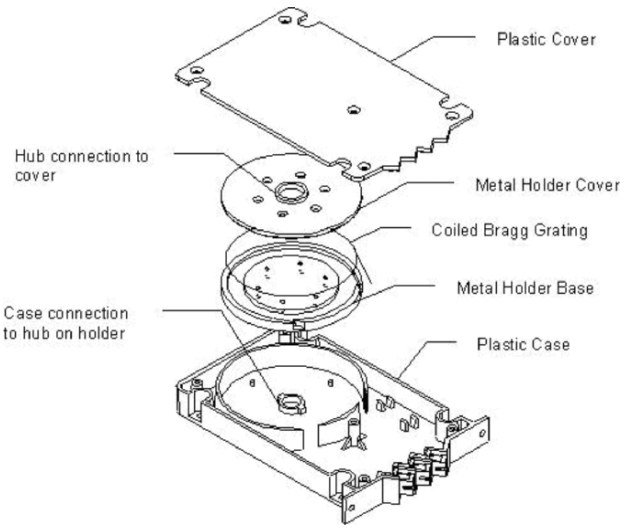

Fig. 8. Exploded view of a package designed to minimize thermal gradients along the length of long fiber gratings.

The effects of thermal gradients can be reduced across a DCG package by embedding the grating in a thermal conductor surrounded by a thermal insulator, which keeps the grating length at a nearly uniform temperature. The package performance was modeled with finite element methods, confirmed the results experimentally, and have found no measurable perturbation in the device dispersion during thermal testing, even as 80°C thermal gradients were imposed across the module. One could also actively stabilize the temperature along the length of a grating, say, thermo-electrically, which may be a desirable approach when the grating is incorporated into optical amplifier designs.

The DCG package, detailed in Fig. 8, is 19 cm long, 12 cm wide, and 2.5 cm thick. As shown, the grating is coiled and placed in a groove that is machined into an aluminum 10-cm-diameter metal base, and then a metal lid is secured on top of the base, effectively encasing the grating inside a 1-cm-thick thermal conductor. The metal holder is then positioned inside a plastic housing and spaced from the housing walls to ensure that an air gap >1 mm exists between the plastic housing and the metal holder, thereby surrounding the metal holder with a thermal insulator. The outer housing may also be made from thermally conductive materials, such as aluminum or copper, instead of insulating plastic, but a metal outer package offers little additional thermal stability of the DCG module and is considerably more expensive in high volume manufacturing than molded plastic parts. As will be shown, the DCG dispersion is unaffected when the plastic outer package is used, even under extreme temperature gradients by telecommunications standards.

Finite element techniques were employed to evaluate the thermal properties of initial package designs (ANSYS, Version 5.7). Temperature gradients were imposed

across various regions of a DCG package, and the temperature profiles in the grating chamber were simulated. [66] Fixed temperature values were imposed on the outer surface of the plastic case to create a sharp temperature variation of 80°C across the top and bottom surfaces, which was considered to represent a worse case scenario in telecommunications applications. The model indicated <0.6°C temperature variation within the fiber chamber.

We fabricated –1360-ps/nm-dispersion ∼1.6-m-long gratings and built these devices into dispersion compensation modules with the package of Fig. 8. The gratings were annealed before packaging at 200°C for 30 minutes to stabilize them. To monitor the temperature of the metal holder, we embedded 75-μm-diameter thermocouples at four locations around its periphery in the DCG horizontal plane to within 150 μm of the grating, and then we directed hot and cold air streams onto opposing corners of the package to create temperature gradients across it. The temperature gradient along the fiber length after making the two package extremes –10°C and +70°C (80°C gradient) was measured to be ∼0.4°C. Although the fine structure of the fiber grating, such as phase ripple and residual dispersion, shifted in wavelength with the overall temperature of the fiber holder, the overall dispersion of the DCG remained at a constant –1360 ps/nm. [66] We estimate that temperature gradients >2°C are needed across the fiber holder to alter the DCG optical performance, which will not occur with the proposed package until a temperature gradient >300°C is imposed across the entire package.

4. Device Specifications

With the availability of gratings of sufficient quality for use in optical communications systems, grating manufacturers and system designers need a means to specify these devices. A telecommunications system supplier must be able to clearly stipulate grating specifications to a grating vendor and must be confident that gratings that meet these specifications will perform well in their system. This section discusses parameters of a chirped grating that need to be characterized before being designed into telecommunications systems. We start with a 'legacy' specification called group delay ripple and show how phase ripple characterization is more informative. We mention the effects of insertion loss ripple and residual dispersion, and then offer a short discussion on polarization mode dispersion in chirped gratings.

4.1. Group Delay Ripple

Early studies focused on using the group delay ripple amplitude to characterize grating quality, but found that this amplitude correlated poorly with device performance in optical communications systems. [70, 71] Ripple amplitude specifications did indicate general device quality and could roughly separate useful and faulty gratings, yet often gratings with relatively low ripple amplitude did not work well in a system compared with those with much larger ripple amplitude. Several researchers conducted numerical simulations of the effects of group delay ripples on system performance and found that these effects classified as either dispersion error or inter-symbol interference. [72–74] The magnitude of each effect depended on the ripple period, explaining why system performance predictions with delay ripple amplitude alone were difficult. When the

delay ripple periodicity is large compared to the signal bandwidth, the dominant effect is a modification of the gradient of the delay curve and thus the dispersion of the device varies across its bandwidth, called residual dispersion. When the ripple period approaches the signal bandwidth, the ripple effect is much smaller than that estimated by dispersion error predictions and is eventually averaged out by the signal bandwidth. The mathematical definition of dispersion fails with very dense ripple, since it is correct for a linear group delay change only, which is clearly not the case for dense delay ripples.

As discussed in previous sections, grating defects reflect some of the transient light, form etalon cavities, and give rise to multipath interference. If the cavity has a round trip transit time shorter than the duration of a single bit, then the resulting phase distortions generate dispersion. When the cavity becomes longer and the round trip time exceeds the duration of the bit, the individual reflections separate from each other and the grating responds by creating echoes of the impinging pulse. The magnitude of the echo is proportional to the group delay ripple amplitude multiplied by its period, which is the amplitude of the phase ripple. [74] To illustrate this point, assume the group delay ripple t_g is co-sinusoidal with period f_r and amplitude Δt_g as

$$t_g(\omega) = -\Delta t_g \cos \frac{\omega}{f_r}. \tag{20}$$

The transfer function of this perturbation is

$$H(\omega) \equiv e^{i\theta_r} = K e^{i(\Delta t_g f_r \sin \omega / f_r)}, \tag{21}$$

where the phase ripple θ_r is the integral of the group delay ripple and K is a constant. The resulting impulse response can then be calculated as

$$\begin{aligned} h(t) &\propto \sum_{i=-\infty}^{\infty} J_i(\Delta t_g f_r) e^{ji\varphi_0} \delta(t + i/f_r) \\ &\approx \delta(t) + \frac{\Delta t_g f_r}{2} \left[e^{j\varphi_0} \delta(t + 1/f_r) - e^{-j\varphi_0} \delta(t - 1/f_r) \right] \end{aligned} \tag{22}$$

with the assumption that $\Delta t_g f_r \ll 1$. In Eq. (22), J_i are Bessel functions of the first kind, δ are delta functions, and φ_0 is the relative phase between the signal-carrier frequency and the group delay ripple. Note that the impulse response in Eq. (22) has echoes that are proportional to the amplitude of the group delay ripple multiplied by its frequency, which is the phase amplitude of Eq. (21). Indeed researchers have found that for a chirp-free NRZ signal, the worst case relative eye closure (REC), when $\varphi 0 = n\pi$, is given by

$$\text{REC} \propto \begin{cases} \Delta t_g f_r & f_r \le f_{\text{bit}} \\ \Delta t_g f_r \left[1 - g(1/f_r)\right] & f_r > f_{\text{bit}} \end{cases}, \tag{23}$$

where $g(t)$ is the normalized pulse shape in the electric field representation. The REC is proportional to the amplitude of the phase ripple.

Group delay ripple measurements. Group delay can be measured directly or calculated from phase measurements. [75] Since the group delay ripple in chirped gratings is typically dense, one must carefully measure the device with the highest resolution possible to extract useful information. As discussed, early researchers were confounded

when trying to relate group delay ripple amplitude to system performance because they neglected the ripple frequency information, but often researchers didn't clearly specify their measurement parameters when the delay ripple was characterized. Here we illustrate how measurement parameters must be carefully selected to yield uncorrupted data.

A common method of determining group delay is the modulation phase-shift method. [75–77] Typically the output of a narrowband tunable optical laser is intensity modulated and applied to the device under test (DUT). The transmitted signal from the DUT is detected and the phase of its intensity modulation is measured relative to that driving the input signal. These phase measurements are repeated at intervals across the wavelength range of interest, and then a relative time delay between the measurement points is calculated. The next discussion, which closely follows the presentation in [76], considers the case of amplitude modulation of a light carrier with angular frequency ω_0 by a sinusoidal signal of angular frequency ω_m. The input signal electric field E_i can be written as

$$\begin{aligned}\frac{E_i(t)}{E_0} &= \cos\omega_0 t\,(1+\hat{x}\cos(\omega_m t)) \\ &= \cos\omega_0 t + \frac{\hat{x}}{2}\cos\left[(\omega_0+\omega_m)\,t\right] + \frac{\hat{x}}{2}\cos\left[(\omega_0-\omega_m)\,t\right]. \end{aligned} \tag{24}$$

This signal is launched into the DUT, which uniquely modifies the amplitude and phase of each of the three discrete spectral lines in Eq. (24), to yield an output electric field E_{out} as

$$\begin{aligned}\frac{E_{\text{out}}(t)}{E_0} &= \hat{x}_0\cos\left(\omega_0 t+\varphi_0\right) + \frac{\hat{x}_+}{2}\cos\left[(\omega_0+\omega_m)\,t+\varphi_+\right] \\ &\quad + \frac{\hat{x}_-}{2}\cos\left[(\omega_0-\omega_m)\,t+\varphi_-\right], \end{aligned} \tag{25}$$

where

$$\begin{aligned}&\hat{x}_0 \equiv |H(\omega_0)|\,,\ \hat{x}_+ \equiv \hat{x}\cdot|H(\omega_0+\omega_m)|\,,\ \hat{x}_- \equiv \hat{x}\cdot|H(\omega_0-\omega_m)|\,, \\ &\varphi_0 \equiv \varphi(\omega_0),\ \ \varphi_+ \equiv \varphi(\omega_0+\omega_m),\ \ \varphi_- \equiv \varphi(\omega_0-\omega_m). \end{aligned} \tag{26}$$

At a direct detection receiver, the output signal is proportional to the mean optical power and can be calculated as

$$\left|\frac{E_{\text{out}}(t)}{E_o}\right|^2 \propto x_{\text{out}} = A + B\cos(\omega_m t+\Psi) + C\cos(2\omega_m t+\Phi). \tag{27}$$

Typically a network analyzer or vector voltmeter is used to determine the amplitude and phase of the sinusoidal component at the modulation angular frequency ω_m. These terms in Eq. (27) are defined as

$$B = \hat{x}_0\sqrt{\hat{x}_+^2+\hat{x}_-^2+2\hat{x}_+\hat{x}_-\cos(\varphi_++\varphi_--2\varphi_0)} \tag{28}$$

for the amplitude and

$$\Psi = \frac{\varphi_+-\varphi_-}{2} + \arctan\left(\frac{\hat{x}_+-\hat{x}_-}{\hat{x}_++\hat{x}_-}\tan\frac{\varphi_++\varphi_--2\varphi_0}{2}\right) \tag{29}$$

for the measured phase. From measurement of either the amplitude or phase, the group delay characteristics of the DUT can be derived.

In the amplitude method, the phase distortion is evaluated by sweeping the modulation frequency over a given frequency range. A plot of the amplitude measurements exhibits characteristic dips corresponding to amplitude modulation of the output signal. [75, 76] Chirped gratings often exhibit rapidly varying amplitude and phase variations, which complicates calculations relying on Eq. (28). The most common measurement is to determine the phase Ψ of the output signal. In a simplified case where the amplitude distortions are negligible,

$$\Psi \approx \frac{\varphi_+ - \varphi_-}{2}. \tag{30}$$

The measured phase is the average of the phase distortions between the locations of the two sidebands created by the modulation in Eq. (24). If the modulation frequency is too large compared to the delay ripple frequency, the measurement will create a moving-average of the phase ripple amplitude across the grating bandwidth, effectively smoothing the ripples, and decreasing the measured ripple amplitude. [77]

The best method to correctly characterize a given grating design is to take measurements at a relatively low modulation frequency, say 200 MHz, and then compare these measurements with even lower frequency measurements. The amplitude of the delay ripple should not increase with decreasing modulation frequency when the modulation frequency is sufficiently low. For chirped gratings of a few cm in length, this frequency is typically <200 MHz, but for very long length gratings this frequency can be <25 MHz. Generally measurements made with ∼1 GHz modulations or greater will significantly under-represent the actual ripple amplitude.

4.2. Phase Ripple [78]

The amplitude of the phase ripple, as opposed to that of the group delay ripple, is more indicative of the performance of a chirped grating in a communications system. [66,68,78–80] Here we develop a theory that relates this performance to the variance of the amplitude of the phase ripple that has been weighted by the incoming signal spectrum. The phase ripple in a spectral window,$\phi(\omega)$, may be expressed with a Fourier series as

$$\phi(\omega) = \sum_{k>0} A_k \cos(\omega\, t_k + \theta_k), \tag{31}$$

where ω is the optical frequency, and A_k and θ_k are the weight and phase associated with the kth Fourier component. Studies have shown that variations in grating insertion loss have a much smaller impact on system performance than the phase distortions [e.g., 73]. This model can be extended to account for insertion loss variations, but here we set the amplitude of the grating reflectivity to unity, and thus its transfer function becomes

$$H(\omega) = e^{j\phi(\omega)} = \prod_{k>0} \sum_{n=-\infty}^{+\infty} J_n(A_k) j^n e^{jn(t_k\omega+\theta_k)}. \tag{32}$$

By transforming the transfer function into the time domain, one finds that each component of the Fourier decomposition creates echo pulses centered about the original input pulse, as detailed in the previous section. For small A_k's, this expression simplifies considerably to $H(\omega) \approx 1 + j\phi(\omega)$, where the second term of the expansion

identifies the unwanted phase perturbations to the transfer function. For a given input signal consisting of one high bit with spectrum $S_i(\omega)$, the energy loss from this bit due to phase ripples can be calculated by integrating the energy in the output signal with time t, excluding $t = 0$, which is equivalent to integrating the spectral power of the output signal spectrum $S_o(\omega)$ without the DC component (Parseval's Theorem), i.e.,

$$\Delta E = \int |S_i(\omega)[H(\omega) - 1]|^2 d\omega \approx \int |S_i(\omega)\phi(\omega)|^2 d\omega \equiv \int |\phi_w(\omega)|^2 d\omega, \quad (33)$$

where ϕ_w is the phase ripple weighted by signal spectrum. The power penalty is related to the system eye closure as

$$\text{Power Penalty (dB)} \propto -10\log_{10}(1 - \Delta E - \varepsilon\sqrt{2\Delta E}), \quad (34)$$

where the input energy has been normalized. The incoming pulse loses energy ΔE due to the phase ripple and may also be reduced by interference with echoes from neighboring pulses, each of height $\Delta E/2$. This energy reduction due to inter-symbol interference is expressed as $\varepsilon\sqrt{2\Delta E}$, which is scaled by the factor ε to account for the relative phase between the echo and the input pulse and the temporal distribution of the echo energy. In previous studies, grating ripple was modeled as a single-frequency sinusoid, which would create distinct echoes of the incoming pulse. The worst-case scenario for power penalty estimation, where ε becomes unity, occurs when the echoes are fully overlapped and π-shifted relative to the input pulse.

The phase ripple of typical gratings consists of several frequencies, instead of a distinct single periodicity, and therefore the echoed pulse energy is smeared temporally. In this scenario, the scaling factor ε is significantly reduced, and the energy loss from the pulse dominates the power penalty due to the phase ripple,

$$\text{Power Penalty (dB))} \propto -10\log_{10}(1 - \Delta E) \approx K\sigma_w^2, \quad (35)$$

where σ_w is the standard deviation of ϕ_w and K is a scaling coefficient.

When the nonreturn-to-zero (NRZ) modulation format is used, different bit lengths with unique spectral extents occur and therefore the spectral weighting used to calculate the variance of the phase varies. In this instance, σ_w^2 should taken as the weighted average of the weighted variance of each bit length as

$$\overline{\sigma_w^2} = \sum_{i=1} P_i \cdot \sigma_{w_i}^2, \quad (36)$$

where P_i is the probability of occurrence of pulses of "i" bit length units and σ_{wi} is their respective standard deviations.

This analysis method is illustrated in Fig. 9 by analyzing the phase ripple from an actual fiber grating. The unweighted and weighted ripple in a 20 GHz window is displayed as the center wavelength of the weighting function moves by 40 pm from 1597.058 to 1597.018 nm. The solid curves give the phase ripple weighted by the spectrum of an isolated high-bit in a 10-Gb/s NRZ signal (100 ps duration), which is shown as a dotted curve in Fig. 9(a). We simulated the performance of this grating as a dispersion compensator in a 10 Gb/s NRZ communications system with a 2^9-1 pseudo-random binary sequence (PRBS) and obtained the eye diagrams in Fig. 10. The

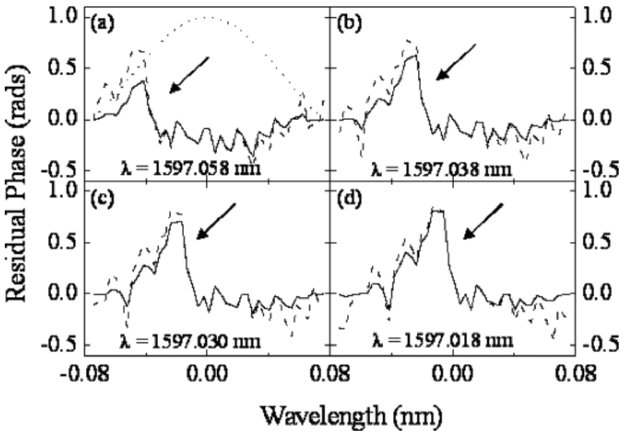

Fig. 9. Dashed curves show the phase ripples within a 20 GHz spectral window at four different center wavelengths and the solid curves correspond to the phase ripples weighted by a sinc-function [(dotted curve in (a)].

dramatic change in eye closure as the center wavelength of the test signal is moved < 40 pm is due mainly to the location of the large phase variation (indicated by an arrow) in Fig. 9 relative to the input signal center wavelength. By weighting the phase ripple with the signal spectrum before taking its variance, one accounts for both ripple magnitude and its relative position to the signal center wavelength.

We measured the distortion-induced power penalty of scores of chirped gratings with various bandwidths, dispersions, and quality on the 10 Gb/s NRZ optical communications test-bed described in [67]. With these comparisons, K was found to be $\sim$ 70 dB/radian^2, which corresponds to $\sigma_w = 120$ milliradian for a 1-dB power penalty.

In practice, this method of weighting the phase ripple by the signal spectrum is difficult to implement in a manufacturing and sales environment where customer systems vary, so simpler, less accurate methods are often used to specify devices. A common specification for this is the amplitude of the phase ripple. [80]

4.3. Residual Dispersion and Insertion Loss Ripple

Phase variations within a given spectral window feature typically a fast oscillatory structure (phase ripple) superimposed on a slowly varying curve (residual dispersion). [79] The residual dispersion broadens a pulse and forces energy into neighboring time slots, while phase ripples carry the energy generally further from the pulse. Estimates of system power penalties due to residual dispersion can be estimated with conventional techniques. [81]

If the amplitude variations are significant, then they must also be included when estimating the performance of a given grating device [72]. Amplitude and phase ripples constitute the real and imaginary part of the grating transfer function, i.e.,

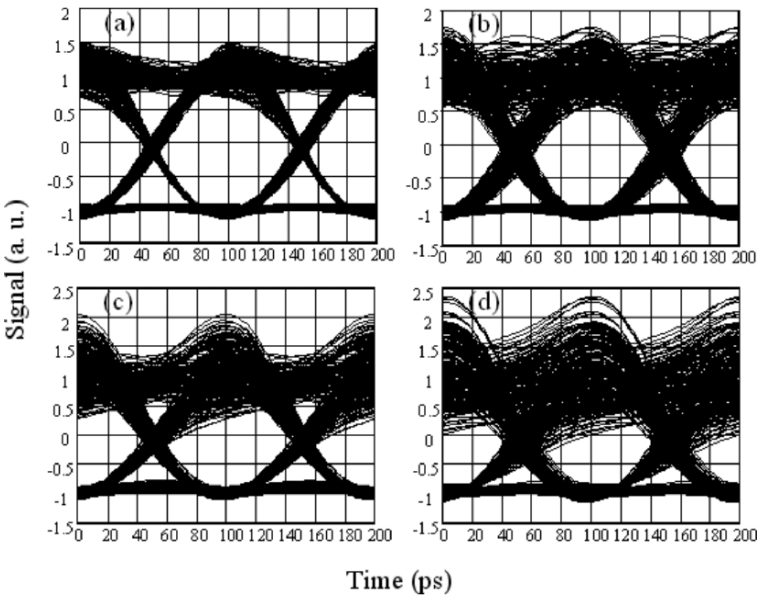

Fig. 10. Eye diagrams simulated at the wavelength positions given in Fig. 9.

$$H = [1 + \beta(\omega)]e^{j\phi(\omega)} \approx 1 + \beta(\omega) + j\phi(\omega),$$

where $\beta(\omega)$ is the amplitude variation from unity, so amplitude ripples can be handled in a manner similar to that presented in the previous section.

4.3.1. Polarization Mode Dispersion

Many effects may cause birefringence Δn in fiber gratings, but generally the largest effect is due to the side-write fabrication process. [82] Polarization mode dispersion (PMD) measurements are complicated by group delay ripple, which may cause the measured differential group delay (DGD) between polarizations at a given wavelength to imply nonsensically large PMD values if common definitions are used, [83] i.e. the measured DGD implies complete eye-closure, yet little measurable difference in system performance is seen as the polarization space is explored in system test bed measurements. While it is common, and sometimes desirable, to measure both DGD and GDR with high resolution, this information is redundant in the case of chirped FBGs. A proper discussion of PMD in chirped gratings is beyond the scope of this chapter and we direct the reader to other sources for more information. [84–88]

The delay ripple in chirped gratings causes the differential group delay (DGD) to vary rapidly with wavelength, making measurements difficult to interpret. The value that system designers need for budgeting PMD in the system design is related to the underlying birefringence of the device, but this is masked by the GDR-dominated DGD measurements made with low-bandwidth techniques. A ‘low-bandwidth’ technique is

one where the spectral bandwidth of each point in the measurement is much less than that of the system signal for which the grating device is intended, while a 'high-bandwidth' technique has a bandwidth comparable to or greater than that of the signal. Phase ripple should be measured with low-bandwidth measurements, as discussed in Section IVA, while PMD should be measured with high-bandwidth techniques to avoid double-counting the phase ripple. [83,88]

The differential group delay Δt can be well approximated as $\Delta t \approx D\Delta\lambda$, where D is the grating dispersion and $\Delta\lambda/\lambda = \Delta n/n$. This simple relation implies that the DGD increases linearly with dispersion. However, in practice weaker gratings having less induced birefringence are needed for higher dispersion devices, since the coupling interaction length for a given wavelength increases with dispersion. Recent reports indicate that photoerasure techniques may be able to reduce the induced birefringence and lower the overall DGD of a device. [89]

5. Applications

The advantages that chirped grating solutions offer for dispersion management over competing technologies cannot be overlooked. Gratings can be fabricated with complex dispersion profiles to solve system design challenges that other technologies cannot address. The desirability of grating modules over conventional techniques will likely change as grating technology matures, market conditions force component and system designs to change, and higher speed and power systems are deployed. This section mentions four potential areas where long length chirped gratings may eventually find significant commercial interest: long-haul, submarine, and metropolitan telecommunications, and chirped pulse amplification.

5.1. Long-Haul Telecommunications

Dispersion compensating fiber (DCF) is used widely today to solve chromatic dispersion problems in high-speed optical communications systems. New DCF designs attempt to match the dispersion and dispersion slope to be opposite to that of a given transmission fiber, but often these DCF designs don't exactly match the dispersion characteristics of their intended fiber and thus leave a residual dispersion that accumulates over multiple spans of transmission fiber. Since DCF designs can be complicated and difficult to manufacture, several transmission fibers do not yet have a matching DCF solution. In addition, it seems very unlikely that a perfectly matched DCF design will ever be developed for some fibers with highly complex dispersion characteristics.

Single-channel dispersion compensating gratings, with bandwidths <1 nm, have been deployed in communications systems, but multi-channel large-bandwidth devices have yet to gain widespread acceptance. As discussed, fabrication errors create ripples in the delay curve and thus inaccuracies in the dispersion correction. The wavelength of a given channel in a system may be adjusted finely to make a particular grating performance acceptable, but if the laser wavelength or the grating structure drifts slightly, the system power penalty with a poor grating could increase by several dB, rendering the device useless.

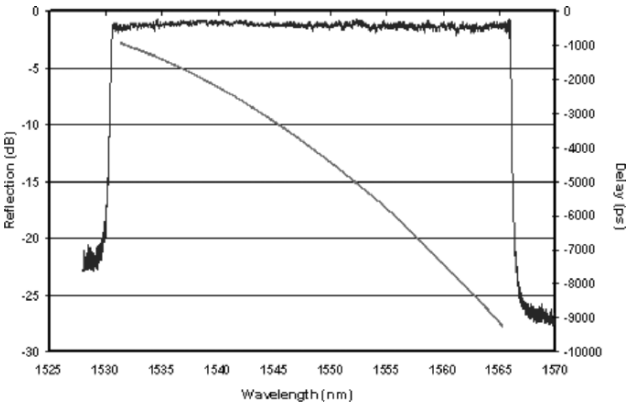

Fig. 11. Reflection amplitude and delay spectra from a >30 nm bandwidth chirped fiber Bragg grating.

As an example, we discuss a full-band grating that yielded <0.3 dB power penalty due to distortion across its full device bandwidth in a 10 Gb/s NRZ optical communications system. [65] This grating, fabricated in DLF-coated fiber, matched the dispersion characteristics of an 80 km length of LEAF optical fiber and had a central wavelength at ∼1546 nm, >30 nm wide bandwidth, ∼ −330 ps/nm dispersion at 1550 nm, and a dispersion slope of ∼ −7 ps/nm^2. The resulting reflection and its group delay from the grating are shown in Fig. 11. We measured the group delay with the modulation-phase shift method at a 60-MHz modulation frequency and 1-pm step size and then integrated the result to obtain the reflected optical phase information. The standard deviation of the phase ripple was calculated after weighting it with a 20 GHz sinc-function moving-window and was <50 milliradians across the full bandwidth of the device, indicating that this device has <0.4 dB of distortion-induced system power penalty in an externally-modulated 10 Gb/s NRZ system (see section 4.2). The power penalty was measured with a communications test system across its full bandwidth in 10 pm steps, and the power penalty was <0.3 dB across the full bandwidth of the device. [65]

The excellent performance of this device was obtained likely because the delay ripple period was <20 MHz, which significantly reduced the magnitude of the echo pulses. Other testing at 40 Gb/s showed similar system performance levels as the 10 Gb/s system, but these grating devices performed poorly at *low* data rates (!), such as at 155 Mb/s (OC-3) and 622 Mb/s (OC-12) bit rates [unpublished data]. One can hypothesize that this reduction in system performance at low rates is because the spectral bandwidth of the signal does less smoothing of the ripple, as detailed in section 3, but verification of this point is needed. Some system designs have channels operating at different data rates across their bandwidth, so the low data rate performance may limit the application of these gratings in some instances. The PMD of this device was also 2 to 3 ps, which is high and must be reduced for deployment in high-speed

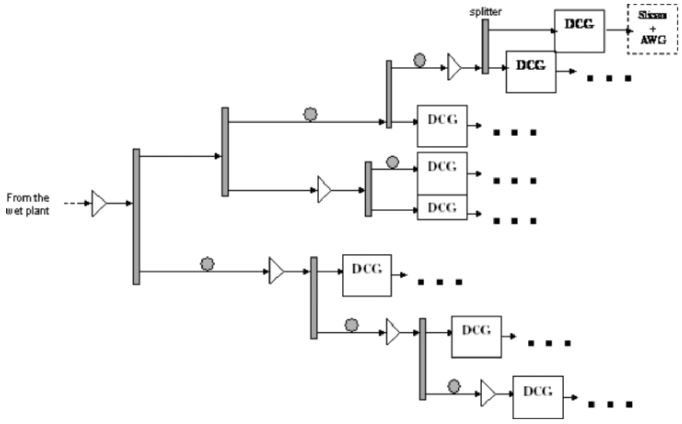

Fig. 12. Sub-sea 'tree' terminal architecture used to correct for residual dispersion.

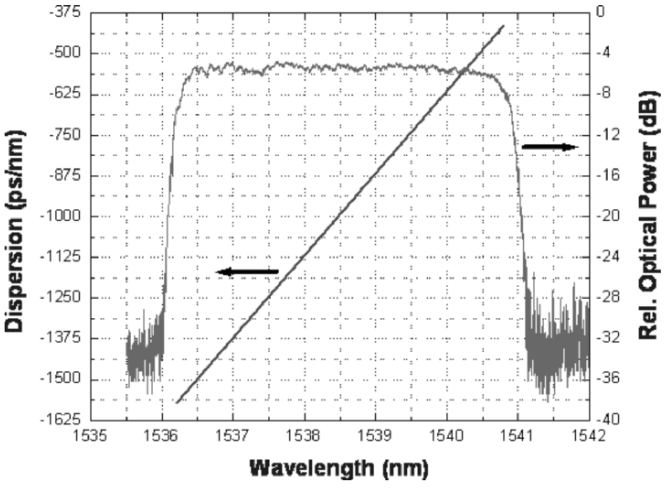

Fig. 13. Nonlinearly chirped grating designed for the terminal architecture of Fig. 12.

systems. Perhaps the most troubling specification of this grating was that the insertion loss ripple was $\sim$1 dB, which makes it difficult for a system designer to maintain acceptable signal-to-noise ratios across the channels.

5.2. Submarine Telecommunications Systems

Sub-sea communications systems often deploy alternating links of normal and anomalous dispersion fiber to minimize the accumulated dispersion across thousands of kilo-

meters of transmission fiber. The dispersion slopes of the fibers used in these alternating links do not match one another exactly, so the only the channels in the center of the system bandwidth accumulate little dispersion after very long transmission lengths. Channels at the edges of the bandwidth accumulate large amounts of residual dispersion that often varies considerably from one channel to the next. Designers of these systems often create a tree-like structure in the terminal architecture to combat this problem, shown in Fig. 12, where successive layers of splitters, DCF, and amplifiers correct the residual dispersion in each channel. The grating shown in Fig. 13 has a 250 ps/nm^2 dispersion slope over a $>$4 nm bandwidth, where the dispersion across this bandwidth ranges from –1500 to –500 ps/nm. By including these devices into the sub-sea terminal architecture, a designer can save considerably on terminal cost and volume. Long-length gratings, as opposed to channelized dispersion management solutions such as sampled fiber gratings and Gire-Tournois etalons, are particularly well suited for this application, since often the channel spacings are irregular. Another fiber grating device, demonstrated by Ibsen et al., could also address this system design issue. [90] The design of this device employed a sophisticated apodization technique to create a dispersion-slope correction grating.

5.3. Metropolitan Telecommunications Systems

Metropolitan and regional network expansion is expected to drive communications systems growth in the near term. As low cost and high-speed components become readily available, an evolution of these networks to 10 Gb/s is expected, in part to ensure compatibility with backbone networks. These systems must be cost effective, flexible, and occupy little space. To meet these needs, system designers employ directly-modulated or electro-absorption modulated lasers (DMLs or EMLs) as transmitters. These devices are simple and inexpensive, but they produce pulses that are considerably chirped. The carrier frequency of the transmitted pulse varies with time, which causes a broadening of the transmitted spectrum and degrades dispersion limits compared to unchirped pulses.

Dispersion compensating fiber is a choice for dispersion management in metropolitan systems, but fiber-based solutions restrict system design and flexibility. Often system designers want to pre-compensate for the dispersion and launch very high powers into the lines to avoid in-line amplifiers. Partial-band DCGs can have low insertion loss ($<$ 2 dB), reduced nonlinear optical interactions, and a small package size. System users can expand the capability of their system with gratings by single- or few-channel increments in an effective manner. In earlier work, we demonstrated that chirped gratings would work well with EML transmitters. We used a 12-nm-bandwidth 1360-ps/nm-dispersion fiber gratings and an EML transmitter in a 10-Gb/s communications system and demonstrated a maximum power penalty $<$2 dB over a wide range of standard fiber lengths (30 to 110 km). [91] Chirped gratings may find early acceptance in the very cost-sensitive metropolitan systems market if they can be produced in a cost-effective manner.

5.4. Chirped Pulse Amplification

A number of important applications for femtosecond lasers have appeared over the past several years, which has initiated a demand for practical turnkey technologies

for optical pulse generation. [92] Generally, ultrashort-pulse solid-state lasers are very complex systems with a large number of components inside a long free-space cavity. New generations of these lasers are emerging that use chirped pulse amplification techniques with optical fiber and semiconductor amplifiers. Long length optical fiber gratings are likely to play a part in pulse stretching, since enormous stretches ($>$10s of ns) are possible at a low insertion loss. Often these stretches are needed at wavelengths, such as 980 nm, where the insertion losses of fiber-based approaches are prohibitive. Preliminary work has been reported in this area and more reports are likely in this rapidly evolving area of research. [93]

6. Summary

Many technical obstacles that have prevented chirped gratings from being used as dispersion compensators in optical communications systems have been overcome. Their adaptation by system designers is likely to begin in areas where DCG specifications significantly outweigh existing solutions, such as high figure-of-merit metro applications and large dispersion slope correction.

References

1. K.O. Hill, B. Malo, F. Bilodeau, and D.C. Johnson, Photosensitivity in optical fibers, Ann. Rev. Mater. Sci., **23**, 125–157 (1993).
2. W.W. Morey, G.A. Ball, and G. Meltz, Photoinduced Bragg gratings in Optical fibers, Opt. Photon. News, **5**, 8–14 (1994).
3. R.J. Campbell and R. Kashyap, The properties and applications of photosensitive germanosilicate fibre, Int. J. Optoelectron., **9**, 33–57 (1994).
4. P.St.J. Russel, J.-L. Archambault, and L. Reekie, Fibre gratings, *Physics World*, 41–46, October 1993.
5. I. Bennion, J.A.R. Williams, L. Zhang, K. Sugden, and N.J.Doran, UV-written in-fibre gratings, Opt. Quant. Electron., **28**, 93–135 (1996).
6. See the invited papers in the special issue of J. Lightwave Technol., **15**, (1997).
7. T.A. Strasser and T. Erdogan, Fiber gratings devices in high-performance optical communications systems, in *Optical Fiber Telecommunications IVA*, edited by I. Kaminow and T. Li. (Academic Press, San Diego, 2002).
8. A. Othonos and K. Kalli, *Fiber Bragg Gratings, Fundamentals and applications in telecommunications and sensing* (Artech House, Boston, 1999).
9. R. Kashyap, *Fiber Bragg Gratings* (Academic Press, San Diego,1999).
10. K.O. Hill Y. Fujii, D.C. Johnson, and B.S. Kawasaki, Photosensitivity in optical fiber waveguides: applications to reflection filter fabrication, Appl. Phys. Lett., **32** 647–649 (1978).
11. J.L. Zyskind, J.A. Nagel, and H.D. Kidorf, Erbium-doped fiber amplifiers for optical communications, in *Optical Fiber Telecommunications IIIB*, edited by I.P. Kaminow and T.L. Koch (Academic Press, San Diego, 1997), pp. 13–68.
12. F. Ouellette, Dispersion cancellation using linearly chirped Bragg filters in optical waveguides, Opt. Lett., **12**, 180–182.

13. A.D. Kersey, M.A. Davis, H.J. Patrick, M. LeBlanc, K.P. Koo, C.G. Askins, M.A. Putnam, and E.J. Friebele, Fiber gratings sensors, J. Lightwave Technol., **15**, 1442–1463 (1997).
14. A. Galvanauskas, M.E. Fermann, D. Harter, K. Sugden, and I. Bennion, All-fiber femtosecond pulse amplification circuit using chirped Bragg gratings, Appl. Phys. Lett., **66**, 1053–1055 (1995).
15. A. Grunnet-Jepsen, A. Johnson, E. Maniloff, T. Mossberg, M. Munroe, and J. Sweetser, Spectral phase encoding and decoding using fiber Bragg gratings, in Proceedings of 1999 Optical fiber Communications, San Diego, CA, 1999, Paper PD33.
16. P.C. Chou, H.A. Haus, and J.F. Brennan III, Reconfigurable time-domain spectral shaping of an optical pulse stretched by a fiber Bragg grating, Opt. Lett., **25**, 524–526 (2000).
17. N.G.R. Broderick, D.J. Richardson, and M. Ibsen, Nonlinear switching in a 20-cm-long fiber Bragg grating, Opt. Lett., **25**, 536–538 (2000).
18. J.A.R. Williams, L.A. Everall, I. Bennion, and N.J. Doran, Fiber Bragg grating fabrication for dispersion slope compensation, IEEE Photon. Tech. Lett., **8**, 1187–1189 (1996).
19. L. Quetel, L. Rivoallan, M. Morvan, M. Monerie, E. Delevaque, J.Y. Guilloux, and J.F. Bayon, Chromatic dispersion compensation by apodized Bragg gratings within controlled tapered fibers, Opt. Fiber Technol., **3**, 267–271 (1997).
20. M.G. Xu, A.T. Alavie, R. Maaskant, and M.M. Ohn, Tunable fibre bandpass filter based on a linearly chirped fibre Bragg grating for wavelength demultiplexing, Electron. Lett., **32**, 1918–1919.
21. T. Imai, T. Komukai, and M. Nakazawa, Dispersion tuning of a linearly chirped fiber Bragg grating without a center wavelength shift by applying a strain gradient, IEEE Photon. Tech. Lett., **10**, 845–847 (1998).
22. J.A. Rogers. B.J. Eggleton, J.R. Pedrazzani, and T.A. Strasser, Distributed on-fiber thin film heaters for Bragg gratings with adjustable chirp, Appl. Phys. Lett., **74**, 3131–3133 (1999).
23. B.J. Eggleton, J.A. Rogers, P.S. Westbrook, and T.A. Strasser, Electrically tunable power efficient dispersion compensating fiber Bragg grating, IEEE Photon. Tech. Lett., **11**, 854–856 (1999).
24. R. Kashyap, P.F. McKee, R.J. Campbell, and D.L. Williams, A novel method of writing photo-induced chirped Bragg gratings in optical fibers, Electron. Lett., **30**, 996 (1994).
25. R. Kashyap, H.-G. Froehlich, A. Swanton, and D.J. Armes, 1.3 m long super-sep-chirped fibre Bragg grating with a continuous delay of 13.5 ns and bandwidth 10 nm for broadband dispersion compensation, Electron. Lett., **32**, 1807–1809 (1996).
26. H. Rourke, B. Pugh, S. Kanellopoulos, V. Baker, B. Napier, D. Greene, D. Goodchild, J. Fells, R. Epworth, A. Collar, and C. Rogers, Fabrication of extremely long fibre gratings by phase matched concatenation of multiple short sections, in proceedings of Bragg Gratings, Photosensitivity, and Poling in Glass Waveguides, 23–25 September 1999, OSA: Stuart, Florida, OSA, pp. 32–34.
27. M.J. Cole, W.H. Loh, R.I. Laming, M.N. Zervas, and S. Barcelos, Moving Fibre/phase mask-scanning beam technique for enhanced flexibility in producing fibre gratings with uniform phase mask, Electron. Lett., **31**, 1488–1489 (1995).
28. R. Stubbe, B. Sahlgren, S. Sandgren, and A. Asseh, Novel technique for writing long superstructured fiber Bragg gratings, in proceedings of Photosensitivity and Quadratic Nonlinearity in Glass Waveguides: Fundamentals and Applications, 9–11 September 1995, OSA 1995 Technical Digest 22: Portland, Oregon, 1995, pp. PD1.
29. A. Asseh, H. Storoy, B.E. Sahlgren, S. Sahlgren, and R.A.H. Stubbe, A writing technique for long fiber Bragg gratings with complex reflectivity profiles, J Lightwave Technol., **15**, 1419–1423 (1997).

30. M. Ibsen, M.K. Durkin, M.J. Cole, and R.I. Laming, Optimised square pass-band fibre Bragg grating filter with in-band flat group delay response, Electron. Lett., **34**, 800–802 (1998).

31. J.F. Brennan III and D.L. LaBrake, Realization of >10 m long chirped fiber Bragg gratings, 1999 OSA Topical conference on Bragg gratings, Photosensitivity, and Poling in Glass Waveguides, Stuart, FL, Paper ThD2, 1999.

32. J.F. Brennan III, E. Hernandez, J.A. Valenti, P.G. Sinha, M.R. Matthews, D.E. Elder, G.A. Beauchesne, and C.H. Byrd, Dispersion and dispersion-slope correction with a fiber Bragg grating over the full C-band, in proceedings of Optical fiber Communications, Anaheim, CA, 17–22 March 2001, Paper PD12.

33. J.A. Stone and L.P. Howard, A simple technique for observing periodic nonlinearities in Michelson interferometers, Precision Engineering, **22**, 220–232 (1998).

34. J.F. Brennan III and D.L. LaBrake, Fabrication of long-period fiber gratings with arbitrary refractive index profiles and lengths, 1999 OSA topical conference on Bragg gratings, Photosensitivity, and Poling in Glass Waveguides, Stuart, FL, paper ThE13, 84–86, 1999.

35. L. Poladian, Understanding profile induced group-delay ripple in Bragg gratings, Appl. Opt., **39**, 1920–1923 (2000).

36. K Ennser, M.N. Zervas, and R.I. Laming, Optimization of Apodized linearly chirped fiber gratings for optical communications, IEEE J Quant. Electron., **34**, 770–778 (1998). and references therein.

37. N.S. Bergano, Undersea amplified lightwave systems design, in *Optical Fiber Telecommunications IIIA*, edited by I.P. Kaminow and T.L. Koch (Academic Press, San Diego, 1997), pp. 302–335.

38. T.A. Strasser, T. Nielson, and J.R. Pedrazzani, Limitations of dispersion compensation gratings including impact on system performance, proceedings of 1998 National Fiber Optic Engineers Conference, Orlando, FL 13–17 September 1998, pp. 79–85.

39. L.L. Blyler Jr., F.V. DiMarcello, J.R. Simpson, E.A. Sigety, A.C. Hart Jr., and V.A. Foertmeyer, UV-radiation induced losses in optical fibers and their control, J. Non-Crystal. Solids, **38 & 39**, 165–170 (1980).

40. E.M. Dianov, V.M. Mashinsky, V.B. Neustruev, and O.D. Sazhin, "Origin of excess loss in single-mode optical fibers with high Ge)2-doped silica core, Opt. Fiber Technol., **3**, 77–86 (1997) and references therein.

41. J. Stone, Interactions of hydrogen and deuterium with silica optical fibers: a review, J. Lightwave. Tech., **LT-5**, 712–733 (1987).

42. D.L. LaBrake, D.A. Sloan, and J.F. Brennan III, Optical losses due to grating fabrication processes in germanosilicate optical fibers, 1999 OSA Topical conference on Bragg Gratings, Photosensitivity, and Poling in Glass Waveguides, Stuart, FL, Paper ThE29, 130–133, 1999.

43. F.M. Araujo, E. Joanni, M.J. Marques, and O.G. Okhotnikov, Dynamics of IR absorption caused by hydroxyl groups and its effect on refractive index evolution in UV-exposed, hydrogen-loaded Ge)2-doped fibers, in proceedings of Conference on Lasers and Electro-optics, 1998 OSA Technical Digest, vol. 6, paper CWE3, 225–226, 1998.

44. R.M. Atkins and P.J. Lemaire, Effects of elevated temperature hydrogen exposure on short-wavelength optical losses and defect concentrations in germanosilicate optical fibers, J. Appl. Phys., **72**, 344–348 (1992).

45. V. Mizrahi and J.E. Sipe, Optical properties of photosensitive fiber phase gratings, J. Lightwave Technol., **11**, 1513–1517 (1993).

46. T. Erdogan, Cladding-mode resonances in short- and long-period fiber grating filters, J. Opt. Soc. Am. A, **14**, 1760–1773 (1997).

47. S.J. Hewlett, J.D. Love, G. Meltz, T.J. Bailey, and W.W. Morey, Cladding-mode coupling characteristics of Bragg gratings in depressed-cladding fibre, Electron. Lett., **31**, 820–822 (1995).

48. M.K. Durkin, M. Ibsen, R.I. Laming, and V. Gusmeroli, Equalization of spectral non-uniformities in broad-band chirped fibre gratings, in proceedings of Bragg Gratings, Photosensitivity, and Poling in Glass Fibers and Waveguides: Applications and Fundamentals, OSA 1997 Technical Digest Volume 17, Paper BMG16, pp. 231–233, 1997.

49. V. Finazzi and M.N. Zervas, Cladding mode losses in chirped fibre Bragg gratings, in proceedings of Bragg Gratings, Photosensitivity, and Poling in Glass Waveguides, OSA 2001 Technical Digest, Paper BThB4, 2001.

50. F. Ghiringhelli and M.N. Zervas, Inverse scattering design of fiber Bragg gratings with cladding mode losses compensation, in proceedings of Bragg Gratings, Photosensitivity, and Poling in Glass Waveguides, OSA 2003 Technical Digest, Paper TuD2, pp. 226–228 (2003).

51. N.K. Viswanathan and D.L. LaBrake, Accelerated-aging studies of chirped Bragg gratings written in deuterium-loaded germano-silicate fibers, J. Lightwave Technol. **22**, 1990–2000 (2004).

52. R. Feced, and M.N. Zervas, Effects of random phase and amplitude errors on optical fiber Bragg gratings, J. Lightwave Technol., **18**, 90–101 (2000).

53. M. Sumetsky, B.J. Eggleton, and C. Martijn de Sterke, Theory of group delay ripple generated by chirped fiber gratings, Opt. Express, **10**, 332–340 (2002).

54. B.J. Eggleton, P.A. Krug, L. Poladian, and F. Ouellette, Long superstructure Bragg gratings in optical fibers, Electron. Lett., **30**, 1620–1622 (1994).

55. M.R. Matthews, J. Porque, C.D. Hoyle, M.J. Vos, and T.L. Smith, Simple model of errors in chirped fiber gratings, Optics Express, **12**, 189–197 (2004).

56. L. Poladian, Graphical and WKB analysis of nonuniform Bragg gratings, Phys. Rev. E, **48**, 4758–4767 (1993).

57. Transmission characteristics of optical components and subsystems, International Telecommunications Union, ITU-T G.671, 2002.

58. Generic requirements for fiber optic dispersion compensators, Telcordia document, GR-2854-CORE.

59. M.M. David, J.F. Brennan III, B. Cronk, B. Gates, B. Nelson, C. Jorgensen, D.L. LaBrake, D. Paolucci, C. Byrd, and J. Valenti, Diamond-like film encapsulated fibers for long-length fiber grating production, in proceedings of 2000 Optical Fiber Communication, OSA Technical Digest, Baltimore, MD, Paper PD1, 2000.

60. R.P. Espindola, R.M. Atkins, D.A. Simoff, K.T. Nelson, and M.A. Paczkowski, Fiber Bragg gratings written through a fiber coating, in proceedings of 1997 Optical Fiber Communication, OSA Technical Digest Volume 6, Dallas, TX, Paper PD4, 1997.

61. K. Imamura, T. Nakai, K. Moriura, Y. Sudo, and Y. Imada, Mechanical strength characteristics of tin-doped germanosilicate fibre Bragg gratings by writing through UV-transparent coating, Electron. Lett., **34**, 1016–1017 (1998).

62. L. Chao and L. Reekie, Grating writing through the fibre coating using a 248 nm excimer laser, in proceedings of 1999 Optical Fiber Communication, OSA/IOOC Technical Digest, San Diego, CA, paper ThD5, 1999.

63. M. Ibsen and R.I. Laming, Fibre non-uniformity caused Bragg grating imperfections, in proceedings of 1999 Optical Fiber Communication, OSA/IOOC Technical Digest, San Diego, CA, Paper FA1, 1999.

64. J. Mort and F. Jansen, *Plasma Deposited Thin Films* (CRC Press, Baco Raton, FL, 1986).

65. J.F. Brennan III, M.R. Matthews, W.V. Dower, D.J. Treadwell, W. Wang, J. Porque, and X. Fan, Dispersion correction with a robust fiber grating over the full C-band at 10 Gb/s rates with a <0.3-dB power penalties, IEEE Photon. Tech. Lett., **15**, 1722– 1724 (2003).

66. J.F. Brennan III, P.M. Bungarden, C.E. Fisher, and R.M. Jennings, Packaging to reduce thermal gradients along the length of long fiber gratings, IEEE Photon. Technol. Lett., **16**, 156–158 (2004).

67. M.J. Li, Recent Progress in fiber dispersion compensators, in European Conference on Optical Communications 2001, Amsterdam, The Netherlands, Paper Th.M.1, (2001.

68. W.W. Morey and W.L. Glomb, Incorporated Bragg Filter Temperature Compensated Optical Waveguide Device, United States Patent # 5,042,898 (27 August 1991).

69. J.A. Rogers, B.J. Eggleton, J.R. Pedrazzani, and T.A Strasser, Distributed on-fiber thin film heaters for Bragg gratings with adjustable chirp, Appl. Phys. Lett., **74**, 3131–3133 (1999).

70. J.F. Brennan III, M.R. Matthews, and P.G. Sinha, The modulation transfer-function of chirped fiber Bragg gratings, in proceedings of Bragg Gratings, Photosensitivity, and Poling in Glass Waveguides, OSA 2001 Technical Digest, Stresa, Italy, Paper BThC21, 2001.

71. B.J. Eggleton, A. Ahuja, P.S. Westbrook, J.A. Rogers, P. Kuo, T.N. Nielson, and B. Mikkelson, Integrated tunable fiber gratings for dispersion management in high-bit rate systems, J. Lightwave Technol., **18**, 1418–1432 (2000).

72. D. Garthe, G. Milner, and Y. Cai, System performance of broadband dispersion compensating gratings, Electron. Lett., **34**, 582–583 (1998).

73. K. Ennser, M. Ibsen, M. Durkin, M.N. Zervas, and R.I. Laming, Influence of nonideal chirped fiber grating characteristics on dispersion cancellation, IEEE Photon. Technol. Lett., **10**, pp. 1476–1478 (1998).

74. C. Scheerer, C. Glingener, G. Fischer, M. Bohn, and W. Rosenkranz, Influence of filter delay ripples on system performance, in proceedings of 1999 European Conference on Optical Communication, Nice France, Volume I, pp. 410–411, 1999.

75. P. Hernday, Dispersion Measurements, in *Fiber Optic Test and Measurement*, edited by D. Derickson (Prentice-Hall, New Jersey, 1998), chapter 12, pp. 475–518.

76. C. Scheerer, Phase distortions in optical transmission systems, Frequenz, **54**, 42–46 (2000).

77. T. Niemi, M. Uusimaa, and H. Ludvigsen, Limitations of phase-shift method in measuring dense group delay ripple of fiber Bragg gratings, IEEE Photon Technol. Lett., **13**, 1334–1336 (2001).

78. X. Fan and J.F. Brennan III, Performance effect in optical-communication systems caused by phase ripple of dispersive components, Appl. Opt., **43** (26), 5033-5036 (2004). Also, X. Fan, D.L. LaBrake, and J.F. Brennan III, Chirped fiber grating characterization with phase ripple, in proceedings of 2003 Optical Fiber Communications, OSA Technical Digest, Atlanta, Georgia, Paper FC2, 2003.

79. M. Eiselt, C.B. Clausen, and R.W. Tkach, Performance characterization of components with group delay fluctuations, Photon. Technol. Lett., **15**, 1076–1078 (2003). Also in Symposium on Optical Fiber Measurements, NIST, Boulder, CO, 2002, Session III.

80. H. Yoshimi, Y. Takushima, and K. Kikuchi, A simple method for estimating eye-opening penalty caused by group-delay ripple of optical filters, in proceedings of 2002 European Conference on Optical Communications, Copenhagen, Denmark, 2002, Paper 10.4.4.

81. G.P. Agrawal, *Fiber-Optic Communication Systems*, 2nd edition (John Wiley & Sons, New York, 1997).

82. T. Erdogan and V. Mizrahi, Characterization of UV induced birefringence in photosensitive Ge-doped silica optical fiber , J. Opt. Soc. Am. B, **11**, 2100–2105 (1994).

83. D. Wang, M. Matthews, and J.F. Brennan III, PMD measurement of dispersion compensation grating and its effect on system penalty estimation, in proceedings of 2003 Optical Fiber Communications, OSA Technical Digest, Atlanta, Georgia, Paper WC3, 2003.

84. M. Schiano, and G. Zaffiro, Polarisation mode dispersion in chirped fiber gratings, in 24th European Conference on Optical Communication, Madrid, Spain, pp. 403–404, 1998.

85. S. Bonino, M. Norgia, E. Riccardi, and M. Schiano, Measurement of polarization properties of chirped fiber gratings, in 1997 Optical Fiber Measurement Conference, pp. 49–55, 1997.

86. E. Ciaramella, E. Riccardl, and M. Schiano, System penalties due to polarisation mode dispersion of chirped gratings in 24th European Conference on Optical Communication, Madrid, Spain, pp. 515–516, 1998.

87. L.C.B. Linares, A.O. Dal Forno, and J.P. von der Weid, Polarimetric measurements of PMD and differential group delay ripple in chirped fiber Bragg gratings, Microwave Opt. Technol. Lett., **34**, 270–273 (2002).

88. D. Wang, M.R. Matthews, and J.F. Brennan III, Polarization mode dispersion in chirped fiber Bragg gratings, Opt. Express, **12** , 5741–5753 (2004), http://www.opticsexpress.org/abstract.cfm?URI=OPEX-12-23-5741.

89. N.K. Viswanathan, Photoerasure of ultraviolet-induced birefringence and polarization-mode dispersion of chirped fiber Bragg gratings, Optics Lett., **29** , 2470–2472 (2004).

90. M Ibsen and R Feced, Broadband fibre Bragg gratings for pure third-order dispersion compensation, in proceedings of 2002 Optical Fiber Communications, OSA Technical Digest, Anaheim, CA, Paper FA7, 2002.

91. B.J. Koch and J.F. Brennan III, Dispersion compensation in an optical communications system with an electroabsorption modulated laser and a fiber grating, IEEE Photon Technol. Lett., **15**, 1633–1635 (2003).

92. M.E. Fermann, A. Galvanauskas, and G. Sucha, *Ultrafast Lasers, Technology and Applications* (Marcel Dekker, New York, 2003).

93. K. Kim, S. Lee, P.J. Delfyett Jr., X-CPA (extreme chirped pulse amplification)—Beyond the energy storage limit of semiconductor gain media, in proceedings of 2004 Conference on Lasers & Electro-Optics, San Francisco, CA, Paper CTuY2, 2004.

DOI: 10.1007/s10297-006-0072-6
Originally published in J. Opt. Fiber. Commun. Rep. 4, 41–85 (2007)

Fiber-based tunable dispersion compensation

N.M. Litchinitser, M. Sumetsky, and P.S. Westbrook

OFS Labs, Somerset, NJ 08873

Abstract. Tunable dispersion has been implemented in various technology platforms, including fiber gratings, planar waveguides, thin film etalons, and bulk optic technologies. This paper will focus on fiber grating based tunable dispersion compensation, because fiber gratings are at present one of the best developed TDC technologies available. The paper is divided into three parts. In the first part we describe grating based TDC technologies and discuss their advantages and disadvantages. We focus on thermally tuned linearly chirped fiber gratings, as these have to date been the most successful grating technology for 40 Gbit/s. We also compare grating TDCs to two other prominent tunable dispersion technologies: thin film etalons and planar waveguide ring resonators. In the second section we describe the techniques used to fabricate high performance dispersion compensation gratings as well as the theory of the primary defect of fiber grating dispersion compensation: group delay ripple (GDR). In the third section we describe the telecom system related issues for tunable gratings, including characterization of grating performance, tunability requirements and results from actual system trials using tunable FBGs.

Introduction

Tunable dispersion compensation (TDC) refers to a range of optical technologies that allow for a controlled amount of chromatic dispersion to be added to a signal over a given bandwidth. Tunable dispersion can be distinguished from "adjustable" dispersion which requires switching and hence loss of data during the change in dispersion [1]. Tunability implies continuously variable chromatic dispersion that can be employed in feedback loops to stabilize high bit rate channels or compensate for reconfiguration of a network. This technology has been recognized as essential for the proper functioning of telecom systems at bit rates of 40 Gbit/s and above [2]. At these high bit rates, the sensitivity to dispersion is at the level of 10s to a few 100 ps/nm. As this paper will

show, such dispersion can be designed into a discrete device with a practical signal bandwidth. At lower bit rates, 10 Gbit/s and below, tunable dispersion is required only for static trimming of the system to compensate dispersion slope mismatch, or system reconfiguration. However, because of the higher dispersion tolerances, the useful tuning range is several 100s to 1000s of ps/nm, and this dispersion is more difficult to achieve in a single discrete device. Moreover, as electronic equalizers improve in speed and performance, the need for tunable optical dispersion compensation at 10 Gbit/s also diminishes. Therefore, tunable dispersion compensation is primarily geared toward 40 Gbit/s, where cost per bandwidth is more favorable, dispersion range is more easily realized, and electronic equalizers are less practical. Our primary focus will therefore be on the TDC technologies that have been most extensively developed and tested to meet 40 Gbit/s TDC requirements.

Tunable dispersion has been implemented in various technology platforms, including fiber gratings, planar waveguides, thin film etalons, and bulk optic technologies. This paper will focus on fiber grating based tunable dispersion compensation, because fiber gratings are at present one of the best developed TDC technologies available. The paper is divided into three parts. In the first part we describe grating based TDC technologies and discuss their advantages and disadvantages. We focus on thermally tuned linearly chirped fiber gratings, as these have to date been the most successful grating technology for 40 Gbit/s. We also compare grating TDCs to two other prominent tunable dispersion technologies: thin film etalons and planar waveguide ring resonators. In the second section we describe the techniques used to fabricate high performance dispersion compensation gratings as well as the theory of the primary defect of fiber grating dispersion compensation: group delay ripple (GDR). In the third section we describe the telecom system related issues for tunable gratings, including characterization of grating performance, tunability requirements and results from actual system trials using tunable FBGs.

1. Fiber Grating TDC Technology Overview

In section 1 we review fiber grating TDC technology. We first discuss the basic concept behind fiber grating dispersion compensators and give simple design rules. We then describe different methods of making fiber gratings tunable and discuss different fiber grating TDC designs. Finally we compare fiber gratings to other well developed TDC technologies.

1.1. Fiber Gratings as Dispersion Compensators

The basic principle behind almost all fiber grating dispersion compensators is Bragg reflection in a fiber grating. It has been known since 1978 that periodic modulations of the refractive index may be inscribed into the Ge-doped core of the standard single mode step index fibers used in optical telecommunications [3]. These Fiber Bragg Gratings (FBGs) reflect light over a narrow range of wavelengths determined by the period of the grating. Such reflectors have been used as laser mirrors and narrowband WDM filters for adding and dropping channels as well as optical taps and broadband filters [4,5]. A significant aspect of the fiber grating technology is that the grating

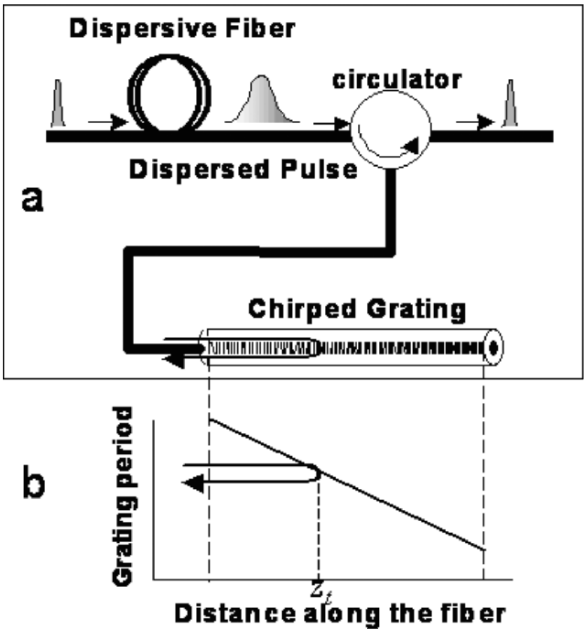

Fig. 1. (a) Chirped fiber grating dispersion compensator concept. (b) Grating period vs distance along fiber which gives rise to group delay that is linearly related to wavelength.

index modulation profile along the fiber can be controlled to a high degree through a variety of grating fabrication techniques. Thus, FBGs can have a chirped period, or a superstructure modulation, or a variety of different aperiodic perturbations to the basic uniform Bragg grating.

The first suggestion of the use of FBGs for dispersion compensation, and the method most in use today, was by Ouellete [6]. The basic idea of this work was to inscribe a Bragg grating in a fiber with a linearly chirped grating period. In such a grating, longer wavelengths reflecting off of the grating would travel either more or less than shorter wavelengths, depending on the sign of the chirp. As long as the grating had a uniform index modulation amplitude, the amplitude response would be flat. As a result, the response of the grating in reflection would be a small uniform attenuation and constant chromatic dispersion. The concept of chirped fiber grating dispersion compensation is shown in Fig. 1.

The chromatic dispersion D of a chirped FBG is very simply related to the chirp of the grating through ray tracing arguments by the approximate expression

$$D \sim 1/cC, \tag{1}$$

where C is the dimensionless linear chirp rate of the grating period and c is the speed of light. Note that the units are ps/nm as opposed to ps/nmkm used for dispersion compensating fiber. Gratings are a discrete chromatic dispersion element with a fixed

dispersion. Typical chirp rates required to compensate 60 km of standard single-mode fiber (SSMF), which has a dispersion of 1060 ps/nm at 1550 nm, is ∼0.036 nm/cm.

For any chirped Bragg grating, bandwidth, B, dispersion, and effective length L are always related:

$$B \sim 2n_0LC \sim 2n_0L/cD. \tag{2}$$

Here n_0 is the effective index of the guided mode (n_0 ∼1.45). For a 1060-ps/nm grating at 1550 nm with 0.5 nm (60 GHz) of bandwidth, Eq. (2) implies an effective grating length of ∼5 cm. We use the term effective length here to refer the uniform middle portion of the grating. Actual grating lengths are typically a few cms longer because smooth turn-on and turn-off of the grating index modulation at either end of the grating must be included. Another useful rule of thumb is that 10 cm of fiber corresponds to roughly 500 ps of delay, making 1000 ps the maximum delay attainable from reflection off of a 10-cm grating. Therefore, although very large dispersions are possible with short gratings, the bandwidth over which the grating will have the desired response may be very small. As we discuss below, this bandwidth-dispersion tradeoff can be overcome in at least two ways.

The tradeoff between bandwidth and dispersion for a given grating length is one of the fundamental limitations of fiber gratings as dispersion compensators. Mass production of gratings is generally carried out using phase masks, and since these are produced using standard semiconductor equipment, they are usually no longer than 10 cm. Therefore 10 cm represents a threshold length defining the boundary between mass produced phase mask manufactured gratings and alternate grating fabrication technologies, such as point by point writing.

Two basic methods have been considered to overcome the bandwidth-dispersion tradeoff. The first method simply requires the fabrication of very long fiber gratings. Methods of fabricating gratings with lengths in excess of 1m have been suggested by various researchers. These involved either very long stages [7,8] or some form of rotary mount [9,10] to hold the long lengths of fiber. Such gratings have been demonstrated in telecom systems [11] and may provide almost arbitrary dispersion and dispersion slope over large bandwidths. They cannot easily be tuned, though, since their long length precludes the strain and thermal tuning possible with shorter gratings. They must also be packaged in a coiled manner similar to standard fiber dispersion compensation modules (DCMs) [12], unlike short fiber gratings that can be held straight.

The other approach to increasing the bandwidth of a chirped fiber grating is known as sampling [13–18]. (See Fig. 2.) If the index modulation comprising the Bragg resonance is modulated or sampled at a much longer period, then the grating response will be repeated at fixed frequency intervals which are integral multiples of the sampling frequency. As a result, the dispersion of one grating can be repeated over a large bandwidth. In effect, the sampling technique puts multiple chirped gratings in the same region of fiber. Thus a sampled grating can achieve a broad bandwidth in the same 10 cm length of fiber as a single channel grating. Therefore they can be mass produced with phase masks, much like the single channel gratings.

An important design issue with sampled gratings is the degree to which the channels repeat reliably. This is controlled by the sampling function. If this function is a simple on-off sampling of the grating, then the repeated channels will have an envelope that is roughly a sinc function. On the other hand, if the sampling function is roughly a sinc function, then the repeated channels will all be the same strength and there will be no additional channels [16]. Another important issue with sampled gratings is the scaling

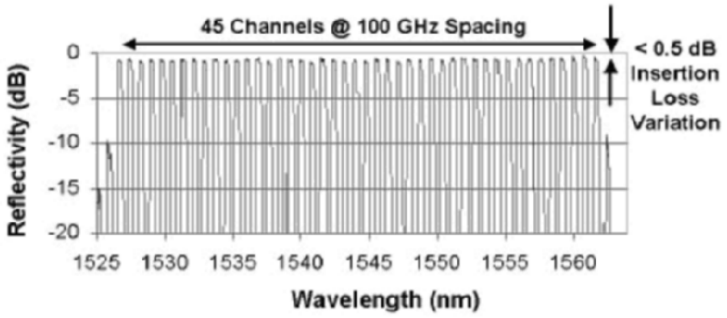

Fig. 2. Multichannel sampled chirped fiber grating dispersion compensator covering more than 30 nm of bandwidth with 100 GHz spaced channels. After [18]. (© 2003 OSA and IEEE)

of the required refractive index change with number of channels. Since the amount of index change achievable in a fiber is typically no more than 0.01, there is a limit on the number of channels that can be present. For some types of sampling such as on-off, this scaling is linear, meaning that doubling the number of channels requires doubling the index change. However, for other sampling techniques, such as phase optimized [17] or phase only [18], the scaling can be improved to square root of the number of channels. Thus doubling the index change would give four times the number of channels. Therefore, multichannel dispersion compensators require complex grating and/or phase mask profiles. Such techniques have resulted in multichannel dispersion compensation gratings with channels covering more than 30 nm, as shown in Fig. 2. A drawback of such multichannel fiber gratings is that they are usually more lossy than single or few channel gratings, and they also have more system penalty due to group delay ripple. (See section 2.) However, unlike long fiber gratings, the chromatic dispersion of sampled chirped fiber gratings can be tuned. We discuss an example below.

1.2. Tunable Linearly Chirped Fiber Grating Dispersion Compensators

In this section we consider tunable linearly chirped fiber gratings, since these are the most successful grating TDC technology to date. Tunable chromatic dispersion has been achieved in linearly chirped FBGs through either strain or thermal variation of the fiber properties. It is well known that the effective index of the core mode is temperature dependent. Bragg resonances near 1550 nm in germanosilicate fibers will change at 0.011 nm/$^\circ$C. Strain can also be used in either compression or in tension to modify a Bragg resonance. Tolerable strain levels can shift Bragg resonances by a few nms, however shifts of 10s of nm have also been achieved for gratings near 1550 nm.

In what follows we cover primarily the thermal route to tunability for two reasons. Most importantly, thermal methods have to date been the most successful path to commercialization because of their higher reliability, low PMD, and lack of moving parts. Secondly, the basic dispersion tuning mechanism in thermal methods is very similar

conceptually to that used in most strained tuned TDCs. Therefore an understanding of thermal tuning can be easily translated to strain tuned TDCs.

Thermally Tuned TDCs

In order to control the chromatic dispersion a variable temperature gradient must be imposed on the fiber grating. Changing the magnitude of the gradient changes the grating chirp rate and hence the dispersion according to Eq. (1). For the case of a thermal gradient, the first demonstrations simply used a bulk heater and cooler on either end of the grating [19]. This design has the disadvantage of large size, slow response time and inefficient power use. A more compact approach employs nonuniform thin film heaters. [2,20] These may be fabricated onto the fiber itself or onto a capillary tube into which the fiber is inserted. Figure 3 shows a typical film profile. Where the film is thicker, current flow will give a lower temperature. The relationship between film thickness and temperature is somewhat complicated, due to the dependence of film resistance on thickness and temperature. However, for a given drive current, the required film thickness is roughly inversely proportional to the desired temperature. Typical film thicknesses are a few microns to a few 10s of microns. Thinner films are less stable, but require a lower operating voltage due to higher resistance. The film may be deposited on the fiber or capillary using standard techniques such as electrochemical deposition or e-beam evaporation. For additional thermal stability, the grating or capillary can be placed inside another insulating enclosure. In this way, the grating is protected from air currents which might affect the temperature gradient. Any nonuniformity in this gradient will appear as group delay ripple. Figure 4 shows a grating packaged in an insulating glass tube, as well as a final grating package with electrical connections. Typical dimensions are $\sim$16 cm$\times$1 cm$\times$1 cm.

It is well known that the index modulation of FBGs must be annealed at high temperature in order to achieve the long term stability required in telecom or other applications [21]. Gratings used in thermal tuning applications must be annealed at very high temperatures. The hot side of the grating can reach temperatures in excess of 200°C, so a specialized annealing procedure that includes very high temperatures must be developed for thermally tuned TDCs.

Another significant problem that must be overcome in a successful TDC is that the center wavelength of the device must not drift, thereby reducing the usable bandwidth of the device. Therefore, the thermal gradient should not have a bias which causes the entire grating spectrum to increase with temperature. In practice this can be achieved by ensuring that one end of the thin film heater is sufficiently thick that the temperature changes there are small, or by providing an additional uniform heater to maintain a constant minimum temperature.

A typical set of optical responses for a thermally tuned 40 Gbit/s FBG TDC is shown in Fig. 5. The top plot shows the grating reflectivity for various tuning voltages. Below this is the group delay response. The designed bandwidth is indicated by vertical lines. The group delay ripple for all voltages is plotted in the lowest plot. Group delay ripple (GDR) is computed by subtracting a linear fit from the group delay response and plotting the residual. GDR is discussed further in sections 2 and 3. The figure also shows the dispersion tuning curve. Two important properties of fiber grating TDCs are evident in these plots. Firstly, they have only one control voltage to change dispersion. This important characteristic makes them advantageous in feedback loops

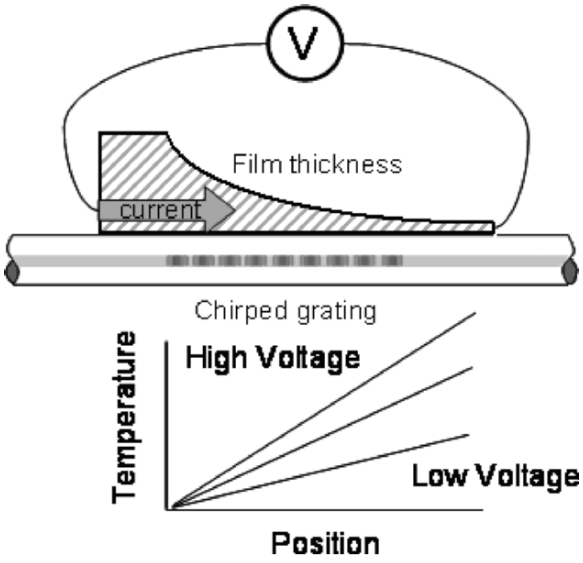

Fig. 3. Tunable dispersion compensator using linearly chirped fiber grating and a thin film heater that provides a variable temperature gradient. See [2].

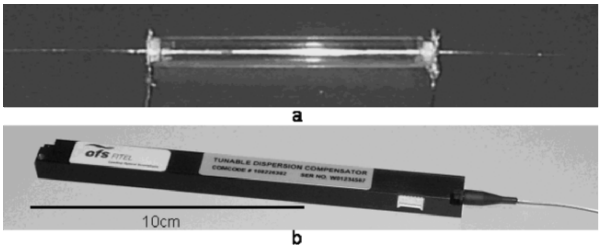

Fig. 4. (a) Chirped fiber grating TDC packaged in glass tube for stability. (b) Fully packaged thermal fiber grating TDC with approximate dimensions.

used to stabilize chromatic dispersion degradations, since only one control voltage is necessary to change dispersion. Secondly, the bandwidth of the grating increases as the dispersion is changed [see Eq. (2)]. Therefore, a fiber grating TDC requires additional bandwidth outside of its designed bandwidth. This is a primary difference between chirped gratings and resonator-based TDCs, which do not change their bandwidth as dispersion is tuned (see below).

The response time of a thermally tuned FBG depends on the thermal mass of the heater and fiber, and is usually no faster than a few seconds. Figure 6 shows the time response of the grating. The plot shows the recovery of the bit error ratio (BER) of a bit

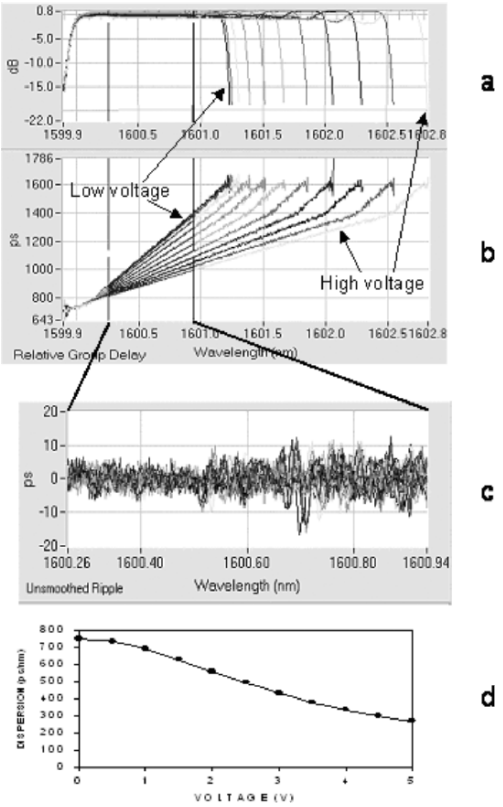

Fig. 5. Typical optical characteristics of a 40-Gbit/s chirped fiber grating tunable dispersion compensator employing thermal tuning. (a) Grating reflectivity versus wavelength for several values of the tuning voltage. (See Fig. 3.) (b) Grating group delay versus wavelength for several values of the tuning voltage. In both plots, the vertical lines indicate the operation bandwidth of the device. (c) Group delay ripple within the bandwidth for each group delay curve. Group delay ripple is computed by subtracting a best linear fit from each group delay curve of (b). (d) Grating dispersion vs. tuning voltage.

stream compensated by a grating TDC after a large change (few volts) of the grating dispersion.

Sampled gratings have also been considered for tunable dispersion compensation at 40 Gbit/s. Figure 7 shows the response of such a broadband TDC. (See [14]). In this experiment, the sampling period allowed four strong channels in a 10-cm-long grating. A single thin film heater controlled the dispersion of all of the channels simultaneously. An additional strain tuning mechanism allowed independent and continuous tuning of the grating's wavelengths by up to 200 GHz, enabling the device to cover any wavelength within an 8.8-nm bandwidth when used as a single channel device. This device was meant for "colorless" operation, in which a single device can cover channels over a broad range of wavelength. Colorless operation must be distinguished from

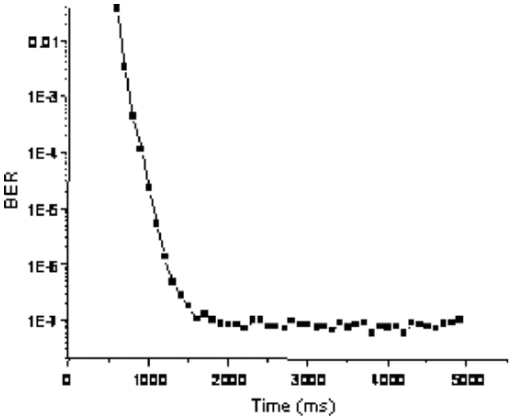

Fig. 6. Time response of thermal TDC. Bit error ratio (BER) of a signal compensated by the grating was measured as TDC restored low error operation.

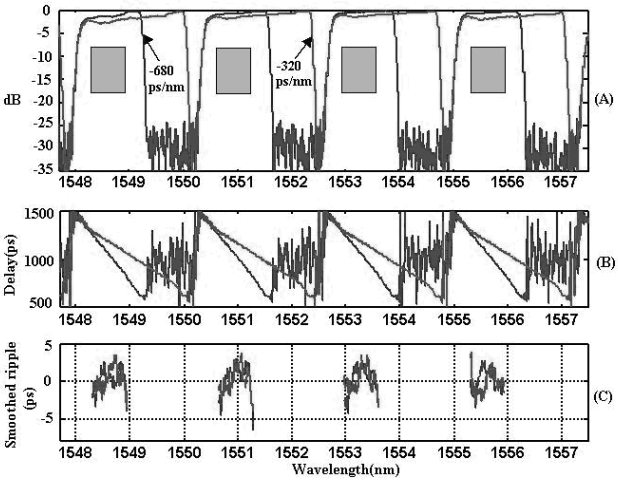

Fig. 7. Multichannel "colorless" TDC using linearly chirped sampled FBG with a single thermal heater. Reflectivities (top), group delay (middle), and ripple (bottom) are shown for channels and two values of the control voltage driving the chirped heater. Boxes indicate the usable bandwidth for 40 Gbit/s operation.

multichannel operation in which a single device is meant to compensate dispersion in many channels simultaneously. In general, colorless operation is more readily achieved, since only one channel at a time must meet a given specification. Extra bandwidth between the gratings was essential to accommodate the change in bandwidth of each

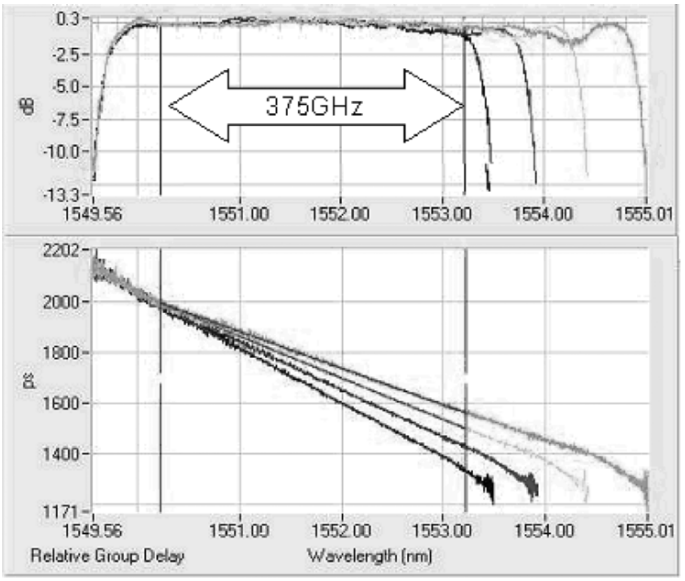

Fig. 8. Reflectivity and group delay for a broadband linearly chirped fiber grating for several values of the tuning voltage. This bandwidth and dispersion tuning range is suitable for compensating 160 Gbit/s signals.

sampled grating resonance. The performance of this device is summarized in table 1 and is discussed in detail in section 3.

One of the strengths of the FBG TDC technology is that the bandwidth can be made very large simply by increasing the chirp rate of the grating. Thus FBG TDCs can be employed at very high bit rates, including 160 Gbit/s [22,23]. Figure 8 shows a 160 Gbit/s fiber grating TDC with over 350 GHz of bandwidth. The grating was 10cm long and the thermal gradients were the same as those of Fig. 5. The dispersion tuning range of this device was -144 to -213 ps/nm [23]. Such large bandwidths are at present only achievable using FBGs. The system performance of 160 Gbit/s TDCs are also summarized in Table 1 and discussed in [22] and [23].

Whether the grating is tuned through changes in a strain or temperature gradient, the dispersion tuning range of a grating of length L is always related to the dispersion and grating bandwidth through:

$$\delta D \sim \tau_{\mathrm{total}}/B - \tau_{\mathrm{total}}/(B+\delta B) = \tau_{\mathrm{total}}\delta B/B(B+\delta B). \tag{3}$$

Here δD is the dispersion tuning range and τ_{total} is the total round trip delay for light reflecting from the farthest end of the grating (1000 ps for a 10-cm-long grating). Therefore the tuning range for a single grating is roughly proportional to $\sim 1/B^2$. As will be discussed below, a similar result is valid for other TDC technologies. The change in bandwidth δB is always determined by the tuning mechanism. For thermal tuning, a 100°C change in temperature across the grating yields 1.1 nm of additional bandwidth at 1550 nm. The dispersion can then be changed by the fractional change

in bandwidth corresponding to this change in temperature:

$$\delta D/D_{\min} \sim \delta B/B, \tag{4}$$

where $D_{\min} = \tau_{\text{total}}/(B + \delta B)$. Here the usable device bandwidth is B, and a guard band of δB is needed to accommodate the change in bandwidth during tuning. Therefore, broadband gratings (with B greater than a few nm) can have only limited thermal tuning range, no matter what their length is, since δB <1.5 nm, typically (see Figs. 5 and 8). A similar result holds for mechanical tuning, however, as discussed below, mechanical tuning can yield greater changes in wavelength, and therefore can yield larger tuning ranges.

Strain Tuned TDCs

Gratings can also be tuned by applying strain gradients. Strain gradients were first demonstrated by simply potting a fiber in elastic material [24]. A more controlled method employs piezo materials. The grating may be bonded to a piezo stack which provides the strain gradient when actuated [25–27], or the grating may bonded onto a nonuniform piezo block [28]. Figure 9 shows one of the more successful designs [25]. A piezo stack is attached to the grating and expansion and contraction of the stack gives the variable strain gradient. Another strain tuning method employs bending of the grating. With an appropriate noncircular bend, either of the free grating [29] or of a grating held within a bendable material [30] a variable linear chirp may be added. In all strain tuning methods, it is possible to ensure that the center of the grating is unchanged. This is achieved by assuring that the center of the grating remains unstrained. Thermal tuning methods usually shift the center wavelength of the grating unless there is both cooling and heating.

The biggest advantage of strain tuned gratings is speed. They can be tuned with response times >100 times faster than thermally tuned gratings. Another advantage is that straining can in principle change a Bragg resonance by more than 10 times the maximum thermal change, meaning that strain can yield larger tuning ranges. In practice, though, long term reliability constraints preclude grating devices with very large strain gradients. Like thermal tuning there is typically only one control voltage making active control loops straight forward to implement. All straining methods rely critically on the ability to bond the fiber to a given substrate. This is typically accomplished using epoxies or glass solder or combinations of these. The reliability requirements of such mechanical bonding has made strain tuning unattractive for telecom applications that demand high reliability and typically no moving parts. As discussed in the next section, the applicability of strained tuned gratings is also greatly limited by excess PMD.

Polarization Mode Dispersion in Fiber Grating TDCs

Another issue with all chirped fiber gratings, which is exacerbated in strain tuned gratings is polarization mode dispersion (PMD). Most straining techniques require mechanical motion along a preferred plane or axis, and this can result in fiber birefringence and hence PMD. Thermally tuned gratings also have some PMD due to native and UV-induced fiber birefringence. Fiber birefringence results in a splitting of the

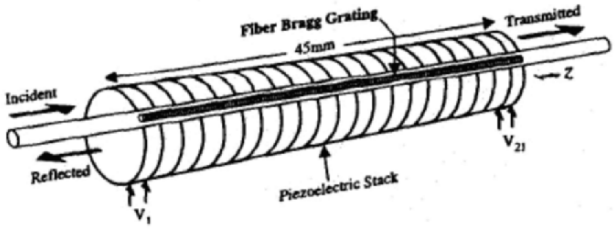

Fig. 9. Fiber grating with piezo stack to provide linear strain gradient. Strain gradient changes the local Bragg condition in a chirped fiber grating and hence controls grating dispersion. Single drive voltage on piezo stack changes gradient. After [25]. (© 1997 OSA and IEEE)

Bragg resonance wavelength for the two principal states of the fiber grating (usually just two orthogonal linear states aligned with the fiber birefringence axes). The wavelength splitting manifests as a polarization dependent group delay difference at a given wavelength. In the language of PMD, such a polarization dependent group delay difference is known as first-order PMD, and is characterized by a given differential group delay (DGD). Using simple geometric arguments as in Fig. 1, the DGD can be related to the dispersion, fiber birefringence, $B_{\rm fiber}$, and wavelength through [31]

$$DGD = B_{\rm fiber} D \lambda. \tag{5}$$

Within this approximation the variation of the DGD with wavelength can be computed by simply differencing the group delay including its ripple [31]. Using Eq. (5), a birefringence of 1e-5 and dispersion of 500 ps/nm at 1550 nm gives a DGD of $\sim$8 ps. This level of DGD would be unacceptable for bit rates of 40 Gbit/s where tunable dispersion is most often required. Thermally tuned fiber gratings designed for 40 Gbit/s applications typically have less than 1 ps of PMD. This low PMD results from the very low native birefringence of standard step index fibers (1e-6 or lower), and also from the very low UV-induced birefringence observed in these fibers after the index change has been annealed (also $\sim$1e-6). Because of this high sensitivity to fiber birefringence, strain tuned TDCs have been less attractive for telecom applications than have thermally tuned TDCs. As discussed below, most of the other highly developed non-grating TDC technologies also use thermal tuning.

1.3. Other Fiber Grating Tunable Dispersion Compensators

While we have focused on linearly chirped fiber gratings tuned by linear strain or thermal gradients, fiber gratings may also be fabricated with nonlinear chirps and may also be subjected to nonlinear strain or temperature gradients. Quadratically chirped gratings have been investigated as TDCs at 10 Gbit/s [32]. The quadratic chirp results in a response in reflection that has both chromatic dispersion and dispersion slope. To change dispersion, the quadratically chirped grating need only be tuned in wavelength. In principle, large dispersion tuning ranges can be achieved by increasing the dispersion

slope. The drawback of this technique is that the grating response will never be a pure linear dispersion. The additional dispersion slope, especially at higher bit rates (>40 Gbit/s) adds penalty to the response of a system employing such gratings. The slope penalty may be eliminated through the use of a grating pair. In such a TDC the light must reflect off of both gratings and the dispersion slope is cancelled [33]. As the two gratings are tuned, the dispersion changes, but the slope remains zero. This technique of course requires two gratings and is thus twice as lossy as the single grating case. Both nonlinearly chirped grating TDCs also have the problem of requiring more bandwidth outside the device bandwidth, just as linearly chirped compensators do.

An alternative approach to tunable dispersion compensation using fiber gratings employs fiber grating Gire-Tournois etalons (GTEs) [34]. Etalons are discussed further in the next section. GTEs are resonant devices whose response is periodic in frequency (free spectral range, or FSR). The resonant cavity comprises a pair of highly chirped fiber gratings. In this case, the grating chirp functions only to provide broadband reflectivity. The reflection bandwidth determines the bandwidth over which the device functions. In order to achieve the correct cavity dimensions, the two gratings forming the resonant cavity can be overlapping. Typically, one grating has very high reflectivity, and the second grating has a lower reflectivity. The result is an "all-pass" response, which means a constant amplitude response over the operation bandwidth. The phase response is periodic, though, with an FSR that is determined by the cavity spacing of the two highly chirped gratings. By adjusting the reflectivity of the weaker grating the phase response can be designed to approximate a linearly varying group delay. Tunability is achieved by concatenating two or more grating pairs and tuning the Bragg resonances of the cavities with respect to each other.

The primary advantage of GTEs is that they are inherently multichannel devices. They also have the advantage of low-loss, compact, all-fiber construction, requiring only a circulator to extract the reflected response. However, they also have the disadvantages of resonant devices, namely a bandwidth and tunability that is limited by the FSR (see below). This limited bandwidth has restricted their use in telecom applications to primarily 10 Gbit/s applications. For improved tuning they require multiple cavities, increasing loss, complexity and number of control voltages. GTEs will be discussed more in the next section.

While tunable chromatic dispersion may be the only requirement for 40 Gbit/s systems, at higher bit rates, there may be a need for tunable dispersion slope as well. At 160 Gbit/s, linear dispersion compensation alone may not be sufficient and tunable slope compensation may be required [35]. These requirements are discussed further below. Tunable intra-channel slope compensators have been demonstrated using strain tuning [36,37] as well as thermal tuning [38,39] Figure 10 shows the tuning of the slope of a linearly chirped grating using a quadratic thermal gradient. Slope compensation sufficient for 10s of km of fiber was observed.

Lastly, Bragg gratings can be used as dispersion compensators in transmission. Linearly chirped FBGs operate in reflection mode and thus an optical circulator or 3-dB coupler is required to access the reflected light (see Fig. 1). However, gratings also have dispersion in transmission. Dispersion compensation using an unchirped, apodized FBG in transmission has been demonstrated both experimentally and theoretically [40–42]. The performance of the transmission based dispersion compensator relies on the strong dispersion introduced by the grating at frequencies close to but outside the FBG band gap (or reflection bandwidth). The most challenging aspect of these

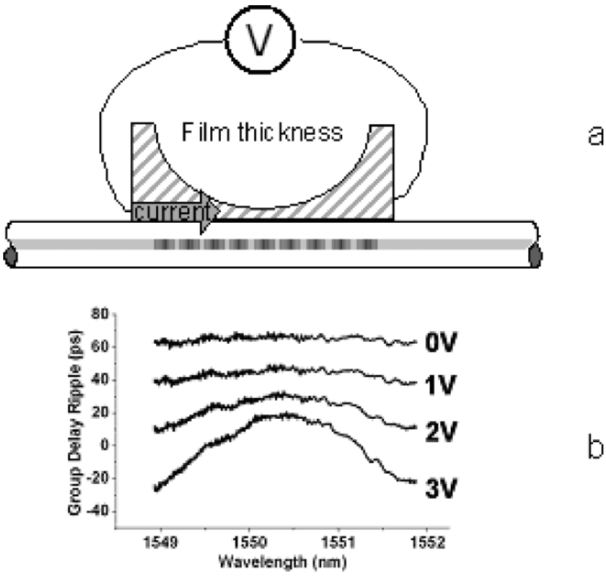

Fig. 10. Chirped fiber grating with quadratic temperature profile to provide tunable dispersion slope. (a) Chirped fiber grating with symmetric quadratically varying thin film heater. (b) Dispersion slope after subtraction of linear fit for several tuning voltages. See [38].

devices is the reduction of higher order dispersion that naturally accompanies the linear dispersion outside the reflection bandwidth. There are strict limits on this dispersion and the achievable bandwidth [43], and as a result transmissive gratings are limited to lower bit rates (10 Gbit/s and below). Tunability may be achieved through simple tuning of the grating and designs have been proposed [44]. There has also been some progress in designing specific grating profiles with transmissive dispersion, although at the cost of a more complex grating profile [45].

1.4. Comparison With Other TDC Technologies

Other technologies have also been considered for tunable dispersion compensation. Prominent among these are resonator based devices [46]. In such devices the dispersion of one or more resonant cavities is concatenated to yield an overall chromatic dispersion. By changing the coupling to these cavities as well as the phase shifts within them, the dispersion may be tuned. The most important characteristic of resonant dispersion compensators is that the resonant response is periodic in frequency. This spacing is known as the free spectral range (FSR), and it is a characteristic of all of the resonators used in the device. Therefore, such devices are inherently multichannel or "colorless" in their function since the same response is repeated every FSR. Once resonators with the same FSR are adjusted to function at one wavelength, they will work at many wavelengths separated by the FSR. The two most common realizations of the resonator based tunable dispersion compensators are the waveguide ring resonantor [47,48] and

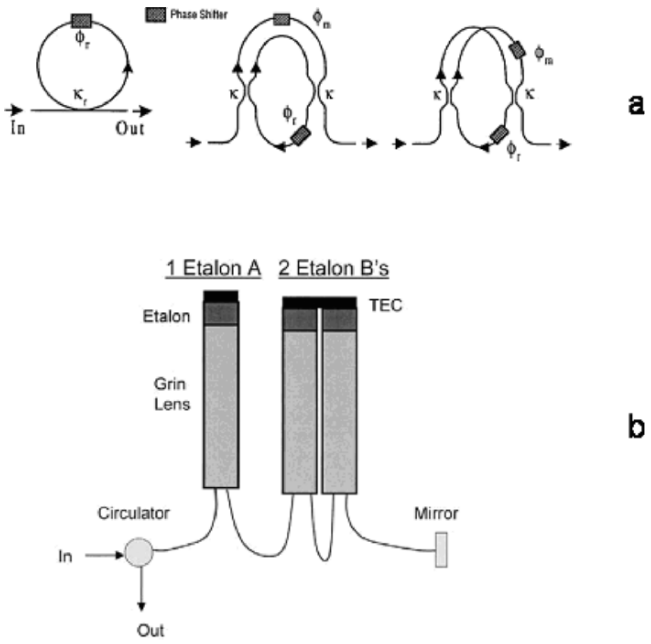

Fig. 11. Two types of resonator-based tunable dispersion compensators. (a) Ring resonators After [47] (© 1999 IEEE) (b) Thin film etalon resonators. After [51] (© 2002 IEEE).

the thin film stack Gire-Tournois etalon [49–51], however, as previously mentioned, fiber grating etalon TDCs have also been demonstrated using Gires-Tournois etalons. [34]

Figure 11 shows the two most prominent resonator devices: ring resonantors and thin film etalons. Note that the ring resonators are transmissive devices that do not require a circulator to operate. On the other hand, GTEs are reflective and therefore require a circulator to access the reflective response.

As mentioned above, the primary advantages of resonant TDCs is that they are inherently "colorless" or multichannel. Colorless operation means that any channel in the WDM system can be compensated with a single device. Therefore, a single device with one "code" can be used for an entire band of wavelengths. Fiber gratings, on the other hand, require a different grating period, or code, for each channel. This can be overcome to some degree with sampled fiber gratings, with higher loss and higher system penalty. However, since chirped fiber gratings require extra bandwidth for tunability, (see Figs. 5 and 8), either channel spacing must increase or tuning range must decrease in multichannel or colorless operation. Resonant devices do not change their amplitude response as significantly during tuning. Nor do they require additional bandwidth outside of the usable bandwidth as dispersion is tuned. This makes them better suited to multichannel operation with closely spaced channels. Finally, resonator

Table 1. Comparison of several well developed TDC technologies. In the loss column, (*) indicates that the circulator loss is included. The planar ring resonators do not require a circulator.

	B (GHz)	Bite rate (GB/s)	No. of ch.	Ch. spacing (GHz)	Format	Loss (dB)	System penalty (dB)	Carrier freq. range tested (GHz)	D tuning (ps/nm)	CV	Ref.
LC FBG	100	40	1	N/A	CSRZ	2	0.7	20	300–700	1	[98]
LC FBG	320	160	1	N/A	RZ (30%)	2.5	1.3	0	80–130	1	[22]
SC FBG	100	40	12	100	CSRZ	3	1.1	20	300–700	1	[14]
TFE	80	40	20	200	CSRZ	5.2*	2	20	−200–200	2	[51]
PRR	60	40	>6	75	NRZ	6	4	4	−100–100	8	[48]

LC=linearly chirped; SC=sampled chirped;TFE=thin film etalons; PRR=Planar ring resonators; CV=Control voltages.

based TDCs have dispersion tuning ranges that are symmetric about 0 ps/nm, whereas fiber gratings have an offset dispersion value, unless they are used in pairs.

The greatest drawback of resonant devices is that there are limitations to how large the FSR can be made. Since the FSR controls the device characteristics, this puts limitations on device performance. The operational bandwidth is always some fraction of the FSR and the tuning range varies as $1/\mathrm{FSR}^2$. This is a similar scaling rule as fiber gratings, but the FSR depends on a resonant cavity, and this cavity must be made very small to achieve large bandwidths. In practice, the number of cavities is also typically increased to accommodate more bandwidth, increasing complexity. Another drawback of tunable resonant dispersion compensators is that they typically have large loss due to coupling to bulk optics or planar waveguides. Typical insertion loss is 4–6 dB as compared to 2–3 dB for tunable fiber gratings. They are also larger on average then Bragg gratings. Usually two dimensions are similar to the FBG TDC ($\sim$1 cm and $\sim$10 cm), and one dimension is $\sim 10\times$ larger in the resonator TDC ($\sim$10 cm).

Lastly, resonant devices usually require more than one control voltage, since several resonators are required to form a given dispersive response. On the other hand, fiber gratings typically require only one control voltage, since a single heater or piezo stack can provide the required change in linear chirp gradient. This gives fiber grating dispersion compensators an advantage in applications that require feedback, since the single drive voltage can simplify the control algorithms. Moreover, the resonant devices require a calibration of the various control voltages, which, if it drifts over time can result in additional GDR.

Table 1 compares three well developed tunable dispersion technologies: thermally tuned chirped fiber gratings, thin film resonant devices, and planar waveguide ring resonator devices. Fiber gratings and thin film etalons are currently available as commercial products. The table focuses on 40 Gbit/s systems, since these are most likely to require tunable dispersion compensation. The numbers are taken from representative examples in the literature. The GDR of these devices was all roughly 10 ps peak-to-peak. However, as we describe below, this measure is only a rough indication of performance. Calculation of eye opening penalty (EOP, see below) or actual system measurements of the received power penalty are the only true measures of system performance. The cases considered in Table 1 all had system tests as well. The "system

penalty" column gives received power penalties at 10^{-9} BER (bit error ratio). The next column gives the range of carrier frequencies over which the power penalty was measured. This number is significant since tunable dispersion devices can often be tuned to a "sweet spot" to give optimal performance, but such freedom is not necessarily present in an actual system. Therefore the system performance must be measured as the signal carrier frequency or the device resonant wavelength are tuned to different wavelengths. As the table shows, the relatively small bandwidth of the etalons typically give them more penalty over the same range of carrier detuning. The data format is also given in one column. Bandwidth requirements per channel increase from NRZ (lowest) to CSRZ (middle) to RZ (highest).

Finally, the table shows the design parameters for a fiber grating dispersion compensator designed for 160 Gbit/s. As previously discussed, the bandwidth of fiber grating TDCs can easily be increased simply by increasing the chirp. Note that, as expected, the resulting tuning range is decreased by roughly $1/B^2$ as for the resonator devices.

In general the regimes of interest for the resonantor and fiber grating technologies is somewhat complementary. Resonantor devices are more attractive for multichannel applications. Moreover, thin film and waveguide technologies are well developed and can in principle provide lower cost per channel. Fiber gratings on the other hand are clearly most useful in single channel applications, since many of their characteristics (size, loss, OSNR penalty, bandwidth, number of control voltages) are superior. However, their main drawback is that they do not scale easily to many channels without incurring the same penalties that the resonator technologies have, and at some number of channels (4–8) they become less attractive. For fixed and tunable 10 Gbit/s applications, they are limited primarily to single channel systems. Because FBGs can have very large bandwidths, they can be applied in very high bit rate systems. Gratings with bandwidth in excess of 300 GHz and 50 ps/nm tuning range have been used with 160 Gbit/s RZ systems [22]. These fiber grating dispersion compensators have also been employed in applications that require closed loop stabilization and used in actual field trials [23].

Many other techniques for optical TDC have been proposed. These filters can be categorized broadly as "finite impulse response" (FIR) and "infinite-impulse response" (IIR). Loosely speaking, all resonant TDC devices with optical feedback paths, such as etalons, ring resonators, and Bragg gratings are categorized as IIR. There is some ambiguity in this definition, though [46]. On the other hand, transmissive TDC devices which do not have signal feedback paths, such as mach-zehnder structures [52,53], virtual imaged phase arrays [54], long period fiber gratings [55], arrayed waveguide structures [56] hybrid planar waveguide-MEMs structures [57] and optical fiber can be categorized as FIR. Full description of all of these technologies goes beyond the scope of this review. As we have previously discussed, we have limited our discussion to fairly well developed technologies that have been tested in systems and/or deployed in commercial 40 Gbit/s telecom systems, and their comparison to the most successful fiber based technologies. While fiber-based technologies such as chirped gratings have been successful to date, planar based technologies are still in development and have the promise of greatly reducing cost and required product codes. Research into optical TDC continues and improved solutions may be realized in the future.

Finally, the problem of tunable dispersion compensation is part of a larger problem of optical and electrical equalization of signals at a receiver [58–61]. Numerous meth-

ods exist for compensation of signal degradations in the electrical domain, including decision feedback equalizers, feed forward equalizers, and maximum likelihood sequence estimation [62,52]. These approaches can also be implemented in the optical domain with even greater control of the signal distortions and the possibility of inverting the linear transfer function of any transmission line [52,61]. Such techniques can compensate any signal distortion, including modal dispersion in multimode fibers, polarization mode dispersion (PMD) and nonlinear effects such as self phase modulation. These techniques require fast processing to be implemented at the receiver. This challenge is being overcome at 10 Gbit/s and below as system tests have shown. [63,64] Moreover, electrical precompensation methods have also been demonstrated in single channel 10 Gbit/s experiments. Such electrical precompensation enabled transmission over 5120 km of standard step index fiber without any optical chromatic dispersion compensation [65]. Because such schemes allow for tunable precompensation, they can in principle also be configured to include a tunable dispersion function. Therefore the need for optical tunable dispersion at 10 Gbit/s is expected to greatly decrease due to these competing low cost techniques in the electrical domain.

At 40 Gbit/s and above, though, receiver electronics are still too slow for implementation of electrical compensation, and optical TDC is to date the only viable and cost effective method of equalizing signals with chromatic dispersion. Moreover, because they act in the optical domain, TDCs can recover signals with many bit periods of chromatic dispersion, which is very difficult for most methods in the electronic domain. While still in its early stages, current research on SiGe [66] and InP [67] electronics may also yield such electronic feedback at 40 Gbit/s. Any optical chromatic dispersion compensator will also enhance the capabilities of electrical equalizers. When an optical TDC has already eliminated the dominant chromatic dispersion penalty, then electrical equalizers can reduce other penalties due to PMD and nonlinearities, that are not easily or cost effectively corrected in the optical domain.

2. Theory and Fabrication of FBG Dispersion Compensators

In section 2 we focus on linearly chirped FBG TDCs. We discuss the primary optical defect of such TDCs, namely group delay ripple (GDR). GDR is the deviation of the phase response from the desired linear group delay. It is a property of all TDC technologies and arises from physical imperfections in these devices. Section 2.1 describes the general features of FBGs necessary to understand GDR. Section 2.2 then describes the relationship between GDR and the physical imperfections of FBGs. Sections 2.3 and 2.4 describe a general method of removing GDR through post processing of fiber gratings. Both theoretical and experimental results are given.

2.1. Dispersion Compensation Grating Design and Specifications

As previously discussed, FBGs used in optical communications may be classified by their bandwidth and separated into single-channel, multi-channel, and broadband gratings. The bandwidth of a single-channel grating is around 1 nm, while the bandwidth of a multi-channel and broadband grating is up to several tens of nm. Gratings may also be classified by the profile of the period and amplitude of their index modulation. In this classification scheme, the gratings are separated into uniform, linearly or

non-linearly chirped, phase- and amplitude-modulated sampled, and others. The phase masks used to fabricate fiber gratings may be classified similarly to the corresponding FBG. Thus, there exist single-channel, multi-channel, broadband, chirped, sampled, and other types of phase masks.

The principal property of a FBG is the ability to reflect light at certain wavelengths. A prime advantage of fiber gratings over other technologies is that their reflectivity R can be made close to unity,

$$R \sim 1. \tag{6}$$

High grating reflectivity translates into low loss for chirped grating dispersion compensators, since the desired phase response is always realized in reflection. When reflectivity is close to 100% the loss will be determined by the accompanying circulator (see Fig. 1), typically no more than 2–3 dB. Since high reflectivity is usually required to make gratings attractive in applications, this condition places a lower limit to the FBG length and index modulation amplitude and also an upper limit on its chirp.

For a uniform grating, the *maximum* reflectivity achieved at the Bragg condition is equal to

$$R = \tanh^2(\pi \Delta n_{\mathrm{AC}} L/\lambda_0), \tag{7}$$

where Δn_{AC} is the effective index modulation amplitude, λ_0 is the wavelength of light, and L is the length of grating [4]. In this case Eq. (6) yields $\pi \Delta n_{\mathrm{AC}} L/\lambda_0 \gtrsim 1$. Typically, Δn_{AC} is less than or of order 10^{-3} and therefore the grating length should be greater or of order 1 mm.

For a chirped FBG, the maximum reflectivity achieved at the local Bragg condition is $R = 1 - \exp(\pi^2 \Delta n_{\mathrm{AC}}^2/2n_0^2|C|)$, where n_0 is the effective refractive index and C is the chirp of grating period $\Lambda(x)$, $C = d\Lambda(x)/dx$ [4]. Then Eq. (6) gives $\pi^2 \Delta n_{\mathrm{AC}}^2/2n_0^2|C| \gtrsim 1$. For $\Delta n_{\mathrm{AC}} \lesssim 10^{-3}$ we have that the chirp of FBG should be less or of order 10 nm/cm. Typically, the chirp value of single-channel chirped gratings is of the order 0.1 nm/cm. For multi-channel and broadband gratings, the chirp may be of order 10 nm/cm.

As discussed above, for superstructure gratings the magnitude of reflectivity is "shared" between channels and, in order to achieve reflectivity equal to similar single-channel grating, one must increase the index modulation amplitude by a factor which is of order the number of channels for simple on-off sampled gratings and is of order square root of the number of channels for the phase-modulated superstructure FBG [17,18].

In order to suppress the GDR caused by reflections from the ends of the FBG, the grating is apodized. Apodization is usually performed by smooth transition of the grating strength down to zero on the interval of $\sim$ 1 cm near the ends of the grating. The actual shape of apodization matters but not that significantly, once the apodization is smooth enough [4]. For typical chirped gratings of $\sim$ 100 mm length providing dispersion $\sim$ 1000 ps/nm, the unapodized grating may have the GDR $\sim$ 100 ps. However, as illustrated in Fig. 12, after apodization, the GDR of an ideal grating reduces to the values below 0.1 ps.

2.2. Relation Between GDR and Spatial Noise of Chirped FBG Parameters

While apodization of the grating index modulation profile greatly reduces group delay ripple, GDR arising from imperfections in the grating profile remains. This GDR is

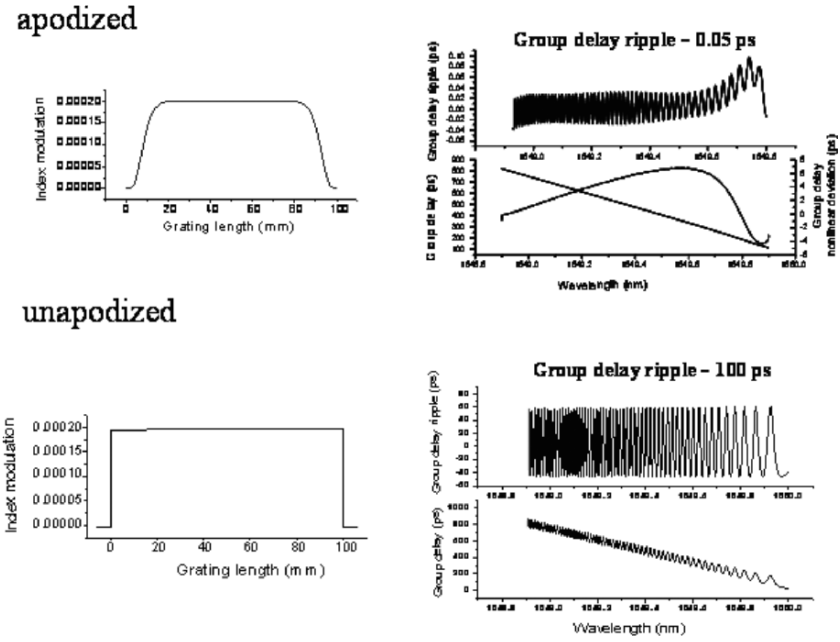

Fig. 12. Group delay ripple for apodized and unapodized gratings.

the principal impediment restraining the practical implementation of chirped FBGs as dispersion compensators. Analysis and calculations of GDR in chirped FBGs has been addressed in several publications [4,68–74]. In particular, the authors of [73,74], conducted a general study of random spatial variations of strength and period of gratings. They showed that these variations could have significant effect on group delay characteristics. In [68] the effects of fiber diameter variation for ultra-long fiber gratings, which have been proposed for broadband dispersion compensation, are studied. In this section we review a theory [74], which yields further understanding and establishes a simple relationship between the high-frequency spatial noise in grating parameters and the corresponding GDR. As discussed above, the order of magnitude parameters for a typical single-channel dispersion compensation FBG are $L \sim 10$ cm, chirp $C \sim 0.1$ nm/cm, bandwidth ~ 1 nm, and the corresponding dispersion is ~ 1000 ps/nm. To analyze GDR it is useful to consider its Fourier transform. In our discussion we consider high- and low-frequency GDR. The GDR Fourier components having the characteristic periods of ~ 1 nm are referred to as low-frequency ripples, while the GDR components with smaller periods ~ 0.01 nm are designated high-frequency ripples.

We is assume that there is no spatial ripple in the grating parameters other than in the period $\Lambda(z)$,

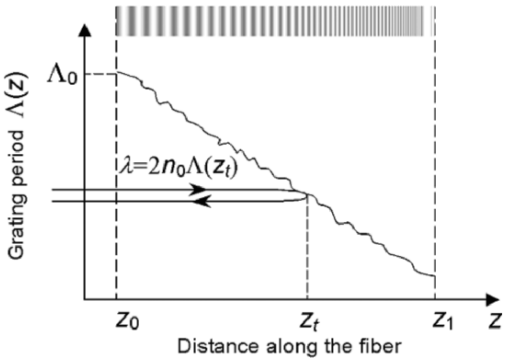

Fig. 13. Reflection of light from chirped fiber Bragg grating.

$$\begin{aligned} \Lambda(z) &= \Lambda_0 + C(z - z_0) + \Delta\Lambda(z), \\ \Delta\Lambda(z) &= \sum_{q>0} \Delta\Lambda_q \exp[iq(z - z_0)] + \text{c.c.}, \end{aligned} \tag{8}$$

where, for convenience, we use the spectral representation of the grating period noise, $\Delta\Lambda(z)$. The spatial ripple of the other grating parameters, like the amplitude of the index modulation, can be described similarly.

Let us consider first the description of GDR based on a simplistic classical ray approximation, which, as shown below, is somewhat useful to understand low-frequency ripple, but not is valid for high-frequency ripple. In this approximation, grating period variations are assumed to be slowly varying along the grating, and GDR appears only due to the ripple in the position of the turning point z_t, and follows this variation adiabatically. The grating period noise elsewhere in the grating does not matter (see Fig.13). Simple calculation using Eq.(8) defines GDR in a form demonstrating its inverse proportionality to the chirp C:

$$\Delta\tau(\lambda) = \frac{2n_0}{cC}\Delta\Lambda(z_t), \qquad z_t = z_0 + (\lambda - 2n_0\Lambda_0)/2n_0C, \tag{9}$$

where n_0 is the effective index of the guided mode, and c is the speed of light.

While the adiabatic ripple due to turning point variation can contribute to imperfection in dispersion compensation, there is also a large contribution to the GDR which is non-local and does not follow any grating defect adiabatically. This GDR is predominantly generated by the interference of the waves reflected from weak inhomogeneities of grating parameters along the whole grating length traveled by the light. In terms of noise components with frequency q [see Eq.(8)] this reflection can be understood as a secondary Bragg reflection governed by the coupled wave equations [4] with $(2\pi/q)$-periodic coefficients.

A simple explanation of the properties of GDR is given in Fig.14, which is a band diagram [75,76] of a chirped FBG with a weak long-period modulation representing a frequency component of the spatial noise $\Delta\Lambda(z)$ defined by Eq.(8). This modulation produces narrow and weak reflection sidebands, or photonic bandgaps, shaded in Fig. 14, spaced by interval $\Delta\lambda_q \propto q$(superstructure effect[76]). The GDR arises due to the

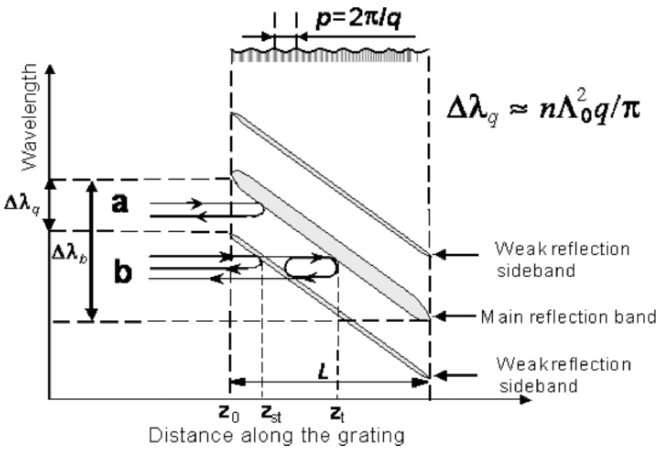

Fig. 14. Physical picture of the GDR cutoff effect.

interference of the light reflected from the main band and its sideband. There are two different wavelength regimes:

a.(*above cutoff*): If the light is reflected from the main reflection band only, without intersecting the sidebands then no GDR is observed.

b.(*below cutoff*): If the light also crosses the sideband then the interference of the wave reflected from the main band and the sideband causes GDR.

Thus, the formation of sidebands is accompanied by GDR if the ripple period is below the cutoff magnitude. It is also clear from Fig. 14 that if the main band is partly transparent then, even in region a, the grating will exhibit GDR because of interference with the wave reflected from the upper sideband. Below we assume that the grating is sufficiently reflective that the GDR produced by this interference is negligible. It is seen from Fig. 14 that whenever $z_{\rm st}$ is outside the interval (z_0, z_t) the component with frequency q does not generate GDR. The cutoff spatial frequency, q_c, and the cutoff GDR frequency, ν_c, in the form

$$q_c = \frac{\pi \Delta\lambda}{n_0 \Lambda_0^2}, \qquad \nu_c = \frac{\pi \Delta\lambda}{2C n_0^2 \Lambda_0^2}. \tag{10}$$

Figure 15(a) demonstrates typical group delay and GDR measurements for a phase mask fabricated chirped FBG. Figure15(b) shows the Fourier spectra of this GDR calculated for different bandwidths $\Delta\lambda$ measured from the high-wavelength edge of the reflection band. It is seen that the experimental cutoff frequencies are in excellent agreement with the ones predicted by Eq.(10).

Thus, the high frequency noise exhibits a cutoff as a function of wavelength and the underlying spatial noise frequency giving rise to the GDR. The cutoff effect is demonstrated here for the spatial noise in the grating period. It can be similarly shown that Eq. (10) holds for the spatial noise in any grating parameter. Generally, the results of this section also demonstrate the link between noisy gratings and superstructure

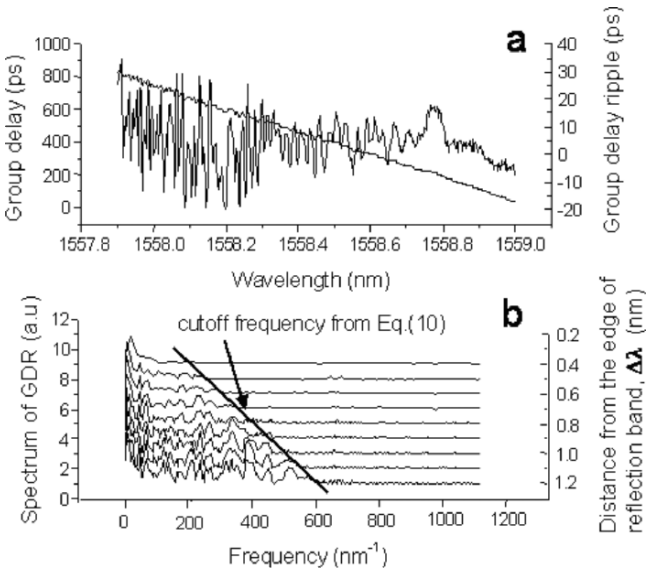

Fig. 15. (a) Group delay and GDR of a typical chirped FBG. (b) Fourier spectrum of this GDR calculated for different bandwidths $\Delta\lambda$ measured from the high-wavelength edge of the reflection band and demonstrating the cutoff frequencies coincident with the ones predicted by Eq. (10).

Bragg gratings. These results are important both for basic understanding and for the further improvement of the grating performance.

2.3. Correction of Chirped Fiber Bragg Gratings

As discussed above, GDR originates from random and systematic errors introduced during fiber grating fabrication. While fabrication methods can be fine tuned to eliminate much of this noise, an alternate approach is to improve grating performance through post processing based on the measured response of a grating. Several research groups have reported on modification of the fiber grating fabrication process to achieve reduced GDR [77–80]. The authors of [80] proposed a method for adjusting the grating profile to account for systematic grating imperfections by numerical solution of the inverse problem for the coupled wave equations. Though these approaches allow for significant reduction of GDR, they do not deal with random errors introduced in fiber grating fabrication, which in typical fiber grating fabrication systems are larger than or comparable to systematic errors. [81] demonstrates a technique for reducing the GDR in chirped FBGs by iteratively characterizing and subjecting the grating to additional UV corrective post-processing. This technique does not fully rely on the accuracy of the solution of the coupled wave equations, using them as iterations only and, thus, equally well suited for correction of systematic as well as random deviations in chirped FBG parameters.

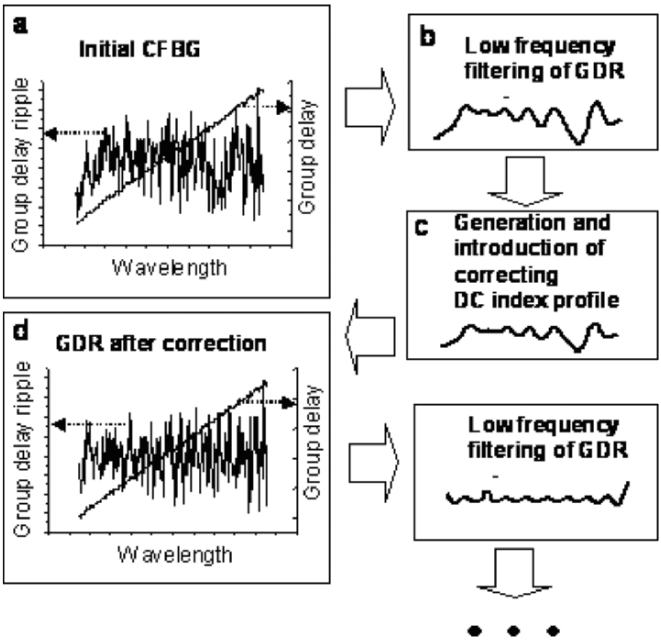

Fig. 16. Iterative chirped FBG correction. (a) Group delay and GDR of initial chirped FBG. (b) The result of low frequency filtering of the GDR shown in Fig. 14(a). (c) Determination of corrective DC index and inscription onto chirped FBG by direct UV exposure. (d) Group delay and GDR after first correction. See [81].

The idea of the approach of [81] is illustrated in Fig. 16 and described further below in this section. After fabrication of a chirped FBG using the conventional UV grating writing technique, e.g., with a phase mask, the GDR of the grating is characterized [Fig.16(a)]. This grating correction is based on the fact that, it is only relatively low frequency GDR that affects the performance of chirped FBG devices [2,74,69]. For this reason, the correction of chirped FBGs can be performed in the adiabatic or classical ray approximation when compensating slowly varying grating defects and can be determined by a simple rescaling of the low-frequency GDR component as schematically shown in Fig. 16b and c and described further below. This algorithm is useful for strong gratings for which the numerical inverse solution of coupled wave equations becomes unstable and its accuracy is questionable [82]. The corrective index variation is introduced by direct UV exposure to obtain GDR having reduced low frequency component of GDR [Fig. 16(d)]. The iterative steps (b→c→d→b) are continued until the desired reduction of the GDR is achieved.

The correction algorithm of [81] is based on an "adiabatic" solution of the inverse problem for the coupled wave equation for chirped FBG. The GDR is usually relatively small and therefore the relation between the refractive index variation and corresponding GDR is linear. In the simplest adiabatic approximation, which is valid for slowly varying GDR, the "direct current" (DC) index variation, $\delta n_{\rm dc}(x)$ [4] needed

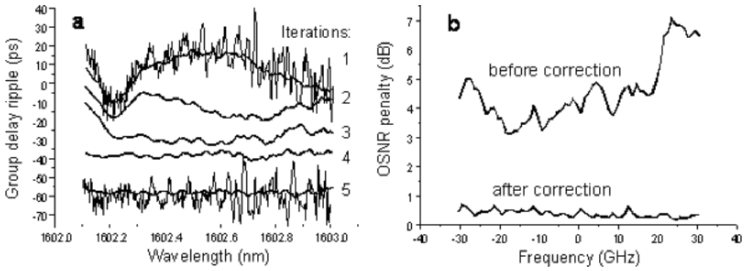

Fig. 17. (a) Iterative process of grating correction: GDR (fine) and GDR averaged over 0.1 nm (bold) after several correction steps, from 1 (initial) to 5 (final). For better visualization, the zero GDR of iterations has been arbitrarily shifted along the GDR axis. (b) Computed OSNR penalties for initial (1) and final corrected (5) gratings. See [81].

for compensation of the GDR, $\delta\tau(\lambda)$, is defined by

$$\delta n_{\rm dc}(z) = \text{const}\frac{cC}{\Lambda}\delta\tau(2n_0Cz), \tag{11}$$

where c is the speed of light in vacuum, n_0 is the effective index, $C = d\Lambda/dx$ is the chirp rate of the grating period Λ, and *const* is of order 1. This constant is determined by experimental calibration. Equation (11) shows that in the adiabatic approximation the DC index needed to compensate the GDR is simply determined by rescaling the plot of GDR. It follows from Eq. (11) that $\delta n_{\rm dc}(x)$ which compensates 10 ps in GDR amplitude is $\sim 10^{-5}$. Note that if the grating is strong (as in the experiment considered below) the reflection amplitude is very close to unity and the reflection amplitude ripple introduced by $\delta n_{\rm dc}(x)$ is negligible. Interestingly, the described inverse procedure is valid in the limit of strong gratings and is therefore suitable for strong gratings where layer-peeling algorithms are prone to errors [82].

If the characteristic frequency of the GDR becomes large enough Eq.(11) fails. In this case the local spatial peak in DC index no longer corresponds to a local peak in group delay but generates a complex GDR as described in the previous section. In order to enable local correction of the higher frequency ripple, it is necessary to determine a DC index profile, which corresponds to a narrow peak in GDR. Generally, this can be done by solving the inverse problem for the coupled wave equation [82]. For practical purposes and also for general understanding it is desirable to have a simple relation, which determines the DC index profile corresponding to a local GDR peak. This relation was found in [81].

[81] considers a chirped FBG written in hydrogen loaded single mode fiber, which has a grating period $\Lambda = 548$ nm, chirp $C = 0.048$ nm/cm, grating length 10 cm, and amplitude of index modulation $\sim 3 \times 10^{-4}$ corresponding to reflection coefficient 99.998%. The dispersion generated by this chirped FBG is around 780 ps/nm, bandwidth ~ 1.2 nm, and the GDR observed is $\pm$ 25 ps peak-to-peak. For these grating parameters, Eq. (11) is reasonably accurate if the spatial resolution of index variation is ≥ 1 cm and, respectively, the characteristic wavelength of GDR variation is ≥ 0.1 nm.

Fortunately, this range of wavelength variation corresponds to low-frequency GDR, which introduces the major contribution to the OSNR penalty for the 40 Gbit/s systems [2,74,69].

Figure 17(a) shows the original GDR of the grating considered (1, fine curve), and the result of its averaging over 0.1 nm (1, bold curve). The correction of the averaged GDR was performed in several iterations by successive elimination of individual ripples using a 5 mm wide UV laser beam. The corresponding DC index variation was found using Eq. (11) with *const* determined by calibration of the beam power at each step of GDR trimming. Figure 17(a) demonstrates reduction of averaged GDR from ± 15 (curve 1) to ± 2 ps (curve 5). The OSNR penalty curves of Fig. 17(b) calculated for the unsmoothed GDR demonstrate the dramatic improvement obtained when the corrected device was implemented in a 40-Gbit/sec CSRZ transmissions system simulation. The OSNR penalty is reduced from 7 to less than 1 dB in the ± 30-GHz bandwidth. Note that this comparison also highlights the dominant contribution of the low-frequency GDR, which can be improved through the described procedure, relative to the small effect of high-frequency GDR component.

Systematic errors in FBG fabrication could also be eliminated through correction of phase masks. Methods of diffraction grating modification through nonuniform heating and stretching have been developed [83]. These approaches allow changes to the phase mask grating period in the range between a few pm and a few nm and spatial resolution of a few mm. It was shown that the grating period can be modified iteratively with negligible effect on the profile of the gratings.

2.4. GDR in Sampled Bragg Gratings

As mentioned above, sampled FBGs are gratings having a long-period change of refractive index on the top of the short-period FBG. Chirped sampled FBG (CSFBG) can be used for colorless or multi-channel dispersion compensation (MDC). The development of MDC devices is of significant interest due to their use in single channel applications requiring "colorless" or broadband components that are valid for many channels over a large range of wavelengths, as well as applications requiring operation for multiple channels simultaneously.

A brief review of the sampled FBG is given in section 1.2. Here we will dwell only on the discussion of the GDR problem for the sampled FBG, which is the most serious limiting factor in the performance of MDC devices. For CSFBGs, the GDR reduction is even more critical than for the single channel chirped FBG because these gratings require stronger UV-induced index change, and GDR grows with increased UV-induced index. Moreover it is expected that in superstructure gratings, the corrective profile derived from a single channel may be applicable to all of the channels, making UV correction a useful tool for such CSFBGs just as it is for single channel gratings.

The reproducibility of GDR for all channels is critical for the application of multi-channel grating correction. To examine the origins of GDR in multi-channel gratings we consider the simplest example of a two-channel grating which has the following variation of the refractive index:

$$\begin{aligned}\Delta n_{\mathrm{ac}}(z) &= \Delta n_0[\sin(k_1 z + Cz^2 + \varphi(z)) = \sin(k_2 z + Cz^2 + \varphi_2(z))] \\ &= \Delta n_0 \sin\left(\tfrac{k_1+k_2}{2} z + Cz^2 + \tfrac{\varphi_1(z)+\varphi_2(z)}{2}\right)] \\ &\quad \times \cos\left(\tfrac{k_1-k_2}{2} z + \tfrac{\varphi_1(z)-\varphi_2(z)}{2}\right). \end{aligned} \tag{12}$$

The first line of Eq. (12) corresponds to the AC index $\Delta n_{\mathrm{ac}}(z)$ of two single channel gratings having channel separation $k_1 - k_2$. Here the coefficient C determines the chirp of the gratings and functions $\varphi_1(z)$ and $\varphi_2(z)$ determine the spatial phase noise at each exposure. We ignore amplitude noise in this simplified analysis. Clearly, the two phase terms are in general independent and a corrective profile derived from one of the channels will not be applicable to the other channel. The second line of Eq. (12) corresponds to the AC index introduced by a single exposure through a sinusoidal amplitude modulated phase mask. In this case the spatial noise is separated into the noise in the high-frequency AC index modulation $\varphi_{\mathrm{Bragg}}(z) = (\varphi_1(z) + \varphi_2(z))/2$, and noise in the low-frequency superstructure period variation,

$$\varphi_{\mathrm{superstructure}}(z) = (\varphi_1(z) - \varphi_2(z))/2.$$

In this case, provided that $\varphi_{\mathrm{superstructure}}(z)$ is small, each channel will see the same high-frequency phase noise, $\varphi_{\mathrm{Bragg}}(z)$, and grating correction derived from one channel will be applicable for both channels. Therefore, just as phase noise in the grating period causes GDR in the single channel grating, phase noise in the superstructure period will cause channel-to-channel variations of GDR. This effect may also be understood with a simple Fourier argument: The noise in the superstructure period may be understood as the addition of Fourier components to the superstructure that are not simply multiples of the fundamental superstructure period. Such superstructure Fourier components would have the effect of generating grating GDR with a different wavelength spacing from that of the fundamental superstructure period. This "aperiodic" grating GDR will be roughly added to the fundamental periodic grating response, thus resulting in an overall grating response that is different for each channel. Note that this argument employs Fourier components and superstructure side bands similar to the GDR cutoff arguments described in [74].

However, even if the grating has a single superstructure period, there are other sources of noise that can make each channel profile different from another. In particular, the presence of cladding mode loss, which occurs on the short wavelength side of a fiber Bragg resonance, can cause the superstructure grating response to vary from channel to channel. This can be most easily understood by considering the longest wavelength resonance of a multi-channel fiber Bragg grating, which will not overlap with any cladding mode resonances from the other channels, unlike the shortest wavelength resonance, which will coincide with the cladding mode resonances from all of the longer wavelength channels.

Another source of channel irreproducibility originates from differences in channel reflectivities. The strong channels display mostly phase ripple, and very little amplitude ripple, whereas for weak channels, amplitude ripple is more pronounced and affects the channel's response to the correction.

[15] demonstrated correction of the low frequency GDR of chirped superstructure FBGs using the UV post-processing technique described above. It was shown that for dispersion compensation of 40 Gbit/s signals this method can significantly reduce the

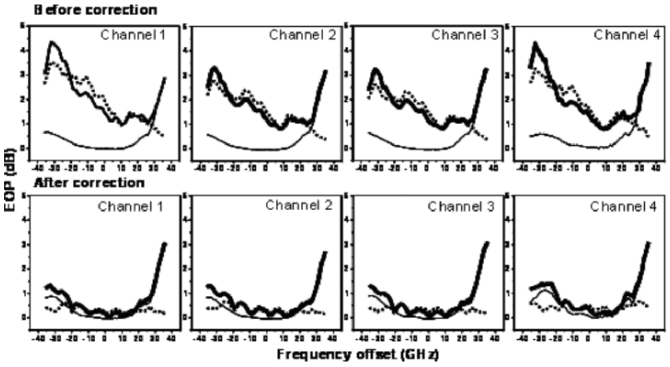

Fig. 18. EOP simulation plots for the four strongest channels before and after correction of the superstructure grating GDR. Zero detuning corresponds to approximate center of the reflection band. Solid: amplitude, dashed: phase, bold: both. EOP near zero frequency offset improves by 0.5 to 1 dB in all channels. See [15].

low frequency GDR for all channels of a multichannel grating. It was also shown that the resulting eye opening penalty (EOP) is also improved substantially (from 1 to 0.5 dB).

Figure 18 shows simulation plots of the 43-Gbit/s NRZ EOP (see section 3 for definition of EOP) of each channel before and after grating correction from [15]. It was demonstrated that after correction the EOP due to the superstructure grating was reduced from $\sim$2 to $<$ 1 dB over a range of $\sim$15 GHz of carrier frequency tuning near the band center. These plots show the EOP due to only the phase noise, only the amplitude noise, and both noises together. We note that the phase noise contribution is dominant, and that the adiabatic correction technique reduces the EOP from the phase noise while leaving the contribution from the amplitude noise small. This is to be expected, since the reflectivity is large and thus insensitive to variations in the local Bragg wavelength, and moreover, the data used in generating the corrective profiles was derived from the GDR. We will discuss the relation between GDR and EOP further in section 3.

3. Dispersion Compensation Using Fiber Bragg Gratings: System Aspects

In section 3 we discuss the details of the system impact of fiber grating TDCs. In the first two sections, we consider the system impact of the dispersion and the dispersion slope and the need for tunable dispersion compensation. Then we describe methods of approximating the system impact of GDR through simulations and we focus on one measure in particular: the EOP. We then consider applications of EOP to characterization of gratings in systems and also during grating fabrication. Lastly we discuss system tests of fiber gratings. As previously mentioned, we consider primarily 40 Gbit/s (and higher) systems, since these are most likely to require tunable dispersion compensation.

3.1. Dispersion Limitations in Optical Transmission Systems

High-speed systems operating at bit rates of 40 Gbit/s and beyond are more sensitive to dynamic variations such as channel peak power deviations, network reconfigurations, as well as temperature changes in the fiber [2,22,84,85]. Fiber dispersion has a significant impact on propagation of short optical pulses. Different frequency components of the pulse propagate at different speeds and, therefore, arrive at slightly different times, eventually leading to pulse broadening. Dispersion-induced pulse broadening is more detrimental for higher bit rate communication systems. For example, the dispersion tolerance of 40 Gbit/s transmission is 16 times tighter than that of the 10 Gbit/s and 256 times tighter than that of 2.5 Gbit/s. These problems can be exacerbated by incomplete dispersion slope compensation in transmission fiber and uncertainties in the actual dispersion of installed fiber spans. As a result, precise and tunable dispersion compensation becomes an essential part of high bit rate transmission system design.

Fiber dispersion imposes limitations on the maximum distance that signals can propagate at a particular bit rate with the maximum acceptable penalty not exceeding a certain limit. One can relate fiber dispersion β_2, maximum tolerable fiber length L and a signal bit rate B as [86]

$$B\sqrt{|\beta_2|L} \leq 1/4. \tag{13}$$

The coefficient in the right-hand side generally depends on the modulation format and the criterion used to define maximum acceptable penalty. In Eq. (13), we use the dispersion parameter β_2, which is related to the fiber dispersion D_{fiber} through: $\beta_2 = -\lambda^2 D_{\text{fiber}}/2\pi c$, where λ is the center wavelength of the pulse. Equation (13) is often referred to as the dispersion limit.

At higher bit rates (>40 Gbit/s), the pulse spectrum is broad enough so that even for a single channel the dispersion changes across the channel bandwidth. Therefore, even if β_2 is fully compensated, the maximum transmission distance can be limited by higher order dispersion, $\beta_3 = d\beta_2/d\omega$, or dispersion slope. The dispersion slope limit of a system may be derived according to arguments in [86]. From the pulsewidth–bandwidth product criterion, it follows that maximum allowed transmission length (L) limited by cubic dispersion is given by [86]

$$B(|\beta_3|L)^{1/3} \leq 0.324. \tag{14}$$

This shows that there is an inverse cubic dependence of transmission distance limit on bit rate, unlike the linear dispersion length limit, which is proportional to the inverse square of the bit rate. To verify this simple argument, we computed EOPs for 40- and 160-Gbit/s 50% return-to-zero (RZ) data pulse trains subjected to a purely cubic dispersion. Figure 19 shows the cubic decrease of the maximum tolerable dispersion slope (for a given EOP) as the bit rate increases. These plots also allow a rough estimate of the dispersion slope limited distance for transmission fibers, i.e., the maximum transmission distance when linear dispersion is completely compensated and only dispersion slope predominates. For 160 Gbit/s, the EOP rises to 0.5 dB at about 0.04 ps/nm^{2}km, and a transmission distance of 50 km. Typical transmission fibers have dispersion slopes in the range from 0.04 to 0.1 ps/nm^{2}km, giving 160-Gbit/s slope limited distances of between 50 and 20 km.

Dispersion slope compensation with the fixed DCMs only is difficult at higher bit rates due to the extreme sensitivity to dispersion variations. Therefore, transmission

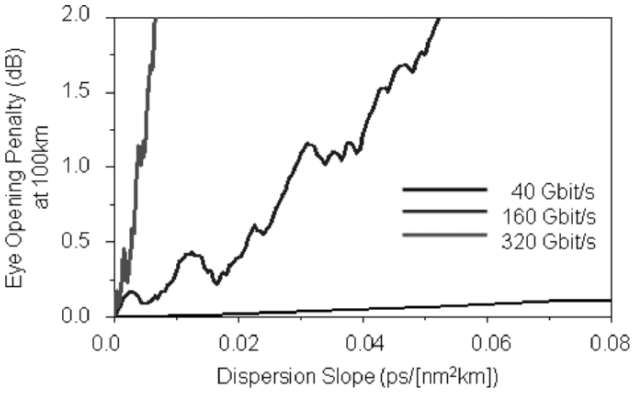

Fig. 19. Eye opening penalty at 100 km as a function of dispersion slope.

systems operating at 160 Gbit/s and higher bit rates are likely to require additional dynamic dispersion slope compensation.

3.2. Dispersion Management in Optical Networks

Dispersion management is one of the most critical parts of high bit rate and high capacity optical networks [86–89]. Figure 20 shows a schematic of a typical WDM transmission system. Broadband fixed dispersion compensation (DC) devices are usually placed in the middle of two stage in-line optical amplifiers. Typically, in-line dispersion compensation is accomplished by inserting dispersion compensating fiber (DCF) modules periodically in the network. DCF serves to reverse some of the effects of transmission fiber dispersion. However, it is difficult to compensate accumulated dispersion precisely for all WDM channels due to the dispersion slope mismatch. A slope matching can be improved using so-called enhanced DCF, although additional adaptive per-channel based compensation is still necessary for high-speed networks. A residual slope accumulated over multiple transmission spans can be compensated by a broadband compensator that is typically inserted after the multiplexer or before the demultiplexer (pre- or post-compensation). Broadband fixed dispersion compensators cannot compensate for dynamic dispersion variations, and therefore, accumulated dispersion may exceed dispersion tolerances of the receiver. This excessive dispersion is compensated by the TDCs. They are often located in front of the receiver after the demultiplexer and complement broadband fixed DC modules. In addition, channel rerouting in optical networks may cause variations in accumulated dispersion of different channels depending on the route traveled by a particular channel. Sub-band dynamic tunable dispersion compensators with adjustable slope and a large tuning range are likely to become a viable solution in long reconfigurable networks.

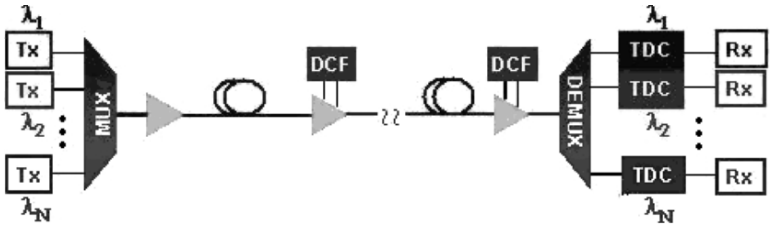

Fig. 20. Schematic of a typical high-speed transmission system.

3.3. System Performance of FBG-Based DCs and Effect of GDR

As we discussed in section 2, in an ideal dispersion compensating device, group delay should vary linearly with wavelength, but in practice, as with any optical resonant device, FBGs exhibit group delay ripple (GDR). GDR is more precisely defined as pseudo-random amplitude and phase noise that gives rise to optical degradation of pulses propagating through the grating [2,69,70,90–97]. GDR is simply the frequency derivative of the grating phase response versus frequency. GDR impacts optical pulse propagation in several ways depending on the amplitude and period of the ripple and data bit rate/modulation format. These include pulse broadening and reshaping, amplitude and timing jitter, and inter-symbol interference. Pulse distortions of this type manifest in system penalty, thus reducing the benefit of the TDC device.

It is useful to divide GDR into two categories: ripple with the oscillation periods larger than the bit rate will be referred to as *slow* ripple, while ripple with oscillation periods smaller than bit rate will be referred to as *fast* ripple. (Note that this definition of slow and fast GDR is not necessarily the same as that used in the previous section when relating GDR to physical grating defects.) Several studies have shown that slow ripple is typically more detrimental for the system performance whereas fast ripple is averaged over the optical signal bandwidth. Both slow and fast GDR cause degradation in system performance that can be characterized by eye-opening penalty.

We may relate GDR to transmission system penalties through analysis of the grating and signal spectra. The complex amplitude $A_{\mathrm{out}}(t)$ for a particular pulse shape/data modulation format at the output of the FBG may be obtained by convolving the input complex amplitude $A_{\mathrm{in}}(t)$ with the impulse-response function $H(t)$ of the FBG as

$$A_{\mathrm{out}}(t) = \int_{-\infty}^{\infty} A_{\mathrm{in}}(t')H(t-t')dt. \tag{15}$$

The fiber grating is modeled as a linear filter with constant amplitude and non-uniform phase. We assume that the linear part of the grating chirp perfectly compensates for transmission fiber dispersion [93] and, therefore, can be subtracted from total grating chirp, leaving the GDR only.

The GDR that can be represented as

$$\tau(\Delta\omega) = a \sin\left(\frac{\Delta\omega}{p} + \varphi\right), \tag{16}$$

where $\Delta\omega = \omega - \omega_0$ is frequency offset from the central frequency of the optical signal, a is amplitude of GDR, is the period of the ripple. The full GDR is then a Fourier sum of these harmonic components.

The impulse response function $H(t)$ is more directly related to the phase characteristics of the FBG rather than to the GDR. Phase ripple can be obtained by integrating Eq. (16) over ω:

$$\varphi(\Delta\omega) = ap \cos\left(\frac{\Delta\omega}{p} + \varphi\right). \tag{17}$$

There are two important cases that should be considered: (a) when the central frequency of the pulse is aligned with the GDR peak point $\varphi \propto \cos(\omega)$ corresponding to φ =0, and (b) when it is aligned with the GDR quadrature point $\varphi \propto \sin(\omega)$ corresponding to $\varphi = \pi/2$.

General results for the impulse response were first derived in [70]. For two special cases of φ =0 and $\varphi = \pi/2$ the impulse response is given by

$$H(t) = \begin{cases} J_0(ap)\delta(t) + \sum_{n=1}^{\infty} i^n J_n(ap)[\delta(t - n/p) + \delta(t + n/p)], \\ \qquad\qquad\qquad\qquad\qquad\qquad \text{if } \varphi = 0, \\ J_0(ap)\delta(t) + \sum_{n=1}^{\infty} J_n(ap)[\delta(t - n/p) + (-1)^n \delta(t + n/p)], \\ \qquad\qquad\qquad\qquad\qquad\qquad \text{if } \varphi = \pi/2, \end{cases} \tag{18}$$

Equations (18) can be further simplified if we assume that $ap \to 0$.

$$H(t) \approx= \begin{cases} \delta(t) + i\frac{ap}{2}[\delta(t - 1/p) + \delta(t + 1/p)], & \text{if } \varphi = 0, \\ \delta(t) + i\frac{ap}{2}[\delta(t - 1/p) - \delta(t + 1/p)], & \text{if } \varphi = \pi/2. \end{cases} \tag{19}$$

3.4. Eye-Opening Penalty Estimations

Several approaches for translation of the GDR to system penalties have been proposed [70,91–97]. Based on a simple analytical result in Eqs. (19), GDR can be related to expected system penalty through

$$\text{EOP} = -10 \log_{10}(1 - ap), \tag{20}$$

where ap is the amplitude of phase ripple. The penalties predicted by this simple relation have been shown to be in a good agreement with experimental results [70]. Estimation of the worst EOP based on peak-to-peak phase ripple measured within the signal bandwidth was proposed by Yoshimi et al. [92]. In [94] the system penalty has been estimated using standard deviation of the phase ripple within a spectral window. This method has been further refined in [94] by weighting the standard deviation of the phase ripple by the signal spectrum. A comparison of system penalty simulations, testbed results and predictions of different models is shown in Fig. 21 [96]. Note that while Fig. 21 shows good agreement with experiment, such estimations of system penalty and comparison with experiment become less reliable when the penalty

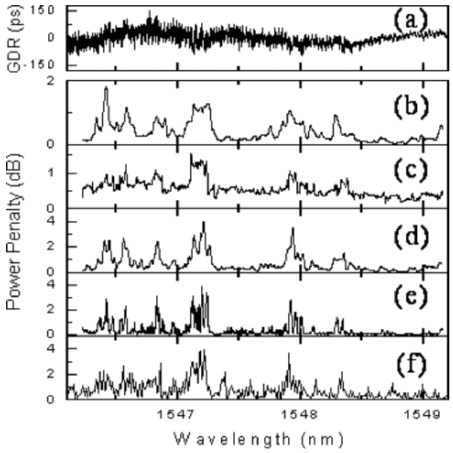

Fig. 21. System measurements, simulations, and model predictions. (a) Measured GDR. (b) Power penalty calculated from the unweighted phase ripple standard deviation [94] (c) Power penalty calculated from the phase ripple peak-to-peak amplitude [92]. (d) Power penalty calculated from the phase ripple weighted by the signal spectrum [96]. (e) Simulated power penalty. (f) Testbed results. After [96] (© [2003] IEEE).

approaches the low levels required by system designers ($\sim$0.5 dB). In this range, numerical simulations provide at best a guide to an upper bound for system penalty.

Depending on the application, system length and a particular design various modulation formats are utilized. These include on-off-keying (OOK) type of formats such as non-return-to-zero (NRZ), return-to-zero (RZ), carrier suppressed RZ (CSRZ), and differential phase shift keying (DPSK). Analytical results together with numerical simulations can be used to predict the effect of GDR periodicity on different data modulation formats. It can be inferred from Eqs. (19) that larger period ripple results in an intra-symbol interference and leads to distortions similar to those caused by dispersion, while small ripple periods result in inter-symbol interference [70,90]. Figure 22 shows the calculated penalties due to GDR for NRZ and RZ signals, with the signal being aligned with a GDR peak (left column), as well as the quadrature point (right column). Independent of modulation format, the largest sensitivity to GDR occurs when the ripple period equals the bit rate [70,2,93]. DPSK, unlike OOK, has been found to be very tolerant to GDR with $\varphi = 0$ (peak point), while quite sensitive to GDR with $\varphi = \pi/2$ (quadrature point) [2].

3.5. System Simulations and Experimental Results

Computation of EOP is a useful measure of grating performance that can be applied when experimental system results are not available. Figure 23 illustrates a definition of EOP. Shown in this figure are the 43-Gbit/s NRZ eye diagrams for the signals after the electrical Bessel filter without the grating (left plot), and with the grating (right plot).

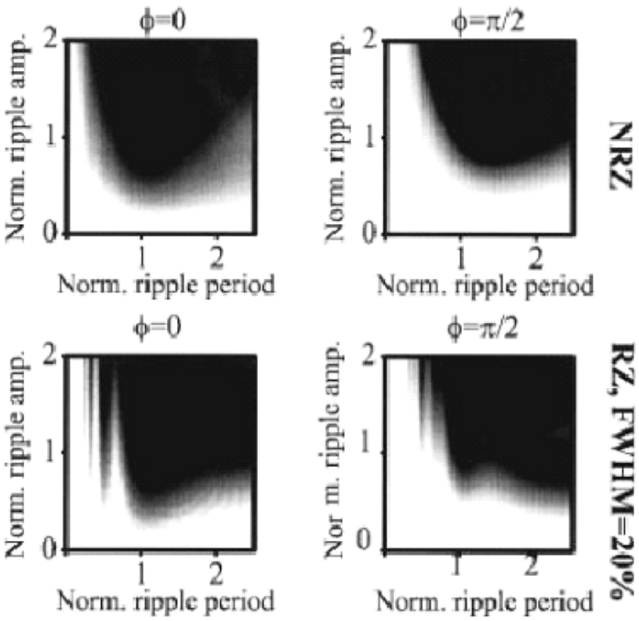

Fig. 22. Calculated penalties with the signal being aligned with a GDR peak (left column), and with the quadrature point (right column). Penalties range from 0 (white) to 2 dB and higher (black). From [2].

Rectangles of fixed width (20% of the bit period) are fitted within each eye diagram by adjusting their heights. The EOP due to the grating GDR can be conceptually described as the reduction of the height of the rectangle from the eye diagrams with the grating compared to the height of the rectangle from the eye diagram without the grating. If we take account only the effects of the dispersion compensator in the system then the OSNR penalty due to the device is roughly twice the EOP.

The EOP measure can also be used in the grating fabrication process, for example, to quantify the improvement in chirped FBG TDCs made using post-processing correction techniques [98]. Figure 24(b) shows the improvement in OSNR computed using the EOP as a measure of performance. Such improvement may be computed efficiently during the writing process and included in iterative grating fabrication schemes.

A TDC device was fabricated from the grating of Fig. 17. Both system tests at 40 Gbit/s and EOP computations were performed. As discussed in section 1, an important test for any TDC is its performance as the carrier frequency is tuned. Figure 24(a) shows OSNR penalty calculated from the EOP as both dispersion and carrier frequency are tuned. These simulations show that the OSNR penalty was less than 0.8 dB for carrier frequency variation of ± 30 GHz and dispersion variation between 750 and 270 ps/nm. The OSNR penalty was also measured experimentally using the setup shown in Fig. 24(b). The 43-Gbit/s CSRZ signal was controlled by adjusting the input power into an EDFA. The dispersion was varied by sending the signal through various lengths

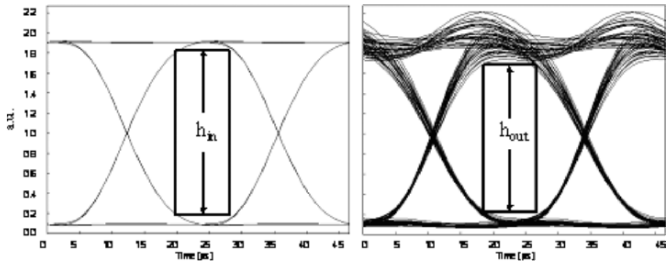

Fig. 23. 43-Gbit/s NRZ eye diagrams at the output of the electrical Bessel filter of the simulation setup without the grating (left plot) and with the grating (right plot). Rectangles of fixed width (20% of the bit period) are fitted within each eye diagram by adjusting their heights. The reduction in height gives a measure of the EOP.

of DCF. The TDC was inserted in front of the receiver. Figure 24(c) shows the result of OSNR penalty measurement for carrier frequency shifts of –10, 0, and 10 GHz as a function of applied voltage. This carrier frequency deviation accounts for possible drift of the laser and grating central frequency. The measured OSNR penalties did not exceed 0.5 dB and were in reasonable agreement with numerical simulations. As mentioned previously, it is important to note that system penalties at the level of 0.5 dB are difficult to measure with great accuracy, and any method of characterizing penalty due to grating GDR will at best provide a typical value of the system penalty.

A number of other system experiments have been reported utilizing FBG-based tunable dispersion compensating devices [2,22,36,39,84,99,100]. In principle, FBG TDCs could be implemented in the pre-, post-, or in-line compensation modules of the transmission system. In [99] a tunable FBG was utilized for dynamic optimization of a nonlinear system where the optimum amount of dispersion compensation changes with the power level. In this case, the FBG was placed at the receiver of a 40-Gbit/s NRZ system. Figure 25 compares the measured and calculated receiver sensitivities versus span launch power for a system with fixed (DCF) and optimized tunable (FBG) post-compensation. This result shows that an FBG TDC used as a per-channel post-compensator can significantly reduce the penalties arising from variations in the launch power compared to a similar system with fixed dispersion compensation.

As previously mentioned, chirped FBG TDC devices enabling a dispersion management of 160 Gbit/s systems has been proposed and demonstrated [2,22,23]. The tuning ability of the device in [2] is illustrated in Fig. 26. FBG-based tunable dispersion slope compensators for 160 Gbit/s transmission have been proposed in [36,38,39,100].

Finally, as discussed in section 1 multi-channel TDC devices have been demonstrated based on multi-channel sampled fiber gratings. One such device used a single linearly chirped sampled FBG providing a continuous compensation of chromatic dispersion from -700 to -300 ps/nm simultaneously for four channels with 300 GHz spacing [14]. In 40 Gbit/s CSRZ transmission experiments the power penalty did not exceed 1.1 dB for any of the twelve 100-GHz spaced channels. Figure 27(a) shows the received power versus bit-error rate (BER) and measured eye diagrams obtained in experiments at one of the channels (channel 5) for back-to-back configuration and for

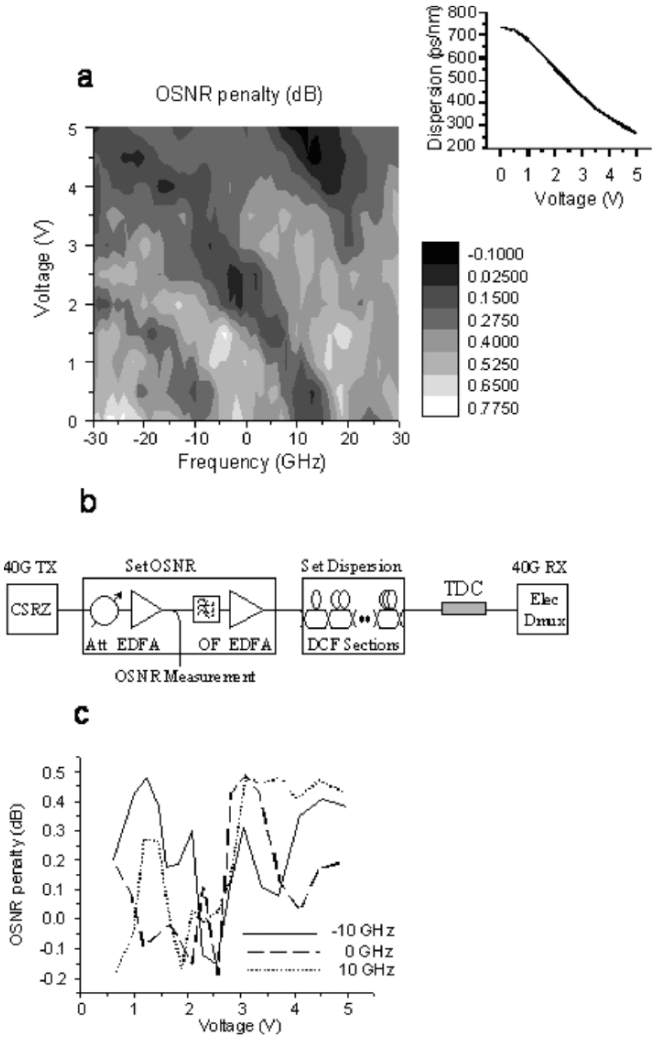

Fig. 24. (a) OSNR penalty calculated for the TDC device as a function of voltage and carrier frequency for a 43- Gbit/s CSRZ system. The insert shows the introduced dispersion as a function of applied voltage. (b) Experimental setup for OSNR measurement (Att—attenuator, OF—optical filter, DCF—dispersion compensating fiber). (c) Measured OSNR penalty for the same device for −10, 0, and 10 GHz carrier frequency shifts. From [98] (© [2003] IEEE).

two values of link dispersion compensated by the TDC. In addition, detuning of the channel center wavelength up to 20 GHz resulted in a less than 1.1 dB power penalty [shown in Fig. 27(b)] demonstrating suitability of this device for both dynamic reconfiguration and cost reduction in 40 Gbit/s systems. This device is summarized in Table 1 as well.

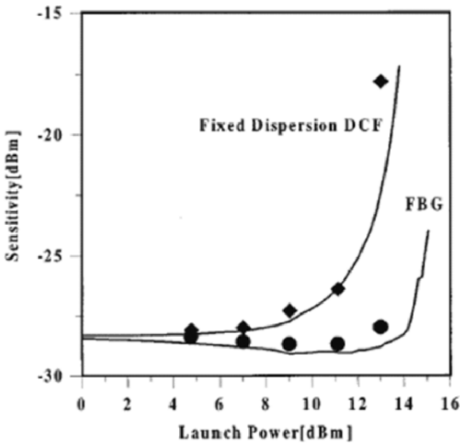

Fig. 25. Comparison of measured and calculated receiver sensitivity versus span launch power for the system with fixed and tunable post-compensation. Solid line corresponds to simulated results, diamonds and circles correspond to measured results. After [2] (© [2000] IEEE).

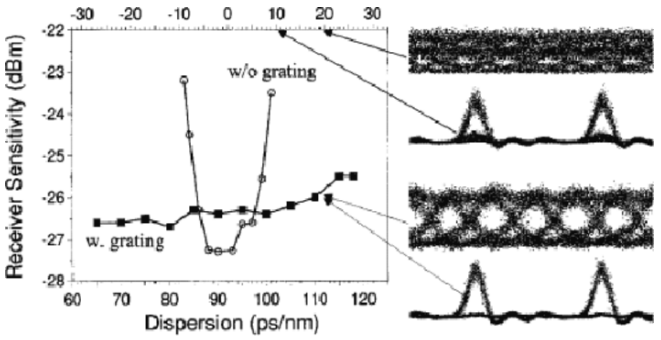

Fig. 26. Measured receiver sensitivity versus preset dispersion with and without the tunable FBG-based dispersion compensator. Measured eye-diagrams at 80 and 160 Gbit/s (after demultiplexing to 10 Gbit/s) for different amount of preset dispersion. After [2] (© [2000] IEEE).

Conclusions

In this work, we have discussed fiber grating based tunable dispersion compensators. There are numerous types of fiber grating TDCs. These include linearly and nonlinear chirped fiber Bragg gratings used in reflection and/or transmission, long period gratings, and fiber grating etalons. Tuning mechanisms exploit either the strain or temperature dependence of the fiber refractive index and grating period. In discussing fiber grating TDCs we focused on the most prominent example: the linearly chirped fiber

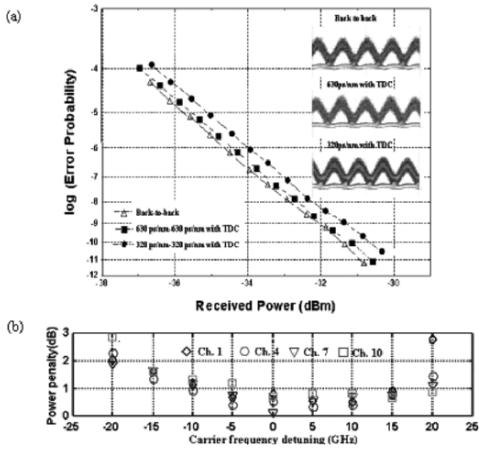

Fig. 27. (a) Received power versus BER and measured eye diagrams. (b) The effect of signal frequency detuning for different channels. After [14] (© [2003] IEEE).

grating tuned with a variable linear temperature gradient. We compared the thermally tuned grating TDC to two other well developed technologies: thin film etalons and ring resonantors. Although many TDCs have been demonstrated, only thermally tuned chirped fiber gratings, thin film etalons and ring resonators have been examined extensively in 40 Gbit/s systems. Many other TDCs have been examined at 10 Gbit/s, but as we discussed, this bit rate does not have the same stringent requirements for optical TDC and moreover, electrical dispersion compensation methods are becoming increasingly attractive at lower bit rates. Our comparison shows that at 40 Gbit/s the FBG TDCs have very good performance, but in multichannel applications, they have the drawback of being single channel or requiring complex sampling profiles and are therefore less attractive than the inherently multichannel thin film etalons and ring resonators.

We then discussed the origin of group delay ripple (GDR) in chirped fiber gratings the fabrication and characteristics of chirped FBGs in detail. Our analysis of group delay ripple made clear the origins of both high and low frequency ripple and related these to physical grating parameters. An intuitive model showed that GDR can be related to out of band reflections of a grating, which in turn can be understood as superstructure sidebands arising from individual sinusoidal components describing the grating defects. This theory clearly shows the primary property of GDR: It exhibits a high spectral frequency cutoff. GDR with higher frequencies will always occur on the long delay side of the grating spectrum, implying that chirped fiber gratings have lowest GDR (and best performance) if the light penetrates the least into the grating, i.e., has lowest delay. Lastly we discussed how GDR can be corrected through the use of post processing. The grating GDR may be measured and used in an iterative scheme to reduce the GDR. An example of a high performance grating was given

showing improvement over several post processing iterations. We also discussed the origins of GDR in multichannel sampled gratings, in particular the variations in GDR from channel to channel that arise from noise in the sampling period, variations in channel reflectivity, and cladding mode resonances. Finally, we discussed experiments showing that post processing may be applied to improve the GDR of multichannel sampled gratings.

In our last section, we discussed the system aspects of chirped fiber grating TDCs. We discussed the dispersion limits of telecom systems. At 40 Gbit/s the problems of precise dispersion compensation and drift in fiber dispersion make TDC a necessity. At 10 Gbit/s, where dispersion tolerance is 16 times higher, TDC is not necessary and therefore not cost effective, and 10 Gbit/s systems are generally designed without optical TDC. We then described several methods of relating GDR to system penalty. In particular, we showed how FBG TDCs can be characterized using the eye opening penalty. Several examples were given, including comparison between system penalty measurements and EOPs computed from the grating GDR. General agreement is observed, however, at the levels that are typically required for real devices (OSNR penalty$\sim$0.5dB), these measurements are quite difficult to do reliably, and all measures of system penalty extracted from GDR will have some error as well. Therefore GDR and measures extracted from it, including actual system measurements, can only give an upper bound on actual performance. Generally speaking, a typical number of 10–15 ps peak-to-peak GDR is a high performance specification and gives typically 0.5 to 1 dB of OSNR penalty in 40 Gbit/s systems measurements.

References

1. S. Ramachandran, S. Ghalmi, S. Chandrasekhar, Fellow, IEEE, I. Ryazansky, M.F. Yan, F.V. Dimarcello, W.A. Reed, and P. Wisk, "Tunable Dispersion Compensators Utilizing Higher Order Mode Fibers", IEEE Photon. Technol. Lett. **15** (5), 727–729 (2003).
2. B.J. Eggleton, A. Ahuja, P.S. Westbrook, J.A. Rogers, P. Kuo, T.N. Nielsen, and B. Mikkelsen, "Integrated tunable fiber gratings for dispersion management in high-bit rate systems", J. Lightwave Technol. **18**, 1418–1432 (2000).
3. K.O. Hill, Y. Fujii, D.C. Johnson, and B.S. Kawasaki, "Photosensitivity in optical fiber waveguides: Application to reflection filter fabrication," Appl. Phys.s Lett. **32**, 647–649 (1978).
4. R. Kashyap, *Fiber Bragg Gratings* (San Diego: Academic Press, 1999).
5. A. Othonos and K. Kalli, *Fiber Bragg Gratings: Fundamentals and Applications in Telecommunications and Sensing* (Boston: Artech House, 1999).
6. F. Ouellette, "Dispersion cancellation using linearly chirped Bragg grating filters in optical waveguides," Opt. Lett. **12**, 847–849 (1987).
7. R. Stubbe, B. Sahlgren, S. Sandgren, and A. Asseh, "Novel technique for writing long superstructured fiber Bragg gratings," Photosensitivity and quadratic nonlinearity in glass waveguides: fundamentals and applications, vol. 22, PD1-1 PD1-3 (1995).
8. M.J. Cole, W.H. Loh, R.I. Laming, M.N. Zervas, and S. Barcelos, "Moving fibre/phase mask-scanning beam technique for enhanced flexibility in producing fibre gratings with uniform phase mask," Electron. Lett. **31**, 1488–1490 (1995).
9. M. Brienza, "Extended length embedded Bragg grating manufacturing method and arrangement," USA Patent 5066133: United Technologies, Hartford, Conn., 1991.

10. J.F. Brennan, D. LaBrake, G.A. Beauchesne, and R.P. Pepin, "Method for fabrication of in-line optical waveguide index grating of any length," USA Patent, 5912999: Minnesota Mining and Manufacturing Company, 1999.

11. J.F. Brennan, M.R. Matthews, W.V. Dower, D.J. Treadwell, W. Wang, J. Porque, and X.D. Fan, "Dispersion correction with a robust fiber grating over the full C-band at 10-Gbit/s rates with $<$ 0.3-dB power penalties," IEEE Photon. Technol. Lett. **15**, 1722–1724 (2003).

12. J.F. Brennan, P.M. Bungarden, C.E. Fisher, and R.M. Jennings, "Packaging to reduce thermal gradients along the length of long fiber gratings," IEEE Photon. Technol. Lett. **16**, 156–158 (2004).

13. F. Ouellette, P.A. Krug, T. Stephens, G. Dhosi, and B.J. Eggleton, "Broadband and WDM dispersion compensation using chirped sampled fibre Bragg gratings," Electron. Lett. **31**, 899–901 (1995).

14. Y. Li, B. Zhu, C. Soccolich, L. Nelson, N. Litchinitser, and G. Hancin, "Multi-Channel High-Performance Tunable Dispersion Compensator for 40 Gbit/s Transmission Systems," Optical Fiber Communication Conference and Exhibition, Atlanta, GA, paper ThL4, pp. 517–519 (2003).

15. P.I. Reyes, M. Sumetsky, N.M. Litchinitser, and P.S. Westbrook, "Reduction of group delay ripple of multi-channel chirped fiber gratings using adiabatic UV correction," Opt. Express **12**, 2676 (2004).

16. M. Ibsen, M.K. Durkin, M.J. Cole, and R.I. Laming, "Sinc-Sampled Fiber Bragg Gratings for Identical Multiple Wavelength Operation," IEEE Photon. Technol. Lett. **10**, 842–844 (1998).

17. A.V. Buryak, K.Y. Kolossovski, and D.Y. Stepanov, "Optimization of refractive index sampling for multichannel fiber Bragg gratings," IEEE J. Quantum Electron. **39**, 91–98 (2003).

18. J. Rothenberg, F. Babian, Z. Brodzeli, P. Chou, H. Li, Y. Li, J. Popelek, and R. Wilcox, "Phase-Only Sampling for Fabrication and Design of High Channel-Count Fiber Bragg Gratings," Technical Digest, Optical Fiber Communications Conference, Atlanta, GA, 2003, paper ThL3, pp. 516–517.

19. J. Lauzon, S. Thibault, J. Martin, and F. Ouellette, "Implementation and characterization of fiber Bragg gratings linearly chirped by a temperature gradient," Opt. Lett. **19** (23), 2027–2029 (1994).

20. B.J. Eggleton, J.A. Rogers, P.S. Westbrook, and T.A. Strasser, "Electrically tunable power efficient dispersion compensating fiber Bragg grating," IEEE Photon. Technol. Lett. **11**, 854–856 (1999).

21. S. Kannan, J.Z.Y. Guo, P.J. Lemaire, "Thermal stability analysis of UV-induced fiber gragg gratings", J. Lightwave Technol. **8**, 1478–1483 (1997).

22. B.J. Eggleton, B. Mikkelsen, G. Raybon, A. Ahuja, J.A. Rogers, P.S. Westbrook, T.N. Nielsen, S. Stulz, and K. Dreyer, "Tunable Dispersion Compensation in a 160-Gbit/s TDM System by a Voltage Controlled Chirped Fiber Bragg Grating," IEEE Photon. Technol. Lett. **12**, 1022–1024 (2000).

23. S. Wielandy, P.S. Westbrook, M. Fishteyn, P. Reyes, W. Schairer, H. Rohde, and G. Lehmann, "Demonstration of automatic dispersion control for 160 Gbit/s transmission over 275 km of deployed fibre," Electron. Lett. **40**, 690–691 (2004).

24. P.C. Hill and B.J. Eggleton, "Strain gradient chirp of fibre Bragg gratings," Electron. Lett. **30**, 1172–1173 (1994).

25. M.M. Ohn, A.T. Alavie, R. Maaskant, M.G. Xu, F. Bilodeau, and K.O. Hill, "Tunable fiber grating dispersion using a piezoelectric stack," Technical Digest, Optical Fiber Communication Conference 1997, paper WJ3, pp. 155–156.

26. M.M. Ohn, A.T. Alavie, R. Maaskant, M.G. Xu, F. Bilodeau, and K.O. Hill, "Dispersion variable fibre Bragg grating using a piezoelectric stack," Electron. Lett. **32**, 2000–2001 (1997).

27. Junhee Kim, Junkye Bae, Young-Geun Han, Sang Hyuck Kim, Je-Myung Jeong, and Sang Bae Lee, "Effectively tunable dispersion compensation based on chirped fiber Bragg gratings without central wavelength shift", Photon. Technol. Lett. IEEE **16** (3), 849–851 (March 2004).

28. M. Pacheco, A. Mendez, L.A. Zenteno, and F. Mendoza-Santoyo, "Chirping optical fibre Bragg gratings using tapered-thickness piezoelectric ceramic," Electron. Lett. **34**, 2348–2349 (1998).

29. T. Imai, T. Komukai, and M. Nakazawa, "Dispersion Tuning of a Linearly Chirped Fiber Bragg Grating Without a Center Wavelength Shift by Applying a Strain Gradient," IEEE Photon. Technol. Lett. **10**, 845–847 (1998).

30. X. Dong, P. Shum, N.Q. Ngo, C.C. Chan, J.H. Ng, and C. Zhao, "Largely tunable CFBG-based dispersion compensator with fixed center wavelength," Opt. Express **11**, 2970–2974 (2003).

31. R. Caponi, E. Ciaramella, E. Riccardi, M. Schiano, T. Tambosso, G. Zaffiro, "Origin and system effects of polarization mode dispersion in chirped Bragg gratings", Fiber Int. Opt. **19**, 295–309 (2000).

32. A.E. Willner, K.-M. Feng, J. Cai, S. Lee, J. Peng, and H. Sun, "Tunable compensation of channel degrading effects using nonlinearly chirped passive fiber Bragg gratings," IEEE J. Select. Topics Quantum Electron. **5**, 1298–1311 (1999).

33. J.A.J. Fells, S.E. Kanellopoulos, P.J. Bennett, V. Baker, H.F.M. Priddle, W.S. Lee, A.J. Collar, C.B. Rogers, D.P. Goodchild, R. Feced, B.J. Pugh, S.J. Clements, and A. Hadjifotiou, "Twin fiber grating tunable dispersion compensator," IEEE Photon. Technol. Lett. **13**, 984–986 (2001).

34. X.W. Shu, K. Sugden, and K. Byron, "Bragg-grating-based all-fiber distributed Gires-Tournois etalons", Opt. Lett. **28** (11), 881–883 (June 1 2003).

35. S. Vorbeck and R. Leppla, "Dispersion and Dispersion Slope Tolerance of 160-Gbit/s Systems, Considering the Temperature Dependence of Chromatic Dispersion," IEEE Photon. Technol. Lett. **15** (10), 1470–1472 (Oct. 2003).

36. C.S. Goh, S.Y. Set, K. Taira, S.K. Khijwania, K. Kikuchi, "Nonlinearly strain-chirped fiber Bragg grating with an adjustable dispersion slope," IEEE Photon. Technol. Lett. **14** (5), 663–665 (May 2002).

37. C.S. Goh, S.Y. Set, and K. Kikuchi, "Design and Fabrication of a Tunable Dispersion-slope Compensating Module Based on Strain-Chirped Fiber Bragg Grating," IEEE Photon. Technol. Lett. **16** (2), 524–526 (Feb. 2004).

38. P.I. Reyes, N. Litchinitser, M. Sumetsky, and P.S. Westbrook, "160-Gbit/s tunable dispersion slope compensator using a chirped fiber Bragg grating and a quadratic heater", IEEE Photon. Technol. Lett. **17** (4), 831–833 (2005).

39. S. Matsumoto, M. Takabayashi, K. Yoshiara, T. Sugihara, T. Miyazaki, and F. Kubota, "Tunable Dispersion Slope Compensator With a Chirped Fiber Grating and a Divided Thin-Film Heater for 160-Gbit/s RZ Transmissions," IEEE Photon. Technol. Lett. **16** (4), 1095-1097 (April 2004).

40. P.S.J. Russell, "Bloch Wave Analysis of Dispersion and Pulse Propagation in Pure Distributed Feedback Structures," J. Mod. Opt. **38**, 1599–1619 (1991).

41. B.J. Eggleton, T. Stephens, P.A. Krug, G. Dhosi, Z. Brodzeli, and F. Ouellette, Electron. Lett. **32**, 1610–1611 (1996).

42. N.M. Litchinitser and D.B. Patterson, "Analysis of fiber Bragg gratings for dispersion compensation in reflective and transmissive geometries," IEEE J. Lightwave Technol. **15**, 1323–1328 (1997).

43. N.M. Litchinitser, B.J. Eggleton, and D.B. Patterson, "Fiber Bragg gratings for dispersion compensation in transmission: Theoretical model and design criteria for nearly ideal pulse recompression," J. Lightwave Technol. **15**, 1303–1313 (1997).

44. D.B. Patterson and B.C. Moore, US Patent US 6,356,684 B1 (2002).

45. J. Skaar, "Synthesis of fiber Bragg gratings for use in transmission," J. Opt. Soc. Am. A **18**, 557–564 (2001).

46. C.K. Madsen and J.H. Zhao, *Optical Filter Design and Analysis* (New York: Wiley, 1999).

47. C.K. Madsen, G. Lenz, A.J. Bruce, M.A. Cappuzzo, L.T. Gomez, and R.E. Scotti, "Integrated all-pass filters for tunable dispersion and dispersion slope compensation," IEEE Photon. Technol. Lett. **11**, 1623–1625 (1999).

48. C.K. Madsen, S. Chandrasekhar, E.J. Laskowski, M.A. Cappuzzo, J. Bailey, E. Chen, L.T. Gomez, A. Griffin, R. Long, M. Rasras, A. Wong-Foy, L.W. Stulz, J. Weld, and Y. Low, "An integrated tunable chromatic dispersion compensator for 40 Gbit/s NRZ and CSRZ," Optical Fiber Communications Conference and Exhibition, Anaheim, CA, postdeadline paper FD-9, 2002.

49. M. Jablonski, Y. Takushima, K. Kikuchi, Y. Tanaka, and N. Nigashi, "Adjustable coupled two-cavity allpass filter for dispersion slope compensation of optical fibres," Electron. Lett. **36**, 511–512 (2000).

50. D.J. Moss, S. McLaughlin, G. Randall, M. Lamont, M. Ardekani, P. Colbourne, S. Kiran, and C.A. Hulse, "Multichannel tunable dispersion compensation using all-pass multicavity etalons," Technical Digest of the Optical Fiber Communications Conference and Exhibit, Anaheim, CA, paper TuT2, 2002, pp. 132–133.

51. L.M. Lunardi, D.J. Moss, S. Chandrasekhar, L.L. Buhl, M. Lamont, S. McLaughlin, G. Randall, P. Colbourne, S. Kiran, and C.A. Hulse, "Tunable Dispersion Compensation at 40-Gbit/s Using a Multicavity Etalon All-Pass Filter With NRZ, RZ, and CS-RZ Modulation," J. Lightwave Technol. **20**, 2136–2144 (2002).

52. M. Bohn, W. Rosenkranz, and P.M. Krummrich, "Adaptive Distortion Compensation With Integrated Optical Finite Impulse Response Filters in High Bitrate Optical Communication Systems," IEEE J. Select. Topics Quantum Electron., **10**, 273–280 (2004).

53. C.R. Doerr, S. Chandrasekhar, M. Cappuzzo, E. Chen, A. Wong-Foy, L. Gomez, S. Patel, and L. Buhl, "Two Mach-Zehnder, tunable dispersion compensators integrated in series to increase bandwidth and/or range while maintaining single knob control", IEEE Photon. Technol. Lett. **17**, 828–830 (2005).

54. M. Shirasaki, "Chromatic-dispersion compensator using virtually imaged phased array," IEEE Photon. Technol. Lett. **9**, 1598–1600 (1997).

55. F. Ouellette, "All-fiber filter for efficient dispersion compensation," Opt. Lett., **16**, 303–305 (1991).

56. C.R. Doerr, L.W. Stulz, S. Chandrasekhar, and R. Pafchek, "Colorless Tunable Dispersion Compensator With 400-ps/nm Range Integrated With a Tunable Noise Filter," IEEE Photon. Technol. Lett. **15**, 1258–1260 (2003).

57. C.R. Doerr, D.M. Marom, M.A. Cappuzzo, E.Y. Chen, A. Wong-Foy, L.T. Gomez, and S. Chandrasekhar, "40 Gbit/s colorless tunable compensator with 1000 ps/nm tuning range employing a planar lightwave circuit and a deformable mirror", Proceeings of the Optical Fiber Communications Conference, Anaheim, CA, postdeadline paper PDP5, 2005.

58. R.D. Gittlin, J.F. Hayes, and S.B. Weinstein, *Data Communications Principles* (New York: Plenum, 1992).

59. S. Benedetto, E. Biglieri, and V. Castellani, *Digital Transmission Theory* (Englewood Cliffs, NJ: Prentice-Hall, 1987).

60. J.G. Proakis, *Digital Communications, 3rd ed.* (New York: McGraw-Hill, 1995).

61. T. Nielsen and S. Chandrasekhar, "OFC 2004 workshop on optical and electronic mitigation of impairments", J. Lightwave Technol. **23**, 131–142 (2005).

62. H.F. Haunstein, W. Sauer-Greff, A. Dittrich, K. Sticht, and R. Urbansky, "Principles for Electronic Equalization of Polarization-Mode Dispersion," IEEE J. Lightwave Technol. **22**, 1169–1182 (2004).

63. S.L. Woodward, S.-Y. Huang, M.D. Feuer, and M. Boroditsky, "Demonstration of an Electronic Dispersion Compensator in a 100-km 10-Gbit/s Ring Network," IEEE Photon. Technol. Lett. **15**, 867–869 (2003).

64. M.D. Feuer, S.-Y. Huang, S.L. Woodward, O. Coskun, and M. Boroditsky, "Electronic Dispersion Compensation for a 10-Gbit/s Link Using a Directly Modulated Laser," IEEE Photon. Technol. Lett. **15**, 1788–1790 (2003).

65. D. McGhan, C. Laperle, A. Savchenko, C. Li, G. Mak, and M. O'Sullivan, "5120 km RZ-DPSK transmission over G652 fiber at 10 Gbit/s with no optical dispersion compensation", Proc. of the Optical Fiber Communications Conference, Anaheim, CA, postdeadline paper PDP27, 2005.

66. H. Jiang, R. Saunders, S. Colaco, "SiGe IC for PMD mitigation and signal optimization of 40 Gbit/s transmission", Proc. Opt. Fiber Commun. 2005, Anaheim, CA, paper OWO2.

67. M. Nakamura, H. Nosaka, M. Ida, K. Kurishima, and M. Tokumitsu, "Electrical PMD equalizer Ics for a 40 Gbit/s transmission", Opt. Fiber Commun. Conf., Los Angeles, CA, paper TuG4, 2004.

68. M. Ibsen, M.K. Durkin, R. Feced, M.J. Cole, M.N. Zervas, and R.I. Laming, "Dispersion compensating fibre Bragg gratings", in Active and Passive Optical Components for WDM Communication, Proc. SPIE **4532**, 540–551 (2001).

69. K. Ennser, M. Ibsen, M. Durkin, M.N. Zervas, and R.I. Laming, IEEE Photon. Technol. Lett. **10**, 1476–1478 (1998).

70. C. Scheerer, C. Glingener, G. Fischer, M. Bohn, and W. Rosenkranz, "Influence of filter group delay ripples on system performance," in Proc. ECOC 1999, pp.1410–1411.

71. F. Ouellette, "The effect of profile noise on the spectral response of fiber gratings" in Bragg Gratings, Photosensitivity, and Poling in Glass Fibers and Waveguides: Applications and Fundamentals, Paper BMG13-2, Williamsburg, 1997.

72. R. Feced and M.N.Zervas, "Effect of random phase and amplitude errors in optical fiber gratings", J. Lightwave Technol. **18**, 90–101 (2000).

73. R. Feced, J.A.J. Fells, S.E. Kanellopoulos, P.J. Bennett, and H.F.M. Priddle, "Impact of random phase errors on the performance of fiber grating dispersion compensators", Opt.l Fiber Commun. Conf. (OFC), 2001, Anheim, CA, Paper WDD89, 2001.

74. M. Sumetsky, B.J. Eggleton, and C.M.de Sterke, "Theory of group delay ripple generated by chirped fiber gratings", Opt. Express **10**, 332–340 (2002).

75. L. Poladian, "Graphical and WKB analysis of nonuniform Bragg gratings", Phys. Rev. E **48**, 4758–4767 (1993).

76. N.G.R. Broderick and C.M. de Sterke, "Theory of grating superstructures", Phys. Rev. E **55**, 3634–3646 (1997).

77. I. Riant, S. Gurib, J. Gourhant, P. Sansonetti, C. Bungarzeanu, and R. Kashyap, "Chirped fiber Bragg gratings for WDM chromatic dispersion compensation in multispan 10-Gbit/s transmission," IEEE J. Select.Topics Quant. Electron. **5**, 1312–1324 (1999).

78. S.J. Mihailov, F. Bilodeau, K.O. Hill, D.C. Johnson, J. Albert, and A.S. Holmes, "Apodization technique for fiber grating fabrication with a halftone transmission amplitude mask," Appl. Opt. **39**, 3670–3677 (2000).

79. T. Komukai, T. Inui, and M. Nakazawa, "Very low group delay ripple characteristics of fibre Bragg grating with chirp induced by an S-curve bending technique," Electron. Lett. **37**, 449–451 (2001).

80. A.V. Buryak and D.Yu. Stepanov, "Correction of systematic errors in the fabrication of fiber Bragg gratings," Opt. Lett. **27**, 1099–1101 (2002).

81. M. Sumetsky, P.I. Reyes, P.S. Westbrook, N.M. Litchinitser, and B.J. Eggleton, "Group delay ripple correction in chirped fiber Bragg gratings," Opt. Lett. **28**, 777–779 (2003).

82. J. Skaar and R. Feced, "Reconstruction of gratings from noisy reflection data," J. Opt. Soc. Am. A **19**, 2229–2237 (2002).

83. M. Sumetsky, Y. Dulashko, J. W. Fleming, A. Kortan, P.I. Reyes, and P.S. Westbrook, "Thermomechanical modification of diffraction gratings," Opt. Lett. **29**, 1315–1317 (2004).

84. B. Mikkelsen, C. Rasmussen, P. Mamyshev, F. Liu, S. Dey, F. Rosca, "Real-world issues for High-capacity and long-haul transmission at 40 Gbit/s," ECOC 2003.

85. W.H. Hatton and M. Nishimure, "Temperature dependence of chromatic dispersion in single mode fibers," J. Lightwave Technol. **4**, 1552–1555 (1986).

86. G.P. Agrawal, *Fiber-Optic Communication Systems*, 2nd ed. (Wiley, 1997).

87. S. Lelièvre, E. Pelletier, A.W. Farr, Y. Painchaud, R. Lachance, and M. Brown, "Grating based solutions for chromatic dispersion management in DWDM systems," NFOEC 2002.

88. A.H. Gnauck, J.M. Weisenfield, L.D. Garrett, R.M. Dersier, F. Forghieri, V. Gusmeroli, and D. Scarano, "4×40 Gbit/s 75 km WDM transmission over conventional fiber using a broadband fiber grating," IEEE Photon. Technol. Lett. **11**, 1503–1505 (1999).

89. R. DeSalvo, A.G. Wilson, J. Rollman, D.F. Schneider, L.M. Lunardi, S. Lumish, N. Agrawal, A.H. Steinbach, W.Baun, T. Wall, R. Ben-Michael, M.A. Itzler, A. Fejzuli, R.A. Chipman, G.T. Kiehne, and K.M. Kissa, "Advanced components and sub-system solutions for 40 Gbit/s transmission," J. Lightwave Technol. **20**, 2154–2181 (2002).

90. S.G. Evangelides, Jr., N.S. Bergano, C.R. Davidson, "Intersymbol interference induced by delay ripple in fiber Bragg gratings," ECOC'99 Paper FA2, pp. 5–7.

91. R.L. Lachance, M. Morin, and Y. Painchaud, "Group delay ripple in fibre Bragg grating tunable dispersion compensators," Electron. Lett. **38**, (2002).

92. H Yoshimi, Y. Takushima, and K. Kikuchi, "A simple method for estimating the eye-opening penalty caused by group-delay ripple of optical filters," ECOC 2002, Paper 10.4.4.

93. N. Litchinitser, Y. Li, M. Sumetsky, P. Westbrook, B. Eggleton, "Tunable dispersion compensation devices: group delay ripple and system performance," OFC 2003, Paper TuD2, 163–164.

94. M.H. Eiselt, C.B. Clausen, R.W. Tkach, "Performance characterization of components with group delay fluctuations," IEEE Photon. Technol. Lett. **15**, 1076–1078 (2003).

95. M. Derrien, D. Gauden, E. Goyat, A. Mugnier, P. Yvernault, and D. Pureur, "Wavelength-frequency analysis of dispersion compensator group delay ripples," OFC 2003, Paper MF31, pp. 34–35.

96. X. Fan, D. Labrake, and J. Brennan, "Chirped fiber grating characterization with phase ripples," OFC 2003, Paper FC2, pp. 638–640.

97. X. Liu, L.F. Mollenauer, X. Wei, "Impact of group-delay ripple on differential-phase-shift-keying transmission systems, ECOC 2003.

98. M. Sumetsky, N.M. Litchinitser, P.S. Westbrook, P.I. Reyes, B.J. Eggleton, Y. Li, R. Deshmukh, C. Soccolic, F. Rosca, J. Bennike, F. Liu, and S. Dey, "High performance 40 Gbit/s fibre Bragg grating tunable dispersion compensator fabricated using group delay ripple correction technique," Electron. Lett. **39**, 1196–1198 (2003).

99. T.N. Nielsen, B.J.Eggleton, J.A. Rogers, P.S. Westbrook, P.B. Hansen, and T.A. Strasser, "Dynamic post dispersion optimization at 40 Gbit/s using a tunable fiber Bragg grating," IEEE Photon. Technol. Lett. **12**, 173–175 (2000).

100. T. Inui, T. Komukai, M. Nakazawa, K. Suzuki, K.R. Tamura, K. Uchiyama, and T. Morioka, "Adaptive dispersion slope equalizer using a nonlinearly chirped fiber Bragg grating pair with a novel dispersion detection technique," IEEE Photon. Technol. Lett. **14**, 549–551 (2002).

DOI: 10.1007/s10297-006-0071-7
Originally published in J. Opt. Fiber. Commun. Rep. 3, 221–291 (2006)

Impact of DCF properties on system design

René-Jean Essiambre[1], Peter J. Winzer[2] and Diego F. Grosz[3]

[1] Lightwave Systems Dept., Bell Labs, Lucent Technologies, Holmdel, NJ 07733
E-mail: rjessiam@lucent.com,
[2] Photonic Networks Dept., Bell Labs, Lucent Technologies, Holmdel, NJ 07733
[3] Instituto Tecnológico de Buenos Aires (ITBA), Eduardo Madero 399, C1106AD Buenos Aires, Argentina

Abstract. The dispersion-compensating fiber is an important optical element of current and future optical networks. In this paper, we review the impact that various properties of dispersion-compensating fibers has on the performance of optical communication systems.

1. Introduction

Dispersion compensating fibers (DCFs) have become an important building block making up today's high-capacity optical transport networks. To appreciate the importance of DCF for high-capacity lightwave systems, we briefly look at the historic evolution of optical fiber transmission [1,2].

The first single-mode optical fibers to be fabricated with low loss were step-index silica fibers [3], now referred to as standard single-mode fibers (SSMFs) and specified in the International Telecommunication Union (ITU) standard G.652. In the late 1970s and early 1980s, transmission over such fibers was performed in the spectral window around 1300 nm, where this fiber's chromatic dispersion (hereafter just referred to as "dispersion") is lowest, and permitted loss-limited transmission over about 100 km at about 1 Gb/s using Fabry-Perot lasers. However, the minimum intrinsic loss of SSMFs at 1300 nm is still $\sim$0.4 dB/km, twice the minimum value of $\sim$0.2 dB/km found in the wavelength band around 1550 nm. But even at such low loss, and with the use of both distributed feedback (DFB) lasers and highly sensitive coherent detection, transmission distances were attenuation-limited to about 200 km at 1-Gb/s data rates. With the development of erbium-doped optical amplifiers (EDFAs) operating in the

1550 nm window, the limitation from fiber loss was circumvented, and transmission over distances of thousands of kilometers became possible. However, since dispersion of SSMFs in the 1550-nm window amounts to around 17 ps/(nm km), it was now the accumulated dispersion that limited transmission distances to a few hundred kilometers at 2.5 Gb/s. To overcome this dispersion limit, new optical fibers with a dispersion zero shifted from 1300 to the 1550-nm region were designed and fabricated (ITU standard G.653). Using such dispersion-shifted fibers (DSFs), the dispersion limit was pushed out to a few thousand kilometers without the need for DCFs. However, with the advent of wavelength-division multiplexing (WDM), it was discovered [4] that the effects of Kerr fiber nonlinearities over fibers having low-dispersion values [$\lesssim 2$ ps/(nm km)], such as DSFs, leads to signal distortions from four-wave mixing (FWM) [4] and nonlinear mixing of signal and noise [5], which strongly limits transmission distance. As a result, non-zero dispersion-shifted fibers (NZDFs) were developed to provide a sufficient value of dispersion [$\gtrsim 2$ ps/(nm km)] in the 1550-nm window to prevent FWM (ITU standard G.655). The presence of NZDFs and SSMFs in optical networks along with the increase in signal speed and growth in the bandwidth of optical amplifiers all contributed in making dispersion compensation needed in current and future optical networks.

The need for dispersion compensation in the low-loss amplification window has been identified as early as 1980 [6] to extend the dispersion-limited transmission distance. Among the early technologies used to demonstrate dispersion compensation were chirped fiber Bragg gratings [7], all-pass filters [8] and micro strip delay equalizers in combination with coherent detection [9]. The first use of negative-dispersion optical fibers as dispersion compensators in system experiments has been demonstrated starting in 1993 [10] where eight wavelength-division multiplexed (WDM) channels operating at 10 Gb/s were transmitted over 280 km of NZDFs. Many experimental demonstrations followed [11–14] in terrestrial applications as well as in submarine systems [14–16]. The capacity of WDM transport then increased dramatically as dispersion compensated transmission lines became efficient (see [17] for an early review).

The beginning of the deployment of 10-Gb/s-based WDM communication systems near the end of the 1990s fostered the incorporation of dispersion compensation in various optical transmission systems. By the beginning of the 3rd millennium, deployment of 10-Gb/s technologies had become widespread in backbone terrestrial networks, making dispersion compensation omnipresent in the fabric of the worldwide fiber-optic communication infrastructure. The types of backbone terrestrial networks requiring dispersion compensation includes ultra long-haul (ULH, > 3000 km), long-haul (LH, 1000–3000 km) and regional (300–1000 km). A few years after its apparition in backbone networks, dispersion compensation also started to appear in regional and metropolitan optical networks (< 300 km) as they started to adopt 10-Gb/s technologies.

The increased demand in transport capacity, first in backbone and later in metropolitan networks, and the cost reduction of 10-Gb/s transponders is what allowed the large-scale deployment of dispersion compensation to take place. Nowadays, fiber-optic communication systems are, de facto, designed with dispersion compensation built in, so as to accommodate transport at any bit rate from 2.5 to 40 Gb/s.

This paper focuses on the basic properties of DCFs and how they impact systems. The chapter is organized as follows. The Introduction section presents the basic properties of DCFs and the way DCFs are used in systems. Section 2 describes the tools

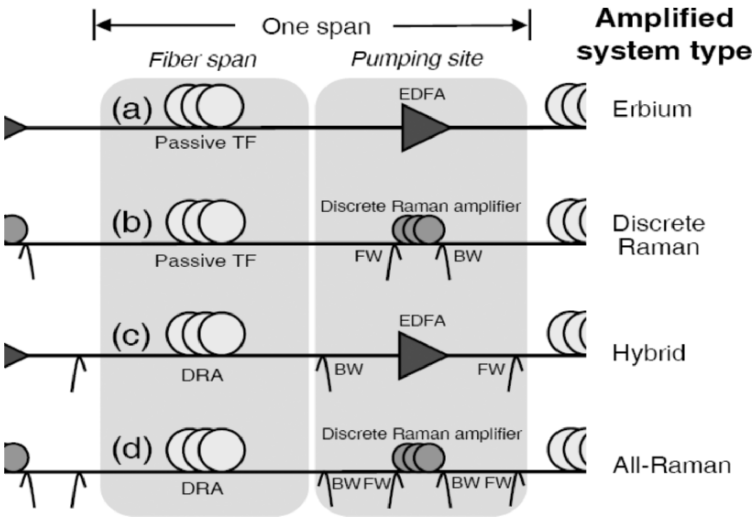

Fig. 1. Classification of transmission line types according to amplification technologies and amplifiers locations: a) EDFA; b) Discrete Raman; c) Hybrid (EDFA and Raman) and d) All-Raman. (FW/BW: Forward/Backward Raman pumping, TF: transmission fiber, DRA: Distributed Raman amplifier, EDFA: erbium-doped fiber amplifier)

used to quantify the effects of noise and fiber properties on transmission. The analysis of the impact of DCFs in various system configurations is presented in Sec. 3 which focuses on providing physical understanding of the impact of DCFs' properties on basic dispersion compensation schemes. Finally, the last section discusses the system impacts of using non-DCF-based dispersion compensation technologies.

1.1. System Layouts and Classification

Optical transmission lines can differ from one another in various ways. The most common features that are used to differentiate transmission lines are *amplification technologies*, *fiber types* and *dispersion compensation schemes*. Owing to the overwhelming importance of optical amplification in overcoming the attenuation limit, it has become customary to classify transmission lines according to the amplification scheme used in the line.

In terrestrial systems, one generally distinguishes four types of amplification schemes, as represented in Fig. 1. In the first two transmission line types (Fig. 1a and 1b), the fiber spans are made of passive transmission fibers, separated by *discrete optical amplifiers*. Depending on whether the discrete amplification scheme is based on EDFAs [1] or on discrete Raman amplifiers [18], we distinguish between *'EDFA'* and *'discrete Raman'* systems. Discrete amplification is also known as *lumped* amplification. In the situation where in addition to lumped amplification, the transmission fiber is transformed into a distributed optical amplifier using Raman pumping, one

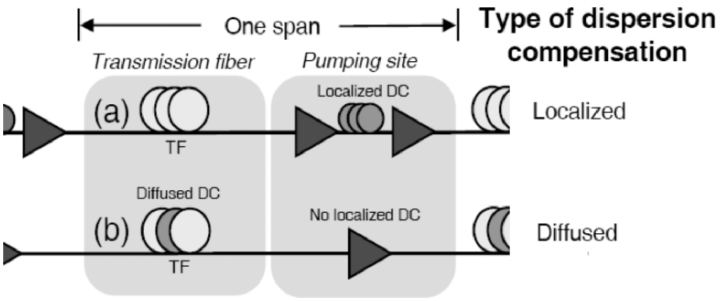

Fig. 2. Dispersion compensation placed at a specific physical location within the transmission line (a), and dispersion compensation diffused within the transmission fiber (b). In a) the DCF does not contribute to extend the transmission distance while in b) the full length of the DCF is used to bridge distance. (TF: Transmission fiber, DC: dispersion compensation)

either refers to a *'hybrid'* transmission line (if EDFAs are used as discrete amplifiers) or an *'all-Raman'* system (if *all* amplifiers in the system are based on Raman pumping). Discrete Raman amplification is generally implemented by Raman pumping the DCF [19] even though other fibers could be used as well [20]. Raman amplifiers, like EDFAs, can use both forward and backward pumping. However, unlike most EDFAs[4], Raman amplification can be used on very long fibers [22–24] that can exceed 100 km in length. Typically, the Raman gain remains large for not more than a few tens of kilometers inside the fiber, after which the Raman pumps are too attenuated to provide appreciable gain. Because of the long fiber lengths involved, one often refers to such Raman amplifiers as *distributed Raman amplifiers* (DRAs). Whether or not a Raman amplifier can be considered as a DRA also depends on the importance of other fiber properties (such as Rayleigh backscattering and fiber Kerr nonlinearity) occurring within the fiber. Rayleigh backscattering and fiber nonlinearity are treated in Secs. 2.2 and 2.3, respectively. Note that the most commonly used amplification schemes described in Fig. 2 are, in order of prevalence, discrete EDFA, hybrid, all-Raman and discrete Raman. The discrete Raman amplification scheme is generally used only to access amplification bands that lie outside the amplification window of EDFAs and other rare-earth doped fiber amplifiers [24]. Note that even though the strongest natural gain of EDFAs is the 1530–1565 nm range (C-band), the amplification window has been extended at wavelength as short as 1500 nm [25] (S-band) and as long as 1610 nm (L-band).

A second way to classify systems is according to their dispersion compensation scheme. One generally uses two broad dispersion compensation categories: *localized* and *diffused* dispersion compensation (see Fig. 2). Localized dispersion compensation applies to systems where DCFs are localized at the amplification or Raman pumping sites between transmission spans, but are not used to bridge distance. In commercially deployed systems, localized dispersion compensation is implemented by inserting reels of DCFs in huts, periodically located along a transmission line. In contrast, diffused

[4] A noticeable exception is a 68-km long EDFA developed to become a transmission fiber [21].

dispersion compensation is generally implemented by using advanced transmission fibers that are composed of fiber segments with opposite-sign dispersion [26–37]. Such fibers are referred to as dispersion-managed fibers (DMFs) and cables containing such fibers are called dispersion-managed cables (DMCs). Note that, even though the DCF is shown near the center of the fiber span in Fig. 2b, it could be placed anywhere within the fiber span. From a practical standpoint, the favored locations are the center of the fiber span (symmetric configuration) or the end of a fiber span, to minimize the number of fiber segments and fiber nonlinearity.

An important difference between the two types of dispersion compensation schemes mentioned above is that in localized dispersion compensation, the DCF is *not* used to bridge transmission distance; therefore, the actual propagation distance (i.e., the total fiber length) can significantly exceed the transmission distance (the physical path length connecting two locations). Typically, the amount of negative dispersion provided by a DCF per unit length is about 5 to 25 times higher than that of a transmission fiber. Using localized dispersion compensation, the propagation length thus exceeds the transmission distance by 4 to 20%. This excess propagation length can have several negative impacts, including potentially larger fiber cost from the additional fiber length required to bridge a given distance, additional amplification needed to compensate for the larger total loss that the signal experiences during propagation, and extra transit time in a network. However, there are also benefits to localized dispersion compensation, including the ability to easily deploy new dispersion compensation technologies as they become available, as well as more flexibility in changing the dispersion map when upgrading a system, as discussed in the next section.

1.2. Dispersion Maps

In the absence of fiber Kerr nonlinearity during propagation in optical fiber, the *total cumulative dispersion* or the *net residual dispersion* at the end of the line uniquely determine the signal distortion from dispersion (see Sec. 2.3). However, in order to maximize the optical signal-to-noise ratio (OSNR) delivered to the receiver (see Sec. 2.2), it is generally desirable to operate a system at the highest possible signal launch power into the fiber spans. The maximum power is dictated by the onset of severe signal distortions through fiber nonlinearity (see Sec. 2.3). In the presence of fiber nonlinearity, transmission is no longer linear, and hence the precise location and value of dispersion compensation becomes critical in determining the overall signal distortion after propagation. The technique of managing dispersion in a transmission line in order to minimize the effects of fiber nonlinearity is referred to as *dispersion mapping*. The evolution of the cumulative dispersion along the transmission line is referred to as the *dispersion map*.

Dispersion maps are commonly represented in two different ways (Fig. 3). In the first representation (Fig. 3a), the cumulative dispersion is plotted as a function of the *physical fiber length*, while the fiber length is replaced by the *transmission distance* in the second representation (Fig. 3b). The largest difference between fiber length and transmission distance occurs in transmission lines having localized dispersion compensation where DCFs are not used to bridge distance.

With both the amount and the location of dispersion compensation as free parameters, a large number of dispersion maps can be envisioned. Figure 4 shows a few possible dispersion maps with relevance to optical networking. In Fig. 4a, no dispersion

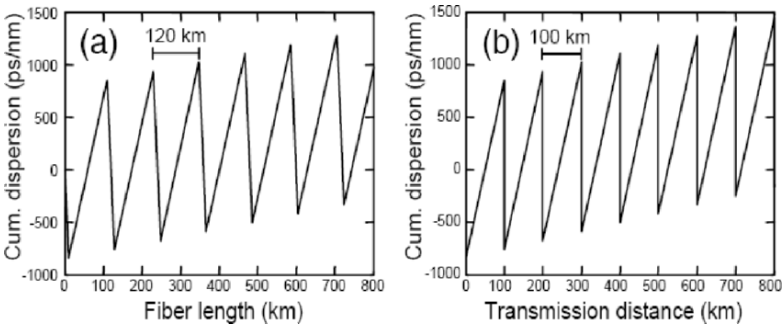

Fig. 3. Representations of dispersion maps for localized dispersion compensation. In a) the dispersion map is plotted as a function of fiber length, while in b) it is plotted as a function of the transmission distance. The dispersions of the TF and DCF are 17 and −85 ps/(nm km), respectively.

compensation is present. Dispersion maps like this are used in short-range ($\sim$100 km) and/or low data rate ($<$10 Gb/s) systems, where neither accumulated dispersion nor fiber nonlinearity are of major concern. More recently, this type of dispersion map has also gained some attention for regional and long-haul systems in the context of electronic pre-distortion [38–41]. In Fig. 4b, equal amounts of dispersion compensation are applied periodically along the transmission line, leaving the same amount of residual dispersion per span. Such dispersion map is referred to as *singly-periodic dispersion map* (SPDM). In the dispersion map of Fig. 4c, additional dispersion is inserted or removed every few transmission spans. As a result, a second period of dispersion compensation appears, which gives this *doubly-periodic dispersion map* (DPDM) its name; DPDMs are considered for optically-routed networks [42–44], where it is important to bring the dispersion to reasonably low values at optical add-drop multiplexer (OADM) sites. Finally, if no periodic pattern is visible in dispersion compensation (Fig. 4d), the dispersion map is referred to as an *aperiodic dispersion map*. Aperiodic dispersion maps can arise for instance in SPDM when dispersion accuracy (either of the transmission fibers or the DCFs) is insufficient to accurately achieve the target RDPS. Although even a larger variety of dispersion maps can be envisioned, a dispersion map that leads to simple and robust engineering rules for system deployment is highly desirable. For that purpose, the SPDM of Fig. 4b is attractive, because each span is compensated in the same manner so that only knowledge of one span is necessary to implement dispersion compensation. For this reason, SPDM is the most widely used dispersion map today.

Note that, regardless of the employed dispersion map, inaccuracies in the dispersion values of transmission fibers and dispersion compensators, the dependence of dispersion with wavelength, and the granularity in dispersion compensation may result in significant deviations from the original dispersion map design as discussed in Sec. 3.2. The impact of such deviations have to be evaluated for each system individually.

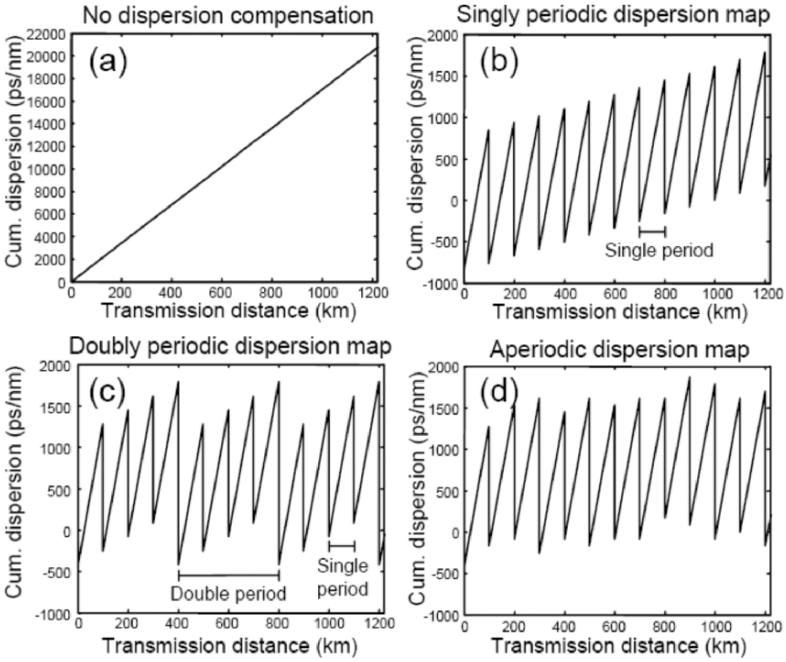

Fig. 4. Examples of dispersion maps: a) No dispersion compensation; b) Singly periodic dispersion map (SPDM); c) Doubly periodic dispersion map (DPDM); d) Aperiodic dispersion map. Fiber dispersion values are the same as in Fig. 3.

1.3. Properties of Dispersion Compensators

Even though the primary role of dispersion compensation is to reduce the accumulated dispersion, the system impact of inserting dispersion compensating elements into the transmission line is manyfold. The properties of dispersion compensating modules (DCMs) that impact transmission and system design include the following:

– The *insertion loss* of the DCM affects the delivered OSNR at the receiver (Sec. 3.1).

– The DCM bandwidth impacts the accuracy of the dispersion map (see Fig. 5) and the number of WDM channels supported.

– If a DCM is channelized, it limits the per-channel data rates and the WDM channel spacings supported by the system as opposed to a non-channelized DCM (see subsection 'Channelized and tunable dispersion' in Sec. 3.2).

– Polarization-Mode Dispersion (PMD) within the DCM adds to the total PMD of a system, which may impact systems operating at high bit rates (Sec. 3.2).

– Polarization-Dependent Loss (PDL) that adds to the system PDL and increases polarization-dependent signal power variations.

– Fiber nonlinearity (for fiber-based dispersion compensation) that increases signal distortions (Sec. 3.2).

– Multi-Path Interference (MPI), including Double-Rayleigh Backscattering (DRB), that acts like an additional source of signal degradation (Sec. 3.1).

– Group delay fluctuations with wavelength (for interferometric devices) that generates additional signal distortions.

The presence and the importance of each property listed above in a system implementation strongly depend on the dispersion compensation technology. In this chapter, we focus mainly on the system impact of DCF technologies, even though some of the analysis may be applied to other dispersion compensation technologies as well. A perspective on alternative technologies to DCFs is presented in Sec. 4, where the impact on system performance and the benefits trade-offs between different technologies are discussed.

1.4. Dispersion-Compensating Fibers

The DCF is, by far, the most commonly used dispersion compensation technology in optical networks. The main advantages of DCFs over other technologies include low (splice) loss ($\lesssim 0.5$ dB) to transmission fibers, low insertion loss, non-channelized compensation allowing arbitrary per-channel bit rates and WDM channel spacings as well as the concatenation of a large number of DCFs, broadband compensation, low PMD, and low PDL. On the other hand, drawbacks of DCF technologies include, long fiber lengths resulting in bulky DCMs, no tunability in dispersion or dispersion slope, and the presence of Kerr nonlinearity in the DCF.

In an effort to capture the impact of various different DCF designs on system performance, certain fiber properties have been combined to form a single parameter characterizing the DCFs [45–47]. An example of such parameter combination is the (linear[5]) *figure of merit* (FOM), defined as [46]

$$\mathrm{FOM} = \frac{|D|}{\alpha}, \tag{1}$$

where D is the local dispersion [ps/(nm km)] of the fiber and α is the fiber loss parameter [dB/km]. Clearly, a high FOM indicates that large dispersion compensation can be accomplished with low loss, helping to lower the impact of inserting a DCF in a line on the OSNR degradation (Sec. 3.1).

Another parameter used to characterize DCFs is the relative dispersion slope (RDS), defined as

$$\mathrm{RDS} = \frac{S}{D}, \tag{2}$$

where S is the dispersion slope, i.e., the first-order derivative of dispersion with wavelength, $\mathrm{d}D/\mathrm{d}\lambda$. A DCF that has an RDS that matches the RDS of a transmission fiber can achieve broadband dispersion compensation, a desired feature for WDM systems. However, the slope S itself often varies considerably across the signal band and, with

[5] An extension of this figure of merit to include fiber nonlinearity [45,46] will be given in Sec. 3.3.

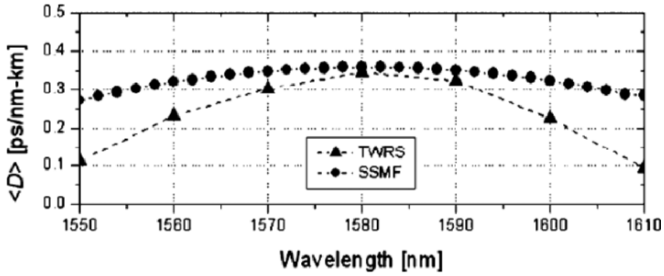

Fig. 5. Example of accuracy of broadband dispersion compensation. Average dispersion, $\langle D \rangle$, as a function of wavelength for two fiber types. TWRS: Truewave® reduced slope and SSMF: standard single-mode fiber.

state-of-the-art DCFs, dispersion slope can only be compensated on *average* across the signal band, leaving residual uncompensated dispersion. For broadband dispersion compensators, a better measure of the quality of the dispersion compensation is the maximum deviation of the cumulative dispersion across the signal band or, alternatively, the maximum deviation of the average dispersion across the signal band. Figure 5 shows an example of how the average dispersion varies across a wavelength band after dispersion compensation for Truewave® Reduced Slope (TWRS), a commercial fiber belonging the NZDF family, and SSMF fibers. Note that the residual dispersion per span is simply given by $\langle D \rangle L$, where is L the transmission fiber length.

With the development of new types of transmission fibers, a large number of DCFs have become available. Most DCFs are designed to target compensation of a transmission fiber type. The properties of DCFs can vary greatly depending on the fiber type they compensate. Table 1 shows the range of parameters of the main DCF properties for commercially available DCFs. The choice of DCF for a particular optical network is guided by many factors, such as the transmission fiber type, the transmission distance, the signal bandwidth, the average span loss and the bit rate of the signal.

Table 1. Range of parameters of commercially available DCFs. A_{eff}: fiber effective area, DGD: Differential group delay, and PDL: Polarization-Dependent Loss.

A_{eff}	FOM	RDS	PMD	PDL
μm^2	ps/(nm dB)	nm^{-1}	ps/$\sqrt{km}$	dB
14-21	160-240	0.0036-0.017	< 0.1	< 0.1

2. General Design Principles of Transmission Lines

Designing an optical transmission system with optical in-line amplifiers, dispersion management, as well as elements for optically adding, dropping, or routing wavelength channels requires a skillful balance between various sources of *noise* and *signal distortion*. The distinction between noise and distortion depends on which quantities are

considered *deterministic* and which quantities are considered *random* in the context of a particular system.

In a typical long-haul transmission system, the most important sources of noise and random impairments are

– *Amplified Spontaneous Emission* (ASE), generated by in-line optical amplification.

– *Multi-Path Interference* (MPI), either due to imperfect extinction properties of OADMs and optical cross-connects (OXCs), or due to DRB. The latter becomes particularly important in Raman-pumped fiber amplifiers.

– *Coherent Crosstalk* between WDM channels in ultra-dense WDM systems.

The most important sources of signal distortion are

– *Net residual dispersion* (NRD) at the end of a transmission line, caused by deviations from the prescribed dispersion map.

– *Kerr nonlinearity*-induced signal distortions of various types, including self-phase modulation (SPM), inter and intra-channel cross-phase modulation (XPM or IXPM), and inter and intra-channel four-wave mixing (FWM or IFWM); these effects are exacerbated if the dispersion map does not follow its prescribed optimum.

– *Polarization-mode dispersion* (PMD), which can severely impair systems operating on older transmission fiber and at bit rates exceeding 10 Gb/s.

– *Narrow-band optical filtering*, which occurs in the presence of multiple OADMs or OXCs along optically-routed transmission paths.

In this section, we will study those sources of noise and distortion that determine system performance. A more detailed discussion of the trade-offs involved in system design due to the presence of DCF in a transmission line is presented in Sec. 3.

2.1. Noise Characterization of Optical Receivers

In order to understand the impact of noise and distortion on the design of lightwave systems, it is crucial to understand the process of signal detection and receiver performance quantification. Both topics will be treated in this section.

Figure 6 shows the basic structure of a direct-detection WDM receiver. The optical field of all WDM signal channels passes through a WDM demultiplexer along with the random optical field of ASE generated from optical amplification along with the random field due to DRB. The latter is especially important in Raman-pumped systems. The demultiplexer spectrally separates the WDM channels and suppresses out-of-band ASE. A photodiode followed by a band-limiting electronic circuitry converts the optical power at the detector into an electrical signal, which is then sampled at the bit rate. In today's state-of-the art receivers, the transmitted digital information is restored using simple threshold detection[6]. Detection errors are quantified using the *bit error ratio* (BER).

[6] More advanced receiver structures will be discussed in Sec. 2.3.

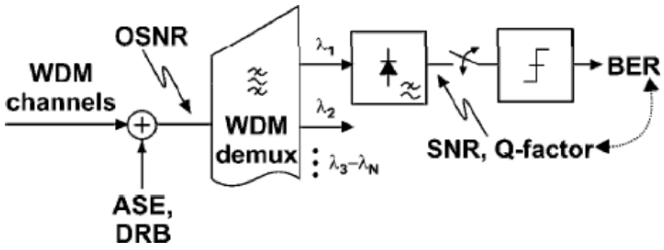

Fig. 6. Basic structure of a direct-detection WDM receiver. The WDM channels, impaired by ASE and DRB, are demultiplexed, and each wavelength is detected using a photodiode. Sampling and decision circuits extract a digital data stream from the (analog) detected signal waveform with some bit error ratio (BER).

Performance Measures: BER, SNR, and Q

Bit Error Ratio (BER)

The BER is the ultimate performance measure of optical communication systems. It is *statistically* defined as the time-averaged fraction of wrong bits contained in a bit stream. For long averaging times, the BER can also be considered as the *probability* of having a detection error for an individual bit,

$$\mathrm{BER} = \left\{ \frac{\text{bits in error}}{\text{total number of bits}} \right\}_{\text{time average}} \xrightarrow{\text{long averaging time}} P[\text{bit error}] \; . \quad (3)$$

The BER target that has to be met by a system depends on the system application. Typical values for target BERs are 10^{-12} or 10^{-15} for carrier-class optical transport systems without error-correcting coding, and 6×10^{-5} or 2×10^{-3} for systems employing forward error correction (FEC). In order to measure statistically meaningful values of BER, the average number of detected errors per measurement interval should be at least 10 but preferably 100. If one restricts the BER measurement time to a few minutes, typical for laboratory experiments, the lowest BER that can be accurately measured is $\sim 10^{-9}$ to 10^{-10} at current bit rates used in the Synchronous Optical NETwork (SONET) hierarchy (2.5 Gb/s to 40 Gb/s)[7]. As a consequence, comparisons of system performance in research laboratory experiments have traditionally been done at BER=10^{-9}, the lowest BER that can be reliably measured in a few minutes time period. Additional comments on the impact of target BER specification on the design of systems with FEC can be found at the end of Sec. 2.3.

The Q-Factor

The *Q-factor* is an important parameter that is widely used in optical communications to describe system performance. It appears in several different contexts, with different

[7] Long-term error measurements, i.e. counting errors over days, weeks or even months, becomes necessary for systems with BER specification well below 10^{-10}. Such tests are generally performed in the course of product development and system procurement.

underlying assumptions. Understanding these assumptions is crucial to making proper use of the Q-factor.

In one of its uses, most frequently employed by experimentalists, the Q-factor is just a different and more convenient way of expressing BER. The strict fundamental equivalence between the Q-factor and the BER is given by

$$\text{BER} = 0.5\ \text{erfc}[Q/\sqrt{2}]\ , \tag{4}$$

where $\text{erfc}[x] = (2/\sqrt{\pi})\int_x^\infty \exp(-\xi^2)\mathrm{d}\xi$ denotes the complementary error function. Note that Eq. (4) is a *mere definition* that as such does *not* rely on any assumptions regarding noise or signal distortion. Typically, the Q-factor is specified in dB, using $Q_{[\mathrm{dB}]} = 20\log(Q_{[\mathrm{lin}]})$. Note that this conversion of the Q-factor to a dB-scale, using $20\log(\cdot)$ rather than $10\log(\cdot)$, is convenient, given the relation between the Q-factor and the signal to noise ratios defined below. Table 2 gives the correspondence between Q and BER for several frequently used BER values.

Table 2. Correspondence between Q-factor and BER.

BER	10^{-2}	$2\cdot10^{-3}$	10^{-3}	$6\cdot10^{-5}$	10^{-6}
Q-factor	7.3 dB	9.2 dB	9.8 dB	11.7 dB	13.5 dB
BER	10^{-9}	10^{-10}	10^{-12}	10^{-15}	10^{-16}
Q-factor	15.6 dB	16.1 dB	16.9 dB	18.0 dB	18.3 dB

Another use of the Q-factor is the experimental extrapolation of system performance to BER values that are too small to be measured directly [48]: Here, the BER is measured as a function of the receiver's decision threshold, which gives a V-shaped curve. If the minimum BER escapes direct measurement, the two legs of the V-curve are extrapolated towards the center. The intersection then yields the estimated BER at the optimum decision threshold. Obviously, this method relies on proper knowledge of the extrapolation function, which is most often taken to be the complementary error function, reflecting Gaussian detection statistics.

Yet another important use of the Q-factor is the *prediction* of system performance, based on the observation of mean and standard deviation of the electrical signal at the receiver's decision gate. In fact, this is the way the Q-factor was first introduced by Personick in 1973 [49]. Leaving detailed derivations to more comprehensive texts [50–52], we restrict ourselves to the key predictive equation,

$$Q = \frac{|s_1 - s_0|}{\sigma_1 + \sigma_0}\ , \tag{5}$$

where $s_{0,1}$ are the noise-free electrical signal amplitudes for a logical '0' and '1' at the decision gate, and $\sigma_{0,1}$ are the associated noise standard deviations. Inserting Eq. (5) in Eq. (4) yields a rough approximation of the BER to be expected in a system.

Note that although Eq. (5) allows for valuable interpretations of system performance trends, and gives reasonable 'first-guess' estimates of the BER, it is based on a series of key assumptions. If violated, the resulting system performance estimate may be severely off its true value. In particular, critical assumptions are

– **Absence of inter-symbol interference (ISI) and pattern effects**
If ISI or other pattern effects are present in a system due to signal distortions or

timing jitter from the transmitter, from propagation, or from receiver elements, there is typically no single value for s_1 and s_0 or for σ_1 and σ_0, but each bit has its individual signal mean level and an associated variance. In this case, the eye diagram exhibits several different traces for '1'-bits and '0'-bits, and $s_{0,1}$ is typically taken from the *worst-case* traces forming the inner rim of the eye.

– **Gaussian noise approximation and single-ended detection**
The entire theory around the Q-factor is built upon Gaussian statistics of the electrical signal at the decision gate. It turns out that this assumption is very well met for the important case of ASE-induced beat-noise limited reception of on/off keyed (OOK) modulation [53], but completely fails for, e.g., balanced detection of phase-shift keyed (PSK) transmission [54]. Furthermore, other sources of optical noise, such as in-band crosstalk arising from a limited number of interferers, may lead to non-Gaussian detection statistics, and may therefore not be accurately captured by the Q-factor.

– **Optimized decision threshold**
Both the Gaussian approximation and the Q-factor only work well if the receiver is assumed to operate with optimized decision threshold. Although most modern optical receivers have threshold adaptation built in, caution has to be exerted when studying the impact of temporally varying distortions, which are faster than the threshold adaptation control loop.

As a final remark, we want to emphasize that, in optical communications, the noise variances can be different for each bit, reflected explicitly by the appearance of σ_1 and σ_0 in Eq. (5): as we will see below, many important noise terms are *signal-dependent*, i.e., the noise variance is a function of the optical signal power. For purely *signal-independent* noise ($\sigma_1 = \sigma_0 = \sigma$), Eqs. (5) and (4) reduce to BER$= 0.5\ \mathrm{erfc}[|s_1 - s_0|/(2\sqrt{2}\sigma)]$, a well known expression in classical communication theory [55].

Electrical Signal-to-Noise Ratio (SNR)

While the Q-factor accounts for different noise variances of '1'-bits and '0'-bits, and approximately relates to system performance via Eq. (4), the *electrical signal-to-noise ratio* (SNR) at the receiver's decision gate (cf. Fig. 6) only accounts for the '1'-bit; the SNR is defined as the ratio of the electrical peak power of a '1'-bit (s_1^2) to the associated noise variance (σ_1^2),

$$\mathrm{SNR} = \frac{s_1^2}{\sigma_1^2}\ . \tag{6}$$

Since the SNR only accounts for the statistics of the '1'-bits, analyses based on SNRs generally lead to simpler analytic expressions than using the Q-factor, which also includes '0'-bit statistics. Nevertheless, SNR-based analyses are often sufficient for crude system performance estimates, even for beat-noise limited reception: Under the frequently met assumptions of a good signal extinction ratio ($s_1 \gg s_0$) and dominance of the '1'-bit noise over the '0'-bit noise ($\sigma_1 \gg \sigma_0$), we use Eqs. (5) and (6) to find the useful relation

$$Q = \sqrt{\mathrm{SNR}}\ . \tag{7}$$

Beat Noise, Shot Noise, and Electronics Noise

Since photodetection converts the *power* of the total optical field incident to the photodiode to an electrical signal $s(t)$, we observe beating effects between the signal field $E_{\text{sig}}(t)$ and the noise fields $E_{\text{noise}}(t)$,

$$s(t) = S|E_{\text{sig}}(t)+E_{\text{noise}}(t)|^2 = S|E_{\text{sig}}(t)|^2+2S\text{Re}\{E_{\text{sig}}(t)E^*_{\text{noise}}(t)\}+S|E_{\text{noise}}(t)|^2, \tag{8}$$

where * is the complex conjugate, and S [A/W] is the photodiode's responsivity, given by

$$S = \eta e/h\nu \ , \tag{9}$$

with $\eta < 1$ being the detector's quantum efficiency, and $e = 1.602 \times 10^{-19}$ A·s denoting the elementary charge.

The first term on the right-hand side of Eq. (8) represents the desired signal information. The second term represents the beating of the signal field with the optical noise field. Since the optical noise field varies randomly in time, this beat term is also random, and therefore acts as noise on the detected electrical signal $s(t)$. Thus, this term is called *signal-ASE beat noise* or *signal-DRB beat noise*, depending on the optical noise field under consideration. The third term on the right-hand side of Eq. (8) represents the instantaneous power of the noise field, which also fluctuates randomly, and thus acts as noise on $s(t)$. Since this term can be viewed as the beating between different frequency components of the optical noise, it is called *ASE-ASE beat noise*, or *DRB-DRB beat noise*, depending on the optical noise field under consideration.

Leaving more complex expressions for the beat noise terms to specialized texts (e.g., [56,18,57]), we give here a useful approximation for systems with Gaussian filters and Gaussian optical pulses, under the assumption that the optical filter bandwidth of the receiver significantly exceeds both the bandwidth of the optical signal and the electrical bandwidth of the receiver[8]. In this case, the signal-ASE and signal-DRB beat noise variances read [18,57]

$$\sigma^2_{1,s-\text{ASE}} = \frac{4S^2N_{\text{ASE}}P_sB_e}{[1+B_s^2/(4B_e^2)]^{1/2}} \ , \tag{10}$$

$$\sigma^2_{1,s-\text{DRB}} = \frac{2S^2P^P_{\text{DRB}}P_s}{[1+B_s^2/(2B_e^2)]^{1/2}[1+B_s^2/(4B_e^2)]^{1/2}} \ , \tag{11}$$

where N_{ASE} [W/Hz] is the ASE power spectral density in the same state of polarization as the signal, P_s [W] is the optical power of a '1'-bit incident to the photodetector, B_e [Hz] is the receiver's electrical bandwidth, and B_s [Hz] is the optical signal bandwidth; P^P_{DRB} [W] is the DRB power co-polarized with the signal.

Simplifying further, by assuming quasi-CW signaling ($B_s \ll B_e$), we arrive at the frequently used approximations for signal-ASE and signal-DRB beat noise variances [58,59],

$$\sigma^2_{\text{signal-ASE}} \approx 4S^2N_{\text{ASE}}P_sB_e \ , \tag{12}$$

$$\sigma^2_{\text{signal-DRB}} \approx 2S^2P^P_{\text{DRB}}P_s \ . \tag{13}$$

[8] This approximation is reasonably accurate, unless highly spectrally efficient systems are considered. In that case, one has to resort to the more accurate expressions given in [18,57].

The differences in the expressions for the signal-ASE beat noise and the signal-DRB beat noise have their origin in the different spectral distribution of ASE and DRB, as we will see below. The noise-noise beat terms (ASE-ASE, ASE-DRB, and DRB-DRB) are typically small compared to the signal-noise beat terms, and we will neglect these terms in our discussions to follow.

Apart from beat noise, the electrical signal is also corrupted by fundamentally unavoidable *shot noise*, originating in the quantized (photonic) interaction between light and matter. Leaving the exact expressions for shot noise to more detailed literature (e.g., [60]), we state here an approximation based on Gaussian receive filters and Gaussian optical pulses [18]. Assuming again that the optical receive filter bandwidth exceeds the signal bandwidth, we find

$$\sigma^2_{\text{shot}} = \frac{2eSP_sB_e}{[1 + B_s^2/(4B_e^2)]^{1/2}} \ . \tag{14}$$

Assuming further quasi-CW signaling ($B_s \ll B_e$), this expression reduces to the well-known approximation [60]

$$\sigma^2_{\text{shot}} \approx 2eSP_sB_e \ . \tag{15}$$

Like the signal-noise beat terms, signal shot noise is also *signal-dependent*. Shot noise arising from the detection of ASE and DRB is well below signal shot noise, and can be safely neglected in evaluating system performance. Although signal shot noise is typically well below signal-ASE beat noise, it plays an important role as a reference noise source for defining the optical noise figure, as we will see in Sec. 2.2.

Other types of detection noise, generated within the detection electronics and independent of the optical signals incident to the photodetector, are summarized under the term *electronics noise*. Examples are thermal noise, $1/f$-noise, or transistor shot noise. Since all detection noise sources are statistically independent, their variances may be added up, and the overall system performance is determined by the *sum* of the individual noise variances. Taking into account the most important noise terms only, we thus have

$$\sigma^2_{total} \approx \sigma^2_{\text{s-ASE}} + \sigma^2_{\text{s-DRB}} + \sigma^2_{\text{signal-shot}} + \sigma^2_{\text{electronic}} \ . \tag{16}$$

Beat Noise Limit and Required OSNR

The beat noise terms, Eqs. (10) and (11), or Eqs. (12) and (13), are proportional to the optical power of signal and optical noise incident on the photodetector. When detecting the highly attenuated signal directly at the end of a fiber span, the beat noise terms are thus comparatively small compared to electronics noise. In such a scenario, electronics noise would dominate system noise, and almost exclusively determine the system's BER. In this case, designing a receiver with lower electronics noise would directly improve system performance up to the point at which beat noise would start to limit system noise. However, reducing electronics noise in uncooled, high-speed electronic circuitry is a non-trivial engineering task. Luckily, receiver performance can be improved by other means: optical amplification prior to detection. Optical pre-amplifiers amplifies the optical signal power, together with the optical noise power coming from the line, by some gain G. As a result, the electrical signal amplitude is increased by G,

and the beat noise variances are increased by G^2 [cf. Eqs. (12) and (13)]. As long as the beat noise terms are still below the electronics noise floor, increasing the pre-amplifier gain will linearly increase the electrical signal amplitude, and will thus quadratically increase the SNR. Increasing the pre-amplifier gain further, so that the beat noise terms grow above the electronics noise, no further SNR improvement will be seen, since electrical signal power and electrical noise variance both scale with G^2, and the sum of all noise terms, Eq. (16) is then dominated by beat noise. Since the optically pre-amplified receiver is then largely independent of the specific noise properties of the receiver electronics and is limited by beat noise, this mode of receiver operation is referred to as *beat-noise limited*.

If ASE-induced beat-noise limits receiver noise, the receiver's noise performance can be fully characterized by the *optical signal-to-noise ratio* (OSNR), defined as the ratio of average optical signal power to optical noise power. To see this, consider for simplicity[9] a receiver limited by signal-ASE beat noise only. Using Eq. (12), the SNR [which is approximately related to the Q-factor and the BER through Eqs. (4) and (7)] can then be written as

$$\mathrm{SNR} = \frac{S^2 P_s^2}{4S^2 N_{\mathrm{ASE}} P_s B_e} = \mathrm{OSNR}\frac{B_{\mathrm{ref}}}{2B_e} \ . \tag{17}$$

with the definition

$$\mathrm{OSNR} = \frac{P_s}{2N_{\mathrm{ASE}} B_{\mathrm{ref}}} \ . \tag{18}$$

The factor of 2 in the denominator of Eq. (18) accounts for the fact that the total ASE power is made up of *two* ASE polarization states; B_{ref} is a reference optical bandwidth, which is typically taken to be 12.5 GHz, corresponding to a convenient value of 0.1 nm for a standard resolution setting of optical spectrum analyzers.

The minimum OSNR that is needed at the receiver input to guarantee detection with some specified BER is called the *required OSNR*, and quantifies the amount of optical noise a receiver can tolerate to still maintain transmission performance at the target BER. Obviously, successful system design requires that the OSNR that is actually *delivered* to the receiver equals or exceeds the required OSNR. Table 3 lists the OSNR requirements for some important optical modulation formats at 42.7 Gb/s and for a target BER of 10^{-3}, obtained by numeric simulation [61].

Table 3. Required OSNR for different modulation formats at 42.7 Gb/s and at a target BER of 10^{-3}. NRZ: Non return-to-zero, RZ: Return-to-zero, CSRZ: Carrier-suppressed return-to-zero, DPSK: Differential phase shift keying, DQPSK: Differential quadrature phase shift keying.

Modulation format	required OSNR
NRZ-OOK	16.5 dB
Duobinary	17.4 dB
33% duty cycle RZ-OOK	14.9 dB
67% duty cycle CSRZ	15.1 dB
67% duty cycle RZ-DPSK	11.1 dB
50% duty cycle RZ-DQPSK	12.2 dB

[9] Including ASE-ASE beat noise does not change the fact that beat-noise limited receiver performance depends on the OSNR only.

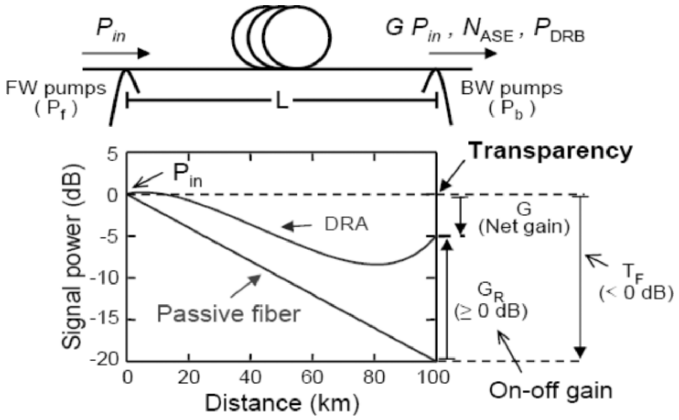

Fig. 7. Definition of parameters for a Raman amplifier.

Note from Eq. (17) that the data-rate independent choice of B_{ref} lets the required OSNR become *data-rate dependent*: For a given system performance, i.e., for fixed BER, fixed Q-factor, or fixed SNR, an increase in bit rate requires the same increase in OSNR, since B_e linearly increases with data rate.

2.2. *Optical Noise From the Transmission Line*

Having considered the impact of optical noise on receiver performance in the preceding section, we discuss in this section the generation and accumulation of optical noise along an optical communication line. This allows us to quantify the OSNR that is actually *delivered* to the receiver in a particular system; a system can only guarantee a specific BER if the delivered OSNR exceeds the required OSNR for that BER.

Amplified Spontaneous Emission

Amplified spontaneous emission (ASE) is caused by spontaneous relaxations of excited energy states in optical amplifiers, and is therefore intimately related to the gain process [1].

For *discrete* optical amplifiers, such as Erbium-doped fiber amplifiers (EDFAs), the ASE power spectral density at the output of the amplifier is given by [1]

$$N_{\text{ASE}} = n_{\text{sp}}(G-1)h\nu \ , \tag{19}$$

where $h\nu$ is the energy of a photon at the wavelength at which ASE is to be evaluated, G is the amplifier gain, and $n_{\text{sp}} > 1$ is the amplifier's spontaneous emission factor. Note that Eq. (19) denotes the ASE power spectral density per *transversal waveguide mode*, which in a single-mode optical fiber corresponds to one *state of polarization*.

For *distributed* optical amplification, such as Raman-pumped transmission fiber or for *discrete* Raman amplifiers such as Raman-pumped DCF, N_{ASE} is given by [62,18]

$$\mathrm{N_{ASE}} = \mathrm{h}\,\nu \int_0^L \mathrm{C_r}(\lambda_\mathrm{s}, \lambda_\mathrm{p}) \left[P_b e^{-\alpha_p (L-z)} + P_f e^{-\alpha_p z} \right] G(z, L) dz, \tag{20}$$

where

$$G(z_1, z_2) = T_F(z_1, z_2)\, G_R(z_1, z_2) \tag{21}$$

is the net gain from distance z_1 to z_2, $T_F(z_1, z_2) = \exp[-\alpha_s(z_2 - z_1)]$ is the passive fiber transmission at the signal wavelength from z_1 to z_2, and

$$\mathrm{G_R}(z_1, z_2) = \exp\left\{ \frac{\mathrm{C_r}(\lambda_\mathrm{s}, \lambda_\mathrm{p})}{\alpha_\mathrm{p}} \left[P_b \left(e^{-\alpha_p (L-z_2)} - e^{-\alpha_p (L-z_1)} \right) + P_f \left(e^{-\alpha_p z_1} - e^{-\alpha_p z_2} \right) \right] \right\}, \tag{22}$$

is the Raman gain, also from z_1 to z_2; $G_R = G_R(0, L)$ is the Raman on-off gain and $T_F = T_F(0, L)$ is the passive fiber transmission (≤ 1) (see Fig. 7). In Eqs. (20) and (22), $C_r(\lambda_s, \lambda_p)$ is the Raman gain efficiency (gain factor per unit of length and power) for signal and pump wavelengths λ_s and λ_p, respectively, α_p and α_s are the loss coefficients at the pump and signal wavelengths, and P_b and P_f are the backward and forward pump powers at the ends of the fiber, respectively. Equations (20) and (22) apply to the general case of a bidirectionally-pumped DRA, and are derived using the undepleted-pump approximation [62]. Under the assumption of perfectly depolarized pumps, the ASE from Raman amplification is randomly polarized.

For both types of amplifiers considered here (EDFA or Raman), the spectral distribution of ASE follows closely the amplifier's gain profile. Since spectral gain variations occur on wavelength scales much larger than the bandwidth of typical communication signals, ASE can be considered white over the signal bandwidth, i.e. the ASE spectral density can be considered constant over the optical signal frequency.

Double-Rayleigh Backscatter

Rayleigh scattering of light is an elastic scattering process caused by small-scale inhomogeneities of the refractive index of the media. The fraction of light that is backscattered depends on the composition of the glass, the waveguide properties of the fiber, and the recapture fraction, which determines the fraction of backscattered optical power that is actually captured in a guided fiber mode. The amount of optical power that is Rayleigh backscattered into a guided fiber mode per unit length is quantified by the Rayleigh backscatter coefficient r. For NZDFs at 1550 nm, with an effective mode area of $A_{\mathrm{eff}} = 53\ \mu\mathrm{m}^2$, we have $r = 9.6 \times 10^{-5}\ \mathrm{km}^{-1}$. For typical DCF, we have $r = 3.7 \times 10^{-4}$ (see Table 5).

Using the Rayleigh backscatter coefficient, the optical power that is Rayleigh backscattered to the fiber input reads

$$\mathrm{P_{RB}} = \mathrm{P_{in}} r \int_0^L G(0, z)^2 dz \tag{23}$$

In an un-pumped (passive) optical fiber, with $G(0, z) = \exp[-\alpha z]$, this expression simplifies to

$$\mathrm{P_{RB}} = \mathrm{P_{in}} \frac{r}{2\alpha} (1 - \exp[-2\alpha L])\ , \tag{24}$$

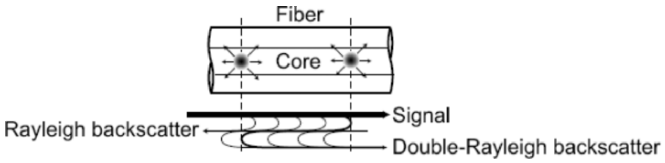

Fig. 8. Generation of Double-Rayleigh Backscatter (DRB) in an optical fiber.

which for long fibers and $\alpha = 0.05$ Np/km $= 0.2$ dB/km gives the well-known Rayleigh backscatter ratio of about 30 dB.

Being a linear process, Rayleigh scattering fully preserves the spectral content of the signal, i.e., the power spectral density of the Rayleigh-scattered power matches the magnitude of the launched optical signal spectrum. However, since the scattering process occurs at random locations within the fiber, the spectral frequency components of the backscattered signal are randomly de-phased, and any phase correlation in the backscattered spectrum is lost. This makes the Rayleigh backscattered signal a random process.

If Rayleigh scattering occurs twice within a fiber, such that a doubly-scattered portion of the original signal eventually co-propagates with the original signal, we observe beat noise between the signal and the DRB field at the receiver. The generation of DRB is schematically depicted in Fig. 8.

Under the undepleted pump approximation, the total DRB power, $\mathrm{P_{DRB}}$, is given by [63,18],

$$\mathrm{P_{DRB}} = G\,\mathrm{P_{in}}\,r^2 \int_0^L G(0,z)^{-2} \int_z^L G(0,\zeta)^2\; d\zeta\; dz, \tag{25}$$

where $\mathrm{P_{in}}$ is the signal input power to the DRA. Oftentimes it is more convenient for system design to specify the amount of DRB in terms of the ratio $\mathrm{P_{DRB}}/\mathrm{P_{out}}$ where $\mathrm{P_{out}} = \mathrm{G\,P_{in}}$ is the signal power at the fiber output. This leads to the definition of the *crosstalk ratio*, $\mathrm{R_c}$, as [18]

$$\mathrm{R_c} \equiv \frac{\mathrm{P_{DRB}}}{\mathrm{G\,P_{in}}} = r^2 \int_0^L G(0,z)^{-2} \int_z^L G(0,\zeta)^2\; d\zeta\; dz. \tag{26}$$

For a passive fiber, this equation becomes

$$\mathrm{R_c} = \frac{r^2}{4\alpha^2}(\exp[-2\alpha L] - 1 + 2\alpha L)\;, \tag{27}$$

which yields a typical crosstalk ratio of -50 dB. If the transmission fiber is made active through DRA, the crosstalk ratio can reach unacceptably high values, as will be discussed in Sec. 3.1.

It is worth noting that DRB is *not* completely depolarized, but has a degree of polarization of 5/9, co-polarized with the signal [64], which has to be taken into account in evaluating beat noise, since beating at photodetection only occurs between co-polarized optical fields [cf. Eq. (8)]. Together with the non-white spectral characteristics, this fundamentally distinguishes DRB from ASE, and leads to the different beat noise expressions (12) and (13).

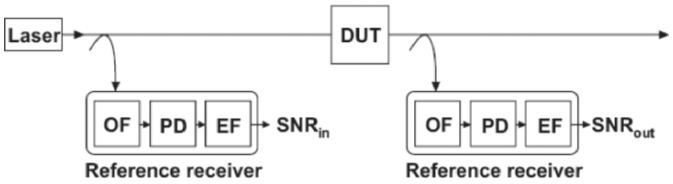

Fig. 9. The definition of noise figure. OF: Optical filter, EF: Electrical filter, PD: Photo detector.

Amplifier Noise Figure

In analogy to microwave amplifiers, optical amplifiers are conveniently characterized by their *noise figure* NF, which quantifies the noise enhancement by the amplifier. The noise figure is generally defined as the signal-to-noise ratio (SNR) at the amplifier input divided by the SNR at the amplifier output,

$$\mathrm{NF} = \frac{\mathrm{SNR_{in}}}{\mathrm{SNR_{out}}}, \tag{28}$$

where $\mathrm{SNR_{in}}$ is given by accounting for a baseline noise reference. In microwave engineering, this baseline noise is typically considered to be thermal noise at room temperature. At optical frequencies it is more convenient to consider the fundamentally unavoidable *signal shot noise* as a noise reference, and consequently to define the noise figure with the help of the *electrical* SNR *after* photodetection. This engineering approach to the definition of noise figure[10] is visualized in Fig. 9, where the *device under test* (DUT) could be an optical amplifier or any other optical component whose noise figure is to be assessed.

Using Eq. (14) for the shot noise variance, we find for the SNR at input of the DUT,

$$\mathrm{SNR_{in}} = \frac{S^2 P_s^2}{\sigma^2_{\text{shot}}} \approx \frac{S P_s}{2eB_e/[1 + B_s^2/(4B_e^2)]^{1/2}} \approx \frac{P_s}{2h\nu B_e}\ , \tag{29}$$

where the last approximation holds for quasi-CW ($B_s \ll B_e$) signaling, and Eq. (9) was substituted for S, assuming a perfect photodiode ($\eta = 1$). The SNR at the output of the DUT, $\mathrm{SNR_{out}}$, is obtained by considering all sources of noise that are present in an ideal receiver (i.e., a receiver with no electronics noise) following the DUT.

In the case of a purely *passive optical element* with transmission $T_F < 1$, we only encounter shot noise, and the output SNR becomes

$$\mathrm{SNR_{out}} = \frac{S^2 T_F^2 P_s^2}{\sigma^2_{\text{shot, out}}} = \frac{S^2 T_F^2 P_s^2}{T_F \sigma^2_{\text{shot, in}}} = T_F\ \mathrm{SNR_{in}}\ . \tag{30}$$

Therefore, the noise figure of a passive element is equal to its loss ($F = 1/T_F$), in complete analogy to lossy elements in microwave engineering.

[10] Related definitions of the noise figure, which are directly based on quantum theory, and are thus more rigorous but less used in an engineering context are discussed in [65,66].

If the DUT represents an *optical amplifier* with gain G, the noise within the ideal output reference receiver will contain beat noise in addition to shot noise, and the output SNR becomes

$$\mathrm{SNR}_{\mathrm{out}} = \frac{S^2 G^2 P_s^2}{\sigma^2_{\mathrm{s-ASE}} + \sigma^2_{\mathrm{ASE-ASE}} + \sigma^2_{\mathrm{shot,out}}}. \tag{31}$$

If we neglect the ASE-ASE beat noise term, which can typically be well justified in the context of optical communication systems[11], we find by substituting Eqs. (10) and (14), and taking note of $\sigma^2_{\mathrm{shot,out}} = G\sigma^2_{\mathrm{shot,in}}$,

$$\mathrm{SNR}_{\mathrm{out}} = \frac{S^2 G^2 P_s^2}{4S^2 N_{\mathrm{ASE}} G P_s B_e + 2eSGP_s B_e}[1 + B_s^2/(4B_e^2)]^{1/2}\,. \tag{32}$$

Thus, using Eqs. (29), (32), and (9), the noise figure for an optical amplifier, assuming an ideal ($\eta = 1$) reference photodiode, becomes

$$\mathrm{NF} = \frac{1}{G}\left(\frac{2N_{\mathrm{ASE}}}{h\nu} + 1\right)\,. \tag{33}$$

Inserting expression (19) for N_{ASE}, we obtain

$$\mathrm{NF} = 2n_{\mathrm{sp}}(1 - 1/G) + 1/G\,. \tag{34}$$

Since n_{sp} is lower-bounded to unity, the theoretically minimum noise figure of a high-gain optical amplifier is 3 dB. EDFAs with noise figures approaching this limit to within a few tenths of a dB have been demonstrated [67]. Typical values of noise figures for system-deployable, wide-band EDFAs are between 5 and 7 dB.

One of the main advantages of introducing noise figures is the possibility of assessing the noise performance of an entire system consisting of a concatenation of various elements with individually known gain (or loss) and noise figure, such as a chain of optical amplifiers inserted between transmission fiber and DCF. It is easy to show that in the case of concatenation of DUT_1 (noise figure NF_1) and DUT_2 (noise figure NF_2), the noise figure NF_{12} of DUT_{12} (= DUT_1 immediately followed by DUT_2) is given by [1,68]

$$\mathrm{NF}_{12} = \mathrm{NF}_1 + \frac{\mathrm{NF}_2 - 1}{G_1}, \tag{35}$$

where G_1 is the net gain (or loss) of DUT_1. The noise figure for concatenation of more than two amplifiers can be obtained by using Eq. (35) recursively.

We next consider the noise figure of an entire transmission span [1], consisting of a lossy transmission fiber (transmission $T_F < 1$, and hence noise figure $\mathrm{NF}_{\mathrm{fiber}} = 1/T_F$) in combination with either lumped or distributed optical amplification (noise figure $\mathrm{NF}_{\mathrm{amp}}$ and amplifier gain $G = 1/T_F$, such that the span loss is fully compensated by the optical amplifier). If, as shown in Fig. 10a, a lumped amplifier (e.g., an EDFA) is placed at the end of the fiber span, we find with the help of Eq. (35),

$$\mathrm{NF}_{\mathrm{span}} = G\mathrm{NF}_{\mathrm{amp}} \qquad [\text{ linear units }], \tag{36}$$

[11] Note that this assumption is crucial to our engineering definition of the noise figure of optical amplifiers. If this assumption breaks down, a more rigorous approach has to be taken, as pointed out by Haus [65].

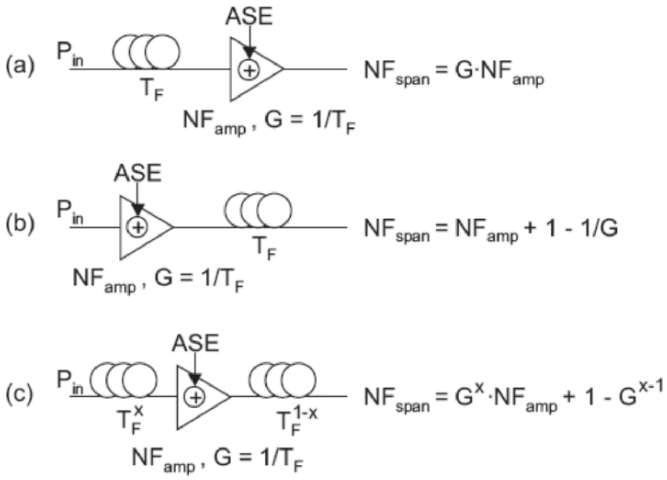

Fig. 10. The benefit of distributed amplification on ASE generation.

or

$$\mathrm{NF_{span}} = G + \mathrm{NF_{amp}} \qquad [\text{ in dB }]. \tag{37}$$

Since typical fiber span losses are on the order of 20 dB, the noise figure of an amplified fiber span is usually dominated by the span loss, and amounts to about 25 to 27 dB. If we were to place the optical amplifier *in front* of the fiber span, and keep the optical power levels as indicated in Fig. 10b, the noise figure of the amplified span would only be $\mathrm{NF_{span}} = \mathrm{NF_{amp}} + 1 - 1/G$, significantly less than in the first case, where the amplifier was placed at the end of the span. The general advantage obtained by putting amplification prior to attenuation can be intuitively understood by the fact that any attenuation *after* the injection of noise acts on *signal and noise*, leaving the OSNR constant. On the other hand, any attenuation *prior to* amplification degrades the signal only, while the full amount of noise is injected at the amplifier at the end; this leads to a substantial OSNR degradation. Unfortunately, it is typically not possible to compensate for the full span loss at the fiber input, since the optical signal launch power would be prohibitively high, and would severely degrade the signal due to fiber nonlinearity. Therefore, discrete amplification has to be employed at the end of each transmission span in practice.

A viable compromise between the two extreme cases shown in Figs. 10a and b can be achieved using *distributed amplification*, which we will now illustrate by a simple example, specializing the more general framework found in, e.g., [1]: Turning the transmission fiber into an amplifier across its entire length is conceptually equivalent to pushing a lumped amplifier at the span output inside the transmission fiber, as shown in Fig. 10c. Doing so, the span loss is divided into a pre-amplifier portion T_F^x and a post-amplifier portion T_F^{1-x}, with $0 < x < 1$; note that the overall fiber span loss is kept constant ($T_F^x T_F^{1-x} = T_F$). Using Eq. (35), we find $\mathrm{NF_{span}} = G^x \mathrm{NF_{amp}} + 1 - G^{x-1}$ for the noise figure of the entire span, which is mainly determined by the first term,

representing the amount of attenuation before amplification. We therefore note that pushing amplification inside a span by means of distributed amplification (as emulated by Fig. 10c) results in a better span noise figure without increasing the launch power into the span.

Since the noise figure of an isolated amplifier by itself looses its significance in systems with distributed amplification, it is convenient to benchmark the noise performance of such systems by means of an *effective noise figure*, which is defined as the noise figure of a *hypothetical* discrete amplifier placed at the end of a passive transmission span (according to the setup of Fig. 10a) that would give the *same span noise figure* as the actual transmission span, which uses distributed amplification (e.g., as modeled by the setup of Fig. 10c). To give an example, we calculate the effective noise figure of the system of Fig. 10c: To this end, we equate the noise figure $G\text{NF}_{\text{eff}}$ of the hypothetical system and the noise figure $G^x\text{NF}_{\text{amp}} + 1 - G^{x-1}$ of the actual system, and solve for NF_{eff}. Assuming a 20-dB span loss and mid-span ($x = 0.5$) amplification with a noise figure of $\text{NF}_{\text{amp}} = 8$ dB, we obtain $\text{NF}_{\text{eff}} = -1.9$ dB. Note that the effective noise figure, being the characteristic of a *hypothetical* amplifier, can well be smaller than 3 dB. As our numerical example shows, the effective noise figure can even be smaller than unity (negative when expressed in dB), even if the noise figure of the amplifier within the span is rather high. This reiterates the noise benefits of distributed amplification.

Expanding one step further, we consider as a DUT a distributed optical amplifier with appreciable DRB on top of ASE. Then, neglecting again all noise-noise beat terms, the output SNR is given by

$$\text{SNR}_{\text{out}} = \frac{S^2 G^2 P_s^2}{\sigma^2_{\text{s-ASE}} + \sigma^2_{\text{s-DRB}} + \sigma^2_{\text{shot,out}}} \,, \tag{38}$$

which translates to

$$\text{NF} = \frac{1}{G}\left(\frac{\sigma^2_{\text{s-ASE}}}{G\,\sigma^2_{\text{shot,in}}} + \frac{\sigma^2_{\text{s-DRB}}}{G\,\sigma^2_{\text{shot,in}}} + 1\right), \tag{39}$$

and after substitution of Eqs. (14), (10), (11), and (9) to

$$\text{NF} = \frac{1}{G}\left(\frac{2\,N_{\text{ASE}}}{h\,f} + \frac{5/9\,P_{\text{DRB}}}{hf\,(B_e^2 + B_s^2/2)^{1/2}} + 1\right). \tag{40}$$

The factor of $5/9\ P_{\text{DRB}}$ accounts for the fact that only 5/9 of the total DRB power is co-polarized with the signal [64,18], as mentioned above. Note that the relative importance of signal-DRB beat noise to shot noise decreases as either the signal bandwidth or the receiver's electrical bandwidth increases [69,70].

Both N_{ASE} and P_{DRB} refer to quantities evaluated at the amplifier output. Note that the noise figure incorporating DRB now depends on signal power, since P_{DRB} is proportional to the signal power. This implies that the signal power is a required parameter to evaluate the noise figure of a system impaired by DRB.

Delivered OSNR

The quality of a transmission line with respect to ASE generation is characterized by the *delivered OSNR*, OSNR_{del}. To calculate OSNR_{del}, one can first calculate the

OSNR at the end of a transmission line, $\mathrm{OSNR_{line}}$, due to the generation of ASE by in-line amplification only. For identical spans, this can be written as [68]

$$\mathrm{OSNR_{line}} = 58 + \mathrm{P_{in}} - \mathrm{NF_{eff}} - \mathit{\Gamma}_{\mathrm{F}} - 10\log \mathrm{N_{amp}} \qquad [\text{ in dB }], \quad (41)$$

where $\mathrm{P_{in}}$ is the signal launch power at the input of each span [dBm], $\mathrm{NF_{eff}}$ is the effective noise figure of the optical amplifiers [dB], $\mathit{\Gamma}_{\mathrm{F}}$ is the span loss [dB], and $\mathrm{N_{amp}}$ is the number of amplifiers that follows each fiber span and, here, is equal to the number of spans, $\mathrm{N_{span}}$.

Assuming that the OSNR at the input of the transmission line, $\mathrm{OSNR_{TX}}$, is of finite value, the delivered OSNR, $\mathrm{OSNR_{del}}$, at the end of a transmission is given by

$$\frac{1}{\mathrm{OSNR_{del}}} = \frac{1}{\mathrm{OSNR_{TX}}} + \frac{1}{\mathrm{OSNR_{line}}} [\text{ linear units }]. \quad (42)$$

2.3. Signal Distortions

This section describes the most important signal distortions affecting optical communication links. Knowledge of the trade-offs between noise and distortions is important to understand system design. For example, although a highly distorted signal with little noise (good OSNR) can yield the same BER as a signal with little distortion but a lot of noise (poor OSNR), system designers will always prefer the latter case. This is because noise *gradually* accumulates in a system over its length, and thus *slowly* deteriorates system performance. On the other hand, most types of signal distortion show a threshold effect, beyond which an *abrupt* decrease in BER occurs. Operating at high signal distortions leaves little margin to a system as any additional impairment from defective components or aging can lead to catastrophic deterioration in system BER.

Dispersion-Induced Signal Distortions

Dispersion-induced signal distortions (e.g., pulse broadening in intensity modulated systems, or phase distortions in phase modulated systems) often limit the performance of digital fiber-optic communications systems. The impact of dispersive pulse broadening on system design depends significantly on the system under consideration: single-span, unamplified access systems (10-100 km), such as coarse wavelength-division multiplexed (CWDM) links, are sufficiently dispersion-tolerant, if the signal distortions due to dispersion are acceptably low for all channels, given the system's power budget. In metropolitan area and regional systems, a large dispersion tolerance for 10-Gbit/s channels may allow the installation of 10-Gbit/s channels on a system built for 2.5-Gbit/s with little or no need for installing DCMs. In terrestrial LH and ULH transport, dispersion tolerance usually measures the ability of a system to accommodate variations in fiber dispersion without having to resort to per-channel fixed or tunable dispersion compensators (TDCs); if unavoidable, one strives to at least minimize the TDC's required tuning range. Note that even slight uncertainties or variations in fiber dispersion may accumulate to substantial values over system lengths of many hundred kilometers: as discussed in Sec. 3.2, limited characterization accuracies of installed fiber, manufacturing tolerances, imperfect dispersion slope matching (i.e., non-ideal

broadband compensation) of DCMs, the availability of a limited set of DCMs with a selection of fixed dispersion values only (*granularity* of DCMs), and appreciable temperature-induced changes in fiber dispersion make dispersion-tolerant transmission attractive. In future transparent optical mesh networks, dispersion tolerance is likely to imply a signal's robustness to propagating over different physical paths with mixed fiber types and changing dispersion maps. Several techniques can be used to achieve dispersion tolerance, including modulation format and modulator technology, optical and electrical equalization, and FEC. We will briefly review these techniques here, which either compete with the use of DCFs or complement it. Understanding these techniques allows us to place the role of DCFs in a broader systems context.

Modulation Formats and Modulator Technology

Access systems predominantly use low-cost, highly integrated transmitter hardware, such as directly modulated lasers or electro-absorption modulators, and are therefore restricted to intensity modulation, in its simplest form non-return-to-zero on/off keying (NRZ-OOK). More sophisticated direct modulation techniques, such as dispersion-supported transmission [71], optical phase modulation [72], and optically filtered or reduced-chirp laser designs [73,74] increase dispersion tolerance at the expense of higher transmitter and/or receiver complexity.

In regional or LH system design, on the other hand, advanced optical modulation formats, typically generated by chirp-free Mach-Zehnder modulators (MZMs) are important to guarantee sufficient dispersion tolerance as well as robustness to fiber nonlinearity and concatenated optical filtering. Table 4 lists the simulation results for linear dispersion tolerance at 1 dB and 2 dB OSNR penalty for the selection of modulation techniques presented in Table 3 [61], attractive for 10-Gb/s and 40-Gb/s regional and long-haul transport systems (see, e.g., [75,61,76] and references therein for an introduction to optical modulation formats). In contrast to the direct modulation techniques used in access systems, all formats listed in Table 3 are generated by chirp-free Mach-Zehnder modulators (MZMs). Return-to-zero (RZ) formats typically (but not exclusively) use two-stage modulator setups, with a first (data) modulator and a second modulator to carve pulses [77]. Typical duty cycles are between 33% and 67%, and are indicated by the percentage numbers in Table 3. Differential quadrature phase shift keying (DQPSK) is either implemented by a cascade of two phase modulators [78] (straight-line or MZM), or by two sub-MZMs nested in a super-MZM [79]. The fact that spectrally narrow formats, in general, yield good dispersion tolerance [80] is reflected by the numbers for Duobinary and DQPSK. However, good dispersion tolerance may come at the expense of reduced back-to-back performance (note the higher required OSNR for Duobinary in Table 3) or higher hardware complexity (DQPSK requires more complex transmitters and receivers [79]). These trade-offs show the importance of assessing the dispersion tolerance of a modulation format with a comprehensive view on all the implications associated with it.

Equalization to Increase Dispersion Tolerance

In contrast to DCMs and TDCs, which both counteract residual dispersion by passing the optical signal through an element of opposite-sign dispersion (an *inverse filter*) prior to detection, equalizers do not try to undo the physical effect of dispersion.

Table 4. Dispersion tolerance (OSNR penalty) for different modulation formats at 42.7 Gb/s and at a target BER of 10^{-3}. NRZ: Non return-to-zero, RZ: Return-to-zero, CSRZ: Carrier-suppressed return-to-zero, DPSK: Differential phase shift keying, DQPSK: Differential quadrature phase shift keying.

Modulation format	1-dB penalty	2-dB penalty
Units	ps/nm	ps/nm
NRZ-OOK	39	56
Duobinary	182	206
33% duty cycle RZ-OOK	37	49
67% duty cycle CSRZ	37	50
67% duty cycle RZ-DPSK	43	59
50% duty cycle RZ-DQPSK	122	158

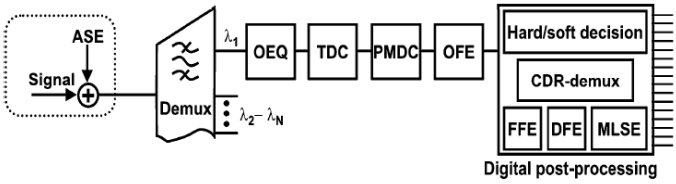

Fig. 11. General layout of an advanced optical receiver [89], using compensators (TDC, PMDC), optical equalizers (OEQ), electrical equalizers, and generic signal processing. OFE: Optical front-end, FFE: Feed-forward equalizer, DFE: Decision feedback equalizer, MLSE: Maximum-likelihood sequence estimator, CDR: Clock and data recovery, ASE: Amplified spontaneous emission.

Equalizers rather address the *symptoms* of dispersive pulse broadening on the signal quality by minimizing inter-symbol interference (ISI), which is simultaneously generated by residual dispersion [81–84] and other signal distortions, such as PMD [83–85] limited-bandwidth transmit or receive hardware [86,87], narrow-band in-line optical filtering [88] or fiber nonlinearity. Equalization can be performed in the optical domain and in the electrical domain, and can either substitute or complement impairment-specific compensators (TDC, PMDC), as shown in the advanced optical receiver setup of Fig. 11 [89].

Optical equalization (OEQ), placed before photo-detection, can use the full optical field information rather than only information on the optical intensity [88,90]. Also, if properly designed, OEQ can work *simultaneously* on many WDM channels by placing the OEQ in front of the WDM demultiplexer [88]. This is in contrast to electronic equalization, which always acts on the signals after photo-detection, and therefore is inherently a *per-channel* device. On the other hand, logic processing and bitwise feedback at high data rates is not easily implemented in the optical domain.

Studied for over 10 years for lightwave systems [81–86], electronic equalization at 10 Gb/s has recently experienced a boost by progress in high-speed integrated circuits, and has proven a powerful tool to increase dispersion tolerance [91–95]. Equalization techniques range from multi-tap feed-forward and decision feedback

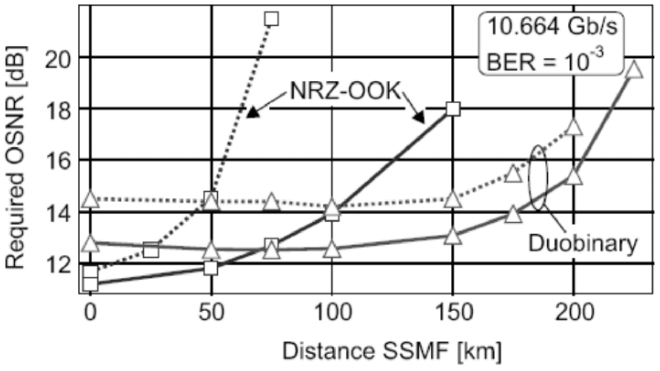

Fig. 12. Required OSNR at BER=10^{-3} vs. SSMF transmission distance at 10.7 Gb/s [61]. Squares: NRZ-OOK. Triangles: Duobinary. Dotted: un-equalized. Solid: using electronic equalization [83].

structures to sophisticated schemes employing multiple thresholds in conjunction with FEC. Advanced schemes using maximum-likelihood sequence estimation (MLSE) have now also been demonstrated at 10 Gb/s [96].

Figure 12 [61] visualizes the benefit of equalization for chirp-free NRZ-OOK and Duobinary modulation, both generated at 10.7 Gb/s using an x-cut $LiNbO_3$ MZM. The required OSNR, measured at BER=10^{-3} is shown as a function of transmission distance over SSMF at 1550 nm. Using electronic equalization [83], the permissible dispersion for 2 dB OSNR penalty could be shifted from 700 to 1650 ps/nm for NRZ in this experiment. At the same time, the 2-dB penalty point for Duobinary could only be pushed from 3200 to 3490 ps/nm, essentially by improving performance by a dispersion-independent amount. It is evident from this example that the increase in dispersion tolerance can substantially depend on the chosen modulation format and equalization scheme.

Forward Error Correction

Over the past few years, FEC has become an invaluable tool to increase system margins [97], which can be traded for enhanced tolerance to propagation impairments, most notably ASE accumulation. FEC schemes are characterized by their bit rate overhead and their correction curve, which is typically specified for uncorrelated (non-bursty) detection errors and translates the *raw channel* BER at the FEC input to a *corrected* (or decoded) BER at the FEC output (cf. inset to Fig. 13).

Alternatively, an FEC scheme may be specified by its coding gain, which is the gain in required OSNR for achieving the same target BER with FEC as for an uncoded system [97]. However, when assessing the benefits of FEC in a particular system scenario, coding gains alone are insufficient: firstly, the FEC overhead implies a higher data rate, which changes the impact of certain propagation impairments. For example, the tolerance to dispersion shrinks with the square of the bit rate, which implies a 14% reduction in dispersion tolerance for a typical FEC overhead of 7% and reduces

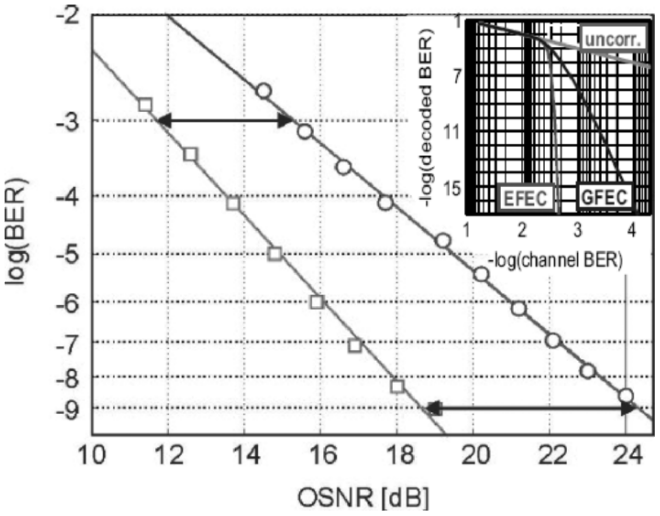

Fig. 13. BER vs. OSNR for NRZ-OOK at 10.7 Gb/s. Squares: back-to-back; circles: after 60 km of SSMF; arrows: BER-dependent dispersion penalties. - Inset: Correction curves for generic FEC (GFEC) and enhanced FEC (EFEC).

the coding gain. Secondly, many impairments (including dispersion) lead to higher penalties at good BER than at poor BER (cf. double-headed arrow in Fig. 13), or even to error floors, which together with the steep correction curve of FECs results in enhanced coding gains in the presence of impairments. Thirdly, the occurrence of burst errors can degrade FEC characteristics for certain kinds of impairments [98].

Fiber Nonlinearity

Transport systems spanning more than a few hundred kilometers of transmission fiber are likely to induce nonlinear distortions on the optical signal. The most important nonlinear phenomenon that results in signal distortion is the instantaneous Kerr effect [99], which occurs as a result of the very high optical intensities inside the core of single-mode optical fibers, typically exceeding 1 MW/cm^2. Such high intensities lead to the fiber's refractive index becoming proportional to the signal intensity.

Kerr nonlinearity can be decomposed into a host of nonlinear interactions that are referred to as self-phase modulation (SPM) [99], cross-phase modulation (XPM) [99], four-wave mixing (FWM) [99], intra-channel cross-phase modulation (IXPM) [100] and intra-channel four-wave mixing (IFWM) [100,101].

Cumulative Nonlinear Phase

The distortions imprinted on a signal by nonlinear effects depend, in general, on both the transmission line parameters and the operating conditions. The line parameters affecting nonlinear transmission include the fiber nonlinear coefficient, the fiber length,

the fiber dispersion and the dispersion map [102], as discussed in more detail in Sec. 3.2. The operating conditions impacting nonlinear transmission are the signal launch power into each optical fiber span, the signal power evolution along the fiber length (e.g., discrete versus distributed amplification), the bit rate, the channel spacing and the modulation format.

Accurately evaluating the effects of fiber nonlinearity on the signal involves solving the *Generalized Nonlinear Schrödinger Equation* (GNSE) [99] that describes the evolution of the optical field along the transmission line. Solving the GNSE with high accuracy can be done numerically using the split-step algorithm [99], but is computationally intensive. However, it is possible for some systems to *approximate* the effects of fiber nonlinearity analytically. In transmission lines where propagation is limited by SPM, XPM or IXPM (after optimization of the dispersion map), one can approximate that the distortions induced on the signal by fiber nonlinearity is determined by the cumulative nonlinear phase shift given by

$$\phi(L) = \int_0^L \gamma(z)\,\mathrm{P}(z)\,dz\ , \tag{43}$$

where $\mathrm{P}(z)$ is the evolution of the average signal power along a fiber of length L having a nonlinear coefficient $\gamma(z)$ [99]. The nonlinear coefficient $\gamma(z)$ is given by

$$\gamma(z) = \frac{\mathrm{n}_2\,\omega_0}{\mathrm{c}\,\mathrm{A}_{\mathrm{eff}}}\ , \tag{44}$$

where n_2 is the nonlinear refractive index coefficient, an intrinsic material property of the fiber, ω_0 is the angular frequency at the signal wavelength, c the speed of light in vacuum and $\mathrm{A}_{\mathrm{eff}}$) the fiber effective mode area [99]. Equation (43) is useful to compare, for instance, the relative impact of fiber nonlinearity on two transmission lines having different signal power evolutions at a fixed bit rate, modulation format and fiber dispersion. For example, we can compare a transmission line consisting of passive fiber spans with a line containing distributed (Raman) amplification by using the ratio of nonlinear phases,

$$\mathrm{R}_{\mathrm{NL}} \equiv \frac{\phi_{\mathrm{DRA}}(L)}{\phi_{\mathrm{Pas}}(L)}, \tag{45}$$

where $\phi_{\mathrm{DRA}}(L)$ and $\phi_{\mathrm{Pas}}(L)$ are the integrated nonlinear phase for a DRA and a passive fiber, respectively. Assuming constant γ and fixed signal input power to the fiber, the nonlinear phase ratio factor R_{NL} can be written as

$$\mathrm{R}_{\mathrm{NL}} = \frac{\alpha_{\mathrm{s}}}{1-\exp(-\alpha_s\,L)} \int_0^L G(0,z)\,dz, \tag{46}$$

which can be interpreted as the ratio of *path-averaged signal powers* in the DRA as compared to the passive fiber. Raman pumping of fibers provides gain to the signal, which increases the path-averaged signal power, and thus results in an effective increase in nonlinear signal distortion. This is illustrated in Fig. 14a, showing the signal power evolution within a passive optical fiber as well as within two different DRAs, one using backward Raman pumping only, and the other using 50% backward and forward Raman pumping. Both pumping configurations are operated at transparency (i.e., producing identical output and input power levels). As seen in the figure, using forward pumping

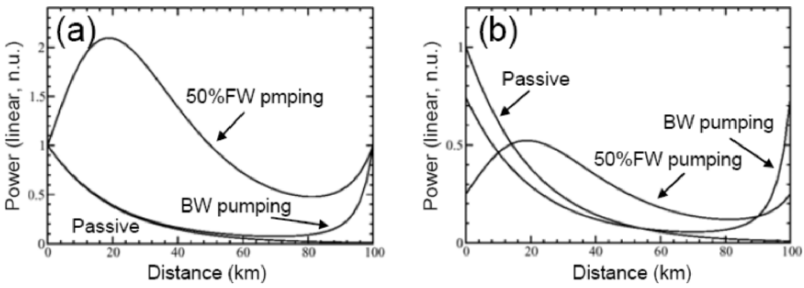

Fig. 14. Signal power evolution along a fiber span at a) fixed signal launch power and b) constant cumulative nonlinear phase. Three configurations are shown: passive fiber and DRAs with full backward (BW) and 50% forward (FW) pumping. Both DRAs are pumped at transparency (0 dB net gain).

rapidly increases the signal power, as it amplifies the signal at the *input* end of the fiber where the signal power is highest. In contrast, a large backward Raman gain is necessary to bring the signal at the fiber output end to a level comparable to the level at the fiber input end. As a result, only a small increase in nonlinearity occurs with backward Raman pumping relative to a passive fiber. For the two Raman pumping scenarios of Fig. 14a, one can make the cumulative nonlinear phase equal by decreasing the signal power by the factor $\mathrm{R_{NL}}$ at the input of the span. This is illustrated in Fig. 14b where the launch powers have been reduced to achieve equal cumulative nonlinear phases.

Figure 15 shows how the nonlinear phase increases with increasing Raman pumping in a DRA for different levels of forward and backward Raman pumping. Because backward Raman pumping mainly increases the low signal power levels towards the end of the transmission span, it features the lowest increase in nonlinear phase. Thus, backward Raman pumping is very efficient to provide distributed signal gain with minimum impact on fiber nonlinearity. However, large backward Raman gain leads to excessive DRB generation that limits transmission [102]. As a result, backward Raman pump powers should not exceed certain levels; optimized Raman pumping configuration therefore include some amount of forward pumping to minimize the effect of DRB while still providing large Raman gain [103,63]. A typical ratio of forward to total Raman pump powers to optimize transmission is around 30%. Specialized fiber designs can also be developed to minimize the impact of nonlinearity and DRB in DRAs [104,105].

Dispersion Tolerance and Fiber Nonlinearity

Signal distortions due to fiber nonlinearity can affect the signal in many ways. Two important effects of fiber nonlinearity are a change in the value of NRD at which detection is optimum, and a reduction in dispersion tolerance. As a consequence, the dispersion tolerance in the nonlinear regime can be substantially different from the linear dispersion tolerance values listed in Table 4.

Figure 16 shows simulation results of the required OSNR for Duobinary, CSRZ, and NRZ-OOK modulation at 42.7 Gb/s and BER=10^{-3} as a function of NRD in

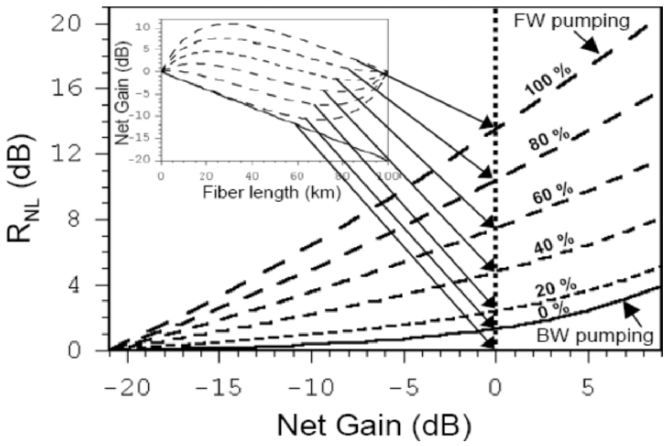

Fig. 15. Increase in nonlinear phase ratio, R_{NL}, in a DRA as a function of the net Raman gain for various percentage values of forward pump power to total Raman pump power. 0% forward pumping corresponds to backward pumping only. The DRA is 100 km, and the signal and pump losses are $\alpha_s = 0.21$ dB/km and $\alpha_p = 0.26$ dB/km, respectively. The inset shows the signal power evolution within the fiber when pumping to transparency (0 dB net Raman gain).

the linear regime (dashed) and after 3,200 km of single-channel propagation (solid) over TrueWave® fiber (4.5 ps/nm dispersion, 55 μm^2 effective area). Each 100-km span was followed by discrete optical amplification (see Fig. 1a). A SPDM with a pre-compensation of -500 ps/nm and an RDPS of 25 ps/nm was used. The per-span launch power was chosen to generate a 1.5-dB OSNR penalty due to fiber nonlinearity at the optimum NRD, as compared to the back-to-back performance (zero NRD and linear propagation). As evident from Fig. 16, the 2-dB dispersion tolerance windows are reduced to 50%, 60%, and 80% of their widths in the linear regime for Duobinary, NRZ, and CSRZ, respectively, and the shift in optimal NRD is different for each modulation format. Note that the effect of fiber nonlinearity on the dispersion tolerance of various modulation formats can also be observed at much *shorter* transmission distances, for example if the signal launch power has to be increased to compensate for higher span losses or more amplification noise, or if the system is composed of a large number of shorter but lossier transmission spans (e.g., 32 highly lossy spans of 20 km each), which may occur in metropolitan area networks.

In addition to the tolerance to NRD, the tolerance to temperature-induced dispersion variations of the transmission fiber, as well as to the granularity of DCMs (pre-compensation, in-line compensation, post-compensation) has to be considered to assess a format's dispersion tolerance, as discussed in more detail in [106].

Dispersion Mapping

As mentioned in Sec. 1.2, SPDMs are the simplest to implement and facilitate the writing of engineering rules for system deployment. Figure 17 shows the three parameters

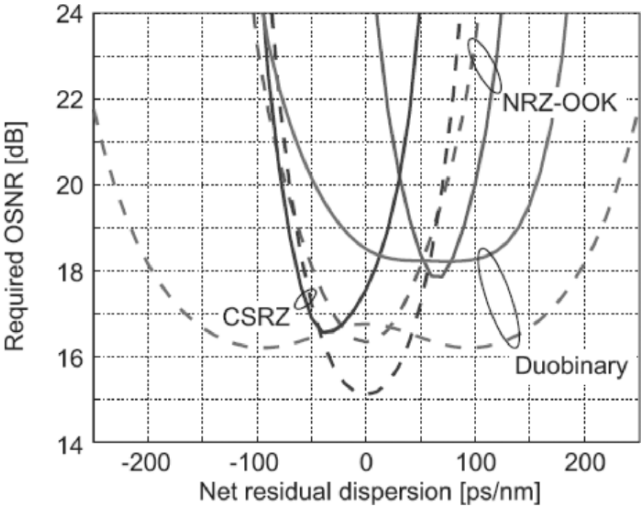

Fig. 16. Dispersion tolerance of various modulation formats without (dashed) and with (solid) fiber nonlinearity. The bit rate is 42.7 Gb/s.

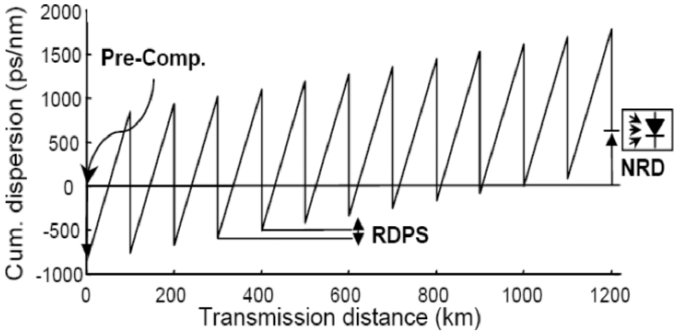

Fig. 17. The three parameters defining a singly-periodic dispersion map (SPDM): Pre-compensation, residual dispersion per span (RDPS) and net residual dispersion (NRD).

that define a SPDM: pre-compensation, RDPS and NRD. Varying these three map parameters leads to all possible dispersion maps that are singly periodic.

The effects of dispersion mapping on transmission can be seen in Fig. 18 that shows transmission of a NRZ signal in the absence of nonlinearity (Fig. 18a) and after nonlinear transmission (Fig. 18b) over 15 spans of 80 km of SSMF at 3.67 mW launch power per channel. The WDM channel spacing is 50 GHz, and the back-to-back required OSNR is 10.9 dB. SSMF parameters are D = 17 ps/(nm km) and S = 0.055 ps/(nm^{2}km). The fiber's nonlinear coefficient is $\gamma = 1.3 \quad (\mathrm{W\,km})^{-1}$. The DCF is

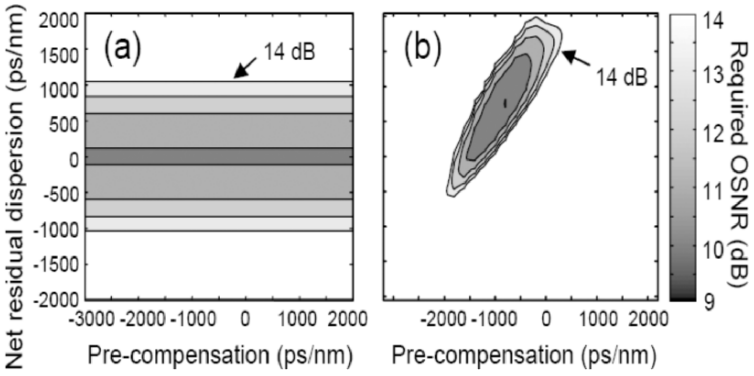

Fig. 18. Required OSNR at 10^{-3} BER as a function of pre-compensation and NRD: a) in the absence of fiber nonlinearity; b) after nonlinear transmission (parameters in main text). The outermost contour indicates 14 dB of required OSNR and decreasing by step of 1 dB going inwards. The bit rate is 10.7 Gb/s.

assumed to have the same RDS as the transmission fiber, and nonlinearity in the DCF is neglected.

Figure 18 demonstrates how critical dispersion mapping is to minimize signal distortions. Deviations of a few hundred ps/(nm km) in pre-compensation or in NRD can lead to a significant OSNR penalty.

Polarization-Mode Dispersion

PMD and System Outage

The transversal index profile of real optical fibers deviates from ideal circular symmetry, which can be due to manufacturing imperfections or due to bending stress when the fiber is cabled and deployed in the field. As a consequence, the fiber becomes slightly birefringent, i.e., different polarizations of light travel at different speeds within the fiber. The two polarization eigenstates are referred to as the *principal states of polarization* (PSP), and the difference in group velocity between them is called *differential group delay* (DGD). The impact of the DGD on digital communication systems manifests itself in dispersive pulse broadening, called *polarization-mode dispersion* (PMD). If the DGD is constant over wavelength, only *first-order* PMD is present, while we need to include *higher-order* PMD if the DGD changes with wavelength (see, e.g., [107] for a detailed overview on the broad topic of PMD).

Figure 19 shows simulations of the OSNR penalty for NRZ, CSRZ, and 33% duty cycle RZ signals for typical beat-noise limited receiver parameters, and for first-order PMD with the signal split equally between the fiber's PSPs. It can clearly be seen that RZ formats are generally more robust to first-order PMD than NRZ formats [108]. The 1-dB OSNR penalty occurs at a DGD of around 30% of the bit duration for NRZ systems. This suggests that signal distortions due to PMD could be fully accounted

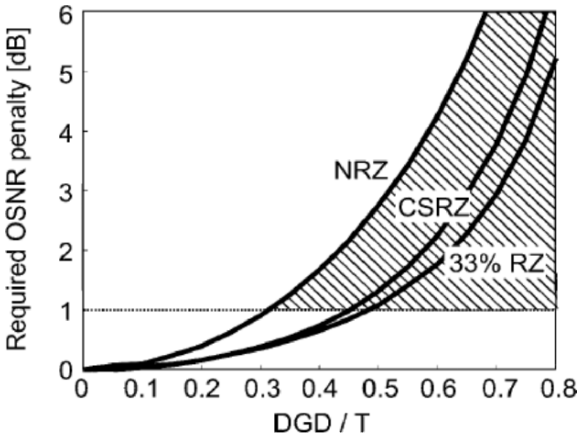

Fig. 19. OSNR penalty versus DGD, normalized to the bit duration T, for first-order PMD and various OOK modulation formats.

for by allocating a 1-dB margin in the system's OSNR budget, provided the fiber PMD does not exceed 30% of the bit duration. However, this simple link budgeting approach, which can be successfully applied to most types of signal distortion, fails for PMD, since fiber PMD is a fundamentally random process: neither the amount of DGD nor the fiber's PSPs are deterministic, but may fluctuate randomly over time, obeying Maxwellian statistics; the probability density function (PDF) of the DGD is given by

$$\mathrm{PDF}[\mathrm{DGD}] = \frac{8}{\pi^2 \langle \mathrm{DGD} \rangle} \left(\frac{2\mathrm{DGD}}{\langle \mathrm{DGD} \rangle} \right)^2 \exp\left[- \left(\frac{2\mathrm{DGD}}{\langle \mathrm{DGD} \rangle} \right)^2 / \pi \right] \quad (\mathrm{DGD} > 0) \,, \tag{47}$$

with mean $\langle \mathrm{DGD} \rangle$.

It is important to understand that the tail of the Maxwellian PDF is unbounded, which implies that arbitrarily high values of DGD may be encountered with some low, but finite probability. This fact can pose severe problems on system design, since any OSNR margin that is allocated to accommodate penalties due to PMD in a system's link budget may be occasionally exceeded, leading to infrequent (but fundamentally unavoidable) instances of *system outage*. If a 1-dB OSNR margin is assigned, as shown in Fig. 19, the outage probability for a system using NRZ modulation can be obtained by calculating the Maxwellian probability that the DGD of a fiber with some given mean DGD exceeds 30% of the bit duration (hatched area in Fig. 19). Thus, the effect of PMD drags system specifications from a purely deterministic approach to probabilistic characterizations.

Specifying the most appropriate value for system outage is a matter of trading system complexity (and cost) against system reliability and a method for PMD specification is not completely defined among network operators; outage probability targets ranging between 10^{-3} to 10^{-7} are mentioned in this context.

Specification of Fiber PMD

For long fibers typically encountered in communication systems, it can be shown that the mean fiber DGD is proportional to the square-root of the fiber length [107]. Therefore, fiber PMD is specified by the *PMD coefficient*, given in ps/$\sqrt{\text{km}}$. Multiplying this value by the square-root of the fiber length yields the mean fiber DGD. While older fiber, installed in the 1980s, may have PMD coefficients as high as 0.8 ps/$\sqrt{\text{km}}$, the PMD coefficients of modern transmission fiber are well below 0.1 ps/$\sqrt{\text{km}}$.

To illustrate the impact of fiber PMD on system performance, consider a beat-noise limited NRZ system with an allocated margin for PMD of 1 dB, leading to system outage whenever the instantaneous DGD exceeds 30% of the bit duration (cf. Fig. 19). Assume a system outage specification of 4×10^{-5}. Integrating the Maxwellian PDF, Eq. (47), we identify this outage probability as the probability that the instantaneous DGD exceeds three times its mean value, i.e., $P[\text{DGD} > 3\langle\text{DGD}\rangle] = 4 \times 10^{-5}$. Therefore, the mean fiber PMD has to be lower than 10% of the bit duration to let the system stay within the outage specifications. At 10 Gb/s operating over old fiber (0.8 ps/$\sqrt{\text{km}}$), this limits the transmission distance only to some 160 km. Using new fiber (0.04 ps/$\sqrt{\text{km}}$), PMD could be tolerated for system lengths up to 4000 km, even for a 40 Gb/s system. Even longer system reach can be achieved by going to RZ formats.

3. Impact of DCF on Transmission

As mentioned in previous sections, dispersion compensation is necessary in systems operating at 10 Gb/s and above to limit the accumulation of dispersion and the resulting inter-symbol interference through pulse broadening. In addition, careful dispersion mapping is also used to minimize the impact of fiber nonlinearity. The presence of dispersion compensation in a transmission line also impacts transmission in many other ways. In the case of DCFs, the main impact on transmission are, additional generation of noise (i.e., ASE and DRB), signal distortions from fiber nonlinearity within the DCF, a possible increase in PMD, and signal distortions from a mismatch in dispersion between the practically achieved and the targeted dispersion maps. In this section, we will describe the general framework and the basic tools for evaluating the impact of DCFs on each of these aspects.

The parameters of the optical fibers that are used in this section are summarized in Table 5.

3.1. Noise

Noise generation along a transmission line takes mainly two forms, ASE and DRB (see Sec. 2.2). Inserting DCFs in a line system can increase both sources of noise through the additional amplification required by DCF loss as well as through Rayleigh scattering within the DCF, the latter increasing when the DCF is Raman pumped.

Table 5. Parameters of the optical fibers considered in this section. $\mathrm{A_{eff}}$ and r are evaluated at the signal wavelength $\lambda_s = 1550$ nm while $\mathrm{C_r}(\lambda_\mathrm{s}, \lambda_\mathrm{p})$ is the Raman gain efficiency for a signal at a given $\lambda_s = 1550$ nm for a pump located at $\lambda_p = 1450$ nm.

Property	Units	NZDF	SSMF	DCF
$\mathrm{A_{eff}}$	$\mu\mathrm{m}^2$	52.8	78.9	17.0
α_s	dB/km	0.2	0.2	0.5
α_p	dB/km	0.25	0.25	0.6
$\mathrm{C_r}(\lambda_\mathrm{s}, \lambda_\mathrm{p})$	1/(W km)	0.691	0.470	2.41
r	1/km	9.64×10^{-5}	6.63×10^{-5}	3.70×10^{-4}
n_2	m^2/W	2.5×10^{-20}	2.5×10^{-20}	2.5×10^{-20}

Optical Signal-to-Noise Ratio

As described in Sec. 2.2, the accumulation of ASE generated by optical amplification in the transmission line degrades the delivered OSNR, $\mathrm{OSNR_{del}}$, at the receiver. The insertion of dispersion compensation in the line introduces additional loss that requires additional amplification, and thus leads to additional ASE generation. It is important to note that, at large net gain G, the OSNR degradation from a single optical amplifier is virtually independent of the gain value [see Eqs. (18) and (19) noting that $P_s = G\,\mathrm{P_{in}^A}$, where $\mathrm{P_{in}^A}$ is the input power to an amplifier]. In contrast to the gain G (for large values of G), $\mathrm{P_{in}^A}$ has a direct impact on the OSNR at the output of an amplifier. The impact that a specific optical amplifier has on the delivered OSNR in a transmission line thus depends mainly on the input power of this amplifier relative to the input powers of the other amplifiers present in the line. As a result, the location of the DCFs in a line, either localized or diffused, greatly impacts $\mathrm{OSNR_{del}}$ as it determines the signal power evolution in each span. Such signal power evolution is represented schematically in Fig. 20 for a span using discrete optical amplification in the absence of dispersion compensation (Fig. 20a), with localized dispersion compensation (Fig. 20b) and with diffused dispersion compensation (Fig. 20c).

In transmission lines using localized dispersion compensation (Fig. 20b), the reduction in $\mathrm{OSNR_{del}}$ relative to a line without localized dispersion compensation (Fig. 20a) originates from the additional ASE generated by the second stage of amplification of the dual-stage amplifier that contains the dispersion-compensating element. As mentioned previously, the importance of the contribution of the second amplification stage relative to the first stage on the OSNR degradation depends on their relative signal input power (for similar noise figures of both stages). For instance, when the input power to the second amplification stage is identical to the input power of the first stage, the dual-stage amplifier degrades $\mathrm{OSNR_{del}}$ nearly twice as much as a single-stage amplifier with the same noise figure. The impact on $\mathrm{OSNR_{del}}$ of a dual-stage amplifier can also be viewed in terms of noise figure. The dual-stage amplifier is then considered as a single amplifier with an effective noise figure that is the weighted sum of the individual stages' noise figures by combining the expression for the noise figure of a single-stage optical amplifier, Eq. (33), with the noise figure concatenation rule, Eq. (35),

$$\mathrm{NF_{loc}} = \mathrm{NF_1} + \frac{\mathrm{NF_2} - \mathrm{T_{DCF}}}{G_1 \mathrm{T_{DCF}}}, \qquad [\text{ linear units }], \tag{48}$$

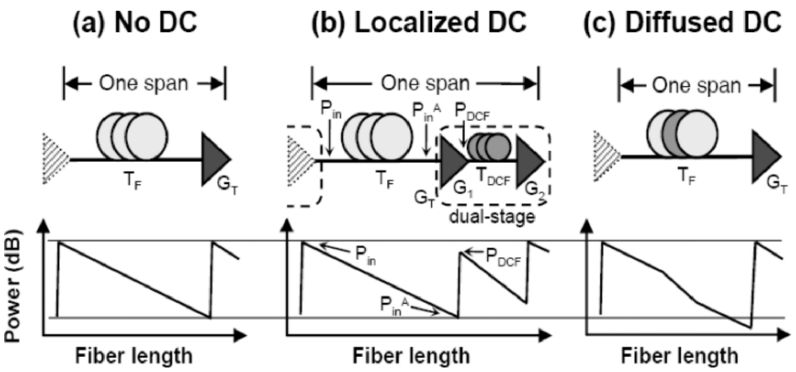

Fig. 20. Evolution of the signal power (in dB) over one span in a system a) without dispersion compensation, b) with localized dispersion compensation, and c) with diffused dispersion compensation.

where NF_1 and NF_2 are the noise figure of the first and second amplification stages of a dual-stage amplifiers, respectively. The noise figure can also be expressed explicitly in terms of spontaneous emission factors,

$$\mathrm{NF_{loc}} = 2\,\mathrm{n_{sp,1}}\left(1-\frac{1}{G_1}\right)+\frac{2\,\mathrm{n_{sp,2}}}{G_1\,\mathrm{T_{DCF}}}-\frac{2\,\mathrm{n_{sp,2}}-1}{G_T}, \qquad [\text{ linear units }], \quad (49)$$

where $\mathrm{n_{sp,1}}$ and $\mathrm{n_{sp,2}}$ are the spontaneous emission factors of the first and second amplification stages, respectively, and G_1 and G_T ($= G_1\mathrm{T_{DCF}}G_2$) are the net gains of the first amplification stage and of the entire dual-stage amplifier, respectively. (The insertion loss of the DCF, expressed in dB, is $\Gamma_{\mathrm{DCF}} = -10\log \mathrm{T_{DCF}}$.) In a transmission line exceeding a few spans, the total gain G_T of the dual-stage amplifier is set to exactly compensate the fiber span loss, so that the launch power into each transmission span is equal. Note that the gain G_1 can also be expressed as the ratio of powers $\mathrm{P_{in}^{A}/P_{DCF}}$ where $\mathrm{P_{in}^{A}}$ and $\mathrm{P_{DCF}}$ are the signal powers at the input of the first amplification stage and at the input of the DCF, respectively. $\mathrm{P_{in}^{A}}$ and $\mathrm{P_{DCF}}$ are typically monitored in transmission systems.

Following Eqs. (41) and (42), and assuming a noise-free transmitter (i.e. infinite $\mathrm{OSNR_{TX}}$) as well as identical spontaneous emission factors for both amplification stages (i.e., $\mathrm{n_{sp,1}} = \mathrm{n_{sp,2}} \equiv \mathrm{n_{sp}}$), the delivered OSNR for localized dispersion compensation, $\mathrm{OSNR_{del}^{loc}}$ can be written as

$$\mathrm{OSNR_{del}^{loc}} = 58 + \mathrm{P_{in}} - 10\,\log\left[\mathrm{NF}+\frac{2\,\mathrm{n_{sp}}}{G_1}\left(\frac{1}{\mathrm{T_{DCF}}}-1\right)\right] - \Gamma_{\mathrm{F}} - 10\log \mathrm{N_{amp}} \qquad [\text{ in dB }], \quad (50)$$

where NF (linear units) is the noise figure of a single-stage amplifier of gain G_T (compensating for the fiber span loss Γ_{F} (in dB)) and spontaneous emission factor $\mathrm{n_{sp}}$.

Using Eq. (50), one can easily see that the degradation in delivered OSNR, $\mathrm{OSNR_{deg}}$, due to the presence of the DCF in the dual-stage amplifier is given by

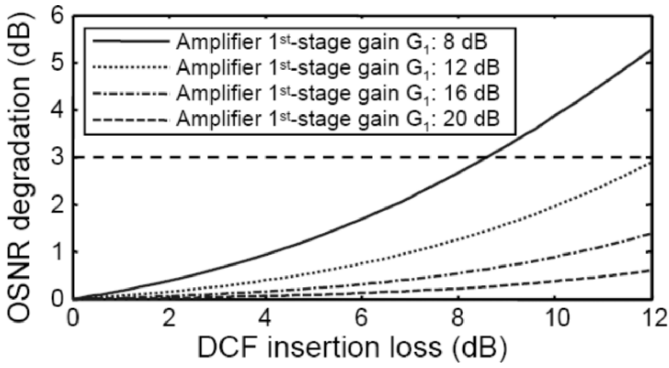

Fig. 21. Degradation in delivered OSNR caused by inserting localized dispersion compensation in a transmission line as a function of the DCF insertion loss. The DCF is assumed to sit in a dual-stage amplifier (Fig. 20b) and the delivered OSNR is compared the a line without DCF (Fig. 20a). The fiber span loss, $\Gamma_{\rm F}$, is assumed to be 20 dB.

$$\mathrm{OSNR}_{\rm deg}^{\rm loc} = 10\,\log\left[\mathrm{NF} + \frac{2\,\mathrm{n_{sp}}}{G_1}\left(\frac{1}{\mathrm{T_{DCF}}} - 1\right)\right] - 10\,\log \mathrm{NF} \qquad [\text{ in dB }], \tag{51}$$

where the last term of Eq. (51) is obtained by noting that the absence of DCF is equivalent to having $\mathrm{T_{DCF}} = 1$.

Figure 21 shows the OSNR degradation, $\mathrm{OSNR}_{\rm deg}^{\rm loc}$, for a span loss $\Gamma_{\rm F}$ of 20 dB and a spontaneous emission factor, $\mathrm{n_{sp}} = 2$ (noise figure at high gain of 6 dB). Note that when the gain of the first amplification stage equals the insertion loss of the DCF, the input power to the two amplification stages are identical. This leads to nearly a doubling of the ASE level (at identical noise figures) and thus an OSNR reduction close to 3 dB as expected (see dashed horizontal line in Fig. 21). The same figure also suggests that one can minimize the OSNR degradation by having a large gain for the first stage of amplification. However, as we will see in Sec. 3.2, nonlinear effects within the DCF may start to contribute significantly to the overall nonlinearity of transmission, thereby offsetting the advantages gained in delivered ONSR. Typical maximum DCF insertion loss for 100-km of SSMF is 10 dB and can decrease to as low as 3 dB for NZDF family fibers because of their low dispersion values.

For diffuse dispersion compensation such as shown in Fig. 20c, the DCF is part of the transmission fiber itself. Since DCFs generally have higher loss than state-of-the-art transmission fibers, the insertion of DCFs in the fiber span generally results in higher fiber span losses, as depicted in the signal power evolution of Fig. 20c. Consequently, a lower signal power enters the amplifier following the fiber span, resulting in a degradation of the delivered OSNR.

The delivered OSNR, $\mathrm{OSNR}_{\rm del}^{\rm dif}$, of a passive diffused dispersion compensation differs from the passive fiber delivered OSNR, $\mathrm{OSNR_{del}}$ in two ways: An increase in fiber loss $\Gamma_{\rm F}$ and a very slight increase in effective noise figure, $\mathrm{NF_{eff}}$ due to the extra gain G_T necessary to compensate the extra loss. Neglecting the small difference in $\mathrm{NF_{eff}}$ and using Eq.(41), one can easily show that the delivered OSNR for diffused

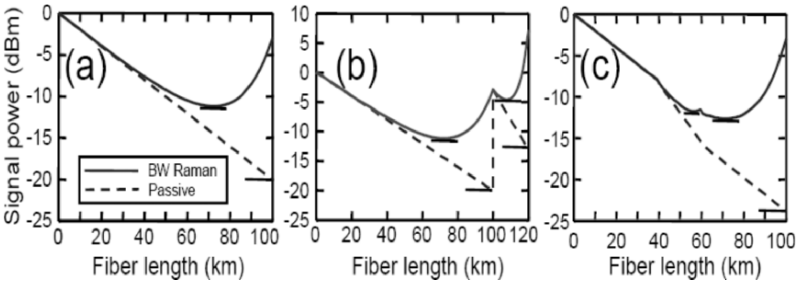

Fig. 22. Signal power evolution in passive and in backward Raman-pumped fibers: a) over NZDF, b) over SSMF compensated by a DCF and c) over a DMF. The fiber span length L, input power $\mathrm{P_{in}}$, and DRA net gain are 100 km, 0 dBm, and -3 dB, respectively, for all three scenarios. Short horizontal lines indicate the location of lowest power for all fiber segments.

dispersion compensation can be written as,

$$\mathrm{OSNR_{del}^{dif}} = \mathrm{OSNR_{del}} \; + \; 10 \; \log \left[\frac{\exp(-\alpha_{\mathrm{F}} \; \mathrm{L_{DCF}})}{\exp(-\alpha_{\mathrm{DCF}} \; \mathrm{L_{DCF}})} \right] \quad [\text{ in dB }], \qquad (52)$$

where α_{F} is the loss coefficient [dB/km] of the fiber that the DCF replaces in the DMF and $\exp(-\alpha_{DCF}\mathrm{L_{DCF}})$ is the DCF insertion loss $\mathrm{T_{DCF}}$ introduced previously. The last term of Eq. (52) can be rewritten as,

$$\mathrm{OSNR_{deg}^{dif}} = 10 \; \log(e) \, (\alpha_{\mathrm{DCF}} - \alpha_F) \, \mathrm{L_{DCF}} \qquad [\text{ in dB }]. \qquad (53)$$

which is the difference [in dB] between the insertion loss of the DCF and the insertion loss of the transmission fiber of the same length it replaces. Consequently, every additional 'dB' of loss to the DMF due to the presence of the DCF results in a 'dB' of delivered OSNR degradation. Note that typical DMFs are nearly 100% dispersion compensated so that the condition $\mathrm{L_{DCF}} \approx (\mathrm{L_{DCF}} - \mathrm{L}) \, \mathrm{D_F}/\mathrm{D_{DCF}}$ approximately holds.

The above considerations are valid for transmission lines using *discrete amplification* (e.g., discrete erbium or discrete Raman amplification, Figs. 1a and 1b). However, for hybrid or all-Raman systems (Figs. 1c and 1d), establishing simple analytic expressions to calculate the OSNR degradation due to the presence of localized dispersion compensation turns out to be challenging [109,110]. For such systems, an accurate evaluation of $\mathrm{OSNR_{deg}}$ can be obtained by numerically solving the equations of Sec. 2.2.

Despite the large variety of possible Raman pumping configurations, one can develop an understanding of the OSNR degradation resulting from the insertion of localized dispersion compensation based on physical considerations of ASE generation and power evolution (Fig. 22). Assuming that the noise figure remains constant, the ASE generated by an amplifier is independent of the input signal power. The maximum impact of ASE generation on OSNR degradation in such amplifier occurs near the location of lowest signal power within the amplifier [62]. The minimum signal powers in segments of passive fibers and DRAs are indicated in Fig. 22, for the three scenarios

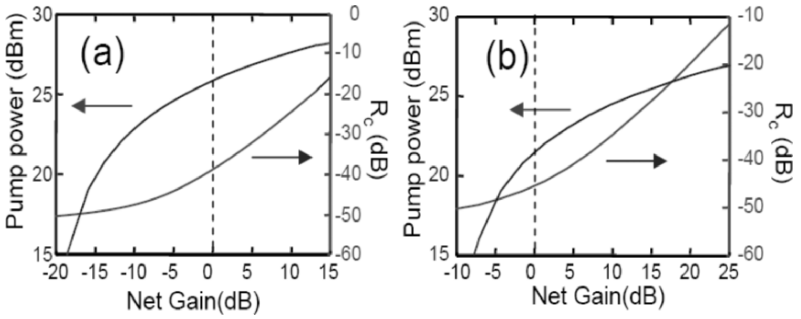

Fig. 23. Generation of DRB in a) a transmission fiber, SSMF, and b) a DCF for backward pumping. Fiber parameters are given in Table 5. The vertical dash line indicates when the amplifier is transparent.

depicted in Fig. 20. As shown in Fig 22, the minimum signal power in a DRA increases significantly relative to a passive fiber, reducing the OSNR degradation from this fiber section. Consequently, in a hybrid system (Fig. 1c), the minimum signal power in a span may occur at the end of the localized DCF (see Fig. 22b), increasing the impact of DCF loss on the delivered OSNR. In an all-Raman system (Fig. 1d) on the other hand, the relative impact of the presence of the DCF in the system is lowered relative to a hybrid system as the minimum power of a Raman-pumped DCF can be much higher than a passive DCF because the DCF is Raman pumped (see Fig. 22b). Even though the picture developed above on OSNR degradation is qualitative, it is a helpful guideline to estimate the relative contributions of each fiber segment in a transmission line without having to resort to elaborate calculations.

The use of Raman amplification helps reducing the impact of ASE generation but can also enhance other impairments. We will see in the next two sections (Secs. 3.1 and 3.2) that the net Raman gain possible in fiber spans and in DCFs is limited by the generation of DRB and by signal distortions from fiber Kerr nonlinearity.

Double Rayleigh Backscatter

As discussed in Sec. 2.2, the generation of DRB in hybrid systems becomes particularly important because the fiber span becomes a DRA. Similarly, generation of DRB in DCF becomes important only when the DCF itself is Raman-pumped. This situation occurs in systems using discrete Raman amplification (Fig. 1b) and in all-Raman systems (Fig. 1d).

The impact of DRB on a signal is best described by the crosstalk ratio, R_c (see Sec. 2.2). Figure 23 shows how R_c grows with the net Raman gain for a transmission fiber (Fig. 23a) and a DCF (Fig. 23b) for backward Raman pumping. The Raman pump power required to achieve such net gain is also presented for reference. In the absence of Raman pumping, the crosstalk ratios for both fibers, SSMF and DCF, are comparable, at a value around -50 dB. As the net Raman gain increases, the crosstalk ratios increase in such a way that, at transparency (0 dB of net gain, dashed vertical

line), R_c for SSMF is higher than R_c for the DCF by about 7 dB. At 10 dB of net Raman gain, the difference has grown to 11 dB. This indicates that signal degradation from DRB in DCFs occurs at higher values of net gain than for SSMF. Knowing that the generation of DRB in DRAs forces to operate a few dBs below transparency [111,103], Fig. 23 indicates that DCF can operate as a DRA with positive net gain with only a small increase in R_c. This property of DCF relative to DRB has been used to design all-Raman systems with DCFs used as Raman amplifiers with positive net gain.

3.2. Signal Distortions

As discussed in Sec. 2.3, in addition to the generation of noise, propagation over transmission lines also introduces deterministic signal distortions. In this section, we discuss how the insertion of DCFs in a line contributes to deterministic signal distortions.

Dispersion Compensation

It is well known that dispersion compensation has been introduced in transmission lines to control the accumulation of dispersion in order to provide optimum transmission. However, achieving the target dispersion values and dispersion map can be a difficult task. The challenges associated with generating a target dispersion value at a given wavelength include the dispersion accuracy of the DCFs, the commercial availability of a finite set of DCFs with discrete dispersion values, and temperature-induced fluctuations of dispersion.

Dispersion Accuracy

The dispersion characteristics of an optical fiber depend on many fiber parameters such as material concentration and the physical fiber parameters [112]. Any variations in the fiber parameters translate into changes in fiber dispersion. Variations in dispersion of individual fibers in a transmission line can lead to significant dispersion walk-off from the target dispersion values along the line. As a result, both the NRD at the receiver as well the dispersion map can be affected.

Assuming a random distribution of fiber dispersion around a nominal value, the variance of the dispersion in a transmission line evolves as

$$\sigma^2_{\mathrm{line}} = \sum_{i=1}^{N_{\mathrm{span}}} \sigma^2_{\mathrm{F,i}} + \sum_{i=1}^{N_{\mathrm{DCF}}} \sigma^2_{\mathrm{DCF,i}} \ , \tag{54}$$

where $\sigma_{\mathrm{F,i}}$ and $\sigma_{\mathrm{DCF,i}}$ are the standard deviations of dispersion of the i^{th} fiber segment around the mean dispersion value for the transmission fibers and DCF, respectively. Equation (54) indicates that, even though inserting DCFs in a line may be necessary to limit the dispersion, it also increases the uncertainty of the dispersion value at detection. This equation can then provide an estimate of the magnitude of dispersion deviations in transmission lines. Such deviations need to be compared to dispersion tolerances of the modulation format and receiver design used in the system.

Finally, we want to mention that some fibers have their local dispersion values accurately measured after fabrication. Through a selection process, fibers with large

deviations from the nominal dispersion value are not made available under the fiber type denomination. Such a selection process is particularly efficient in reducing large deviations of cumulative dispersion in a transmission line that may result from the inadvertent concatenation of a large number of fibers having either large positive or negative dispersion deviations from the nominal dispersion value.

Dispersion Granularity

Practical and commercially attractive deployment of fiber-optic communication systems requires the use of a finite set of dispersion compensation modules, resulting in a *granularity* in the dispersion compensation values. Such a granularity results in deterministic deviations in the prescribed dispersion map of installed systems relative to the optimum possible dispersion map. As an example, if one allows six different dispersion values for DCMs to compensate up to 120 km of SSMF (2,040 ps/nm), one can choose to have a DCM starting at -340 ps/nm of cumulative dispersion up to $-2{,}040$ ps/nm by steps of -340 ps/nm. Equipped with such DCMs, deviations from a target dispersion value at each DCF location in a point-to-point system can reach ± 170 ps/nm, i.e., $\pm$ half the magnitude of the dispersion granularity. On the other hand, in mesh networks, individual channels can be directed in multiple directions and deviations from a target map can increase as channels can go through paths dominated by positive or negative dispersion deviations. A monitoring of the maximum deviations over all possible paths may need to be done at the design stage of mesh networks to prevent large dispersion deviations.

Even though a reduced granularity is generally desirable to better achieve the dispersion target values, a larger set of DCFs modules become required, which potentially increases system cost. This cost increase may offset the advantages that accurate dispersion mapping brings to system design. Therefore, the best choice of DCF granularity depends on the system design and on the distance of interest.

Dispersion Fluctuations

Temperature fluctuations of optical fibers can lead to changes in dispersion [113–117], which may occur on at least two time scales: a few *hours*, typically showing diurnal periodicity, or a few *months*, showing seasonal periodicity [117,118].

The dependence of dispersion variation on temperature has been measured extensively and is on the order of $\pm 2 \times 10^{-3}$ ps/nm/km/°C for most fiber types [116]. For large diurnal variations in temperature on the order of 25°C, aerial fibers of most fiber types will experience dispersion variations of many tens of ps/nm after several hundreds of kilometers, exceeding the 40-Gb/s dispersion tolerance (see Table 3 and Fig. 16). Since the dispersion tolerance of any modulation format can shrink considerably (up to a factor of $\sim$10 times) after nonlinear transmission (see for instance Figs. 18 and 17 for 10 Gb/s), the impact of temperature-dependent dispersion fluctuations is more severe for systems operating in the nonlinear transmission regime. Such dispersion variations with temperature, along with the dispersion uncertainty of transmission fiber and the granularity of DCFs may result in significant BER degradations [117].

Channelized and Tunable Dispersion

To address dispersion variations with temperature and uncertainties in dispersion from various sources, *tunability* in dispersion compensation is desirable. Such tunability

can be provided by different technologies (see Sec. 4 for a review). Most of these technologies operate over a limited bandwidth around a single channel central frequency or over a comb of channels if the device has a periodic frequency response. In both cases, discontinuities in dispersion occur between the channel frequencies. Dispersion compensation exhibiting such discontinuities in frequency is referred to as *channelized dispersion compensation*. Channelized dispersion compensators with non-periodic frequency response, such as fiber Bragg gratings (FBGs) [119], can offer independent dispersion tunability on a per-channel basis, a feature that may become desirable in networks incorporating multiple OADMs, where channels with different propagation histories share common physical paths and may be dropped at the same OADM site. On the other hand, for WDM systems having a large number of channels, many FBGs become necessary with a potential increase in system cost. This can be partially circumvented using broadband tunable dispersion compensation based on devices having periodic responses, where the dispersion of all WDM channels can be simultaneously tuned. For such tunable dispersion compensators, a single device can in principle be used for all channels, potentially reducing cost in high-capacity WDM systems. It is worth mentioning that, for all devices exhibiting channelized dispersion compensation, fixed or tunable, cascadability may become an important issue, especially in systems operating at very high spectral efficiency (> 0.4 bit/s/Hz). This aspect will be discussed further in Sec. 4.

Fiber Nonlinearity

Along with noise generation, fiber nonlinearity is one of the two main effects limiting transmission in optical fibers. The impact of DCF on nonlinear transmission is twofold. First, a DCF impacts nonlinear transmission through control of the dispersion map (see Sec. 2.3). For this purpose, the accuracy of the dispersion compensation parameters is critical to achieve the desired dispersion map. Second, for sufficiently high launch power into the DCF, the presence of a DCF increases the total fiber nonlinearity present in the transmission line by adding its own nonlinear contribution.

Dispersion Mapping

As described in Sec. 2.3, dispersion mapping is a key technique to reduce signal distortions from fiber nonlinearity. Figure 24 shows the result of a proper numerical exploration of SPDMs in a form of a matrix of plots, each one similar to the plot shown in Fig. 18b. From the upper to the lower row, the RDPS is increasing from zero to 100 ps/nm by steps of 25 ps/nm. Each column represents a transmission distance (measured by the length of the transmission fiber) from 400 to 1600 km by steps of 400 km. Note that in the calculations of Fig. 24, the nonlinearity in the DCF has been neglected (see Fig. 26 for the effect of nonlinearity in the DCF). The system parameters are the same as Fig. 18: 10-Gb/s NRZ signals on a 50-GHz grid at a launch power per channel P_{in} of 3.67 mW. At lower powers, the areas of each plot enlarge to eventually become like Fig. 18a at sufficiently low power ("linear regime"). At higher powers, the areas shrink to eventually disappear when the required OSNR exceeds 14 dB. Arrays of plots similar to Fig. 24 need to be recalculated for different systems types to determine their optimum dispersion maps. It is generally required to recalculate the 'good performance' regions of the array of plots at higher and lower powers to

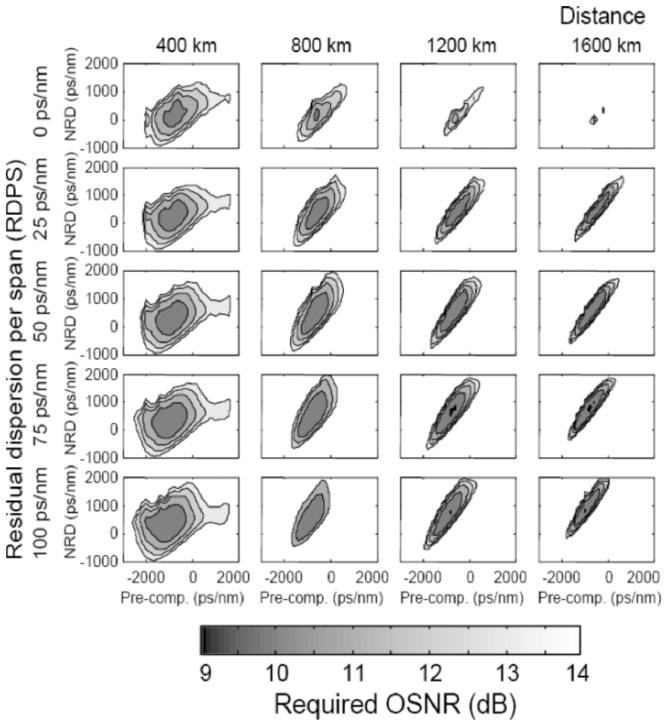

Fig. 24. Dispersion mapping for various RDPS and transmission distances for SPDMs (see Fig. 17). As seen in the figure, the required OSNR depends critically on the dispersion map parameters. The system parameters are identical to those of Fig. 18 except that the RDPS and the transmission distance are varied here.

establish the maximum power for the optimum dispersion map and the performance for the low power channels, respectively.

From Fig. 24, one can clearly see the variations in system performance occurring by changes in RDPS, and how these variations depend on the transmission distance. Even though a SPDM with full dispersion compensation per span may appear attractive due to its simplicity, Fig. 24 shows dramatic signal degradations from nonlinear transmission at distances beyond a few hundred kilometers. Such degradations originate from XPM between 10-Gb/s channels in WDM system [120]. The best ULH nonlinear transmission for the parameters of Fig. 24 occurs for an RDPS above 25 ps/nm. One should note, however, that signal degradations from XPM at zero RDPS can be mitigated by periodically introducing additional time delays between the WDM channels by using, for instance, a channelized dispersion compensator [121–124]. Such an approach has the advantage of providing a simple rule of full dispersion compensation per span but has the drawback of limited cascadability at high spectral efficiency (0.4 bit/s/Hz and above) for the channelized elements generally required to generate such relative time delays.

Transmission systems operating a 40 Gb/s also benefit greatly from dispersion mapping. An important difference to 10-Gb/s systems is that most 40-Gb/s systems operate in the pseudo-linear regime of transmission [102] where the dominant nonlinearities are single-channel nonlinear effects: IXPM and IFWM. For such high-speed systems, dispersion mapping on a single channel is generally sufficient to establish the optimum dispersion map that provides optimum transmission even for a WDM configuration.

Nonlinear Phase

The second impact of DCF on nonlinear transmission is an increase in the total nonlinearity of the transmission line due to the presence of the DCF. In the localized dispersion compensation scheme (Fig. 2a) the signal power at the input of the DCF can be controlled in a dual-stage amplifier configuration (Fig. 1a). Reducing the input signal power to the DCF, $\mathrm{P_{DCF}}$, reduces the impact of fiber nonlinearity in the DCF, but at the expense of an OSNR degradation, as described in Sec. 3.1. If one approximates the effect of fiber nonlinearity by the integrated nonlinear phase ϕ (see Sec. 2.3), the ratio of nonlinearity in the DCF to the nonlinearity in the transmission fiber is given by

$$\mathrm{R_{DCF}} \equiv \frac{\phi_{\mathrm{DCF}}}{\phi_{\mathrm{F}}} = \frac{\int_0^{\mathrm{L_{DCF}}} \mathrm{P_{DCF}}(z)\,\gamma_{\mathrm{DCF}}(z)\,dz}{\int_0^{\mathrm{L_F}} \mathrm{P_F}(z)\,\gamma_{\mathrm{F}}(z)\,dz}, \tag{55}$$

where $\gamma(z)$ is the nonlinear coefficient defined in Eq. (44) of Sec. 2.3.

For systems using localized dispersion compensation and passive fibers (Fig. 2a), the ratio $\mathrm{R_{DCF}}$ can be written as

$$\mathrm{R_{DCF}} = \frac{\gamma_{\mathrm{DCF}}}{\gamma_{\mathrm{F}}}\,\frac{\alpha_{\mathrm{F}}}{\alpha_{\mathrm{DCF}}}\,\frac{[1-\exp(-\alpha_{\mathrm{DCF}}\,\mathrm{L_{DCF}})]}{[1-\exp(-\alpha_{\mathrm{F}}\,\mathrm{L_F})]}, \tag{56}$$

where we assumed that γ and α are independent of distance. For fibers that are Raman pumped, $\mathrm{R_{DCF}}$ can be evaluated by integrating explicitly Eq. (55) or in some cases using approximate solutions [110].

Figure 25 shows the integrated nonlinear phase for a SSMF transmission fiber and a DCF for an identical input power of 0 dBm (fiber parameters in Table 5). As seen on the figure, even without Raman pumping, the nonlinear phase in the DCF can exceed the nonlinear phase in the transmission fiber at identical signal launch powers. However, because the insertion loss of DCFs is generally much smaller than the loss of fiber spans, the launch power into the DCF, $\mathrm{P_{DCF}}$, can be set below the input power to the fiber span, $\mathrm{P_{in}}$, which minimizes the degradation of the delivered OSNR (see Sec. 3.1). The nonlinear phase in the DCF decreasing linearly with the launch power, a reduction of the launch power to the DCF by a few dBs generally lowers the nonlinear phase in the DCF below the nonlinear phase of the transmission span.

To illustrate the impact of nonlinearity in the DCF, Fig. 26 shows required OSNR contour plots for different signal powers launch into the DCF. The parameters are the same as in Fig. 24, with RDPS = 100 ps/nm and at 1200 km [12]. The number in the lower corner of each contour plot is $10\log(\mathrm{P_{DCF}}/\mathrm{P_{in}})$, the power in the DCF relative to the input power to the span, expressed in dB. Nonlinearity in the DCF starts to

[12] The slight difference between the low-power plots of Fig. 26 and the corresponding plot of Fig. 24 comes from small differences in dispersion slopes of the DCF used for both figures.

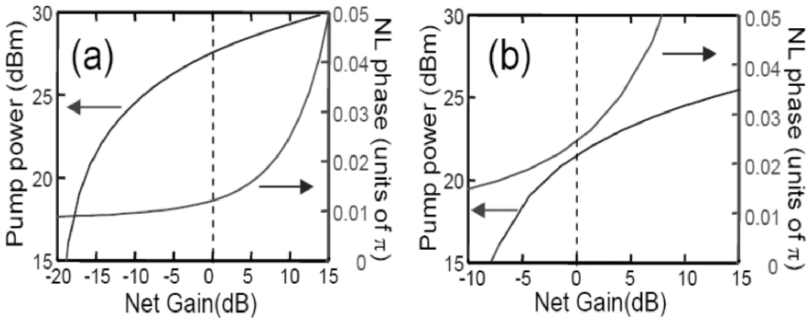

Fig. 25. Integrated nonlinear phase for a) a transmission fiber, SSMF and b) a DCF for identical input signal powers of 0 dBm. As seen in the figure, the nonlinear phase in the DCF can exceed the nonlinear phase in the transmission fiber if input power levels are comparable. The vertical dash line indicates when the amplifier is transparent.

significantly impact nonlinear transmission in the system at around -4 dB of relative power or $\mathrm{P_{DCF}} = 1.46$ mW. This corresponds to a nonlinear phase in the DCF, ϕ_{DCF}, of 67.2% of the nonlinear phase in the transmission fiber, ϕ_{F}.

For systems using *diffused dispersion compensation* and Raman amplification, the increase in nonlinear phase in the DCF generally depends on the location of the DCF in the DMF as well as the Raman pumping scheme. One should note however, that, even though DCFs can be located far from the fiber span input and output ends where Raman pumps are located, the small effective areas of DCFs make them simultaneously more efficient to produce Raman gain with low pump powers [18] and to generate more nonlinear phase [see Eqs. (43) and (44)] at identical signal powers. As a result, detailed analyses need to be performed for each fiber design to determine the importance of the nonlinearity in the DCF present in a DMF [31].

Polarization Mode Dispersion

Polarization-mode dispersion of fibers can cause significant impairments in transmission, especially at 40 Gb/s and above [107]. This section describes how inserting DCF in a line affects its PMD value.

If a system is comprised of N sections of fiber (transmission fiber and DCF), each section with PMD coefficient x_i and length l_i, the total PMD coefficient (in ps/$\sqrt{\mathrm{km}}$) of the line is given by

$$x_{\mathrm{line}} = \sqrt{\frac{\sum_{i=1}^{N} x_i^2 l_i}{\sum_{i=1}^{N} l_i}} \,. \tag{57}$$

Assuming a system composed of N_{span} spans of transmission fiber of length L and N_{DCF} DCFs of length L_{DCF}, we find for the system's PMD coefficient

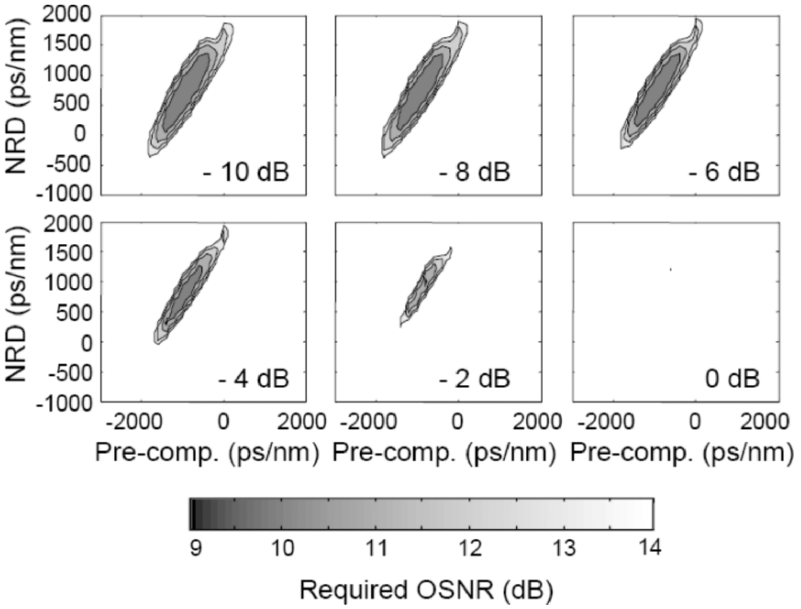

Fig. 26. Effect of the nonlinearity in DCF on transmission. The system parameters are the same as in Fig. 24 with RDPS = 100 ps/nm and a distance of 1200 km. The numbers in the lower corners indicate the power in the DCF relative to the fiber span (see main text). As the power in the DCF increases, nonlinear distortions from the DCF reduces the area of low required OSNR.

$$x_{\text{line}} = \sqrt{\frac{N_{\text{span}}\, x_{\text{span}}^2\, L_{\text{span}} + N_{\text{DCF}}\, x_{\text{DCF}}^2\, L_{\text{DCF}}}{L_{\text{line}}}}\ , \tag{58}$$

where $L_{\text{line}} = N_{\text{span}} L_{\text{span}} + N_{\text{DCF}} L_{\text{DCF}}$ is the total fiber length in the system.

Equations (57) and (57) for calculating the PMD coefficient of a transmission line assumes that the PMD coefficients of the individual fiber spans are known precisely. However, PMD coefficients of commercial fiber depend randomly on stress imposed on the fiber during manufacturing and cabling, which lets nominally identical fiber cables have statistically different PMD coefficients. In an actual transmission line, many fiber cables are concatenated, and the probability that *all* cable sections simultaneously exhibit high PMD coefficients is low. Therefore, it is convenient to specify the PMD of fiber cables using the *probability* $P_Q(M)$ that the PMD coefficient of a transmission line ('*link*') composed of M cable sections exceeds a certain value. This value is called the *link design value* PMD_Q, and is given in conjunction with the number of cable section M and the probability $P_Q(M)$ according to [125],

$$P[x_{\text{line}} > \text{PMD}_Q] = P_Q(M)\ . \tag{59}$$

Therefore, the PMD coefficient of an individually purchased fiber cable may well exceed PMD_Q, but the concatenation of at least M such cables in a transmission line will not, at least not with appreciable probability. Typically, fiber manufacturers specify $M = 20$ and $P_Q(20) = 10^{-4}$.

3.3. DCF Design Issues: The Figure of Merit (FOM)

As we have seen, the insertion of a DCF in a transmission line has an impact on both the delivered OSNR (Sec. 3.1) and on fiber nonlinearity (Sec. 3.2). The design of a DCF should take into account both phenomena to minimize the impact on system performance.

The figure of merit (FOM) [45,46] defined in Eq. (1) is often used to compare different DCF designs [126] for localized dispersion compensation. A high value of FOM indicates that a DCF can offer a large value of dispersion compensation with relatively low insertion loss. However, since Eq. (1) only takes into account OSNR aspects, it often happens that DCFs with identical FOM but different fiber designs have a different system impact, depending on how much additional degradation from *fiber nonlinearity* they impose on transmission (see Fig. 26). For this reason a FOM parameter that includes the effect of fiber nonlinearity has been introduced [45,46]. Assuming passive fibers, the 'nonlinear' FOM is given by

$$\mathrm{FOM_{NL}} = \frac{A_{\mathrm{eff}}^{\mathrm{DCF}}}{A_{\mathrm{eff}}^{\mathrm{F}}} \frac{\alpha_{\mathrm{DCF}}}{\alpha_{\mathrm{F}}} \frac{(T_{\mathrm{F}}-1)^2}{T_{\mathrm{F}}} \frac{T_{\mathrm{DCF}}}{(T_{\mathrm{DCF}}-1)^2}. \tag{60}$$

Neglecting shot noise, one can show that Eq. (51) on the OSNR degradation for localized dispersion, $\mathrm{OSNR}_{\mathrm{deg}}^{\mathrm{loc}}$, can be put in the form,

$$\mathrm{OSNR}_{\mathrm{deg}}^{\mathrm{loc}} = T_{\mathrm{F}} \frac{(G_1-1)G_2 T_{\mathrm{DCF}} + (G_2-1)}{1-T_{\mathrm{F}}} \qquad [\text{ linear units }], \tag{61}$$

where G_1 and G_2 are the gains of the two stages of a dual-stage amplifier. By defining the ratio $\eta \equiv \phi_{\mathrm{NL}}^{\mathrm{DCF}}/\phi_{\mathrm{NL}}^{\mathrm{F}}$ [see Eq. (43) for the definition of nonlinear phase] and using Eq. (60) for a two-stage amplifier with identical spontaneous emission factors ($\mathrm{n_{sp}}$), one can show that [45,46],

$$\mathrm{OSNR}_{\mathrm{deg}}^{\mathrm{loc}} = 1 + \frac{1}{\eta \mathrm{FOM_{NL}}} \qquad [\text{ linear units }]. \tag{62}$$

At constant nonlinearity, the signal power in a system with DCF needs to be reduced by a factor $(1 + \eta)$ to insure constant nonlinear phase ϕ_{NL}. The ratio of OSNR without and with DCF *at constant nonlinearity* can be expressed as,

$$\mathrm{OSNR}_{\mathrm{deg}}^{\mathrm{loc}}(\eta) = (1+\eta)\left(1 + \frac{1}{\eta \mathrm{FOM_{NL}}}\right) \qquad [\text{ linear units }]. \tag{63}$$

Figure 27 shows the degradation of delivered OSNR for different values of gain G_1 of the first-stage of a dual-stage amplifier for different DCF loss coefficient values. There is an optimum gain G_1 that minimizes the impact of the DCF on delivered OSNR. At low values of G_1, the first stage provides insufficient gain so that the power at the output of the DCF is very low, creating OSNR degradation through amplification by the second stage. At high gain values, the additional nonlinearity generated in the DCF exceeds the benefits in delivered OSNR brought by a large value of G_1. Notice that higher DCF loss coefficients produce larger reduction in delivered OSNR and shift the optimum value of G_1 upwards. A similar approach to the one described in this section can be taken to study systems using Raman amplification and generating DRB.

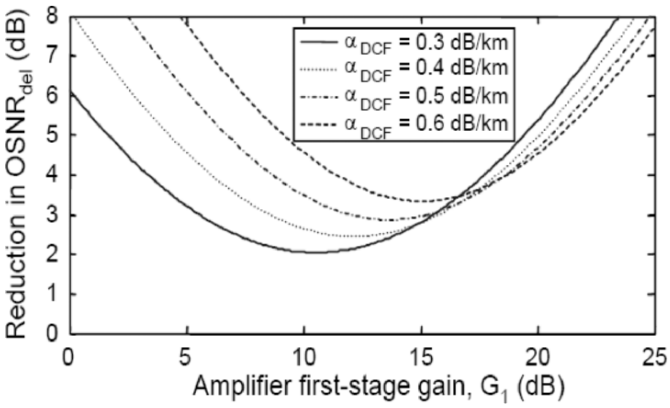

Fig. 27. Reduction in delivered OSNR due to the presence of DCF in a transmission line as a function of the first-stage gain G_1 of a dual-stage amplifier. Curves for different DCF loss coefficients α_{DCF} are shown. The total nonlinearity (transmission fiber plus DCF) is kept constant. A different optimal gain exists for each value of DCF loss.

4. Alternatives to DCF-Based Dispersion Compensation

As discussed in Sec. 1, the per-channel bit rate upgrade from 2.5 to 10 Gb/s in optical communication systems required the implementation of dispersion compensation in order to transmit information beyond a few tens to a few hundred kilometers. For virtually all such systems, dispersion compensation is provided by DCF-based DCMs. However, depending on the application, dispersion compensation can also be implemented by dispersion compensation technologies that are *not* based on DCF.

For systems operating at 10 Gb/s per channel, non-tunable (i.e., fixed) values of dispersion compensation are typically used, because, in 10-Gb/s systems, fixed dispersion compensation is generally sufficiently accurate to achieve the target NRD and near optimum system performance. For such systems, both fiber and non-fiber DCMs can be used for pre-, in-line, and post-compensation. At 40 Gb/s per channel , a given modulation format has a 16-fold reduction in dispersion tolerance relative to 10-Gb/s transmission. As mentioned in Sec. 3.2, 40-Gb/s systems impose stringent dispersion requirements that often necessitate TDC at the receiver to accommodate net residual dispersion variations, especially those produced by temperature fluctuations in optical fibers [113–117].

Systems needing TDC require some form of performance monitoring to provide feedback to adjust the degree of compensation. At the turn of the millennium, state-of-the-art optical transmission systems started to incorporate FEC which provides a convenient feedback on the BER that can be used to control parameters of the TDC. Demonstrations of TDC implementations include per-channel dispersion tuning using Fiber Bragg Gratings (FBGs) [127] in 40-Gb/s systems as well as fixed broadband or tunable broadband dispersion compensation based on Gires-Tournois Etalons (GTEs) [128]. At the time of writing, GTEs and broadband FBGs are commercially available for 2.5 and 10-Gb/s systems (both for fixed and tunable dispersion compensation

applications), whereas FBGs are available for tunable dispersion compensation on a per-channel basis or for a group-of-channels at 40 Gb/s [127].

Besides dispersion tunability, advantages of non-DCF devices over DCFs include total immunity to Kerr nonlinearities (see Sec. 2.3), a smaller form factor, cost, and the possibility of engineering arbitrary dispersion profiles. A high FOM and small form factor make non-DCF devices attractive candidates for use in dispersion compensation in OADMs.

In this section we will review the challenges and perspectives of various dispersion compensation technologies, and discuss the trade-offs in different contexts of metropolitan, LH and ULH transmission systems.

4.1. Challenges for Future DCF Designs

Current systems requiring dispersion compensation mostly use DCF. In systems employing either discrete EDFA (Fig. 1a) or hybrid amplification (EDFA and Raman amplification, see Fig. 1c), it is particularly important to achieve a high FOM (see Sec. 1.3). Using high-FOM DCMs is particularly efficient in reducing the degradation of the delivered OSNR from the presence of dispersion compensation in the line (see Sec. 3.1). For instance, in the case where the DCF is inserted within a dual-stage EDFA, the lower DCF loss (or larger transmittivity $\mathrm{T_{DCF}}$) of a high-FOM DCF (i.e., larger $\mathrm{T_{DCF}}$) leads to less degradation in delivered OSNR [see Eq. (51)].

For systems using discrete Raman (Fig. 1b) or all-Raman (Fig. 1d), additional challenges in DCF design arise. These stem from the need for DCMs to simultaneously provide Raman gain and broadband dispersion compensation [129] with low generation of DRB. In particular, ULH systems require precise control of the RDPS in order to mitigate fiber nonlinearity (see Fig. 24). The DCF design challenge in this case is to achieve an adequate level of Raman gain from the DCM, with low DRB and low PMD while simultaneously providing broadband dispersion compensation across the entire WDM band.

The introduction of 40-Gb/s-based transmission into optical networks will most likely bring scenarios of mixed data rates (10 Gb/s and 40 Gb/s) with different modulation formats present on the same transmission line [130]. Furthermore, state-of-the-art ULH terrestrial systems will incorporate OADMs to optically route transmitted signals [131,132]. These OADMs should be able to handle mixed data rate traffic with different dispersion compensation requirements. Such mixed data rate applications may require large TDC dynamic ranges at OADM sites, especially when the system dispersion compensation is provided by a SPDM which lets dispersion continuously accumulate along the line. One way to alleviate the required TDC dynamic range is to use a DPDM (see Sec. 1.2) [42–44]. In DPDM, the dispersion accumulation is 'reset' periodically to a low value, thereby reducing the excursion of dispersion seen at the OADM sites.

4.2. Non DCF-Based Dispersion Compensation

In recent years, alternatives to DCF-based dispersion compensation have emerged, and some technologies matured sufficiently to become commercially available. Among the most important technologies are devices based on FBGs [127,128,133] and on GTEs [134–136].

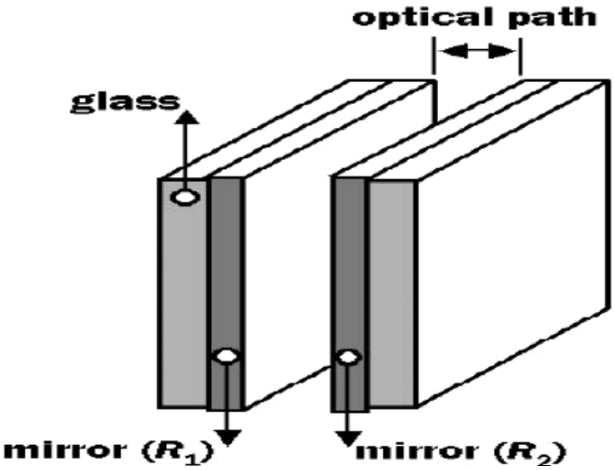

Fig. 28. Fabry-Perot (R_1 and $\mathrm{R}_2 < 1$) and Gires-Tournois etalons ($\mathrm{R}_1 < 1$, $\mathrm{R}_2 = 1$).

Technologies employed for 40-Gb/s TDC (and higher bit rates) are typically based on FBG. FBGs, being fiber-based devices, are fully compatible with optical fibers in the sense that they do not incur any extra fiber-to-device-to-fiber insertion losses, have low PMD, and are generally low cost. Drawbacks of FBGs include a Group Delay Ripple (GDR) of, typically, $\pm$10-20 ps peak-to-peak, and a limited dispersion tuning range of approximately 400 ps/nm. With the advent of ULH systems, this limited tuning range can become an important factor limiting the reach of 40-Gb/s systems.

In 10-Gb/s applications, in addition to FBG-based TDCs, there are also devices based on GTEs. GTE-based technologies have recently started to make way into 10-Gb/s applications as an alternative to DCF-based DCMs due to their large tuning range, small form factor, low cost, and, in some cases, better FOM; in particular, at the time of writing, DCMs based on GTEs are commercially available for high-capacity 10-Gb/s WDM dispersion-compensation applications. Interestingly, in addition to dispersion compensation, GTEs can also be used to build interleavers when placed within the arms of a Michelson Interferometers [137].

A GTE is represented schematically in Fig. 28. Etalons are cavities formed by two reflecting interfaces, with reflectivity coefficients R_1 and R_2 respectively, separated by a fixed gap that provides an optical path difference. If both interfaces are imperfect reflectors (i.e. R_1 and $\mathrm{R}_2 < 1$) the device is called a Fabry-Perot Etalon (FPE), first introduced in 1899. If one of the surfaces is a perfect reflector the device is called a Gires-Tournois Etalon, first introduced in the mid 1960s.

The optical path length can be adjusted to produce reflection resonances coincident with the ITU grid by setting the channel spacing $\delta\nu$ according to

$$\delta\nu = \frac{c}{2\,n\,\mathrm{d}}, \tag{64}$$

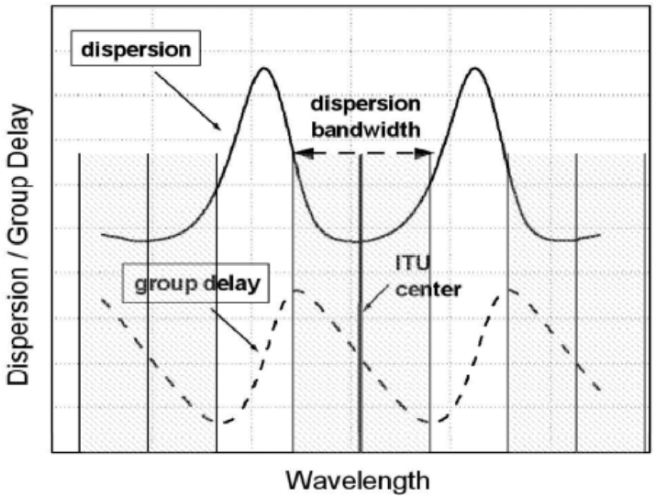

Fig. 29. Dispersion and group delay characteristics of a GTE dispersion compensator.

where c is the speed of light in vacuum, n is the refractive index of the etalon medium, and d is the distance between reflecting surfaces. $\delta\nu$ is called the Free Spectral Range (FSR) of the etalon and can be set to 100 or 50 GHz, for instance. In connection with the reflection resonances, there is a periodic optical delay response that can be used to compensate the dispersion of the transmission fiber simultaneously for all transmitted WDM channels. Typical optical delay and dispersion characteristics of a GTE device are shown in Fig. 29.

GTEs belong to a broad category of filters called *all-pass filters* (APFs); these filters are characterized by a constant amplitude response and a frequency-dependent phase response. For a cascade of N GTEs there is a relation between the dispersion, D, and the half-width dispersion bandwidth Δ, given by [138]

$$D \cong \frac{N}{\mathrm{FSR}^2\,\Delta^2}. \tag{65}$$

Current GTE-based DCMs for 10-Gb/s applications typically have a dispersion bandwidth of 25 GHz centered around an ITU frequency. As seen in Fig. 29, GTEs are providing channelized dispersion compensation that can pose cascadability issues at high spectral efficiency (see end of Sec. 3.2). Note that since the number of GTEs scales linearly with *D*, compensating the dispersion of SSMFs requires, typically, four times more GTEs than to compensate the dispersion of NZDF, thus having higher insertion loss of the device for SSMF than for NZDF. We can also estimate the number of GTEs needed to achieve a desired level of dispersion compensation for 40-Gb/s applications. At such bit rate, GTE-based DCMs will require a dispersion bandwidth of, typically, 80 GHz with an FSR = 100 GHz. According to Eq. (65), the number of GTEs needed to compensate the dispersion of a given fiber type is approximately 40 times larger than that for 10-Gb/s applications. This will seriously impact both the

insertion loss and the form factor of a potential GTE-based DCM for use in 40-Gb/s transmission.

There are a number of non-DCF-based dispersion devices, other than FBGs and GTEs, that at the time of writing are not yet commercially available but represent promising technologies. These include devices based on Ring Resonators (RR) [139,140], cascaded Mach-Zehnder Interferometers (MZI) [88], Waveguide-Grating Routers (WGR) [87], all of which can be built on planar waveguides, High-Order Mode (HOM) fibers [141], and Virtually-Imaged Phased Arrays (VIPA) [142]. Schematics of some of these devices are shown in Fig. 30. RRs, MZIs, WGRs, and VIPAs offer channelized and tunable dispersion compensation for 10 and 40-Gb/s applications; HOM-based DCMs offer broadband non-channelized tunable dispersion compensation when combined with 2×2 mode-converting switches (see Fig. 30). Finally, Photonic Crystal Fibers (PCFs) made from a single material and with a regular array of empty holes running along the length of the cladding may provide very large negative dispersion values in excess -2000 ps/nm km [143,144].

4.3. System Applications and Impact on Non-DCF Dispersion Compensation

Table 6 summarizes current applications and some relevant characteristics of various dispersion compensation technologies currently available to the system designer.

Tunable dispersion compensation is generally used as post-compensation before a receiver to compensate for dispersion fluctuations and uncertainties, especially in 40-Gb/s systems [145] where the tolerable residual dispersion is only on the order of a few tens of ps/nm (see Sec. 2.3). One should point out that in some 10-Gb/s systems, designed such that different dispersion compensation values are required for different network configurations, tunable dispersion compensation can find applications. In such systems, tunability in DCMs can be used to generate arbitrary values of pre-, in-line, and post- dispersion compensation, resulting in a reduction in the DCM inventory.

FBG-based devices have the highest FOM due to an insertion loss that does not depend on the amount of dispersion, unlike GTE-based devices where higher dispersion values are obtained by concatenating more GTEs, thus increasing the device loss. Both FBG and GTE-based devices exhibit channelized dispersion compensation. FBG-based dispersion compensation devices are currently available for single-channel and broadband 10-Gb/s applications [133], and for single-channel and group-of-channels 40-Gb/s applications. Devices for 40-Gb/s transmission typically exhibit an 80-GHz dispersion bandwidth and a channel spacing of 200 GHz. For tunable devices, the dynamic tuning range is currently 400 ps/nm and, in order to compensate for both signs of residual dispersion, higher insertion-loss setups including a circulator and two FBGs are required [127].

DCMs based on GTEs are currently available for 10-Gb/s WDM applications with dispersion passbands of typically 25 GHz and a channel spacing of 50 GHz (parameters also found in their FBG counterparts).

The main disadvantages of FBG and GTE DCMs originate from their channelized dispersion compensation. The existence of dispersion passbands may lead to limitations in spectral efficiency (due to dispersion discontinuities between channels). For this reason channelized dispersion compensators are generally limited to systems with spectral efficiencies up to 0.2 bit/s/Hz. A potential disadvantage of non-DCF based

Table 6. Typical properties and system applications of several commercial dispersion compensation technologies. DC: Dispersion compensation.

DC technology	Current application	Systems types	Tunable range	Channelized	Broadband	FOM
Units			ps/nm			ps/(nm dB)
DCF	Pre-comp., in-line comp., post-comp.	Metro, Regional, LH and ULH	Not tunable	No	Yes	160-420
FBG	post-comp.	40 Gb/s: Regional, LH and ULH	400	Yes	No	< 500
GTE	Pre-comp., in-line comp., post-comp.	2.5 and 10 Gb/s: Metro ?, Regional ? and LH ?	2800	Yes	Yes	80-200

dispersion compensation is its inability to provide Raman gain, a desirable feature especially in ULH all-Raman systems [146].

Long fiber links require DCMs for pre-, in-line, and post-compensation to mitigate nonlinear effects (Sec. 3.2). In this context, the question of whether there will be deleterious effects due to cascading effects in long haul applications arises. Two experiments have been recently reported addressing this problem. In one experiment [136] at 0.2 bit/s/Hz, 40×10 Gb/s NRZ C-Band channels were transmitted over 3200 km of SSMF in a loop configuration. GTEs provided in-line dispersion compensation every 80 km, inserted between the stages of a dual-stage EDFA [136]. In this experiment, GTEs were shown to perform as well as their fiber-based counterparts and no additional penalty was observed due to group-delay and/or insertion loss ripple. In another experiment [147] also at 0.2 bit/s/Hz, 80×10 Gb/s 50% RZ L-band channels were transmitted over 1200 km of NZDF (12×100 km in a loop configuration). An average system margin and a transmission penalty of 4.5 dB and less than 2 dB, respectively, were measured. In this experiment, the additional penalty due to the wavelength drift of the transmitters was also measured. It was found that a drift of ± 2.5 GHz (consistent with commonly found system specifications) led to less than 0.5 dB additional penalty. Note that when evaluating penalties due to the wavelength drift at the transmitter, all filters are misaligned relative to the laser which represents a stringent test. In straight-line systems each filter will have slightly different center frequencies relative to the ITU grid providing some degree of averaging of the concatenated filtering effect.

Both experiments point to the feasibility of employing GTE-based devices, not only for pre- and post-dispersion compensation, but also for in-line dispersion compensation, for LH and ULH high-capacity optical communication systems at moderate to low spectral efficiency (0.2 bit/s/Hz and below).

4.4. Perspective of Non-DCF Compensators

The advent of 40-Gb/s transmission has ushered in the use of tunable dispersion compensation, mostly provided by FBG-based devices. Technologies based on FBGs and

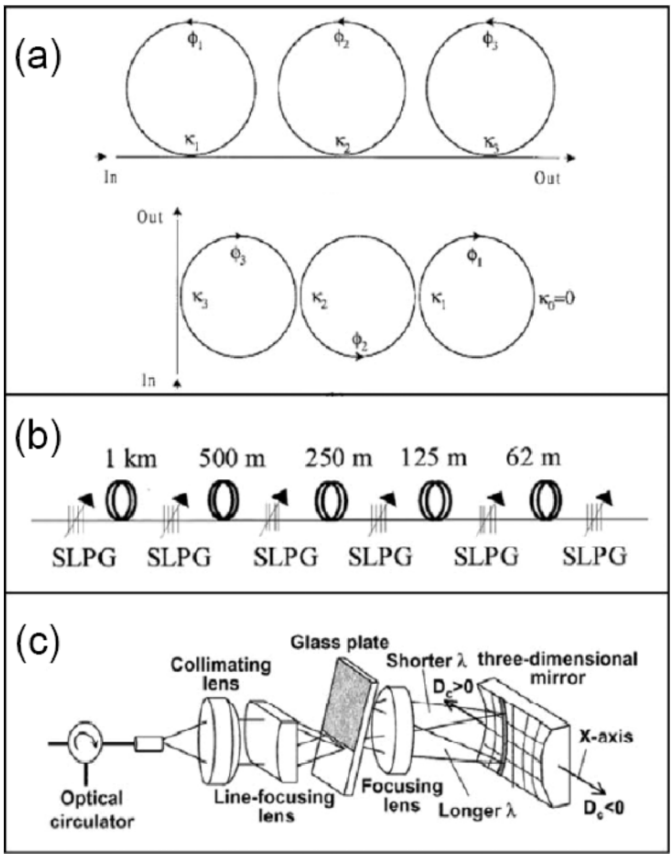

Fig. 30. Non-fiber dispersion compensation technologies: a) ring resonators (RR), b) higher-order mode (HOM) fiber, and c) virtually imaged phased arrays (VIPA). The upper graph in a) is a ring cascade while the lower graph is a ring lattice. κ and ϕ are the power coupling ratio and relative phase delay, respectively. SLFG: Switchable Long-period Fiber Gratings. D_c is the dispersion parameter value. Graphs (a) to (c) are from [140–142], respectively.

GTEs are currently available for tunable as well as fixed dispersion compensation applications. Low loss FBG-based DCMs find applications in both 10-Gb/s and 40-Gb/s single- and multi-channel dispersion compensation, whereas GTE-based devices are becoming attractive candidates for multi-channel pre-, in-line, and post-dispersion compensation in LH 10-Gb/s systems at moderate or low spectral efficiencies (i.e., 0.2 bit/s/Hz or lower).

Non-DCF dispersion compensation devices have generally the advantage of a small footprint, immunity to Kerr nonlinearities, the ability of engineering arbitrary dispersion profiles, and low cost. A small footprint and a high FOM make non-DCF DCMs especially attractive for use in dispersion compensation at OADM sites. Disadvantages of non-DCF DCMs are their channelized nature and, potentially, group-

delay and insertion-loss ripple. Recent high-capacity WDM experiments have been performed to evaluate transmission impairments due to GTE-based DCMs for long-haul and ultra-long-haul 10-Gb/s systems. These experiments showed no degradation attributable to group-delay and/or insertion-loss ripple, cascading effects of dispersion bandwidths, and wavelength drift of transmitters, thus pointing at the feasibility of employing such devices to provide dispersion compensation at 10 Gb/s as required along the signal path.

At the time of writing, there is a number of not yet commercially-available but very promising dispersion-compensation technologies such as Ring Resonators, cascaded Mach-Zehnder Interferometers, Waveguide-Grating Routers , High-Order Mode Fibers, Virtually Imaged Phased Arrays, and Photonic Crystal Fibers, all of which will add to the tools system designers have at their disposal to address the various dispersion-compensation needs arising in next-generation high-speed optical communication systems.

5. Summary

The insertion of dispersion compensation in fiber-optic communication systems has allowed high-speed optical signals, at 10 Gb/s per channel and above, to be transmitted over hundreds and thousands of kilometers without electrical regeneration. Signal propagation over such large distances becomes challenging as many physical phenomena enter into play.

In the first part of this paper, we introduced the tools and models required to assess the performance of an optical transmission system. This included the modeling and performance assessment of optical receivers, the calculations of the accumulation of amplified spontaneous emission generated by EDFA and Raman amplifiers, and the evaluation of double Rayleigh backscatter in Raman amplifiers. It also included phenomena that generally lead to signal distortions such as the accumulation of dispersion, fiber Kerr nonlinearity and polarization-mode dispersion. We also described how the judicious placement of dispersion compensation in a transmission line (i.e., dispersion mapping), can significantly reduce the effects of fiber nonlinearity. A brief description of technologies that can be used to mitigate various impairments has also been presented. Such technologies include forward error correction, advanced modulation formats and optical and electrical equalizations.

The second part of this paper has been devoted to describe the tools necessary to assess the impact of the presence of dispersion-compensating fiber in transmission lines that include erbium-doped amplifiers and Raman amplification. It was shown, for instance, that the impact of dispersion-compensating fiber on the delivered optical signal-to-noise ratio greatly depends on the fiber type of the transmission fiber and whether or not Raman amplification is used in the transmission line. The system impact of Raman pumping dispersion-compensating fibers to compensate their intrinsic loss and to provide some net gain has also been presented. It was shown that the positive net gain of Raman-pumped dispersion-compensating fiber is limited by the generation of double Rayleigh backscatter that becomes excessive at large values of positive gain. The impact of dispersion compensating fiber on signal distortions has also been evaluated. It was shown that one should carefully choose the signal power launched into the dispersion-compensating fiber to prevent fiber nonlinearity in that fiber to become

comparable to the nonlinearity in the transmission fiber. It was also shown, by way of example, what dispersion map parameters are optimum for a wavelength-division multiplexed system operating at 10 Gb/s per channel. The effect of polarization-mode dispersion within the dispersion-compensating fiber has also been described.

Finally, a review of alternative technologies to dispersion-compensating fibers was presented in the last section of this chapter. A description of the trade-offs between various commercial technologies as well as a discussion of novel dispersion-compensation technologies was given at various stages.

Acknowledgments

We would like to thank Andy Chraplyvy, Jake Bromage, Greg Raybon, Sethumadhavan Chandrasekhar, Aref Chowdhury, Dan Fishman, Paul Claisse, Bob Jopson, Lars Grüner-Nielsen, Lynn Nelson, Anjali Agarwal, Christopher Doerr, Dan Marom and Christi Madsen for contributing to this chapter through numerous discussions, advice and reading of the manuscript.

Acronyms

Acronym	Signification
APF	All-pass filter
ASE	Amplified spontaneous emission
BER	Bit-error rate
BW	Backward
CDR	Clock and data recovery
CSRZ	Carrier-suppressed return-to-zero
CW	Continuous wave
CWDM	Coarse wavelength-division multiplexing
DC	Dispersion compensation
DCF	Dispersion-compensating fiber
DCM	Dispersion-compensating module
DFE	Distributed feedback equalizer
DGD	Differential group delay
DMC	Dispersion-managed cable
DMF	Dispersion-managed fiber
DRA	Distributed Raman amplifier
DRB	Distributed Rayleigh scattering
DSF	Dispersion-shifted fiber
DUT	Device under test
DPDM	Doubly periodic dispersion map
DPSK	Differential phase-shift keying
DQPSK	Differential quaternary phase-shift keying

Acronym	Signification
EDFA	Erbium-doped fiber amplifier
EF	Electrical filter
EFEC	Enhanced forward error correction
FBG	Fiber Bragg grating
FEC	Forward error correction
FFE	Feed-forward equalizer
FOM	Figure of merit
FPE	Fabry-Perot Etalon
FSR	Free spectral range
FW	Forward
FWHM	Full width at half maximum
FWM	Four-wave mixing
GDR	Group delay ripple
GFEC	Generic forward error correction
GTE	Gires-Tournois Etalon
GNSE	Generalized nonlinear Schrödinger equation
HOM	Higher-order mode
IFWM	Intra-channel four-wave mixing
ISI	Inter-symbol interference
ITU	International telecommunication union
IXPM	Intra-channel cross-phase modulation
LH	Long-haul
MLSE	Maximum-likelihood sequence estimator
MPI	Multiple-path interference
MZI	Mach-Zehnder interferometer
MZM	Mach-Zehnder modulator
NL	Nonlinear or nonlinearity
NRD	Net residual dispersion
NRZ	Non-return to zero
NZDF	Non-zero dispersion-shifted fiber
OADM	Optical add-drop multiplexer
OEQ	Optical equalization
OF	Optical filter
OFE	Optical front-end
OOK	On-off keying
OSNR	Optical signal-to-noise ratio
OXC	Optical cross connect
PCF	Photonic crystal fiber
PD	Photodiode
PDL	Polarization-dependent loss
PMD	Polarization-mode dispersion
PMDC	Polarization-mode dispersion compensation
PSP	Principal states of polarization

Acronym	Signification
RB	Rayleigh backscatter
RR	Ring resonator
RDPS	Residual dispersion per span
RZ	Return-to-zero
RDS	Relative dispersion slope
SLFG	Switchable long-period fiber gratings
SNR	Signal-to-noise ratio
SONET	Synchronous Optical NETwork
SPDM	Singly-periodic dispersion map
SPM	Self-phase modulation
SSMF	Standard single-mode fiber
TDC	Tunable Dispersion Compensators
TF	Transmission fiber
TWRS	Truewave® reduced slope
ULH	Ultra-long haul
VIPA	Virtually-imaged phase array
WDM	Wavelength-division multiplexing
WGR	Waveguide-grating router
XPM	Cross-phase modulation

References

1. E. Desurvire, *Erbium-doped Fiber Amplifiers: Principles and Applications* (John Wiley & Sons, 1994).

2. P.S. Henry, R.A. Linke, and A.H. Gnauck, *Introduction to Lightwave Systems, in Optical Fiber Telecommunications II*, edited by Stewart E. Miller and I.P. Kaminov (Academic Press, 1988), Chapter 21, pp. 781–831.

3. F.P. Kapron, D.B. Keck and R.D. Maurer, "Radiation losses in glass optical waveguides," Appl. Phys. Lett. **17**, 423–425 (1970).

4. D. Marcuse, A.R. Chraplyvy, and R.W. Tkach, "Effect of fiber nonlinearity on longdistance transmission," J. Lightwave Technol. **9**, 121–128 (1991).

5. D. Marcuse, "Single-channel operation in very long nonlinear fibers with optical amplifiers at zero dispersion," J. Lightwave Technol. **9**, 356–361 (1991).

6. C. Lin, H. Kogelnik, and L.G. Cohen, "Optical-pulse equalization of low-dispersion transmission in single-mode fibers in the 1.3–1.7-μm spectral region," Opt. Lett. **5**, 476–478 (1980).

7. F. Ouellette, "Dispersion cancellation using linearly chirped Bragg grating filters in optical waveguides," Opt. Lett. **12**, 847–849 (1987).

8. L.J. Cimini, L.J. Greenstein, and A.A.M. Saleh, "Optical Equalization to Combat the Effects of Laser Chirp and Fiber Dispersion," J. Lightwave Technol. **8**, 649–659 (1990).

9. K. Iwashita and N. Takachio, "Chromatic dispersion compensation in coherent optical communications", J. Lightwave Technol. **8**, 367–375 (1990).

10. A.R. Chraplyvy, A.H. Gnauck, R.W. Tkach, and R.M. Derosier, "8 × 10 Gb/s transmission through 280-km of dispersion-managed fiber," IEEE Photon. Technol. Lett. **5**, 1233–1235 (1993).

11. C. Kurtzke, "Suppression of fiber nonlinearities by appropriate dispersion management," IEEE Photon. Technol. Lett. **5**, 1250–1253 (1993).

12. A.H. Gnauck, R.M. Jopson, P.P. Iannone, and R.M. Derosier, "Transmission of two wavelength-multiplexed 10 Gbit/s channels over 560 km of dispersive fibre," Electron. Lett. **30**, 727–728 (1994).

13. A. Naka, and S. Saito, "Transmission distance of in-line amplifier systems with groupvelocity- dispersion compensation," J. Lightwave Technol. **13**, 862–867 (1995).

14. M. Suzuki, I. Morita, N. Edagawa, S. Yamamoto, H. Taga, and S. Akiba, "Reduction of Gordon-Haus timing jitter by periodic dispersion compensation in soliton transmission," Electron. Lett. **31**, 2027–2029 (1995).

15. R.A. Jensen, R.E. Tench, D.G. Duff, C.R. Davidson, C.D. Chen, O. Mizuhara, T.V. Nguyen, L.D. Tzeng, and P.D. Yeates, "Field Measurements of 10 Gb/s Line Rate Transmission on the Columbus-2B Submarine Lightwave System," IEEE Photon. Technol. Lett. **7**, 1366–1368 (1995).

16. J.C. Feggeler, D.G. Duff, N.S. Bergano, C.C. Chen, Y.C. Chen, C.R. Davidson, D.G. Ehrenberg, S.J. Evangelides, G.A. Ferguson, F.L. Heismann, G.M. Homsey, H.D. Kidorf, T.M. Kissell, A.E. Meixner, R. Menges, J.L. Miller Jr., O. Mizuhara, T.V. Nguyen, B.M. Nyman, Y.K. Park, W.W. Patterson, and G.F. Valvo, "10 Gb/s WDM Transmission Measurements on an Installed Optical Amplifier Undersea Cable System," Electron. Lett. **31**, 1676–1678 (1995).

17. A.R. Chraplyvy and R.W. Tkach, "Terabit/Second Transmission Experiments," IEEE J. Quantum Electron. **34**, 2103–2108 (1998).

18. J. Bromage, P.J. Winzer, and R.-J. Essiambre, *Multiple-path interference and its impact on system design*, in Raman Amplifiers and Oscillators in Telecommunications, edited by M.N. Islam (Springer Verlag, 2003).

19. P.B. Hansen, G. Jacobovitz-Veselka, L. Grüner-Nielsen, and A.J. Stentz, "Raman amplification for loss compensation in dispersion compensating fibre modules," Electron. Lett. **34**, 1136–1137 (1998).

20. P.B. Hansen, L. Eskildsen, A.J. Stentz, T.A. Strasser, J. Judkins, J.J. DeMarco, R. Pedrazzani, and D.J. DiGiovanni, "Rayleigh Scattering Limitations in Distributed Raman Pre-Amplifiers," IEEE Photon. Technol. Lett. **10**, 159–161 (1998).

21. A. Altuncu, L. Noel, W.A. Pender, A.S. Siddiqui, T. Widdowson, A.D. Ellis, M.A. Newhouse, A.J. Antos, G. Kar, and P.W. Chu, "40 Gbit/s error free transmission over a 68-km distributed erbium-doped fibre amplifier," Electron. Lett. **32**, 233–234 (1996).

22. L.F. Mollenauer, R.H. Stolen, and M.N. Islam, "Experimental demonstration of soliton propagation in long fibers: Loss compensated by Raman gain," Opt. Lett. **10**, 229–231 (1985).

23. L.F. Mollenauer and K. Smith, "Demonstration of soliton transmission over more than 4000 km in fiber with loss periodically compensated by Raman gain," Opt. Lett. **13**, 675–677 (1988).

24. M.N. Islam (Ed.), *Raman Amplifiers for Telecommunications 1: Physical Principles and Raman Amplifiers for Telecommunications 2: Sub-Systems and Systems*, Springer Series in Optical Sciences (Springer-Verlag, 2003).

25. H.J. Thiele, L. Molle, T. Eggert, F. Raub, and R. Freund, "S-band Erbium-Doped Fibre Amplifiers for 40 Gb/s WDM Transmission," Proc. of the European Conference on Optical Communications (ECOC'04), paper Tu1.5.7 (2004).

26. R. Ohhira, Y. Yano, A. Noda, Y. Suzuki, C. Kurioka, M. Tachigori, S. Moribayashi, K. Fukuchi, T. Ono, and T. Suzuki, "40 Gbit/s $\times$ 8-ch NRZ WDM transmission experiment over 80 km $\times$ 5-span using distributed Raman amplification in RDF," Proc. of the European Conference on Optical Communications (ECOC'99), pp. 176–177 (1999).

27. T. Okuno, T. Tsuzaki, and M. Nishimura, "Novel lossless optical transmission line with distributed Raman amplification," Proc. of the European Conference on Optical Communications (ECOC'00), Vol. 2, pp. 7576 (2000).

28. I. Morita, K. Tanaka, N. Edagawa, and M. Suzuki, "40 Gbit/s $\times$ 16 WDM transmission over 2000 km using dispersion managed low-nonlinear fiber span," Proc. of the European Conference on Optical Communications (ECOC'00), Vol. 4, pp. 2526 (2000).

29. H.S. Chung, H. Kim, S.E. Jin, E.S. Son, D.W. Kim, K.M. Lee, H.Y. Park, and Y.C. Chung, "320-Gb/s WDM Transmission with 50-GHz Channel Spacing Over 564 km of Short-Period Dispersion-Managed Fiber (Perfect Cable)," IEEE Photon. Technol. Lett. **12**, 1397–1399 (2000).

30. T. Yamamoto, E. Yoshida, K. R. Tamura, K. Yonenaga, and M. Nakazawa, "640-Gbit/s Optical TDMTransmission Over 92 km Through a Dispersion-Managed Fiber Consisting of Single-Mode Fiber and Reverse Dispersion Fiber," IEEE Photon. Technol. Lett. **12**, 353–355 (2000).

31. S.N. Knudsen, M.O. Pedersen, and L. Grüner-Nielsen, "Optimisation of dispersion compensating fibres for cabled long-haul applications," Electron. Lett. **36**, 2067–2068 (2000).

32. S.N. Knudsen, B. Zhu, L. E. Nelson, M.O. Pedersen, D.W. Peckham, and S. Stulz, "420 Gbit/s (4210 Gbit/s) WDM transmission over 4000 km of UltraWave fibre with 100 km dispersion-managed spans and distributed Raman amplification," Electron. Lett. **37**, 965–967 (2001).

33. B. Zhu, S.N. Knudsen, L.E. Nelson, D.W. Peckham, M.O. Pedersen, and S. Stulz, "800 Gbit/s (80 × 10.664 Gbit/s) WDM transmission over 5200 km of fibre employing 100km dispersion Managed spans," Electron. Lett. **37**, 1467–1469 (2001).

34. R. Hainberger, T. Hoshida, T. Terahara, and H. Onaka, "Comparison of Span Configurations of Raman-Amplified Dispersion-Managed Fibers," IEEE Photon. Technol. Lett. **14**, 471–473 (2002).

35. C. Rasmussen, T. Fjelde, J. Bennike, F. Liu, S. Dey, B. Mikkelsen, P. Mamyshev, P. Serbe, P. van der Wagt, Y. Akasaka, D. Harris, D. Gapontsev, V. Ivshin, and P. Reeves- Hall, "DWDM 40G Transmission Over Trans-Pacific Distance (10 000 km) Using CSRZDPSK, Enhanced FEC, and All-Raman-Amplified 100-km UltraWave Fiber Spans," J. Lightwave Technol. **22**, 203–207 (2004).

36. T. Tsuritani, K. Ishida, A. Agata, K. Shimomura, I. Morita, T. Tokura, H. Taga, T. Mizuochi, N. Edagawa, and S. Akiba, "70-GHz-Spaced 40 42.7 Gb/s Transpacific Transmission Over 9400 km Using Prefiltered CSRZ-DPSK Signals, All-Raman Repeaters, and Symmetrically Dispersion-Managed Fiber Spans," J. Lightwave Technol. **22**, 215–223 (2004).

37. D.F. Grosz, A. Agarwal, A.P. Küng, S. Banerjee, D.N. Maywar, and T.H. Wood, "Performance of a ULH Single Wide-Band All-Raman DWDM Transmission System Over Dispersion-Managed Spans," IEEE Photon. Technol. Lett. **16**, 1197–1199 (2004).

38. M.M.E. Said, J. Sitch, and M.I. Elmasry, "An electrically pre-equalized 10-Gb/s duobinary transmission system," J. Lightwave Technol. **23**, 388–400 (2005).

39. D. McGhan, C. Laperle, A. Savchenko, C. Li, G. Mak, and M. O'Sullivan, "5120 km RZ-DPSK transmission over G.652 fiber at 10 Gb/s with no optical dispersion compensation," Proc. of the Optical Fiber Communication (OFC'05), paper PDP27 (2005).

40. R.-J. Essiambre and P.J. Winzer, "Fibre Nonlinearities in Electronically Pre-Distorted Transmission," Proc. of the European Conference on Optical Communication (ECOC'05), invited paper Tu3.2.2 (2005).

41. P.J. Winzer and R.-J. Essiambre, "Electronic pre-distortion for advanced modulation formats," Proc. of the European Conference on Optical Communication (ECOC'05), paper Tu4.2.2 (2005).

42. H. Sugahara, "Analysis of power jitter induced by interchannel interactions in dispersion-managed optical soliton transmission systems," IEEE Photon. Technol. Lett. **13**, 963–965 (2001).

43. S. Banerjee, A. Agarwal, D.F. Grosz, A.P. Küng, and D.N. Maywar, "Doubly periodic Dispersion Maps for 10 Gb/s and 40 Gb/s Ultra-Long-Haul Transmission," Electron. Lett. **40**, 1287–1288 (2004).

44. C. Xie, "A doubly periodic dispersion map for ultralong-haul 10- and 40-Gb/s hybrid DWDM optical mesh networks," IEEE Photon. Technol. Lett. **17**, 1091–1093 (2005).

45. F. Forghieri, R.W. Tkach, A.R. Chraplyvy, and A.M. Vengsarkar, "Dispersion Compensating Fiber: Is There Merit in the Figure of Merit?" Proc. of the Optical Fiber Communications Conference (OFC'96), paper ThM5 (1996).

46. F. Forghieri, R.W. Tkach, and A.R. Chraplyvy, "Dispersion Compensating Fiber: Is There Merit in the Figure of Merit?" IEEE Photon. Technol. Lett. **9**, 970–972 (1997).

47. P. Sillard, B. Dany, A. Bertaina, L. Curinckx, C. Bastide, O. Courtois, J.-C. Antona, and S. Bigo, "Simple criterion of quality to evaluate DCM impact on WDM system performance," Proc. of the Optical Fiber Communications Conference (OFC'04), paper FA3 (2004).

48. N.S. Bergano, *Undersea communication systems*, in Optical Fiber Telecommunications IV B, edited by I. Kaminow and T. Li (Academic Press, 2002).

49. S.D. Personick, "Receiver design for digital fiber optic communication systems, I," Bell. Syst. Technol. J. **52**, 843–874 (1973).

50. G. Einarsson, *Principles of Lightwave Communications* (John Wiley & Sons, 1996).

51. G. P. Agrawal, *Fiber-optic communication systems* (John Wiley & Sons, 3rd edition, 2002).

52. L. Kazovsky, S. Benedetto, and A. Willner, *Optical Fiber Communication Systems* (Artech House, Inc., 1996).

53. P.J. Winzer, "Receiver noise modeling in the presence of optical amplification," Proc. of the Optical Amplifiers and their Applications (OAA'01), OTuE16 (2001); P.J. Winzer, Performance estimation of receivers corrupted by optical noise, in OSA Trends in Optics and Photonics (TOPS), vol. 60, (N. Jolley, J.D. Minelly, and Y. Nakano, eds.), pp 268–273, (2001).

54. P.J. Winzer, S. Chandrasekhar, and H. Kim, "Impact of filtering on RZ-DPSK reception," IEEE Photon. Technol. Lett. **15**, 840–842 (2003).

55. R.D. Gitlin, J. F. Hayes, and S. B. Weinstein, Data Communications Principles, Plenum Press (1992).

56. P.J. Winzer and A. Kalmar, "Sensitivity Enhancement of Optical Receivers by Impulsive Coding," J. Lightwave Technol. **17**, 171–177 (1999).

57. P.J.Winzer, R.-J. Essiambre, and J. Bromage, "Combined Impact of Double-Rayleigh Backscatter and Amplified Spontaneous Emission on Receiver Noise," Proc. of the Optical Fiber Communications Conference (OFC'02), Paper ThGG87, pp. 734–735 (2002).

58. N.A. Olsson, "Lightwave Systems with Optical Amplifiers," J. Lightwave Technol. **7**, 1071–1082 (1989).

59. P. Wan and J. Conradi, "Impact of Double Rayleigh Backscatter Noise on Digital and Analog Fiber Systems," J. Lightwave Technol. **14**, 288–297 (1996).

60. B.E.A. Saleh and M.C. Teich, *Fundamentals of Photonics* (John Wiley & Sons, Inc., 1991).

61. P.J. Winzer, R.-J. Essiambre, and S. Chandrasekhar, "Dispersion-tolerant optical communication systems," Proc. of the European Conference on Optical Communications (ECOC'04), paper We2.4.1 (2004).

62. R.G. Smith, "Optical Power Handling Capacity of Low Loss Optical Fibers as Determined by Stimulated Raman and Brillouin Scattering," Appl. Opt. **11**, 2489–2494 (1972).

63. M. Nissov, K. Rottwitt, H.D. Kidorf, and M.X. Ma, "Rayleigh Crosstalk in Long Cascades of Distributed Unsaturated Raman Amplifiers," Electron. Lett. **35**, 997–998 (1999).

64. M. Oskar van Deventer, "Polarization Properties of Rayleigh Backscattering in Single- Mode Fibers," J. Lightwave Technol. **11**, 1895–1899 (1993).

65. H.A. Haus, *Electromagnetic noise and quantum optical measurements* (Springer Verlag, 2000).

66. E. Desurvire, D. Bayart, B. Desthieux, and S. Bigo, *Erbium-Doped Fiber Amplifiers, Device and System Developments* (John Wiley & Sons, 2002).

67. R.I. Laming, M.N. Zervas, and D.N. Payne, "Erbium-doped fiber amplifier with 54 dB gain and 3.1 dB noise figure," IEEE Photon. Technol. Lett. **4**, 1345–1347 (1992).

68. P.C. Becker, N.A. Olsson, and J.R. Simpson, *Erbium-Doped Fiber Amplifiers Fundamentals and Technology* (Academic Press, San Diego, 1999).

69. A. Yariv, H. Blauvelt, and S.-W. Wu, "A Reduction of Interferometric Phase-to-Intensity Conversion Noise in Fiber Links by Large Index Phase Modulation of the Optical Beam," J. Lightwave Technol. **10**, 978–981 (1992).

70. K. Shimizu, T. Horiguchi, and Y. Koyamada, "Charateristics and Reduction of Coherent Fading Noise in Rayleigh Backscattering Measurement for Optical Fibers and Components," J. Lightwave Technol. **10**, 982–987 (1992).

71. B. Wedding, "New method for optical transmission beyond dispersion limit," Electron. Lett. **28**, 1298–1300 (1992).

72. R.S. Vodhanel, A.F. Elrefaie, M.Z. Iqbal, R.E. Wagner, J.L. Gimlett, and S. Tsuji, "Performance of directly modulated DFB lasers in 10-Gb/s ASK, FSK, and DPSK lightwave systems," J. Lightwave Technol. **8**, 1379–1386 (1990).

73. F.N. Timofeev, P. Bayvel, V. Mikhailov, O.A. Lavrova, R. Wyatt, R. Kashyap, M. Robertson, and J.E. Midwinter, "2.5 Gbit/s directly-modulated fibre grating laser for WDM networks," Electron. Lett. **33**, 1406–1407 (1997)

74. L. Nelson, I. Woods, and J. K. White, "Transmission over 560 km at 2.5 Gb/s using a directly modulated buried heterostructure gain-coupled DFB semiconductor laser," Proc. of the Optical Fiber Communication Conference (OFC'02), pp. 422–423 (2002).

75. P.J.Winzer and R.-J. Essiambre, "Advanced optical modulation formats," Proc. of the European Conference on Optical Communications (ECOC'03), paper Th2.6.1, pp. 1002–1003 (2003).

76. P.J. Winzer and R.-J. Essiambre, "System trade-offs for different optical modulation formats," Proc. of the Optical Amplifiers and Their Applications (OAA'04), OTuC4 (2004).

77. P.J. Winzer, C. Dorrer, R.-J. Essiambre, and I. Kang, "Chirped return-to-zero modulation by imbalanced pulse carver driving signals," IEEE Photon. Technol. Lett. **16**, 1379–1381 (2004).

78. H. Kim and R.-J. Essiambre, "Transmission of 8×20 Gb/s DQPSK signals over 310-km SMF with 0.8-b/s/Hz spectral efficiency," IEEE Photon. Technol. Lett. **15**, 769–771 (2003).

79. R. Griffin, R. Johnstone, R. Walker, S. Wadsworth, A. Carter, and M. Wale, "Integrated DQPSK transmitter for dispersion-tolerant and dispersion-managed DWDM transmission," Proc. of the Optical Fiber Communications Conference (OFC'03), pp. 770–771 (2003).

80. S. Walklin and J. Conradi, "On the relationship between chromatic dispersion and transmitter filter response in duobinary optical communication systems," IEEE Photon. Technol. Lett. **9**, 1005–1007 (1997); [comments by D. Penninckx: IEEE Photon. Technol. Lett. **10**, 902 (1998).]

81. J.H. Winters and R.D. Gitlin, "Electrical signal processing techniques in long-haul fiber-optic systems", IEEE Trans. Commun. **38**, 1439–1453 (1990).

82. F. Buchali, H. Bulow, and W. Kuebart, "Adaptive decision feedback equalizer for 10 Gbit/s dispersion mitigation," Proc. of the European Conference on Optical Communications (ECOC'00), Vol. 2, pp. 101–102 (2001).

83. D. Castagnozzi, "Digital signal processing and electronic equalization (EE) of ISI," Proc. of the Optical Fiber Communications Conference (OFC'04), paper WM6 (2004).

84. H.F. Haunstein, K. Sticht, A. Dittrich, M. Lorang, W. Sauer-Greff, and R. Urbansky, "Implementation of near optimum electrical equalization at 10 Gbit/s," Proc. of the European Conference on Optical Communications (ECOC'00), Vol. 3, pp. 223–224 (2000).

85. F. Buchali and H. Bulow, "Adaptive PMD compensation by electrical and optical techniques," J. Lightwave Technol. **22**, 1116–1126 (2004).

86. G.S. Kanter, A.K. Samal, O. Coskun, and A. Gandhi,"Electronic equalization for enabling communications at OC-192 rates using OC-48 components," Optics Express **11**, 2019–2029 (2003).

87. C.R. Doerr, A.H. Gnauck, L.W. Stulz, and D.M. Gill, "Using an optical equalizer to transmit a 43-Gb/s signal with an 8-GHz bandwidth modulator," IEEE Photon. Technol. Lett. **15**, 1624–1626 (2003).

88. C.R. Doerr, S. Chandrasekhar, P.J. Winzer, A.R. Chraplyvy, A.H. Gnauck, L.W. Stulz, R. Pafchek, and E. Burrows, "Simple multichannel optical equalizer mitigating intersymbol interference for 40-Gb/s nonreturn-to-zero signals," J. Lightwave Technol. **22**, 249–256 (2004).

89. P.J. Winzer and R.-J. Essiambre, "Receivers for advanced optical modulation formats," Proc. of the 16th annual meeting of IEEE/LEOS (LEOS"03), paper ThA1 (2003).

90. A.J. Weiss, "On the performance of electrical equalization in optical fiber transmission systems," IEEE Photon. Technol. Lett. **15**, 1225–1227 (2003).

91. S.L. Woodward, S.-Y. Huang, M.D. Feuer, and M. Boroditsky, "Demonstration of an electronic dispersion compensator in a 100-km 10-Gb/s ring network," IEEE Photon. Technol. Lett. **15**, 867–869 (2003).

92. M.D. Feuer, S.-Y. Huang, S.L. Woodward, O. Coskun, and M. Boroditsky, "Electronic dispersion compensation for a 10-Gb/s link using a directly modulated laser," IEEE Photon. Technol. Lett. **15**, 1788–1790 (2003).

93. P.J. Winzer, F. Fidler, M.J. Matthews, L.E. Nelson, S. Chandrasekhar, L.L. Buhl, M. Winter, and D. Castagnozzi, "Electronic equalization and FEC enable bidirectional CWDM capacities of 9.6 Tb/s-km," Proc. of the Optical Fiber Communications Conference (OFC'04), paper PDP7 (2004).

94. C.R.S. Fludger, J.E.A. Whiteaway, and P.J. Anslow, "Electronic Equalisation for Low Cost 10 Gbit/s Directly Modulated Systems," Proc. of the Optical Fiber Communications Conference (OFC'04), paper WM7 (2004).

95. M. Cavallari, C.R.S. Fludger, and P.J. Anslow, "Electronic Signal Processing for Differential Phase Modulation Formats," Proc. of the Optical Fiber Communications Conference (OFC'04), paper TuG2 (2004).

96. A. Faerbert, S. Langenbach, N. Stojanovic, C. Dorschky, T. Kupfer, C. Schulien, J.P. Elbers, H. Wernz, H. Griesser, and C. Glingener, "Performance of a 10.7 Gb/s receiver with digital equalizer using maximum likelihood sequence estimation," Proc. of the European Conference on Optical Communication (ECOC'04), paper Th4.1.5 (2004).

97. T. Mizuochi, K. Kubo, H. Yoshida, H. Fujita, H. Tagami, M. Akita, and K. Motoshima, "Next generation FEC for optical transmission systems," Proc. of the Optical Fiber Communications Conference (OFC'03), paper ThN1 (2003).

98. S. Chandrasekhar and L. L. Buhl, "Performance of forward error correction coding in the presence of in-band crosstalk," Proc. of the Optical Fiber Communications Conference (OFC'02), paper WP1 (2002).

99. G.P. Agrawal, *Nonlinear Fiber Optics, 3rd Edition* (Academic Press, San Diego, 2001).

100. R.-J. Essiambre, B. Mikkelsen, and G. Raybon, "Intra-channel cross-phase modulation and four-wave mixing in high-speed TDM systems," Electron. Lett. **35**, 1576–1578 (1999).

101. P.V. Mamyshev and N.A. Mamysheva, "Pulse-overlapped dispersion-managed data transmission and intra-channel four-wave mixing," Opt. Lett. **24**, 1454–1456 (1999).

102. R.-J. Essiambre, G. Raybon, and B. Mikkelsen, *Pseudo-linear transmission of highspeed TDM signals: 40 and 160 Gb/s*, in Optical Fiber Telecommunications IV B, edited by I. Kaminov and T. Li, pp. 232–304 (Academic Press, 2002).

103. R.-J. Essiambre, P. Winzer, J. Bromage, and C.H. Kim , "Design of Bidirectionally Pumped Fiber Amplifiers Generating Double Rayleigh Backscattering," IEEE Photon. Technol. Lett. **14**, 914–916 (2002).

104. C. Fukai, K. Nakajima, J. Zhou, K. Tajima, K. Kurokawa, and I. Sankawa, "A Study of the Optimum Fiber Design for a Distributed Raman Amplification Transmission System, " IEEE Photon. Technol. Lett. **15**, 1642–1644 (2003).

105. H.S. Seo, Y.G. Choi, and K.H. Kim, "Design of Transmission Optical Fiber With a High Raman Gain, Large Effective Area, Low Nonlinearity, and Low Double Rayleigh Backscattering," IEEE Photon. Technol. Lett. **16**, 72–74 (2004).

106. P. Pecci, S. Lanne, Y. Frignac, J-C. Antona, G. Charlet and S. Bigo, "Tolerance to dispersion compensation parameters of six modulation formats in systems operating at 43Gbit/s," Proc. of the European Conference on Optical Communications (ECOC'03), paper We3.5.5 (2003).

107. H. Kogelnik, L.E. Nelson, and R.M. Jopson, *Polarization-mode dispersion*, in Optical Fiber Telecommunications IV B, edited by I. Kaminow and T. Li (Academic Press, 2002).

108. P.J. Winzer, H. Kogelnik, C.-H. Kim, H. Kim, R.M. Jopson, L.E. Nelson, and K. Ramanan, "Receiver Impact on first-order PMD Outage," IEEE Photon. Technol. Lett. **15**, 1482–1484 (2003).

109. S.R. Chinn, "Analysis of counter-pumped small-signal fibre Raman amplifiers," Electron. Lett. **33**, 607–608 (1997).

110. A. Kobyakov, M. Vasilyev, S. Tsuda, G. Giudice, and S. Ten, "Analytical model for Raman noise figure in dispersion-managed fibers," IEEE Photon. Technol. Lett. **15**, 30–32 (2003).

111. A. Carena, V. Curri, and P. Poggiolini, "On the Optimization of Hybrid Raman/ Erbium-Doped Fiber Amplifiers," IEEE Photon. Technol. Lett. **13**, 1170– 1172 (2001).

112. E.M. Dianov, "Advances in Raman fibers," J. Lightwave Technol. **20**, 1457–1462 (2002).

113. W. Hatton and M. Nishimura, "Temperature dependence of chromatic dispersion in single mode fibers," J. Lightwave Technol. **4**, 1552–1555 (1986).

114. K.S. Kim and M.E. Lines, "Temperature dependence of chromatic dispersion in dispersion-shifted fibers: Experiment and analysis," Appl. Phys. Lett. **73**, 2069–2074 (1993).

115. K. Yonenaga, A.Hirano, S. Kuwahara, Y. Miyamoto, H. Toba, K. Sato, and H. Miyazawa, "Temperature-independent 80 Gbit/s OTDM transmission experiment using zero-dispersion-flattened transmission line," Electron. Lett. **36**, 343–345 (2000).

116. M.J. Hamp, J. Wright, M. Hubbard, and B. Brimacombe, "Investigation into the temperature dependence of chromatic dispersion in optical fiber," IEEE Photon. Technol. Lett. **14**, 1524–1526 (2002).

117. H.C. Ji, J.H. Lee, and Y.C. Chung, "Evaluation on system outage probability due to temperature variation and statistically distributed chromatic dispersion of optical fiber," J. Lightwave Technol. **22**, 1893–1898 (2004).

118. A. Walter, G.S. Schaefer, "Chromatic dispersion variations in ultra-long-haul transmission systems arising from seasonal soil temperature variations," Proc. of the Optical Fiber Communication Conference (OFC'02), paper WU4, 332–333 (2002).

119. R. Kashyap, *Fiber Bragg Gratings* (Harcourt Brace & Company, 1999).

120. L.E. Nelson, R.M. Jopson, A.H. Gnauck, and A.R. Chraplyvy, "Resonances in cross-phase modulation impairment in wavelength-division-multiplexed lightwave transmission," IEEE Photon. Technol. Lett. **11**, 907–909 (1999).

121. G. Bellotti and S. Bigo, "Cross-phase modulation suppressor for multispan dispersionmanaged WDM transmissions," IEEE Photon. Technol. Lett. **12**, 726–728 (2000).

122. M.H. Eiselt, "Does spectrally periodic dispersion compensation reduce nonlinear effects?," Proc. of the European Conference on Optical Communications (ECOC'99), paper TuC1.2 (1999).

123. G. Bellotti, S. Bigo, P.-Y. Cortes, S. Gauchard, and S. LaRochelle, "10/spl times/10 Gb/s cross-phase modulation suppressor for multispan transmissions using WDM narrow-band fiber Bragg gratings," IEEE Photon. Technol. Lett. **12**, 1403–1405 (2000).

124. M.H. Eiselt, C.B. Clausen, and R.W. Tkach, "Performance Characterization of Components With Group Delay Fluctuations," IEEE Photon. Technol. Lett. **15**, 1076–1078 (2003).

125. International Standard IEC 60794-3, Part 3: "Optical fiber cables," September 2001, Appendix A.

126. L. Grüner-Nielsen, S.N. Knudsen, B. Edvold, T. Veng, D. Magnussen, C.C. Larsen, and H. Damsgaard, "Dispersion Compensating Fibres," Opt. Fiber Technol. **6**, 164–180 (2000).

127. Y. Painchaud, M. Lapointe, and M. Guy, "Slope-matched tunable dispersion compensation over the full C-band based on fiber Bragg gratings," Proc. of the European Conference on Optical Communication (ECOC'04), paper We3.3.4 (2004).

128. L.M. Lunardi, D.J. Moss, S. Chandrasekhar, L.L. Buhl, M. Lamont, S. McLaughlin, G. Randall, P. Colbourne, S. Kiran, and C.A. Hulse, "Tunable Dispersion Compensation at 40-Gb/s Using a Multicavity Etalon All-Pass Filter With NRZ, RZ, and CS-RZ Modulation," J. Lightwave Technol. **20**, 2136–2144 (2002).

129. D.N. Maywar, S. Banerjee, A. Agarwal, D.F. Grosz, M. Movassaghi, A.P. Küng, and T.H. Wood, "Impact of relaxed dispersion map and gain ripple on ultra-wideband 10-Gb/s transmission," Electron. Lett. **39**, 1266–1267 (2003).

130. A. Agarwal, S. Banerjee, D.F. Grosz, A.P. Küng, D.N. Maywar, T.H. Wood, "Ultralong- haul transmission of 40 Gb/s RZ-DPSK in a 10/40G hybrid system over 2500 km of NZ-DSF," IEEE Photon. Technol. Lett. **15**, 1779–1781 (2003).

131. M. Vasilyev, I. Tomkos, J.-K. Rhee, M. Mehendale, B.S. Hallock, B.K. Szalabofka, M. Williams, S. Tsuda, M. Sharma, "Broadcast and Select OADM in 80 $\times$ 10.7 Gb/s ultra-longhaul network", J. Lightwave Technol. **15**, 332–334 (2003).

132. D.F. Grosz, A. Agarwal, S. Banerjee, D.N. Maywar, and A.P. Küng, "All-Raman Ultralong-Haul Single-Wideband DWDM Transmission Systems With OADM Capability," J. Lightwave Technol. **22**, 423–432 (2004).

133. M. Morin, M. Poulin, A. Mailloux, F. Trepanier, and Y. Painchaud, "Full C-Band slope-matched dispersion compensation based on a phase sampled Bragg grating," Proc. of the Optical Fiber Communication Conference (OFC'04), paper WK1 (2004).

134. X. Shu, K. Sugden, P. Rhead, J. Mitchell, I. Felmeri, G. Lloyd, K. Byron, Z. Huang, I. Khrushchev, and I. Bennion, "Tunable Dispersion Compensator Based on Distributed Gires-Tournois Etalons," IEEE Photon. Technol. Lett. **15**, 1111–1113 (2003).

135. S. Doucet, R. Slavk, and S. LaRochelle, "Tunable Dispersion and Dispersion Slope Compensator Using Novel Gires-Tournois Bragg Grating Coupled-Cavities," IEEE Photon. Technol. Lett. **16**, 2529–2531 (2004).

136. D. Yang, C. Lin, W. Chen, and G. Barbarossa, "Fiber Dispersion and Dispersion Slope Compensation in a 4-Channel 10-Gb/s 3200-km Transmission Experiment Using Cascaded Single-Cavity Gires-Tournois Etalons," IEEE Photon. Technol. Lett. **16**, 299–301 (2004).

137. C.-H. Hsieh, R. Wang, Z.J. Wen, I. McMichael, P. Yeh, C.-W. Lee, and W.-H. Chen, "Flat-Top Interleavers Using Two Gires-Tournois Etalons as Phase-Dispersive Mirrors in a Michelson Interferometer," IEEE Photon. Technol. Lett. **15**, 242–244 (2003).

138. G. Lenz and C.K. Madsen, "General Optical All-Pass Filter Structures for Dispersion Control in WDM Systems," J. Lightwave Technol. **17**, 1248–1254 (1999).

139. C.K. Madsen and G. Lenz, "Optical All-Pass Filters for Phase Response Design with Applications for Dispersion Compensation," IEEE Photon. Technol. Lett. **10**, 994– 996 (2003)

140. C.K. Madsen, E.J. Laskowski, J. Bailey, M.A. Capuzzo, S. Chandrasekhar, L.T. Gomez, A. Griffin, P. Oswald, and L.W. Stulz, "The Application of Integrated Ring Resonators to Dynamic Dispersion Compensation," Proc. of the Optical Fiber Communication Conference (OFC'02), Paper TuJ2, pp. 29–30 (2002).

141. S. Ramachandran, S. Ghalmi, S. Chandrasekhar, I. Ryazansky, M.F. Yan, F.V. Dimarcello, W.A. Reed, and P. Wisk, "Tunable Dispersion Compensators Utilizing Higher Order Mode Fibers," IEEE Photon. Technol. Lett. **15**, 727–729 (2003).

142. H. Ooi, K. Nakamura, Y. Akiyama, T. Takahara, T. Terahara, Y. Kawahata, H. Isono, and G. Ishikawa, "40-Gb/s WDM Transmission With Virtually Imaged Phased Array (VIPA) Variable Dispersion Compensators," J. Lightwave Technol. **20**, 2196–2203 (2002).

143. T.A. Birks, D. Mogilevtsev, J.C. Knight, and P. St.J. Russell, "Dispersion Compensation Using Single-Material Fibers," IEEE Photon. Technol. Lett. **11**, 674–676 (1999).

144. Y. Ni, L. Zhang, L. An, J. Peng, and C. Fan, "Dual-Core Photonic Crystal Fiber for Dispersion Compensation," IEEE Photon. Technol. Lett. **16**, 1516–1518 (2004).

145. M. Yagi, S. Satomi, S. Tanaka, S. Ryu, and S. Asano, "Field Trial of Automatic Chromatic Dispersion Compensation for 40-Gb/s-Based Wavelength Path Protection," IEEE Photon. Technol. Lett. **17**, 229–231 (2005).

146. D.F. Grosz, A. Küng, D.N. Maywar, L. Altman, M. Movassaghi, H.C. Lin, D.A. Fishman, and T.H. Wood, "Demonstration of All-Raman Ultra-Wide-Band Transmission of 1.28 Tb/s (128 $\times$ 10 Gb/s) over 4000 km of NZ-DSF with Large BER Margins," Proc. of the European Conference on Optical Communication (ECOC'01), Paper PD B.1.3, pp. 72–73 (2001).

147. D.F. Grosz, D.N. Maywar, A.P. Küng, A. Agarwal, and S. Banerjee, "Performance of Non-Fiber Based Dispersion Compensation for Long-haul 10.7 Gb/s DWDM Transmission," Electron. Lett. **40**, 825–827 (2004).

DOI: 10.1007/s10297-006-0075-3
Originally published in J. Opt. Fiber. Commun. Rep. 3, 340–398 (2006)

Survey of systems experiments demonstrating dispersion compensation technologies

Lara Denise Garrett

Celion Networks, 1 Sheila Drive, Suite 2, Tinton Falls, NJ 07701, USA
Email: lara@ieee.org

Abstract. Chromatic dispersion compensation is an integral part of WDM transmission system design. Compensator properties such as insertion loss, dispersion slope and effective mode area have a large impact on WDM system performance due to nonlinear optical propagation effects. Dispersion compensator imperfections, such as multi-path interference, group delay ripple, insertion loss ripple and limited per-channel compensation bandwidth, place additional limitations on the achievable transmission distance and capacity. In this paper, a survey of key WDM transmission system experiments is undertaken to 1) review the development of chromatic dispersion compensation technologies, 2) discuss the device characteristics that most impact system design for each technology, and 3) hopefully enable the reader to better evaluate compensator technologies for specific applications.

1. Introduction

The goal of this paper is to reinforce awareness of the impact of dispersion compensation choices on wavelength division multiplexed (WDM) optical transmission system design through the review of key WDM transmission experiments for each technology. It is critical to understand the strengths and weaknesses of the various compensation technologies in order to make intelligent design choices. For an ultra-longhaul system designer, the primary design issue might be accuracy of dispersion slope compensation or optical power handling. For a metro system designer, the primary issue might be an understanding of which performance parameters can least detrimentally be traded off for cost and size reduction.

Dispersion compensation is an integral part of WDM transmission system design. The distribution of dispersion along a WDM transmission system, or "dispersion map",

is a critical design parameter for high-performance systems. The optimal dispersion map depends on the number and density of wavelengths, the per-wavelength data rate and modulation format, and the length of the system. Dispersion compensator properties such as insertion loss, dispersion slope and effective mode area have a large impact on WDM system performance due to non-linear optical propagation effects. Dispersion compensator imperfections, such as multi-path interference, group delay ripple, insertion loss ripple and limited per-channel compensation bandwidth, place additional limitations on the achievable transmission distance and capacity.

Optical transmission experiments that include chromatic dispersion compensation vary widely in level of complexity. Dispersion compensating fiber (DCF), Raman-pumped DCF, and dispersion managed fiber spans are sufficiently advanced to be used primarily to facilitate record-breaking transmission results in terms of channel count, channel data rate and/or transmission distance. The higher-order mode (HOM) compensators and etalon-compensators have been demonstrated in multi-span transmission experiments that may not break records but demonstrate the capability of these technologies as reasonable competitors for DCF. Broadband chirped gratings tend to have either sufficient quality or sufficient optical bandwidth for full C-band, multi-span applications, but not both. The remaining fiber-based technologies, in general, have been evaluated in single-span configurations to date to demonstrate the basic competence of the devices.

For WDM systems designers, the proof of a technology has to be in the demonstrated performance. Multi-span performance can be numerically simulated based on measurements of technology-dependent impairments such as group delay variation or multi-path interference (MPI). The best proof that a technology will work in a given application, however, is demonstration in a realistic WDM transmission experiment using the correct modulation rate and format, WDM channel count, number of concatenated fiber spans, and dispersion compensation modules. Any narrow-band or channelized device should also be evaluated over the entire range of operating temperature to look for changes in central frequency, dispersion magnitude, and the optical bandwidth of both insertion loss and dispersion, because deployed systems do not operate at room temperature.

The assigned topic for this document was fiber-based technologies for the compensation of chromatic dispersion in optical fiber transmission systems. However, a few additional non-fiber-based compensators including all-pass filters, virtually imaged phased arrays (VIPA) and electronic equalizers will be covered so that the reader has a more complete understanding of the available dispersion compensation options.

1.1. A Brief Overview of DWDM Transmission Systems

A brief discussion of Dense Wavelength Division Multiplexing will provide some background for our review. DWDM technology increases the traffic capacity of a fiber-optic link by transmitting multiple data channels on different wavelengths of light within the same fiber. The linear transmission properties of glass ensure that there is little crosstalk between the wavelength channels as they propagate through the optical fiber. The sharing of the transmission media between the wavelength-multiplexed channels decreases the cost-per-bit of the link.

At each endpoint of the optical fiber link, incoming electrical data channels are modulated onto light from lasers with different wavelengths. The modulated optical

signals are then multiplexed onto a single fiber for transmission. Optical amplifiers may be placed at distributed sites along the link to provide analog optical gain to all wavelength channels. Depending on the total transmission distance, the channel data-rate of the system, and the fiber type, the amplifier sites may also contain dynamic gain equalizers to actively correct for power level variations between optical channels, and dispersion compensation modules to correct for the transmission fiber dispersion. At the opposite endpoint of the system, the optical wavelengths are demultiplexed and then converted back into the electronic domain by optical receivers.

The earliest optical fiber transmission in the 1980s used a single wavelength at 1300 nm, where the dispersion of "conventional" single mode fiber (SMF) was very low. However, the attenuation of SMF is much lower at 1550 nm, so transmission soon migrated to this wavelength. "WDM" initially referred to the addition of a channel at 1550 nm to the original channel at 1300 nm. These early systems had to use electronic regenerators every 40 km or so. The cost of electronic regeneration dominated the system cost, so it did not make sense to add more channels on a single fiber. The development of erbium-doped fiber amplifiers (EDFAs) in the early 1990s provided uniform optical gain over a 35-nm bandwidth, and soon we had early WDM systems with eight widely-spaced channels separated by 3.2 nm (400 GHz). The development of DWDM systems was driven by the fundamental cost advantage of the EDFA as a single parallel "optical regenerator" replacing N single-channel electronic regenerators, and this cost advantage generally holds true today.

In-line dispersion compensation is traditionally placed between the stages of a two-stage EDFA amplifier to minimize the noise impact of the compensator insertion loss. The optical signal-to-noise ratio (OSNR) in dB after N identical optically amplified spans, measured in a reference optical bandwidth of 0.1 nm, is given by

$$\mathrm{OSNR(dB)} = 58 + P_{\mathrm{out}}(\mathrm{dBm}) L(\mathrm{dB}) \mathrm{NF(dB)} 10 \log 10(N), \tag{1}$$

where P_{out} is the amplifier output power per channel in dBm, L is the span loss in dB, NF is the amplifier noise figure in dB, and N is the number of spans [1]. This equation is derived from the ASE noise generated by a single amplifier, P_{noise}, with all terms in linear units:

$$P_{\mathrm{noise}} = (h\nu) B_0 \mathrm{NF}(G-1), \tag{2}$$

$$\mathrm{OSNR} = \frac{P_{\mathrm{out}}}{N P_{\mathrm{noise}}} \approx \frac{P_{\mathrm{out}}}{N[(h\nu) B_0 G \mathrm{NF}]}, \tag{3}$$

assuming $G \gg 1$, where $(h\nu)$ is the photon energy, B_0 is the reference optical bandwidth of 12.5 GHz for 0.1 nm, and G is the amplifier gain in linear terms, which should be equal to the fiber span loss L.

Placing a device with 5 dB insertion loss between the span output and the EDFA input of every span would add 5 dB directly to the span loss in our OSNR equation, reducing the length of a noise-limited system by a factor of 5 dB (3×). Placing the device instead at the EDFA output would require 5 dB higher EDFA output power to maintain a constant power into the fiber. Increasing EDFA output power is an expensive modification because the pump lasers generally dominate EDFA cost, and additional or higher-power pumps would be required. The EDFA output is also the highest power location in the WDM system, so the nonlinear impairment from any dispersion compensator would also be maximized.

Putting the dispersion compensation in the amplifier mid-stage reduces the impact of insertion loss on system noise accumulation. The concatenated noise figure of a two-stage EDFA with a mid-stage loss budget allocated for dispersion compensation has a small NF penalty proportional to the mid-stage loss divided by the first stage gain. The mid-stage compensator location also allows the power levels in the compensator to be optimized separately from the transmission fiber, requires the same total amplifier gain, and is implemented in two lower-power stages that may be more cost effective than a single higher-power stage. The "dense" in DWDM refers to tightly spacing channels within the bandwidth of an optical amplifier technology. Today, a typical DWDM implementation might have 40 channels operating at 10 Gbps separated by 0.8 nm (100 GHz) within a 35-nm wavelength range, although densities as high as 160 channels separated by 0.2 nm (25 GHz) have been demonstrated. However, maintaining 25 GHz channel spacing imposes many system complications because of the extremely tight wavelength stability required of all optical components and the extremely sharp filter shapes required of all optical filters. Also, cross-talk effects between channels increase as the channels are spaced more closely together. The channel spacing is also limited by the data rate of the channels because the spectral components of the modulated optical carriers should not overlap, so that 10 Gbps channels can be more closely spaced than 40 Gbps channels for the same modulation format. The more complex DWDM transmission experiments are generally implemented in a "recirculating loop" configuration. We will see many recirculating loop experiments in our survey of system experiments. Proposed by N. Bergano et al. in 1995 [1], this is now a standard experimental technique that provides a cost-effective method to test extremely long transmission distances with a limited amount of equipment. As it is generally not possible to obtain multiple units of a new experimental compensator technology, the next best thing is a recirculating loop. For realistic multi-span performance, however, it is best to acquire more than a single unit, preferably at least three. In a recirculating loop, optical switches and precision timers allow data to be circulated through a short section of transmission system multiple times to emulate longer transmission distances. Loop experiments require some polarization-scrambling element within the loop to more realistically emulate the polarization state evolution of a signal in a "straight-line" system [2]. This is significant because the optical components have both polarization dependent losses and polarization-mode dispersion, and because the nonlinear interactions between wavelength channels can depend on the relative polarization states of the wavelengths. References [3] and [4] are early publications on margin measurement and optical noise evolution, respectively, in optically amplified transmission systems that everyone should have.

Coarse WDM, or "CWDM", refers to combining 8 or 16 channels spaced at 20 nm intervals over the entire range from 1310 to 1610 nm. CWDM is primarily used for low-cost OC-48 or 1GigE access and metro applications, because the wide wavelength range results in extreme variations in fiber loss and difficulty in providing broadband optical amplification or dispersion compensation. There will be little further mention of CWDM, since the system designs tend to be limited by available optical power rather than fiber dispersion.

2. Dispersion Compensating Fiber

The development of optical amplification technologies in the early 1990s removed the limitation of optical attenuation on the maximum length of optical transmission systems [5,6]. This allowed 2.5 Gbps data to be transmitted up to 1000 km in SMF fiber without electronic regeneration, limited primarily by the linear dispersion limit at 2.5 Gbps of 16,000 ps/nm. These distances were quite sufficient in a time when transmission systems were usually less than 500 km in length. However, growing interest in the transmission of 10 Gbps data and the large amount of deployed SMF fiber with a linear dispersion limit of only 60 km at 10 Gbps soon turned researchers to the field of dispersion compensating fiber [7,8]. This work was concurrent with research on dispersion-shifted fiber (DSF) with zero dispersion at 1550 nm, and later on non-zero DSF fibers (NZDSF) with low but non-zero dispersion at 1550 nm to suppress the four-wave mixing problem for C-band WDM channels in DSF fiber [9]. The growth in WDM system channel count next required DCF technology with dispersion-slope as well as dispersion compensation [10] to maintain uniform dispersion across all channels. The early 2000s kept DCF developers busy generating fiber designs to match the dispersion and slope of the many varieties of NZDSF, all requiring significantly higher ratio between negative dispersion and dispersion slope, known as "RDS" for "relative dispersion slope", than DCF-for-SMF [11]. Most recently, DCF fibers have been produced that can be wound onto significantly smaller spools for installation in cost- and size-sensitive extended-metro applications [12].

An early article from Antos and Smith of Corning Inc. [12] nicely stated the basic argument for dispersion compensating fiber modules in 1994: "The compensating fiber is envisioned as possibly being quite long but deployed on a compact reel; the reel may be located at the transmission or receiver site or at any point along the transmission path. A standard transmission system would not tolerate the additional loss that results from propagation through the additional length of dispersion compensating fiber. In an amplified system, however, the additional loss is compensated by EDFAs that are present in the system."

Dispersion compensating fiber (DCF) modules are currently the dominant technology in commercial optical transmission equipment. There has been significant improvement in the nonlinear performance and the insertion loss of DCF in recent years, reflected in a higher figure of merit (FOM) given by the magnitude of dispersion divided by the attenuation. Early DCF designs provided negative dispersion at the center wavelength of the optical amplifier band, but still had positive dispersion slope that limited the number of WDM channels and the number of fiber spans over which the dispersion match was sufficient at the edge channels for 10 Gbps transmission. DCF modules have been commercially available with accurate dispersion slope matching for the major SMF and NZDSF transmission fibers since approximately 2002.

The primary feature of DCF that has made it the preferred choice for commercial WDM system deployment is that it has been continuously available from multiple sources. The years from 1996 to 2004 saw the development of many innovative alternative dispersion compensator technologies with promising performance that quickly disappeared from the marketplace due to the market downturn, while DCF continued to improve each year. Another good feature of DCF is the broadband performance across a 35-nm operating window, for instance the EDFA C-band from 1530 to 1565 nm, that allows a standard DCF module to be used for WDM systems with any wavelength

spacing and with any channel modulation scheme. Channelized compensators such as sampled gratings [93] or all-pass filters [116] are designed for some fixed wavelength spacing such as 50 or 100 GHz, and may have sufficient optical bandwidth in each channel for 10 Gbps NRZ-encoded wavelengths but not for 12.5 Gbps RZ-encoded wavelengths with high-gain forward error correction or for 40 Gbps wavelengths. It should be noted that, while uncommon, DCF modules have been developed with reasonably good slope matching across multiple amplifier windows, such as the C+L band from 1530 to 1605 nm [13,14].

In a typical DCF module, the several kilometers of DCF are wound with precise tension about a metal spool for thermal uniformity and low bend loss, so that the complete DCF module is fairly substantial. The small effective mode area of the DCF requires a specialized and proprietary splice process to attach SMF pigtail fibers to the DCF endpoints [15]. The two splice losses (approximately 0.5 dB each, but very design dependent and constantly improving) puts a minimum floor on a DCF module insertion loss, and cause the FOM to be lower for low-dispersion modules than for high-dispersion modules using the same DCF fiber. Because of the special packaging conditions, DCF is only sold as modules with a specified DGD value (i.e., 500 ps/nm at 1550 nm) rather than as loose fiber. We will see below that DCF that has been optimized for module-style packaging is quite different from negative-dispersion fiber optimized for transmission spans, and can incur high bending losses when cabled [31,32].

Insertion loss has traditionally been an issue for DCF modules. The cost of any additional optical amplification from either erbium doped fiber amplifiers (EDFAs) or Raman amplification required to compensate for this loss adds to the effective cost of any dispersion compensation solution. There are several variations of DCF available for any fiber type, and insertion loss will depend on what amount of slope compensation the DCF fiber provides (0%, 66%, 100%), and on the operating band, i.e., C-band versus L-band or S-Band. As an example, commercial insertion loss values are about 6 dB for an 80-km DCF-for-SMF module and 4 dB for an 80-km DCF-for-NZDSF module, for C-band operation and 100% slope compensation. Another disadvantage of DCF has been that the complicated waveguide structure required to produce negative dispersion fiber with large negative dispersion slope result in fibers with small effective mode areas typically in the range of 15–25 μm^2 compared to $80\mu m^2$ for SMF, resulting in large nonlinear coefficients [16]. Both the insertion loss and the total module nonlinear impact have been improved by increasing the dispersion per unit length of the DCF, so that less fiber is required for a given dispersion value [16]. This provides an economic incentive for DCF to be sold as modules for the compensation of a certain distance rather than as fiber-by-the-meter.

In an early DCF demonstration in 1994, C.D. Chen et al. from AT&T Bell Labs used a non-slope matched DCF technology in a single-wavelength 10 Gbps transmission experiment over three field-deployed 120-km spans of standard SMF fiber [17]. Without the DCF modules, transmission through even a single 120-km span would have been impossible as the linear dispersion limit at 10 Gbps in SMF is approximately 60 km. The DCF modules in this experiment had a typical dispersion coefficient of 80 ps/nm km and figure of merit values that ranged from 80 to 120, compared to the 200 to 240 of a commercial DCF-for-SMF module today. The wide variation in DCF properties was apparently due to separate sources for each module, since the authors thank three early DCF pioneers, Corning [8], Furukawa-Fitel [18], and Sumitomo-Litespec for providing the DCF modules. The authors claim that this was the first 10-Gbps long

haul transmission through embedded standard fiber cable. The system ran with a bit error rate (BER) of less than 10^{-16}, corresponding to "less than a single error" or error-free operation over the 11 days of measurement.

The 120-km spans in that experiment were three times longer than the common 40-km spans of the time, and notably longer than the 80- to 100-km spans of terrestrial systems today. There was a great debate at the time over whether amplified optical transmission systems should be deployed with equipment huts spaced at 80 km (22 dB) or 120 km (33 dB), a tradeoff between number of amplifier sites and total system length. Recall from Eq. (1) that for a total amount of required gain, the generation of amplified spontaneous emission (ASE) noise and the resulting OSNR degradation is lowest for many distributed units of low gain, which explains why submarine systems use 40 km spans to traverse trans-oceanic distances. But there are operational costs including such mundane details as lawn mowing and real estate taxes associated with each amplifier site in terrestrial networks, and the 80- to 100-km span length has predominated. For a 1200-km system, dividing the length into 15 amplified spans of 80 km (22 dB gain per EDFA) will result in an OSNR 9.2 dB higher than dividing the length into 10 spans of 120 km (33 dB gain per EDFA), assuming the same EDFA Pout and NF.

The AT&T Bell Labs group reported an early "WDM" transmission experiment over this field route in 1995, with two 10 Gbps channels at 1552 nm and 1558 nm [19]. This work demonstrated that the dispersion match between the SMF and DCF was adequate at both wavelengths, with +326 ps/nm and +173 ps/nm total dispersion corresponding to 92% and 95% "under-compensation" of the total dispersion of the SMF spans for the 1558 and 1552 nm channels, respectively. The optical power level required at the receiver to produce a 10^{-9} bit error rate was increased by 1.5 to 2.5 dB after transmission over the three fiber spans relative to the back-to-back receiver sensitivity. The authors noted what is now a rule of thumb for 10-Gbps transmission, that "a slight under-compensation provides a wider eye opening and therefore a better system performance than the exact compensation of the chromatic dispersion" in amplified systems because of the interaction between dispersion and self-phase modulation (SPM). The authors also noted "the input power levels into the DCFs must be carefully adjusted to control the SPM effect in the DCFs." Because of the inherently smaller effective mode area of DCF fibers, nonlinear impairments occur at lower per-channel optical power levels than in the transmission fiber spans. This property of DCF adds complexity to the distribution of optical gain throughout an optical transmission system.

In 1995, N. Kikuchi et al. from Hitachi published a paper studying the optimal per-channel optical power level for DCF modules designed for SMF fiber [20]. The experiment transmitted one 10 Gbps NRZ channel at 1557.6 nm over 25 passes through a recirculating loop containing a 89.9-km span of SMF with DCF dispersion compensation, for a total distance of 2245 km. The loop contained 3 single-stage EDFAs: one before the SMF span, one before the DCF module, and one after the DCF module. The residual dispersion of the entire loop was +45.7 ps/nm. With a dispersion of -1505 ps/nm and a loss of 9.2 dB, the FOM of the DCM module was 163. The authors measured the achievable transmission distance with a BER of at least 10^{-9} for optical power levels into the DCF ranging from -9 to +3 dBm, and found the optimum level to be -2.4 dBm. Although the power level into the SMF spans was +8.2 dB, the system performance was notably degraded for power levels higher than

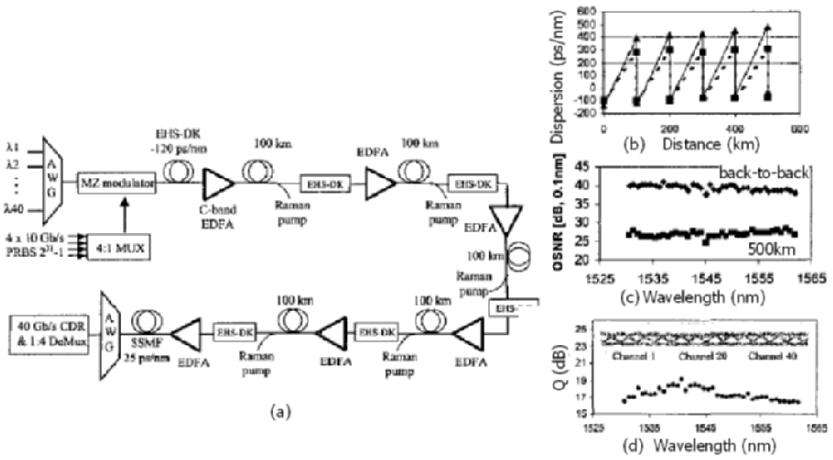

Fig. 1. Ultra-high slope DCF for compensation of TrueWave-RS$^{\mathrm{TM}}$ fiber, demonstrated in 40 $\times$ 40 Gbps WDM transmission over five 100 km spans with hybrid EDFA/Raman amplification. (a) Experimental diagram, (b) dispersion map versus distance for longest and shortest wavelengths, (c) OSNR and (d) Q of all channels after 500 km transmission.

only +1 dBm into the DCF, emphasizing the high optical nonlinearity of 1995-vintage DCF compared to SMF. If the two EDFA stages surrounding the DCF and the DCF itself are considered as a single "dual-stage EDFA" that compensates for the SMF span loss, there is a design trade-off between the noise figure of the EDFA (high first-stage gain) and the power into the DCF (lower first stage gain).

There is a very brief window in the literature between the development of slope-matched DCF fibers for NZDSF and the transition of most ultra-longhaul (ULH) transmission experiments to all-Raman amplification with Raman pumped DCF, the topic of the next section. In 2002, L. Leng et al. from OFS transmitted 40 $\times$ 40 Gbps over 500 km of TrueWave-RS$^{\mathrm{TM}}$ fiber using newly developed "extra-high slope dispersion compensators", or EHS-DK in Danish [21]. The experiment, shown in Fig. 1(a), used Raman amplification of the spans with EDFA post-amps to compensate for the DCF loss. The accumulation of dispersion versus distance, or dispersion map, is shown in Fig. 1(b) for the longest (1561.8 nm) and shortest (1530.7 nm) wavelength. The small amount of variation between the two maps indicates small dispersion slope error between the NZDSF fiber and the EHS-DK DCF modules across the C-band. The dispersion slope match was sufficient so that the 40 Gbps channels required no per-channel or per-band dispersion optimization at the receiver. For all channels, the OSNR was better than 26 dB and Q was better than 16.4 dB (2.4×10^{-11} BER). Note that this experiment narrowly predates the presumption of forward error correction (FEC) in WDM experiments, and so used 40 Gbps channels rather than 43.7 Gbps, and presumed the traditional 10^{-9} "acceptable" bit error rate.

2.1. Raman-Amplified DCF Modules

For multi-span WDM systems, DCF has traditionally been placed between the stages of a two-stage EDFA optical amplifier. This reduces the impact of the DCF insertion loss on the system noise accumulation, but can increase both the cost and complexity of the amplifier. The small effective mode area of DCF suggests the transformation of the DCF module into a Raman amplifier as proposed by Hansen et al. in 1998 [22], since Raman gain is proportional to power density in the optical fiber mode, and power density increases with decreasing mode area. Achieving flat gain across a 35-nm window requires a set of pump wavelengths at about 100 nm shorter wavelength, with the number of pump wavelengths determined by the required gain flatness. To date, Raman-amplified DCF has primarily been used to facilitate high spectral efficiency hero experiments, although there are commercial WDM systems available with all-Raman amplification using Raman-amplified DCF.

Figure 2 illustrates a C-band Raman-pumped DCF design from Emori et al. in 1998 [23], with four pumps ranging from 1435 to 1480 nm. In effect, Raman-pumped DCF modules transfer the cost of amplification from an EDFA post-amp to the Raman-DCF itself, with the cost savings determined by the relative pump laser costs. Raman-amplified DCF modules, or "DCA" modules, are commercially available commercially with the required pump lasers and control electronics integrated within the center of the DCF spool for effectively loss-less dispersion compensation in the same footprint as the original DCF module. DCA modules are perhaps most attractive for all-Raman amplified systems, where the optical bandwidth of the system is limited only by the number of Raman pump wavelengths (rather than the EDFA gain bandwidth), the range of acceptable dispersion slope matching between the transmission fiber and the DCF fiber, and the most mundane and practical consideration, the availability of optical components.

T. Miyamoto et al. from Sumitomo Electric in 2002 demonstrated a DCA module that was dispersion slope-matched to 50 km of SMF fiber over 100-nm of optical bandwidth in the C+L window [24], sufficient for 130 WDM wavelengths spaced by 100 GHz. The DCA produced sufficient gain to compensate for the loss of both the 50-km SMF fiber span and the DCF fiber of the module itself, thus completely replacing the per-span EDFA. The noise figure of the DCA was not explicitly noted, but the OSNR of wavelengths measured after transmission through 49 km of SMF and the DCA module varied from 34.5 to 39.3 dB, indicating a fairly high 4.8 dB variation in noise figure. The variation in optical gain across the 100-nm bandwidth was 2.5 dB using pump lasers with five different wavelengths, and could be reduced to the 0.5 dB value typical of gain-flattened EDFA amplifiers by using nine pump wavelengths.

In 2001, Bissessur et al. from Alcatel used distributed Raman amplification in both TeraLightTM fiber and slope-matched DCF in an experiment with eighty 40 Gbps channels spaced at 50 GHz within the C-band [25]. There were many advanced transmission technologies facilitating this result, including a "Phase-Shaped Binary Transmission", or PSBT, modulation format to limit the 40-Gbps signal bandwidth to allow 50 GHz channel spacing. The Raman amplification and Raman-pumped DCF were used primarily for OSNR advantage. Figure 3 below illustrates the testbed configuration and the results from this experiment. The span configuration includes both Raman and EDFA amplification. Figure 3(c) shows best and worst BER results, referring to the four 10 Gbps electrical tributaries that were measured for each 40 Gbps

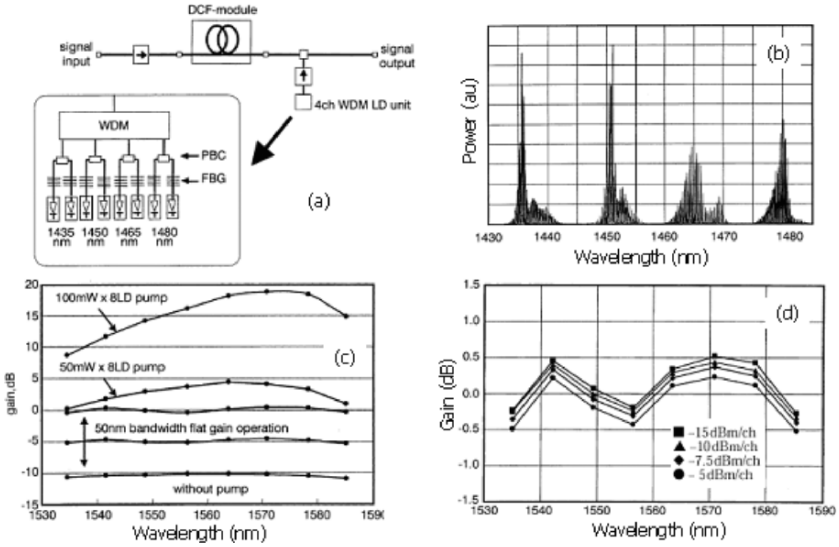

Fig. 2. From Emori et al. [23] in 1998, a Raman pumped DCF with four pump wavelengths: (a) module schematic, (b) pump wavelength spectra, (c) C-band gain shape for increasing pump levels with flat response at 0 dB gain or "lossless operation", and (d) gain shape at "lossless" condition over 10 dB range of input powers.

optical signal. For data rates higher than available test equipment, signals are electrically demultiplexed to lower rates for BER testing and the BER of all tributaries recorded. For this experiment, all tributaries of all eighty channels were better than 10^{-8} BER. Figure 3(d) and (e) indicate that the PSBT format provides tolerance to both residual dispersion and receiver filter alignment. The allowable dispersion variation for one decade of BER degradation is 120 ps/nm, compared to 65 ps/nm for NRZ modulation.

A 2003 experiment from L. Leng et al. from OFS [2.22] used distributed Raman amplification in both the transmission spans and DCF modules to transmitted 160 $\times$ 10.7 Gbps RZ over 4000 km in the L-band with 25 GHz channel spacing. The authors note that in systems with channels spaced this tightly, fiber nonlinearities such as cross-phase modulation (CPM or XPM) and four-wave mixing (FWM) are dramatically elevated. Minimizing the system impairment from these effects requires careful design tradeoff between accumulated optical noise (OSNR) and fiber nonlinearities. With distributed Raman amplification, the optical signals undergo relatively uniform power evolution in the transmission fiber and DCF, in this case from -8.5 dBm/ch at the span input to 10.5 dBm/ch at the span output. This reduces the wide optical power level swings inherent in systems with lumped amplifiers, whether EDFA or Raman, minimizing both nonlinearity impairment from the high power locations and noise accumulation from the low power locations." The higher fiber dispersion in the L-band operation compared to the C-band is also advantageous for systems limited by nonlinear impairment.

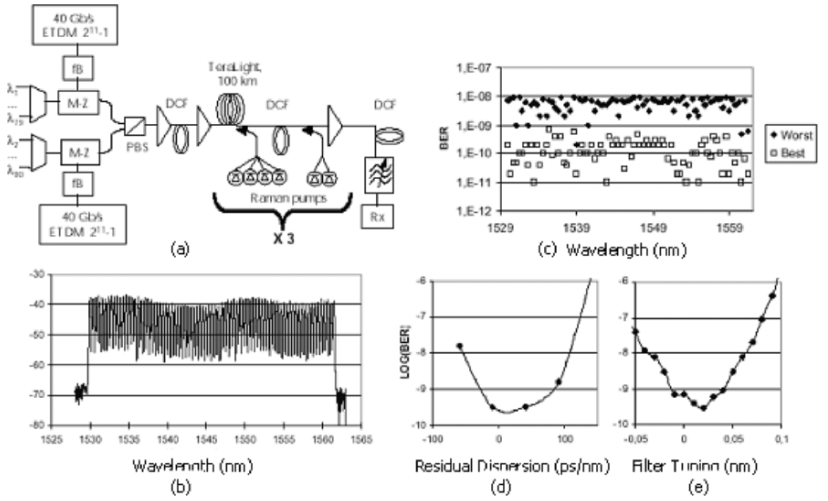

Fig. 3. High-spectral efficiency transmission of 80 × 40 Gbps over 300 km with Raman-pumped DCF by H. Bissessur et al. from Alcatel [251], (a) testbed configuration, (b) optical spectrum and (c) BER of 80 channels after transmission, and tolerance to (d) residual dispersion and (e) receiver filter detuning.

The recirculating loop in this experiment contained four 100-km spans of TrueWave-Reach$^{\mathrm{TM}}$ fiber, a medium-dispersion fiber with low dispersion slope, with corresponding slope-matched DCF modules for spans with residual dispersion variation of only 2 ps/nm over 33 nm. The TW-Reach$^{\mathrm{TM}}$ spans were forward and reverse Raman pumped at 1465 and 1496 nm, and the DCF modules were reverse-pumped at 1460, 1478, and 1503 nm, as illustrated in the span configuration of Fig. 4(a). The "medium-dispersion" fiber types have an advantage for Raman amplification over earlier generations of NZDSF fiber in that the dispersion zero is at a shorter wavelength outside the 1400–1480 nm range of the required Raman pump lasers for C- and L-band operation so that there is less pump-to-pump [27] and pump-to-signal [2.24] four-wave mixing. Figure 4(b) shows the gain distribution across the L-band from the co- and counter-propagating span amplification and from the DCF amplification, and the total gain. A gain equalizer was required in the loop to compensate for the accumulated gain variation because of the low number of Raman pump wavelengths. Figure 4(d) indicates fairly uniform OSNR across the channels, with lower OSNR at short wavelengths. In Fig. 4(c), all channels in the experiment performed better than 10^{-4} BER, acceptable for operation with the assumed 7%-overhead FEC. There is a similar wavelength dependence between the OSNR and Q measurements, indicating that the short wavelength channels with higher error rates may be OSNR limited.

In the previous experiment, the OSNR of the weakest channel after 4000 km was 14.4 dB. To illustrate the noise benefit of distributed Raman amplification, consider a similar system based on 2-stage EDFAs with a typical 7 dB noise figure. For 40 spans with 22.5 dB loss and a 8.2-dBm span input power, the OSNR would a mere 4

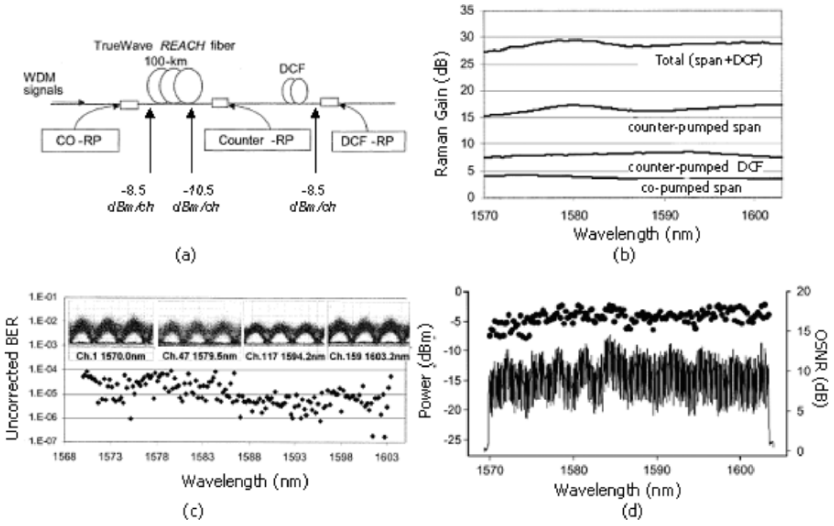

Fig. 4. (a) Span configuration for Leng et al. [26] with co- and counter-pumping of NZDSF fiber span and counter-pumping of DCF module, indicating per-channel power at the span input and output and the DCF output, and (b) resulting gain contributions across the L-band. (c) Uncorrected (Pre-FEC decoding) error rates better than 10^{-4} and (d) OSNR better than 14.4 dB over all channels.

dB according to Eq. (1). To produce a workable EDFA-based system, the reach might have to be reduced to 8 spans (800 versus 4000 km for all-Raman) and the launch power increased to 5 dBm/ch to maintain a 15-dB OSNR with acceptable nonlinear performance.

A 2004 experiment from the OFS group [29] used the same four-span loop configuration to achieve a record capacity-distance result transmitting 160 $\times$ 42.7 Gbps over 3200 km using the C-band and L-band. The Raman span amplification in this case used eight pump wavelengths, and the DCF modules were reverse-pumped with four wavelengths. The gain variation across the C and L bands was 2.3 dB per span, requiring gain equalization every four spans. Although Raman gain can be designed to continuously cover the C+L-bands, gain equalization in the loop required separate C- and L-band gain equalizers and EDFA post-amps with filters to separate the two bands, reflecting the difficulty in designing systems using non-standard optical bandwidth with available standard components. There were many advanced transmission technologies in this result besides the Raman amplification, including CSRZ-DPSK modulation, optimal optical bandwidth filtering to allow 50-GHz channel spacing of 40-Gbps channels, and adjacent channel polarization-interleaving at the transmitter, tunable per-channel dispersion compensation and balanced detection at the receiver, and careful fiber span dispersion management.

There is an important price/performance design tradeoff in Raman amplification, as pump lasers dominate the price of a Raman amplifier. The DCA gain shape is determined by the pump wavelength distribution, so the gain variation of concatenated

modules can add up linearly. After 5 fiber spans using DCA modules with 0.5 or 2.3 dB gain flatness, for instance, the accumulated power variation across the WDM channels without additional gain equalization devices could be as high as 2.5 or 11.5 dB, respectively. The maximum length of a transmission system containing many DCA modules could then be limited by the OSNR of the low-gain channels or the nonlinear impairment of the high-gain channels. Uniformity in optical power level and dispersion map for all channels is an important principal for designing high-channel-count, ultra-longhaul WDM systems, so it would be important in that application to use DCA modules producing the higher gain uniformity spec of perhaps 0.5 dB. In shorter extended-metro applications, the advantage in Raman-amplified DCF modules could lie more in cost reduction by elimination of additional EDFA amplification stages, and the combination of few pumps and higher gain variation might be acceptable.

3. Dispersion-Managed Fiber Spans

3.1. Evolution of Single-Mode Transmission Fiber

Since dispersion-managed fiber is more aptly described as the latest evolution of the transmission fiber industry rather than a dispersion compensation device, it will be useful to first briefly review the evolution of singlemode fiber types. The optical fiber vendors have achieved significant advancements in single-mode fiber technology over the last ten years. These efforts have largely been aimed at developing a fiber with the optimum chromatic dispersion-versus-wavelength characteristics while causing minimal degradation to other fiber properties. It has gradually been realized that the dispersion characteristics of optical transmission fiber are an integral part of the DWDM system design, not merely an annoying side effect to be eliminated. The general perception of "optimal" for C-band operation has changed over the years, shifting from the original value of 16–17 ps/nm/km for SMF at 1550 nm to 0 ps/nm/km for dispersion shifted fiber (DSF), and then slowly increasing back up from 2–4 ps/nm/km (TrueWave Classic$^{\mathrm{TM}}$, LEAF$^{\mathrm{TM}}$, LS$^{\mathrm{TM}}$) to 5 ps/nm/km (TrueWave RS$^{\mathrm{TM}}$, ELEAF$^{\mathrm{TM}}$) towards 7–8 ps/nm/km in some current releases (TrueWave Reach$^{\mathrm{TM}}$, TeraLight$^{\mathrm{TM}}$).

Fiber development in the early 1990s focused on total elimination of the cost and insertion loss of discrete dispersion compensation modules. "Dispersion shifted fiber" (DSF) with D =0 ps/nm/km at 1550 nm was designed and deployed to allow single-channel, multi-span 10-Gbps transmission without dispersion compensation. The advent of WDM led rapidly to the discovery of four-wave mixing (FWM) between channels in early experiments, an effect that strongly limited the acceptable optical power levels in the fiber and thus the OSNR of a transmission system. Increasing the fiber dispersion increased the phase difference between adjacent channels to reduce the FWM efficiency, which led to early "non-zero" dispersion shifted fibers (NZDSF) such as positive TrueWave Classic? (P-TWC) with +2 ps/nm/km and negative TrueWave Classic$^{\mathrm{TM}}$ (N-TWC) with -2 ps/nm/km. The desire to operate with smaller channel spacing and at higher optical power levels has gradually led to the continually increasing of most NZDSF fiber dispersion values to "medium" dispersion levels of about 7 ps/nm/km. At the same time, great effort has gone into reduction of the dispersion slope of NZDSF for more uniform dispersion across the WDM channels and for easier DCF-for-NZDSF fiber designs with the correct amount of negative slope.

For instance, TrueWave-RS^{TM} stands for "reduced slope". It is interesting to notice that although NZDSF fiber was originally marketed to be less expensive to dispersion compensate because of the lower fiber dispersion, dispersion compensators for 100 km of either NZDSF or SMF are currently available for about the same price.

As a result of this rapid fiber development, a wide variety of single-mode fiber types have been deployed in significant quantities in fiber networks around the world. Some of the fiber types currently in the ground include standard single-mode fiber, dispersion-shifted fiber, and the many types of non-zero dispersion shifted fibers (NZDSF), including but not limited to several generations of TrueWave^{TM} from OFS (formerly Lucent); LS^{TM}, LEAF^{TM} and ELEAF^{TM} from Corning; and TeraLight? from Draka (formerly Alcatel).

3.2. Dispersion Managed Cable

Rather than deploying a single type of transmission fiber and adding periodic units of negative-dispersion with additional amplification at amplifier sites, transmission fiber can be deployed with alternating sections of positive and negative dispersion to produce fiber spans with average dispersion that is low, but not too low to suppress FWM [30]. This is often referred to as "Dispersion Managed Cable" (DMC), and can eliminate the cost and loss of the lumped dispersion compensation modules. The development of DCF modules for most NZDSF types slowed work in the DMC area from 2001–2003. However, there has been a renewed interest in DMC for more efficient all-Raman amplification to maximize system OSNR for 40-Gbps applications.

There has been extensive work on negative dispersion fiber designs for transmission spans, as opposed to for DCF modules, with optimum design tradeoffs between magnitude of dispersion and good "cabling qualities" [31]. The effective area and insertion loss of "inverse dispersion fiber" (IDF) designs improve as the dispersion per kilometer is reduced, but are never as good as positive dispersion fibers, so there is an optimal ratio between positive and negative fiber dispersion values that produces the best overall span performance [32]. There have been many proposed fiber pairs ranging widely in fiber dispersion values and dispersion map period, as demonstrated by a partial listing of DMC research results in Table 1. Reference [35], for example, used 47 km spans consisting of 40 km of fiber with +18 ps/nm/km dispersion and 7 km of –90 ps/nm/km fiber. The positive-dispersion fiber generally has a higher effective area, and is therefore placed at the span input where the power level is the highest.

3.3. Submarine Dispersion Managed Cable

DMC is a very common dispersion compensation technique in the submarine system industry. All electrical power to the underwater WDM system to run the optical amplifier sites is supplied from the shoreline, so that minimizing the total insertion loss and therefore the power consumption of the optical amplifiers is crucial [37]. In submarine WDM systems, there is no separation between the fiber selection process and transmission system design process, because the entire system including transmission fiber, amplification and dispersion compensation is designed as a holistic entity and then dropped into the ocean. The system designer always has complete control over the amplifier spacing and the dispersion map, with no consideration of non-optical details such as real estate taxes when placing amplifier huts.

Table 1. Examples of DMC experiments, with characteristics of the two fiber types and span configurations for each example.

Ref.	Year	Company/ Fiber Name	Dispersion (ps/nm/km)	A_{eff} (μm^2)	Dispersion Period (km)	Span (km)	Ch. Count	Rate (Gbps)	Dist. (km)
[33]	1996	Lucent/AT&T	+2.3 / –2.3	35/35	80P+80N	80	8	10.0	200
[34]	1999	Corning LEAF/ SubLS$^{\text{TM}}$	+4 / –4	72/55	45P+45N	90	32	10.0	450
[35]	1999	KDD	+18 / –90	–	40P+7N	47	32	10.0	7,280
[30]	2000	Kaist	+17 / –15	80/65	4.5P+4.5N	63	32	10.0	564
[36]	2001	PerfectCable$^{\text{TM}}$	+17 / –15	80/65	4.5P+4.5N	63	32	20.0	280
[37]	2001	NEC	+20 / –63	106/19	18P+6N 9P+3N	48	5	40.0	2,400
[38]	2002	NEC	+20 / –63	106/19	18P+6N 9P+3N	48	32	42.7	6,050
[39]	2001	Alcatel Teralight$^{\text{TM}}$	+8 / –16	65/25	27P+13L	40	32	40.0	2,400
[40]	2004	Mintera UltraWave$^{\text{TM}}$	+20 / –45	107/31	35P+30N+35P	100	40	40.0	10,000

Early 5 and 10 Gbps WDM transmission systems for submarine deployment used dispersion managed fiber spans typically consisting of a negative NZDSF fiber (N-NZDSF, $D = -2$ ps/nm/km at 1550 nm) with negative dispersion and standard SMF (D =+17 ps/nm/km at 1550 nm). In 1995, Bergano et al. from AT&T Bell Labs, now Tyco Submarine, reported the transmission of eight WDM channels at 5 Gbps over 8000 km using a dispersion map with nine 100-km spans of N-NZDSF fiber followed by a single 100-km span of SMF fiber [41]. This map does not compensate for dispersion slope, so the accumulated dispersion of the N-NZDSF fiber is only accurately compensated at the center of the wavelength band. Since submarine systems tend to operate in the "linear propagation" regime with low optical power levels to conserve electrical power, it is acceptable to use such a low-periodicity dispersion map and to trim the dispersion values at the receiver with short lengths of SMF or N-NZDSF fiber as required. Terrestrial systems, on the other hand, tend to operate in the "nonlinear propagation regime" with higher optical power levels to take advantage of beneficial nonlinear transmission effects, and therefore require more-frequent compensation with slope compensation to maintain well-controlled residual dispersion levels throughout the transmission system [42].

In 1999, Tanaka et al. from KDD Labs demonstrated the transmission of thirty-two channels at 10.7 Gbps over a 7280-km "trans-oceanic distance" using a pair of fiber types with much higher magnitude of dispersion. The 47-km fiber spans consisted of 40 km of standard SMF (D =+18 ps/nm/km, slope = +0.06 ps/nm^2/km) and 7 km of a fiber with large negative dispersion and dispersion slope that was referred to as "SCDCF" (D =90 ps/nm/km, slope = –0.03 ps/nm^2/km) to produce a "dispersion flattened fibre link" [37]. The relatively short span lengths indicate that this experiment emulates a submarine application, because submarine systems use short amplifier spacings to reduce the optical noise accumulation and facilitate such long transmission distances. The high dispersion values of the two fiber types are described as "quite attractive because the high dispersion and large effective area of SMF enable a reduction in nonlinear effects such as four-wave mixing and cross-phase modulation to be obtained." Notice that experiments running at odd data rates such at 10.7, 11.5,

12.5, or 43 Gbps are operating at an increased data rate to allow for the overhead requirements of forward error correction encoding schemes. The actual capacity of the channel should be accounted for as 10 or 40 Gbps, as the overhead bits are not available to the user, so this 32 × 10.7 Gbps experiment has a total capacity of 320 Gbps.

In 2001, Alcatel proposed a dispersion-slope matched dispersion-managed cable for submarine applications with 40 km spans consisting of 27 km of TeraLight$^{\mathrm{TM}}$ (D =+8 ps/nm/km and slope = +0.058 ps/nm^2/km at 1550 nm, 65 μm^2 effective area) followed by 13 km of Reverse TeraLight$^{\mathrm{TM}}$ ($D = -16$ ps/nm/km and slope = 0.116 ps/nm^2/km at 1550 nm, 25 μm^2 effective area) [3.10]. This fiber pair was demonstrated in the WDM transmission of 32 × 40 Gbps RZ signals over 2400 km with error rates between 2×10^{-5} and 8×10^{-5} in a recirculating loop containing seven Raman-pumped 40-km dispersion managed span, a dynamic gain equalizer, and one 20-km Teralight$^{\mathrm{TM}}$ span to under-compensate the total loop dispersion. The authors claim that the improved OSNR and control of optical nonlinearities from Raman-only amplification and dispersion managed spans allowed them to break both the maximum aggregate capacity and transmission distance records for submarine 40-Gbps WDM systems.

Recent submarine work from most groups has used the UltraWave$^{\mathrm{TM}}$ pair of dispersion and dispersion-slope matched fibers from OFS, whether or not it is specifically referred to as such in the publications, so we will only mention a few examples. UltraWave$^{\mathrm{TM}}$ consists of a "super-large effective area" or SLA fiber (+20 ps/nm/km dispersion, +0.06 ps/nm^2/km slope, 107 μm^2 effective area for C-band) and an "inverse dispersion fiber" or IDF (–45 ps/nm km dispersion, −0.12 ps/nm^2/km slope, 31 μm^2 effective area for C-band) [46]. The details of UltraWave$^{\mathrm{TM}}$ will be discussed further below with terrestrial experiments. In 2003, J.-X. Cai et al. from Tyco Submarine used 25 km UltraWave$^{\mathrm{TM}}$ spans in the transmission of 373 × 12.3 Gbps over 11,000 km using hybrid EDFA+Raman amplification in the C+L-Band, 25 GHz channel spacing and RZ-DPSK modulation [43]. In 2004, Turitani et al. from KDDI transmitted 40 × 42.7 Gbps over the "trans-Pacific" distance of 9400 km in a 16-span loop with "submarine-length" 43.5-km dispersion-managed spans of UltraWave$^{\mathrm{TM}}$ fiber [44]. Discussion in the paper focuses on the maximum acceptable level of channel bandwidth pre-filtering of the CSRZ-DPSK signals to reduce inter-channel nonlinear interaction among the 70-GHz-spaced channels while not introducing intolerable levels of signal distortion to produce a system with maximal spectral efficiency. In 2005, Charlet et al. from Alcatel used 65 km UltraWave$^{\mathrm{TM}}$ spans in an experiment comparing the performance of DPSK modulation at 40 Gbps with and without an RZ pulse-carving stage in the transmission of 6 Tbps (149 × 42.7 Gbps) over 6120 km using the C+L-band and all-Raman amplification at 50 GHz channel spacing [45]. The paper concluded that there was no performance benefit from the addition of RZ modulation to the DPSK signal for 40 Gbps channels at 50 GHz channel spacing, allowing for lower cost transponders.

3.4. Terrestrial Dispersion Managed Cable

As an early example of terrestrial DMC, in 1996 a Lucent/AT&T group used alternating fiber spans with either 80 km of Positive-TrueWave (PTW, + 2.3 ps/nm/km at 1550 nm) or 80 km of Negative TrueWave (NTW, 2.3 ps/nm/km at 1550 nm) to demonstrate long-haul transmission of eight channels modulated at 10 Gbps over 2000 km with 200 GHz

channel spacing in a straight line (non-recirculating loop) experiment [33]. There was a strong economic advantage to dispersion managed spans in this application, because single-fiber NZDSF spans would have required twenty DCF modules for NZDSF fiber, if such things had been available at the time, and twenty additional early "home-built" EDFAs to compensate for the DCF loss. The average dispersion in the PTW/NTW spans was quite low and the optical power levels into the fiber spans were limited by FWM, predicting the increasing dispersion of later NZDSF designs. Both fiber types had positive dispersion slope, so the maximum transmission distance was influenced by the accumulated dispersion compensation error of the edge channels.

Management of the fiber cable installation process can be more complex for terrestrial deployment of dispersion managed fiber spans, as the installation crew keeps track of placing positive and negative fiber types in the correct locations. In 2000, Chung et al. from Kaist and LG Cable proposed a dispersion managed cable consisting of alternating 4.5 km sections of +17ps/nm and −15ps/nm fiber, both with an effective area of 80 μm^2 [30]. The short map period was chosen so that one standard 9 km deployment cable could contain one complete dispersion map period for field installation requiring only a single cable type rather than requiring separate positive dispersion and negative dispersion cables. Calculations by the authors show that a map period greater than 3km is required with these fiber dispersion levels to maintain an adequate "average dispersion" to suppress four wave mixing for 50-GHz spaced channels. The authors demonstrated WDM transmission of 32 × 20 Gbps channels spaced at 50 GHz over 564 km with an average Q of 18dB (10 15 BER) in a recirculating loop containing two 70 km spans of this "PerfectCable^{TM}?" with no additional dispersion compensation. The authors compared this result to a 160-km recirculating loop containing two 80-km spans of NZDSF fiber using DCF for dispersion compensation, and found that the BER of many channels in the NZDSF system were unmeasurably poor after only 480 km.

3.5. Dispersion Managed Cable for Raman Amplification

Recent DMC work for terrestrial applications has focused on the optimization of DMC for distributed Raman amplification in applications at 40 Gbps and above, using a three-segment map with a small effective area negative-dispersion fiber in the center of each span to shape the Raman gain distribution and improve the noise figure of the span [46]. The OFS Ultrawave^{TM} fiber pair dominates most experimental work in this area. UltraWave^{TM} consists of a "super-large effective area" or SLA fiber (+20 ps/nm/km dispersion, +0.06 ps/nm^2/km slope, 107 μm^2 effective area for C-band) and an "inverse dispersion fiber" or IDF (45 ps/nm km dispersion, –0.12 ps/nm^2/km slope, 31 μm^2 effective area for C-band) [3.17]. UltraWaveTM spans for terrestrial experiments are typically configured with identical lengths of SLA fiber separated by a section of IDF with the appropriate length to provide the desired residual dispersion, for example (35 km SLA: 30 km IDF: 35 km SLA) to produce a 100 km span with a residual dispersion of +50 ps/nm.

When used in systems with all-Raman amplification using bi-directional pumping of the spans, the SLA fiber provides low nonlinearity transmission where the signal power levels are high at the Raman pump launch points. The IDF fiber provides higher Raman gain efficiency at the span midpoint, where signal power levels are lowest. This distribution of optical gain throughout the span produces lower noise figures and therefore higher OSNR values than lumped EDFA amplification, a key enabler for

WDM transmission using 40 Gbps and higher modulation rates. At these high rates, transmission penalties from nonlinear interaction both between channels (inter-channel interaction) and between pulses in a single channel (intra-channel interaction) are more significant, and the quality of transmitter and receiver components are at present lower than 10 Gbps components, so any improvement in system margin from amplifier noise reduction is extremely valuable in designing a system for a given capacity and reach. In a situation analogous to 2.5 Gbps channels generally not requiring dispersion compensation for distances of commercial interest, 10 Gbps channels generally do not require the noise advantage of Raman-pumped dispersion managed cable.

Table 2 summarizes many of the terrestrial transmission experiments with UltraWaveTM dispersion managed spans. After two 10-Gbps experiments in 2001, work in this area focused on maximizing the transmission distance for forty C-band 40-Gbps signals, with 10,000 km the record to date.

Table 2. Selected examples of experiments with UltraWave$^{\mathrm{TM}}$ dispersion managed fiber spans. Shaded experiments indicate 40 $\times$ 42.7 Gbps experiments with progressively increasing transmission distance. Hybrid amplifier configurations use both EDFA and Raman amplification. The fiber span length is 100 km for all experiments.

Ref	Year	Author	Channel Count	Rate (Gbps)	Distance (km)	Format	$\Delta\lambda$ (GHz)	Ampl. Config.
[46]	2001	Knudsen	42	10.0	4,000	RZ	50	Raman
[47]	2001	Zhu	80	10.7	5,200	RZ	50	Hybrid
[48]	2001	Zhu	40	42.7	2,000	CS-RZ	100	Hybrid
[49]	2002	Liu	40	42.7	3,600	CS-RZ	100	Raman
[50]	2002	Rassmussen	40	42.7	5,200	CSRZ-DPSK	100	Raman
[51]	2003	Zhu	40	42.7	6,000	RZ-DPSK	100	Raman
[52]	2004	Rassmussen	40	42.7	10,000	CSRZ-DPSK	100	Raman
[53]	2003	Gupta	40	80.0	2,100	NRZ-Pol. Int.	100	Raman

In one of the earliest UltraWave$^{\mathrm{TM}}$ demonstrations in 2001, Knudsen et al. from OFS demonstrated WDM transmission of 42 $\times$ 10 Gbps RZ channels spaced at 50 GHz over 4000 km in a recirculating loop with four all-Raman amplified 100 km fiber spans [46]. The 100 km spans consisted of 27 km SLA, 35 km IDF, and 38 km SLA as Fig. 5(a), corresponding to about 100 ps/nm residual span dispersion. The spans were counter-pumped only, using a single pump wavelength at 1450 nm with 630 mW output power to overcome 23.6 dB of average span loss. Figure 5(b) shows that after every four spans, an additional lumped Raman amplifier containing 25.5 km of SLA brought the residual loop dispersion to +100 ps/nm, and a dynamic gain equalizer followed by an EDFA cleaned up the channel power distribution due to the single pump. As mentioned with Raman-pumped DCF, there is a system design tradeoff in Raman amplified systems between the cost of additional gain equalization equipment or the cost of additional Raman pump wavelengths for more uniform Raman gain over the amplifier bandwidth. The authors noted that the number of channels was limited to 40 (16.5 nm optical bandwidth, equivalent to half the C-band) by the gain equalization issues related to the single pump wavelength, with high-power channels performance-limited by cross-phase modulation and low power channels performance-limited by low OSNR. The use of dispersion-managed spans in this experiment did not eliminate the requirement for lumped dispersion compensation, but did reduce

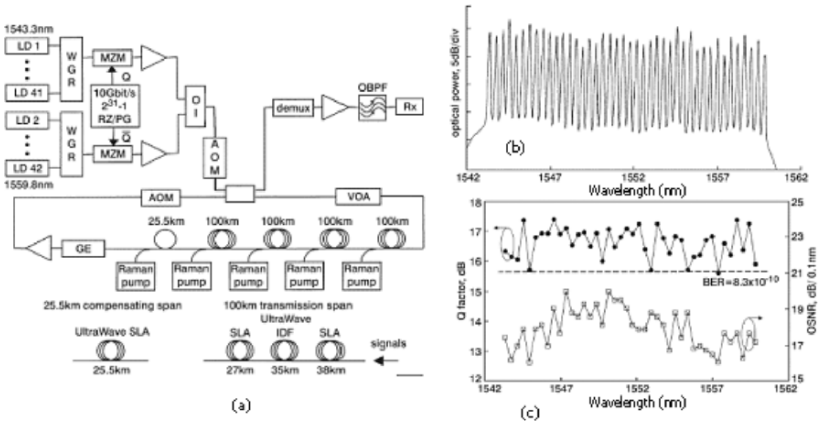

Fig. 5. (a) Recirculating loop configuration including 100 km span configuration, and (b) optical spectrum in 0.1 nm and (c) BER and OSNR for 42 $\times$ 10 Gbps transmission over 4000 km from Knudsen et al. [46].

the number of modules by a factor of four. The authors also note that no additional broadband post-compensation or tunable compensation was required at the receiver, and that the dispersion slope match between the SLA and IDF was sufficient to enable transmission in the full C- and L-bands over this distance.

Later in 2001, this work was extended to double the capacity to 80 channels spaced at 50 GHz [44]. At the same time, the system length was extended from 4000 to 5200 km, a non-intuitive result. This experiment used of hybrid Raman+EDFA amplifiers rather than all-Raman amplification. Power equalization is critical for 50-GHz spaced channels, where the penalty from nonlinear crosstalk is inherently larger than for 100-GHz channels, and the all-Raman approach suffered from gain equalization issues. The hybrid Raman + EDFA amplifiers allowed gain-flattening filters to be placed within each EDFA stage for improved uniformity of optical power levels. This experiment was also performed with the additional advantage of FEC encoding, so the channels were transmitted at 10.7 Gbps indicating the use of a typically FEC with 7% overhead and 7 dB "code gain". The minimum required pre-FEC performance to produce $Q >$ 16.95 dB (BER = 1e-12) after FEC decoding was unspecified but was less than the author's weakest channel of $Q = 11.4$ dB (BER = 9.7e-5). One can see that using $Q >$11.4dB rather than $Q >$15.6 dB as a performance cutoff will significantly enhance the achievable transmission distance. There was a significant jump in the performance of all WDM transmission experiments at about this time in history due to the widespread assumption of FEC-limited system bit error rates rather than the traditional 10^{-9} BER value.

In 2004, Rasmussen et al. from Mintera demonstrated WDM transmission of forty 40 Gbps CSRZ-DPSK channels spaced at 100 GHz over 10,000 km again using all-Raman amplified 100 km OFS UltraWave$^{\mathrm{TM}}$ fiber spans [40]. As can be seen by the long list of co-authors and acknowledgements, this experiment required many enabling technologies, of which dispersion-managed fiber spans were only one aspect.

To achieve this most impressive result, the SLA/IDF configuration of the four 100 km spans in the recirculating loop was carefully optimized by simulation. The authors found that the transmission penalty generally decreased with increasing absolute value of residual dispersion, and that the penalty generally decreased somewhat if the four spans were made non-identical, so that a "3+1" map was used with three spans with net dispersion of +121ps/nm and one span with net dispersion of 276 ps/nm. The resulting dispersion map points out some of the issues mentioned above for actual field deployment. Pre-deployed fiber spans would likely be designed for zero residual dispersion, requiring dispersion "trimmer" modules containing 6km of SLA or IDF to get +121 ps/nm or -276 ps/nm of dispersion compensation, respectively. Also, since access to the midpoint of the fiber spans for dispersion trimming is unlikely, placement of a trimmer based on the small effective-area IDF at the span endpoints rather than in the middle of the spans would be non-optimal from a nonlinear propagation point of view. It is worth noting that this system did require "conventional" dispersion compensators of about -1000 ps/nm at the transmit and receive end, presumably DCF although not explicitly mentioned, to compensate for the 25×100 ps/nm accumulated residual dispersion of the recirculating loop spans.

In 2003, Gupta et al. from Agere raised the channel data rate, demonstrated WDM transmission of forty 80-Gbps channels over 2100 km also using all-Raman amplified 100 km UltraWave$^{\mathrm{TM}}$ fiber spans [3.23]. In this case, the authors used a 300-km loop, containing three asymmetrical spans (50.5 km SLA, 34.5 km IDF, 15 km SLA) with a per-span residual dispersion of 100 ps/nm followed by a single lumped element of 15 km of SLA fiber to bring the loop dispersion to approximately 0 ps/nm residual dispersion. Note that the author's optimized dispersion map utilizes overcompensated spans, unlike the rule of thumb for 10 Gbps channels that advises spans with net-positive (under-compensated) residual dispersion when the dominant system nonlinearity is self-phase modulation. No pre-compensation was required at the transmitter, but at the receiver "net residual dispersion was compensated to near 0 ps/nm with short lengths of SLA or IDF fiber" despite the accuracy of the slope match between the SLA and IDF, reflecting the extremely small dispersion tolerance of 80-Gbps channels. In terms of an actual deployment, such asymmetric fiber spans would likely not be found pre-deployed in the ground, so that trimmer modules of IDF would be required for each span to produce the 100 ps/nm under-compensation. A single-channel tunable compensator such as a tunable chirped grating would likely also be required for optimizing the dispersion at the 80-Gbps receiver in a deployed system.

In the laboratory, scientists are using DMC spans to achieve truly remarkable 40 Gbps and above transmission results. These results have required careful dispersion map design, including a co-optimized group of specifications for pre- and post-compensation at the system endpoints and for the per-span dispersion. The net dispersion of each span is a key parameter in WDM system design that is adjusted based on data rate, modulation format, channel spacing, optical fiber type and even optical power levels. Deployment of fiber spans with the required dispersion accuracy will be more difficult for field installations. Design of 40-Gbps WDM systems for field deployed DMC will require either built in margin to allow for dispersion map imperfections from the fiber installation process, or careful dispersion trimming with short lengths of fiber at the amplifier sites. Of course, there is likewise a reasonably large tolerance on the dispersion of any installed fiber that must be either carefully measured in the field or allowed for in the system margin allocation for high-performance WDM systems.

Also, the dispersion slope match between the two fiber types in a DMC may be less accurate in the S-band or L-band than in the C-band, requiring dispersion trimming at the amplifier sites for non-C-band operation.

The widespread installation of new several-hundred fiber cables in the late 1990s ensures that the installed fiber base will consist largely of SMF and positive-dispersion NZDSF for the near future. The fiber manufacturers have heavily marketed DMC as a key enabler for 40 Gbps commercial DWDM systems. However, recall that we have also reviewed an impressive 160×42.7 Gbps (C+L band) over 3200 km result that used all-Raman pumping of TrueWave-ReachTM fiber spans with Raman-pumped, slope-matched DCF [24] in Section 2.2. The most business-effective choice for single versus multi-fiber spans for future fiber deployments may be more a matter of installation issues rather than raw performance considerations.

4. Higher-Order Mode Fiber Technology For Dispersion Compensation

It has been discussed above that the inherent design tradeoffs in DCF fiber design to produce large negative dispersion result in fibers with a small effective area and correspondingly high nonlinear coefficient. Dispersion compensators based on specialty few-mode fiber ("higher-order mode" or HOM fiber) use the larger effective area and high negative dispersion of higher-order fiber modes, typically the circularly symmetric LP_{02} mode, near cutoff to achieve negative dispersion and dispersion slope with a lower nonlinearity coefficient than DCF. C.D. Poole et al. from AT&T Bell Labs first demonstrated the HOM dispersion compensator concept in 1994 [53], but then there was little follow-up in the field until the late 1990s. At that point, a time lag between the development of new NZDSF transmission fibers and the development of appropriately dispersion slope-matched DCF fibers for 10 Gbps data spurred interest in new technologies capable of high relative dispersion slope (RDS), the ratio between slope and dispersion.

HOM-based dispersion compensation modules contain a pair of spatial mode converters to interface between the fundamental mode of single-mode fiber and the desired higher-order mode of the HOM fiber, as shown in Fig. 6(a). Mode converters have been implemented based on free-space bulk optics [54], long period fiber gratings [55], and even hollow optical fiber [115]. The conversion efficiency of the mode converters for HOM compensators must be very high to minimize multi-path interference (MPI) originating from light propagation in the fundamental mode of the HOM fiber. The HOM fiber itself must also be carefully designed and packaged to minimize distributed mode conversion during propagation within the HOM fiber itself. It has been reported that MPI values of less than 40 dB are required for ultra-longhaul transmission with cascaded HOM devices [56,57]. The accurate measurement of such low MPI values requires specialized techniques [58].

The primary advantages of HOM dispersion compensators are the high RDS values and the low optical nonlinearity. But there is also an opportunity for lower cost, lower insertion loss modules because significantly less HOM fiber is required than DCF fiber for a given amount of dispersion, assuming a cost-effective and low-loss mode converter design. However, high-slope DCF modules with RDS values matched to the various NZDSF fiber types eventually became commercially available, and commercial development of HOM compensators has again faded away as of early 2004 in the face

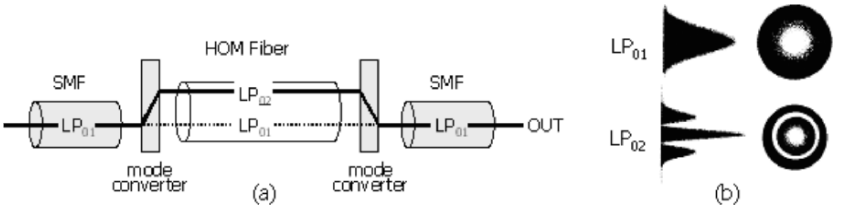

Fig. 6. Schematic diagram of higher-order mode dispersion compensator based on the circularly symmetric LP_{02} mode, and (b) mode profiles of the LP_{01} and LP_{02} modes [62].

of the constant performance improvement and sales volume-based price advantages of DCF products.

In 2000, A.H. Gnauck et al. from AT&T Labs demonstrated HOM modules developed by LaserComm that were designed to compensate for the dispersion and slope of 80 km of NZDSF fiber [54]. The insertion loss of the HOM modules ranged from 5.5 to 6.0 dB. To dispersion match TrueWave-Classic fiber spans with dispersion of 2.5 ps/nm/km and slope of 0.066 ps/nm^2/km, the HOM modules contained SMF "trim" fiber to produce an overall module RDS of 0.025/nm. The effective area of the HOM fiber was 70 μm^2, similar to SMF fiber and much larger than the 20 μm^2 of traditional DCF fibers. The MPI was less than 36 dB over the C-band. At the time of this experiment, DCF modules with full dispersion slope compensation were commercially available for SMF but were still in development for NZDSF fiber types because of the much larger required RDS (0.01 to 0.025 nm^{-1} for various NZDSF fibers versus 0.0034 nm^{-1} for SMF). The HOM modules were therefore compared to DCF modules with RDS of 0.002 nm^{-1} designed for SMF compensation. Dispersion slope compensation is especially critical for 40 Gbps WDM transmission because of the low residual dispersion tolerance at higher data rates and the high cost of per-channel tunable dispersion compensators for dispersion cleanup at each WDM receiver.

To demonstrate the performance of the HOM modules, a tunable 40-Gbps signal was transmitted through a three-span 240-km NZDSF link followed by dispersion compensation from either the three HOM modules or three non-slope-matched DCF modules, as in Fig. 7(a). The accumulated channel dispersion values at the system output relative to the 40 Gbps dispersion limit for each technology are shown in Fig. 7(b). The BER of the 40-Gbps signal was then measured for each compensator technology for laser wavelength settings ranging across the C-band from 1530 to 1560 nm, with resulting eye diagrams as in Fig. 7(c). A low optical power level was used to achieve linear transmission to allow the dispersion compensation to be lumped together with a single EDFA at the end of the system, since the +608 ps/nm dispersion of the 240 km NZDSF was so much greater than the 40 Gbps dispersion limit. With the slope-matched HOM compensators, referred to as DMDs or "dispersion management devices" by the authors, the Q of the 40 Gbps signal was greater than 16 dB across the entire C-band. For DCF compensators without dispersion slope compensation, the Q of the 40 Gbps signal was 18 dB at an optimum wavelength near 1542 nm, but was greater than 16 dB only over about a 4nm bandwidth because of the dispersion slope

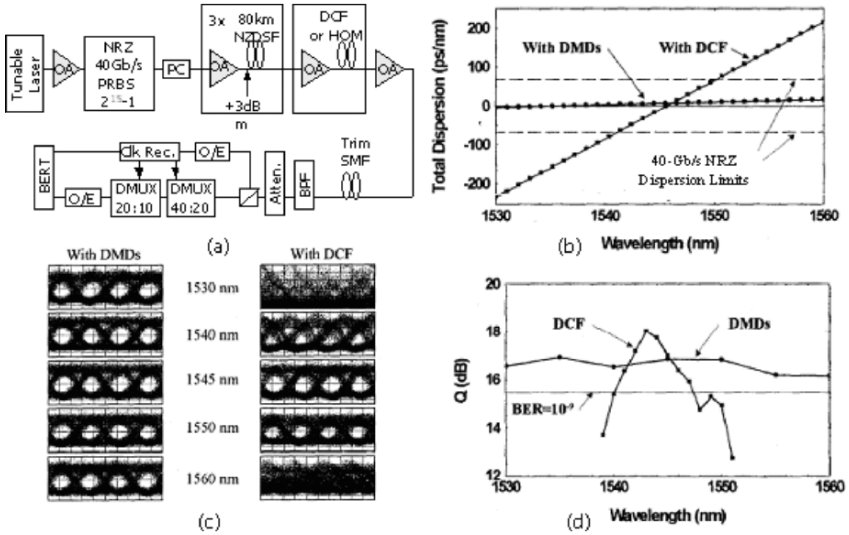

Fig. 7. From Gnauck et al. [54], (a) Experimental diagram, (b) dispersion map, (c) 40 Gbps eye diagrams and (d) measured Q-values across C-band for 240-km transmission with either slope-matched HOM compensators or non-matched DCF compensators.

mismatch between the DCF and the NZDSF transmission fiber. The maximum Q in the HOM measurement was lower than for the DCF measurement because of a total PMD of 8–10 ps for the 3 HOM modules. The authors claimed that the PMD was a side effect of the low volume experimental fiber fabrication process, and not inherent in the HOM technology.

In 2001, S. Ramachandran et al. from Lucent Bell Labs reported a slope-matched HOM compensator for 100 km of TrueWave Reduced Slope (TW-RS) NZDSF fiber with 1 ps PMD, 3.7 dB insertion loss, and effective mode area of 65 μm^2 [4.3]. Novel long-period fiber grating devices (LPGs) written in HOM fiber were used for mode conversion so that the entire module was fiber based, providing advantages of low insertion loss, compact packaging and high-yield manufacturability according to the authors. The LPGs provided better than 99% mode conversion producing an MPI of better than -42 dB with and insertion loss of 0.2 dB over a 30-nm window from 1520 to 1550 nm. The RDS of the HOM module with 2 km of HOM fiber was 0.008/nm, for 80% slope compensation of TW-RS with an RDS of 0.010/nm.

The Lucent authors compared the HOM compensator to a high-slope DCF module with RDS of 0.0065/nm. A tunable 40 Gbps 33%-dutycycle RZ signal was transmitted through the 100-km TW-RS span and either the HOM or DCF compensator, and the BER measured over a 20-nm wavelength range from 1530 to 1550 nm. There was no performance penalty after transmission for the HOM and DCF modules at the 1540 nm wavelength where the dispersion compensation was optimum for both devices. However, the DCF performance degraded more quickly away from the optimum wavelength because of the larger dispersion slope mismatch to the TW-RSTM fiber.

The authors next placed the 100-km fiber span and HOM compensator in a recirculating loop with EDFA amplification and a 4-dBm/ch power level at the HOM input, this time measuring only at 1550 nm with 40 Gbps 10%-dutycycle RZ modulation, and measured a BER penalty of 1 dB at 10^{-9} BER after 1000 km transmission distance. The authors state that to achieve this result without Raman amplification required the high power handling capability of the HOM compensator, but the actual OSNR for the measurement and an equivalent measurement using the DCF module were not provided.

Later in 2001, Ramachandran et al. extended their 1552.6 nm single-channel result from 1000 to 1700 km by adding 15 dB of reverse-pumped Raman gain to the 100 km fiber span [59], claiming the longest transmission distance to date on any fiber type with 100 km amplifier spacing at a data rate of 40 Gbit/s. The 5 dB receiver sensitivity penalty after 1700 km was attributed to both the 25-dB OSNR and to accumulated PMD from both the TW-RS$^{\mathrm{TM}}$ fiber (2.1 ps) and the HOM modules (4.1 ps). The authors reported that the power into the HOM module (PHOM) could be varied from 0 to +5 dBm without affecting the BER results, indicating the lack of nonlinear impairment in the devices. Without knowing the resulting change in OSNR with increasing PHOM, it is difficult to deduce whether the power-independent performance of the HOM modules implied that the improved OSNR with increased PHOM offset the increasing nonlinearity in the HOM module, or whether the performance penalty was independent of PHOM because it was dominated by another factor such as MPI or PMD. Results of BER penalty and OSNR versus distance rather than at a single distance would have clarified the dominant impairment in this experiment.

In 2002, commercial LaserComm HOM modules for LEAF dispersion and slope compensation were one enabling technology in a 10-Gbps RZ-modulated transmission experiment on LEAF fiber from C. Meyer et al. of Corvis-Algety in 2002 [60]. The experiment primarily demonstrated that distributed Raman amplification is necessary for transmission of 25-GHz spaced 10-Gbps channels with the low C-band dispersion of NZDSF fiber. Raman amplification reduces the high inter-channel optical nonlinearity penalty by minimizing the average power levels required to get an adequate OSNR. The authors first demonstrated 80×10 Gbps over 1920 km with a 10^{-9} BER using EDFA amplification and 50 GHz channel spacing. With the channel spacing then reduced to 25 GHz, the authors increased the maximum transmission distance for 10 channels from 1400 to 2800 km with a 10^{-9} BER by switching from an EDFA-only scheme to hybrid Raman-EDFA amplifiers.

In 2003, Ramachandran et al. from OFS demonstrated a unique broadband tunable HOM-based dispersion compensator illustrated in Fig. 8 (a) consisting of five HOM fiber spans arranged in a binary length progression, interconnected by thermally-switched LPG mode converters [61]. The HOM dispersion could be tuned up to -435 ps/nm in discrete, equally spaced steps of 14 ps/nm by switching the signal between the low-dispersion LP_{01} mode and high-dispersion LP_{02} modes in each HOM segment. Figure 8(a) shows the wavelength dependence of the long-period grating-based optical switch, with high isolation between the two switch states from about 1530 nm to 1560 nm. Figure 8(b) shows the device dispersion across a similar wavelength range for incremental tuning states of the device. The device had an average/maximum insertion loss of 3.7 dB/5 dB, dominated by the 12 required splices. The measured MPI was less than -39 dB with a -44 dB average value, although the multiple splices and mode converters provide many potential locations for MPI. The device was demon-

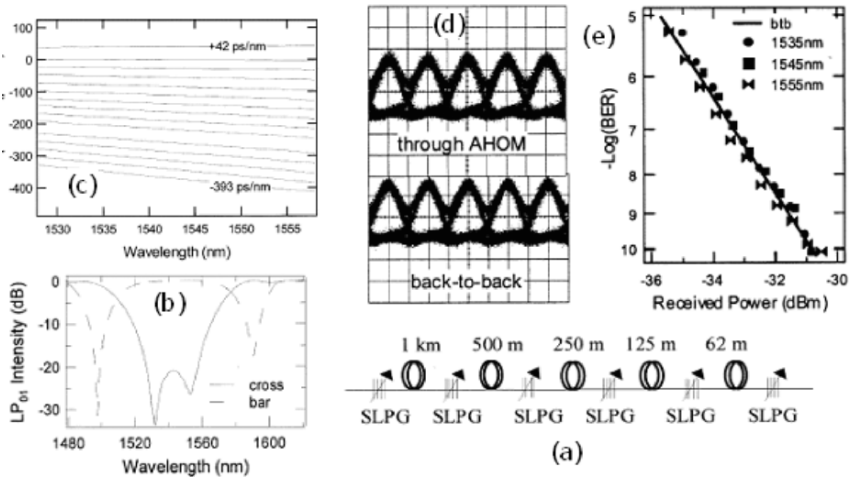

Fig. 8. (a) Schematic of multi-stage tunable HOM compensator from Ramachandran et al, (b) spectrum of switchable mode converter in each state, (c) dispersion versus wavelength over tuning range. For 40 Gbps CS-RZ transmission through +377 ps/nm NZDSF fiber dispersion plus tunable compensator, (d) eye diagrams and (e) sensitivity curves at multiple wavelengths [61].

strated in a single-span experiment by transmitting a 40-Gbps CSRZ signal through an NZDSF fiber span of increasing length followed by the appropriately set tunable compensator, with penalty free transmission over a 20-nm window. Figure 8(d) shows sensitivity curves for transmission through +377 ps/nm of NZDSF fiber and the appropriately tuned compensator. The primary design issue noted by the authors was the requirement for a sufficiently fast thermal switching technique.

Also in 2003, L.D. Garrett et al. from Celion Networks demonstrated ULH transmission of 40 $\times$ 12.5 Gbps RZ-modulated WDM channels over 6000 km of NZDSF using EDFA amplification and commercial LaserComm HOM compensators [62]. The 600-km L-band recirculating loop contained six 100 km LEAF fiber spans compensated by six dispersion and slope-matched HOM modules, so that 60 HOM modules were successfully concatenated in the 6000-km transmission. The dispersion map with the slope-matched HOM modules was sufficiently accurate so that no per-channel or banded-channel compensation was required anywhere in the experiment. The average MPI of all MPI units was less than -41.5 dB, and the insertion losses ranged from 3.1 to 4.3 dB. No polarization adjustment was required. Figure 9(a) shows that over five measurements on separate days of all channels, Q was greater than 11 dB with an average of 12.9 dB after 3000 km, and Q was greater than 8 dB with an average value of 9.9 dB after 6000 km, sufficient for error free transmission with the 25% overhead 9 dB FEC gain. The mean OSNR and Q over the 40 channels were measured versus distance from 600 and 6000 km in 600 km increments as in Fig. 8(b), indicating OSNR-limited performance and no distance-dependent impairment from accumulating MPI. In Fig. 9(c), measurement of all channels at 3000 km as the per-channel power into the

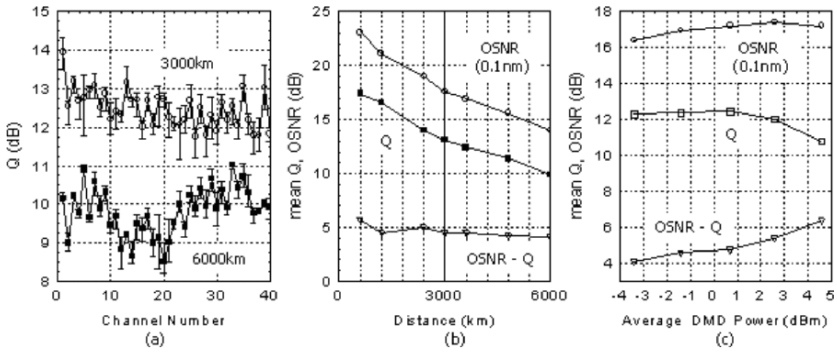

Fig. 9. From Garrett et al. [62], (a) Q-value performance for all channels at 3000 and 6000 km with error bars from five separate measurement sweeps, (b) OSNR and Q versus increasing distance, indicating OSNR-limited performance, and (c) mean OSNR and Q over all channels at 3000 km as the per-channel power in the HOM compensator was increased.

HOM devices was increased showed less than a 2 dB (OSNR-Q) penalty for powers less than +4 dBm/ch. The HOM input power in (a) and (b) was 4 dBm/ch. The average OSNR was maintained at approximately 17 dB as the HOM input power was increased by keeping a constant total mid-stage insertion loss with variable optical attenuators before and after the HOM compensators in the EDFA midstages.

Experimental results have demonstrated that HOM compensators are a viable technology for broadband in-line NZDSF compensation of ultra-longhaul 10- and 40-Gbps WDM transmission systems and a competitor for DCF. The DCF industry has developed so that HOM compensators no longer have their early advantage of being the only technology with 100% slope compensation for high-slope NZDSF fibers. However, HOM modules still require significantly less fiber because of the high HOM fiber dispersion per length, have an effective mode area significantly larger than DCF and even larger than some NZDSF fibers, and can be lightweight and compact with fiber-based mode converters. HOM compensators are not suitable for Raman pumping, primarily because the mode-converters are not sufficiently broadband. While MPI is the dominant design issue for the technology, the most recent commercial modules have been demonstrated with sixty units in series, sufficient for the vast majority of all applications.

5. Chirped Fiber Gratings For Dispersion Compensation

Researchers have been developing chirped reflective gratings in optical fiber for dispersion compensation since at least 1994 [63–65]. Early transmission results from K.O. Hill et al. in 1994 demonstrated 10 Gbps transmission through 100 km of SMF using a single-channel chirped grating for dispersion compensation [65]. J.A.R. Williams et al. extended the concept to dispersion slope compensation in 1996 [66].

In a chirped fiber grating, dispersion compensation is accomplished by varying the period of the grating along the grating length to provide a wavelength-dependent delay

in the grating reflectivity. The chirping function can be designed to provide dispersion slope compensation as well. The grating devices inherently operate in reflection, with a circulator to separate the incoming and outgoing signals. The advantages of chirped fiber gratings for dispersion compensation in WDM systems include low insertion loss, lightweight and compact design, and the absence of nonlinear effects. Chirped gratings were also seen as a potential source of dispersion-slope-matched compensators for the many varieties of NZDSF fiber without requiring the development of a new DCF fiber for each type.

The primary performance challenge for any dispersion compensator of a reflective or resonant nature, including chirped fiber gratings, ring resonators and etalons, is undesirable oscillations in the phase transfer characteristic [67]. In chirped gratings, these oscillations in the group delay with wavelength, or group delay ripple (GDR), arise from various sources of imperfections in the fabrication process [68]. The source of GDR at a given wavelength can be visualized as interference between the main signal reflected at the correct location in the grating and unwanted "echo pulses" reflected from any location in the grating where distortions in the periodicity happen to reflect that wavelength.

The primary point of contention between chirped grating vendors and WDM system designers has always been the quantification of grating quality [69]. The GDR calculated from dispersion measurement of chirped gratings is often reported only as peak-to-peak amplitude, such as ± 20 ps, with no information on the periodicity of the oscillations [70]. However, the prediction of performance based on grating GDR characteristics is both bit rate and modulation scheme dependent. K. Ennser et al. from U. Southampton demonstrated in 1998 that the performance impact of GDR depends strongly on the period of the GDR oscillations relative to the optical bandwidth of the modulated signal, with the largest transmission penalty for ripple features with periods comparable to the bit rate [71]. In 2002, L.-S. Yan et al. from U. Southern California and Phaethon reported measurements at 10, 20, and 40 Gbps through a chirped grating demonstrating both increasing average performance penalty and increasing penalty variation as the central-frequency of the signal was scanned across the grating bandwidth [72].

GDR periods smaller than or equal to the bit rate result in inter-symbol interference by distorting the phase alignment of the spectral components of the modulated signal [67]. Ripple features with periods larger than the bit rate result in a change in the grating dispersion, distorting the grating dispersion at that wavelength [68]. The transmission penalty at a particular wavelength is extremely sensitive to the relative phase between the signal center frequency and the GDR characteristic of the grating, so a slight detuning of the center frequency can drastically change the penalty. This of course is not helpful in a WDM system with ITU-specified channel frequencies, but it can help diagnose whether a transmission problem is due to the presence of high GDR in a system component.

Yoshimi et al. reported in 2002 that a more useful figures of merit (FOM) for chirped grating GDR characteristics should be based on integration of the measured group delay ripple to get the phase ripple (PR) of the grating [70]. In 2003, Eiselt et al. recommended separating the phase response into two separate FOM values [73]. The residual dispersion (D_{res}) reflects the dispersion error within the signal bandwidth caused by long-period phase ripples. The variance of the residual phase [$\sigma^2(\theta_{\mathrm{res}})$] reflects the ISI distortion from higher-frequency phase oscillations within

the signal bandwidth. These two FOMs would need to be reported for the center frequency of each WDM channel compensated by the grating. Also in 2003, X. Fan et al. from 3M recommended a modification to the residual phase FOM to weight the phase by the actual spectral shape of the optical signal [74], and J.C. Cartledge et al. from Queen's University found that modulator chirp characteristics could cause an appreciable performance variation even for signals of the same data rate and modulation format [75].

There are a wide variety of applications for chirped fiber gratings, ranging from single-channel or few-channel tunable devices for use at receivers to broadband devices for use at in-line amplifier sites. The importance of low GDR and PR increases with the number of chirped gratings required in series in a given application, so that low GDR is a significant issue for in-line applications and less of an issue for single-site applications. When multiple gratings with random and independent phase fluctuations are cascaded in a multi-span system, the actual GDR at each wavelength accumulates linearly. However, to evaluate the "cascadability" of a grating technology, it is useful to consider the mean and standard deviation of the residual dispersion and residual phase ripple across all channels [5.11]. The average values accumulate linearly, and the variances accumulate as the square-root of the sum. For ten gratings with $\text{avg}(D_{\text{res}})$ of 20 ps/nm, $\sigma(D_{\text{res}})$ of ± 5 ps/nm, $\text{avg}(\sigma^2_{\theta_{\text{res}}})$ of 0.005 rad^2 and $\sigma[\sigma^2_{\theta_{\text{res}}}]$ of ± 0.002 rad^2, the overall FOM values will be

$$\text{avg}(D_{\text{res}}) \cong \sum_{i=1}^{10} \text{avg}_i(D_{\text{res}}) = 200 \text{ ps/nm},$$

$$\sigma(D_{\text{res}}) = \sqrt{\sum_{i=1}^{10} [\sigma_i(D_{\text{res}})]^2} \approx 16 \text{ ps/nm},$$

$$\text{avg}(\sigma^2_{\theta_{\text{res}}}) \cong \sum_{i=1}^{10} \text{avg}_i(\sigma^2_{\theta_{\text{res}}}) = 0.05 \text{ rad}^2,$$

$$\sigma(\sigma^2_{\theta_{\text{res}}}) = \sqrt{\sum_{i=1}^{10} [\sigma_i(\sigma^2_{\theta_{\text{res}}})]^2} \approx 0.006 \text{ rad}^2.$$

The system impairment from residual dispersion depends on system design variables including bit rate, modulation scheme, and OSNR. A WDM system with 10 Gbps channels may have sufficient margin for the accumulated residual dispersion of (200 $\pm$16 ps/nm) in our example, while a system with 40 Gbps channels would require additional broadband compensation and might require per-channel compensation to correct the dispersion map. The system impairment from residual phase ripple in terms of Q-penalty [76] scales linearly with the variance of phase ripple, with two groups reporting that an accumulated PR variance of between 0.015 and 0.020 rad^2 produces a Q-penalty of 1 dB for 10 Gbps signals [73,74]. For our example, the PR variance could be as high as 0.056 rad^2, significantly higher than the 1-dB penalty level. The concatenation of these gratings in a multi-span system would be PR-variance limited to three or four units for 10 Gbps channels.

5.1. Broadband Fiber Gratings

Chirped fiber Bragg gratings can be designed to compete with DCF modules for broadband applications such as at in-line optical amplifier sites in multi-span WDM transmission systems. The short physical length of a chirped grating in comparison to the multiple kilometers of fiber in a DCF module makes fiber grating broadband compensators attractive for in-line dispersion compensation, because they can have low insertion loss, low optical nonlinearity, compact packaging and a low price. As discussed above, the quality of the grating for this application is much more crucial than for gratings located only in the optical receiver, because there can be as many dispersion compensator modules distributed throughout a WDM transmission system as there are optical amplifier sites. The specifications on optical properties such as polarization- and wavelength- dependent loss, polarization-mode dispersion and group delay ripple will limit the number of chirped gratings that can be concatenated in series, and thus will limit the number of spans of a WDM transmission system. The transmission experiments in this area focus on demonstrating the maximum transmission distance possible with gratings with a certain group delay ripple value.

Broadband Chirped Gratings with Continuous Group Delay

A "continuously-chirped" grating is designed with the correct wavelength-dependent time delay to provide uniform dispersion compensation across a wide operating bandwidth corresponding to multiple WDM channels. Like DCF and HOM compensators, the channels can be aligned at any wavelength with any spacing within the operating bandwidth, and there is no limitation to the modulation-dependent optical bandwidth of an individual signal as in channelized devices. The primary challenge in the commercial development of continuously chirped broadband gratings has been the required stability of the fabrication process to produce long gratings with extremely low group delay ripple across the desired optical bandwidth [77]. The physical length of continuously chirped grating increases with both the optical bandwidth and the chromatic dispersion. For example, a continuous grating designed to compensate for 100 km of SMF over the 35-nm bandwidth of the C-band may be up to 10 m long, while single-channel dispersion-compensating gratings may be only a few centimeters long [63]. Although the resonant frequency of a grating is temperature dependent, continuously chirped gratings do not require thermal stabilization. The grating can be designed with sufficient excess bandwidth to cover the desired operating bandwidth over the entire range of operating temperatures. A package containing only ten meters of fiber grating and a circulator certainly has the potential for low cost and small size. Alternative approaches to chirped gratings for broadband dispersion compensation that require shorter physical lengths have also been developed, including sampled gratings and over-written gratings, although these technologies introduce other significant fabrication issues.

In 1996, Kashyap et al. demonstrated transmission of eight 10 Gbps wavelengths over 100 km of SMF using a 1.3-m chirped grating for dispersion compensation with 1350-ps/nm dispersion and 10-nm bandwidth [78]. To produce the required 13,500 ps delay over 10 nm of bandwidth, thirteen separate phase masks were exposed onto adjacent segments of the fiber in a "super-step-chirped" process to form a grating 1.3 m in length. This "stitching" together of multiple narrower-band gratings to form a

wide bandwidth grating leads to the term "stitching errors" to describe imperfections in the periodicity of a grating that produce group delay ripple.

In 1999 and 2000, Gnauck and Garrett et al. from AT&T Labs-Research did a series of WDM transmission experiments with broadband chirped gratings developed by Pirelli Cavi, as listed in Table 3. The chirped gratings were 1 meter in length with 1330 ps/nm dispersion over a 6.5-nm bandwidth, an insertion loss less than 4 dB, average PMD of 1.5 ps and PDL of less than 0.3 dB. The gratings were placed in the mid-stage of the two-stage EDFA following every fiber span. The experiments explored the maximum number of gratings that could be concatenated with acceptable performance for 10, 20 and 40 Gbps channels, achieving up to 11 concatenated gratings for 10 Gbps operation. Experiments [5.19] and [5.22] contained one grating with –35 ps/nm2 dispersion slope compensation equivalent to 480 km of SMF in addition to the –1300 ps/nm average dispersion. Experiment [5.20] used three 6.5 nm gratings with different center wavelengths to form an 18-nm bandwidth dispersion compensator module. After five 75-km SMF spans compensated by these grating modules, the signal Q-factor at 10 Gbps measured every 0.1nm across the 18-nm grating bandwidth varied from 17.2 dB to 21.7 dB, a 4.5-dB variation that correlated to the accumulated variance in both residual dispersion and phase ripple of the gratings. The outcome of the AT&T/Pirelli work was that while the grating quality was sufficient for reasonable transmission distances at 10 Gbps, it was difficult to increase the optical bandwidth to cover a complete communications band such as the C-band or L-band while maintaining fabrication quality.

Table 3. Early Transmission Results for Continuously Chirped Broadband Fiber Gratings.

Ref.	Year	Lead Author	Grating Bandwidth	Grating Dispersion (ps/nm)	Ch. Count	Ch. Rate	Grating Count	Dist. (km)	Fiber Spans
[79]	1998	Garrett	6.5 nm	–1300	8	10-Gbps NRZ	6	480	80-km SMF
[80]	1998	Gnauck	6.5 nm	–1300	8	20-Gbps RZ	4	320	80-km SMF
[81]	1999	Garrett	6.5 nm	–1300	16	10-Gbps NRZ	11	840	80-km SMF
[82]	1999	Garrett	18 nm	–1300	32	10-Gbps NRZ	5	375	75-km SMF
[83]	1999	Gnauck	6.5 nm	–1300	4	40-Gbps RZ	1	75	75-km SMF
[84]	2000	Gnauck	12 nm	–1300	16	20-Gbps RZ	1	400	80-km NZDSF

In 1999, J.F. Brennan et al. from 3M developed a fabrication process for continuously chirped gratings up to 10 m in length [853]. This process offered the potential for gratings with useful amounts of dispersion over the entire bandwidth of an optical amplifier for in-line compensation. Results published in 2001 demonstrated a single grating with –629 ps/nm dispersion at 1550 nm over 30 nm and insertion loss of 5.5 dB to compensate for 40 km of SMF fiber in the C-band [87]. A similar fabrication concept for "infinite length fibre gratings" was published by R. Kashyap et al. from BT Laboratories the same year [86].

Later 3M results from 2003 demonstrated an improved chirped grating with -330 ps/nm dispersion and –7 ps/nm^2 dispersion slope at 1550 nm over 30 nm to compensate 80 km of LEAF fiber [88]. This grating was evaluated by again transmitting 10 Gbps NRZ data on a tunable wavelength through 80 km of LEAF fiber and the chirped grating, and then measuring the required optical power level into the receiver to achieve a 1×10^{-9} BER using a 0.01-nm wavelength step size. By comparison to the required

receiver power in a back-to-back measurement of the transmitter and receiver without the LEAF fiber or chirped grating, the results show a "system power penalty" of less than 0.6 dB across the entire 30-nm bandwidth. More precise measurement over a 0.2-nm region show a power penalty of less than 0.3 dB, which closely matched the 0.4 dB of distortion-induced system power penalty calculated by the authors from the measured group delay characteristics of the grating.

These results imply that continuously chirped broadband gratings can be a good solution for applications such as metro-area or few-span WDM systems that are more sensitive to cost than performance, but are not yet appropriate for in-line compensation in many-span ultra-longhaul (ULH) systems. In this vein, 3M published a paper in 2003 demonstrating a chirped grating compensator in a metropolitan application [89], generating the 10-Gbps NRZ test signal using a lower-cost electro-absorption modulated laser (EML) source rather than the distributed feedback laser (DFB) with an external Mach-Zehnder (MZ) modulator source typically used in higher-performance long-haul DWDM systems. EML sources can be cost-effective for metropolitan networks consisting of a single or few fiber spans because they are smaller, simpler and less expensive than DFB+MZ sources, but have a lower optical extinction ratio and more data-pattern dependent wavelength chirp on the optical output signal. The 3M experiment demonstrated that the chirped grating with dispersion of -1360 ps/nm could be used to extend the performance of a nominally 40-km EML to greater than 100 km.

Broadband Chirped Gratings with Periodic Group Delay

There are alternative gratings approaches to broadband dispersion compensation that reduce the physical length of the grating in search of improved manufacturability. These techniques produce "channelized" dispersion compensation where the spectral components of each WDM signal are realigned within a single channel but not between channels, equivalent in function to many single-channel compensators in series. Two examples that we will consider are "sampled gratings" and "overwritten gratings". These devices share the low insertion loss, small size and low optical nonlinearity of all fiber-grating based dispersion compensators. There are tradeoffs, of course, in that the exposure pattern for the gratings becomes significantly more complex and precise alignment of the center wavelengths to the ITU grid is required.

The finite optical bandwidth for each WDM channel in a channelized compensator adds a new set of performance specifications in addition to the GDR (group delay ripple) spec of continuously chirped gratings. A multi-channel chirped grating with sufficient optical channel bandwidth for 10 Gbps NRZ signals may be insufficient for forward-error correction (FEC) encoded signals at 10.7 or 11.5 Gbps, for higher-bandwidth modulation formats such as return-to-zero (RZ), or for 40 Gbps signals, adding a strong modulation rate and format dependence to the compensator performance. The wavelength spacing between channels is determined at fabrication, so that compensators have to be specified for both dispersion and passband characteristics i.e., a grating compensates for 80 km of SMF on a 50-GHz grid with 25-GHz channel bandwidth. Also, the frequency alignment of the dispersion compensator relative to the WDM channels is fabrication and temperature dependent, which can require electrical power to the device for active stabilization at a calibrated temperature. Channelized compensators have higher insertion loss between channels, and thus perform a "noise

filtering" function. This can be a useful function, but should be remembered when taking OSNR readings off a spectrum analyzer because the noise in the channel bandwidth may be higher than the noise between channels. These issues apply to other channelized compensators as well including all-pass filters, but are not issues for compensators with broadband group delay characteristics including DCF, HOM-based or continuously-chirped grating compensators.

Overwritten Gratings

In 2002, Painchaud et al. of Teraxion used a superposition approach to fabricate a dispersion compensator that operated over 32 WDM channels spaced at 100 GHz, for a total operation bandwidth of 25 nm [90]. The dispersion of the grating for each channel was adjusted on a per-channel basis to provide dispersion slope compensation. Grating superposition consists of overwriting multiple gratings on the same portion of optical fiber, with the number of superimposed gratings limited by the maximum fiber photosensitivity. The authors state that this superposition approach requires a simpler fabrication procedure than the "sampled grating" approach to producing a multi-channel grating from a single grating structure, effectively because 32 simple single-channel gratings are written rather than writing one more complex pattern with the correct Fourier elements and apodization structure to produce 32 channels. The authors estimated at that time that the maximum number of grating channels that could be superimposed was 48, sufficient for covering the entire C-band with 100-GHz spaced wavelengths. Note also that arbitrary channel plans could be written, with skipped channels or unevenly spaced channels, since there was no inherent periodicity in the grating structure as with sampled gratings or all-pass filter compensators. The insertion loss was between 4.4 and 5.0 dB for the 32-channel grating, with insertion loss ripple within the channels ranging from 0.28 to 0.77 dB. The measured dispersion values of the channels were within 2.1% of target. In 2003, the same group published results on a 16-channel device that was also thermally tunable, with the dispersion slope between the channels scaling appropriately with the dispersion [91].

Another publication by the Teraxion group in 2003 studied the effect of multiple grating concatenation on total group delay ripple and per-channel optical bandwidth in an eight-span WDM link [93]. The experiment used six gratings that covered 45 channels spaced at 100 GHZ on the ITU grid, with a nominal dispersion of –1300 ps/nm and 4.5 ps/nm^2 dispersion slope to compensate 80 km of SMF. The CFBG insertion loss was less than 3.5 dB. Within a 33-GHz bandwidth centered about each ITU channel, the measured group delay ripple (GDR) was less than 35 ps and insertion loss ripple (ILR) was less than 0.6 dB. The receiver-sensitivity power penalty attributed to these devices was measured in a 480-km testbed including six spans of 80-km SMF and EDFA amplifiers using a tunable laser modulated with 10-Gbps NRZ data.

The GDR and optical bandwidth of the individual channels were measured as a function of number of cascaded chirped gratings. As the number of gratings was increased, the overall optical bandwidth of the individual wavelength channels was reduced gradually from the nominal 42 $\pm$ 2 GHz of a single grating to 32 $\pm$2 GHz for six gratings, while the accumulated GDR increased from 30 ps to approximately 110 ps. The insertion loss ripple within the individual channels "remained below 1 dB for most channels". The authors reported that the GDR grew approximately with the square root of the number of cascaded devices for a large number of grating devices

as expected for the predominantly random nature of the GDR. The receiver-sensitivity power penalty due to GDR at a BER of 1×10^{-9} for 10 Gbps NRZ transmission through eight grating-compensated fiber spans was less than 1 dB for signal wavelengths at ITU values and less than 2.5 dB for signal wavelengths within a $\pm$7.5-GHz window of the ITU values. The penalty at offset wavelengths is interesting because while DFB lasers for WDM systems can be wavelength-locked to within $\pm$2.5 GHz, there could be additional thermal drift of the grating central frequency when deployed in actual equipment. A realistic WDM system design would need to allocate margin for Q-penalty due to the maximum expected thermal drift of the grating compensators.

These experimental results were in agreement with contemporary numerical analysis by Jamal and Cartledge [69] that predicted that the system power penalty in a four-span 10 Gbps system would be smaller than 1 dB 98% of the time if the individual grating peak-to-peak GDR was smaller than 40 ps, and nearly 100% of the time if the GDR was less than 20 ps. The Teraxion authors recommended the superimposed CFBG devices with the reported specifications for metro and regional applications, for example in a 400-km ring with eight 50-km spans, and predicted that with improved fabrication techniques, up to 19 devices could be cascaded for long haul and extended long haul systems up to 1000 km in reach.

Sampled Gratings

Sampled gratings were well described by M. Morin et al. from Teraxion in 2004 [99]. The periodic structure of the chirped grating consists of "an underlying linearly chirped function with an overlaid sampling function. The linear chirp determines the dispersion, while the phase sampling produces the multi-channel character. The period of the phase sampling determines the channel spacing, while its harmonic content determines the number and uniformity of channels. A purely periodic sampling produces identical channels that share the same dispersion level. Chirping the sampling period [in addition to the chirp in the underlying grating periodicity] can produce slope-matched dispersion that varies linearly with wavelength." Ibsen argued in 1994 [95] that "sampled gratings are more attractive than overwriting many gratings as different wavelength in that same length of fiber since exact wavelength matching [between] the channels is automatically achieved from the sampling process, and the grating writing time is minimized." However, precise alignment of the central frequencies of the comb of channels to the ITU grid is not automatically achieved.

In theory, sampled chirped gratings can be fabricated with much shorter physical lengths than continuously chirped gratings, with tens of centimeters of fiber rather than tens of meters. In practice, sampled gratings have been in continuous development since 1995 [94–99], with only recent reports of devices providing dispersion compensation at 100 GHz spacing across the entire C-band from M. Morin et al. from Teraxion [99]. The sampling process has, however, found application in transforming single-channel tunable dispersion and slope compensators into few-channel compensators, as will be discussed in the next section. In an interesting note of convergence with the overwritten gratings discussed above, W.J. Loh et al. from E-TEK in 1999 proposed using the blank regions in the grating produced by the sampling process to interleave multiple sampled gratings within the same fiber as an alternative design approach to the large optical index changes required to realize a reasonable number of channels from a single sampled grating [96].

There are few examples in the literature of WDM transmission experiments using sampled gratings for broadband dispersion compensation, and the few examples are single-grating, single-span results without performance comparison to other technologies. The most advanced experiment was reported by M. Ibsen et al. from U. Southampton in 1999 [95], demonstrating a four-channel device from with uniform insertion loss and dispersion of -3200 ps/nm in a 4×10 Gbps WDM transmission experiment over 200 km of SMF with less than 1 dB Q-penalty compared to back-to-back.

5.2. Tunable Single- and Few-channel Gratings

Narrow-band chirped gratings for single-channel operation are much simpler to fabricate than any of the broadband chirped grating techniques. The chirp distribution in a single-channel grating can be tuned by a variety of mechanical or thermal mechanisms. Research in this field has been active since at least 1996 [100,101]. These "per-channel" tunable dispersion compensators are typically placed at the receiver end of the system after the WDM wavelengths have been demultiplexed, and the dispersion can be actively controlled to optimize the channel performance. Unlike the broadband compensators discussed above, these tunable devices are not a competitive device to DCF but a complementary technology.

The tunable gratings are inherently active, requiring transducers for the tuning mechanism and feedback loops for stabilized operation. The optical properties such as GDR, optical bandwidth and insertion loss ripple can vary widely over the dispersion tuning range of the grating device. It is important therefore that the systems performance should be evaluated for a given application over the entire dispersion tuning range of the device. There can also be a significant cost impact from requiring a tunable grating module at the receiver of every channel. However, since this function can be included with the WDM line optics, this cost grows incrementally with number of installed channels and is not part of the first-cost of the system like the in-line dispersion compensators.

Per-channel dispersion is as a rule not necessary for 10 Gbps channels, even in ultra-longhaul WDM systems. There are in-line dispersion compensators with slope compensation available for most NZDSF fiber types so that WDM systems can be designed with sufficiently accurate dispersion maps for 10 Gbps transmission without requiring per-channel cleanup. However, if the price point were acceptable, tunable compensators for 10 Gbps WDM systems could offer benefits in terms of automatic dispersion map optimization that could reduce pre-installation testing of the fiber plant. A single broadband tunable compensator rather than per-channel compensation would be most cost-effective in that application, however.

The capability to do WDM transmission at channel rates of 40 Gbps and above, on the other hand, is greatly facilitated by single-channel or few-channel tunable dispersion compensators [102]. The tolerances on WDM system dispersion maps become very tight at high data rates. The linear dispersion tolerance decreases with the square of the bit rate, so the allowable dispersion map errors for 40 Gbps channels are sixteen times smaller than for 10 Gbps channels. At the same time, the trend to wider total optical bandwidth such as combined "C+L"-band systems also increases the requirement for dispersion compensation with accurate slope compensation. Higher data rates also generally imply higher optical launch powers into the fiber spans, causing further

decrease of the dispersion tolerance due to spectral broadening of signals from fiber nonlinearities such as self-phase modulation, and therefore increasing the per-channel power dependence of WDM system performance. Variations in nonlinear interactions due to per-channel power variations from optical amplifier gain flatness or from reconfigurable OADM devices also can change the optimum post-compensation on a per-channel basis. Thermal drifts in the transmission fiber can also cause seasonal variation in fiber dispersion, with magnitudes dependent on whether the fiber is buried or overhead. Although a linear device such as a tunable chirped grating cannot completely restore a signal that is distorted by distributed interaction between nonlinear effects and the dispersion map along a WDM system, it can reduce much of the incurred performance penalty [102].

Assuming that 40-Gbps systems become a commercial reality, there will likely be a market for tunable dispersion compensation including broadband, few-channel and per-channel. Important characteristics for continued improvement include, size, cost, electrical power consumption and manufacturability. The details of the tuning mechanism, and there are far too many extremely inventive mechanical and thermal approaches in the literature to mention here, in particular, can have a particularly large impact on the manufacturability, stability and power consumption of the tunable grating.

In 2000, B.J. Eggleton et al. from Lucent demonstrated tunable chirped gratings with a distributed thin film heater deposited on the grating to modify the chirp function [103]. A tunable grating was used to compensate a 40 Gbps NRZ signal after 40 km of SMF, with less than 0.5 dB Q-penalty at the optimum dispersion setting. Another interesting experiment demonstrated the utility of tunable compensation in adapting the total dispersion of a system to varying levels of optical nonlinearity in a 40-Gbps three-span transmission system. A three-span link containing NZDSF, DCF and SMF fiber was designed to require post-compensation from either a piece of DCF or a tunable grating. The receiver sensitivity penalty was measured for each technology as the power into the NZDSF spans was increased to cause increasing levels of self-phase modulation (SPM), which leads to optimum performance at increasingly net positive amounts of total link dispersion or "under-compensation" [104]. The dispersion of the tunable grating could be reduced at higher NZDSF launch powers, unlike the DCF module. In a systems application, a feedback signal from the FEC chip, for instance, would be used to actively optimize the grating dispersion in real time. The authors also demonstrated transmission through various amounts of fiber followed by a tunable grating at 80 and 160 Gbps, where the dispersion limit is only ± 7 ps/nm.

In 2001, Fells et al. from Nortel reported a tunable compensator for 40 Gbps that used a twin-fiber grating design to eliminate the higher-order residual dispersion inherent in the tuning mechanism of many tunable gratings [127]. The two gratings have opposite signs of dispersion slope, so that the combined dispersion slopes cancel out as the relative frequency alignment of the two gratings are shifted during tuning. Figure 10(a) illustrates the grating configuration. Figure 10(b) shows the measured group delay and reflectivity of one grating, and Fig. 10(c) shows the group delay across a 0.5-nm window for three different dispersion settings. The device was tested with a 40 Gbps RZ signal, as was found to extend the 2-dB penalty range from ± 50 to ± 300 ps/nm.

It could be advantageous to have tunable dispersion compensators that encompassed a few channels rather than a single channel. This could be useful in system

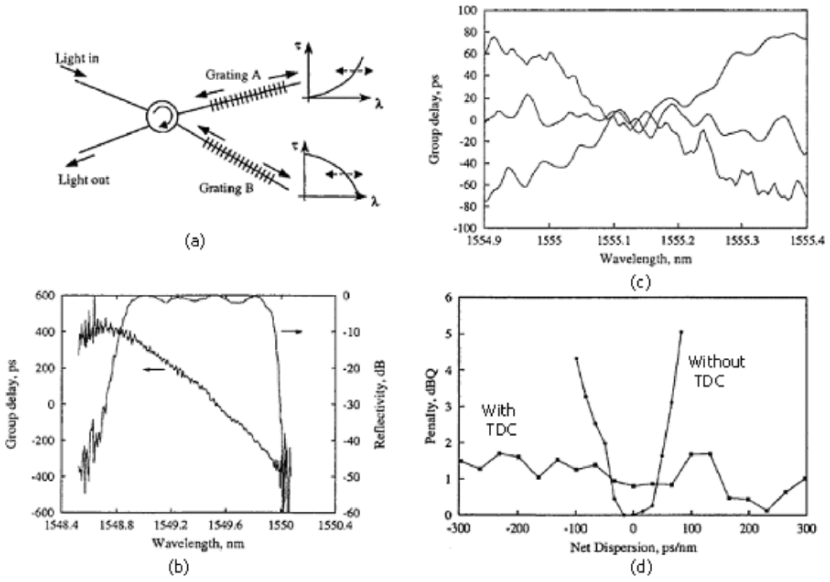

Fig. 10. From Fells et al. [127], (a) schematic of two-grating tuning design, (b) measured group delay and reflectivity (insertion loss) of a single grating, (c) measured group delay of module at three settings, and (d) dispersion tolerance of a 40-Gbps RZ signal with and without the tunable dispersion compensator (TDC).

architectures using 4-channel bands for multiplexing and add/drop, or for a receiver with a dynamically configurable wavelength, or simply for single-channel use to reduce the inventory of parts necessary for an 80-ch WDM system. However, the details of the multi-channel tunable compensator channel plan would need to be considered from the beginning of the WDM system design process. For instance, since these multiple channels are controlled by a shared tuning mechanism, few-channel tunable compensation would not be useful in a system with reconfigurable single-channel add/drop capability where adjacent channels could travel different routes and have significantly different accumulated dispersion.

The sampled grating concept has made more headway in the area of few-channel tunable gratings than in wideband in-line compensators [14–106]. In 2003, D. Gauden et al. from Highwave [108] demonstrated a four-channel sampled grating with 100 GHz channel spacing that was tunable from –370 ps/nm to –1420 ps/nm with better than 3.5% dispersion uniformity over all channels for all dispersion values. However, since the device operates by adjusting the wavelength range over which a fixed time delay occurs, the channel bandwidth varies from 80 GHz at the lowest dispersion value to 23 GHz at the highest value. The usable dispersion tuning range for this device in a given application could be limited on the high end by the acceptable minimum channel bandwidth for data rates higher than 10 Gbps. This compression of the delay-versus-wavelength characteristic also changes the oscillation periodicity of the GDR,

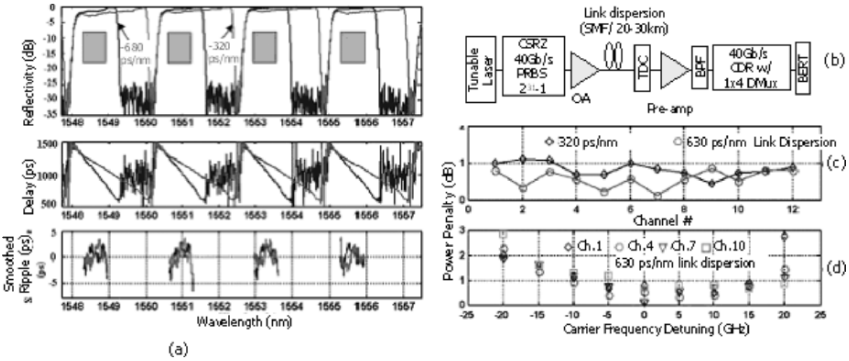

Fig. 11. Results from Y. Li et al. [109] for four-of-twelve tunable grating compensator, showing (a) reflectivity, group delay and smoothed GDR of the four channels at two different dispersion settings with shaded rectangles indicating channel location, (b) setup of 40 Gbps CSRZ transmission, and measured performance penalties (c) for all twelve channels at two different dispersion values and (d) for a few channels as the center frequency is offset for high-dispersion setting.

which can change the performance impact of oscillations with periodicity close to the modulation frequency.

Also in 2003, Y. Li et al. from OFS [109] demonstrated another four-channel sampled grating, with tunability of both the dispersion and the center frequency. The grating channels were separated by 300 GHz, with channel bandwidth of at least 80 GHz for all dispersion settings allowing 40 Gbps operation. The center frequencies of the channel comb could be tuned by 0, 100, or 200 GHz by applying strain, so that the device can be tuned to compensate three different sets of four channels for four-of-twelve operation. The dispersion in the channels could then be tuned from –300 to –700 ps/nm by applying a thermal gradient across the grating, with better than 1% dispersion uniformity. Transmission testing with a tunable 40 Gbps CSRZ signal in a single-span link with SMF fiber showed less than 1.1 dB power penalty both at high and low dispersion settings, as in Fig. 11(c). Figure 11(d) shows that for the highest dispersion, lowest bandwidth tuning condition, the carrier frequency of one set of four channels could be detuned over a 20-GHz range with less than 1 dB penalty indicating sufficient dispersion bandwidth.

6. Photonic-Crystal Fibers for Dispersion Compensation

The chromatic dispersion properties of photonic crystal fiber (“PCF”) are an active field of research, both for application as a transmission fiber and a dispersion compensating fiber [109–114]. There has been a great deal of analytical work demonstrating that arbitrary chromatic dispersion profiles can be generated for slope-matched dispersion compensating fiber based on PCF. Experimental research in the area of PCF for dispersion compensation is currently focused on optimization of the fabrication processes to produce fibers that match the theoretically predicted performance levels.

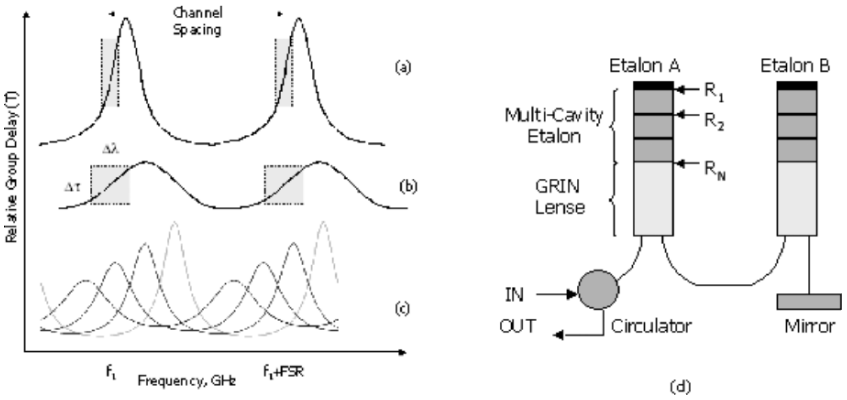

Fig. 12. Group delay characteristics for single stage filter with (a) high dispersion, narrow bandwidth, or (b) low dispersion, wide bandwidth. Part (c) shows combination of multiple filters to achieve intermediate dispersion over a useful bandwidth. Shaded region indicates useful dispersion bandwidth. Part (d) illustrates a multi-stage implementation with bulk-optic Gires-Tournois etalons [129].

Testing in actual optical transmission systems is still in the future for this promising technology.

It is interesting to note that a mode converter structure for HOM-fiber dispersion compensators based on photonic crystal fiber was demonstrated in 2001 by S. Choi et al. from K-JIST [115].

7. Dispersion Compensators Not Based on Optical Fiber

7.1. All-pass Filter Devices

All-pass optical filters must be mentioned in any discussion of viable dispersion compensation options. The filters are often based on bulk optic elements [128, 132] or integrated optical waveguides [123,126] rather than fiber, although fiber-based devices have recently been demonstrated [130]. An "all-pass" filter is a resonant optical cavity that ideally has a flat amplitude response, transmitting or reflecting all incident light. The cavity resonance provides a wavelength-dependent phase response, with relative delay peaks at periodic wavelengths separated by a "free spectral range" (FSR) determined by the resonant cavity length. The phase response to the long-wavelength, short-frequency side of a resonance provides decreasing phase delay with increasing wavelength, i.e., negative dispersion. The magnitude and optical bandwidth of this dispersion are determined by the "finesse" of the cavity resonance, given by the ratio between the FSR and the resonance width. All-pass filter dispersion compensators have the potential advantages of low insertion loss, low nonlinearity, compact size, low cost, and low latency for transit-time sensitive applications.

All-pass filter compensators are WDM channel-spacing specific because of the periodic group delay of the resonant cavities, unlike technologies such as DCF and

HOM-based devices that are broadband and wavelength-plan agnostic. Figure 12 illustrates two possible extremes of single-stage filter design, a high-finesse cavity in (a) providing high dispersion over a very narrow bandwidth relative to the FSR, and a low-finesse cavity in (b) providing lower dispersion, but over a more useful bandwidth. A design with negative dispersion over a useful per-channel "dispersion bandwidth" can be tailored by concatenating multiple filter stages with identical FSR values but different resonance widths and slightly offset resonant wavelengths, as shown in Fig. 12(c). More filter stages are required to produce multi-stage designs with a very linear delay characteristic across the optical bandwidth, or low "GDR" as discussed in the chirped gratings section. When multiple etalon compensators are concatenated in a multi-span system, this in-band dispersion ripple linearly accumulates to contribute distortion of the optical spectrum and can be the limiting factor in maximum system length.

If the FSR values of the multiple filter stages are slightly different, the resonances can be designed to align slightly differently for each WDM signal wavelength, providing both dispersion and dispersion slope compensation. Once a multi-stage filter module with enough stages to achieve acceptable bandwidth and dispersion flatness, multiple units of this basic module can be combined to get higher dispersion values. Figure 12(d) [129] illustrates passing an optical signal through two multi-stage filter modules implemented in Gires-Tournois etalons, consisting of a resonant cavity operating in reflection, with a high rear mirror reflectivity and a low front mirror reflectivity.

The dispersion bandwidth of an all-pass compensation with slope compensation will vary among the channels as the alignment between the filter resonances shifts, ultimately limiting the number of channels that the module can compensate with a specified dispersion bandwidth. The definition of "useful" dispersion bandwidth depends on the intended application, where a 20-GHz channel bandwidth may be adequate for 10 Gbps NRZ data while 30 GHz might be more desirable for 12.5 Gbps FEC-encoded RZ data, or 80 GHz for 43-Gbps RZ data. A very good theoretical analysis of all-pass filter design for dispersion compensation applications, with an overview of the many physical approaches to all-pass filter implementation, has been provided by C.K. Madsen and G. Lenz [116–118].

All-pass filters can be tuned by shifting the alignment of the single-stage filters, either by applying voltages to waveguide ring resonators, thermally adjusting the cavity optical index in bulk optic devices, or applying mechanical strain to fiber-based devices. The proper center-frequency alignment of the multiple filter stages in a fixed all-pass module must be carefully maintained either by active stabilization, or in the case of bulk optic devices, by athermal packaging. Truly athermal packaging with the required stability over the commercial temperature range of 0°C to 70°C is quite difficult, however. Active thermal control has the disadvantage of requiring electrical power, but offers the possibility of dispersion tunability through the temperature setting.

The "modularity" of all-pass filter compensator design can provide a useful cost advantage. A compensator design can contain the bare minimum number of stages required to provide sufficient performance for a given application. In particular, extremely compact and inexpensive etalon compensators can be designed for few-span metro applications that are more sensitive to cost than to performance. Cost-optimized metro compensators can contain significantly fewer etalons than

performance-optimized ultra-longhaul compensators, since short WDM systems require few compensators and can be more tolerant of in-band dispersion ripple.

Although ideally "all-pass", in reality the wavelength-dependent path lengths through the non-zero insertion loss of the cavity material cause small amounts of wavelength-dependent insertion loss ripple (ILR) within each wavelength channel with a design-dependent deterministic shape. Fabrication imperfections in the resonant structures and the thin-film reflector coatings also contribute in-band wavelength-dependent loss. This in-band insertion loss ripple linearly accumulates with the number of compensators to distort the optical spectrum. For instance, an insertion loss ripple of 0.2 dB within each channel in a single compensator could accumulate in a 20-span system to be a 4-dB signal distortion. Reconfigurable gain equalization devices can compensate for power variation between channels, but not for this gain variation within a single channel.

Etalon compensators have typically designed for 100 or 50 GHz channel spacing. It is difficult to design an etalon module with greater than FSR/2 dispersion bandwidth, as can be seen in Fig. 12, limiting a device designed for 50 GHz WDM channel spacing to a 25-GHz dispersion bandwidth. Any channelized device with limited optical bandwidth can be the limiting factor in determining the maximum number of spans before electrical regeneration in a WDM system. As a result, it is important to evaluate these devices in an actual system application with the intended modulation scheme. Compensators that work well up to 10 spans for 10.0 Gbps NRZ-modulated signals may strongly filter the spectral shape after only 6 spans for 12.5 Gbps RZ-modulated signals and be completely inappropriate for 43 Gbps signals. The required optical bandwidth for a particular data rate also depends on the amount of spectral broadening caused by SPM during fiber propagation. If the transmission system uses higher optical power levels, the width of the optical spectrum of a WDM signal will increase with transmission distance. Also, an amplifier chain with etalon compensators designed for 40×10 Gbps channels spaced at 100 GHz would need to be installed with 50 GHz compensators to allow for future upgrade to 80×10 Gbps channels spaced at 50 GHz.

The channelized nature of etalon compensators can be advantageous for suppression of cross-phase modulation (CPM) effects. Data bits in different wavelength channels in a WDM system travel at different velocities because of dispersion, decorrelating the data in adjacent channels due to the "walk-off" effect so that pattern-dependent nonlinear effects between channels are averaged over the transmission system. Traditional dispersion compensators realign the relative position of the bits in all wavelengths at each amplifier site, so that the nonlinear effects will occur between the same groups of bits in each span. Etalon compensators realign the frequency components of each channel, without compensating the temporal shift between channels, resulting in more averaging and slower accumulation of signal distortion [119–121].

Etalon compensators may be of particular interest for latency-sensitive applications such as data storage. DCF and HOM compensators contain kilometers of fiber with the corresponding speed-of-light transit time, although HOM by design typically contains significantly less fiber than DCF. The optical path length through an etalon compensator is only a few centimeters of bulk optics, semiconductor waveguide or fiber gratings with the required circulators. The transit time is about 50 ms for 10-km DCF, 5 ms in 1 km of HOM fiber, and 15 μs in 3 m of resonant cavity optics including circulator fiber pigtails. This same property of short optical path length also implies that very little optical nonlinear interaction will occur in the etalon compensators.

In 1991, Gnauck et al. from AT&T Bell Labs reported one of the earliest applications of Gires-Tournois etalons to dispersion compensation [122]. An interesting historical note, in 1991 the authors stated: "Although the use of dispersion-shifted fiber can greatly increase this [dispersion] limit, much conventional fiber is already installed in commercial networks. For conventional fiber, a device having dispersion equal and opposite to that of the fiber could be used to increase the dispersion-limited distance." These were the days of single-channel transmission, and FWM was not yet an issue with DSF. The authors were using a single tunable resonant cavity in the transmission of an 8-Gbps channel over a single 130-km span of SMF to reduce the dispersion penalty from 3 to 0.9 dB. The use of this single-resonator device was severely limited by the optical bandwidth of the linear dispersion region. The next appearance of etalon compensators was in 1996 from Garthe et al. [123] of BNR Europe and JDS Fitel, exploring the use of two resonators with different finesse and offset resonance in series to increase the dispersion bandwidth.

In addition to their analytical papers on all-pass filters, C.K. Madsen and G. Lenz et al. from Lucent published several papers from 1998–2000 of experimental demonstrations using several different technologies to implement the all-pass filters. In 1999, Madsen et al. demonstrated a two-stage tunable dispersion compensator based on ring-resonator filters fabricated in silica-on-silicon waveguides [124]. Waveguide-based devices are extremely compact and offer the promise of integration with other optical functions on a single substrate. In general, however, waveguide-based ring resonator compensators are limited in FSR by the minimum achievable waveguide bend radius, which is in turn limited by the optical index step of the waveguide fabrication process. Waveguide devices can also have high polarization-dependent loss and high coupling loss to optical fiber because of the non-symmetric waveguide cross-section. The filter in this work, designed for a FSR of 12.5 GHz, a bandwidth of FSR/4, and a dispersion of -4000 ps/nm over 4.5 GHz, was used to transmit a 5-Gbps signal over 250 km of SMF.

Later in 1999, Madsen et al. implemented a tunable dispersion compensator in another technology, based on a Gires-Tournois etalon with a mechanical anti-reflection switch (MARS) for the top partial reflector [125]. The MARS device, shown in Fig. 13(a), is a variable-thickness Fabry-Perot cavity consisting of a silicon substrate, an air gap, and a quarter-wave thick dielectric membrane [126]. The gap between the silicon surface and the dielectric membrane can be varied to modulate the reflectivity by applying a voltage to electrodes on top of the membrane. To make the MARS device into an all-pass filter, a high reflectance coating is added to the opposite side of the silicon substrate. A high front-face partial reflectance yields a sharp peak in the group delay with a large delay at resonance, while lower partial reflectance values have a broader response with a smaller peak delay at resonance. The authors fabricated a 2-stage filter, using the two control voltages and the relative temperatures of the two substrates to obtain the desired overall group delay function. The dispersion in a 47.5-GHz passband could be tuned from +76 ps/nm to –76 ps/nm, equivalent to ± 5 km of SMF, with a group delay ripple compared to a linear fit of less than ± 3 ps. In 2000, the authors used the same devices to implement a dispersion slope compensator, with the group delay characteristics shown in Fig. 13(b).

Turning back to waveguide devices, Horst et al. from IBM Zurich in 2000 used a high-refractive index contrast silicon-oxynitride (SiON) waveguide process to fabricate 4-stage ring resonator-based dispersion compensators with FSR values of 25 and 33

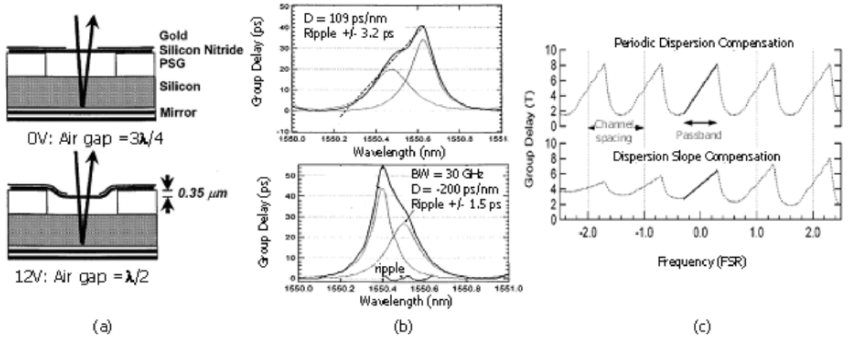

Fig. 13. Gires-Tournois etalon with tunable upper reflector from MARS device [126], (b) alignment of two etalon stages for dispersion settings of +100 ps/nm and −200 ps/nm, and (c) illustration of group delay variation between channels for etalon compensators with and without slope compensation, from Madsen et al. [7.12].

GHz with negligible bending loss, or 50 GHz FSR with small bend losses [128]. The 50-GHz design facilitates operation with WDM channels on the ITU standard 50 GHz wavelength grid. The authors designed the devices for optical bandwidth of FSR/2, achieving a dispersion of 3500 and 500 ps/nm within that bandwidth for the 25-GHz and 50-GHz FSR devices, respectively. The authors noted the issue with polarization in waveguide devices, saying that "this device should be used with a single input polarization, as the filter curves for TE and TM polarized light would be identical in shape but in general slightly displaced in frequency owing to waveguide birefringence."

In 2003, a group from JDS Uniphase published a series of papers on tunable etalon compensators that were based on the two-element technique previously implemented by Fells et al. in tunable chirped gratings [129]. In this technique, the frequency separation between a pair of etalon modules, designed with opposite signs of dispersion slope within the optical channel, is thermally tuned to achieve variable amounts of total dispersion. The intra-channel dispersion slopes of the modules cancel out to provide uniform dispersion across the channel bandwidth. Moss et al. demonstrated a module designed for 10 Gbps channels with a 50 GHz FSR that had a tuning range of +1700 ps/nm to −1500 ps/nm over a 25-GHz dispersion bandwidth, sufficient for in-line compensation of traditional-length fiber spans [130]. With such a tuning range, the authors claimed that perhaps only three part numbers of dispersion compensators might be sufficient for the entire range of fiber span lengths in practical WDM systems.

Lunardi et al. later in 2003 demonstrated another device configuration optimized for 40 Gbps channels with a 200-GHz FSR that had a tuning range of about ±200 ps/nm over an 80-GHz bandwidth [131], primarily useful for dispersion cleanup at terminal sites. This device was demonstrated in a single-channel, single-span link with NRZ, RZ and CS-RZ modulated signals transmitted over up to 45 km of NZDSF fiber. Recall that the dispersion limit at 40 Gbps is a factor of 16 smaller than for 10 Gbps signals, so that the C-band dispersion limit in an NZDSF-type fiber with $D =$ 4–5 ps/nm km is only about 15 km. Another experiment with four wavelengths spread across the C-band demonstrated 40 Gbps transmission over 25 km NZDSF, limited

by imperfect dispersion slope matching to the fiber type. The authors stated that this tunable design could also be implemented with offset FSR values for dispersion slope compensation across the WDM channel plan. The authors also measured the channel performance as the signal frequency was detuned by ±20 GHz. The evaluation with both the different modulation formats and the frequency detuning tolerance indicated that the dispersion characteristics of the tunable etalon module was stable over a sufficiently wide optical bandwidth to allow for higher-bandwidth modulation formats and for source wavelength drift or etalon thermal drift. The authors noted that the group delay ripple performance of these devices is much better than tunable dispersion compensators based on chirped fiber gratings, and so may be more suitable for deployment at in-line amplifier sites in addition to at terminal sites.

In 2003, X. Shu et al. from Indigo Photonics and Aston University demonstrated an interesting tunable dispersion compensator that entailed a similar tunability mechanism to the JDS work above, but with etalons implemented in optical fiber with mirrors formed by overlapped fiber gratings [132], as shown in Fig. 14(c). The authors suggest that a fiber-based etalon device could be easier to manufacture and have lower loss than a bulk-optic device. "These devices have the advantages of chirped fiber grating devices but exhibit low group delay ripple because the delay comes from the cavity and not the grating." The frequency offset between the two etalons in this case was varied by applying strain to the fiber gratings. The device provided a dispersion of ±200 ps/nm over a 20-GHz bandwidth on a 50 GHz grid. The device was evaluated in a creative fashion for a low-dispersion device, placed in a recirculating loop with a 95.7-km SMF span, an EDFA, and enough DCF to compensate the span in combination with the −200 ps/nm etalon dispersion. A 10-Gbps signal survived six round trips through this loop. The actual signal impairment due to the etalon compensator is difficult to state, because the results were not compared to an entirely DCF-compensated loop. The same group also demonstrated a tunable multi-channel dispersion slope compensator based on the same technology in 2004 [133], with results shown in Fig. 14(a,b).

Dispersion compensators with continuous group delay such as DCF and HOM fiber not only reshape the individual WDM channels but also compensates for the temporal shifts between channels, causing the same pattern-dependent inter-channel nonlinear effects to occur in each amplified fiber span. In 1999, M. Eiselt proposed that this effect could be reduced by either designing a system dispersion map with under-compensated spans to leave approximately half a bit per span of "walk-off" between adjacent channels, or by the addition of spectrally-periodic dispersion compensators that inherently do not realign the inter-channel delay [119]. In 2003, Mollenauer et al. from Lucent [120,121] demonstrated this effect, using the periodic group delay of etalon compensators to reduce cross-phase modulation induced jitter in the transmission of 16 × 10 Gbps channels spaced at 50 GHz over greater than 20,000 km (BER of 10^{-3}) with dispersion-managed soliton propagation. Each 100 km NZDSF span was compensated 80% by DCF and 20% by an etalon compensator. Compared to an equivalent system with all-DCF compensation, the transmission distance was approximately doubled by the channel decorrelation provided by the etalon periodic group delay, with the group delay and resulting transmission performance shown in Fig. 15(b,c). The etalon compensator modules for 20 km of NZDSF had GDR of ±0.2 ps [Fig. 15(a)] and insertion loss ripple (ILR) of ±0.2 dB [Fig. 15(b)]. The authors noted that noise accumulation from peaks in the etalon ILR were compensated with an additional periodic amplitude filter, but the GDR of the devices caused no penalty. This

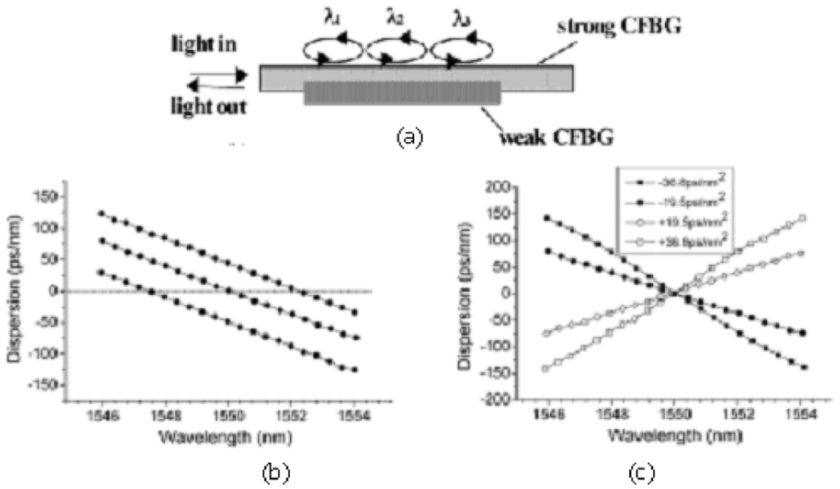

Fig. 14. From Shu et al. [133], (a) A schematic of the fiber-based Gires-Tournois all-pass filter, and plots of dispersion across channels for this device as the (b) dispersion setting and (c) dispersion slope setting were varied.

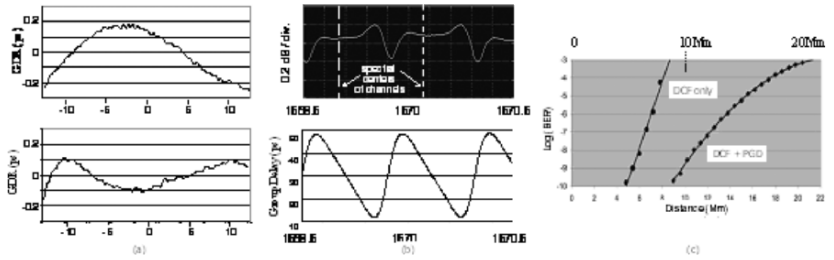

Fig. 15. (a) Group delay ripple for two individual channels, (b) Periodic group delay and insertion loss ripple over two channels, and (c) average bit error rate performance versus distance both for complete compensation with DCF and for compensation with 80% DCF, 20% etalon compensator [120,121].

was a very specialized application of low-dispersion etalon compensators. A standard etalon compensator for 80- or 100-km NZDSF would require more etalon stages and have proportionally higher GDR and ILR. Also, the soliton experiment required only 16 center channels out of the 80 50-GHz spaced channels available across the C-band, so the C-band uniformity of the channel bandwidth, GDR, ILR and dispersion slope was not demonstrated.

In 2004, D. Yang et al. from Avanex published the most advanced transmission paper to date demonstrating etalon-based dispersion compensators in a more commercial configuration [134]. The Gires-Tournois micro-optic air gap etalon modules

with 50 GHz FSR and 25 GHz dispersion bandwidth were designed to compensate for the dispersion and slope of 80 km SMF spans. These modules were compared to slope-matched DCF modules for 80 km SMF in a 400-km C-band recirculating loop experiment. For WDM transmission of 40 × 10 Gbps C-band NRZ channels spaced at 100 GHz covering the entire C-band over eight trips through the loop for 3200 km total distance, the performance difference between the loop with DCF or with etalon DCM modules was "within the margin of error for loop experiments. The authors stated that the micro-optic air-gap etalons don't require thermal stabilization. However, without system testing with the etalons at multiple temperatures such as 25°C, 45°C and 65°C, there is no proof of thermal stability, only proof that the devices were optimized at room temperature.

These types of dispersion-compensation comparison experiments between multiple technologies require that care be taken to maintain all other transmission system factors constant such as OSNR and optical power levels into the transmission fiber. Also, a significant test with channelized devices, or with any device for that matter, is to measure the performance of all channels at several distances, i.e., at 800, 1600, 2400, and 3200 km to look for distance-dependent effects. The performance of the etalon-compensated system could be notably superior to the DCF-compensated system for short distances because of lower optical nonlinearity, but at some point degrade rapidly as the spectral distortion caused by limited dispersion bandwidth and insertion loss ripple become the dominant system impairment. It is also useful to evaluate channelized devices at the actual expected operating temperature. While the ambient temperature of devices in a laboratory is likely 25°C, components within actual equipment often operate at 45°C, and it is important to verify the thermal stability of the channel characteristics such as dispersion amplitude and ripple, and dispersion passband width and frequency alignment.

A few things should be noted about the previous result, related to the bandwidth-limited nature of any channelized compensator. Any source of increased optical bandwidth would decrease the number of bandwidth-limited compensators that could be cascaded without spectral distortion of the optical signal, and there could be a few different sources in a commercial system. The channel rate in the experiment was 10.0 Gbps with NRZ modulation. A more realistic 3200 km ULH commercial systems would likely use higher data rates because of FEC overhead and RZ or CSRZ modulation, both of which would increase the WDM signal optical bandwidth. Also, the lower dispersion of NZDSF fiber types as opposed to the SMF of the previous experiment, and the use of higher per-channel optical power levels such as 5 dBm/ch as is common in EDFA-based ULH systems could introduce more SPM-induced spectral broadening of the WDM signals. In the author's experience, distances up to 2000 km are achievable with temperature-stabilized etalon compensators for 40 × 12.5 Gbps with RZ modulation over NZDSF fiber.

Etalon compensators have low insertion loss and low optical nonlinearity, and can be used successfully for 10 Gbps long-haul transmission. There is very little undesirable polarization-dependent performance or MPI. Modules can also be configured for different applications, using many etalon stages for small GDR in high-performance applications, or a minimum of stages for minimum cost. The GDR is much smaller than chirped grating devices. However, they also have insertion loss ripple in the passband with a deterministic shape that accumulates linearly with compensator count, and have issues with thermal stability of the intra-etalon alignment when not actively

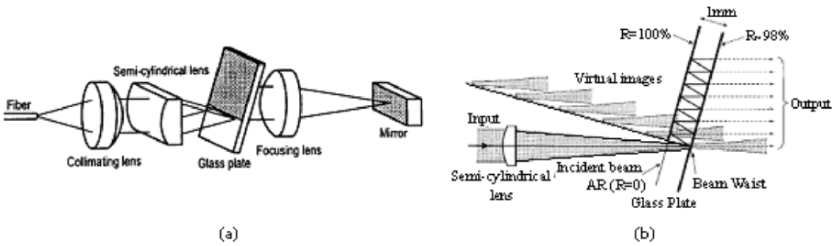

Fig. 16. (a) Group delay ripple for two individual channels, (b) Periodic group delay and insertion loss ripple over two channels, and (c) average bit error rate performance versus distance both for complete compensation with DCF and for compensation with 80% DCF, 20% etalon compensator [7.5, 7.6].

stabilized. To be exceedingly repetitive, the group delay bandwidth, the GDR and the ILR of any compensator with periodic group delay characteristics requires very application-specific performance verification.

7.2. Virtually-Imaged Phased Array (VIPA)

M. Shirasaki from Fujitsu introduced the VIPA dispersion compensator in 1997 [135,136]. A schematic of the device is shown in Fig. 16(a,b). In the VIPA, light is line-focused into a tilted glass plate coated with high reflectivity on one side and low reflectivity on the other, very much like a Gires-Tournois etalon, to form a virtually-imaged phased array that provides high wavelength-dependent angular dispersion. The VIPA is similar to an arrayed-waveguide-grating (AWG) DWDM demultiplexer, except with a small free spectral range so that the spectral components within a WDM channel are separated rather than whole channels. The dispersed spectral components are then translated into wavelength-dependent path length by a translatable focusing lens and mirror for dispersion compensation. The VIPA operates in reflection with an isolator and is periodic like the etalon compensators that we have seen, with the accompanying advantages and disadvantages. It has the unique property among broadband compensators, however, of being manually tunable via the reflecting mirror. Early versions had a large tuning knob on one end.

The VIPA device was demonstrated in 2000 by L.D. Garrett et al. from AT&T and Avanex [137] in 16×10 Gbps NRZ transmission with 100 GHz channel spacing over six 80-km spans of SMF, with comparison to DCF performance. For the same average OSNR after 480 km, there was a performance increase for all channels in the VIPA system relative to the SMF system, with an average value of 0.85 dB. The authors attributed this improvement to reduced nonlinearity in the VIPA devices and reduced cross-phase modulation from the per-channel compensation, as discussed by M. Eiselt in [119]. The VIPA in that experiment was tunable from -1100 to -1500 ps/nm, and had a 100-GHz FSR. In 2002, H. Ooi et al. from Fujitsu [138] used VIPA compensators to provide optimized post-compensation for each channel in the transmission of 88 channels at 43 Gbps over 600 km of NZDSF using the C and L-bands. The broadband

tunability feature of the VIPA is quite appealing both for laboratory and field use. However, the VIPA is not a commercially available device as of publication date.

7.3. Electronic "Dispersion Compensators"

New semiconductor chips have recently become commercially available for the electronic compensation of inter-symbol interference (ISI) at 2.5 and 10 Gbps [139,140], and devices operating at 40 Gbps have also been experimentally demonstrated [7.26]. There has been previous work in this field dating back at least to J.H. Winters et al. in 1990 [143,144], and a great deal of related work on electronic adaptive equalizer filters for non-optical applications. These chips are generally referred to as "electronic dispersion compensation" or "EDC" chips, although they are in reality adaptive receiver equalizers that compensate for signal amplitude distortion in a received signal from many sources including chromatic dispersion, polarization mode dispersion [145] or poor transmitter performance such as low extinction ratio or insufficient electrical bandwidth. The EDC chips are placed after the photoreceiver in each optical channel, and typically incorporate the clock and data recovery (CDR) function. There are also specialized versions of EDC that are optimized to compensate for the modal dispersion of multi-mode fiber [142]. EDC is inherently single-channel, and is not a replacement for broadband dispersion compensators in long multi-span systems. EDC chips thus fit in the same market niche as tunable single-channel chirped gratings, although a single system could use both EDC to compensate for PMD and tunable gratings to compensate for chromatic dispersion. EDC chips have the advantage of cost effectiveness and compact size, but single-channel chirped gratings may compensate for larger amounts of chromatic dispersion and are not limited by electronic bandwidth for 40 Gbps and higher applications.

Like forward error correction (FEC), EDC improves the channel error rate by a specified number of dBs in terms of equivalent Q-value, and these dBs of "link margin" can be used to improve overall system performance in many ways. However, the amount of improvement can be dependent on the nature of the dominant optical impairment [140]. In 2004, Castagnozzi et al. from AMCC reported an all-digital 3-symbol equalizer using FEC feedback with a 10-Gbps NRZ signal and increasing amounts of either chromatic dispersion or polarization mode dispersion [140]. The transmitter chirp and extinction ratio were not specified. Figure 17(a) shows simulation results indicating that while maintaining a 2-dB maximum OSNR penalty and 10^{-7} BER, the equalizer increased the maximum allowable link dispersion by 800 ps/nm, increasing the maximum link distance by 50 km in SMF. Alternatively, at a fixed dispersion of 1530 ps/nm (90 km of SMF), the OSNR penalty was improved by 6 dB by electronic equalization. For PMD compensation at a 10^{-3} BER, Fig. 17(b) shows that the equalizer reduced the OSNR penalty by 3.5 dB for 70 ps DGD, or increased the PMD tolerance from 50 to 60 ps with a 2-dB OSNR penalty. The chromatic dispersion result is more applicable to point-to-point links, and the PMD result to longer multi-span systems with chromatic dispersion compensation provided by other technologies.

The extra link margin provided by EDC might be used in single-span or few-span links to increase the maximum link length without requiring "optical domain" dispersion compensation devices. In a multi-span system, EDC might be used to relax the required tolerance on the broadband in-line dispersion compensators or to increase the maximum transmission system length. The margin from EDC can also be used

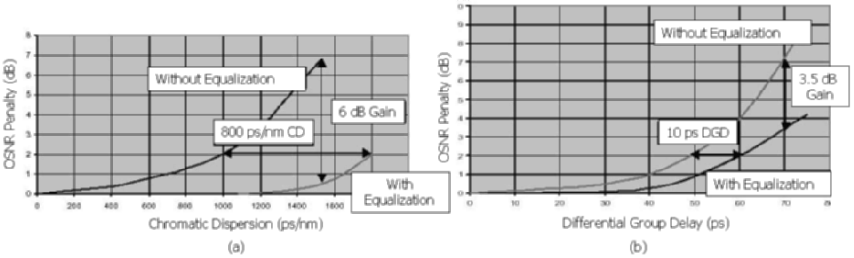

Fig. 17. Performance of electronic dispersion equalization for 10 Gbps NRZ signal impaired by a) chromatic dispersion and b) polarization mode dispersion [140].

by transponder vendors to maintain the transmission distance specifications of their modules (i.e., "2 dB penalty at 16,000 ps/nm dispersion") while using lower-cost, lower-quality optical transmitter and receiver components, in which case the system margin gain from EDC is not available to the optical transmission system designer. Given the low cost of electronics compared to optical components, EDC will likely become as ubiquitous as FEC in optical communications systems.

8. Conclusion

When choosing a dispersion compensation technology for a given application, there are many important factors other than procuring the correct amount of negative dispersion. Each technology has different strengths and weaknesses that should be understood, including but not limited to thermal stability, optical channel bandwidth and channel separation, group delay ripple, and multi-path interference. These properties limit the data rates of the signals being compensated, and limit the maximum length of a multi-span system with compensators for each span.

A statement that "compensator technology "X" shows no additional penalty when compared to DCF" is meaningless without additional information such as "for WDM transmission of 40 $\times$ 10.7 Gbps RZ-modulated signals, spaced by 100 GHz, over a ten-span system with a compensator at each amplifier site, over a temperature range of 25°C to 65°C." Note that stating that a device "worked in a 6000-km system" alone is insufficient. To cite a real example, a single novel compensator may have been used for dispersion slope cleanup at the output of a 6000-km system, but that does not imply that the same technology would perform acceptably for the sixty in-line compensators in the same 6000-km system. Channelized dispersion compensators in particular also need to be tested over the expected operating temperature, to evaluate the temperature stability of the amount of dispersion, the variation across the channels, and the optical bandwidth of the channels. We have not mentioned it much, but compensators for ULH applications should also be tested over an extended period of time with a polarization scrambler in the transmitter to look for polarization-dependent loss, polarization-mode dispersion, and MPI effects that might not be noticed in a short-term measurement. Of course, for single-span, low performance applications, the dominant question may still be "how small and cheap can you make it?"

The combination of the widespread deployment of NZDSF fiber types with high relative dispersion slope, commercial deployment of WDM transmission systems with 10 Gbps channels, and the availability of venture capital funds for the telecomm market caused an explosion of research in the area of chromatic dispersion compensation technology in the late-nineties. Many of the most commercial approaches have been discussed above. There are also many extremely creative dispersion compensation approaches that have not been covered because the technologies are not yet ready for transmission experiments. Unfortunately, the end of the "Telecom Bubble" in approximately 2000 caused the demise of many of the small companies and a few large companies mentioned above, with the hopefully temporary demise of their technological specialties. Hopefully the combination of WDM system designers seeking high-quality dispersion compensators and WDM purchasing managers seeking an extremely good price will lead to the re-animation of the dispersion compensation industry.

In late 2004, the dominant technology for high-performance dispersion compensation applications was still DCF. DCF is available with 100% or nearly 100% slope matching for the dominant installed terrestrial fiber types, with better insertion loss and optical nonlinearity numbers than ever before. DCF is also broadband, with no channel data rate, bandwidth or spacing limitations. Commercial higher-order-mode fiber compensators also provided high quality broadband dispersion and slope compensation with low insertion loss that was capable of long-haul transmission distances at 40-Gbps and ultra-longhaul (3000–6000 km) distances at 10-Gbps, but did not survive the market. The current commercial challenger to DCF for 10 Gbps long-haul applications (say 500–3000 km) appears to be the etalon compensator. For a brief time, there was a broadband etalon compensator with $\pm$ 14% tunability that also did not survive the market. For devices with adequate performance for long-haul systems, competitive forces have led all compensators for a specific span length to cost about the same in volume independent of fiber type or compensator technology, so that performance and not price has to be a differentiator for new products.

To compete commercially, many of the surviving alternative-technology compensator companies have focused their development efforts on devices with just-adequate quality for metro, few-span applications where price and size are the most significant product differentiators and DCF is perhaps more vulnerable to competition. There are broadband-chirped and channelized-chirped gratings with acceptable performance for single or few-module applications, and of course the etalon compensators are interested in producing low-end models for this market. The electronic equalizer also takes aim at the metro market, extending the reach of transponders to eliminate the need for dispersion compensators altogether in short systems. Tunable single or few-channel gratings and dispersion-managed fiber spans, extensively demonstrated in the laboratory, may someday be important enablers for high-performance commercial 40 Gbps WDM systems.

Apologies are due to anyone whose research was not mentioned in the relevant sections of this document. In covering an enormous range of material, the author regrets that many valuable papers may have been inadvertently left out.

References

1. N.S. Bergano and C.R. Davidson, "Circulating loop transmission experiments for the study of long-haul transmission systems using erbium-doped fiber amplifiers," J. Lightwave Technol. **13** (5) 879–888 (May 1995).
2. Y. Sun, B.S. Marks, I.T. Lima, K. Allen, G.M. Carter, C.R. Menyuk, "Polarization state evolution in recirculating loops," Proc. of OFC, Paper ThI4 (2002).
3. N.S. Bergano, F.W. Kerfoot and C.R. Davidson, "Margin Measurements in optical amplifier systems," Photon. Technol. Lett. **5** (3) 304–306 (1993).
4. N.A. Ollson, "Lightwave systems with optical amplifiers," J. Lightwave Technol. **7** (7) 1071–1082 (July 1989).
5. J.L. Zyskind, D.J. DiGiovanni, J.W. Sulhoff, P.C. Becker and C.H. Brito Cruz, "High performance erbium-doped fiber amplifier pumped at 1.48 μm and 0.97 μm," Opt. Ampl. Appl., Monterrey, CA), Paper PD-P6, 1990.
6. M. Nakazawa, Y. Kimura and K. Suzuki, "An ultra efficient erbium-doped fiber amplifier of 10.2 dB/mW at 0.98 μm pumping and 5.1 dB/mW at 1.48 μm pumping, Opt. Ampl. Appl., Monterrey, CA, Paper PD-P1, 1990.
7. C.D. Poole, J. M. Wiesenfeld, A. R. McCormick, K. T. Nelson, "Broadband dispersion compensation by using the higher-order spatial mode in a two-mode fiber," Opt. Lett. **17**, 985 (1992).
8. A.J. Antos and D.K. Smith, "Design and characterization of dispersion compensating fiber based on the LP_{01} mode," J. Lightwave Technol. **12** (10), 1739–1745 (1994).
9. D. Marcuse, "Single-channel operating in very long nonlinear fibers with optical amplifiers at zero dispersion," J. Lightwave Technol **9**, 3 (1991).
10. L. Gruner-Nielsen, S.N. Knudsen, T. Veng, B. Edvold and C.C. Larsen, "Design and manufacture of dispersion compensating fibre for simultaneous compensation of dispersion and dispersion slope," in Proc. of OFC, Paper WM132-1 (1999).
11. M. Wandel, P. Kristensen, T. Beng, Y. Qian, Q. Le and L. Gruner-Nielsen, "Dispersion compensating fibers for non-zero dispersion fibers," Proc. of OFC, Paper WU1 (2002).
12. T. Yokokawa, T. Kato, T. Fuji, Y. Yamamoto, N. Honma, A. Kataoka, M. Onishi, E. Sasaoka, K. Okamoto, "Dispersion compensating fiber with large negative dispersion around -300 ps/nm/km and its application to compact module for dispersion adjustment," Proc. of OFC, Paper FK5 (2003).
13. L. Gruner-Nielsen, Y. Qian, B. Palsdottir, P. Borg Gaarde, S. Drybol and T. Veng, "Module for simultaneous C+L band dispersion compensation and Raman amplification," Proc. of OFC, Paper TuJ6 (2002).
14. M. Hirano, A. Tada, T. Kato, M. Onishi, Y. Madio, M. Nishimura, "Dispersion compensating fiber over 140 nm bandwidth," Proc. of ECOC, Paper Th.M.1.4 (2001).
15. B. Edvold and L. Gruner-Nielsen, "New techniques for reducing the splice loss to dispersion compensating fiber," in Proc. of ECOC, Paper TuP.07, 10996.
16. A.M. Vengsarkar and W.A. Reed, "Dispersion-compensating single-mode fibers: Efficient designs for first-and second-order compensation," Opt. Lett. **18**, 924–926 (1993).
17. C.D. Chen, J.-M. P. Delavaux, B.W. Hakki, O. Mizuhara, T.V. Nguyen, R.J. Nuyts, K.Ogawa, Y. K. Park, R.E. Tench, L.D. Tzeng and P.D. Yeates, "Field experiment of 10Gbit/s, 360 km transmission through embedded standard (non-DSF) fibre cables," Electronics Lett. **30** (14), 1159–1160 (1994).

18. Y. Akasaka, R. Sugizaki, A. Umeda, T. Kamiya, "High-dispersion-compensation ability and low nonlinearity of W-shaped DCF," Proc. of OFC, paper Tha3 (1996).

19. Y.K. Park, P.D. Yeates, J.-M. P. Delavaux, O. Mizuhara, T.v. Nguyen, L.D. Tzeng, R.E. Tench, B.W. Hakki, C.D. Chen, R.J. Nuyts and K. Ogawa, "A field demonstration of 20-Gbps capacity transmission over 360 km of installed standard (non-DSF) fiber," IEEE Photon. Technol. Lett. **7** (7), 816–818 (1995).

20. N. Kikuchi, S. Sasaki and K. Sekine, "10 Gbit/s dispersion-compensated transmission over 2245 km conventional fibres in a recirculating loop," Electronics Lett. **31** (5), 375–377 (1995).

21. L. Leng, B. Zhu, S. Stulz and L.E. Nelson, "1.6 Tb/s (40 × 40 Gbps) transmission over 500 km of nonzero dispersion fiber with 100-km amplified spans compensated by extra-high-slope dispersion-compensating fiber," Proc. of OFC, Paper ThX2 (2002).

22. P.B. Hansen, G. Jacobovitz-Veselka, L. Gruner-Nielsen and A.J. Stentz, "Raman amplification for loss compensation in dispersion compensating fibre modules," Electron. Lett. **34** (11), 1136–1137 (1998).

23. Y. Emori, Y. Akasaka and S. Namiki, "Broadband lossless DCF using Raman amplification pumped by multi-channel WDM laser diodes," Electron. Lett. **34**, 22 (1998).

24. H. Bissessur, G. Charlet, C. Simonneau, S. Borne, L. Pierre, C. De Barros, P. Tran, W. Idler and R. Dischler, "3.2 Tb/s (80×40 Gbps) C-band transmission over 3×10 km with 0.8bit/s/Hz efficiency," Proc. of ECOC, Paper PD.M.1.11 (2001).

25. T. Miyamoto, T. Tsuzaki, T. Okuno, M. Kakui, M. Hirano, M. Onishi and M. Shigematsu, "Raman amplification over 100 nm-bandwidth with dispersion and dispersion slope compensation for conventional single mode fiber," Proc. of OFC, Paper TuJ7, p. 66–67 (2002).

26. L. Leng, S. Stulz, B. Zhu, L.E. Nelson, b. Edvold, L. Gruner-Nielsen, S. Radic, J. Centanni and A. Gnauck, "1.6-Tb/s (160 × 10.7 Gbps) transmission over 4000 km of Nonzero dispersion fiber at 25-GHz channel spacing," IEEE Photon. Technol. Lett. **15** (8), 1153–1155 (2003).

27. R.E. Neuhauser, P.M. Krummrich, H. Bock and C. Glingener, "Impact of nonlinear pump interactions on broadband distributed Raman amplification," Proc. of OFC, Paper MA4 (2001).

28. J. Bromage, P.J. Winzer, L.E. Nelson and C.J. McKinstrie, "Raman-enhanced pump-signal four-wave mixing in bidirectionally pumped Raman amplifiers," Proc. of OAA, Paper OWA-5 (2002).

29. B. Zhu, L.E. Nelson, S. Stulz, A.H. Gnauck, C. Doerr, J.Leuthold, L. Gruner-Nielsen, M.O Pedersen, J. Kim and R. Lingle, "High spectral density long-haul 40-Gbps transmission using CSRZ-DPSK format," J. Lightwave Technol. **22** (1), 208–214 (2004).

30. H.S. Chung, H. Kim, S.E. Jin, E.S. Son, D.W. Kim, K.M. Lee, H.Y Park and Y.C. Chung, "320-Gbps WDM transmission with 50-GHz channel spacing over 564km of short-period dispersion managed fiber (Perfect Cable)," IEEE Photon. Technol. Lett. **12** (10), 1397–1399 (2000).

31. S.N. Knudsen, M.O. Pedersen and L. Gruner-Nielsen, "Optimisation of dispersion compensating fibres for cabled long-haul application," Electronics Lett. **36**, 25 (7 December 2000).

32. S.N. Knudsen, "Design and manufacture of dispersion compensating fibers and their performance in systems," Proc. of OFC, paper WU3, p. 330–331 (2002).

33. L.E. Nelson, L.D. Garrett, A.R. Chraplyvy, and R.W. Tkach, "NZDSF dispersion maps in 2000-km 8×10-Gbps WDM transmission," Proc. of ECOC, pp.315–316 (1998).

34. A. Boskovic and D.L. Butler, "Transmission of 32 channels at 10Gbit/s over 450 km of dispersion managed cable using LEAFTM and sub-LSTM fibres," Electronics Lett. **35** (5) (4 March 1999).

35. K. Tanaka, T. Tsuritani, N. Edagawa and M. Suzuki, "320 Gbit/s (32 × 10.7Gbit/s) error-free transmission over 7280 km using dispersion flattened fibre link with standard SMF and slope compensating DCF," Electronics Lett. **35**, 21 (14 October 1999).

36. H.S. Chung, S.E. Jin, D.W. Lee, D.W. Kim and Y.C. Chung, "640 Gbps (32 × 20 Gbps) WDM transmission with 0.4 bit/s/Hz spectral efficiency using short-period dispersion managed fiber (Perfect CableTM)," Proc. of OFC, Paper ThF6 (2001).

37. Y. Inada, K. Fukuchi, T. Ono, T. Ogata and H. Okamura, "2400-km transmission of 100-GHz-spaced 40-Gbps WDM signals using a "double-hybrid" fiber configuration," Proc. of ECOC, Paper WeF.1.6 (2001).

38. H. Sugahara, K. Fukuchi, A. Tanaka, Y. Inada and T. Ono, "6,050 km transmission of 32 × 42.7Gbps DWDM signals using Raman-amplified quadruple-hybrid span configuration," Proc. of OFC, Paper FC6 (2002).

39. L. du Mouza et al, "1.28 Tbit/s (32 × 40 Gbit/s) WDM transmission over 2400 km of Tera-Lighttm/Reverse TeraLight© fibres using distributed all-Raman amplification," Electronics Lett. **37**, 21 (11 October 2001).

40. C. Rasmussen, T. Fjelde, J. Bennike, F. Liu, S. Key, B. Mikkelsen, P. Mamyshev, P. Serbe, P. van der Wagt, Y. Akasaka, D. Harris, D. Gapontsev, V. Ivshin and P. Reeves-Hall, "DWDM 40G transmission over trans-pacific distance (10 000 km) using CSRZ-DPSK enhanced FEC, and all-Raman-amplified 100-km UltraWave fiber spans," J. Lightwave Technol. **22** (1), 203–207 (January 2004).

41. N.S. Bergano, C.R. Davidson, B.M. Nyman, S.G. Evangelides, J.M. Darcie, J.D. Evankow, P.C. Corbett, M.A. Mills, G.A. Ferguson, J.A. Nagel, J.L. Zysking, J.W. Sulhoff, A.J. Lucero and A.A. Klein, "40 Gbps WDM transmission of eight 5 Gbps data channels over transoceanic distances using the conventional NRZ modulation format," Proc. of OFC, Paper PD-19 (1995).

42. N.S. Bergano and C.R. Davidson, "Wavelength division multiplexing in long-haul transmission system," J. Lightwave Technol. **14** (6), 1299–1308 (June 1996).

43. J.-X. Cai, D.G. Foursa, C.R. Davidson, Y. Cai, G. Domagala, H. Li, L. Liu, W.W. Patterson, A.N. Pilipetskii, M. Nissov and N.S. Bergano, " A DWDM demonstration of 3.73 Tb/s over 11,000 km using 373 RZ-DPSK channels at 10 Gbps," Proc. Of OFC, Paper PD-22 (2003).

44. T. Tsuritani, K. Ishida, A. Agata, K. Shimomura, I. Morita, T. Tokura, H. Taga, T. Mizuochi, N. Edagawa and S. Akiba, " 70-GHz-spaced 40×32.7 Gbps transpacific transmission over 9400 km using prefiltered CSRZ-DPSK signals, all-Raman repeaters, and symmetrically dispersion-managed fiber spans," J. Lightwave Technol. **22** (1) 215–223 (January 2004).

45. G. Charlet, E. Corbel, J. Lazaro, A. Klekamp, R. Dischler, P. Tran, W. Idler, H. Mardoyan, A. Konczykowska, F. Jorge and S. Bigo, " WDM transmission at 6-Tb/s capacity over transatlantic distance, using 42.7 Gb/s differential phase-shift keying without pulse carver," J. Lightwave Technol. **23** (1), 14–107 (January 2005).

46. S.N. Knudsen, B. Zhu, L.E. Nelson, M.O. Pedersen, D.W. Peckham and S. Stulz, "420 Gbit/s (42 × 10 Gbit/s) WDM transmission over 4000 km of UltraWave fibre with 100 km dispersion-managed spans and distributed Raman amplification," Electron. Lett. **37** (15) (19 July 2001).

47. B. Zhu, S.N. Knudsen, L.E. Nelson, D.W. Peckham, M.O. Pedersen and S. Stulz, "800 Gbit/s (80 × 10.664 Gbit/s) WDM transmission over 5200 km of fibre employing 100 km dispersion-managed spans," Electron. Lett. **37** (24) (22 November 2001).

48. B. Zhu, L. Leng, L.E. Nelson, S. Knudsen, J. Bromage, D. Peckham, S. Stulz, K. Brar, C. Horn, K. Feder, H. Thiele and T. Veng, "1.6Tb/s (40 × 42.7Gbps) transmission over 2000 km of fiber with 100-km dispersion-managed spans," Proc. of ECOC, Paper PD.M.1.8 (2001).

49. F. Liu J. Bennike, S. Dey, C. Rassmussen, B. Mikkelsen, P. Mamyshev, D. Gapontsev and V. Ivshin, "1.6 Tb/s (42×42.7Gbps) transmission over 3600 km UltraWave$^{\mathrm{TM}}$ fiber with all-Raman amplified 100-km terrestrial spans using ETDM transmitter and receiver," Proc. of OFC, Paper FC7 (2002).

50. C. Rassmussen, S. Dey, F. Liu, J. Bennike, B. Mikkelsen, P. Mamyshev, M. Kimmitt, K. Springer, D. Gapontsev and V. Ivshin, "Transmission of 40 × 42.7 Gbps over 5200 km UltraWave fiber with terrestrial 100-km spans using turn-key ETDM transmitter and receiver," Proc. of ECOC (2002).

51. B. Zhu, L. Nelson, L. Leng, S. Stulz, M. Pedersen, D. Peckham, "Transmission of 1.6 Tb/s (40 × 42.7 Gbps) over transoceanic distance with terrestrial 100-km amplifier spans," Proc. of OFC, Paper FN2 (2003).

52. G.C. Gupta, L.L. Wang, O. Mizuhara, R.E. Tench, N.N. Dang, P. Tabaddor and A. Judy, "3.2-Tb/s (40 ch × 80 Gbps) transmission with spectral efficiency of 0.8 b/s/Hz over 21×100 km of dispersion-managed high local dispersion fiber using all-Raman amplified spans," IEEE Photon. Technol. Lett. **15** (7) 996–998 (July 2003).

53. C.D. Poole, J.M. Wiesenfeld, D.J. DiGiovanni and A.M. Vengsarkar, "Optical fiber-based dispersion compensation using higher order modes near cutoff," J. Lightwave Technol. **12** (10), 1766–1758 (1994).

54. A.H. Gnauck, L.D. Garrett, Y. Danziger, U. Levy and M. Tur, "Dispersion and dispersion-slope compensation of NZDSF over the entire C band using higher-order-mode fiber," Electronics Lett. **36** (23) (9 November 2000).

55. S. Ramachandran, B. Mikkelsen, L.C. Cowsar, M.F. Yan, G. Raybon, L. Boivin, M. Fishteyn, W.A. Reed, P. Wisk, D. Brownlow, R.G. Huff and L. Gruner-Nielsen, "All-fiber, grating-based, higher-order-mode dispersion compensator for broadband compensation and 1000-km transmission at 40-Gbps," IEEE Photon. Technol. Lett. **13** (6), 632–634 (2001).

56. E.L. Goldstein and S. Eskildsen, "Scaling limitations in transparent optical networks due to low-level crosstalk," IEEE Photon. Technol. Lett. **7**, 93–94 (1995).

57. C. Rasmussen, F. Liu, R.J.S. Pedersen and B.F. Jorgensen, "Theoretical and experimental studies of the influence of the number of crosstalk signals on the penalty caused by incoherent optical crosstalk," Proc. of OFC, Paper TuR5 (1999).

58. S. Ramachandran, J. Nicholson, S. Ghalmi, M. Yan, P. Kristensen, "Measurement of multi-path interference in the coherent cross-talk regime," Proc. of OFC, Paper TuK6, pp. 231–232 (2003).

59. S. Ramachandran, G. Raybon, B. Mikkelsen, M. Yan, L. Cowsar and R.-J. Essiambre, "1700 km transmission at 40 Gbit/s with 100 km amplifier spacing enabled by higher-order-mode dispersion compensation," Electron. Lett. **37** (22) (25 October 2001).

60. C. Meyer, S. Lobo, D. Le Guen, F. Merlaud, L. Billes, T. Georges, "High spectral efficiency wideband terrestrial ULH RZ transmission over LEAF with realistic industrial margins," Proc. of ECOC, Paper 1.1.2 (2002).

61. S. Ramachandran, S. Ghalmi, S. Chandrasekhar, I. Ryazansky, M.F. Yan, F.V. Dimarcello, W.A. Reed, and P. Wisk, "Tunable dispersion compensators utilizing higher order mode fibers," IEEE Photon. Technol. Lett. **15** (5), 727–729 (2003).

62. L.D. Garrett, M. Eiselt, J. Wiesenfeld, R. Tkach, D. Menashe, U. Levy, Danziger and M. Tur, "ULH DWDM transmission with HOM-based dispersion compensation," Proc. of ECOC, Paper We4.P.98, pp. 752–753 (2003).

63. K.O. Hill, S. Theriault, B. Malo, F. Bilodeau, T. Kitagawa, D.C. Johnson, J. Albert, K. Takiguchi, T. Kataoka and K. Hagimoto, "Chirped in-fibre Bragg grating dispersion compensators: linearisation of dispersion characteristic and demonstration of dispersion compensation in 100 km, 10Gbit/s optical fibre link," Electron. Lett. **30** (21), 1755–1756 (1994).

64. R. Kashyap, P.F. Mckee, R.J. Campbell and D.L. Williams, "Novel method of producing all fibre photoinduced chirped gratings," Electron. Lett. **30**, pp. 996–997 (1994).

65. B.J. Eggleton, P.A. Grug, L. Poladian, K.A. Ahmed and H.-F. Liu, "Experimental demonstration of compression of dispersion optical pulses by reflection from self-chirped optical fibre Bragg gratings," Opt. Lett. **19**, 877–879 (1994).

66. J.A.R. Williams, L.A. Everall, I. Bennion and N.J. Doran, "Fiber Bragg grating fabrication for dispersion slope compensation," IEEE Photon. Technol. Lett. **8** (9), 1187–1189 (1996).

67. C. Scheerer, C. Glingener, G. Fischer, M. Bohn and W. Rosenkranz, "Influence of filter group delay ripples on system performance," Proc. of ECOC, Paper I-410 (1999).

68. B.J. Eggleton, A. Ahuja, P.S. Westbrook, J.A. Rogers, P. Kuo, T.N. Nielsen and B. Mikkelsen, "Integrated tunable fiber gratings for dispersion management in high-bit rate systems," J. Lightwave Technol. **18**, 10 (2000).

69. S. Jamal and J.C. Cartledge, "Variation in the performance of multispan 10-Gbps systems due to the group delay ripple of dispersion compensating fiber Bragg gratings," J. Lightwave Technol. **20** (1), 28–35 (2002).

70. H. Yoshimi, Y. Takushima, and K. Kikuchi, "A simple method for estimating the eye-opening penalty caused by group-delay ripple of optical filters," Proc. of ECOC, Paper 10.4.4 (2002).

71. K. Ennser, M. Ibsen, M. Durkin, M.N. Zervas and R.I. Laming, "Influence of non-ideal chirped fiber grating characteristics on dispersion cancellation," IEEE Photon. Technol. Lett. **10** (10), 1476–1478 (1998).

72. L.-S. Yan, T. Luo, Q. Yu, Y. Xie and A.E. Willner, "System impact of group-delay ripple in single and cascaded chirped FBGs," Proc. of OFC, pp. 700–701 (2002).

73. M.H. Eiselt, C.B. Clausen and R.W. Tkach, "Performance characterization of components with group delay fluctuations," IEEE Photon. Technol. Lett. **15** (8), 1076–1078 (2003).

74. X. Fan, D. Labrake, and J. Brennan, "Chirped fiber grating characterization with phase ripples," Proc. of OFC, pp.638-640 (2003).

75. J.C. Cartledge and H. Chen, "Influence of modulator chirp in assessing the performance implications of the group delay ripple of dispersion compensating fiber gratings," J. Lightwave Technol. **21** (7), pp. 1621–1628 (2003).

76. N.S. Bergano, F.W. Kerfoot, and C.R. Davidson, "Margin measurements in optical amplifier systems," IEEE Photon. Technol. Lett **5** (3), 304–306 (1993).

77. R. Kashyap, A. Ellis, D. Malyon, H.G. Froehlich, A. Swanton and D.J. Armes, "Eight wavelength $\times$ 10 Gbps simultaneous dispersion compensation over 100 km single-mode fibre using a single 10 nanometer bandwidth, 1.3 metre long, super-step-chirped fibre bragg grating with a continuous delay of 13.5 nanoseconds," Proc. of ECOC, Paper ThB.3.2 (1996).

78. R. Kashyap, H.-G. Froelhich, A. Swanton and D.J. Armes, "1.3m long super-step-chirped fibre Bragg grating with a continuous delay of 13.5 nm and bandwidth 10 nm for broadband dispersion compensation," Electron. Lett. **32**, 19 (1996).

79. A.H. Gnauck, L.D. Garrett, F. Forghieri, V. Gusmeroli and D. Scarano, "8 $\times$ 20 Gbps 315-km, 8 $\times$ 10 Gbps 480-km WDM transmission over conventional fiber using multiple broad-band fiber gratings," IEEE Photon. Technol. Lett. **10** (10), 1495–1497 (1998).

80. L.D. Garrett, A.H. Gnauck, F. Forghieri, V. Gusmeroli and D. Scarano, "16 × 10 Gbps WDM transmission over 840-km SMF using eleven broad-band chirped fiber gratings," IEEE Photon. Technol. Lett. **11** (4), 484–486 (1999).

81. A.H. Gnauck, J.M. Wiesenfeld, L.D. Garrett, R.M. Derosier, F. Forghieri, V. Gusmeroli and D. Scarano, "4 × 40 Gbps 75-km WDM transmission over conventional fiber using a broad-band fiber grating," IEEE Photon. Technol. Lett. **11** (11), 1503–1505 (1999).

82. L.D. Garrett, A.H. Gnauck, R.W. Tkach, B. Agogliati, L. Arcangeli, D. Scarano, V. Gusmeroli, C. Tosetti, G. DiMaio and F. Forghieri, "Ultra-wideband WDM transmission using cascaded chirped fiber gratings," Proc. of OFC, Paper PD15 (1999).

83. A.H. Gnauck, J.M. Wiesenfeld, L.D. Garrett, M. Eiselt, F. Forghieri, L. Arcangeli, B. Agogliata, V. Gusmeroli and D. Scarano, "16 × 20-Gbps, 400-km WDM transmission over NZDSF using a slope-compensating fiber-grating module," IEEE Photon. Technol. Lett. **12** (4), 437–439 (2000).

84. L.D. Garrett, A.H. Gnauck, R.W. Tkach, B. Agogliati, L. Argangeli, D. Scarano, V. Gusmeroli, C. Tosetti, G. Di Maio and F. Forghieri, "Cascaded chirped fiber gratings for 18-nm bandwidth dispersion compensation," IEEE Photon. Technol. Lett. **12** (3), 356–358 (2000).

85. J.F. Brennan et al, "Realization of greater than 10-m long chirped fiber Bragg gratings," OSA Trends in Optics and Photonics (TOPS) v.33, Bragg gratings, photosensitivity, and poling in glass waveguides, (OSA, Washington DC, 1999), pp. 35–37 (1999).

86. R. Kashyap, A. Swanton and R.P. Smith, "Infinite length fibre gratings," Electronics Lett. **35** (21, 14th October 1999.

87. J.F. Brennan III, E. Hernandez, J.A. Valenti, P.G. Sinha, M.R. Matthews, D.E. Elder, G.A. Beauchesne and C.H. Byrd, "Dispersion and dispersion-slope correction with a fiber Bragg grating over the full C-band," Proc. of OFC, Paper PD-12 (2001).

88. J.F. Brennan III, M.R. Matthews, W.V. Dower, D.J. Treadwell, W. Wang, J. Porque and X. Fan, "Dispersion correction with a robust fiber grating over the full C-band at 10-Gbps rates with $<$0.3 dB power penalties," IEEE Photon. Technol. Lett. **15** (12), 1722–1724 (2003).

89. B. Koch and J.F. Brennan III, "Dispersion compensation in an optical communications system with an electro-absorption modulated laser and a fiber grating," IEEE Photon. Technol. Lett. **15** (11, 1633–1635 (2003).

90. Y. Painchaud, H. Chotard, A. Mailloux and Y. Vasseur, "Superposition of chirped fibre Bragg grating for third-order dispersion compensation over 32 WDM channels," Electronics Lett. **38**, 24 (2002).

91. R. Lachance, S. Lelievre, Y. Painchaud, "50 and 100 GHz multi-channel tunable chromatic dispersion slope compensator," Proc. of OFC, Paper TuD3 (2003).

92. S. Lelievre, H. Chotard, S. LaRochelle, K.-M. Feng, S. Lee, R. Khosvarani, S.A. Havstad and J.E. Rothenberg, "Multi-channel dispersion compensation using cascaded FBGs for 10 Gbps transmission," Proc. of NFOEC, 2003.

93. F. Ouellette, P.A. Krug, T. Stephens, G. Dhosi and B. Eggleton, "Broadband and WDM dispersion compensation using chirped sampled fibre Bragg gratings," Electronics Lett. **31** (11), 899–900 (25 May 1995).

94. M. Ibsen, A. Fu, H. Geiger and R.I. Laming, "All-fibre 4 × 10 Gbit/s WDM link with DFB fibre laser transmitters and single sinc-sampled fibre grating dispersion compensator," Electron. Lett. **35**, 12 (10 June 1999).

95. W.H. Loh, F.Q. Zhou and J.J. Pan, "Sampled fiber grating based dispersion slope compensator," IEEE Photon. Technol. Lett. **11** (100), 1280–1282 (1999).

96. X.-F. Chen, C.-C. Fan, Y. Luo, S.-Z. Xie and S. Hu, "Novel flat Multichannel filter based on strongly chirped sampled fiber Bragg grating," IEEE Photon. Technol. Lett. **12** (11), 1501–1503 (2000).

97. H. Li, Y. Sheng, Y. Li, J.E. Rothenberg, "Phased-only sampled fiber bragg gratings for high-channel-count chromatic dispersion compensation," J. Lightwave Technol. **21** (9), 2074–2083 (2003).

98. M. Morin, M. Poulin, A. Mailloux, F. Trepanier and Y. Painchaud, "Full C-band slope-matched dispersion compensation based on a phase sampled Bragg grating," Proc. of OFC, Paper WK1 (2004).

99. R.I. Laming, N. Robinson, P.L. Scrivener, M.N. Zervas, S. Barcelos, L. Reekie and J.A. Tucknott," A dispersion tunable grating in a 10-Gbps 100-200-km-step index fiber link," IEEE Photon. Technol. Lett. **8** (3), 428–430 (1996).

100. A.E. Willner, K.-M. Feng, J. Cai, S. Lee, J. Peng and H. Sun, "Tunable compensation of channel degrading effects using nonlinearly chirped passive fiber Bragg gratings," IEEE J. Quantum Electronics **5** (5), 1298–1311 (1999).

101. T.N. Nielsen, B.J. Eggleton, J.A. Rogers, P.S. Westbrook, P.B. Hansen and T.A. Strasser, "Dynamic post dispersion optimization at 40 Gbps using a tunable fiber Bragg grating," IEEE Photon. Technol. Lett. **12** (2), 173–175 (2000).

102. B.J. Eggleton, A. Ahuja, P.S. Westbrook, J.A. Rogers, P. Kuo, T.N. Nielsen and B. Mikkelsen, "Integrated tunable fiber gratings for dispersion management in high-bit rate systems," J. Lightwave Technol. **18** (10), 1418–1432 (2000).

103. R.J. Nuyts, Y.K. Park, P. Gallion, "Dispersion equalization of a 10 Gbps Repeatered transmission system using dispersion compensating fibers," J. Lightwave Technol. **15** (1), 31–42 (1997).

104. J.-X. Cai, K.-M. Feng, A.E. Willner, V. Grubsky, D.S. Sarodubov and J. Feinberg, "Sampled nonlinearly-chirped fiber-Bragg grating for the tunable dispersion compensation of many WDM channels simultaneously," Proc. of OFC, Paper FA7-1, pp. 20–22 (1999).

105. Y. Xie, S. Lee, Z. Pan, J.-X. Cai, A.E. Willner, V. Grubsky, D.S. Starodubov, E. Salik and J. Feinberg, "Tunable compensation of the dispersion slope mismatch in dispersion-managed systems using a sampled nonlinearly chirped FBG," IEEE Photon. Technol. Lett. **12** (10), 1417–1419 (2000).

106. J.-X. Cai, K.-M. Feng, A.E. Willner, V. Grubsky, D.S. Starodubov and J. Feinberg, "Simultaneous tunable dispersion compensation of many WDM channels using a sampled nonlinearly chirped fiber Bragg grating," IEEE Photon. Technol. Lett. **11** (11), 1455–1457 (1999).

107. D. Gauden, E. Goyat, A. Mugnier, P. Lesueur, P. Yvernault and D. Pureur, "A tunable four-channel fiber Bragg grating dispersion compensator," IEEE Photon. Technol. Lett. **15** (10), 1387–1389 (2003).

108. Y. Li, B. Zhu, C. Soccolich, L. Nelson, N. Litchinitser, G. Hancin, "Multi-chanel high-performance tunable dispersion compensator for 40 Gbps transmission systems," Proc. of OFC, Paper ThL4 (2003).

109. J.C. Knight, T.A. Birks, P.S.J. Russell and D.M. Atkins, "All-silica single-mode optical fiber with photonic crystal cladding," Opt. Lett. **21**, 1547–1549 (1996).

110. G. Renversez, B. Kuhlmey and R. McPhedran, "Dispersion management with microstructured optical fibers: ultraflattened chromatic dispersion with low losses," Opt. Lett. **28** (12), 989–991 (2003).

111. T.D. Engeness, M. Ibanescu, S.G. Johnson, O. Weisberg, M. Skorobogatiy, S. Jacobs and Y. Fink, "Dispersion tailoring and compensation by modal interactions in OmniGuide fibers," Opt. Express **11** (10) , 1175–1196 (2003).

112. L.P. Shen, W.-P. Huang, G.X. Chen and S.S. Jian, "Design and optimization of photonic crystal fibers for broad-band dispersion compensation," IEEE Photon. Technol. Lett. **15** (4), 540–542 (2003).

113. F. Poli, A. Cucinotta, S. Selleri and A.H. Bouk, "Tailoring of flattened dispersion in highly nonlinear photonic crystal fibers," IEEE Photon. Technol. Lett. **16** (4), 1065–1067 (2004).

114. S. Johnson, "The design and modeling of microstructured fiber," Proc. of OFC, Tutorial WA4 (2004).

115. S. Choi, W. Shin and K. Oh, "Higher-order-mode dispersion compensation technique based on mode converter using hollow optical fiber," Proc. of OFC, Paper WA6, pp. 217–218 (2002).

116. C.K. Madsen and G. Lenz, "Optical all-pass filters for phase response design with applications for dispersion compensation," Photon. Technol. Lett. **10** (7), 994–996 (July 1998).

117. G. Lenz and C.K. Madsen, "General optical all-pass filter structures for dispersion control in WDM systems," J. Lightwave Technol. **17** (7), 1248–1254 (July 1999).

118. C.K. Madsen and J.H. Zhao, *Optical Filter Design and Analysis* (New York: Wiley, 1999).

119. M. Eiselt, "Does spectrally periodic dispersion compensation reduce non-linear effects," Proc. of ECOC, Paper TuC1.2 (1999).

120. L.F. Mollenauer, A. Grant, L. Xiang, W. Xing, X. Chongjin and K. Inuk, "Experimental test of dense WDM using novel, periodic-group-delay-complemented dispersion compensation and dispersion managed solitons: transmission to beyond 20,000 km," Proc. of CLEO, pp. 2121–2122 (2003).

121. L. Mollenauer, X. Wei, X. Liu, A. Grant, and C. Xie, "Reduction of timing jitter in dense WDM by the use of periodic group delay dispersion compensators," Center for Nonlinear Studies Workshop: "Advances in Raman-Based, High-Speed Photonics" Los Alamos National Laboratory, February 3, 2003).

122. A.H. Gnauck, C.R. Giles, L.J. Cimini, Jr., J. Stone, L.W. Stulz, S.K. Korotky and J.J. Veselka, "8-Gbps-130 km transmission experiment using Er-doped fiber preamplifier and optical dispersion equalization," Photon. Technol. Lett. **3** (12), 1147–1149 (December 1991).

123. D. Garthe, J. Ip, P. Colbourne, R.E. Epworth, W.S. Lee and A. Hadjifotiou, "Low-loss dispersion equalizer operable over the entire erbium window," Electron. Lett. **32** (4), 371–373 (1996).

124. C.K. Madsen, G. Lenz, A.J. Bruce, M.A. Cappuzzo, L.T. Gomez, T.N. Nielsen, L.E. Adams and I. Brenner, "An all-pass filter dispersion compensator using planar waveguide ring resonators," Proc. of OFC 1999, Paper FE6, pp. 99–101 (1999).

125. C.K. Madsen, J.A. Walker, J.E. Ford, K.W. Goossen and G. Lenz, "A tunable dispersion compensating MARS all-pass filter," Proc. of ECOC, paper WeB1.3, pp. II-20 and II-21 (1999).

126. J.E. Ford, J.A. Walker, D.S. Greywall and K.W. Goossen, 'Micromechanical fiber-optic attenuator with 3um response," J. Lightwave Technol. **16** (9), 1663–1670 (1998).

127. C.K. Madsen and G. Lenz, "A multi-channel dispersion slope compensating optical allpass filter," Proc. of OFC, Paper WF5 (2000).

128. F. Horst, C. Berendsen, R. Beyeler, G.-L. Bona, R. Germann, H.W.M. Salemink and D. Wiesmann, "Tunable ring resonator dispersion compensators realized in high-refractive-index contrast SiON technology," Proc. of ECOC 2000, Paper PD2.2 (2000).

129. J.J. Fells, S.E. Kanellopoulos, P.J. Bennett, V. Baker, H.F.M. Priddle, W.S. Lee, A.J. Collar, C.B. Rogers, D.P. Goodchild, R. Feced, B.J. Pugh, S.J. Clements and A. Hadjifotiou, "Twin fiber grating tunable dispersion compensator," IEEE Photon. Technol. Lett. **13** (9), 984–986 (2001).

130. D.J. Moss, M. Lamont, S. McLaughlin, G. Randall, P. Colbourne, S. Kiran and C.A. Hulse, "Tunable dispersion and dispersion slope compensators for 10 Gbps using all-pass multicavity etalons," IEEE Photon. Technol. Lett. **15** (5), 730–732 (May 2003).

131. L.M. Lunardi, D.J. Moss, S. Chandrasekhar, L.L. Buhl, M. Lamont, S. McLaughlin, G. Randall, P. Colbourne, S. Kiran and C.A. Hulse, "Tunable dispersion compensation at 40-Gbps using a multicavity etalon all-pass filter with NRZ, RZ and CS-RZ modulation," J. Lightwave Technol. **20** (12), 2136–2143 (2002).

132. X. Shu, K. Sugden, P. Rhead, J. Mitchell, I. Felmeri, G. Lloyd, K. Byron, Z. Huang, I. Khrushchev and I. Bennion, "Tunable dispersion compensator based on distributed Gires-Tournois etalons," IEEE Photon. Technol. Lett. **15** (8), 1111–1113 (2003).

133. X. Shu, K. Chisholm and K. Sugden, "Design and realization of dispersion slope compensators using distributed Gires-Tournois etalons," IEEE Photon. Technol. Lett. **16** (4), 1092–1094 (2004).

134. D. Yang, C. Lin, W. Chen and G. Barbarossa, "Fiber dispersion and dispersion slope compensation in a 40-channel 10-Gbps 3200-km transmission experiment using cascaded single-cavity Gires-Tournois etalons," IEEE Photon. Technol. Lett. **16** (1), 299–301 (2004).

135. M. Shirasaki, "Chromatic-dispersion compensator using virtually imaged phased array," IEEE Photon. Technol. Lett. **9**, 12 (1997).

136. M. Shirasaki, Y. Kawahata, S. Cao, H. Ooi, N. Mitasura, H. Isono, g. Ishikawa, G. Barbarossa, C. Yang and C. Lin, "Variable dispersion compensator using the virtually imaged phased array (VIPA) for 40-Gbit/s WDM transmission systems," Proc. of ECOC, Paper PD-23 (2000).

137. L.D. Garrett, A.H. Gnauck, M.H. Eiselt, R.W. Tkach, C. Yang, C. Mao, and S. Cao, "Demonstration of virtually-imaged phased-array device for tunable dispersion compensation in 16 $\times$ 10 Gbps WDM transmission over 480 km standard fiber," Proc. of OFC, Paper PD7 (2000).

138. H. Ooi, K. Nakamura, Y. Akiyama, T. Takahara, J. Kumasako, J.C. Rasmussen, T. Terahara, Y. Kawahata, H. Isono, G. Ishikawa and N. Yamaguchi, "3.5-Tbit/s (43-Gbit/s $\times$ 88 ch) transmission over 600-km NZDSF with VIPA variable dispersion compensators," Proc. of OFC, Paper ThX3 (2002).

139. G. Kanter, A.K. Samal, and A. Gandhi, "Electronic dispersion compensation for extended reach," Proc. of OFC, Invited Paper TuG1 (2004).

140. D. Castagnozzi, "Digital signal processing and electronic equalization of ISI," Proc. of OFC, Invited Paper WM6 (2004).

141. M. Nakamura, H. Nosaka, M. Ida, K. Kurishima, M. Tokumitsu, "Electrical PMD equalizer ICs for a 40-Gbps transmission," Proc. of OFC, Paper TuG4 (2004).

142. C. Fludger, J. Whiteaway, P. Anslow, "Electronic equalization for low cost 10 Gbit/s directly modulated systems," Proc. of OFC, Paper WM7 (2004).

143. J.H. Winters and R.D. Gitlin, "Electrical signal processing techniques in long-haul, fiber-optic systems, "IEEE Trans. Commun. **38**, 1439–1453 (1990).

144. J.H. Winters and S. Kasturia, "Adaptive nonlinear cancellation for high-speed fiber-optic systems," J. Lightwave Technol. **10**, 971–977 (1992).

145. J. Poirrier, A.G. Gnauck and J.H. Winters, "Experimental nonlinear cancellation of polarization-mode dispersion," Proc. of OFC, Paper ThH4 (2000).

Legend:
OFC = Optical Fiber Communication Conference, sponsored by IEEE/LEOS and OSA
ECOC = European Conference on Optical Communications, sponsored by IEEE/LEOS and EUREL
NFOEC = National Fiber Optic Engineers Conference
OAA = Optical Amplifiers and their Applications, sponsored by IEEE/LEOS and OSA